CRACKING AND TENSION FIELD ACTION

IN COMPOSITE BEAMS

by

Robert William Allison

A thesis for the Degree of

Doctor of Philosophy, submitted

to the University of Warwick

Department of Engineering,
University of Warwick.

February, 1980.

CONTENTS

Contents	i
List of tables	vii
List of figures	viii
Acknowledgements and Declaration	xiv
Summary	xv
Notation	xvi
Dedication	xxiv
INTRODUCTION	1
CHAPTER 1 REVIEW OF PREVIOUS WORK	
1.1 Introduction	3
1.2 Research on reinforced concrete members	4
1.2.1 Bond-slip theory	4
1.2.1.1 General	4
1.2.1.2 Research on large-scale reinforced concrete beams	6
1.2.1.3 Research on partially-prestressed 'I' beams	9
1.2.2 Stress redistribution	12
1.2.2.1 Derivation of average crack spacing	12
1.2.2.2 Calculation of crack widths	14
1.2.2.3 Crack widths in wide members	15
1.2.3 Empirical formulae	16
1.2.4 No-slip theory	18
1.2.4.1 General	18
1.2.4.2 Cracking in reinforced concrete beams	18
1.2.4.3 Cracking in slabs	20
1.2.4.4 Cracking in prisms subjected to pure tension	22
1.2.4.5 Design formula	24
1.2.4.6 Cracking in scale models	24

1.3 Research on composite beams 25

1.3.1 Uniaxial bending 25

1.3.2 Biaxial bending 26

1.4 Prediction of average surface strain 32

CHAPTER 2 TESTS TO INVESTIGATE CRACKING

2.1 Introduction 43

2.2 Test specimens 43

2.2.1 Choice of specimens 43

2.2.2 Detailing of test specimens 44

2.2.2.1 The steel girder 44

2.2.2.2 The reinforced concrete slab 44

2.2.2.3 Shear connection 45

2.2.3 Construction of test specimens 46

2.3 The test rig 47

2.4 Instrumentation 48

2.4.1 Measurements taken 48

2.4.2 Instruments used 48

2.5 Test procedure 50

2.6 Auxiliary tests 51

2.6.1 Material properties 51

2.6.2 Test on instrumentation 51

CHAPTER 3 RESULTS OF TESTS TO INVESTIGATE CRACKING

3.1 Introduction 65

3.2 Formation of the crack pattern 65

3.3 Beam curvature 66

3.4 Concrete surface strain 67

3.5 Slip 68

3.6 Auxiliary tests 68

3.6.1 Shrinkage prisms 68

3.6.2 Material properties 69

3.6.3 Accuracy of the instrumentation 69

CHAPTER 4 ANALYSIS AND DISCUSSION OF TEST RESULTS

4.1 Introduction 89

4.2 Accuracy of test results 89

4.2.1 Accuracy of experimental results 89

4.2.2 Accuracy of theoretical calculations 92

4.3 Moment-curvature and moment-strain relationships 93

4.4 Drying shrinkage in the concrete slab 94

4.4.1 Theoretical consideration of shrinkage strain and curvature 94

4.4.2 Estimation of strains and curvatures due to shrinkage 96

4.5 Moment-curvature relationships 97

4.6 Surface strains 98

4.6.1 Strain along individual grid lines 98

4.6.2 Average surface strain 99

4.6.3 Prediction of mean surface strain 99

4.6.3.1 General 99

4.6.3.2 Before cracking 100

4.6.3.3 After cracking 100

4.7 Crack widths 102

4.8 Crack spacing 104

4.8.1 Effect on crack widths 104

4.8.2 Presentation and discussion of test results 105

4.8.3 Prediction of final crack spacing 107

4.8.3.1 General 107

4.8.3.2 Final crack spacing mid-way between bars 108

4.8.3.3 Final crack spacing over reinforcing bars 109

4.8.3.4 Final crack spacing anywhere on the concrete slab 110

4.8.3.5 Comparison with experimental results 111

4.9 Prediction of crack widths 111

4.9.1 Introduction 111

4.9.2 Mean crack widths 111

4.9.3 Crack widths with a 20% probability of being exceeded 113

4.10 Comparison of various crack width formulae 115

4.10.1 Introduction 115

4.10.2 Equation based on stress-redistribution 116

4.10.3 Equations based on the no-slip theory 116

4.10.4 Equation based on individual crack width theory 118

4.11 Crack widths at low strain 118

4.11.1 Discussion of results 118

4.11.2 Crack widths due to release of shrinkage strain 119

4.11.3 Prediction of crack widths at low strains 121

CHAPTER 5 CONCLUSIONS OF THE WORK ON CRACKING

5.1 Summary of conclusions 150

5.2 Recommendations for design 150

5.3 Scope of proposed design formulae 151

CHAPTER 6 REVIEW OF PREVIOUS WORK

6.1 Introduction 152

6.2 Plain steel girders 152

6.2.1 Behaviour in pure shear 152

6.2.2 Design methods for girders subjected to pure shear 153

6.2.3 Girders subjected to pure bending moment 156

6.2.4 Girders subjected to combined shear and bending 158

6.2.4.1 Empirical methods 158

6.2.4.2 Analytical methods 160

6.2.4.3 Parametric study 165

6.3 Composite beams 167

6.4 Shear in cracked reinforced concrete 169

6.5 Design rules for composite girders 170

CHAPTER 7 TESTS TO INVESTIGATE ULTIMATE STRENGTH

7.1 Introduction 183

7.2 Test specimens 183

7.2.1 Choice of specimens 183

7.2.2 Detailing of test specimens 184

7.2.2.1 Steel girder 184

7.2.2.2 Reinforced concrete slab 184

7.2.2.3 Longitudinal shear 185

7.2.3 Construction of test specimens 186

7.3 The test rig 187

7.4 Instrumentation 188

7.5 Test procedure 190

7.5.1 General 190

7.5.2 PG1A 191

7.5.3 PG1B 192

7.5.4 PG2A and PG3A 192

7.5.5 PG2B 192

7.5.6 PG3B 192

7.6 Auxiliary tests 193

CHAPTER 8 RESULTS OF TESTS ON PLATE GIRDERS

8.1 Introduction 210

8.2 PG1A 210

8.3 PG1B 211

8.4 PG2A 212

8.5 PG2B 213

8.6 PG3A 213

8.7 PG3B 214

8.8 Onset of plasticity 215

8.8.1 The steel girder 215

8.8.2 Slab reinforcement 216

8.9 Out-of-plane web deformations 216

8.10 Slip 217

8.11 Uplift and vertical deformations in the tension flange 217

8.12 Auxiliary tests 217

CHAPTER 9 ANALYSIS AND DISCUSSION OF TEST RESULTS

9.1 Introduction 239

9.2 Accuracy of results 239

9.2.1 Experimental results 239

9.2.2 Theoretical analyses 241

9.3 Discussion of test results 241

9.3.1 Elastic response 241

9.3.2 Onset of plasticity 243

9.3.3 Behaviour at and beyond ultimate limit state 244

9.3.3.1 Uplift and deformation in the tension flange 244

9.3.3.2 Web buckles 245

9.3.3.3 Slab behaviour 246

9.3.3.4 Ultimate loads 246

9.4 Ultimate strength of composite girders subjected primarily to shear 247

9.4.1 General 247

9.4.2 Shear force in the slab 248

9.4.3 Shear strength of the steel girder 251

9.4.3.1 General 251

9.4.3.2 Critical buckling load 251

9.4.3.3 Plastic moment of resistance of the flanges 252

9.4.3.4 Inclination of the yield band 255

9.5 Design method for composite plate girders 258

9.6 Implications for design recommendations 261

CHAPTER 10 CONCLUSIONS OF THE WORK ON TENSION FIELD ACTION

10.1 Experimental observations 274

10.2 Design methods 275

List of references xxv

LIST OF TABLES

CHAPTER 2 (pp 53,54)

2.1 The parameters varied in the UC series of tests

2.2 Instruments used for the UC series of tests

CHAPTER 3 (pp 70-72)

3.1 Measurement of shrinkage in trial prisms up to day (or days) of test

3.2 0.2% proof stress of samples of reinforcement

3.3 Yield strength of steel coupons

3.4 Properties of concrete on last day of beam test

CHAPTER 4 (pp 122-126)

4.1 Estimated strain profiles in UC1-UC7 due to shrinkage

4.2 Experimental values of W_{ave} and W_{20} for Beams UC1-UC7

4.3 Experimental equations of best fit: crack spacing and surface strain

4.4 Exponential lines of best fit to test data: crack spacing and surface strain

4.5 Statistics of slope ratios for various crack width formulae

4.6 Crack widths due to release of shrinkage strains

CHAPTER 7 (pp 194,195)

7.1 List of tests in PG series

7.2 Concrete mixes for Beams PG1-PG3

7.3 Concrete test specimens for Beams PG1-PG3

CHAPTER 8 (p 218)

8.1 Results of tests on steel coupons

8.2 Properties of concrete on last day of girder test

CHAPTER 9 (pp 264,265)

9.1 Loads to cause yield at various levels in the tension flange

9.2 Ultimate load of test panels

9.3 Proportion of total shear carried by slab (α)

9.4 Ratios of theoretical:experimental values for various parameters, using calculated β_o

9.5 Ratios of theoretical:experimental values for various parameters, using measured inclination of web buckles

LIST OF FIGURES

CHAPTER 1 (pp 34-42)

1.1 Cracking in prism subjected to pure tension

1.2 Cracking in beam subjected to pure bending

1.3 Bond and tensile stresses in cracked prism at a section, distance y from a crack

1.4 Models of tensile and flexural members

1.5 Limit of tensile stresses in cracked member

1.6 Development of crack pattern

1.7 Internal cracking in reinforced concrete prism

1.8 Definition of e_1 and e_2 for calculating effective cover

1.9 Prism analysed by finite element method

1.10 Elongation of prism subjected to pure tension

1.11 Strain in prism subjected to pure tension

1.12 Test rig used to study cracking in biaxial tension

1.13 Plot of w/ε against ε: individual crack width readings

CHAPTER 2 (pp 55-64)

2.1 Elevation of Beams UC1 to UC7

2.2 Section through test region: Beams UC1 to UC7

2.3 Spacing of shear connectors

2.4 View of test rig

2.5 Method of loading and stabilising Beams UC2-UC7

2.6 End bearings for Tests UC2-UC7

2.7 Measurement of displacements for Tests UC1-UC7

2.8 Measurement of strains for Tests UC1-UC7

2.9 Location and dimensions of steel coupons

2.10 Instrumentation for Test UC6A

CHAPTER 3 (pp 73-88)

3.1 Final crack patterns for Beams UC1-UC7

3.2 Moment-curvature relationships for UC1

3.3 Moment-curvature relationships for UC2

3.4 Moment-curvature relationships for UC3

3.5 Moment-curvature relationships for UC4

3.6 Moment-curvature relationships for UC5

3.7 Moment-curvature relationships for UC6

3.8 Moment-curvature relationships for UC7

3.9 Variation of ε_{mg} along grid line 8 of Beam UC5

3.10 $\bar{\varepsilon}$ for all grid lines: Beam UC7

3.11 Moment-strain relationships for UC1

3.12 Moment-strain relationships for UC2

3.13 Moment-strain relationships for UC3

3.14 Moment-strain relationships for UC4 and UC7

3.15 Moment-strain relationships for UC5

3.16 Moment-strain relationships for UC6

3.17 Slip along Beams UC1-UC4 and UC7

3.18 Average shrinkage strains in trial prisms

3.19 Comparison of strains from mechanical and electrical gauges

3.20 Moment-curvature relationships for Beam UC6A

CHAPTER 4 (pp 127-149)

4.1 Moment-curvature relationships for a rolled steel girder

4.2 Relationship between true and measured strain

4.3 Relationship between true and measured curvature

4.4 Moment-strain relationships for UC1

4.5 Moment-strain relationships for UC2

4.6 Moment-strain relationships for UC3

4.7 Moment-strain relationships for UC4

4.8 Moment-strain relationships for UC5

4.9 Moment-strain relationships for UC6

4.10 Moment-strain relationships for UC7

4.11 Distribution of crack widths: Grid Line 8, Beam UC5

4.12 Crack width-strain relationships: Grid Lines 2 and 8, Beam UC5

4.13 Crack width-strain relationships

4.14 Relationship between crack slope and crack spacing, Beam UC5

4.15 Relationship between crack slope and crack spacing, Beam UC5

4.16 Relationship between crack slope and crack spacing, Beam UC5

4.17 Crack spacing-strain relationship: Grid Lines 2 and 8, Beam UC5

4.18 Crack spacing-strain relationship: Grid Lines 3 and 7, Beam UC5

4.19 Crack spacing-inverse strain relationship: Grid Lines 2 and 8, Beam UC5

4.20 Crack spacing-inverse strain relationship: Grid Lines 3 and 7, Beam UC5

4.21 Cracking in unreinforced slab of composite beam

4.22 Relationship between λ and $c/(H + S_t)$

4.23 Relationship between $1/L_f$ and $1/a_{cr}$

4.24 Comparison of experimental and predicted final crack spacing

4.25 Comparison of W_{ave} and L_f

4.26 Relationship between η and $c/(H + S_t)$

4.27 Comparison of experimental and predicted values of W_{20}

4.28 Predicted crack widths mid-way between bars, Broms and Allison

4.29 Predicted crack widths over bars, C and CA and Allison

4.30 Predicted crack widths mid-way between bars, CP110 and Allison

4.31 Crack widths due to the release of shrinkage strains

CHAPTER 6 (pp 173-182)

6.1 Stresses in plate girder subjected to shear

6.2 Extent of diagonal yield band

6.3 Collapse modes of a girder subjected to shear

6.4 Vertical flange buckling

6.5 Effect of web slenderness on ultimate moment

6.6 Interaction charts for combined loading

6.7 Collapse mechanism for girder subjected to combined loading

6.8 Interaction diagram from upper bound analysis

6.9 Failure mechanism due to Evans et al

6.10 Interaction chart due to Evans et al

6.11 Web stresses at yield in compression flange

6.12 Anticipated failure mode of composite plate girder

6.13 Failure mode of compact composite beam

6.14 Interaction diagram of BS5400

6.15 Effective flange section

6.16 Collapse mechanism for large axial flange stresses

CHAPTER 7 (pp 196-209)

7.1 Method of conducting two tests on one beam

7.2 Steel girders for Beams PG1-PG3

7.3 Reinforced concrete slabs for Beams PG1-PG3

7.4 Layout of shear connectors for Beams PG1-PG3

7.5 Welding of steel plate girders

7.6 View of test rig from South West

7.7 View of test rig from North East

7.8 Deflection and rotation readings: Tests PG1-PG3

7.9 Instrumentation rig for Tests PG1-PG3

7.10 Location of electrical resistance strain gauges

7.11 Rig for measuring out-of-plane web deformations

7.12 Grid lines on top surface of slab

7.13 Extra stiffening for Beams PG2 and PG3

7.14 Coupons for PG1-PG3

CHAPTER 8 (pp 219-238)

8.1 Load-deflection curves for Beam PG1

8.2 Load-deflection curves for Beam PG2

8.3 Load-deflection curves for Beam PG3

8.4 Final deformations in Beams PG1-PG3

8.5 Developed surface of slab showing final crack pattern

8.6 Residual slab deformation in Beam PG1

8.7 Cracking in top surface of slab, Beam PG1B

8.8 Separation of slab and girder in Beam PG2A

8.9 Local failure in soffit of slab, Beam PG2A

8.10 Local failure in soffit of slab, Beam PG2B

8.11 Contours of web deformation in test panels at ultimate load

8.12 $V-\delta_o$ curves for Beams PG1-PG3

8.13 Load-slip curves for Beam PG1

8.14 Load-slip curves for Beam PG2

8.15 Load-slip curves for Beam PG3

8.16 Deflection and uplift in test panels of Beam PG1

8.17 Deflection and uplift in test panels of Beam PG2

8.18 Deflection and uplift in test panels of Beam PG3

8.19 Calibration of load cells for PG tests

CHAPTER 9 (pp 266-273)

9.1 Properties of tension flange at hogging hinge

9.2 Interaction diagram for Beams PG1-PG3

9.3 Forces in a composite beam

9.4 Forces in a composite plate girder at collapse

9.5 Stresses in 'T' section at location of plastic hinge

9.6 Equilibrium forces in composite plate girder at collapse

9.7 Stresses in a buckled web

9.8 Collapse mode for large axial flange forces

9.9 Interaction diagrams from draft Part 3, BS5400

ACKNOWLEDGEMENTS

I would like first to thank my supervisor, Professor R.P.Johnson, for his valuable guidance and advice throughout my period of study. I am also very grateful to Constrado for providing the opportunity to conduct this research, and for their financial support of both myself and the research contract.

Several members of staff at Warwick University have given freely of their time to advise and assist me, but the help of Dr.I.M.May, Mr.R.J.Buckby, Dr.C.Arnaouti and Mr.A.Redhead has been particularly appreciated. Special thanks are due to Mr.P.O.Ogunronbi for permission to use results from his first test on a cracked composite beam, and for allowing me to take part in the second test.

Finally, the patience and endurance of my mother, who typed the manuscript, and Mrs.B.Howsen, who lettered the drawings, is gratefully acknowledged.

DECLARATION

Experimental data from one of the tests reported in this thesis (UC1) were provided by Mr.P.O.Ogunronbi, and he and the present author were jointly responsible for conducting another test (UC2). Apart from this, and except where reference is made to the work of others, this thesis contains the original work of the author. It has not been submitted for a degree to any other University.

R. W. Allen

SUMMARY

Two aspects of the behaviour of uncased composite 'T' beams of steel and concrete are considered.

Flexural cracking in the reinforced concrete slab was studied by subjecting seven 350-mm deep composite beams to hogging bending moment. Measured strains were found to exceed those calculated from an elastic analysis ignoring concrete in tension. Also, the first cracks to form in the slab were much wider than expected. Both of these effects are shown to be due to drying shrinkage in the slab of the composite beam. A formula for calculating the mean surface strain in the slab, which allows for both drying shrinkage and tension stiffening, is proposed.

Consideration of the parameters which affect cracking leads to a formula for predicting crack widths in composite beams. Comparison with experimental results shows that it is sufficiently accurate for design purposes.

In a second series of tests, three 900-mm deep composite plate girders with slender webs were subjected to combined shear and bending to study their ultimate load behaviour. Failure was due to the formation of a plastic collapse mechanism which closely resembles that observed in plain steel girders under similar loading. The addition of a concrete slab acting compositely with the girder increased the ultimate strength of the beam, but variations in the size of the slab and the strength of the shear connection had negligible effect on the beam's strength.

An idealised collapse model, based on the experimental observations, is described and is used in the development of a method to calculate the ultimate strength of composite plate girders. It is shown that a design method for plain steel girders in the draft Part 3, BS5400 may, with small modifications, be applied to composite plate girders.

NOTATION

A	length of longer side of prism surrounding a reinforcing bar, less the bar diameter
A_c	cross-sectional area of concrete surrounding a reinforcing bar
A_{cf}	cross-sectional area of compression flange of a steel girder
A_f	cross-sectional area of a steel flange
A_r	area of tension reinforcement, taken as that area within the effective breadth of the slab for a composite beam
A_{tf}	cross-sectional area of tension flange of a steel girder
A_w	cross-sectional area of the web
a	constant
a_{cr}	distance from nearest reinforcing bar to point where crack width is measured
a_m	distance from the surface of the reinforcement to the point on the concrete surface mid-way between bars
a'	distance from the compression face to the point where cracking is being considered
B	length of shorter side of prism surrounding a reinforcing bar, less the bar diameter
b	constant (Chapters 1-5); clear breadth of panel between vertical stiffeners (Chapters 6-10)
b_e	effective breadth of composite section at the level of the tensile reinforcement
b_f	half the effective width of a steel flange
b_t	breadth of a plain reinforced concrete section at the level of the tensile reinforcement
C.V.	coefficient of variation
c	minimum cover to reinforcement
c_c	distance between plastic hinges in the compression flange of a steel girder
c_e	effective cover to reinforcement
c_s	minimum side cover to the reinforcing bar assumed to be controlling cracking on the side face of a beam

c_t distance between plastic hinges in the tension flange of a steel girder

c_l greater cover to a centrally reinforced rectangular prism

D diameter of the effective area of concrete surrounding a bar

D_i diameter of the effective area of concrete surrounding bar i

D' distance between the centroids of the two flanges of a steel girder

d clear depth of the web between flanges

d_t depth of the yield band adjacent to a vertical stiffener

$(d/t)_c$ slenderness ratio when the flange yield stress equals the flange buckling stress

d_l depth from neutral axis to the centroid of the tension steel

E modulus of elasticity

E_c modulus of elasticity for concrete

E_s modulus of elasticity for steel (plate or reinforcement)

e_o term used when calculating effective cover

e_1 distance for calculating effective cover (Fig.1.8)

e_2 distance for calculating effective cover (Fig.1.8)

F restraining force in steel beam (Chapters 1-5);
limiting flange force in girder (Chapters 6-10)

F_c axial force in the compression flange at the mid-panel hinge

F_{cs} compressive force in the slab of a composite beam

F_r resultant force in the reinforcing bars when yielding in tension

F_t axial force in the tension flange at the mid-panel hinge

F_w resultant membrane force in the yield band of the web

F_y yield force for a layer of reinforcement in a slab

F'_c axial force in the compression flange mid-way between the two hinges

F'_t axial force in the tension flange mid-way between the two hinges

f function of ....

f_b maximum bond stress

f_{biu} ultimate bond stress of bar i

f_{bu} ultimate bond stress

f_{nt} steel stress at the load considered, assuming no tension-stiffening

f_s stress in steel reinforcement

f_{scr} steel stress at cracking, calculated on the assumption of no tension-stiffening

f_t tensile strength of concrete

f_y yield stress of steel reinforcement

g function of ....

H distance between the shear connectors and the grid line considered, measured transversely

H_{cr} horizontal force in web at elastic buckling load

h overall depth of member

h_f depth of concrete flange in tension in composite beam

h_o initial crack height

h_r lever arm of the resultant force in the reinforcement about the mid-depth of the web of a composite beam

h_w depth of web in the effective flange section

h_1 height of top layer of reinforcement above the slab soffit

h_2 height of bottom layer of reinforcement above the slab soffit

K constant which relates only to the specific equation in which it occurs

K_1, K_2, K_3 constants which depend on the required probability of the calculated crack width being exceeded, tabulated in Ref.22

K'_1, K'_2, K'_3 constants which depend on the required probability of the calculated crack width being exceeded, tabulated in Ref.25

k constant which relates only to the specific equation in which it occurs

k_b a factor which when multiplied by the peak bond stress gives the average bond stress

k_{bi} the factor k_b for bar i

$k_{1...n}$ constants which relate only to the specific equation in which they occur

L crack spacing

L_{ave} average crack spacing

L_b final crack spacing directly over a reinforcing bar

L_c distance defined in Fig.1.10

L_{cr} length along a bar, on one side of an isolated crack, over which the surface strain of the concrete is reduced by the presence of the crack

L_f final crack spacing

L_m final crack spacing mid-way between adjacent reinforcing bars

L_{max} maximum crack spacing

L_{mg} length equal to half the crack spacing on either side of a crack

L_{min} minimum crack spacing

L_o original length of an element of slab

M externally applied moment (Chapters 1-5);
maximum panel bending moment, coexistent with vertical shear force (Chapters 6-10)

M_F plastic moment of resistance of a steel I beam, ignoring the web

M_Q maximum moment in the end panel of a simply supported girder

M_R moment at transition from shear mechanism failure to bending type of failure, ie: when axial forces in the flanges are such that they cannot support any tension field action

M_{cr} moment to cause cracking in concrete (Chapters 1-5);
lower critical moment obtained from separate local and lateral-torsional buckling analyses (Chapters 6-10)

M_f moment that results in the release of all shrinkage strains

M_p plastic moment of resistance of a steel flange

M_{pc} plastic moment of resistance of the compression flange

M_{pg} full plastic moment of resistance of a girder

M_{pt} plastic moment of resistance of the tension flange

M_{pw} plastic moment of resistance of the web

M_u moment corresponding to the ultimate bond stress (Chapters 1-5);
ultimate bending strength of a girder subjected to combined bending and shear (Chapters 6-10)

M_{ult} ultimate bending strength of a girder subjected to pure bending

M_w bending moment in web at elastic buckling load

M_y bending moment that causes yield in tension reinforcement (Chapters 1-5)
bending moment that causes yield in the extreme compression flange fibres of a plate girder (Chapters 6-10)

M_{ynt} bending moment that causes yield in the extreme tension reinforcement, assuming no tension-stiffening

M'_{pc} reduced plastic moment of resistance of the compression flange

M'_{pt} reduced plastic moment of resistance of the tension flange

P pure tensile force

P_c vertical force at the interface of the girder and slab in a composite beam

P_t vertical force at the interface of the girder and slab in a composite beam

P_y pure tensile force that causes yield in the reinforcement

p ratio of reinforcement area to effective concrete area

q perpendicular distance of resultant membrane force from mid-height of the web

R_1 force in top layer of slab reinforcement

R_2 force in bottom layer of slab reinforcement

r ratio of distances from the neutral axis to the point considered and to the centroid of the tension reinforcement

r_t ratio of distances from the neutral axis to the tension face of the member and to the centroid of the tension reinforcement

r_1 factor defining bond stress distribution

S half the clear spacing of the reinforcing bars

S.D. standard deviation

S_t longitudinal spacing of the shear connectors

s length of an element of a composite beam (Fig.9.3a)

t web thickness

t_f thickness of steel flange

V vertical shear force

V_R vertical shear force at transition from shear mechanism failure to bending type of failure, ie: when axial forces in the flanges are such that they cannot support any tension field action

V_{cr} shear force in web at elastic buckling

V_m shear force developed by a plastic collapse mechanism

V_u ultimate shear strength of a girder subjected to combined bending and shear

V_{ult} ultimate strength of a girder subjected to pure shear

V_y shear yield strength of the web of a steel girder

W crack slope

W_{ave} average crack slope

W_b crack slope directly over a reinforcing bar

W_{lim} crack slope for a grid line an infinite distance from a reinforcing bar

W_m crack slope on the surface of concrete, mid-way between adjacent reinforcing bars

W_n crack slope exceeded by n% of the results along a particular grid line

w width of an individual crack

w_{max} maximum crack width

w_{min} minimum crack width

w_n width exceeded by n% of the results along a particular grid line

$\bar{w}$ mean width of cracks along a grid line

x distance from the compression face of a beam to the neutral axis

y distance from a crack to the section considered

Z lever arm of the external load about the mid-panel section

z eccentricity of centre of rotation of a plastic hinge

α proportion of the total shear force carried by the slab of a composite beam

α_A, α_B, α_G proportion of the total shear force carried by the slab at Sections A, B and G in Fig.9.4a

α_c proportion of the total shear force carried by a cracked slab in a composite beam

α_u proportion of the total shear force carried by an uncracked slab in a composite beam

β inclination of the tension field to the flanges

β_d inclination of the web panel diagonal to the flanges

β_o optimum value of β

δ deflection of the tension flange relative to the instrumentation rig at the location of the support stiffeners

δ_o maximum out-of-plane deflection of the web in the test panel

δ_s shear displacement across a crack

$\delta\varepsilon$ reduction in strain due to tension-stiffening

ε_{cm} the mean strain at the surface of uncracked concrete

ε_{mg} mean tensile strain over a length equal to half the crack spacing on either side of an isolated crack

ε_{nt} strain derived on the assumption of no tension-stiffening

ε_s strain in the reinforcing bars

ε_{sh} free shrinkage strain in a concrete slab

ε_{st} tensile strain at top surface of the slab of a composite beam due to shrinkage of the concrete

$\bar{\varepsilon}$ mean surface strain along a grid line

$\bar{\varepsilon}_c$ mean tensile strain at the surface of uncracked concrete over a length equal to half the crack spacing on either side of an isolated crack

$\bar{\varepsilon}_s$ surface strain in a slab, averaged over the length and breadth of the constant moment region

η derived term (see p 114)

λ derived term (see p 110)

ν Poisson's ratio

ρ area of tension steel in a slab, expressed as a proportion of the area of concrete

σ_a net compressive stress at mid-panel section which results in buckling in presence of bending and shearing stresses

σ_{acr} elastic buckling stress of a panel subjected to pure compression

σ_{cf} axial stress in the compression flange mid-way between the two hinges

σ_{cr} elastic buckling stress of a panel subjected to pure bending

σ'_{f} direct stress in flange due to tension field action

σ_{m} extreme compressive stress due to bending at mid-panel section, which results in buckling in presence of either shear stresses, or shear and net compressive stresses

σ_{tf} axial stress in the tension flange mid-way between the two hinges

σ_{ty} membrane yield stress

σ_{tyc} membrane yield stress adjacent to the compression flange at a point mid-way between the two hinges

σ_{tyt} membrane yield stress adjacent to the tension flange at a point mid-way between the two hinges

σ_{yf} yield stress of a flange of a steel girder

σ_{yw} yield stress of the web of a steel girder

τ_{cr} critical shear stress of web plate

τ_{m} shear stress in panel which results in buckling in presence of either bending stress, or bending and net compressive stress

τ_{yw} shear yield stress of the web of a steel girder

ϕ diameter of reinforcing bar

ϕ_{sh} initial sagging curvature due to shrinkage

DEDICATION

To Helen

INTRODUCTION

Several types of composite construction are commonly used in buildings and bridges, but the one considered in this thesis consists of a reinforced concrete slab connected by shear studs to a steel 'I' beam.

The work reported here forms part of a long-term study into the behaviour of continuous composite beams in the region of an intermediate support. Aspects of the problem which have been considered previously include the behaviour of continuous composite floor systems and of shear studs in hogging moment regions, and the design of semi-rigid joints in composite frames. Of particular interest is work conducted by Climenhaga, Johnson and Willmington[41,42] who studied the ultimate load behaviour of compact composite beams subjected to various proportions of hogging bending and vertical shear. It was found that such girders could develop their plastic moment of resistance and maintain it over a large rotation without risk of local flange or web buckling. It was also found that the shear strength of a composite beam with heavy longitudinal reinforcement in the slab exceeded the plastic capacity of the web.

Two further aspects of the behaviour of continuous composite beams are considered in this thesis: the width of cracks which form in the hardened concrete slab due to flexural action, and the ultimate load behaviour of beams with slender webs.

Over the past 15 years, extensive research has been conducted into cracking in plain reinforced concrete beams and slabs, and design formulae are available - for example, in CP110[33] and BS5400, Part 4[34]. Very little attention has been paid to crack widths in composite beams, however, and such design formulae as exist (BS5400, Part 5[34]) are based on the research on plain reinforced concrete, modified slightly in accordance with engineering judgement.

One of the aims of the present study was therefore to determine whether existing crack width formulae adequately predict crack widths in composite beams, and if not, to develop alternative formulae. This work

is reported in Chapters 1 to 5. Chapter 1 contains a review of previous work and Chapters 2 and 3 describe tests on composite beams to obtain experimental crack width data. The results are analysed and discussed in Chapter 4, while Chapter 5 summarises the conclusions and presents recommendations for design.

The normal design procedure for assessing the ultimate strength of continuous composite beams is to assume that the slab and its reinforcement add to the bending strength of the steel girder but not to its shear strength. Research has shown that when a plain steel girder with a slender web is loaded predominantly in shear, a diagonal yield band forms in the web. Collapse finally occurs when the stresses in this yield band cause inward collapse of the flanges.

In continuous composite beams near an internal support, the steel tension flange is attached to the concrete slab, which may increase its resistance to inward collapse substantially. Conversely, the stresses in the yield band impose axial loads on the shear connectors, and this might cause pull-out failure of the slab, leading to a loss of composite action in bending. The second aim of the present study was therefore to determine whether the assumptions normally made in design can reasonably be applied to composite girders with slender webs.

The investigation of ultimate load behaviour has been conducted independently of the work on cracking, and is reported separately in Chapters 6 to 10. This reflects current design practice, which is to consider the attainment of the maximum permitted crack width and of the ultimate strength of the beam as two quite different limit states. Chapter 6 reviews previous work on steel and composite girders, and presents some current design recommendations. Chapters 7 and 8 describe tests on three composite plate girders, the results of which are analysed and discussed in Chapter 9. The conclusions are summarised in Chapter 10.

The notation and references listed elsewhere in this thesis are common to all of Chapters 1 to 10.

CHAPTER 1

REVIEW OF PREVIOUS WORK

1.1 Introduction

Very little work on crack widths in composite steel and concrete beams subjected to hogging moment has been reported and attention has, of necessity, been focussed on work conducted on reinforced concrete members. Such work, of course, is not directly applicable to uncased composite 'T' beams, in which the neutral axis is often well below the concrete slab, so that the stress pattern corresponds more closely to an axial tensile load than to a flexural load. Other factors which affect the distribution of stresses in composite 'T' beams are the presence of large forces due to shrinkage of the concrete slab and of concentrated local forces in the region of the shear connectors.

Previous reports on cracking in concrete subjected to externally applied loads have fallen into one of four categories:

(i) those that accept the "bond-slip" theory, which assumes that failure of the bond between the reinforcement and the concrete occurs as cracking takes place;

(ii) those that consider stress redistribution after cracking;

(iii) those that believe that the bond remains intact - at least until the crack pattern is substantially complete; and

(iv) those that are derived on a mainly empirical basis.

A report by Cattley[1] gives a bald summary of papers from each of the above four categories, but makes no attempt to compare either the results or the conclusions of the numerous workers in the field. A more detailed review of these papers, along with others not considered by Cattley, is therefore given below.

1.2 Research on reinforced concrete members

1.2.1 Bond-slip theory

1.2.1.1 General

This theory hypothesises that stress is uniform at any section of a cracked reinforced concrete member subjected to pure axial tension. The sides of a crack are therefore parallel, as shown in Fig.1.1, and there must be local failure of the bond between the reinforcing bars and the surrounding concrete. For a reinforced concrete member subjected to pure flexure, it is assumed that plane sections remain plane. Hence, the sides of a crack are flat, and the crack is wedge-shaped with zero width at the neutral axis.

The theory also hypothesises that the minimum crack spacing will be the length over which the force transmitted to the concrete by the bond between it and the reinforcement is just sufficient to cause cracking of the concrete. Hence:

$$L_{min} = f_t \, \phi / 4 r_1 \, f_b \, p \qquad (1.1)$$

where: L_{min} = the minimum crack spacing;

f_t = tensile strength of concrete;

ϕ = bar diameter;

r_1 = factor defining bond stress distribution;

f_b = maximum bond stress; and

p = ratio of steel area to effective concrete area.

Since an intermediate crack would form if the initial crack spacing exceeded twice the minimum spacing

$$L_{max} = 2L_{min} \qquad (1.2)$$

where: L_{max} = the maximum crack spacing.

If, as is usual, the strain in the concrete between cracks is assumed to be negligible, the maximum crack width at the level of the reinforcement is given by:

$$w_{max} = L_{max} f_s/E_s$$

where: w_{max} = maximum crack width;

f_s = the steel stress in the member at the section considered, calculated from $f_s = f_y M/M_y$ for a flexural member, and from $f_s = f_y P/P_y$ for a tensile member;

E_s = modulus of elasticity for steel reinforcement;

f_y = yield stress for steel reinforcement;

M = the applied moment at the section considered;

M_y = the moment corresponding to yield in the reinforcement of a flexural member;

P = the applied tensile force at the section considered;

P_y = the tensile force corresponding to yield in the reinforcement of a tensile member.

Hence:

$$w_{max} = \phi f_s/p k_1 \qquad (1.3)$$

where: $k_1 = 2r_1 f_b E_s/f_t$

The derivation of Equations 1.1 to 1.3 is considered in greater detail in a very useful paper by Bianchini, Kesler and Lott[2].

Research at the Cement and Concrete Association[3] has shown that the concrete strain between cracks may in fact reach several times the value normally associated with cracking, so Equation 1.3 may be expected to overestimate the maximum crack width. Nevertheless, this equation has become widely accepted as the basis for research not only in Europe but also in America, although significant modifications are usually made.

The C.E.B.[4] realised that Equation 1.3 overemphasised the importance of p, and altered it, on a purely empirical basis, to:

$$w_{max} = (4.5 + 0.4/p)\ \emptyset\ f_s/k_2 \qquad (1.4)$$

where k_2 is a constant similar to, but not the same as, k_1 in Equation 1.3.

1.2.1.2 Research on large-scale reinforced concrete beams

In the first of a series of reports from the Portland Cement Association, Hognestad[5] showed that for plain reinforcing bars the relationship between crack width and bar diameter was nearly linear, which is the prediction of the bond-slip theory. However, for the old type of deformed reinforcing bar, the relationship was less marked, and for the modern type of deformed bars, the bond-slip theory, even as modified by the C.E.B. (Equation 1.4), overestimated the effect of both the bar diameter and the steel percentage. Instead of confining his attention to crack widths at the level of the reinforcement, Hognestad considered crack widths elsewhere on the beam's surface, and found that at constant strain crack width was proportional to cover from the point considered to the nearest bar orthogonal to the crack. This result, which has been confirmed by many other workers in the field, implies that crack width at the surface of a reinforcing bar is zero. Taken together with Hognestad's conclusions on the effect of bar diameter and steel percentage, it is evidence that the bond-slip theory is not applicable to modern deformed bars.

The next in the series of reports from the PCA was by Kaar and Mattock[6] who had conducted tests on half-scale highway bridge beams of rectangular, 'I' and 'T' sections, reinforced with high strength deformed bars. Crack widths were measured on the side faces of the beams at the level of the reinforcement and found to be proportional to steel stress but independent of the bar diameter. The term (4.5 + 0.4/p) in Equation

1.4 was therefore replaced by $1/0.357p^{\frac{1}{2}}$, which has the same value for the usual range of p, but gives, on rearrangement:

$$w_{max} = 3.16A_c^{\frac{1}{2}} f_s/k_2$$

where: A_c = the concrete area surrounding a reinforcing bar.

Substituting the value of k_2 used by the CEB gave the following equation for predicting maximum crack width at the level of the reinforcement:

$$w_{max} = 0.067A_c^{\frac{1}{2}} f_s \times 10^{-6} \qquad (1.5)$$

where the units are in pounds and inches.

Kaar and Mattock compared the predictions of Equation 1.5 with their own measurements of crack widths as well as those of Hognestad[5] and Clark[17] and found them to be in good agreement for values of p between 0.04 and 0.2. For values of p less than 0.04, however, crack widths were still overestimated, and the equation was modified, on an empirical basis, to:

$$w_{max} = 0.115A_c^{0.25} f_s \times 10^{-6} \qquad (1.6)$$

A similar equation was put forward for predicting the mean crack width, $\bar{w}$, at the level of reinforcement:

$$\bar{w} = 0.077A_c^{0.25} f_s \times 10^{-6} \qquad (1.7)$$

It will be noted that $\bar{w} = w_{max}/1.5$, which was the relationship obtained theoretically by Beeby[7], who used probability theory to obtain the mean crack spacing in terms of the maximum and minimum spacings.

In a later report by Kaar and Hognestad[8], equations were put forward for predicting crack widths on the tension face of flexural concrete members reinforced with high strength deformed bars:

$$w_{max} = 0.115r_t A_c^{0.25} f_s \times 10^{-6} \qquad (1.8)$$

$$\bar{w} = 0.077 r_t A_c^{0.25} f_s \times 10^{-6} \qquad (1.9)$$

where: r_t = the ratio of distances from the neutral axis to the tension face of the member and to the centroid of the tension reinforcement.

The units are again expressed in pounds and inches.

These equations were compared with crack widths measured during the authors' tests on half-scale bridge beams of 'T' cross-section and on a half-scale model of a bridge deck; they were also compared with the results from References 5, 6 and 17. There were therefore a large number of readings for w_{max} - one for each level of stress on each grid line of all the specimens tested, and when these were plotted on a graph of w_{max} against f_s a cloud of points resulted. Equation 1.8 was plotted on the same graph, and although it fell more or less in the middle of this cloud, individual values of w_{max} varied by up to $\pm$50% of the predicted value. The same was true for values of the mean crack width, $\bar{w}$, and it was claimed that this scatter was acceptable in view of the variability of cracking. This argument is not convincing, however: certainly along any grid line at constant f_s (for example, on a member subject to constant moment) there will be a large scatter of crack width readings about the mean value, but any formulae which purport to give this mean value, or the value of the maximum crack width, ought to do so with greater accuracy than 50%.

In the final report in the series[9], Kaar took a more reasonable approach to cracking, and attempted to derive formulae that would predict not the maximum crack width, but crack widths with various probabilities of being exceeded. Experimental data came from yet another series of tests on 'T' section beams representing those found in highway bridges - two at full size, and one each at $\frac{1}{2}$ and $\frac{1}{4}$ scale.

It was found that Equation 1.8, although of little use for

predicting maximum crack widths, agreed very well with measured values of crack widths with a 30% probability of being exceeded. Similarly, the equation:

$$w = 0.172 r_t A_c^{0.25} f_s \times 10^{-6} \qquad (1.10)$$

gave good predictions for the width with a 10% probability of being exceeded.

Equations 1.8 and 1.10 may be represented as:

$$w_n = k\, r_t A_c^{0.25} f_s \times 10^{-6} \qquad (1.11)$$

where: w_n = the width with n% probability of being exceeded;

and k = a constant, whose value varies according to the value of n.

The same approach to prediction of cracking is taken by the Cement and Concrete Association, whose work is yet to be described in detail; indeed, the latter's formula for predicting crack widths in reinforced concrete beams is very similar to Equation 1.11.

Note that although Kaar's early work[6] on cracking in concrete reinforced with high strength bars was based on the bond-slip theory, the equation finally put forward for predicting crack widths contains neither ∅ nor p, the two parameters predicted by the theory to have the greatest influence on cracking.

1.2.1.3 Research on partially-prestressed 'I' beams

More recently, Desayi[10] has revived the bond-slip theory and applied it to cracking in Class 3 partially-prestressed 'I' beams. Tests were conducted on 9 such beams, 6.3m long and 300mm deep, subjected to a constant moment over the central 1.8m of their length. High-tensile wires 7mm diameter were used for prestressing tendons and high-yield bars 10mm diameter for reinforcement; various arrangements of tendons and bars

were used in the tests, but the diameters were kept constant. This is unfortunate, because in the absence of experimental data Desayi has assumed the relationship between crack widths and bar diameter predicted by the bond-slip theory, which has been shown to be invalid for high strength bars. The application of Desayi's crack width formulae to cracking in concrete reinforced with other than 10mm bars must therefore be highly suspect.

By considering the longitudinal equilibrium of the cylindrical element of concrete in Fig.1.3 the following equation for predicting crack spacing was obtained:

$$L = \frac{f_t \Sigma_i (D_i^2 - \phi_i^2)}{4 \Sigma_i (\phi_i k_{bi} f_{biu} M/M_u)} \qquad (1.12)$$

where: L = crack spacing;

D_i = the diameter of the effective area of concrete surrounding bar i;

k_{bi} = a factor which when multiplied by the peak bond stress gives the average bond stress;

f_{biu} = the ultimate bond stress of bar i;

M_u = the moment corresponding to ultimate bond stress.

This equation was said to give the average crack spacing, but in fact it gives the theoretical minimum spacing.

A linear relationship between applied moment and maximum bond stress was assumed in the derivation of Equation 1.12:

$$f_{bi} = f_{biu} M/M_u$$

which may be questioned, but the resulting formula does predict that crack spacing is reduced as the applied moment increases, and this is the behaviour observed in tests. Furthermore, if the effects of tension

stiffening are assumed constant:

$$M/M_u = f_{si}/f_{yi}$$

Substituting into Equation 1.12, and noting that for a typical reinforced concrete element, D, ϕ, k_b, f_s, f_y and f_{bu} are the same for all bars, gives:

$$L = k_1/\varepsilon_s \qquad (1.13)$$

where: $k_1 = \dfrac{f_t\,(D^2 - \phi^2)\,f_y}{4\,\phi\,k_b\,f_{bu}\,E_s}$

and ε_s = the strain in the reinforcing bars, calculated from

$$\varepsilon_s = f_s/E_s$$

Equation 1.13 is the reciprocal relationship between crack spacing and strain found by other workers in the field (e.g. Beeby). Desayi's paper is the first to be based on the bond-slip theory which formulates this relationship.

A serious criticism of Equation 1.12 is that it cannot predict the variation of crack spacing at different levels of a beam, and yet Desayi's test results, in common with those of many other workers, show that spacing is much less at the level of reinforcing bars than elsewhere. The same criticism may be levelled at the bond-slip theory in general. Using estimated values of f_t, f_{bi}, etc., Equation 1.12 gave good predictions of crack spacings in Desayi's tests at the level of the reinforcing bars and prestressing tendons, but underestimated them elsewhere.

Assuming that the average crack spacing could be predicted with reasonable accuracy, the mean crack width would be obtained from:

$$\bar{w} = L_{ave}\,\varepsilon_s\,r \qquad (1.14)$$

where: L_{ave} = average crack spacing;

r = the ratio of distances from the neutral axis to the point considered and to the centroid of the steel reinforcement.

The residual strain in the concrete is ignored in this equation, which is reasonable at the level of the reinforcement where crack spacing is small, but at levels where crack spacing is large residual strain may also be large. Other than at the level of the reinforcement, therefore, Equation 1.14 would be expected to overestimate crack widths, were it not for the fact that crack spacing is underestimated. These two errors tend to balance each other; Desayi's paper shows that predictions of crack widths at all levels of the beams tested were of much the same accuracy.

For each grid line in turn, and at various strains, comparisons were made between maximum measured crack widths and the maximum predicted crack widths, where the latter are derived as follows. For a small increment of load above the load at first cracking, in which L_{ave} remains constant, crack widths increase in proportion to L_{ave}. When further cracks form, spacing is decreased and crack widths increase in proportion to the lower spacing L'_{ave}. It was postulated that the widest crack will be the one that increases in proportion to the initial, and greatest, value of L_{ave}. Maximum crack widths predicted by this method cannot however be expected to give good agreement with experimental results, for the initial value of L_{ave} will be significantly affected by random effects such as irregularity of cross section and concrete strength. In the case of Desayi's results, maximum crack widths along the various grid lines at various strains are underestimated by up to 50% of the measured value.

1.2.2 Stress redistribution

1.2.2.1 Derivation of average crack spacing

Broms presented a series of very useful papers [11-14] on crack widths

in reinforced concrete, based on considerations of stress redistribution in cracked sections. The stress pattern for concentrically loaded tension members and flexural members was derived from the theory of elasticity, using the approximate loading and stress patterns shown in Fig.1.4. It was shown[11] that tensile stresses exist only within a radius equal to half the original crack spacing, as illustrated in Fig.1.5. Once two cracks have formed, therefore, the extent to which a third one propagates is determined by the spacing of the original two. The theoretical predictions of stress pattern were found to correlate well with surface strain measurements taken during tests on 37 tension members and 10 flexural members reinforced with high strength deformed bars. In the next paper in the series[12] Broms showed how the theory might be used to predict crack spacings and crack widths. Fig.1.6 shows the various stages in the formation of the crack pattern for members subjected to either tensile loads or flexural loads. The differences between primary and secondary cracks of the first and second order are also shown; they are distinctions frequently made although not all workers in the field believe them to be meaningful ones. Note that because of the loading patterns assumed by Broms (Fig.1.4) neither the stress pattern nor the crack spacings (nor, by inference, the crack widths) predicted by the theory vary in the y-direction of Fig.1.6. The theory does, however, indicate that these parameters will vary in the z-direction, and is therefore an improvement on the bond-slip theory, which is unable to explain this aspect of observed cracking behaviour.

It is apparent from Fig.1.6 that if two adjacent cracks form at a distance apart of less than twice the cover, any cracks that subsequently form between them cannot penetrate to the surface ABCD. Hence, Broms proposed that the minimum visible crack spacing on these surfaces should equal the cover c. Further, the maximum crack spacing will equal twice the cover, since greater spacing than this would allow another visible

crack to form, and it was concluded that the average crack spacing would be 1.5c. (This need not be the case, of course, for there are more opportunities for cracks to form at small spacings than at large spacings - which brings the average value down. Beeby[7] calculated that $L_{ave} = 1.33c$.) Broms' tests on tensile and flexural members showed that the crack spacing on the surfaces ABCD decreased rapidly with increasing load, and approached an average value which was in fact equal to 2c. The discrepancy was attributed to the differences between the actual and assumed stress distributions.

1.2.2.2 Calculation of crack widths

By assuming that the concrete elongation between cracks was negligible, Broms concluded that the mean crack width on the surface ABCD of a member loaded in tension was given by:

$$\bar{w} = 2c\,\varepsilon_s \qquad (1.15)$$

Crack widths on the tension face of a flexural member could be predicted by:

$$\bar{w} = 2r_t\,c\,\varepsilon_s \qquad (1.16)$$

These equations were found to underestimate crack widths at low stresses and overestimate them at high stresses; the reason for this is not apparent.

The shape of the cracks was investigated by testing tensile specimens of length approximately equal to the crack spacing. The cracks were found to be very narrow at the level of the reinforcement and wider at the surface of the concrete, and Broms thought that this indicated the presence of secondary internal cracks as otherwise very high concrete strains were indicated at the level of the reinforcement. Using a method he had developed earlier[13] he found that these secondary cracks were indeed present, but that they also were narrow at the reinforcement and

widest some distance from it. He suggested that the discrepancy in apparent elongation of the concrete at the level of the reinforcement was due to the presence of minute cracks, which is probably the case, for Goto has detected such cracks in his own experiments[15]. Goto's longitudinal section through an axially loaded specimen is reproduced as Fig.1.7, and it will be seen that the internal cracks are wider at the surface of the reinforcement than elsewhere.

It was stated in Section 1.2.1.1 that the bond-slip theory indicates that the sides of a crack in a member loaded in pure tension will be parallel: neither Broms' nor Goto's results support this. Also, Broms' formulae for crack width are independent of bar diameter and effective area of concrete in tension, which is evidence that bond-slip is not a factor in determining crack widths in concrete reinforced with modern deformed bars.

1.2.2.3 Crack widths in wide members

As noted earlier, a shortcoming of Broms' theory is its inability to predict variation of stress, crack spacing or crack widths across the width of the member (the y-direction in Fig.1.6). This is particularly important in slabs, which are wide by definition. Broms and Lutz[14] attempted to solve this problem by defining an effective cover for points on the surface of reinforced concrete between two adjacent bars. The equation put forward was:

$$c_e = (e_o^2 + [c + \emptyset/2]^2)^{0.5}$$

where: c_e = the effective cover;

$$\frac{1}{e_o} = \frac{1}{e_1} + \frac{1}{e_2} \quad ; \quad \text{and}$$

e_1 and e_2 are defined in Fig.1.8

Substituting c_e into Equation 1.16 gives:

$$\bar{w} = 2 r_t c_e \varepsilon_s \qquad (1.17)$$

which was found to give reasonable predictions of the width of both external and internal cracks. It will be noted that Equation 1.17 is the only one proposed so far that predicts the observed variation of crack width along its length.

1.2.3 Empirical formulae

In 1968 Gergely and Lutz[16] presented a purely statistical analysis of results from References 5, 6, 8, 12, 17 and 18. Using various combinations of the parameters which other workers had thought to be important, they built up an alarming array of more than forty different equations and performed regression analyses on each of them for the various sets of data referred to.

They found that $\emptyset/p$ was a very poor variable in any form, and that the CEB variable $(4.5 + 0.4/p)\emptyset$ greatly overestimated crack width for low values of p. Similarly for all other equations proposed in the past - although most fitted the data from which they were derived, none were found to predict accurately crack widths from other investigations.

This is no doubt due to the rather confined scope of much of the work done to date. Hognestad, for example, measured crack width only between bars, whereas Rusch and Rehm[18] measured only crack widths above bars.

The equations finally recommended by Gergely and Lutz include all the parameters found to be of importance - f_s, A_c and c:

$$w_{max} = 0.091 (c A_c)^{1/3} (f_s - 5) r_t \qquad (1.18)$$

for crack widths on the tension face of a flexural member, and:

$$w_{max} = 0.091\ (c_s\ A_c)^{1/3}\ (f_s - 5)/(1 + c_s/d_1) \qquad (1.19)$$

for side cracks at the level of the reinforcement,

where: c_s = minimum side cover to the reinforcing bar assumed to be controlling cracking on the side of a beam;

and d_1 = depth from neutral axis to the centroid of the tension steel.

These equations are not dimensionally correct, in spite of what Gergely and Lutz say: the units used are not stated, but by inference they must be as follows:

w_{max} in thousandths of an inch;

c, d_1 in inches;

A_c in square inches;

f_s in kips per square inch.

Gergely and Lutz recommend their formulae in preference to Broms', but the grounds on which they do so are not particularly convincing. It is argued that the latter give poor predictions of results from References 6, 17 and 18, but results from the last two are ignored anyway, on the grounds that they are "out-of-line" with other data. The advantage of Gergely and Lutz's formulae is therefore that they give better predictions of crack widths from one series of experiments out of six; the disadvantage is that they have no theoretical backing at all. It is surprising, therefore, that as recently as 1972 Nawy[19] should recommend the use of Equations 1.18 and 1.19 in preference to all others.

More recently, Albandar and Mills[20] attempted to resolve the conflict between the bond-slip theory and the no-slip theory (still to be described) but in practice achieved little more than to add two more crack-width equations to the multitude that already existed. Nine beams were tested at a constant steel stress and a surface fitting computer routine was

used to derive the equation of best fit to the experimental data:

$$\bar{w} = (0.00184a_{cr} + 0.000484A_c^{\frac{1}{2}})\ r$$

where: a_{cr} = distance from nearest reinforcing bar to point where crack width is measured.

Assuming that crack widths are directly proportional to steel stress this was transformed into the recommended equation:

$$\bar{w} = (1.5a_{cr} + 0.4A_c^{\frac{1}{2}})\ \bar{\varepsilon} \qquad (1.20)$$

where: $\bar{\varepsilon}$ = the mean surface strain along the grid line in question.

In view of the variability of cracking in reinforced concrete, however, a total of 9 beams and less than 300 crack measurements is a very small sample on which to base an empirical equation. Further, the scope of the investigation was very limited - steel stress, the cross section and steel percentage were all constant and cracks were only measured on one side face of each beam. In fact the only variables were bar diameter and spacing, which indirectly caused variation in the parameter A_c.

1.2.4 No-slip theory

1.2.4.1 General

The most credible account of cracking in reinforced concrete to date has been given in a series of reports by the C and CA[3,21-26]. Not only is it based on measurements of more than 250,000 crack widths, but theoretical explanations have been sought and found for most of the phenomena which occurred. The work has been summarised by Beeby[39], who also explains the derivation of the formulae for crack width and concrete strain used in current design practice. These formulae are considered in Sections 1.2.4.5 and 1.4 respectively.

1.2.4.2 Cracking in reinforced concrete beams

The new theory was introduced by Base et al[3] who conducted tests on

105 reinforced concrete beams, each simply supported and subject to concentrated loads at one-third points. A series of grid lines were drawn on the surface of the beam parallel to the main reinforcement, and crack widths across these lines were measured at each load stage. It was found that the mean width of cracks crossing a grid line ($\bar{w}$) was proportional to the average strain along that line.

A statistical approach was used to analyse the test results, since variations between nominally identical beams were found to be of the same order as between different ones. This was particularly true of the effect of bar type, and a further 28 beams were tested[21] - 12 each with plain and deformed bars, and 4 with heavily deformed bars. Beams reinforced with plain bars were found to contain fewer but wider cracks, but there was no significant difference between deformed and heavily deformed bars. This is, of course, further evidence that bond failure is not a critical consideration for modern deformed bars.

A combination of theoretical and empirical considerations gave the following equations:

$$\bar{w} = 1.67\, a_{cr}\, \bar{\varepsilon} \qquad (1.21)$$

$$w_1 = 3.3\, a_{cr}\, r\, f_s/E_s \qquad (1.22)$$

where: w_1 is the width exceeded by 1% of the cracks along the grid line.

These equations may be used to predict crack widths anywhere on the surface of a reinforced concrete beam; their similarity to the equations put forward by Broms (1.15 and 1.16) will be noted. Of particular relevance to cracking in composite beams was the finding that stirrups acted as crack inducers - especially where cover was low. Another report by the C and CA[24] confirmed this, but unfortunately insufficient data was available to form any quantitative conclusions on the matter.

1.2.4.3 Cracking in slabs

The next report in the series[22] was also of relevance to composite beams for it considered the effect of the wide bar spacings common in reinforced concrete slabs. The mean crack width on any particular grid line was again found to be proportional to the average strain, but the distribution of crack widths in the slab tests was found to be markedly skew, whereas that for beams had been normal. Each individual measurement of crack width along a grid line (w) was therefore divided by the appropriate mean strain, and the values of $(w/\bar{\varepsilon})$ exceeded by 2, 5, 7.5, 10, 15, 20, 25 and 50% of the results were determined. These values were found to be constant for each grid line and were therefore used to define the crack width distribution. The parameter $(w/\bar{\varepsilon})$ appears frequently in the following pages, where it is termed the "crack slope" and denoted by W; W_n refers to the crack slope exceeded by n% of the results and W_{ave} to the average crack slope, which is not necessarily the same as W_{50}.

Crack widths measured at a distance of less than 2c from the bars were predicted reasonably well using Equation 1.21, but outside this range a further factor, related to the depth of section, was found to have a bearing. Beeby proposed that crack spacing (and hence crack width) at any point on the surface of a reinforced concrete slab was a function of two basic cracking patterns - one immediately over a bar which depended on the cover, and the other at hypothetical points an infinite distance from the bar, which depended on the initial crack height. In fact, since cracks taper to almost zero width at a reinforcing bar, one might say that both patterns depended on the initial crack height.

For W_{ave} and all values of W_n a linear relationship was found to exist between $1/W$ and $1/a_{cr}$, which allowed the cracking pattern at any intermediate point to be given in terms of the two basic patterns. Also, by projecting backward to the axis $1/a_{cr} = 0$, the value of W at infinite

a_{cr} (W_{lim}) for the slab in question could be determined. It was found to be directly proportional to the initial crack height:

$$W_{lim} = K\, h_o \qquad (1.23)$$

where: h_o = initial height of cracks;

K is a constant which depends on the required probability of W_{lim} being exceeded. Values are tabulated in Ref.22.

To determine relationships for the cracking patterns immediately over reinforcing bars, Beeby started with an equation derived by Ferry-Borges[27]:

$$L_{ave} = k_1(A_c/\emptyset) + k_2 c$$

where: k_1, k_2 = constants.

Crack width could be expected to follow a similar relationship.

Beeby suggested that the markedly skew distribution of crack widths observed in his tests was due to slip between the concrete and reinforcement after the crack pattern had formed, allowing greater crack widths to develop. Now, if bond remained intact, the cover would dominate, whereas if bond were to break down completely, the initial crack height would dominate. The ratio (c/h_o) therefore determined the amount of modification possible and either ($\emptyset/p$), or ($A_c/\emptyset$) - the two differ only by a constant - could be looked on as determining the number of cracks at which modification would occur.

Hence, a relationship for crack slope directly over a bar, W_b, was proposed:

$$W_b = k\, c + f(c/h_o)\; g(A_c/\emptyset)$$

where: k = a constant;

$f(c/h_o)$ = a function of (c/h_o);

$g(A_c/\phi)$ = a function of (A_c/ϕ).

The two functions were derived empirically and gave:

$$W_b = K_1 c + \frac{K_2 A_c \exp(-K_3 c/h_o)}{\phi} \qquad (1.24)$$

where $K_{1,2,3}$ are constants which vary according to the required percentage of crack slopes exceeding the calculated slope. Values were found empirically and are tabulated in Reference 22.

Equations 1.23 and 1.24 may be used to determine the crack slopes of the two basic cracking patterns, W_{lim} and W_b. The following equation, derived from the linear relationship of $1/W$ and $1/a_{cr}$, may then be used to calculate the crack slope anywhere on the surface of a reinforced concrete slab:

$$W = \frac{a_{cr} W_{lim} W_b}{c W_{lim} + (a_{cr} - c) W_b} \qquad (1.25)$$

The three Equations 1.23 to 1.25 will be referred to as the "slab equations".

Many workers have assumed that:

$$L_{ave} = \bar{w}/\bar{\varepsilon} = W_{ave}$$

whereas Beeby found that average crack spacing often exceeded the average crack slope. This led him to the conclusion, already noted, that residual strain in cracked concrete was significant, and he proposed the following equation:

$$L_{ave} = W_{ave} + R_1/\bar{\varepsilon} \qquad (1.26)$$

where: $R_1 = 0.05 \exp(-0.0135c)$

1.2.4.4 Cracking in prisms subjected to pure tension

In a later report[25], Beeby described a series of tests on reinforced

concrete prisms loaded in pure tension, the purpose of which was to study in detail the effect of the parameter $A_c/\emptyset$ on the crack pattern immediately over a bar. This parameter had been introduced to predict the likelihood of internal failure at cracks, and is obviously important where such failure takes the form of bond-slip. However, Goto had found[15] that for deformed bars internal cracking was the dominant form of internal failure, and it was not clear how the variable $A_c/\emptyset$ related to this. The parameter finally put forward in its place was $(c_1/c)^{\frac{1}{2}}$ $(c/\emptyset)$ c, where c_1 and c are the greater and lesser covers respectively for a centrally reinforced rectangular prism.

It was argued that the new parameter defined geometric similarity, and hence the stress pattern would be the same in any prism having the same value of $(c_1/c)^{\frac{1}{2}}$ $(c/\emptyset)$ c. The term would therefore be effective whether internal failure took the form of bond-slip or of internal cracking.

Substituting $(c_1/c)^{\frac{1}{2}}$ $(c/\emptyset)$ c for $A_c/\emptyset$ in Equation 1.24 gave the new formula for predicting crack slope immediately over a reinforcing bar:

$$W_b = K'_1\, c + K'_2\, (A/B)^{\frac{1}{2}}\, (cB/2\emptyset)\, \exp(-K'_3\, c/h_o) \qquad (1.27)$$

where: K'_1, K'_2, K'_3 are constants;

$(A + \emptyset)$ = length of longer side of prism surrounding a bar;

and $(B + \emptyset)$ = length of shorter side of prism surrounding a bar.

Values of K'_1, K'_2 and K'_3 were found empirically and are tabulated in Reference 25, which also gives guidance on the dimensions to take for A and B for various arrangements of reinforcing bars.

Equations 1.23, 1.27 and 1.25 may be used to calculate crack widths anywhere on the surface of a reinforced concrete member and will be

referred to as the "tension formulae".

1.2.4.5 Design formula

Present design philosophy in Britain is to check that the crack width with a 20% probability of being exceeded is not greater than some specified limit anywhere on the surface of the concrete. Since the maximum crack width will always occur at the greatest distance from a reinforcing bar, the formula required for design is the one that gives w_{20} on the surface of the concrete mid-way between adjacent reinforcing bars. Beeby has shown[39] how such an equation can be obtained from the "tension formulae".

It is assumed that the initial crack height is proportional to $(h - x)$, where h is the overall depth of the member and x is the distance from the compression face to the neutral axis so that for a 20% probability of the crack width being exceeded, Equation 1.23 gives:

$$W_{lim} = 1.5(h - x)$$

The crack pattern over the bars will have little effect on crack widths mid-way between them, so Equation 1.27 is simplified to:

$$W_b = 3c$$

Substituting in Equation 1.25 gives:

$$w = \frac{3\, a_{cr}\, \bar{\varepsilon}}{1 + 2(a_{cr} - c)/(h - x)} \qquad (1.28)$$

which is the formula given in both CP110[33] and BS5400[34].

1.2.4.6 Cracking in scale models

Finally, we may look at crack similitude in reinforced concrete, which is of course particularly important in composite construction where prototype sizes are such that they cannot conveniently be handled in the

laboratory. Clark[23,26] found that neither crack width nor crack spacing scaled, even at constant stress. Models exhibited a greater cracking strain and greater plasticity than prototypes, due not only to the properties of micro concrete but also to the absolute size of the specimen. It was also very difficult to obtain a scale bond effect between steel and concrete in small models, and for this reason model crack widths would either be greater or smaller than the scaled prototype crack widths. In particular, the greater plasticity of micro concrete and the very poor bond on small gauge wire combined to give a greater degree of internal failure in models reinforced in this manner.

Clark shows how all these differences can take place within the framework of the no-slip theory of cracking, but concludes that we will seldom know the bond and tensile concrete properties of both model and prototype accurately enough to predict prototype crack patterns from the model.

1.3 Research on composite beams

1.3.1 Uniaxial bending

Garcia and Daniels[28,29] subjected uncased 'T' section composite beams to both static and dynamic loads to represent the effect of intermediate columns on continuous beams. Very little numerical data on crack width or spacing is given, but it is apparent that effects of shrinkage and temperature are quite significant, for cracks were first observed in the concrete while stresses due to applied loads were virtually zero. Garcia and Daniels also found that at low steel percentages the steel yields at an early stage and no more cracks form since the steel stress has reached an upper limit. Crack spacing is therefore large, and the cracks widen to an unacceptable degree.

A series of tests on continuous composite 'T' beams has been

conducted at Cambridge University[40-43]. However, the primary aim was to study the various modes of collapse behaviour, and information on cracking is usually limited to photographs of the final cracking pattern after failure had occurred. Hope - Gill[43] subjected beams of the size used in buildings to hogging moment and shear over intermediate supports, and found that individual crack widths sometimes exceeded the value permitted in CP110[33].

1.3.2 Biaxial bending

Concurrently with the author's work on uniaxial bending, Arnaouti has been studying cracking in composite beams subjected to biaxial bending[30-32]. His approach differs in a number of important respects from that of others, as will become apparent.

A finite element analysis was conducted on part of a concrete slab reinforced with a single layer of bars symmetrically placed and subjected to pure tension. The prism analysed is shown in Fig.1.9; its length was taken to be half the crack spacing. Surface ADEH was assumed to be one cracked surface, and ABCD the top of the slab, so both were taken as free of restraint and stress. The planes zx, zy and yx were assumed restrained in the perpendicular direction by symmetry, and Arnaouti argued that because concrete stress falls off rapidly round a bar, the plane ABGH could be assumed free.

The prism was loaded in increments, and once an element had cracked, it was assigned zero direct stiffness and zero shear stiffness for redistribution of stress and further increments of loads. Both these assumptions are reasonable for the case studied (direct tension) although the second would be suspect if any shear forces were to be applied to the element.

Referring to Fig.1.10, which shows a singly reinforced concrete

prism subjected to pure tension, one can write:

$$w = \varepsilon_{mg} L(1 - \bar{\varepsilon}_c/\varepsilon_{mg}) \qquad (1.29)$$

where: w = width of the crack;

ε_{mg} = mean tensile strain over a length equal to half the crack spacing on either side of a single crack;

and $\bar{\varepsilon}_c$ = mean tensile strain at the surface of uncracked concrete, over a length equal to half the spacing on either side of an individual crack.

If L and $\bar{\varepsilon}_c/\varepsilon_{mg}$ are known, therefore, the crack width can be calculated. Arnaouti postulated that:

$$\bar{\varepsilon}_c/\varepsilon_{mg} = f(E_c, \emptyset, S, p, a_{cr}, L)$$

$$L = g\,(S, \bar{\varepsilon}_c, \varepsilon_{mg}, a_{cr})$$

where: f and g = functions of the terms enclosed in brackets;

E_c = Youngs Modulus of concrete;

and S = half the clear spacing of adjacent reinforcing bars.

The finite element analysis was used to conduct a parametric study to determine the above functions, and it was found[30] that:

$$\bar{\varepsilon}_c/\varepsilon_{mg} = (2 + 4400\ \varepsilon_{mg})/(46.9/S + 0.53)a_{cr}$$

which was approximated to:

$$\bar{\varepsilon}_c/\varepsilon_{mg} = (2 + 4400\varepsilon_{mg})/a_{cr} \qquad (1.30)$$

and: $$2\ L_{cr} = 0.82\ (S^2 + c^2)^{\frac{1}{2}} + 86 \qquad (1.31)$$

where: L_{cr} = length along a bar, on one side of an isolated crack, over which the strain at the surface of the concrete is reduced by the presence of a crack;

and L_{cr}, S, c and a_{cr} are measured in millimetres.

Equations 1.30 and 1.31 were substituted into Equation 1.29 to obtain an expression for predicting crack width anywhere on the surface of a reinforced concrete slab:

$$w = \varepsilon_{mg}(0.82\,[S^2 + c^2]^{\frac{1}{2}} + 86)(1 - [2 + 4400\,\varepsilon_{mg}]/a_{cr}) \qquad (1.32)$$

Now, Equation 1.31 only gives one value of "spacing" for a particular slab (assuming cover to be constant and the bars to be uniformly spaced) and is clearly not meant to predict crack spacing along any chosen grid line at a given strain; its substitution for L in Equation 1.29 therefore requires careful consideration.

The parametric study had shown that there was a limiting value of crack spacing, above which the crack width was not influenced. This can be explained by considering the variation of steel and concrete stresses between two adjacent cracks. Referring to Fig.1.11, the crack width is equal to the integral of the difference in strains over the length BD - the area of BCDC'. Concrete surface strain increases with increasing distance from the crack until at distance L_{cr} (points A and B) it reaches a maximum. If the crack spacing is less than twice L_{cr}, points A and B do not exist - and changes in spacing affect the area BCDC'. If the spacing is large however, change of spacing merely alters the length AB, and the area of BCDC' remains constant - as does the crack width. For a constant strain, then, increasing the crack spacing until it equals twice L_{cr} causes an increase of crack width, but increasing it beyond twice L_{cr} results in no alteration of width. A crack spacing of $2L_{cr}$ therefore corresponds to the maximum crack width for a particular grid line and strain.

A further finding from the parametric study was that a linear relationship existed between L_{cr} and distance from the grid line considered to the nearest bar; in fact:

$$2L_{cr} = 0.82a_{cr} + 86$$

For a grid line on the surface of a slab mid-way between two reinforcing bars, $a_{cr} \doteq (S^2 + c^2)^{\frac{1}{2}}$, so for such a grid line substituting Equation 1.31 into Equation 1.29 is legitimate, and would be expected to give maximum crack widths. The justification for making this substitution and using the resulting equation to predict crack widths anywhere on the slab surface is not clear, however.

To provide experimental backing for the theoretical work, a series of five tests were conducted on cruciform-shaped composite beams loaded in biaxial bending. The test rig is shown diagramatically in Fig.1.12. Crack widths were measured where they intersected the grid lines of quadrants Q_1 and Q_3, and concrete strains were measured along all grid lines, parallel to both sets of reinforcing bars, and diagonally as well.

The traditional method of analysing test results is to compare average crack widths along a grid line with average strains, but because each specimen was subjected to a varying moment this was not possible. Instead crack widths were related to the mean strain measured along the particular gauge length which spanned them. Now in Equation 1.32, the strain ε_{mg} is the mean tensile strain over a length L/2 on either side of the crack in question; since Arnaouti argued that L could be replaced by $2L_{cr}$, it followed that the gauge reading could be substituted for ε_{mg} as long as:

(i) the gauge length was approximately equal to $2L_{cr}$: and

(ii) a method was developed for sharing the measured strain between the cracks if two or more formed within one gauge length.

Both of these conditions were met, although the method for sharing strains relies on the crack width formula, and is subject to the criticism that the formula is being used to check itself. However, it was argued that the occasions when more than one crack formed in a single gauge length

are relatively few, so this point could safely be ignored.

Equation 1.32 could therefore be expected to predict experimental results which were presented in the form of individual crack widths and the average strain over the associated gauge lengths. Arnaouti considered the results from grid lines 1 to 4 of the present author's Tests UC4 and UC5, and found very good agreement with the predicted results[30]. Similarly with his own test results - once a method for deriving principal strains for comparison with crack widths had been developed[31], agreement of predicted and measured values was very good. Fig.1.13 is a reproduction of Fig.6 of Reference 32, and shows a typical set of results. The limits of error mark the range within which experimental results should fall, assuming the theory is exact, but allowing for experimental error. Crack widths of less than 0.05mm were not included in the analysis, because reading errors for such narrow cracks had been shown to be as high as 40%.

Two important points are illustrated by Fig.1.13:

(i) results from tests on reinforced concrete showed that the ratio crack width : strain was constant for a given grid line at all strains. This is seen not to be the case for the slabs of composite beams, where w/ε_{mg} is inversely proportional to ε_{mg};

(ii) given the surface strain in the region of a single crack, its width may be predicted with reasonable accuracy by using Equation 1.32. Earlier crack width formulae only allowed the average crack width, or the width exceeded by a specified percentage of results, to be calculated.

Because Arnaouti's method predicts individual crack widths, the concepts of a "mean crack width along a grid line, $\bar{w}$" and a "crack width exceeded by 20% of the results on a grid line, w_{20}" are meaningless. Nevertheless, existing and future Codes of Practice[33,34] give crack

control clauses in terms such as these, so a useful interpretation of $\bar{w}$ is that if there were a large number of bridges of identical geometry, loading and materials, the average of the width of cracks at the point considered would be $\bar{w}$. The definition of w_{20} follows, and by assuming the distribution of w for the population of bridges to be normal (which it might well be) and considering the scatter of test results, it was proposed that:

$$w_{20} = 1.2\bar{w} \qquad (1.33)$$

Equation 1.32, as applied to biaxial bending, was simplified to a form suitable for design purposes: making the same simplification for the case of uniaxial bending gives:

$$\bar{w} = \varepsilon_{mg}(0.8S + 80) \qquad (1.34)$$

Unfortunately, the strength of Arnaouti's method is also its weakness: individual crack widths can be predicted but only if the strain in the region of each crack is known beforehand. This of course will never be the case, but it was postulated that a conservative value of ε_{mg} would be the strain calculated on the assumption of no tension-stiffening (ε_{nt}). Hence:

$$w_{20} = \varepsilon_{nt}(0.96S + 96) \qquad (1.35)$$

However, test results to be described in this thesis (Sections 3.4 and 4.6.1) show that the strain in the region of a single crack may be as large as $2\varepsilon_{nt}$. In this case, the probability of the crack width exceeding w_{20} (as calculated from Equation 1.35) is in fact much greater than 20%. Conversely, a crack sometimes forms in a region where the strain is less than ε_{nt}, and the probability of its width exceeding the calculated value of w_{20} is therefore less than 20%.

1.4 Prediction of average surface strain

It is well established that in a cracked reinforced concrete element, the concrete between cracks is able to develop tensile stress, and contributes to the element's stiffness. This is the "tension-stiffening" effect, and allowance must be made for it if calculations of the mean surface strain, and hence crack widths, are not to be grossly conservative.

Beeby has explained[39] how the design formula for calculating strain in CP110[33] was obtained. The following general equation was used to calculate the reduction in strain due to tension-stiffening ($\delta\varepsilon$):

$$\delta\varepsilon = K f_t f_{scr}/E_s \rho f_{nt} \qquad (1.36)$$

where: K is a constant;

f_{scr} is the steel stress at cracking, calculated on the assumption of no tension-stiffening;

f_{nt} is the steel strain at the load considered, assuming no tension-stiffening;

and p is the area of tension reinforcement, expressed as a proportion of the area of concrete.

The following approximations were made:

$$f_t f_{scr}/E_s = 0.7 \times 10^{-3}$$

$$f_{nt} = 0.58 f_y$$

although, as noted by Beeby[39], the second of these assumptions limits the applicability of the resulting equation without simplifying the design process, since f_{nt} has to be calculated anyway.

Substituting in Equation 1.36 gives the reduction in strain at the tensile face of the member, and results in the CP110 formula for predicting the mean strain at any level:

$$\bar{\varepsilon} = \varepsilon_{nt} - \frac{1.2 b_t h}{A_r f_y} \frac{(a' - x)}{(h - x)} \times 10^{-3} \qquad (1.37)$$

where: b_t is the breadth of the section at the steel level;

a' is the distance from the compression face to the point where cracking is being considered;

A_r is the area of tension reinforcement.

Two formulae are quoted in BS5400 for calculating the mean surface strain: for reinforced concrete construction the CP110 formula is used unaltered, but for composite construction the following definition of ρ has been assumed:

$$\rho = (A_r + A_f)/b_e h_f$$

where: A_r is the area of the tension reinforcement within the effective breadth of the slab;

A_f is the area of the encased tension flange of the structural steel member, where appropriate;

b_e is the effective breadth of the composite section at the level of the tensile steel;

and h_f is the depth of the concrete flange in tension.

Substituting in Equation 1.37 gives the BS5400 formula for predicting the mean strain in the slab of a composite beam. For an uncased 'T' beam, it is simplified to:

$$\bar{\varepsilon} = \varepsilon_{nt} - \frac{1.2 b_e h_f}{A_r f_y} \frac{(a' - x)}{(h - x)} \times 10^{-3} \qquad (1.38)$$

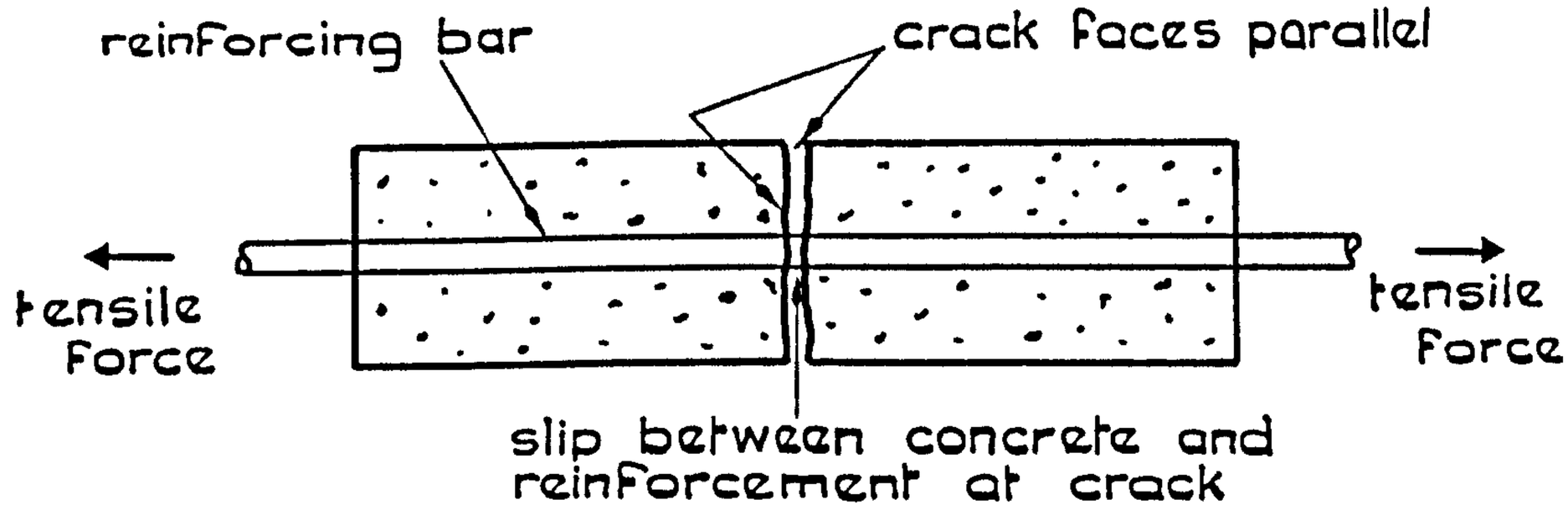

FIG. 1.1 CRACKING IN PRISM SUBJECTED TO PURE TENSION

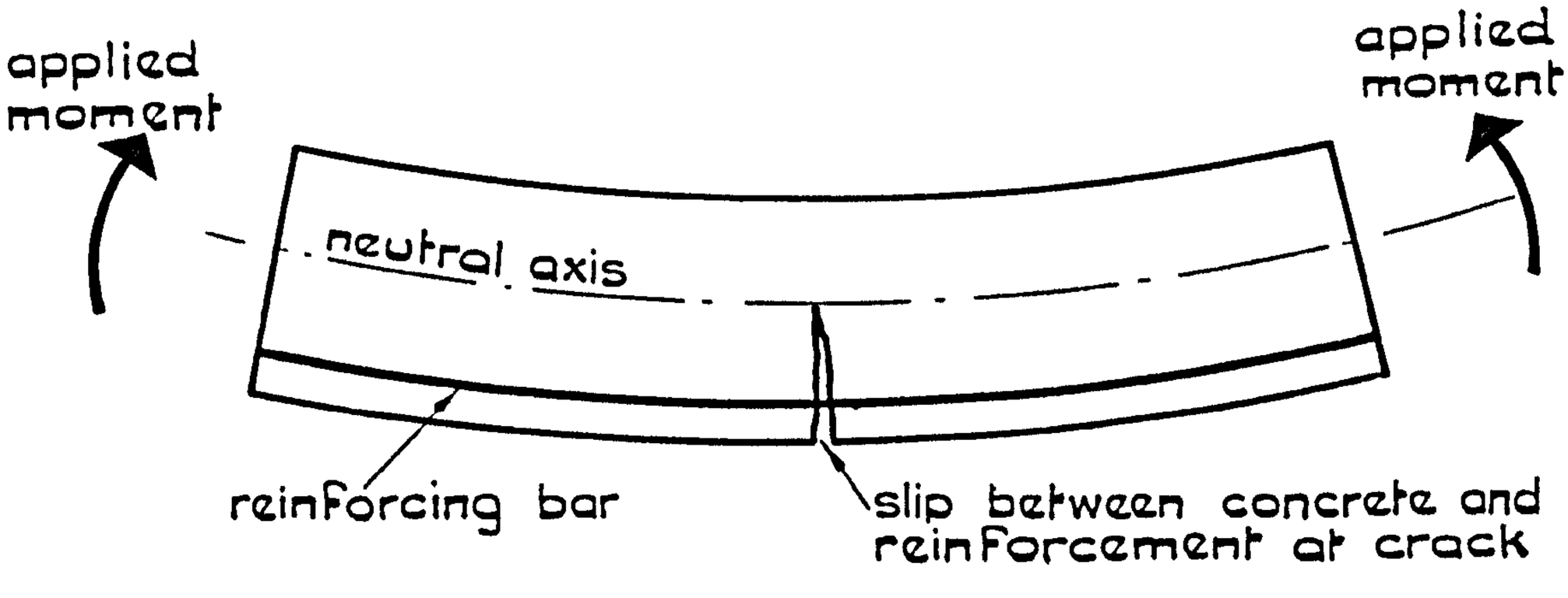

FIG. 1.2 CRACKING IN BEAM SUBJECTED TO PURE BENDING

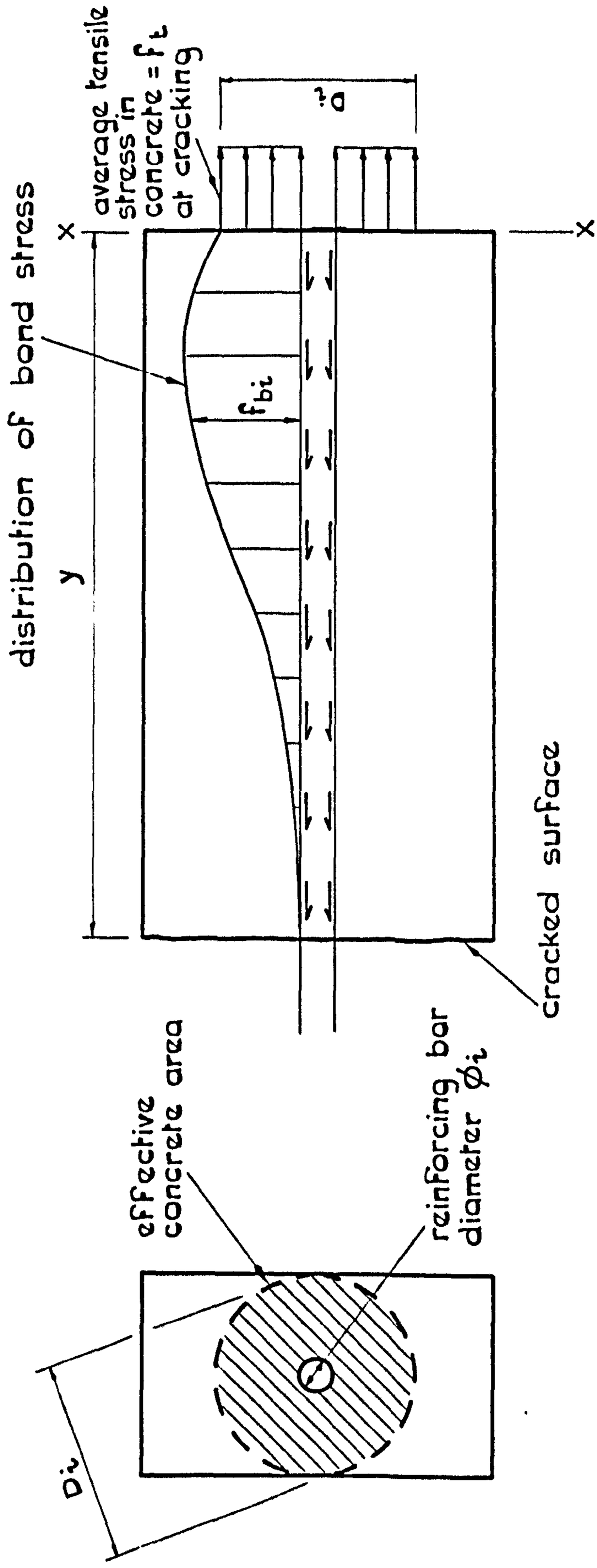

FIG.1.3 BOND AND TENSILE STRESSES IN CRACKED PRISM AT A SECTION, DISTANCE y FROM A CRACK

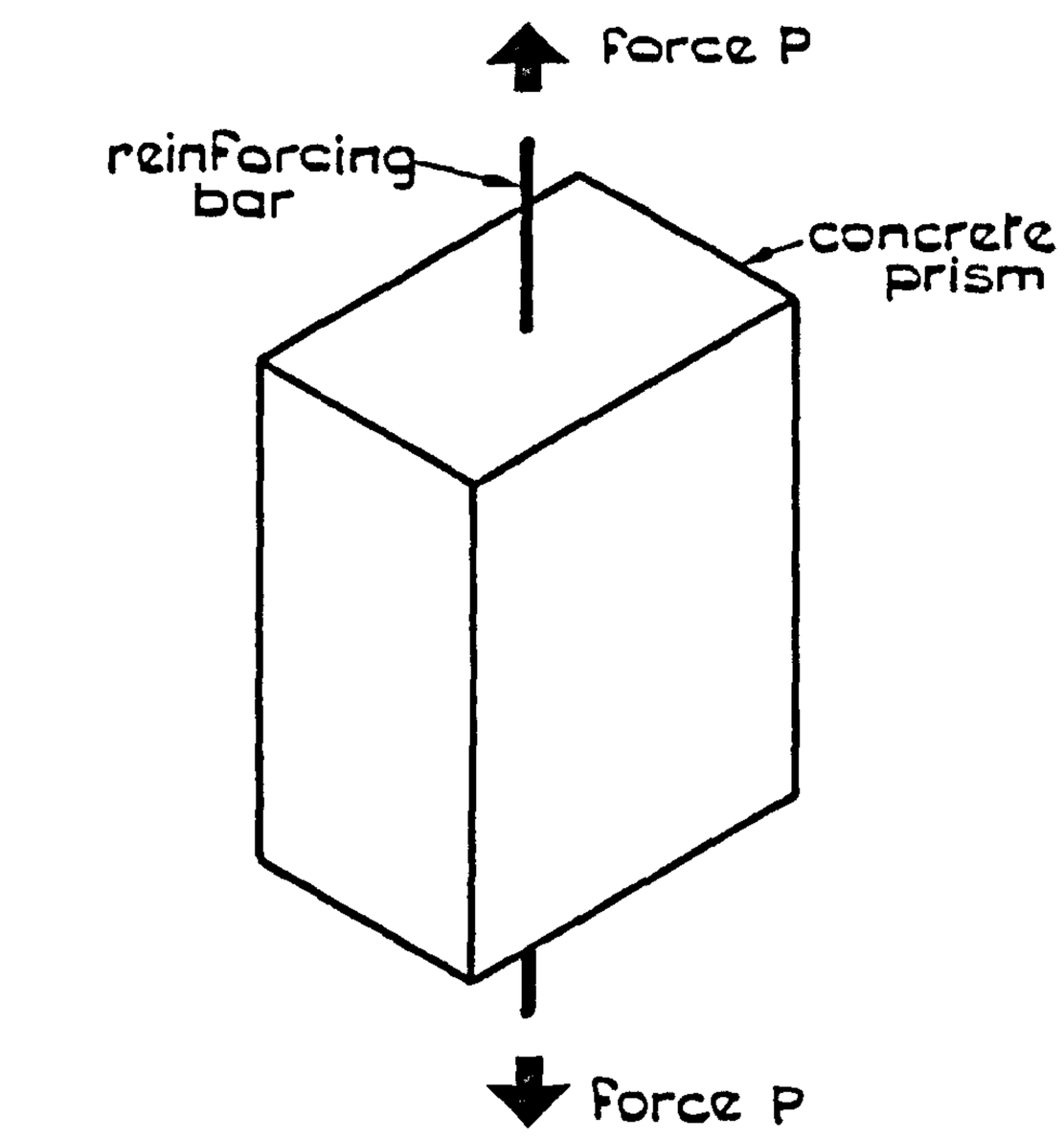

(a) Actual load on tensile member

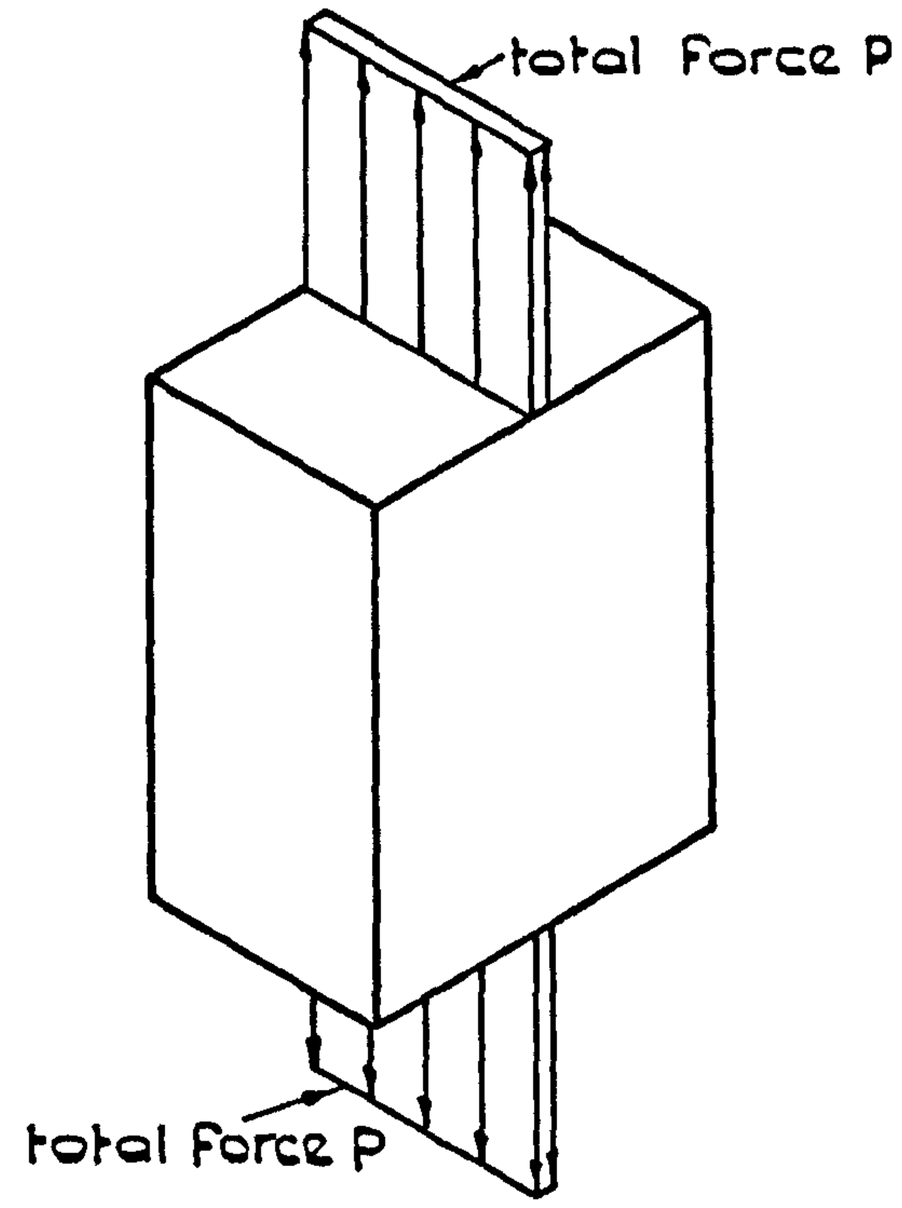

(b) Loading pattern assumed for analysis

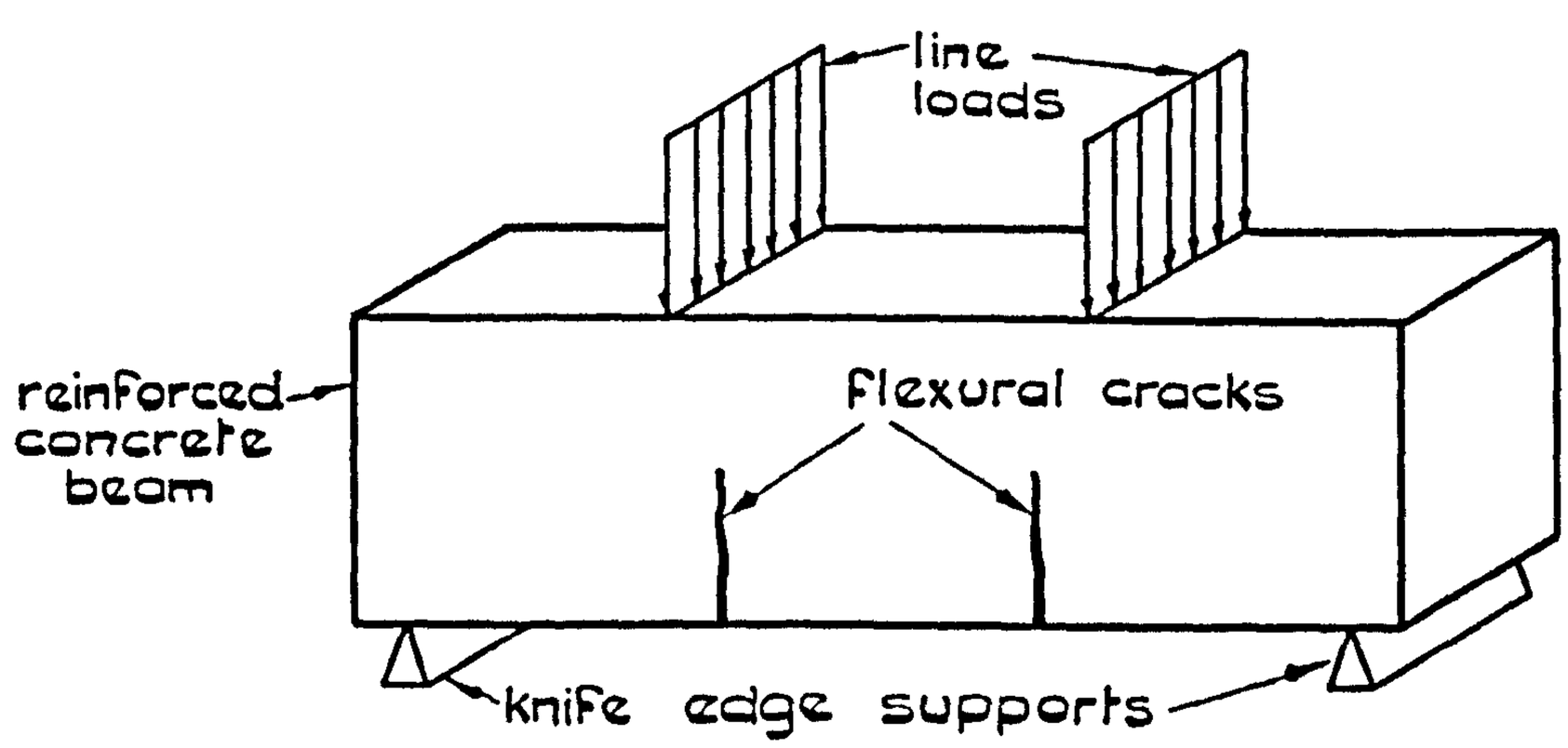

(c) Loading assumed for flexural member

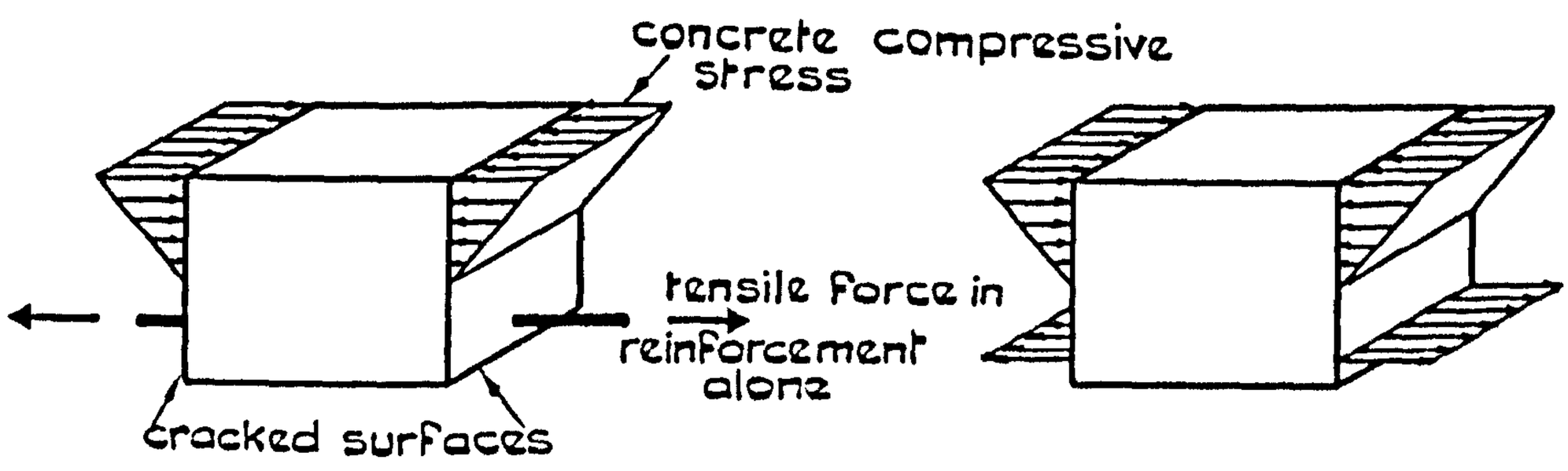

(d) Approximate stress pattern

(e) Idealised stress pattern

FIG. 1.4 MODELS OF TENSILE AND FLEXURAL MEMBERS

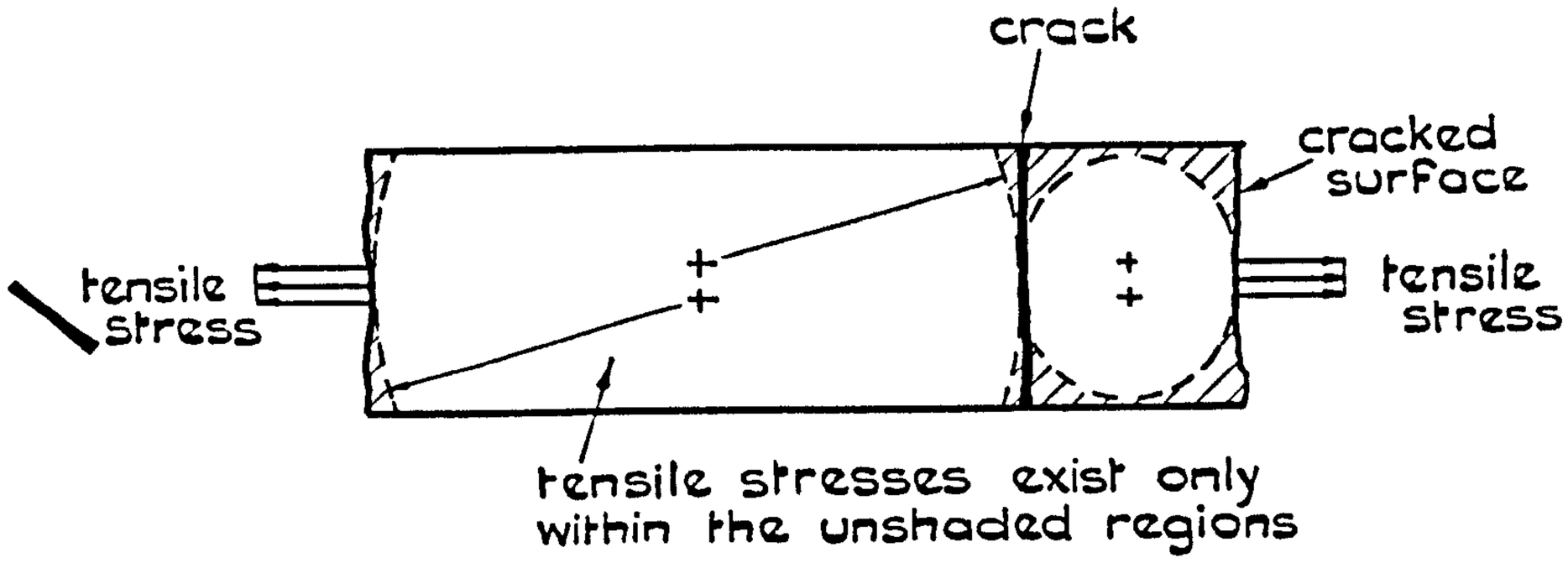

(a) Prism subjected to pure tension

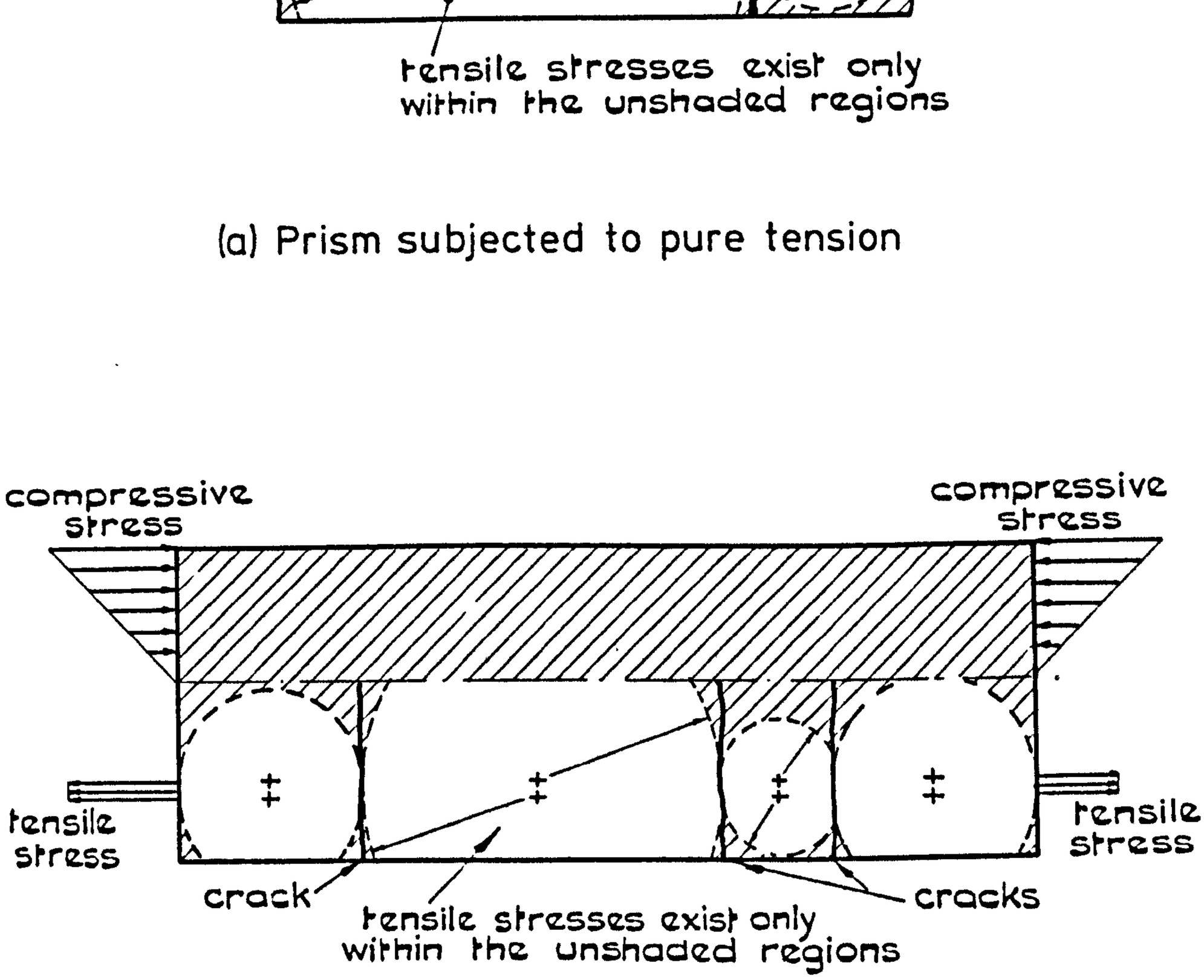

(b) Beam subjected to pure moment

FIG. 1.5 LIMIT OF TENSILE STRESSES IN CRACKED MEMBER

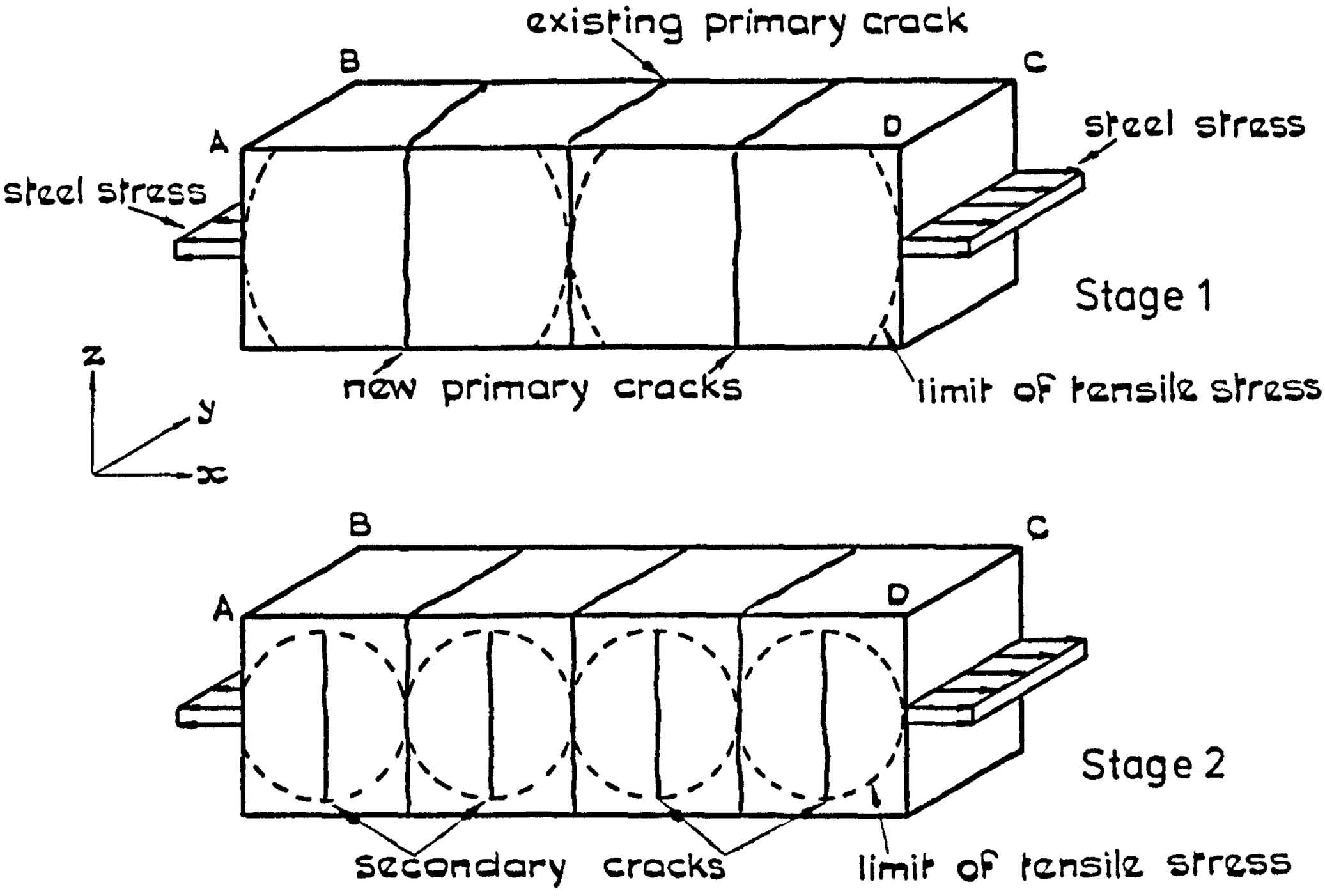

(a) Tensile member

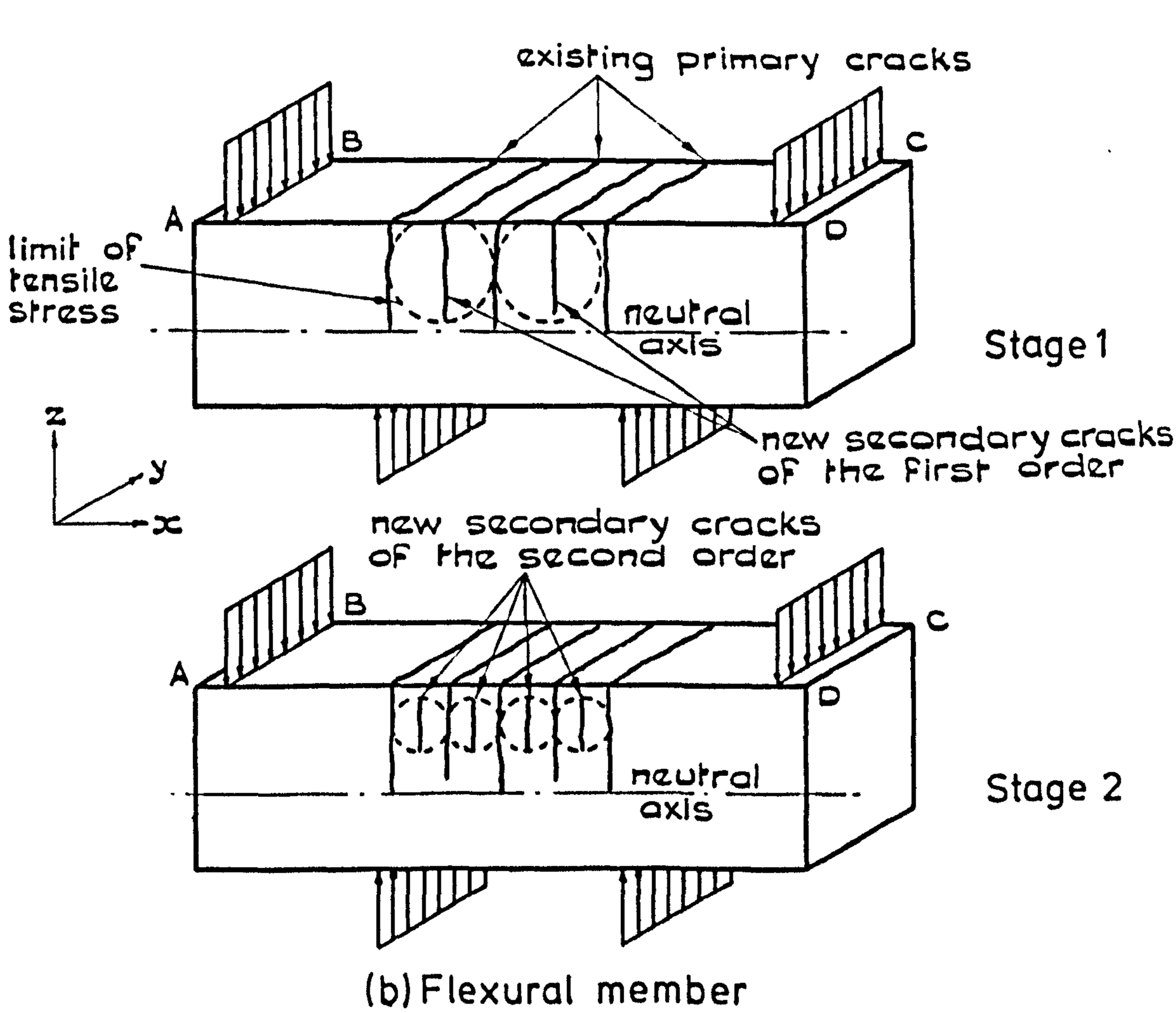

(b) Flexural member

FIG.1.6 DEVELOPMENT OF CRACK PATTERN

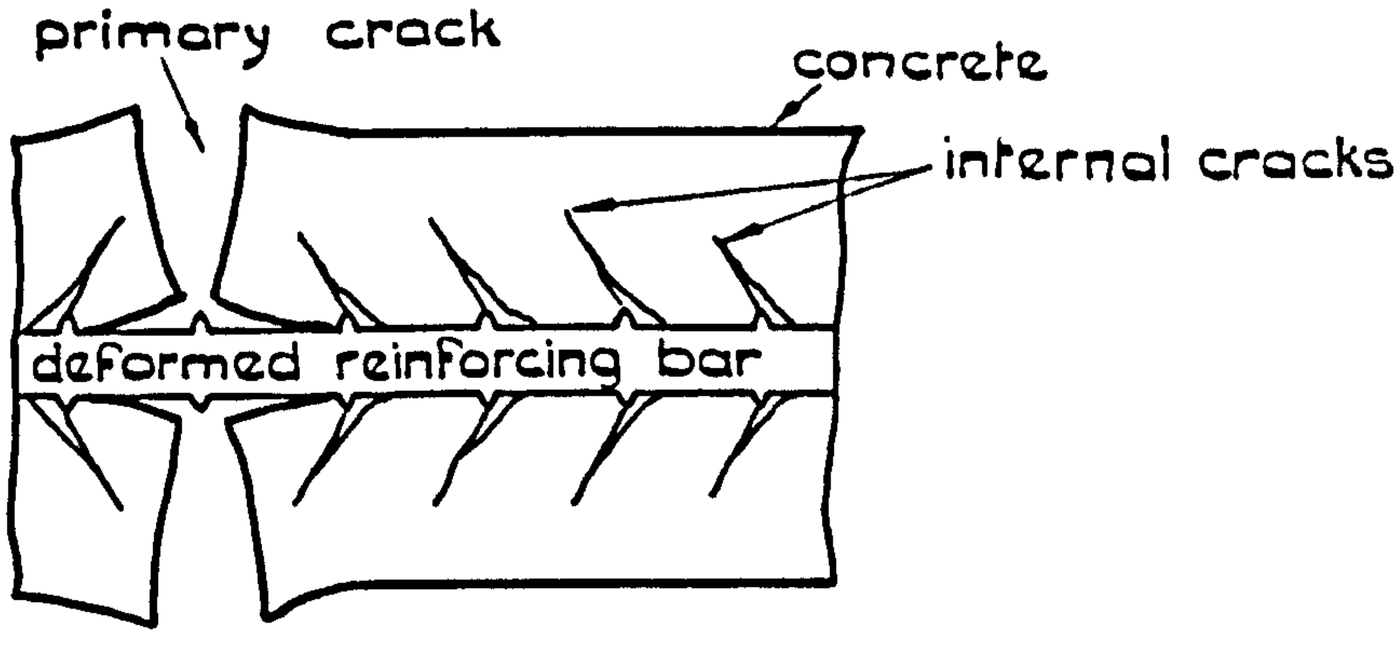

FIG.1.7 INTERNAL CRACKING IN REINFORCED CONCRETE PRISM

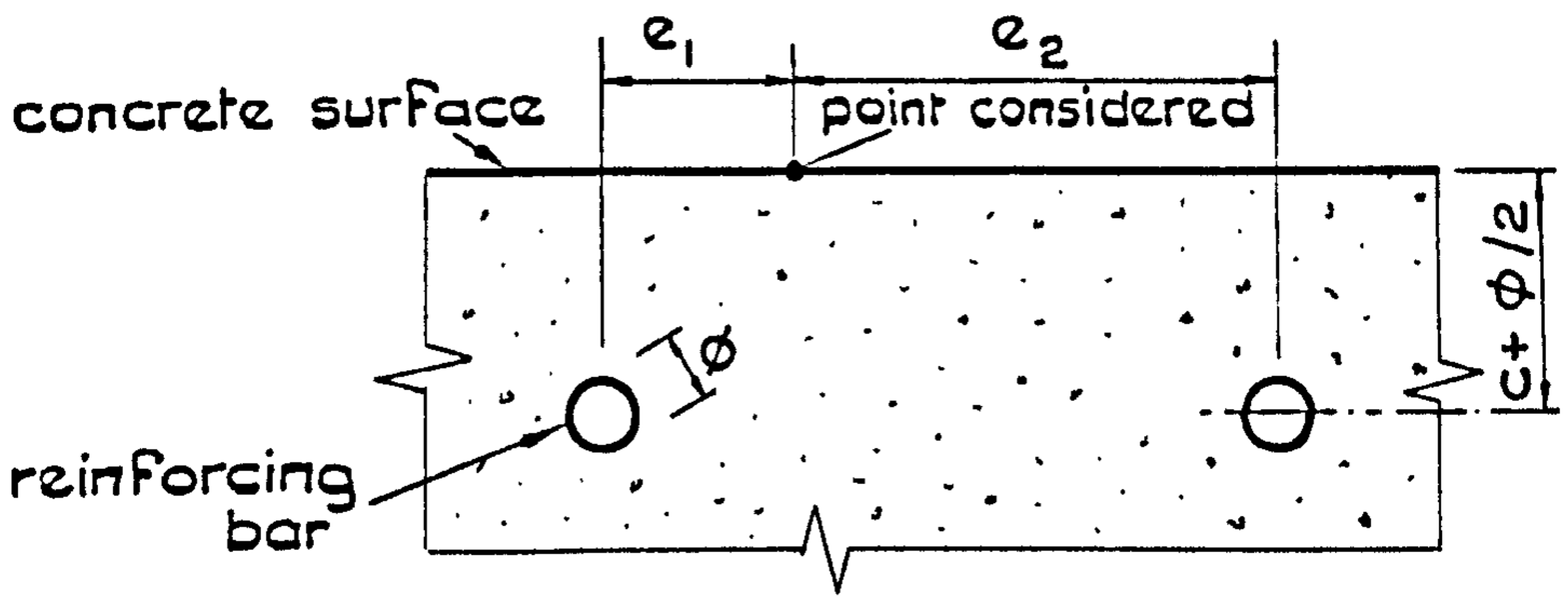

FIG.1.8 DEFINITION OF e_1 AND e_2 FOR CALCULATING EFFECTIVE COVER

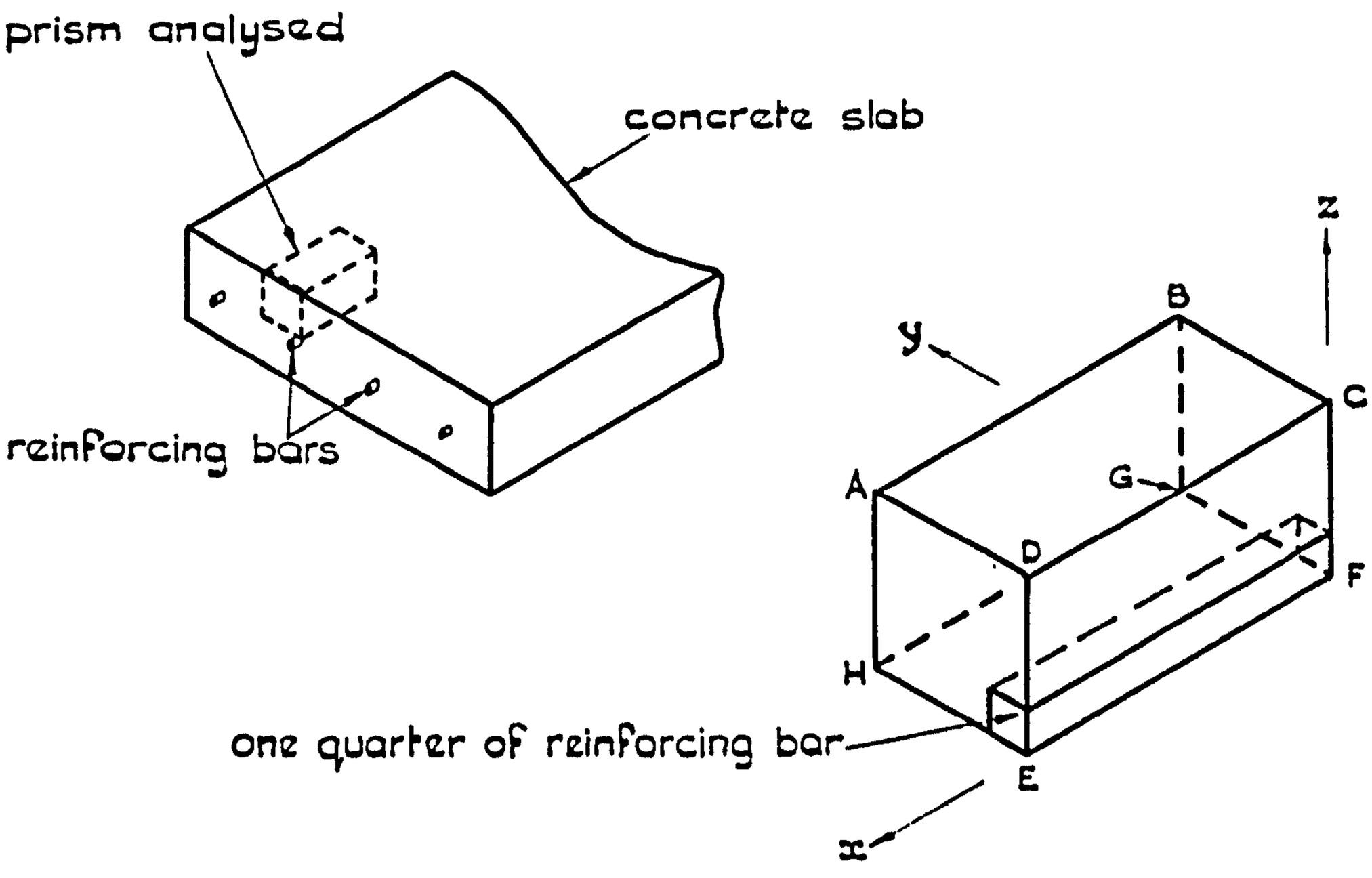

FIG.1.9 PRISM ANALYSED BY FINITE ELEMENT METHOD

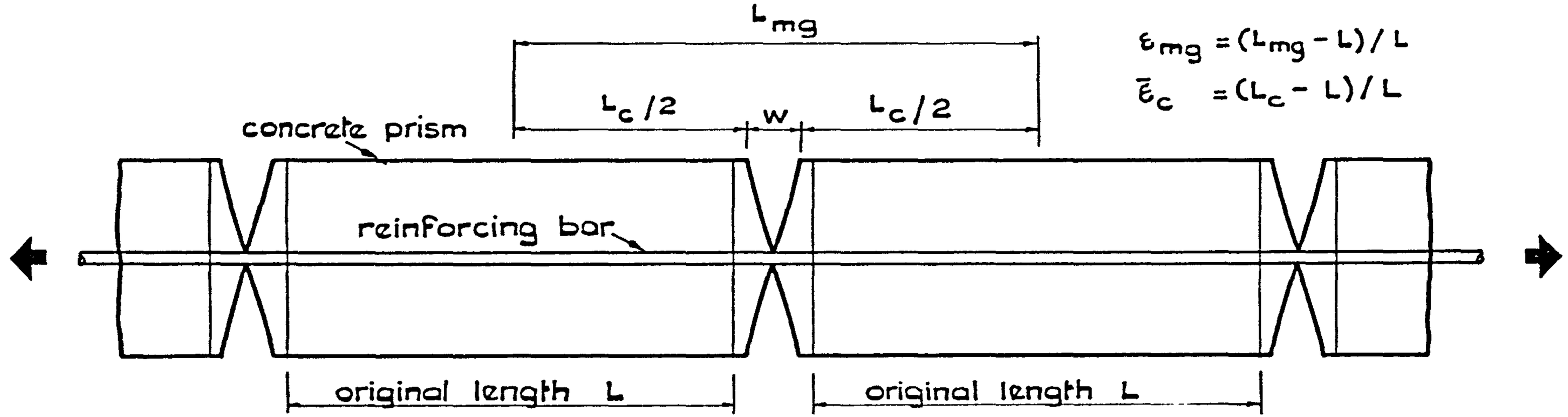

FIG.1.10 ELONGATION OF PRISM SUBJECTED TO PURE TENSION

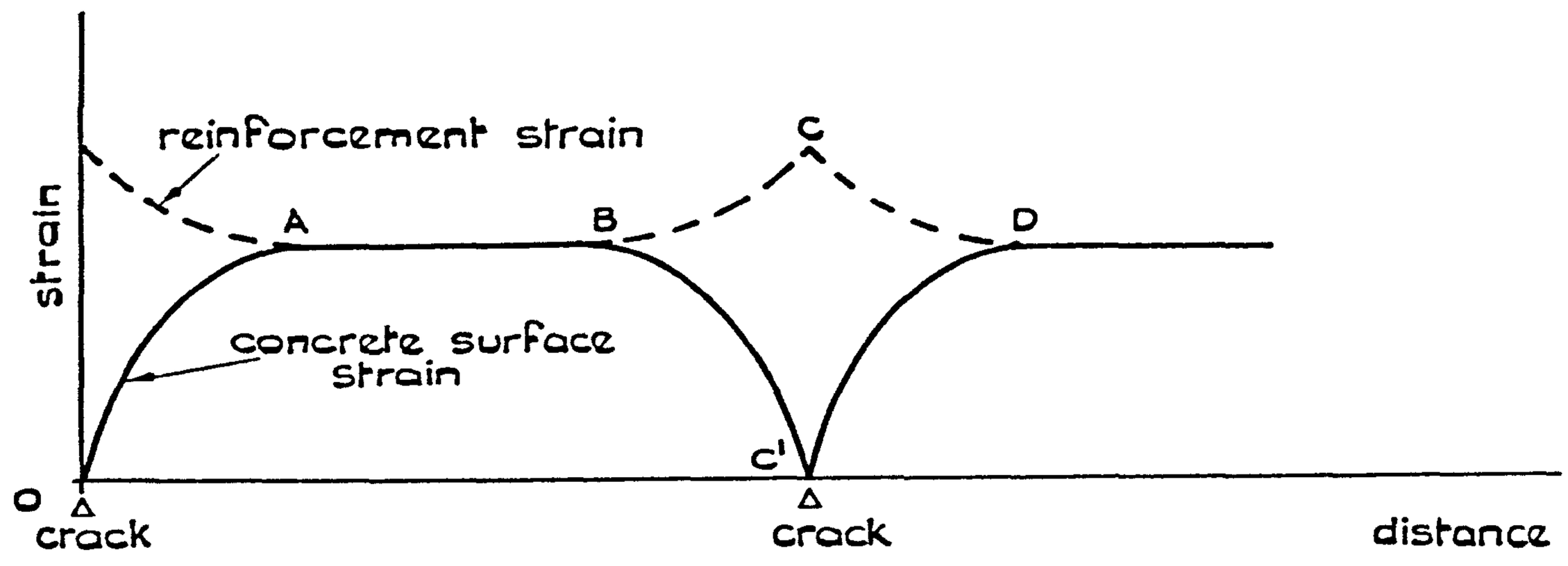

FIG. 1.11 STRAIN IN PRISM SUBJECTED TO PURE TENSION

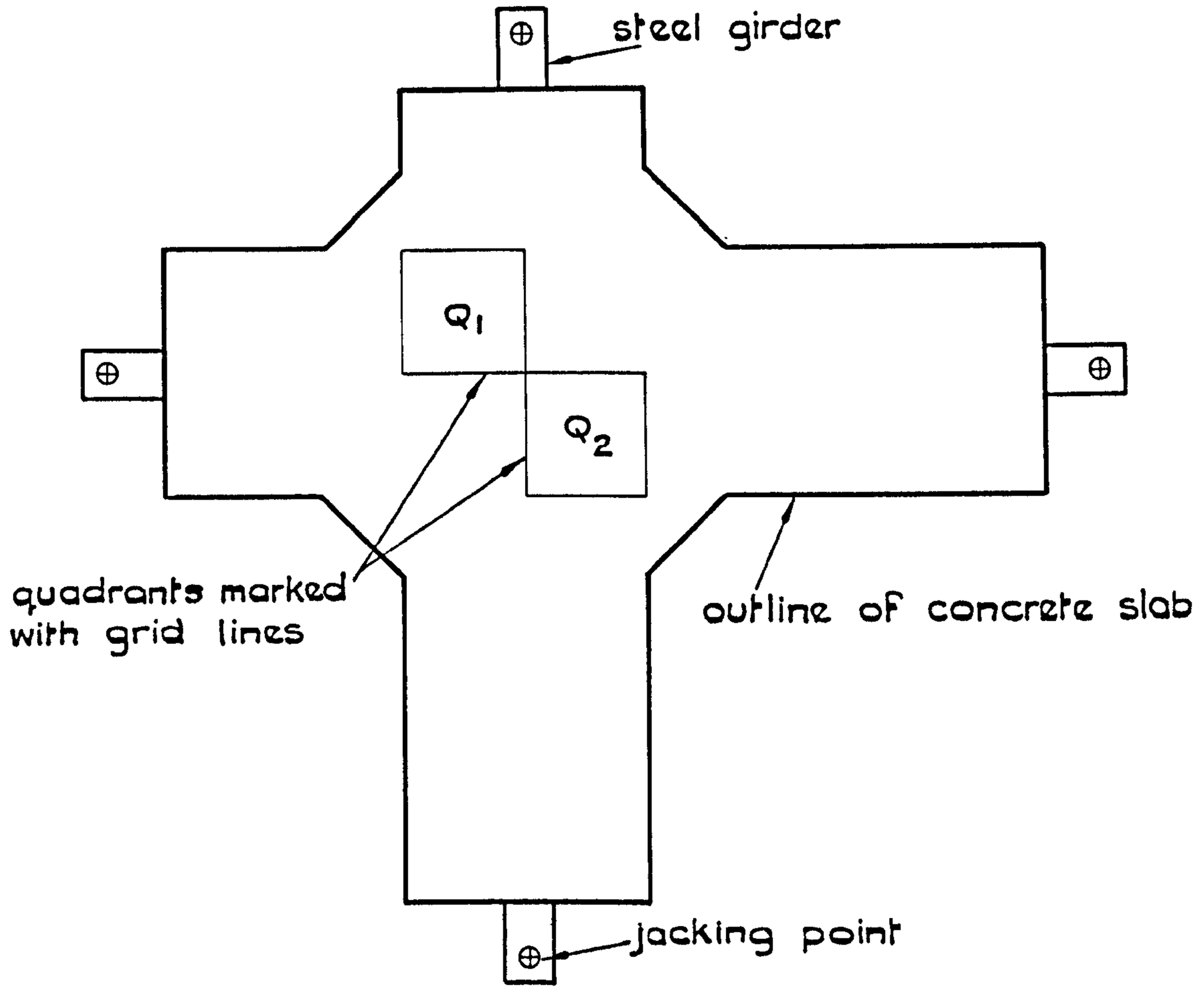

Plan

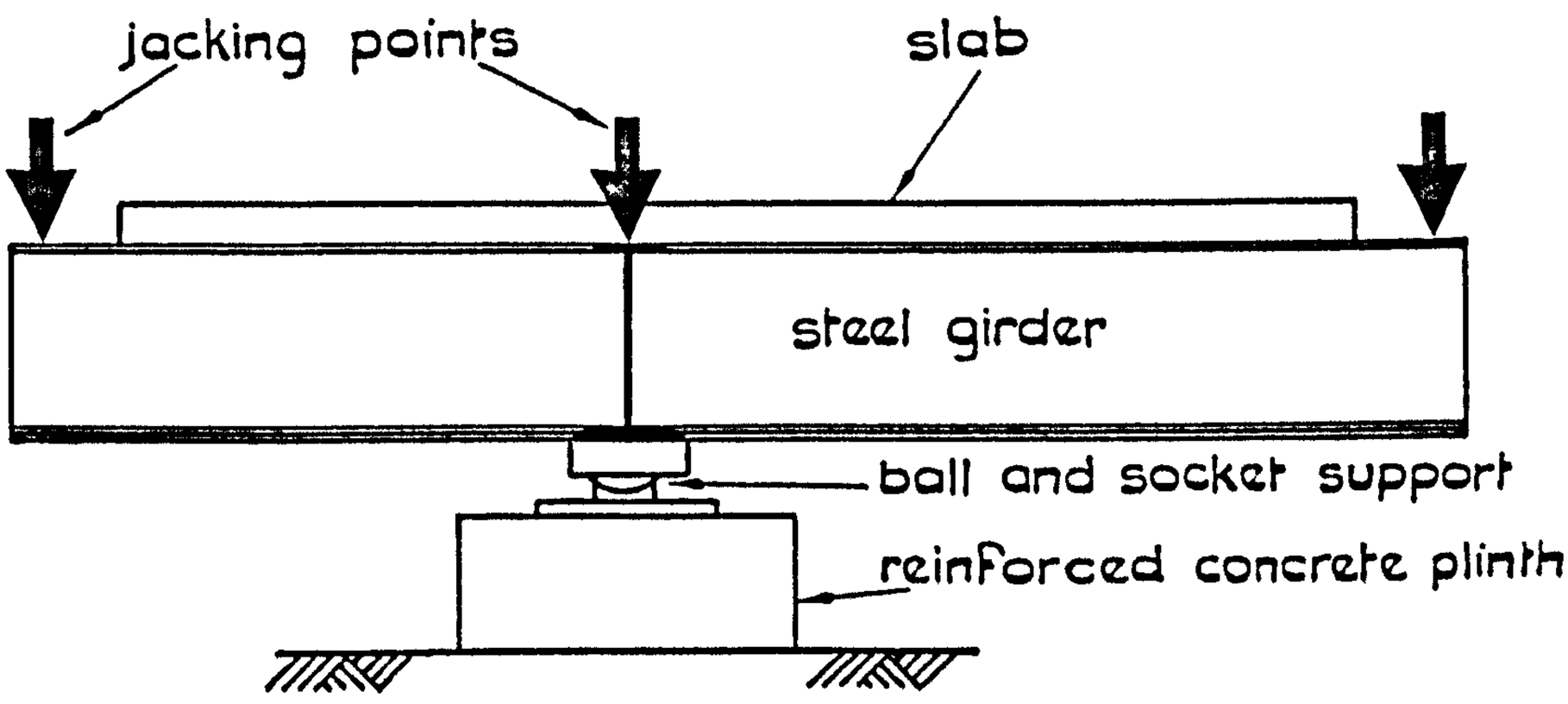

Elevation

FIG.1.12 TEST RIG USED TO STUDY CRACKING IN BIAXIAL TENSION

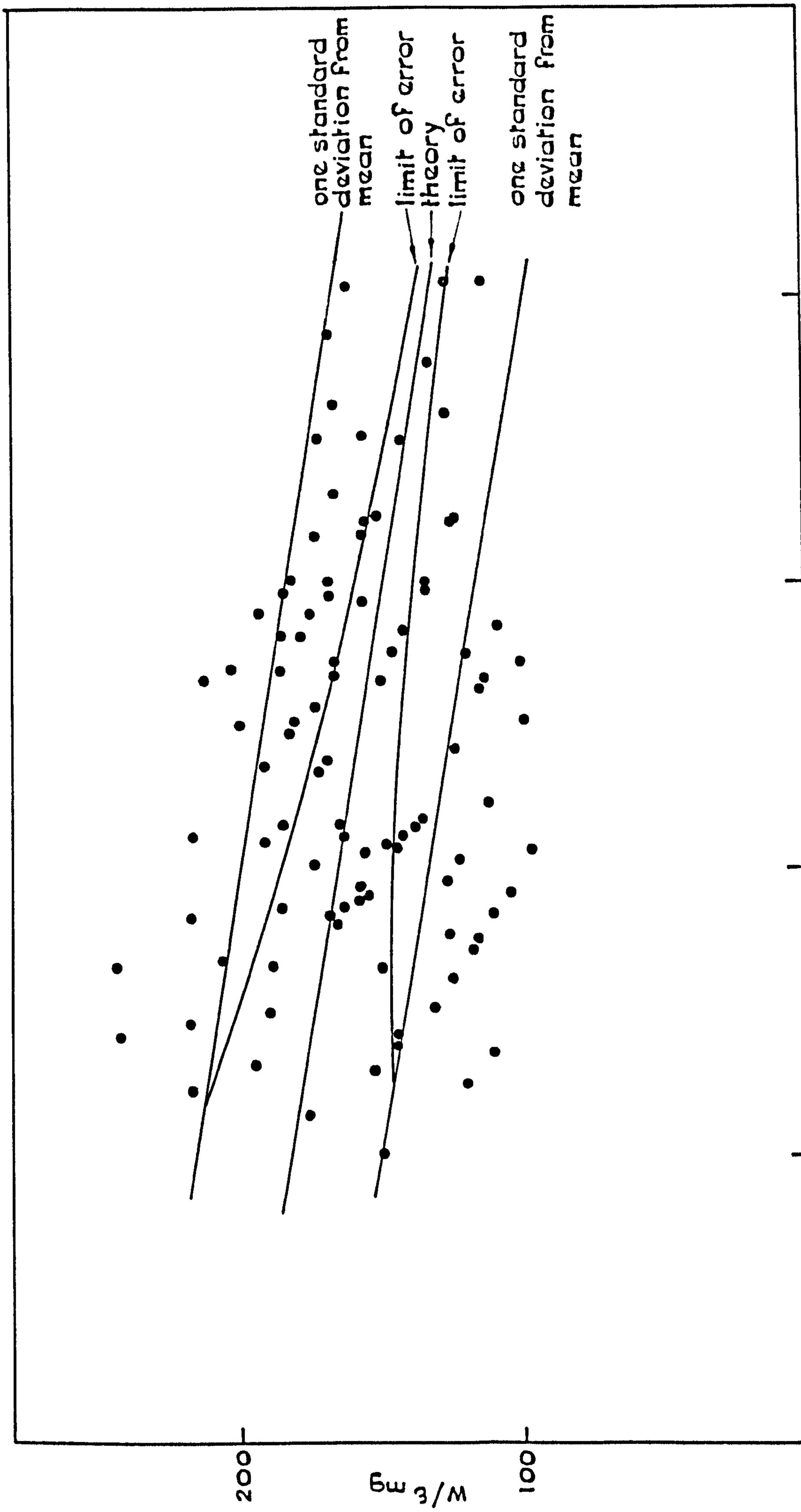

FIG.1.13 PLOT OF w/ε AGAINST ε : INDIVIDUAL CRACK WIDTH READINGS

CHAPTER 2

TESTS TO INVESTIGATE CRACKING

2.1 Introduction

A series of seven composite beams have been tested to observe their cracking behaviour, and to provide experimental data against which proposed crack-width formulae may be checked. Each beam was given a serial number from UC1 to UC7.

Ogunronbi, who tested Beams UC1 and UC2 and assisted the present author with UC3, has already reported on these three tests[35], but details of them are repeated below for convenience, as they will be referred to frequently in the following chapters.

2.2 Test specimens

2.2.1 Choice of specimens

It was decided that the test specimens would all be uncased composite beams of 'T' cross-section, subjected to a constant uniaxial moment over part of their length by applying concentrated loads as shown in Fig.2.1. Measurements of crack width and spacing and steel strain would be taken in the constant moment region, or the "test region".

Beams UC1 and UC2 comprised a 254 x 102 x 28 Universal Beam with a slab 1000mm wide by 90mm deep cast on top, and a 150 x 25mm steel plate welded to the bottom flange. The effect of the latter was to lower the neutral axis of the composite beam, so the slab would behave in a similar manner to one acting compositely with a steel beam about 600mm deep. The test specimen therefore represented a full size model of a typical composite beam for use in buildings, and a 1:3 scale model of a typical composite bridge beam. The problems associated with small scale models of reinforced concrete, referred to in Section 1.2.4.6, made it

inadvisable to use models of a smaller scale, and the proportions of Beams UC1 to UC3 were altered little for subsequent tests.

The parameters considered in each test are listed in Table 2.1. Crack widths were to be measured at a number of load stages and on several grid lines marked on the surface of the slab, so the effect on crack width of distance to the nearest bar and concrete strain could be determined. Hot-rolled, high-yield deformed bars were used for longitudinal slab reinforcement throughout the UC series of tests.

2.2.2 Detailing of test specimens

2.2.2.1 The steel girder

Details of the steel girders are given in Fig.2.2. The same girder, with different concrete slabs cast onto it, was used for Beams UC1 to UC4 and UC7. Similarly, the girder used in UC5 was used again, with an additional flange plate, for UC6. The universal beams for both girders were cut from a single length of grade 43 steel. Flange plates were also of grade 43 steel.

The effects of using the same girder repeatedly on its behaviour during tests are considered in Chapter 4.

2.2.2.2 The reinforced concrete slab

The dimensions of the slab and the arrangement of the reinforcement in the test region are shown in Fig.2.2: the sections of Beams UC1 to UC3 are repeated from Ref.35.

The longitudinal slab reinforcement normally consisted of eight 12mm bars, which represent 1% of the cross-sectional area of the slab.

Transverse reinforcement in the test region was set at a standard spacing of 155mm, which was altered slightly to 150mm for Beams UC5 and

UC6 for ease of setting out. 8mm mild steel reinforcement was used instead of 6mm high-yield reinforcement in later tests in the series because the smaller bars were no longer available. In Beam UC1 the transverse bars were placed outside the longitudinal reinforcement, but except where a test was conducted specifically to study the effect of spacing and position of transverse reinforcement, the present author preferred to place it inside the longitudinal bars. This would reduce any possible effect of the transverse reinforcement on cracking and increase, relatively, the effect of the parameter considered.

Because the vertical shear force in the test region is zero, transverse reinforcement can be varied here without affecting the behaviour of the beam. Thus, in both UC2 and UC3, the arrangement of transverse reinforcement was different in the two halves of the test region, giving in effect two test regions which were designated 'A' and 'B' respectively (Fig.2.1). Results from region 'A' were treated quite separately to those from region 'B'.

Outside the constant moment region the transverse reinforcement was designed by the method proposed by Johnson[36] in the case of Beams UC1 and UC2, and in accordance with the rules now in BS5400, Part 5[34] for all others.

2.2.2.3 Shear connection

Headed studs 65mm long and 13mm diameter were used to provide the shear connection between the universal beam and the concrete slab: Fig.2.3 shows the spacing adopted for each beam. This drawing is at variance with Fig.7 of Reference 35 which is incorrect; as may be verified from Fig.5 of the same work.

Shear studs were used in two successive tests before being ground off and replaced by fresh ones.

2.2.3 Construction of test specimens

Stiffeners and flange plates for both the steel girders were welded in the laboratory's workshops. Studs were welded to the beam using the semi-automatic apparatus provided by Crompton-Parkinson.

Ready mixed concrete supplied by Mix-Concrete had been used for UC1 and UC2, and this practice was continued for all subsequent tests. Ordinary Portland cement and aggregate of 20mm maximum size were used throughout. Usually a 28-day cube crushing strength of 30 N/mm^2 was specified, but for Beams UC5 and UC6 a strength of 40 N/mm^2 was required in order to reduce the time lapse between casting the slab and testing the beam.

The shuttering for the concrete slab was supported rigidly along its outer edges but the inner edges were supported on the steel girder, which was in turn supported on two steel trestles placed as near to the jacking points as possible. The shuttering was removed three to four days after casting, but the damp hessian under which the slab was cured remained in place for seven days.

Samples were taken from the concrete mix to make up specimens as follows:

(i) Five prisms 250 x 50 x 50 for shrinkage measurements;

(ii) Three prisms 500 x 100 x 100 for modulus of rupture tests;

(iii) Three cylinders 200 x 100 diameter for indirect tensile tests;

(iv) Not less than nine 150mm cubes for crushing tests.

All specimens were cured under damp hessian for 24 hours, then the shrinkage prisms were stored with the test beam itself while all other specimens were transferred to a curing tank until they were tested. The only exception to this rule was UC2, in which all test specimens were stored with the beam, for reasons which are explained in Ref.35.

2.3 The test rig

The rig used for Tests UC2 to UC7 is shown in Figs.2.4 to 2.6. The load was applied to the beam through two hydraulic jacks, each of 20-tonne capacity, placed at one-third points under the beam and both fed from a single manual pump. The 'H' shaped reaction frames at each end of the beam and the support frames which surround each jack (Fig.2.4) were all built up from standard laboratory "Meccano". The rig for Test UC1 was similar apart from the bearings at the reaction and jacking points. Some of the present author's modifications to that rig are referred to in Ref.35, but a more complete account is given below.

In Test UC1 cylindrical bearings with their axes transverse to the span of the beam were used at all four jacking and reaction points. Therefore, should the bearings be inclined to each other in the transverse direction at the start of the test, or should they become so during the course of loading, the beam would be forced to twist along its length. This was particularly so at the reaction frames, where the cylindrical bearing was 375mm long, and significant torsional stresses developed in the slab of UC1 - as indicated by the direction of cracks shown in Fig.3.1. The problem was overcome in subsequent tests by using spherical seatings : the ball and socket joints used at the jacking points can be seen in Fig.2.5 and the spherical surface of the end bearings is indicated in Fig.2.6.

Another problem experienced in Test UC1 had been the lack of adequate lateral and torsional restraint to prevent instability of the beam, and the more substantial restraint provided at both jacking points in later tests is shown in Fig.2.5. These restraints and the 'H' frames at the end of the beam provided lateral restraint at four points along the beam, and bending in plan was noted during a subsidiary test (UC4A) conducted immediately after Test UC4. The problem was avoided in

subsequent tests by introducing to the bearings at both reaction frames a layer of rollers with their axes in the direction of the span (Fig.2.6).

2.4 Instrumentation

2.4.1 Measurements taken

Fig.2.7 illustrates the positions at which angular and linear displacements were measured. The extension of the slab was measured along grid lines marked on the surface, parallel to the reinforcement, as shown in Fig.2.8, and the width of each crack was measured wherever it crossed a line. The applied load was measured at both jacking points. The displacement gauges mounted horizontally and bearing against the side of the slab were used in the subsidiary test UC4A only, to monitor bending in plan.

2.4.2 Instruments used

During the course of the UC series of tests the same variables have not always been measured with the same instruments so a summary of the instruments used in each test is given in Table 2.2.

The two 20-tonne Phillips electrical strain gauge load cells used in Tests UC1 and UC2 were used for all subsequent tests - one at each jacking point. They were calibrated by Ogunronbi[35] before Test UC1, and checked again after Test UC7.

Strains on the surface of the concrete slab were determined with an 8-in mechanical demec gauge of sensitivity 10.7×10^{-6} per division. Demec points were mounted at four inch centres to give overlapping gauge lengths. The same gauge was used to determine strain in the steel beam for some tests, but here the readings did not overlap and the demec points were placed at eight inch centres.

Crack widths were measured using a microscope with a magnification

of 20 and a graticule marked in 0.05mm divisions.

Dial gauges, where used, were of sensitivity 0.01mm per division and a maximum travel of 25mm; since the maximum beam deflection usually exceeded 30mm the position of the dial gauges monitoring this movement had to be adjusted during the course of the test. In Tests UC3 and UC4, therefore, deflections of the beam were measured with dial gauge calipers of lower sensitivity (.05mm per division) but with a maximum travel of 100mm.

Strains in the steel beam were always measured with electrical resistance strain gauges (e.r.s.g.s), although they were supplemented sometimes by mechanical demec gauges. Temperature-compensated foil gauges 10mm long were used in conjunction, initially, with a Tequipment strain bridge. The bridge was calibrated to give readings in strain, and had a sensitivity of 10^{-6} per division.

Rotations at four points along the beam were measured in Tests UC5 to UC7 using a demountable inclinometer 3in long and of sensitivity 0.333×10^{-3} radians per division.

A more important change to the instrumentation for Tests UC5 to UC7 was the use of a Solartron data-logging system, instead of the strain bridge, in conjunction with the e.r.s.g.s. The data-logger incorporated 150 channels, and the built-in PDP-11 micro-computer was programmed to read the necessary channels and output the measured strains automatically.

In Tests UC5 and UC6 linear voltage displacement transducers were used to measure deflections, and these also were read automatically by the data-logger. Transducers with a range of ± 50mm and sensitivity in the order of 50mm/V were used to measure beam deflections, and slip and uplift were measured with transducers of range ± 25mm and sensitivity approximately 25mm/V. All transducers were calibrated accurately before each test.

For Test UC7 measurements of linear displacements were again taken

with dial gauges because the accuracy of the transducers was found to be inadequate, as discussed in Section 4.2.

2.5 Test procedure

For Tests UC1 to UC4, the load was increased in increments of 10 to 15kN per jack until the maximum load of 100kN per jack was attained. At each increment, the load was held constant for about 45 minutes while readings were taken, and while new cracks and extensions to old ones were marked on the slab with felt-tip pens. A different colour was used to denote each load increment.

Test UC4 was completed in one day, but Tests UC1 to UC3 continued over two days. There was a slight fall off in load overnight, but the original loading curve was regained on continued loading.

A maximum jacking force of 100kN was applied to Beams UC1, UC3 and UC4; this corresponded to a stress in the reinforcement of approximately 330N/mm^2. In UC2 however, three further load cycles were applied in which the jacking force was increased to a maximum of 120kN. Their results have been reported elsewhere[35] and are not discussed here.

In Tests UC5 to UC7 the load was increased and decreased in several cycles, primarily to study the overall behaviour of beams subjected previously to various amounts of cracking. The load was both applied and released in increments, and readings were taken at each. Crack widths and concrete strains were not normally measured during unloading of a beam or during re-loading to the previous maximum, except in the case of two grid lines (one over and one between reinforcing bars) in UC5 and UC7.

The maximum load applied to Beams UC5 to UC7 corresponded to a stress in the reinforcement of approximately 330N/mm^2.

2.6 Auxiliary tests

2.6.1 Material properties

Tension tests were performed (some of them by Ogunronbi) on samples of the universal beam, cover plates and the longitudinal reinforcement, using a 10-tonne Monsanto Extensometer machine. For the mild steel specimens, with their well defined yield point, stress-strain curves were obtained from the x - y plotter, but for the high-yield reinforcing bars, this was supplemented by measuring extension with a Baty dial gauge of length 2in and sensitivity 1/20000in per division. Fig.2.9 shows the dimensions and locations of the steel coupons.

Tests on the concrete specimens were carried out in accordance with BS1881[37] where appropriate, using a 3MN Denison machine. Cube crushing tests were conducted at regular intervals after casting the slab to determine a suitable date for testing the beam.

Demec points were fixed at 8in centres on two opposite faces of the shrinkage specimens once the prisms had dried sufficiently to allow the points to adhere to the surface - typically this time lapse was five days. Readings of shrinkage were taken at regular intervals thereafter using an 8-in Demec gauge.

In Tests UC4, UC5 and UC7 readings of the e.r.s.g.s mounted on the steel beam were taken immediately before casting the slab and at regular intervals thereafter, in order to determine the effects of shrinkage of the slab on the beam. For the same reason dial gauges were located at mid-span and both jacking points of the beams for Tests UC6 and UC7 and readings of these were taken throughout the period between casting the slab and testing the beam.

2.6.2 Test on instrumentation

A separate test, UC6A, was conducted after UC6 to assess the

relative accuracy of the various instruments used to measure the overall beam behaviour and, particularly, to check the output from the data-logger. Fig.2.10 shows the instrumentation for this test. The steel girder used was the same as that in UC6, but the slab was broken off in order that the section properties of the beam could be calculated with greater accuracy and confidence.

Three cycles of load were applied in Test UC6A; in each one the load was increased to a maximum in approximately equal increments and then reduced to zero, also in increments. All instruments were read at each increment.

Beam No.	Parameter varied (All changes given w.r.t. basic values)	Comments
UC1	Length of side of effective concrete area reduced	Steel percentage maintained constant by using more bars of smaller diameter
UC2A	Transverse bars outside main bars	
UC2B	All parameters have basic values	Used as control
UC3A	Transverse bars outside main bars, at narrow spacing	
UC3B	Transverse bars outside main bars, at wide spacing	
UC4	Cover to main bars increased	The shorter side of effective concrete area is necessarily greater than its basic value
UC5	Depth of neutral axis decreased	Achieved by using smaller compression flange plate
UC6	Bar diameter increased	Additional compression flange plate welded to beam to maintain depth of neutral axis at its basic value
UC7	Identical specimen to that in UC4	Used to check repeatability of results

TABLE 2.1 THE PARAMETERS VARIED IN THE UC SERIES OF TESTS

Test	Load	Concrete strain	Crack widths	Beam deflection	Uplift and slip	Steel strains	Output from ERSGs	Beam rotation
UC1	LC	D	M	DG	DG	ERSG	SB	None
UC2	LC	D	M	DG	DG	ERSG	SB	None
UC3	LC	D	M	DGC	DG	ERSG D	SB	None
UC4	LC	D	M	DGC	DG	ERSG D	SB	None
UC5	LC	D	M	T	T	ERSG	DL	I
UC6	LC	D	M	T	T	ERSG	DL	I
UC7	LC	D	M	DG	DG	ERSG D	DL	I

NOTATION:

LC	Load cell	DG	Dial gauge	ERSG	Electrical resistance strain gauge
D	Demec gauge	DGC	Dial gauge calipers	SB	Strain bridge
M	Crack width microscope	T	Transducers	DL	Data-logger
				I	Inclinometer

TABLE 2.2 INSTRUMENTS USED FOR THE UC SERIES OF TESTS

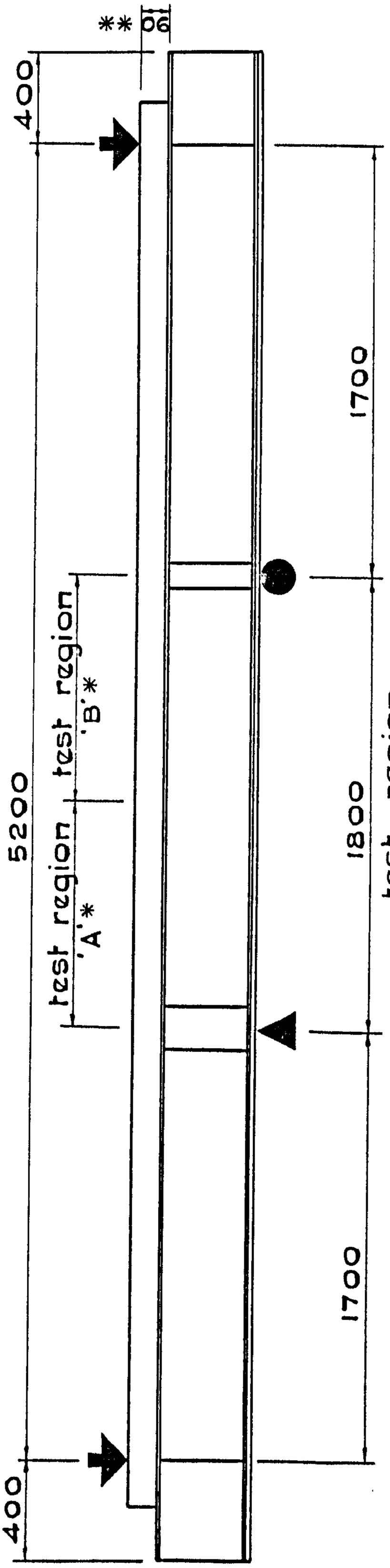

* For beams UC2 and 3 only
** For beams UC4 and UC7
** 110 For beams UC1 to 7

FIG. 2.1 ELEVATION OF BEAMS

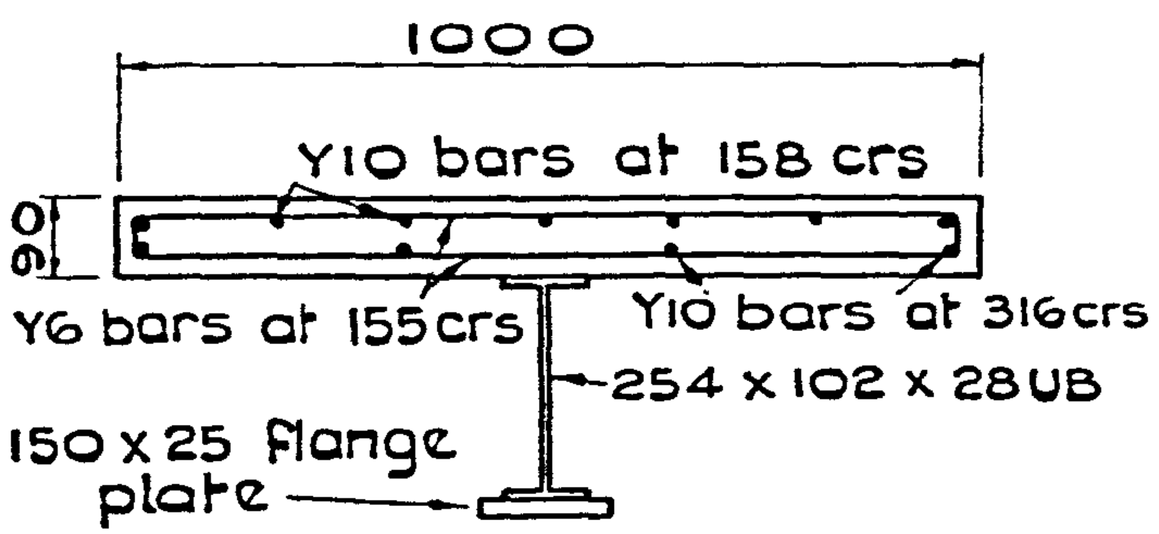

UC1

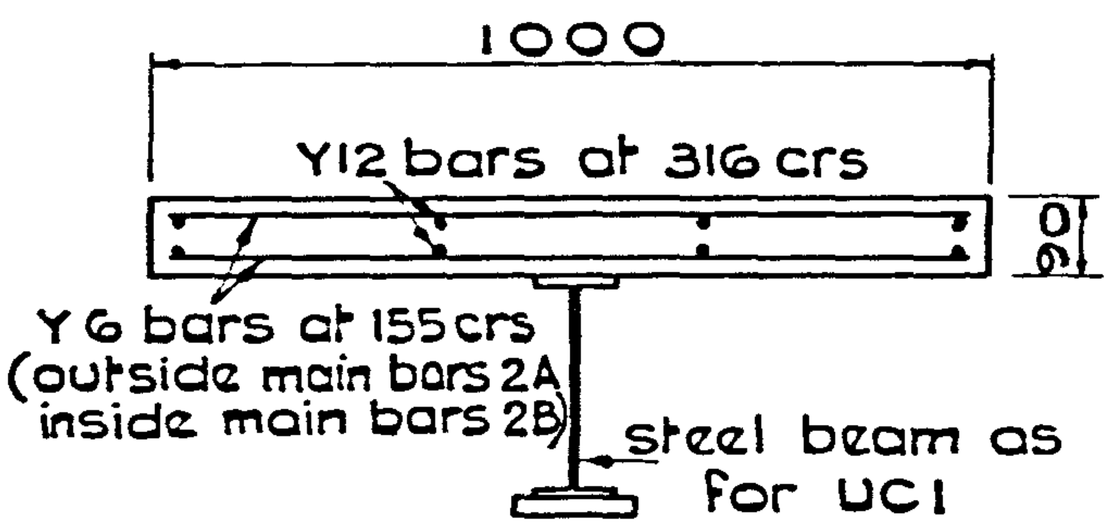

UC2

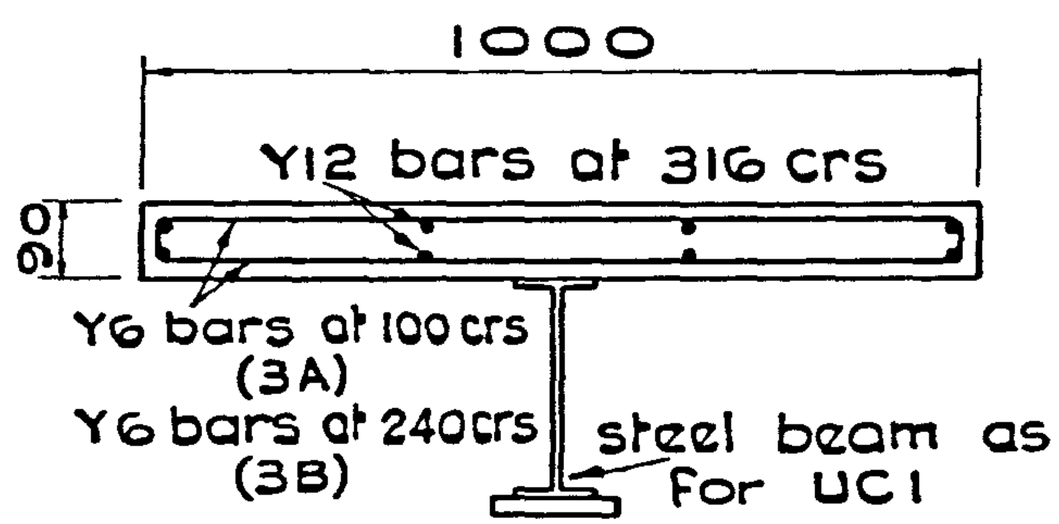

UC3

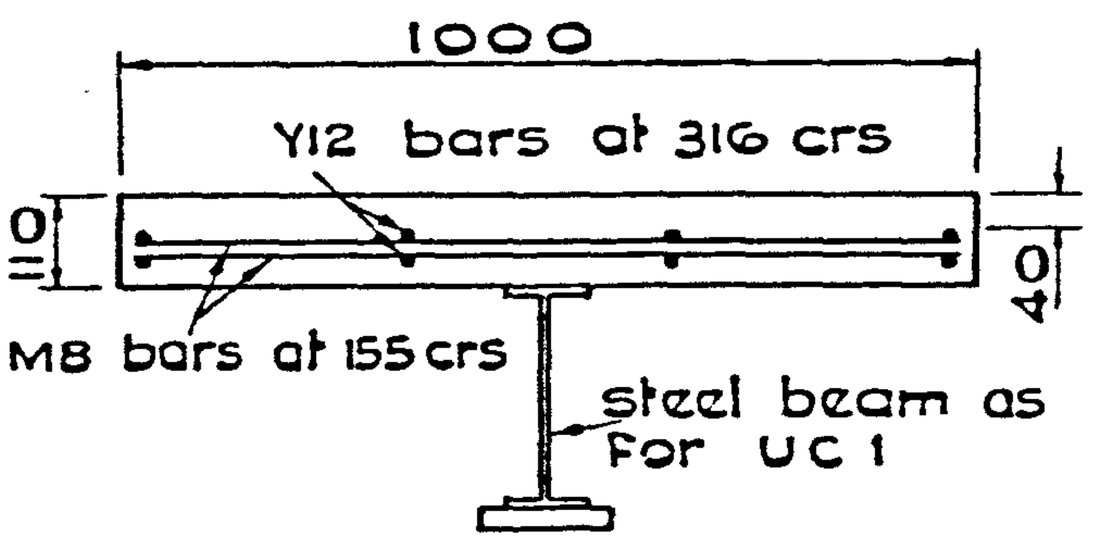

UC4
&7

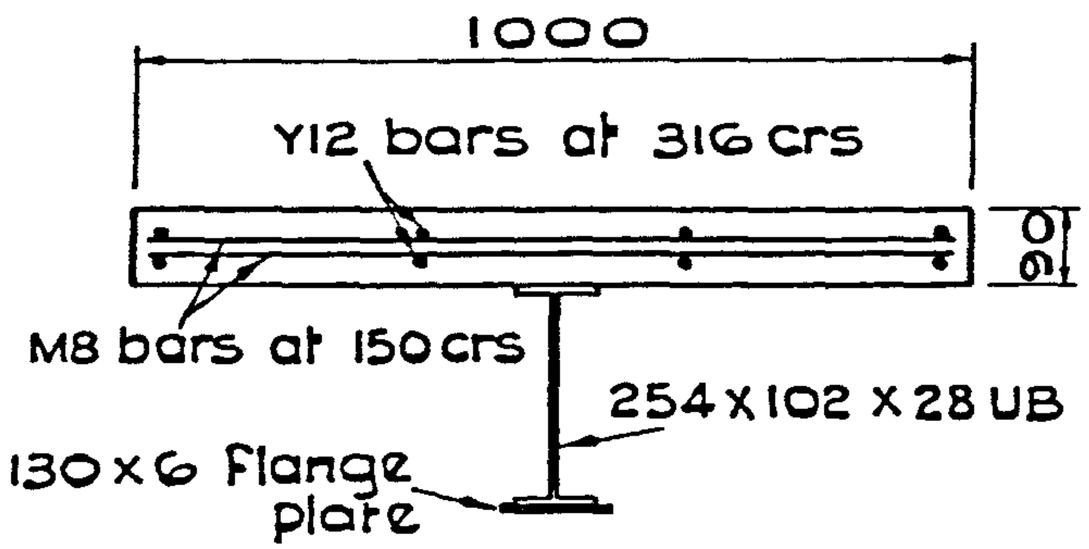

UC5

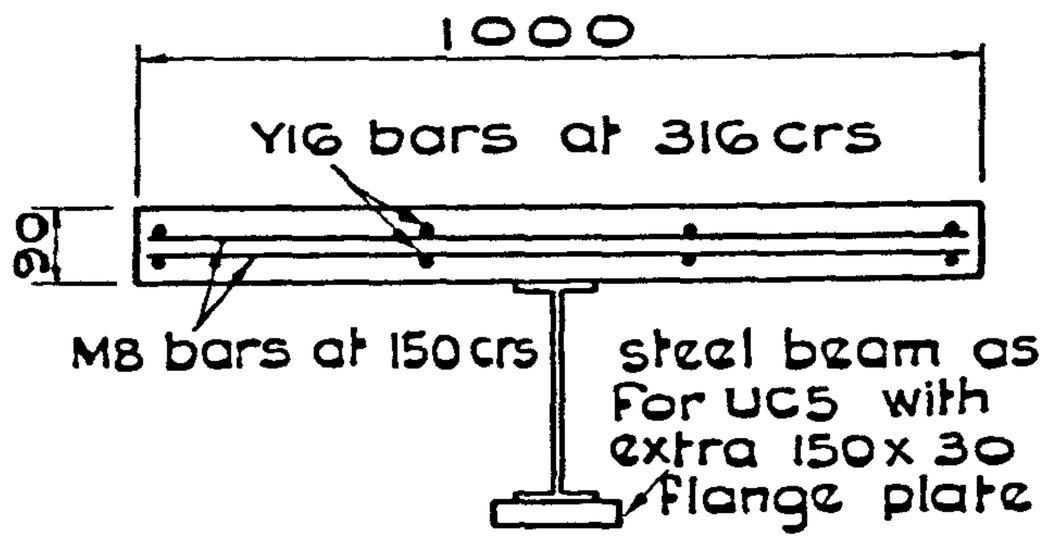

UC6

Notes cover to main bars 20 unless stated.
steel beams and flange plates all grade 43

FIG. 2.2 SECTION THROUGH TEST REGION: BEAMS UC1 to 7

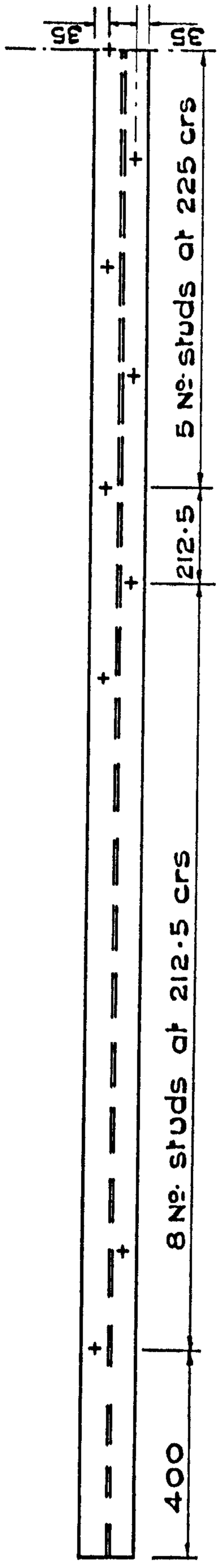

a) Plan on beams UC1-4 & 7

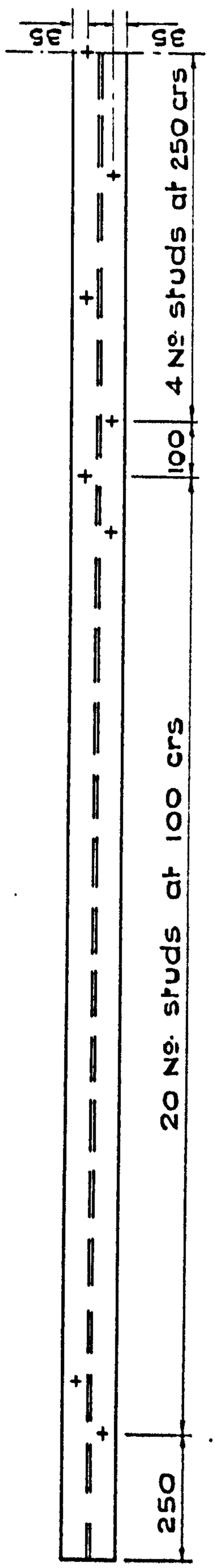

b) Plan on beams UC5 & 6

65mm x 13mm headed studs used throughout

FIG. 2.3 SPACING OF SHEAR CONNECTORS

FIG. 2.4 VIEW OF TEST RIG

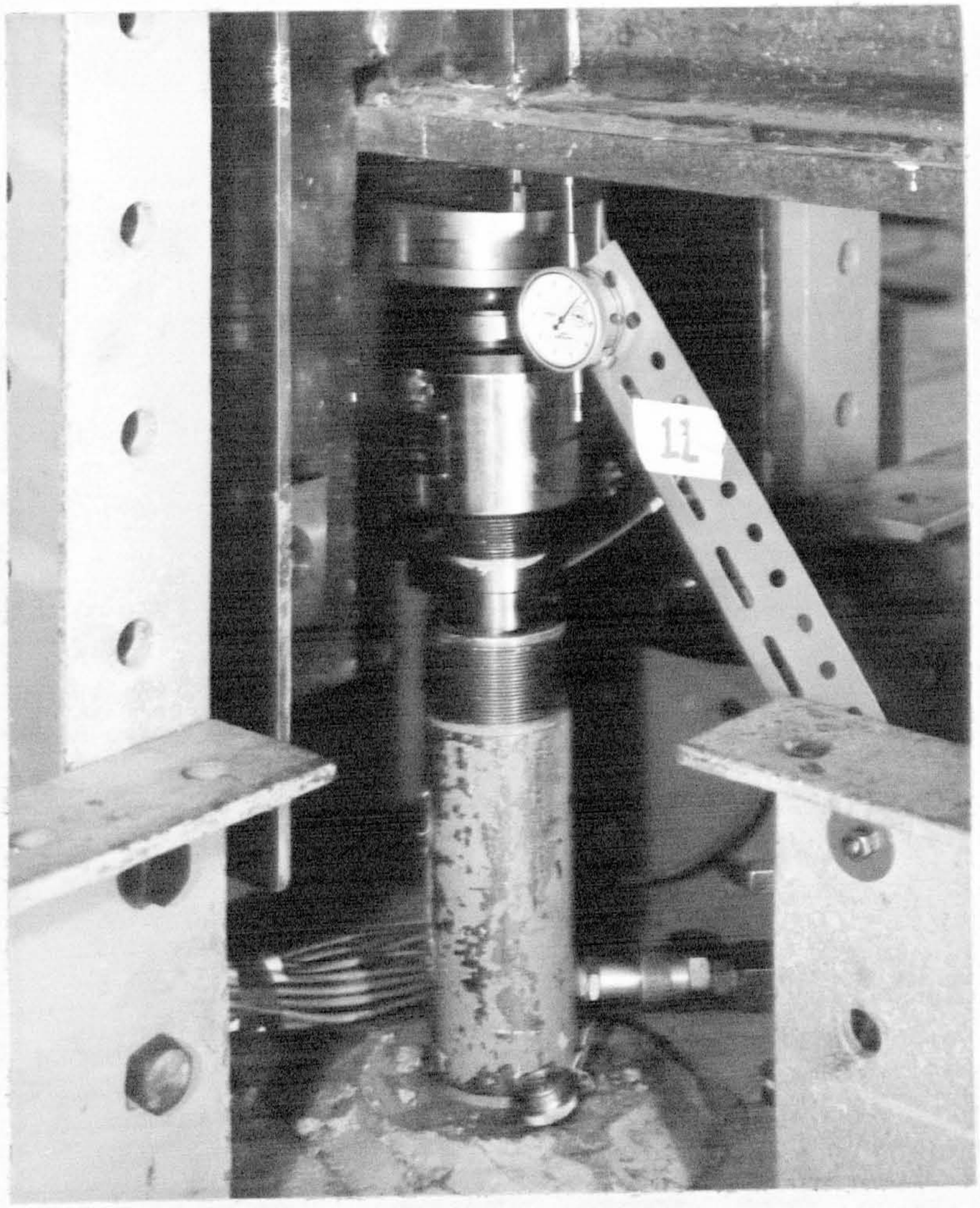

a) Elevation

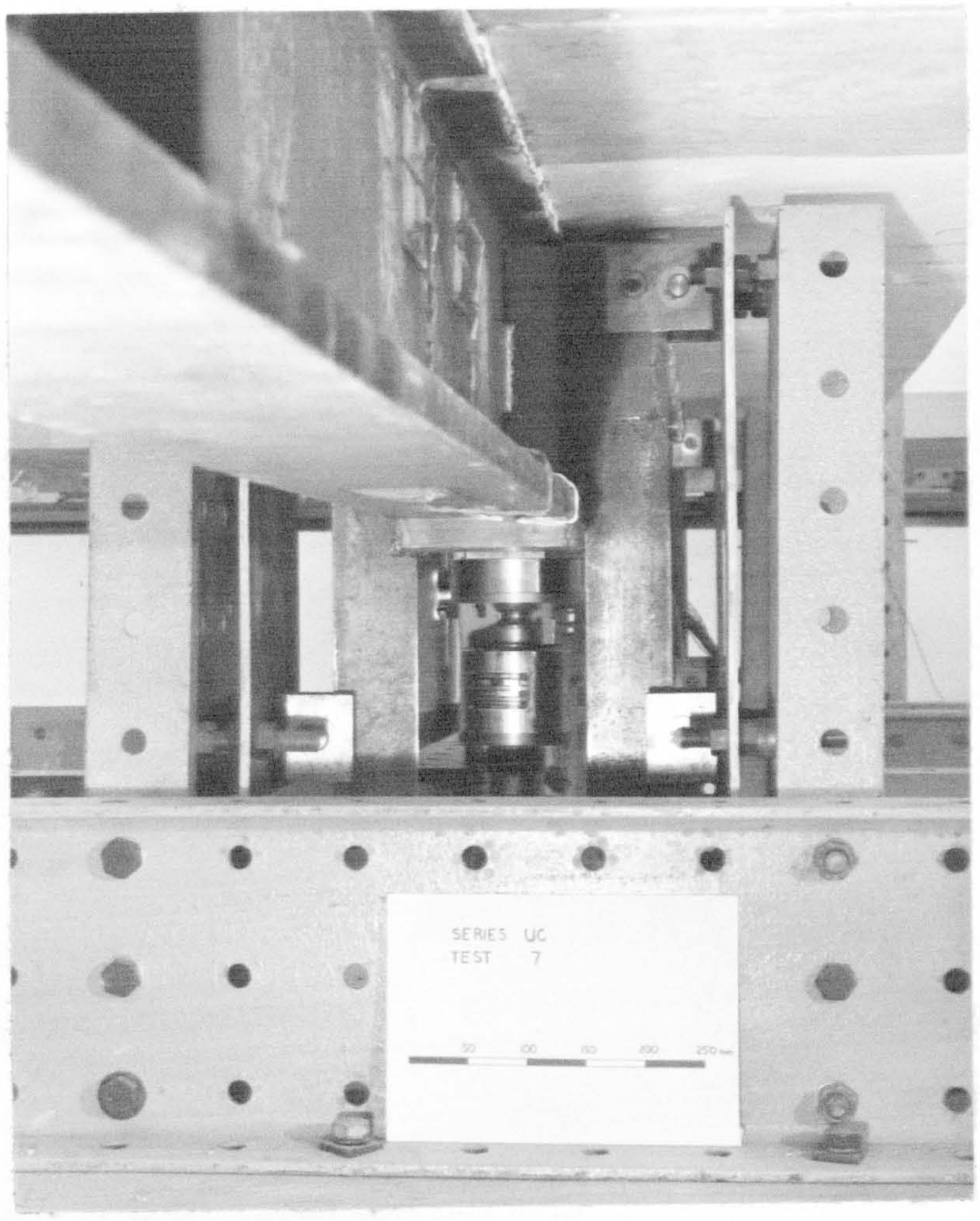

b) End view

FIG. 2.5 METHOD OF LOADING AND STABILISING BEAMS UC2-UC7

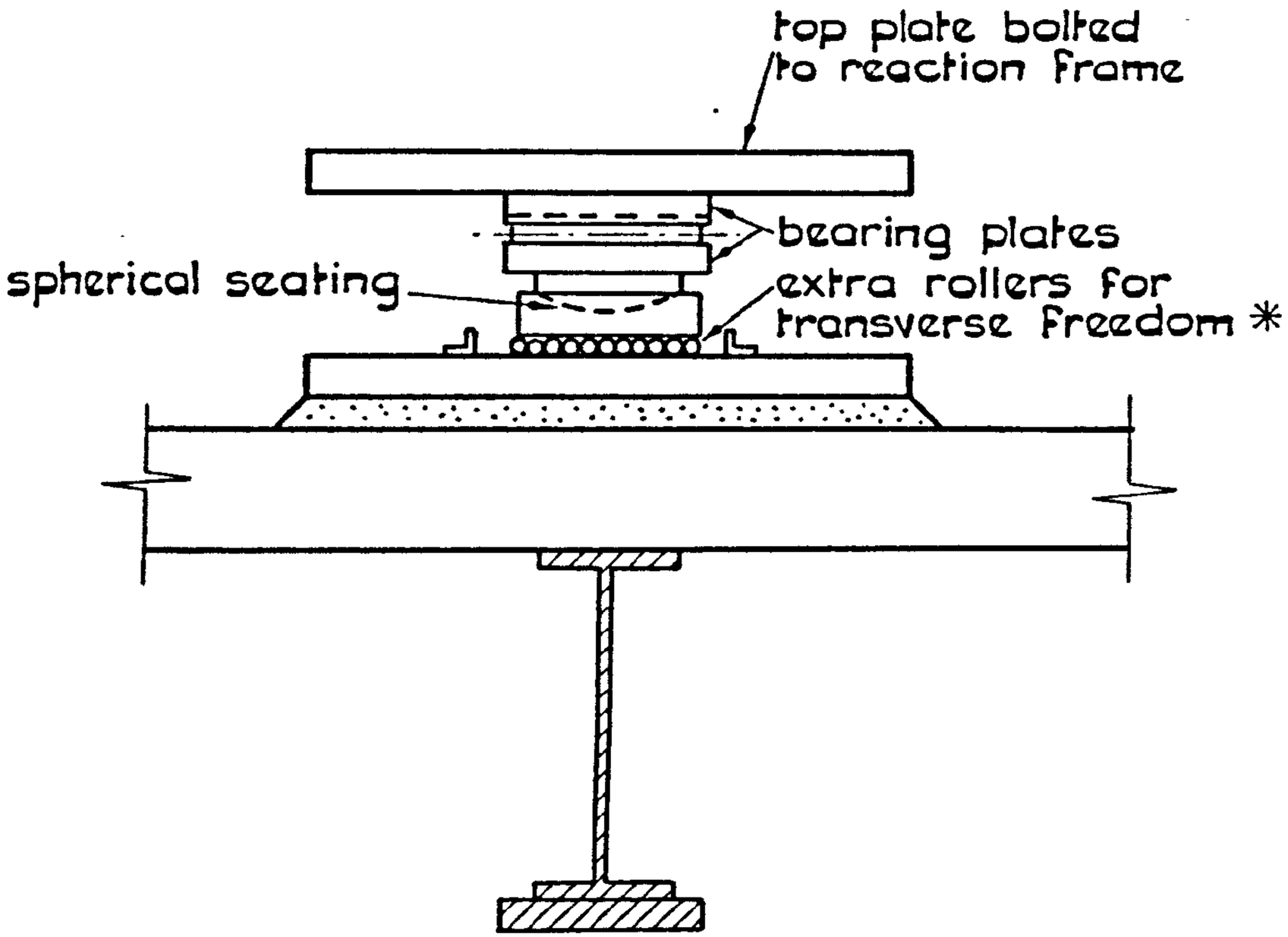

Cross section

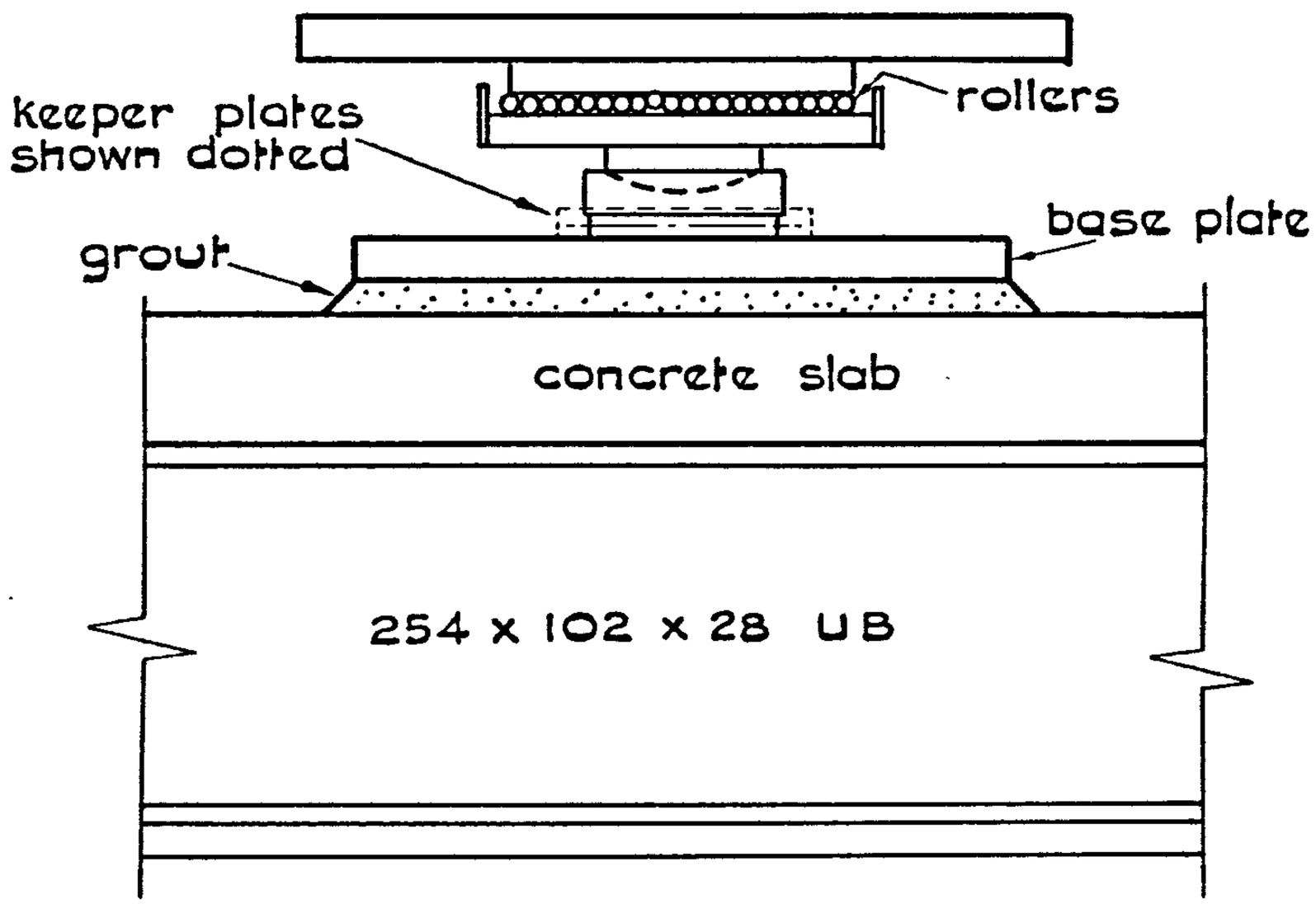

Elevation

* Note keeper plate and extra rollers in tests UC5 to 7 only

FIG. 2.6 END BEARINGS FOR TESTS UC2-7

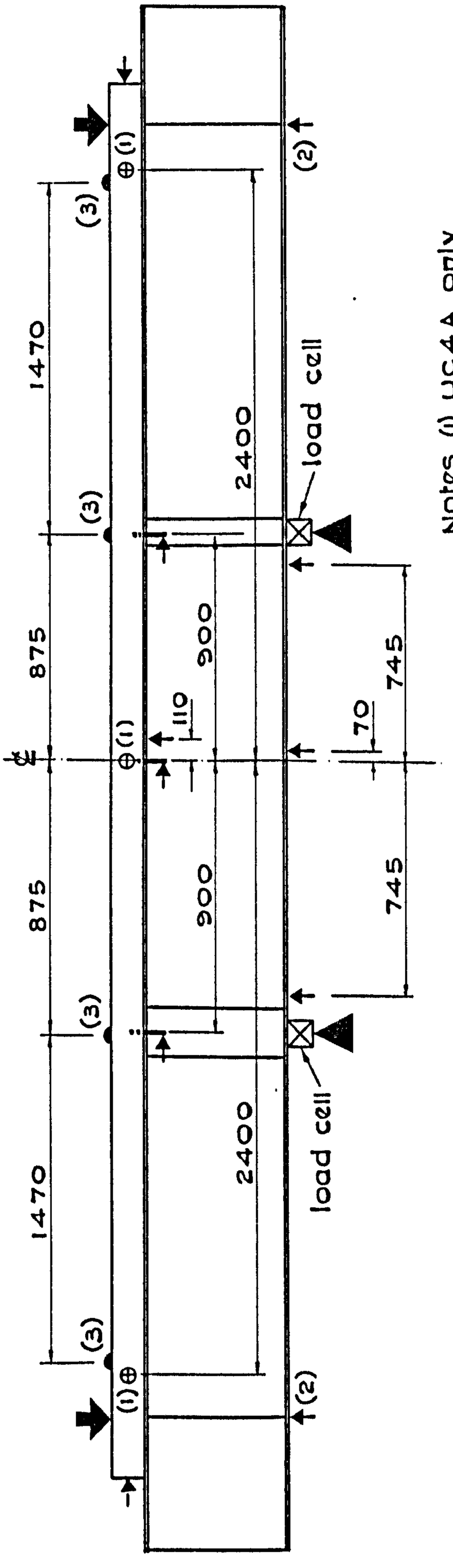

FIG. 2.7 MEASUREMENT OF DISPLACEMENTS FOR TESTS UC1-7

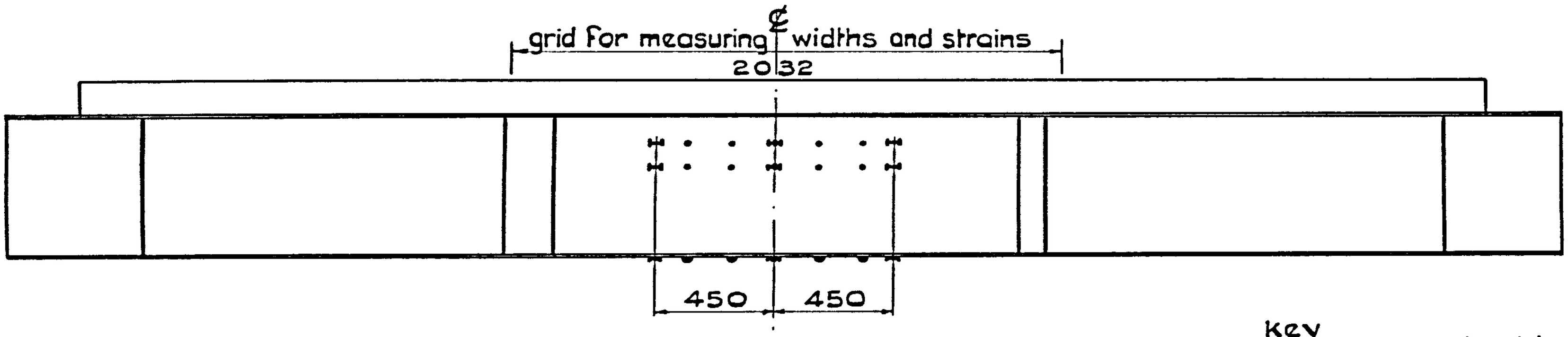

Elevation

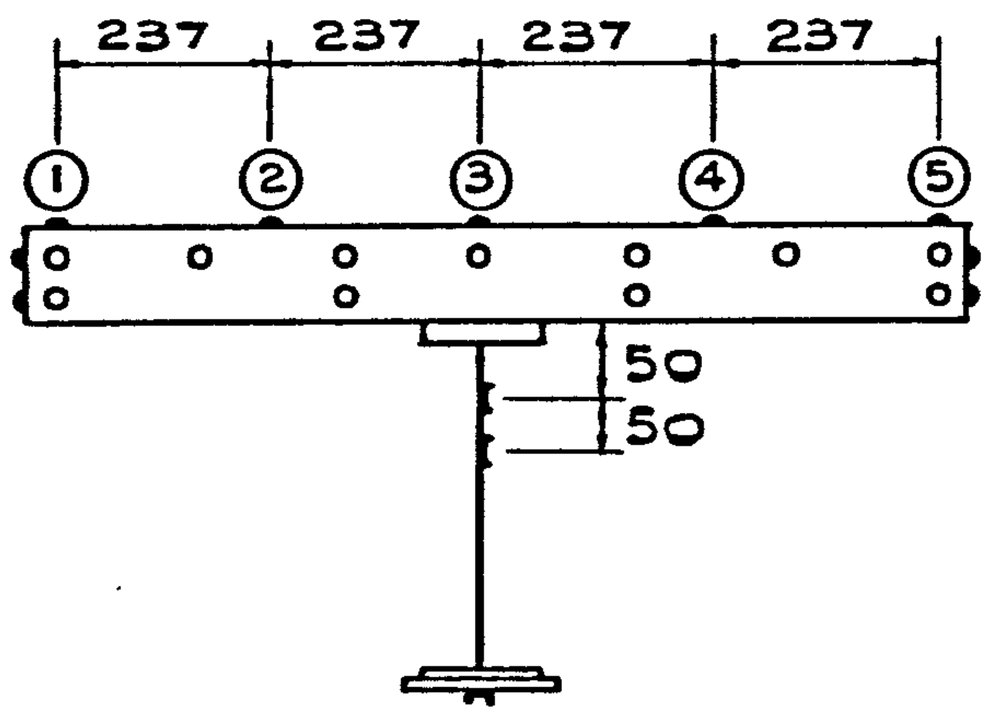

Section UC1

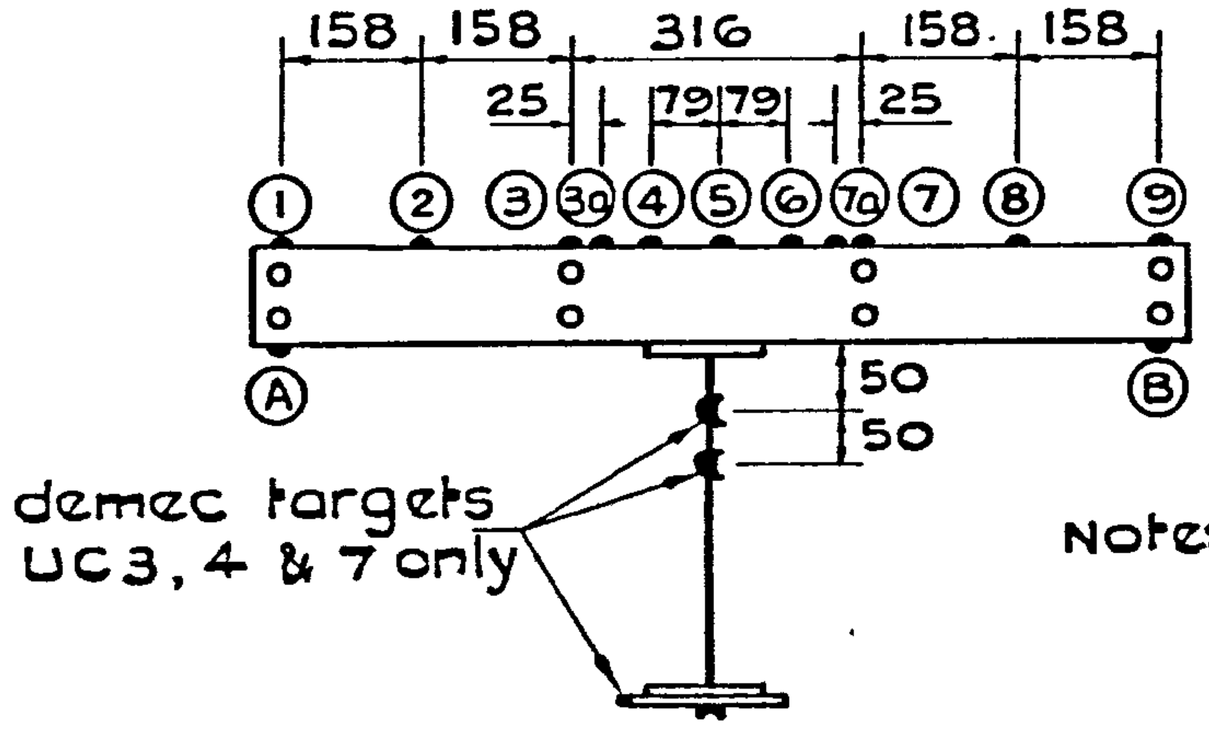

Section UC2-7

Key

Electrical resistance strain gauge

• Targets for demec gauge

③ Grid line number

Notes i) Lines 3A and 7A for UC6 and 7 only.

ii) Lines A and B omitted UC7.

FIG. 2.8 MEASUREMENT OF STRAINS FOR TESTS UC1-7

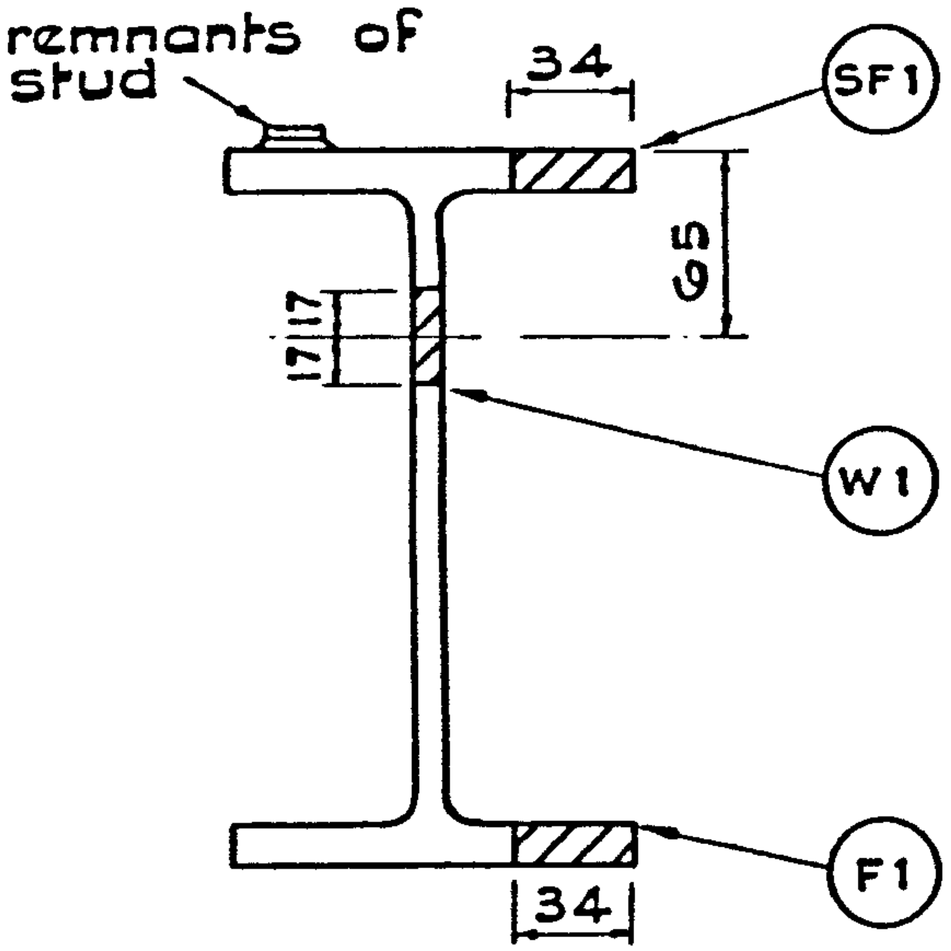

Location

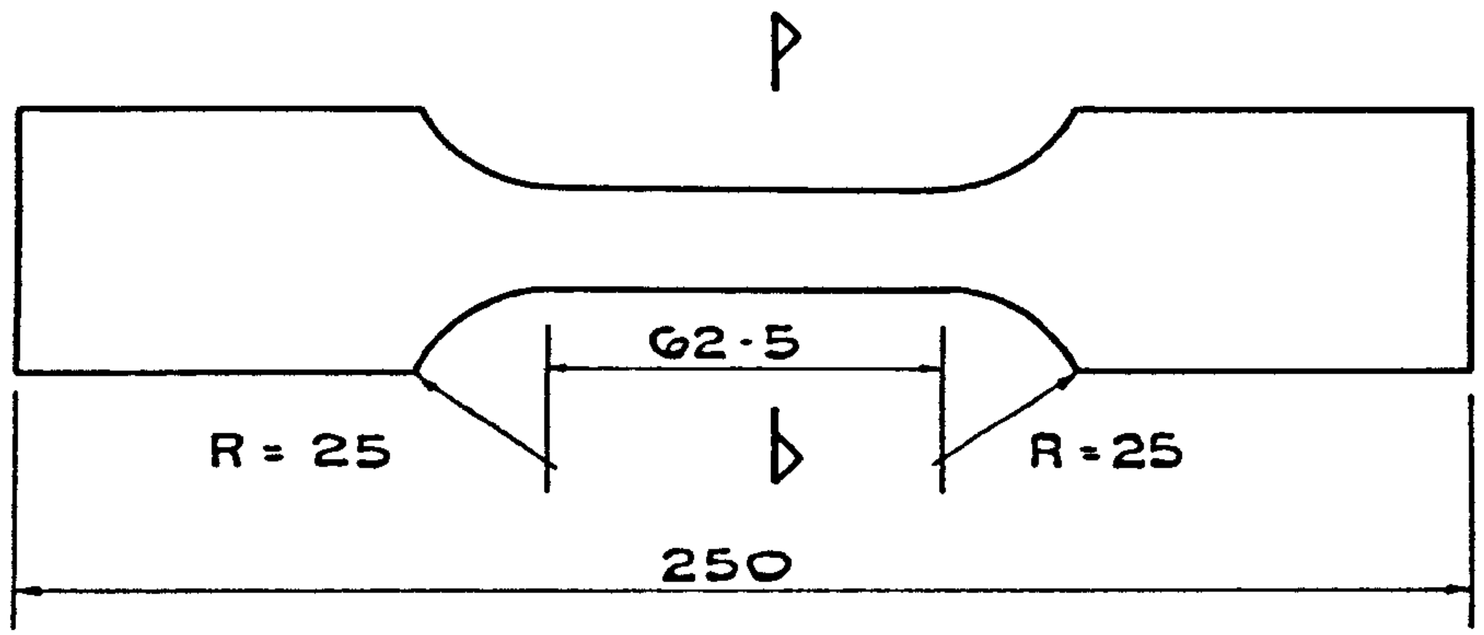

Elevation

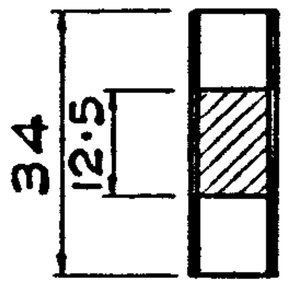

Section

COUPONS FROM 254×102×28 U.B.

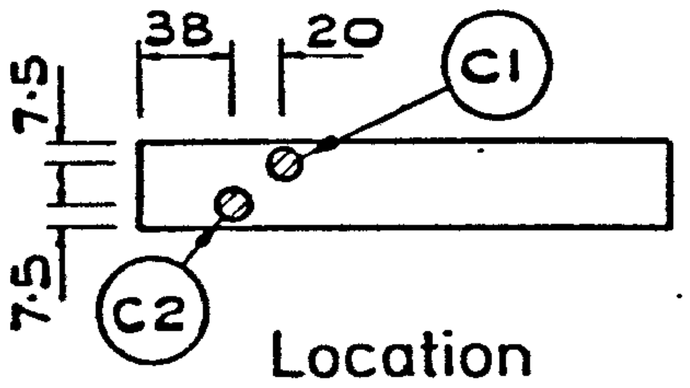

Location

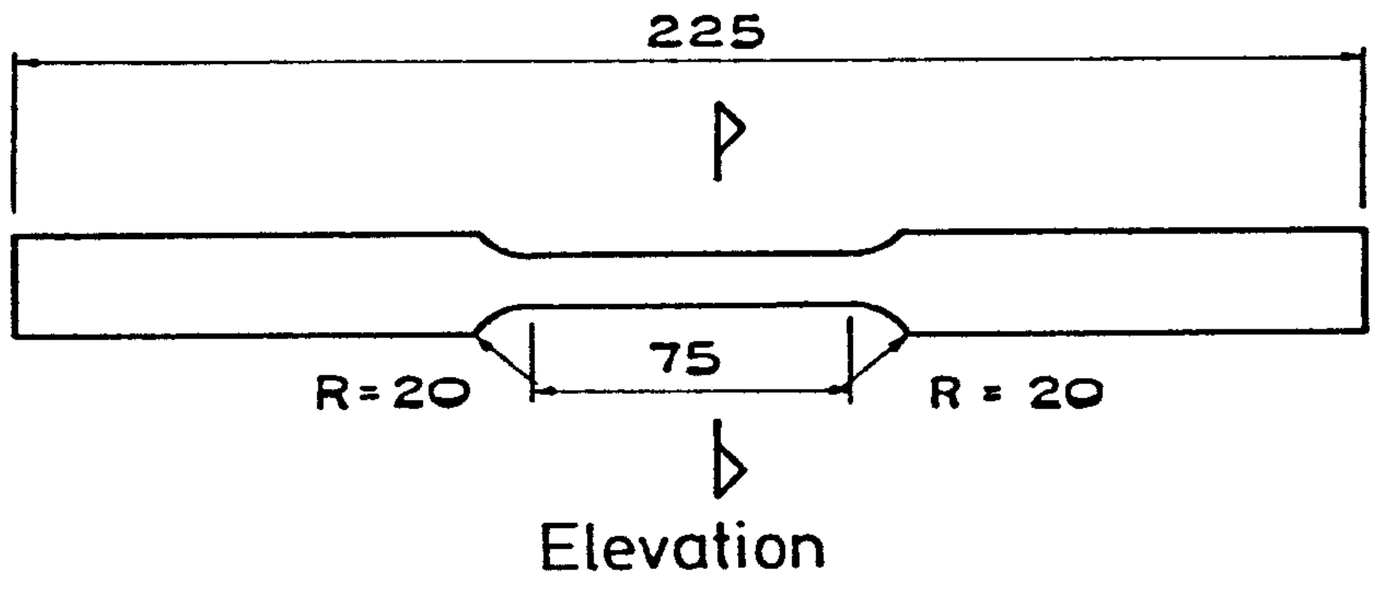

Elevation

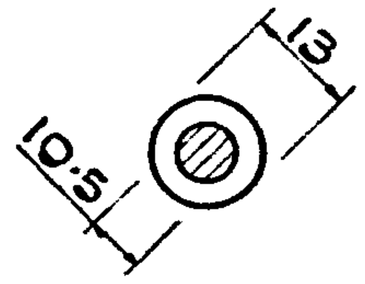

Section

COUPONS FROM 150×30 FLANGE PLATE

FIG. 2.9 LOCATION AND DIMENSIONS OF STEEL COUPONS

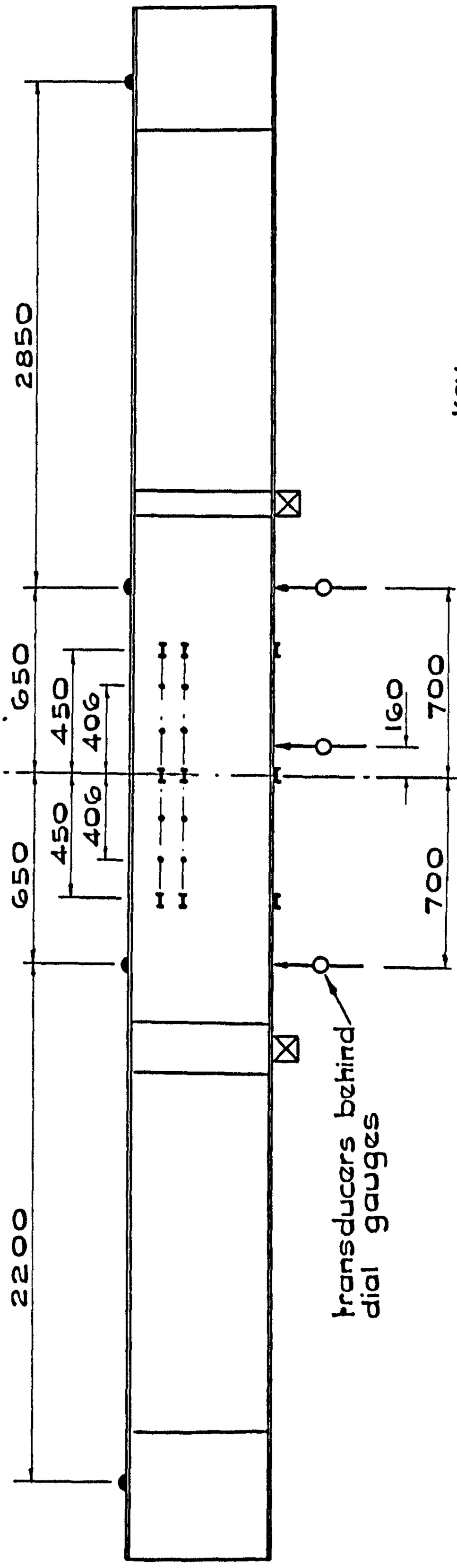

FIG. 2.10 INSTRUMENTATION FOR TEST UC6A

CHAPTER 3

RESULTS OF TESTS TO INVESTIGATE CRACKING

3.1 Introduction

The results which are relevant to the global behaviour of Specimens UC1 to UC7 are presented in this chapter, as are the results of the auxiliary tests.

The large number of measurements of crack width and crack spacing precludes the possibility of listing each individual result here, but this data has been analysed statistically and the results are given in Chapter 4.

3.2 Formation of the crack pattern

Initial cracking occurred when the applied moment was in the range $0.10M_{ynt}$ to $0.23M_{ynt}$, where M_{ynt} is the moment that would cause yield in the upper layer of reinforcement in the absence of tension-stiffening. Usually, two or three wide cracks formed across the full width and depth of the slab, together with a number of smaller cracks which were concentrated around the outermost reinforcing bars. In Specimens UC2A and UC6 a single, short crack formed first, but during the next load increment larger cracks of the type noted above appeared.

In the early stages of cracking, increasing the load caused new cracks to develop both over the reinforcing bars and between them, but later on the only new cracks to form were those over the bars. A further increase of the load resulted in these cracks propagating outwards, and some of them meeting in between the bars. The final crack patterns of each specimen are shown in Fig.3.1; these correspond to a maximum applied moment in the range $0.75M_{ynt}$ to $0.80M_{ynt}$. We note that:

(a) More cracks form over or near to the longitudinal reinforcing bars than between them. This effect is not pronounced in Beam

UC1, where the bar spacing is small, nor in Beams UC4 and UC7 where the minimum cover is quite large, but is apparent in all the other tests.

(b) The different arrangement of transverse steel in the two halves of Beam UC2 has not caused any obvious difference in the final crack spacing.

(c) There is no obvious difference in the crack spacing in the two halves of Beam UC3. However, all of the cracks which have formed across the full width of the slab in UC3B are located over or very near to the transverse reinforcing bars.

(d) A number of short, random cracks were visible on the surface of the slab of Beam UC6, in addition to the normal cracking pattern. Most of these were the result of "crazing" of the surface of the slab before the test commenced, and did not attain a measurable width under the action of external loads.

3.3 Beam curvature

The moment-curvature plots for the Beams UC1 to UC7 are shown in Figs.3.2 to 3.8. These have been derived as follows.

The vertical axis is the externally applied moment (M), which is calculated from the average of two load cell readings - one at each jack. Curvature is the average of three values derived from the three columns of e.r.s.g.s mounted on the steel girder in the constant moment region (Fig.2.8). Strains were measured with respect to the state of the beam immediately before the first increment of external load was applied.

The curvature of the composite beams increased in proportion to the applied moment until first cracking occurred. Thereafter, increasing the moment caused a gradual reduction in the beam stiffness and the curvature increased more rapidly than before. However, if at any stage after cracking the moment was slowly reduced and then increased to its former

value, the moment-curvature relationship during that sequence was linear.

The beam's curvature did not reduce to zero when the external moment was removed. Instead it returned to some value of residual curvature, which was increased when the maximum moment to which the beam had been subjected was increased.

The lines labelled "uncracked", "no-tension" and "no-tension (corrected)" in Figs.3.2 to 3.8 are discussed in Section 4.5.

3.4 Concrete surface strain

The surface strain in the concrete along the various grid lines was obtained from the demec gauge readings using a computer analysis. This gave the mean surface strain along each gauge length (ε_{mg}) and over the length of the grid line ($\bar{\varepsilon}$). Examples of each are illustrated in Figs.3.9 and 3.10 respectively.

The surface strain of the slab increased uniformly with increasing load throughout the constant moment region until cracking occurred. Subsequent loading caused much greater extensions of the slab in the region of the cracks than between them, and this is the reason for the large variation in ε_{mg} along a grid line, as illustrated in Fig.3.9. Where demec gauge readings were taken over a section of uncracked concrete its length was often seen to decrease as the applied moment was increased.

For each load stage the area under the strain diagram (Fig.3.10) has been integrated, and divided by the breadth of the slab to give the average surface strain over the length and breadth of the constant moment region. This average strain is denoted by $\bar{\varepsilon}_s$, and values have been derived for most load stages of Tests UC1 to UC7. However, during the unloading-reloading stages (only) of Tests UC5 and UC7, $\bar{\varepsilon}_s$ has had to be estimated from readings along two grid lines only.

The M-$\bar{\varepsilon}_s$ curves for Specimens UC1 to UC7 are shown in Figs.3.11 to

3.16: the moment is expressed as a proportion of M_{ynt}, and the strain is given with respect to the state of the slab immediately before the first increment of external load was applied. The pattern of the $M-\bar{\varepsilon}_s$ curve is similar to that of the moment-curvature relationship already discussed.

The lines labelled "no-tension" and "uncracked" in Figs.3.11 to 3.16 are explained in Sections 4.3 and 4.6.2 respectively.

3.5 Slip

Fig.3.17 illustrates how the slip at the interface of the girder and the slab varies along Beams UC1 to UC4 and UC7. Results are not available for Beams UC5 and UC6, for the reasons given in Section 4.2.

Two sets of curves are given in Fig.3.17: one corresponds to the maximum load applied to the beam, and the other to approximately 0.4 times the maximum load. The accurate values of the loads applied to each beam are listed in the figure.

3.6 Auxiliary tests

3.6.1 Shrinkage prisms

Two examples of the shrinkage-time relationship of the trial prisms are shown in Fig.3.18. The shrinkage strain has been calculated by taking the average of ten experimental values - one from each side of the five shrinkage prisms. The day on which the first demec gauge readings were taken is indicated.

The average shrinkage of the trial prisms from the seventh day after casting to the day (or days) that each test was conducted has been determined and the values are listed in Table 3.1: no experimental results are available for Test UC1. The figures given are at variance with those in Table 2 of Reference 35 which, it is believed, are estimates of the free shrinkage strain of the slab of the composite beam.

3.6.2 Material properties

The results of the tests on the steel coupons and the concrete specimens are given in Tables 3.2 to 3.4.

3.6.3 Accuracy of the instrumentation

Typical sets of results from Test UC6A are illustrated in Figs.3.19 and 3.20. The first compares the strain profiles in the beam, as derived from electrical and mechanical strain gauges. The strains plotted at each level are the average values of three e.r.s.g. readings and four demec gauge readings.

The curvature in the beam has been calculated using various sets of measurements, and the results are given in Fig.3.20. In the case of the electrical resistance and demec strain gauges, the curvature was taken to be the slope of the line of best fit to the results in Fig.3.19. When deriving the curvature from dial gauge, transducer and inclinometer readings, it was assumed that the test region of the beam deflected in a circular arc of radius equal to the inverse of the curvature. The line labelled "calculated" was derived by taking E is equal to 207kN/mm^2, and by assuming the nominal cross-sectional properties of the universal beam and cover plates.

Test	Period after casting (days)	Measured strain
UC1	-	- (1)
UC2	7-42	430
UC3	7-41	472
UC4	7-18	280
UC5	7-41	630 (2)
UC6	7-25	275
UC7	7-21	271

Notes: (1) Test results not available

(2) Exceptionally weak mix

TABLE 3.1 MEASUREMENT OF SHRINKAGE IN TRIAL PRISMS UP TO DAY (OR DAYS) OF TEST

Bar diameter and type	0.2% proof stress (N/mm^2)		
	Sample 1	Sample 2	Sample 3
Y10	478	475	480
Y12	440	437	434
Y16	507	507	485

TABLE 3.2 0.2% PROOF STRESS OF SAMPLES OF REINFORCEMENT

Location	No. specimens tested	Yield stress (N/mm^2)
Web (W1)	1	339
Flange (SF1)	1	311
Flange (F1)	1	280
Cover plates (C1 and C2)	2	326

TABLE 3.3 YIELD STRENGTH OF STEEL COUPONS

Test	Crushing strength of 150mm cubes (N/mm^2)	Modulus of rupture (N/mm^2)	Indirect tensile strength (N/mm^2)	Age (days)
1	39.6	4.3	3.2	28
2	38.8(1)	2.8	3.1	37
3	40.1	4.3	3.4	40
4	51.6	5.3	3.8	19
5	24.8	3.8	2.5	54
6	43.6	4.8	3.1	36
7	50.1	4.8	4.0	21

Note: (1) Air-cured. All other specimens water-cured to BS1881

TABLE 3.4 PROPERTIES OF CONCRETE ON LAST DAY OF BEAM TEST

(Average results from 3 specimens)

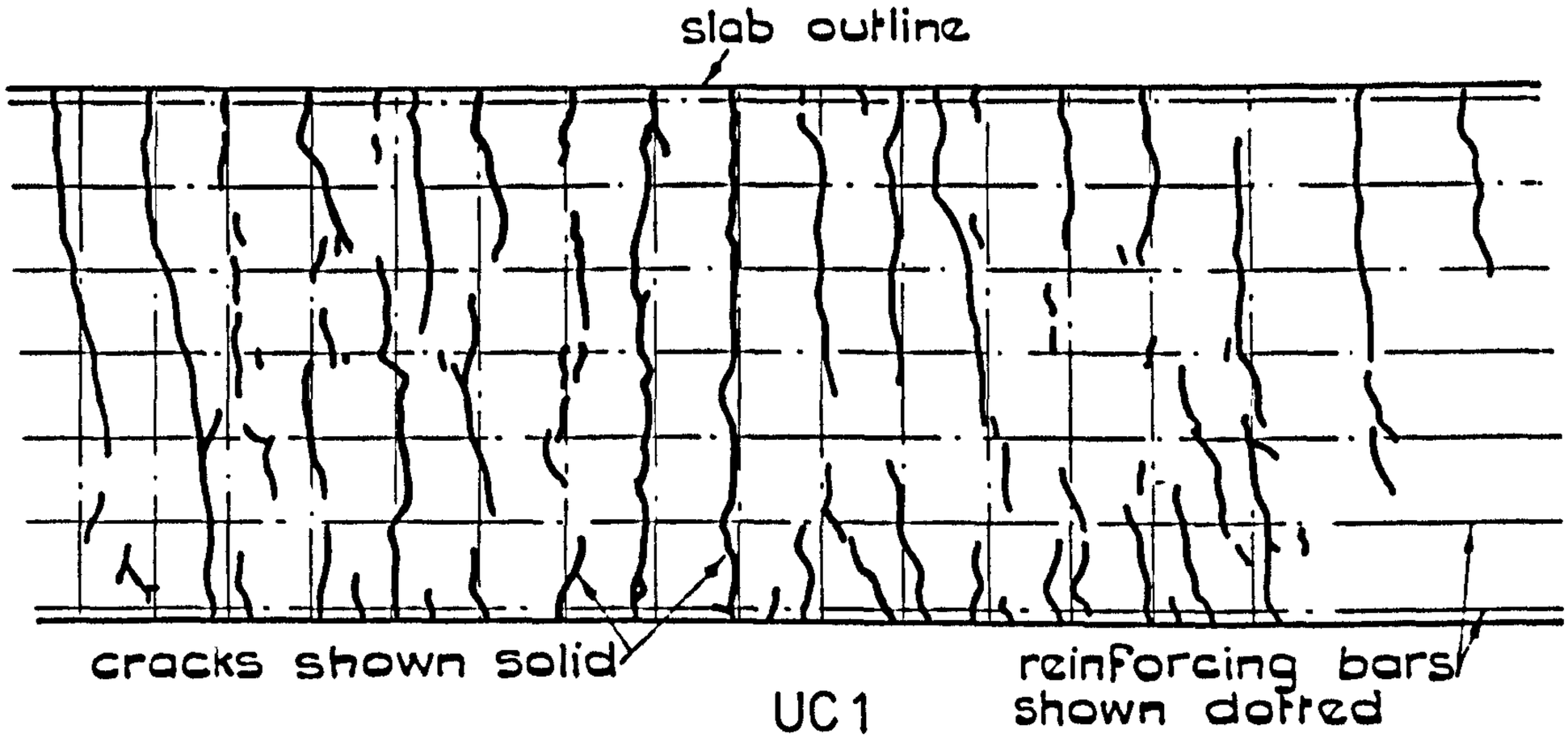

UC 1

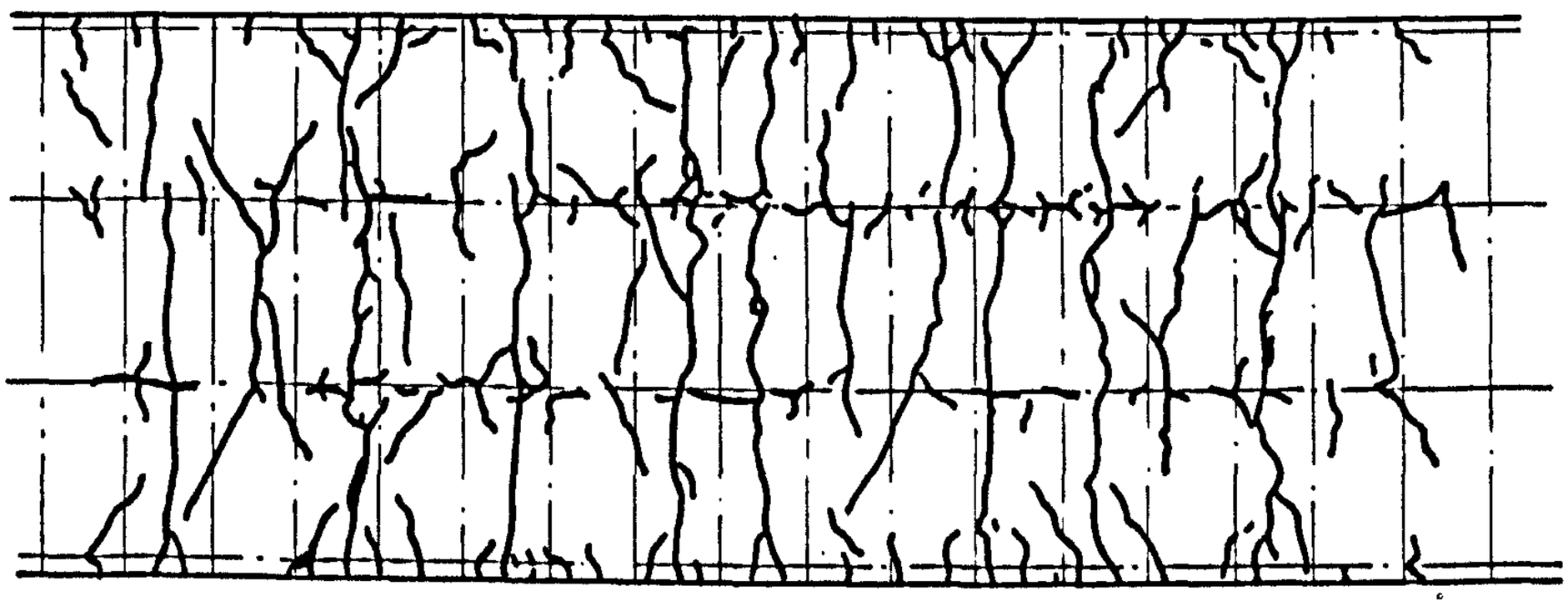

UC 2A

UC 2B

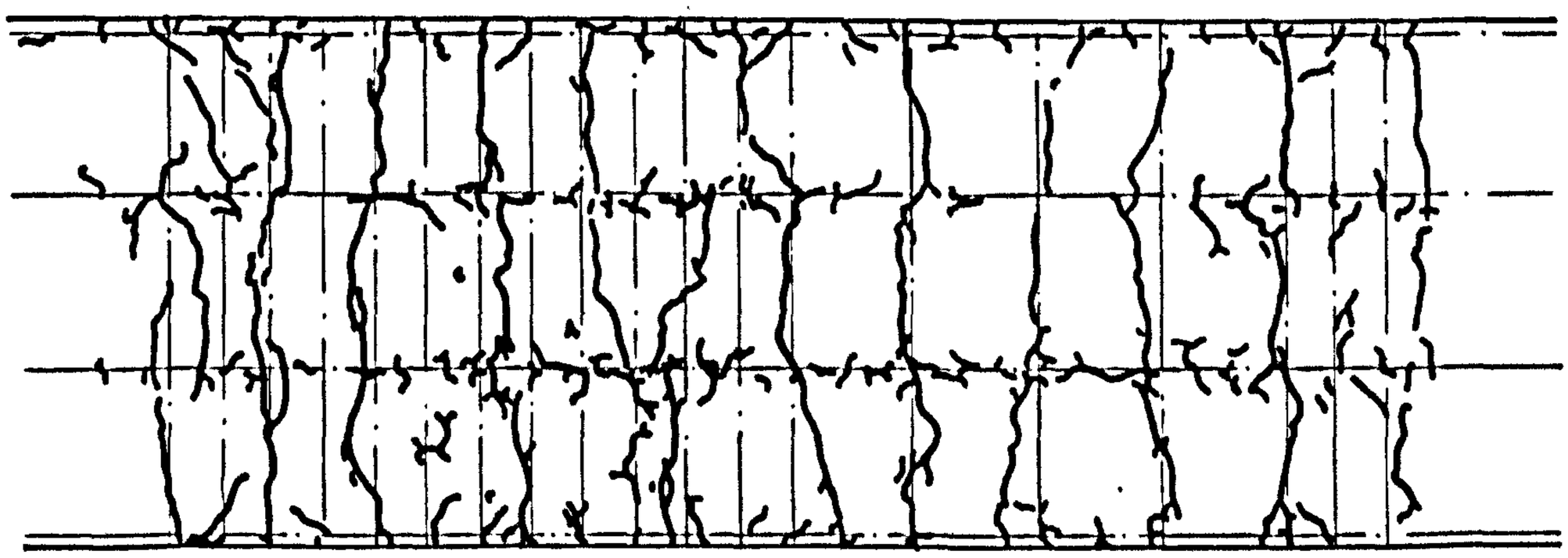

UC 3A

UC 3B

FIG. 3.1 FINAL CRACK PATTERNS FOR BEAMS UC1 - UC7 (continued..)

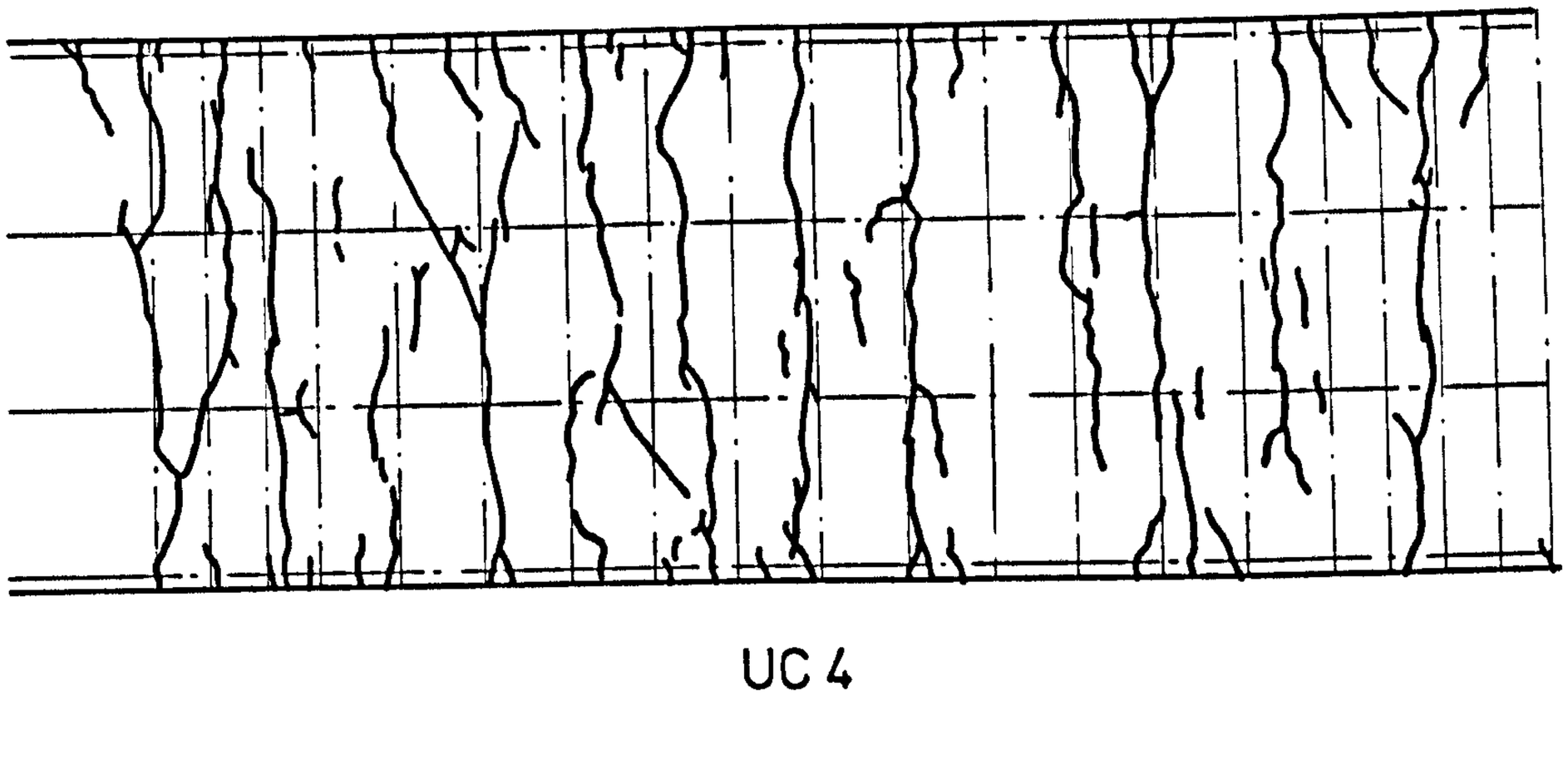

UC 4

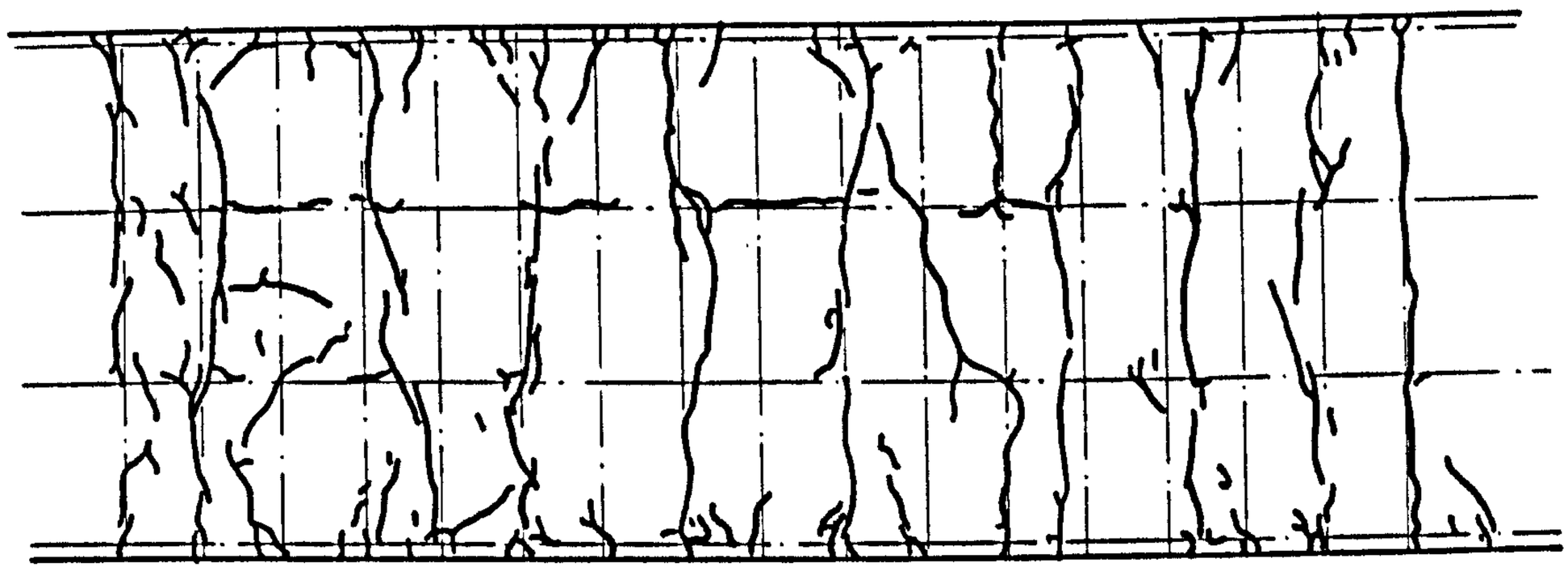

UC 5

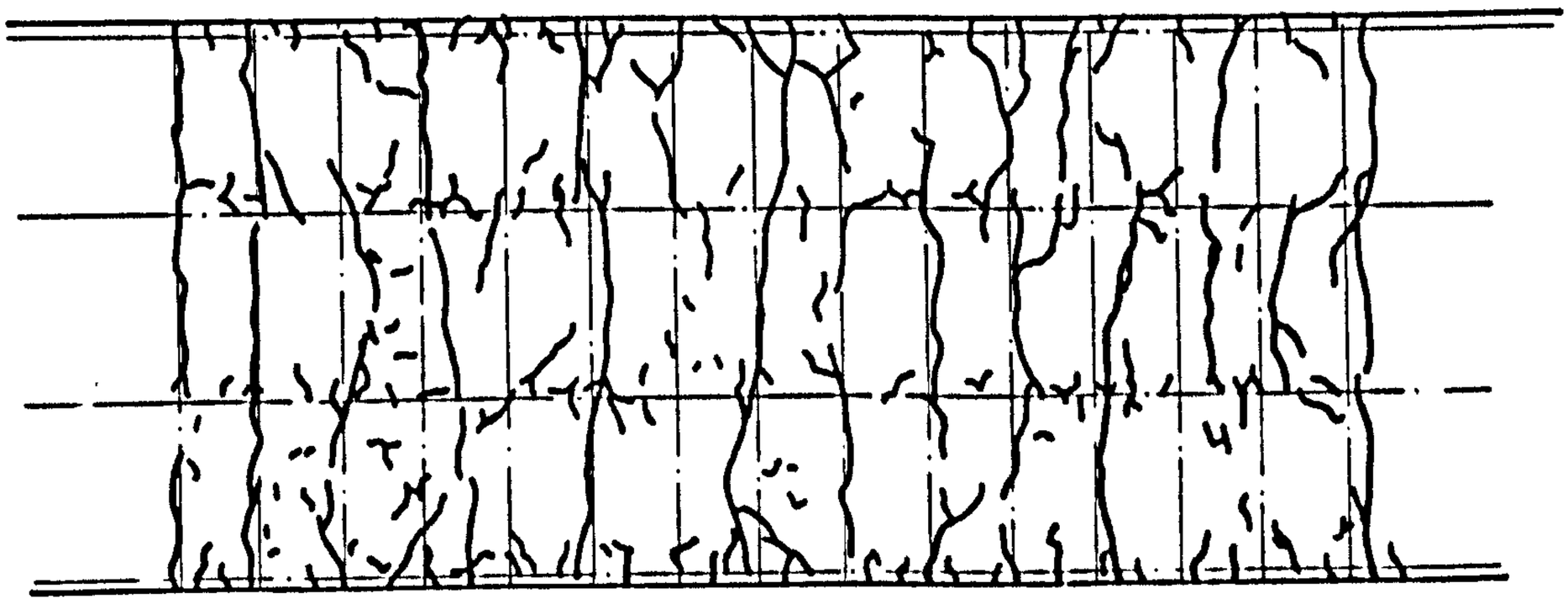

UC 6

FIG. 3.1

(continued...)

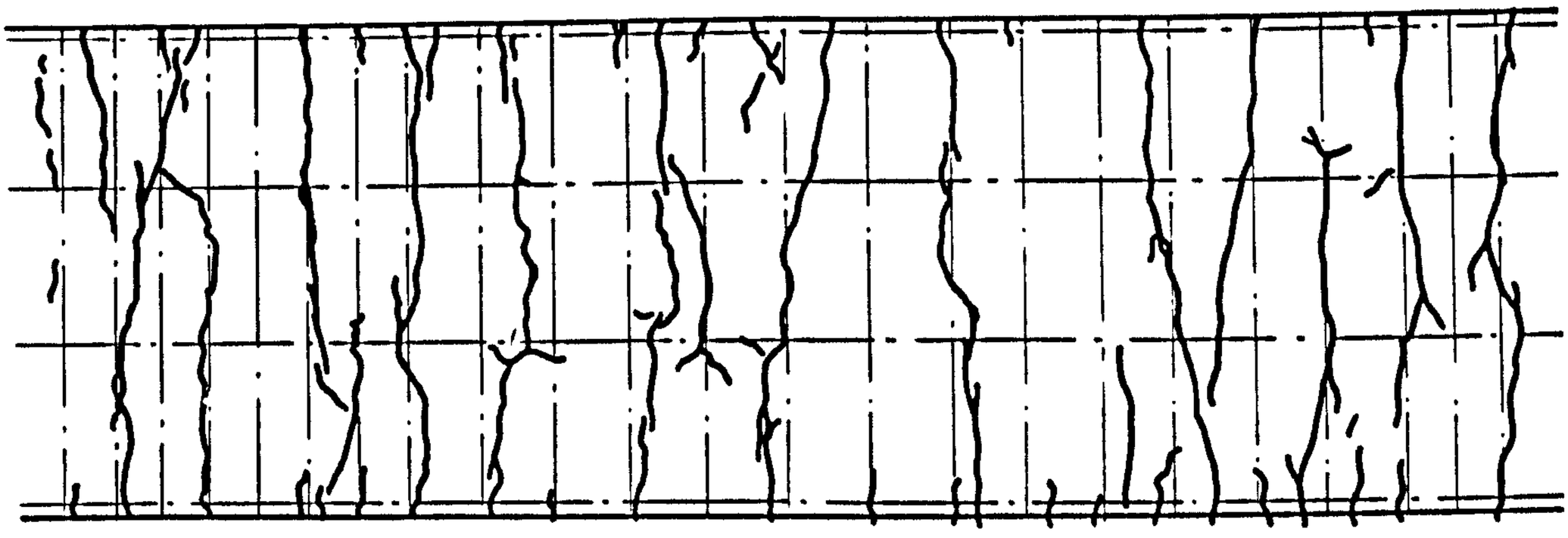

UC 7

FIG. 3.1 (concluded)

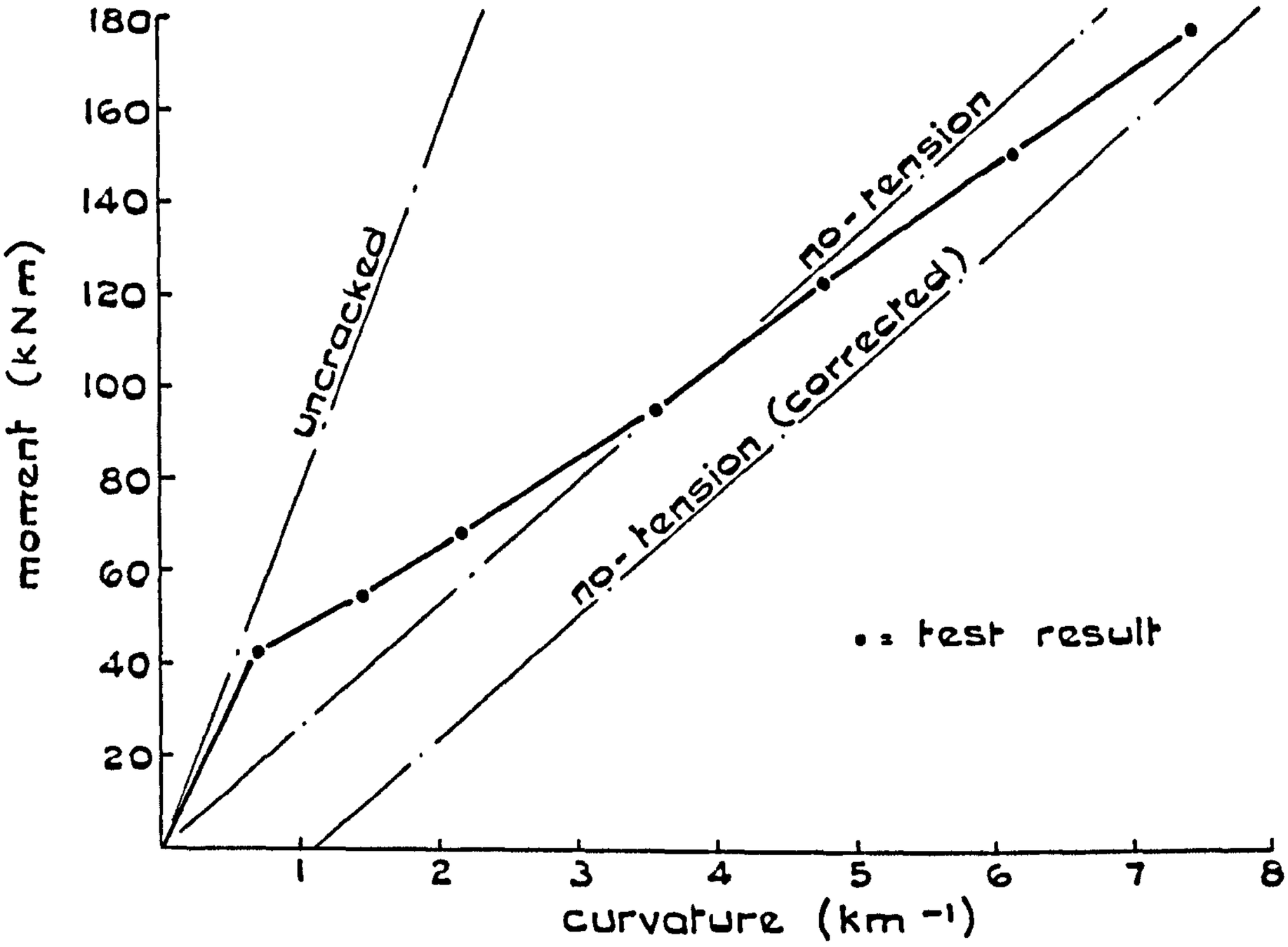

FIG.3.2 MOMENT-CURVATURE RELATIONSHIPS FOR UC1

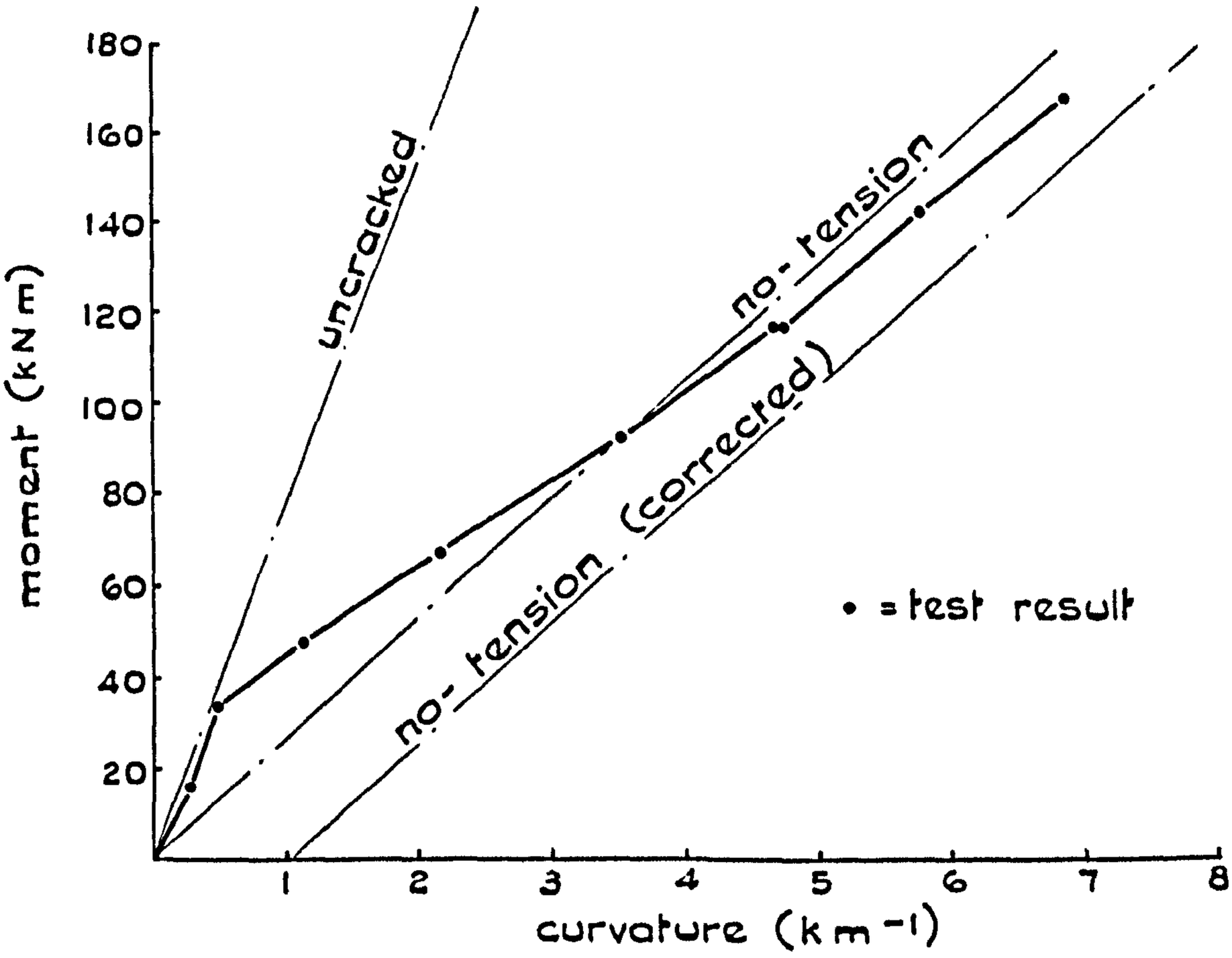

FIG. 3.3 MOMENT-CURVATURE RELATIONSHIPS FOR UC2

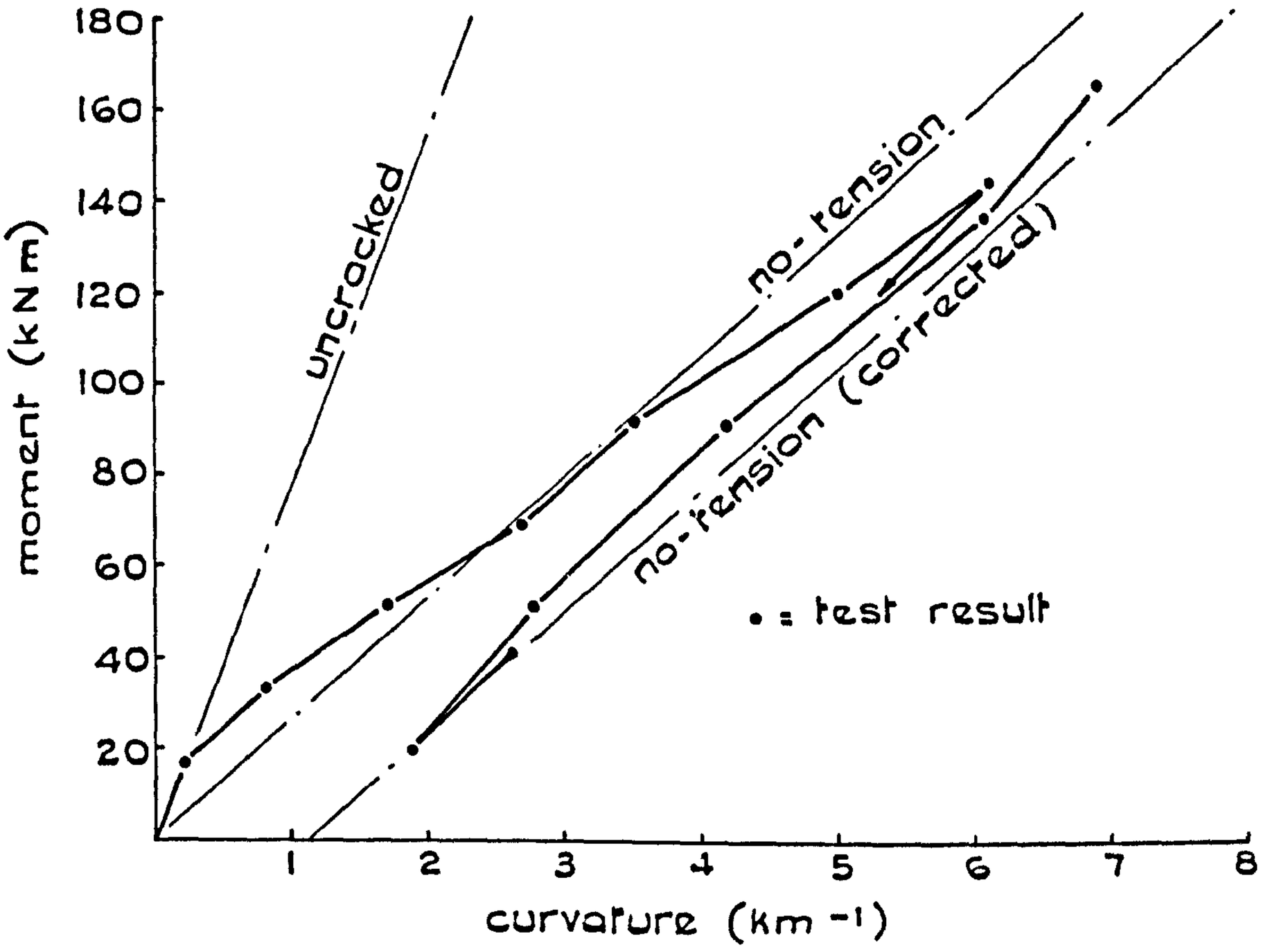

FIG. 3.4 MOMENT-CURVATURE RELATIONSHIPS FOR UC3

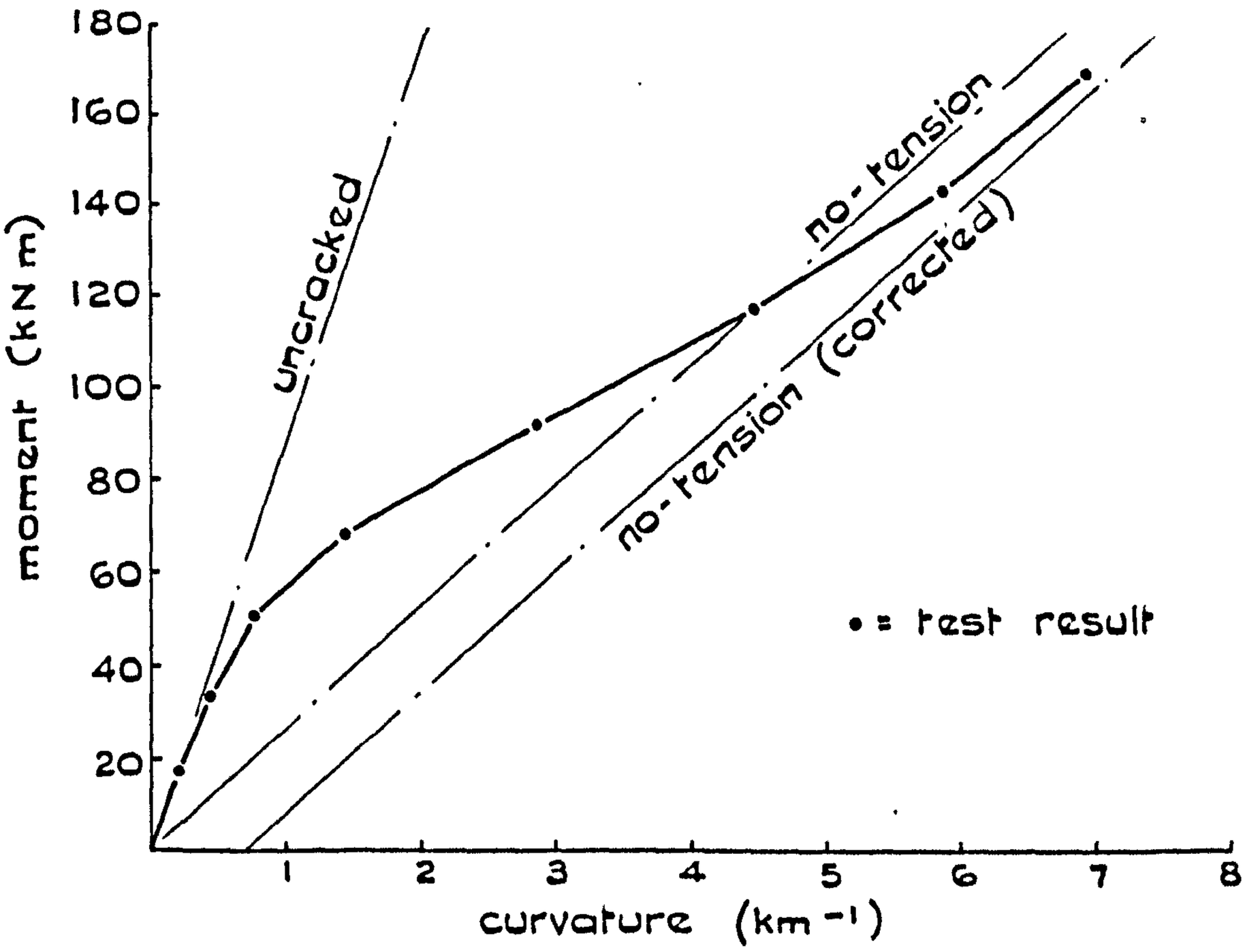

FIG. 3.5 MOMENT-CURVATURE RELATIONSHIPS FOR UC4

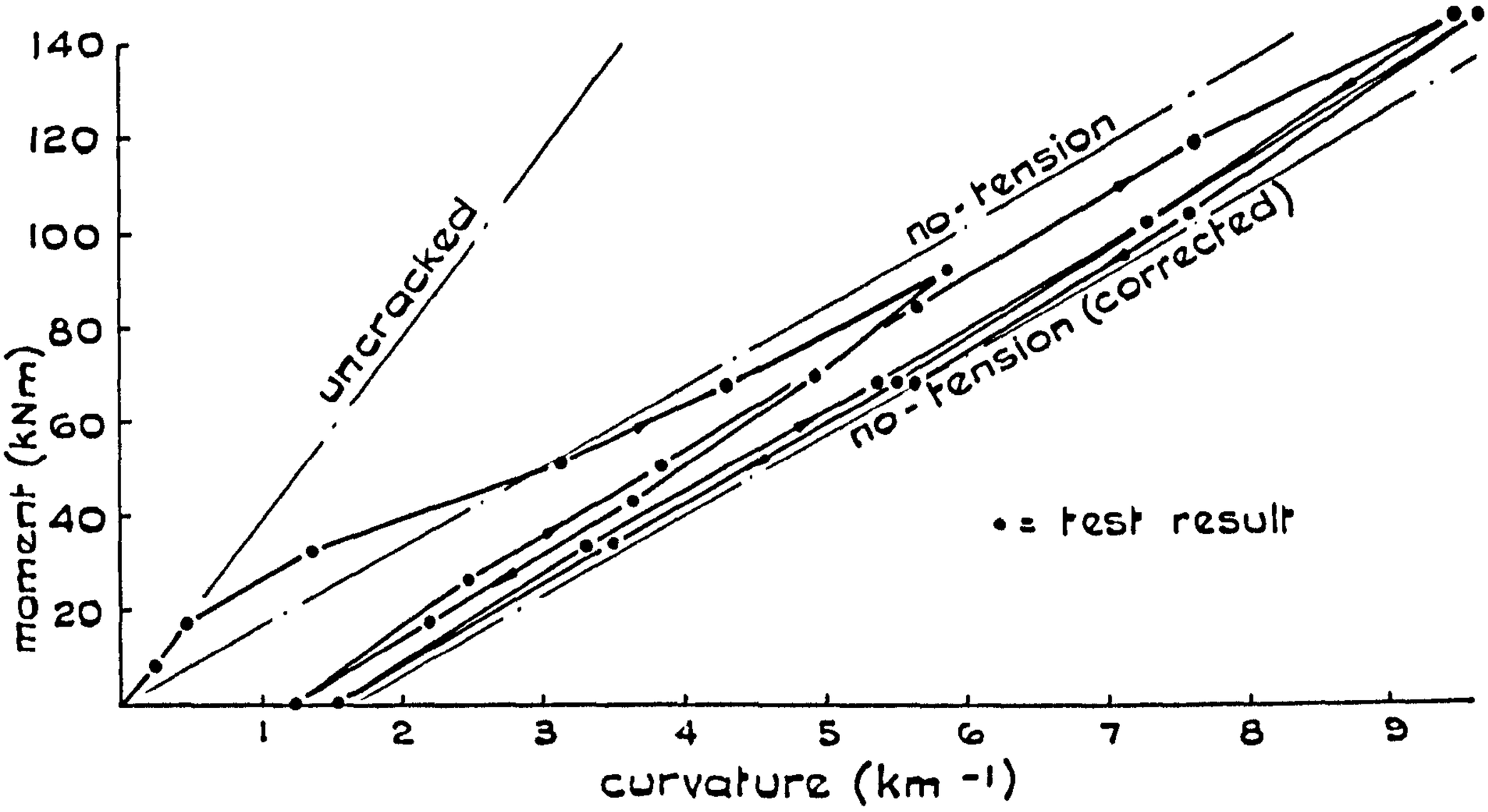

FIG. 3.6 MOMENT-CURVATURE RELATIONSHIPS FOR UC5

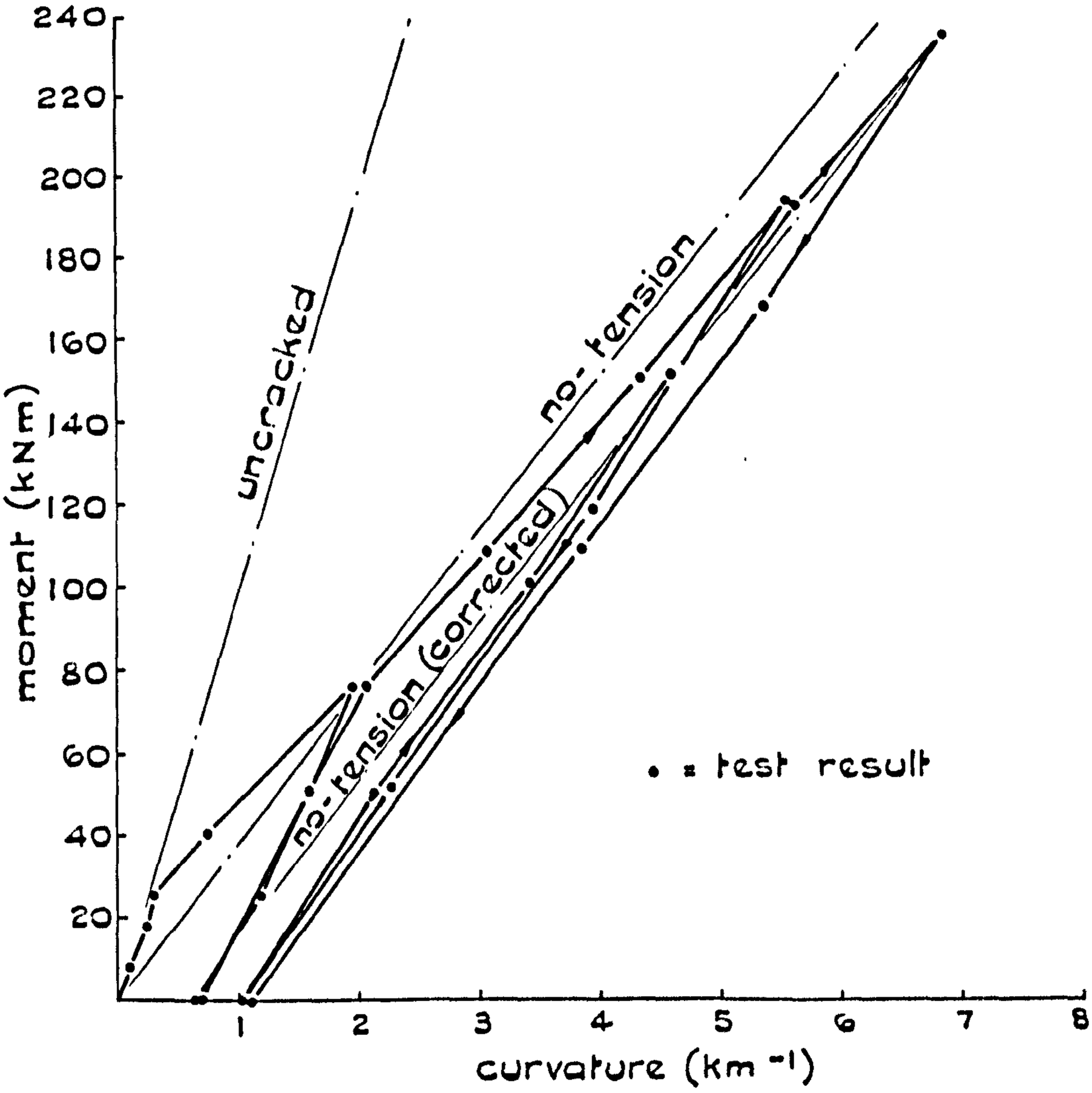

FIG. 3.7 MOMENT-CURVATURE RELATIONSHIPS FOR UC6

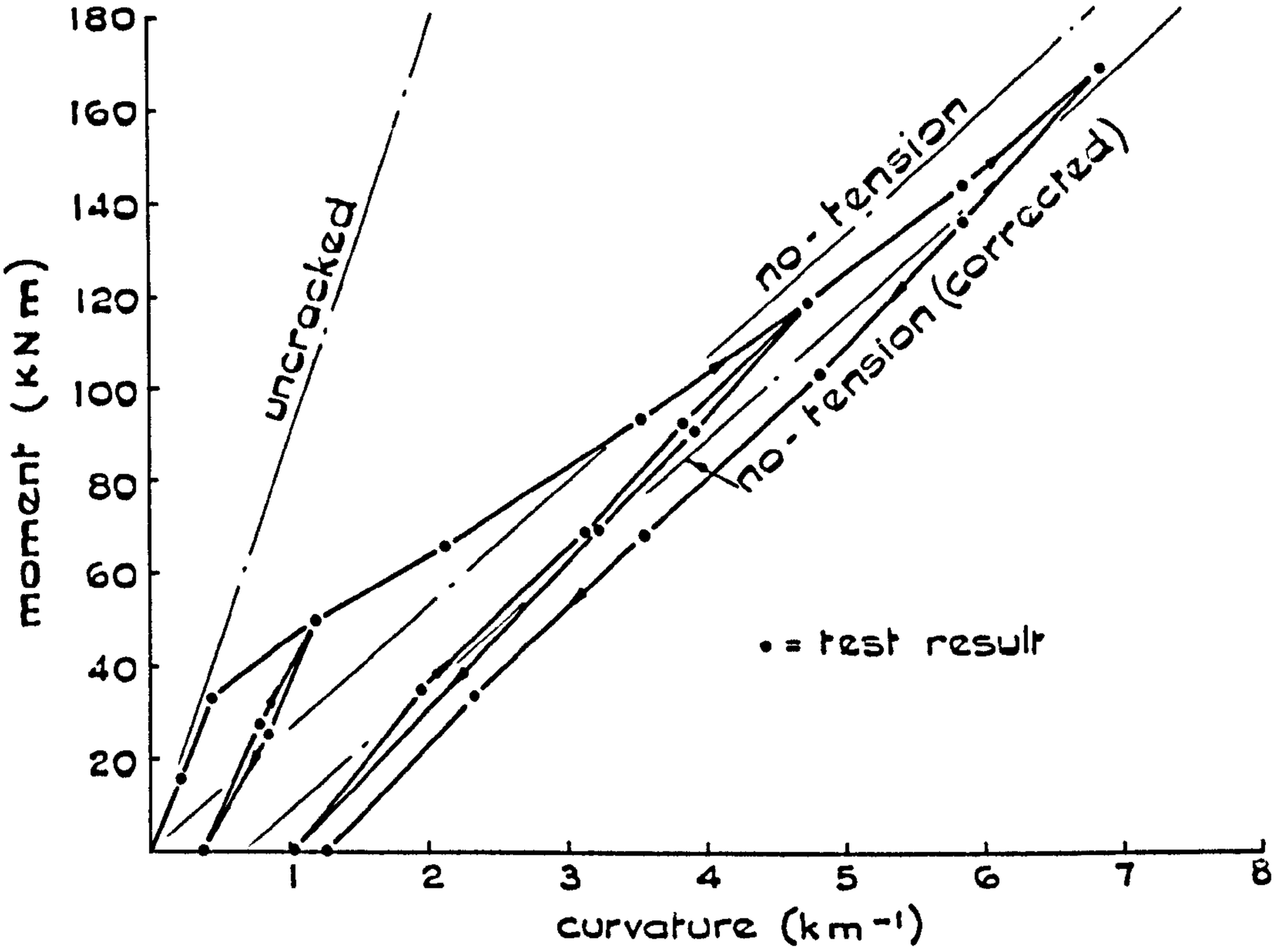

FIG. 3.8 MOMENT-CURVATURE RELATIONSHIPS FOR UC7

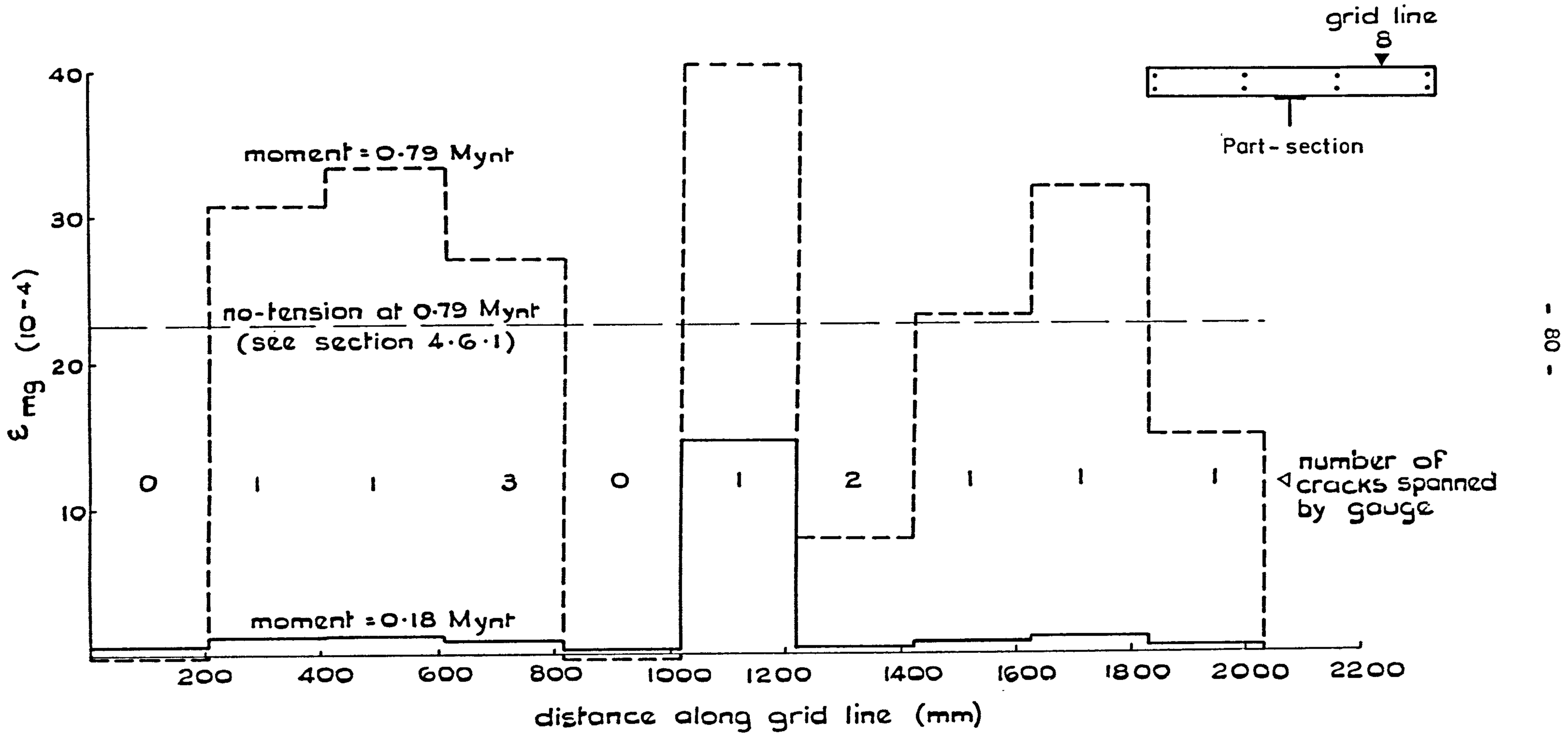

FIG.3.9 VARIATION OF ε_{mg} ALONG GRID LINE 8 OF BEAM UC5

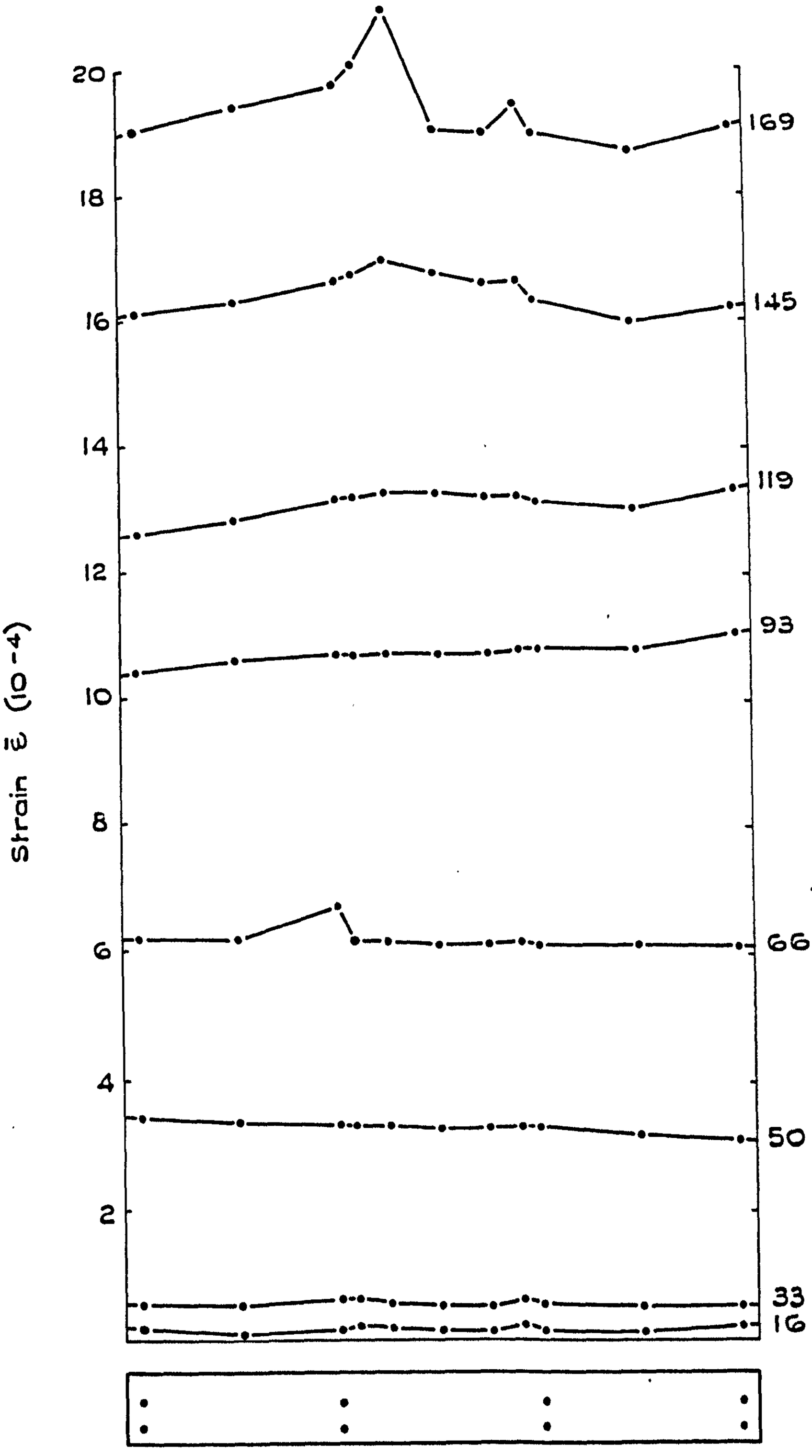

Section through slab

FIG. 3.10 ε FOR ALL GRID LINES: BEAM UC7

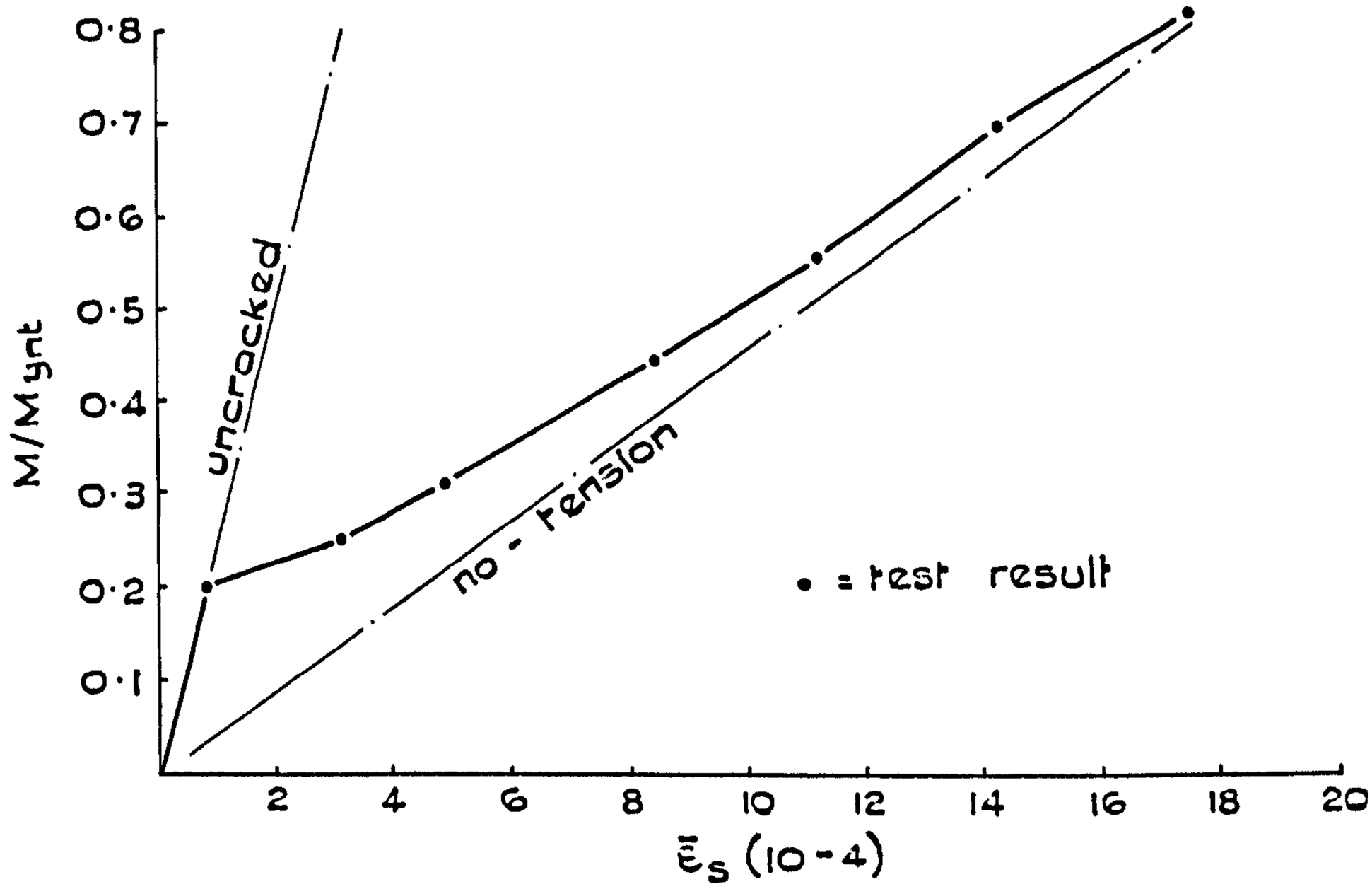

FIG. 3.11 MOMENT-STRAIN RELATIONSHIPS FOR UC1

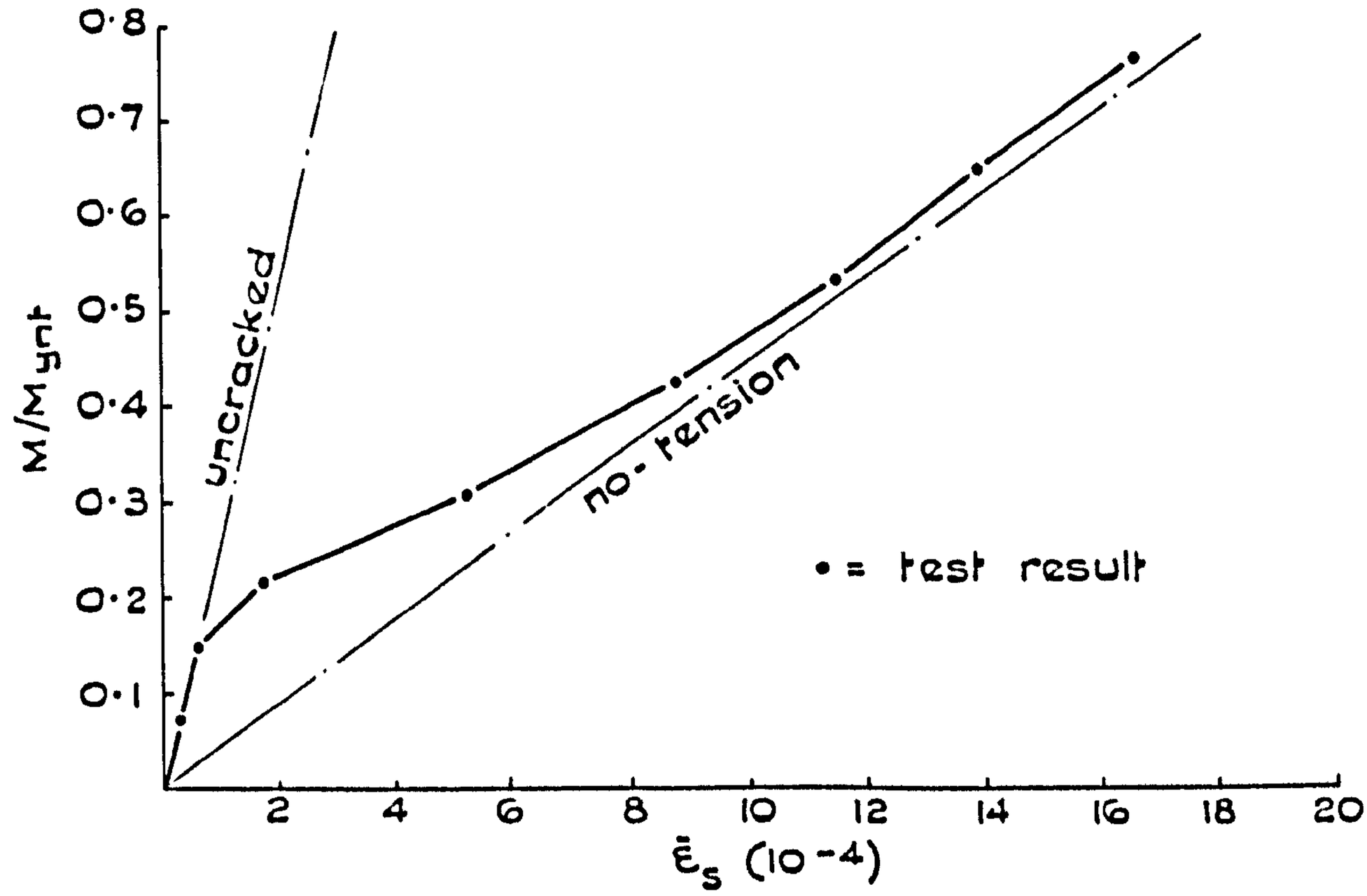

FIG. 3.12 MOMENT-STRAIN RELATIONSHIPS FOR UC2

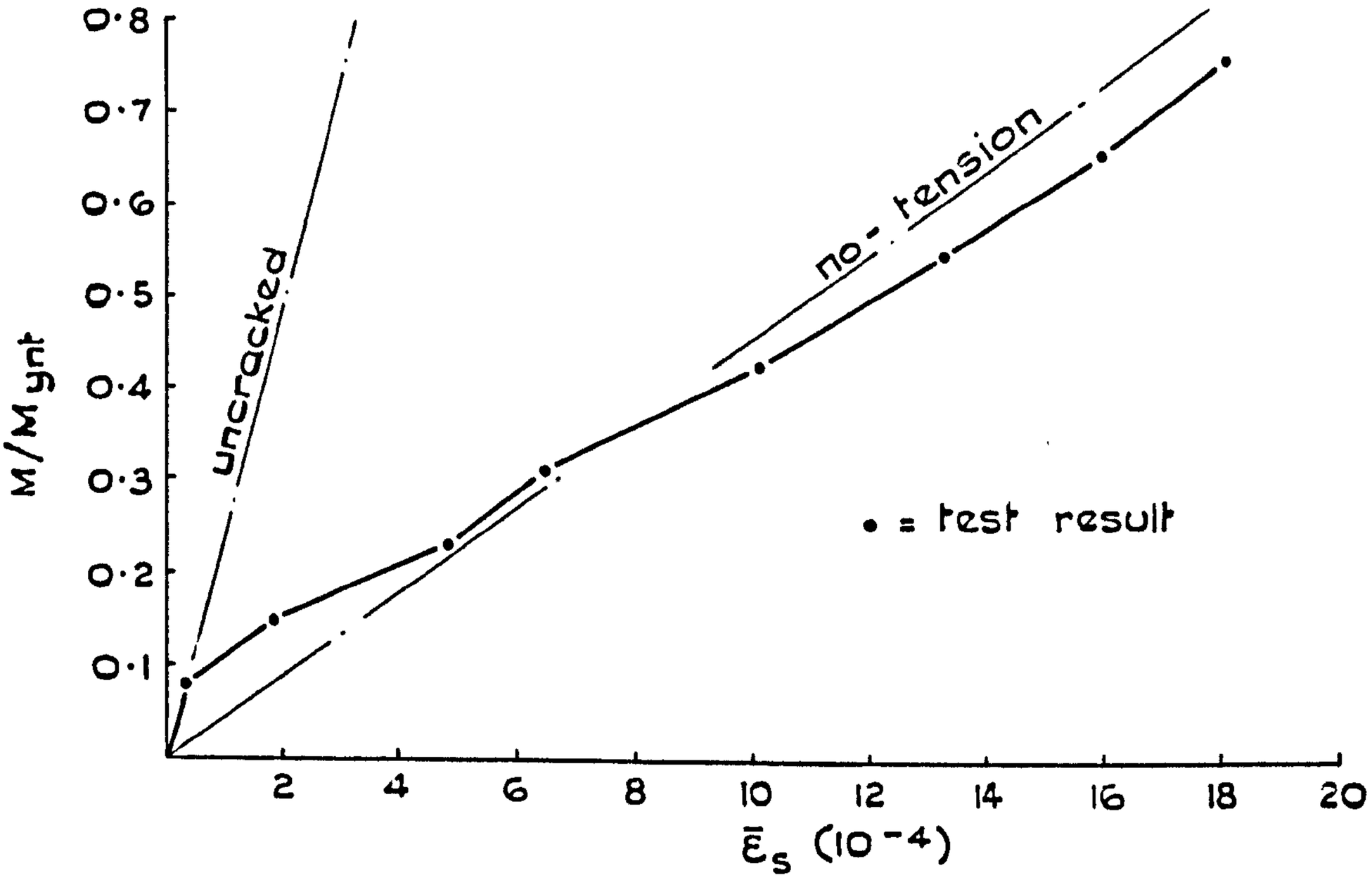

FIG. 3.13 MOMENT-STRAIN RELATIONSHIPS FOR UC3

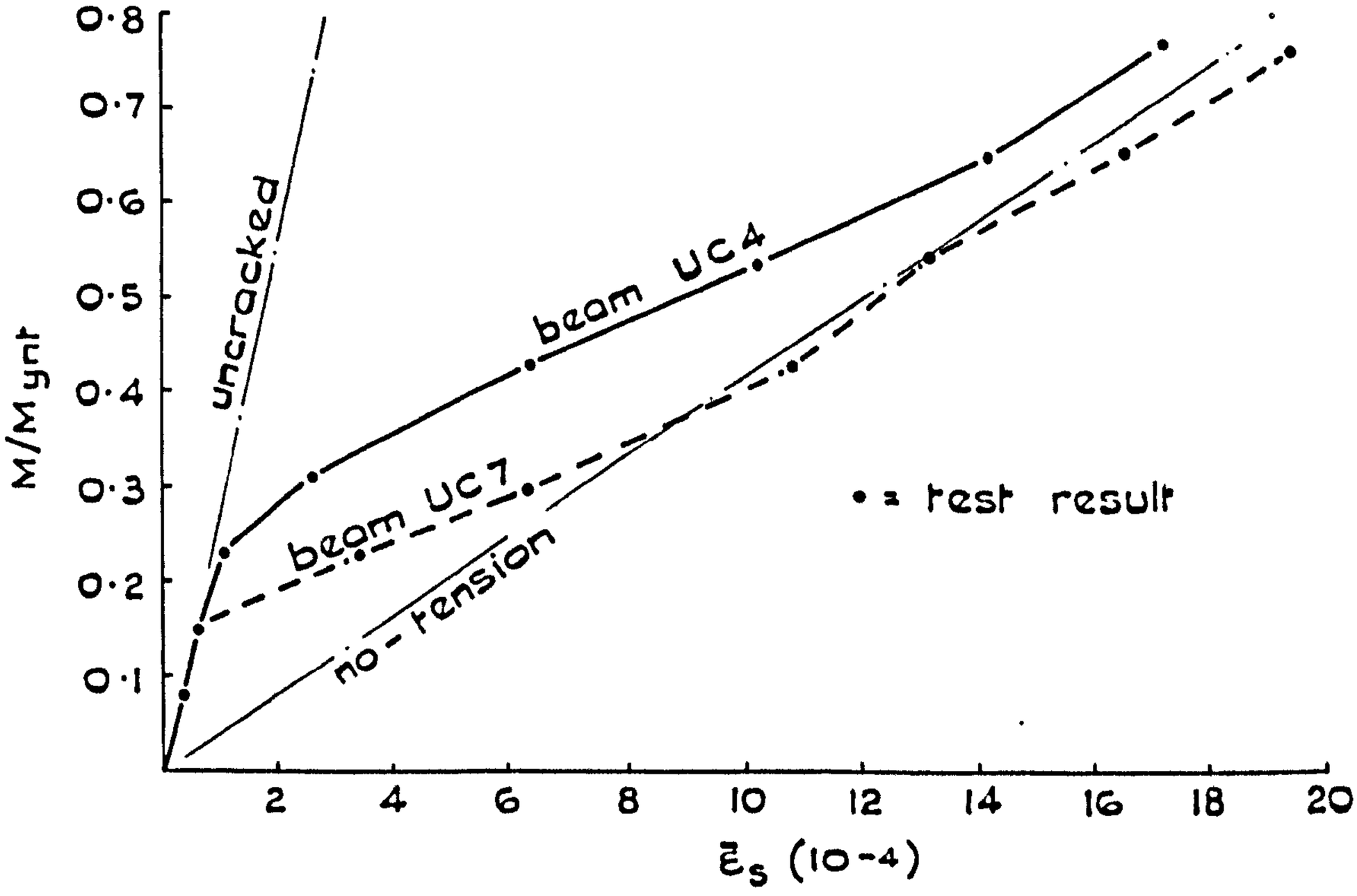

FIG. 3.14 MOMENT-STRAIN RELATIONSHIPS FOR UC4 & UC7

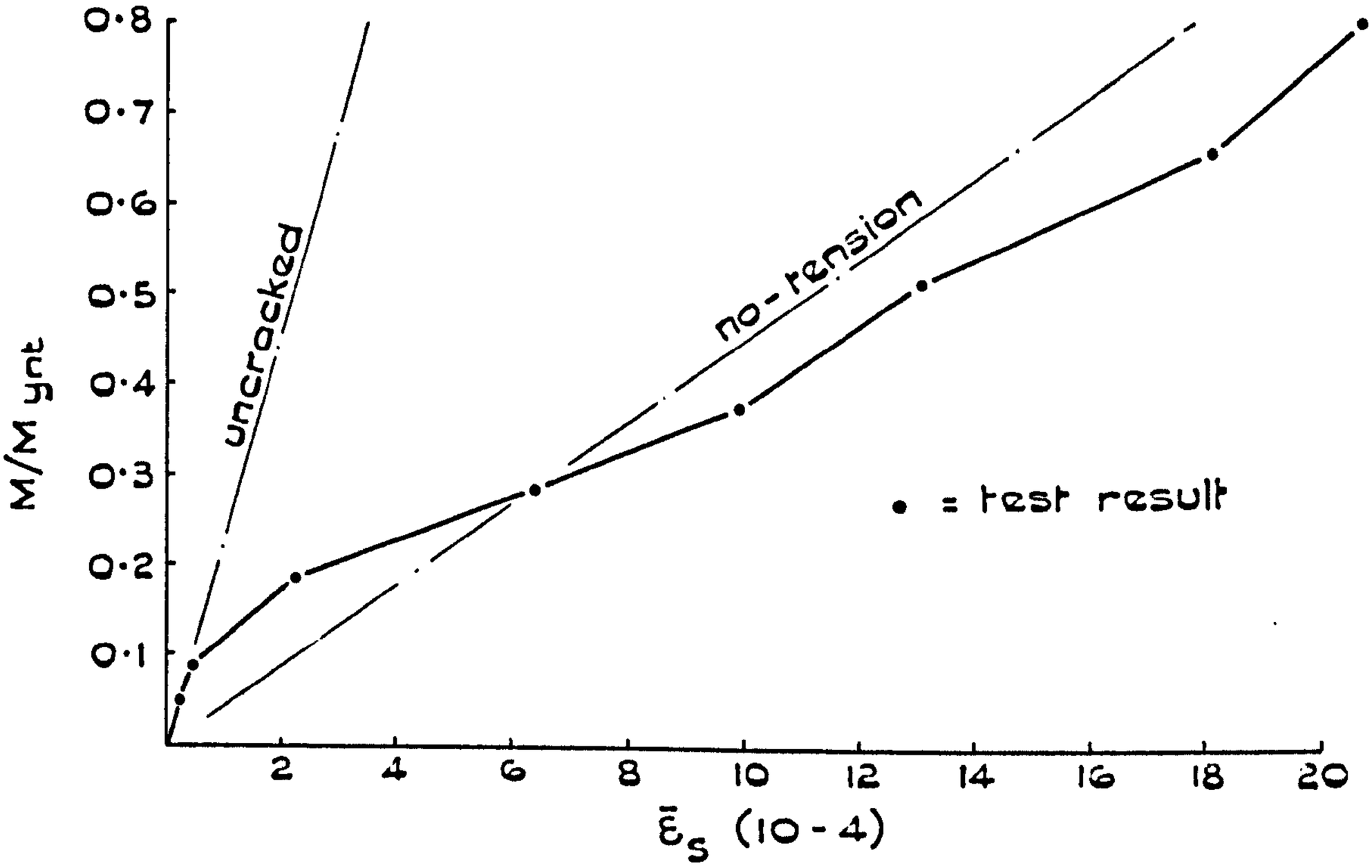

FIG. 3.15 MOMENT-STRAIN RELATIONSHIPS FOR UC5

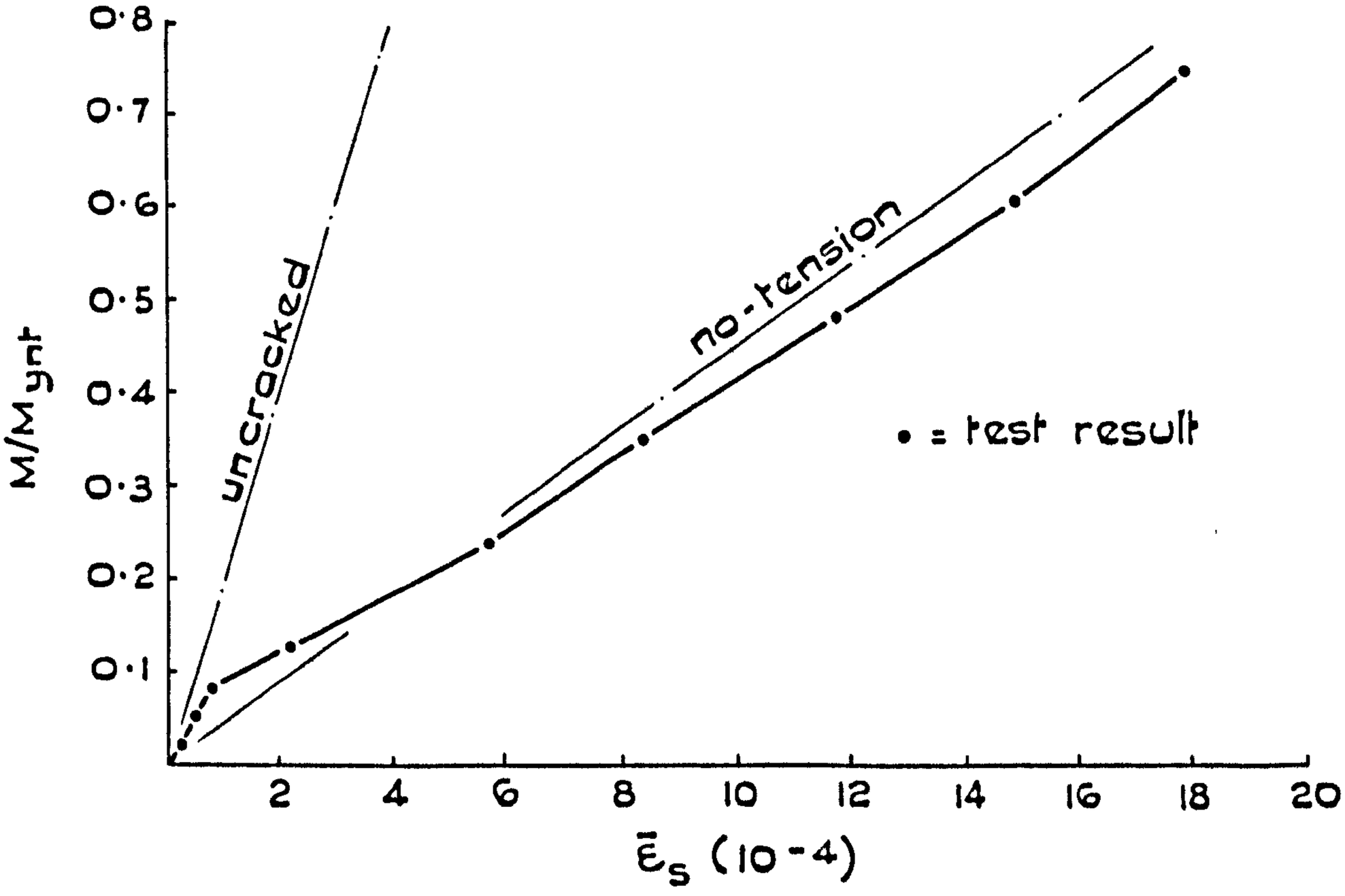

FIG.3.16 MOMENT-STRAIN RELATIONSHIPS FOR UC6

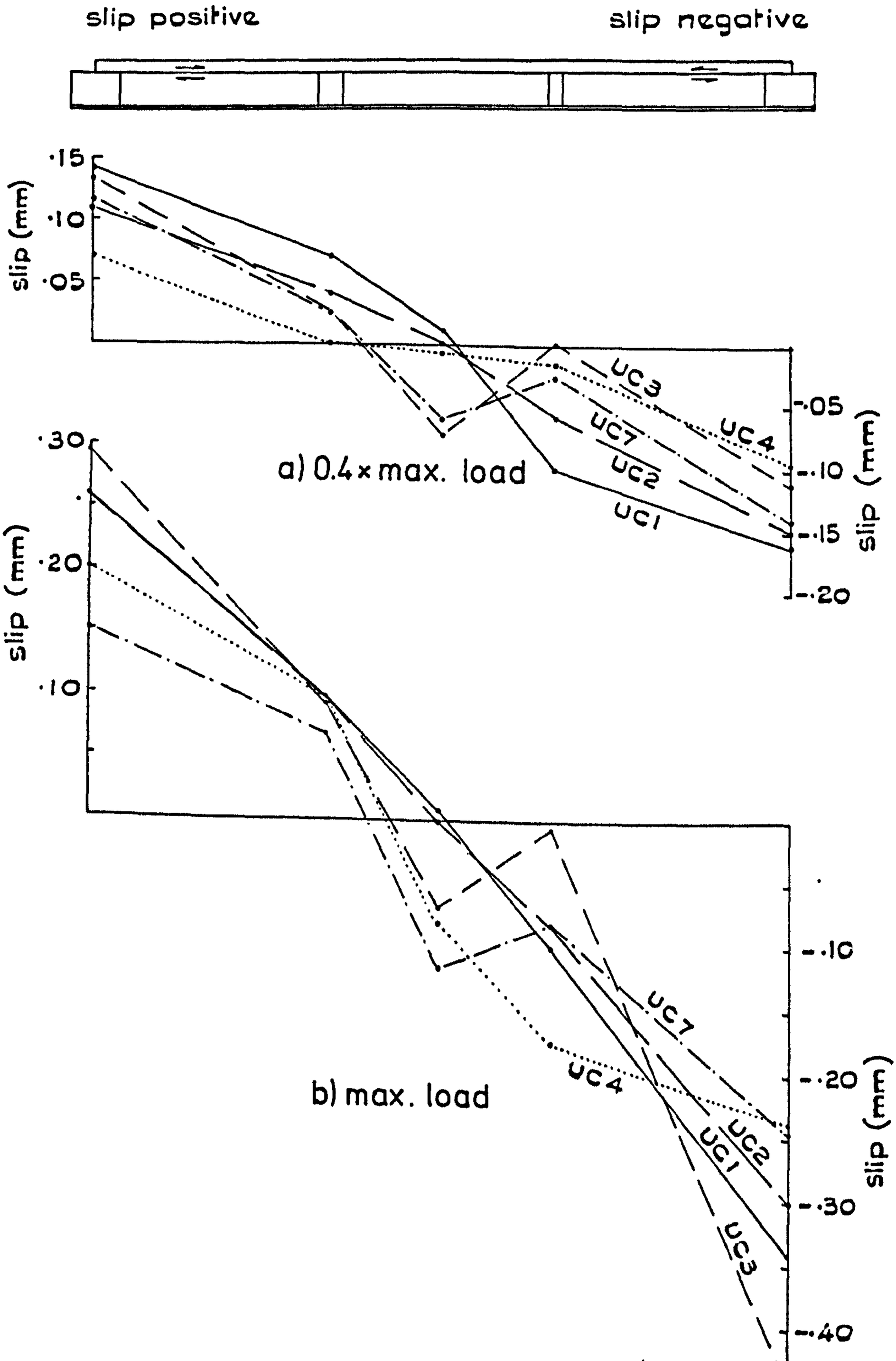

proportion of Mynt in each beam

beam (UC:-)	1	2	3	4	7
at approx 0·4 x max load	·31	·31	·31	·31	·30
at max load	·81	·78	·75	·78	·77

FIG.3.17 SLIP ALONG BEAMS UC1-UC4 & UC7

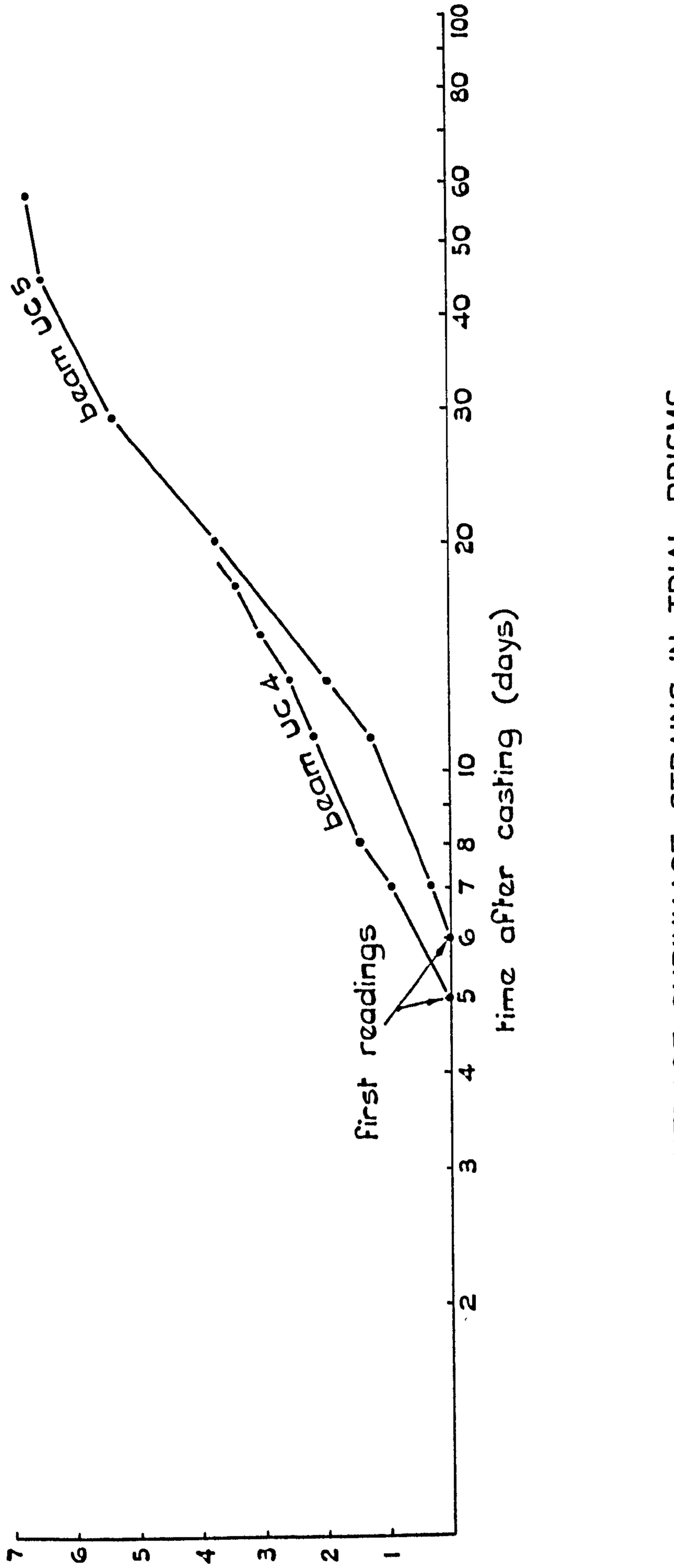

FIG. 3.18 AVERAGE SHRINKAGE STRAINS IN TRIAL PRISMS

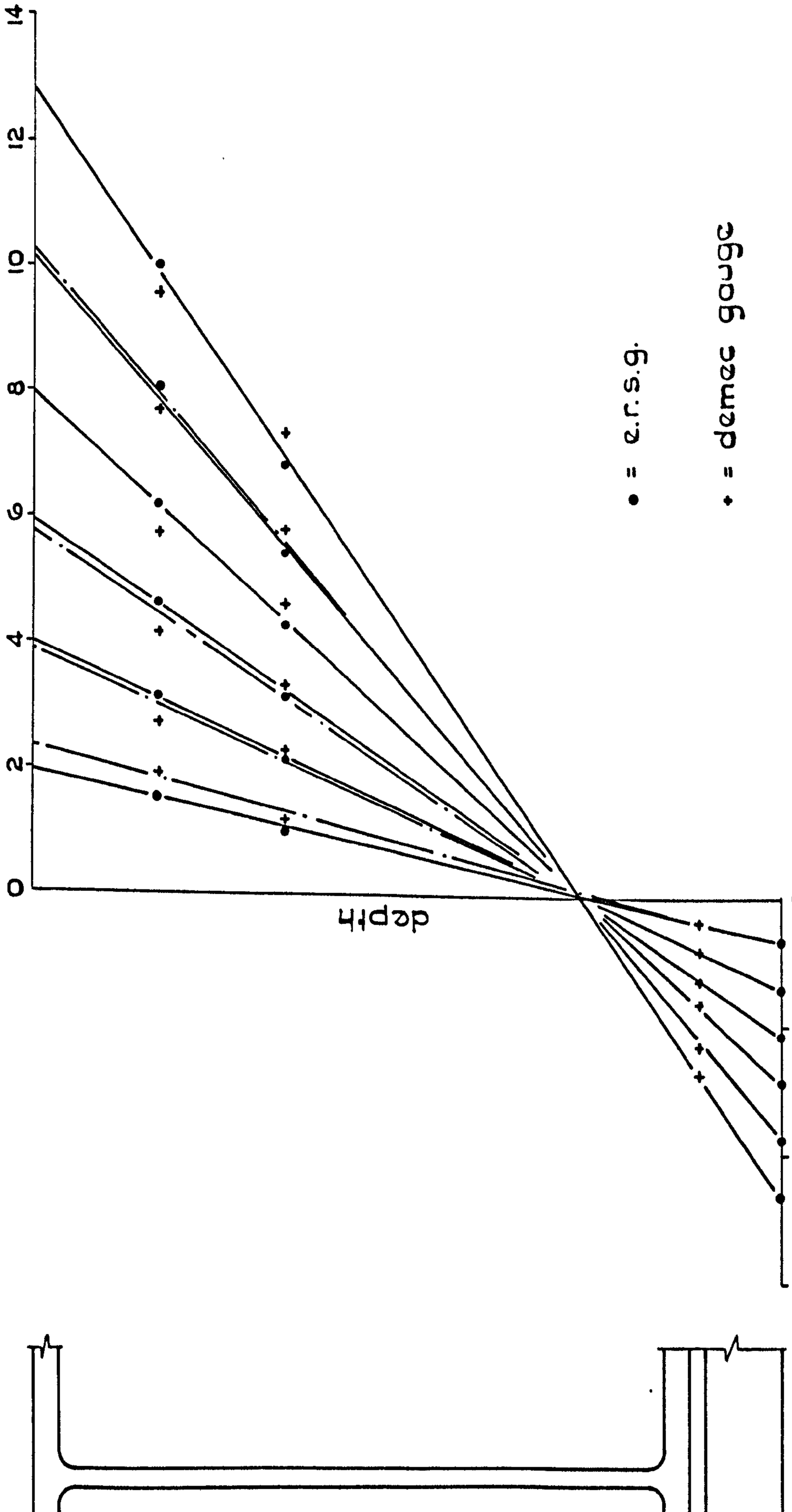

FIG.3.19 COMPARISON OF STRAINS FROM MECHANICAL AND ELECTRICAL GAUGES

Part-section through girder

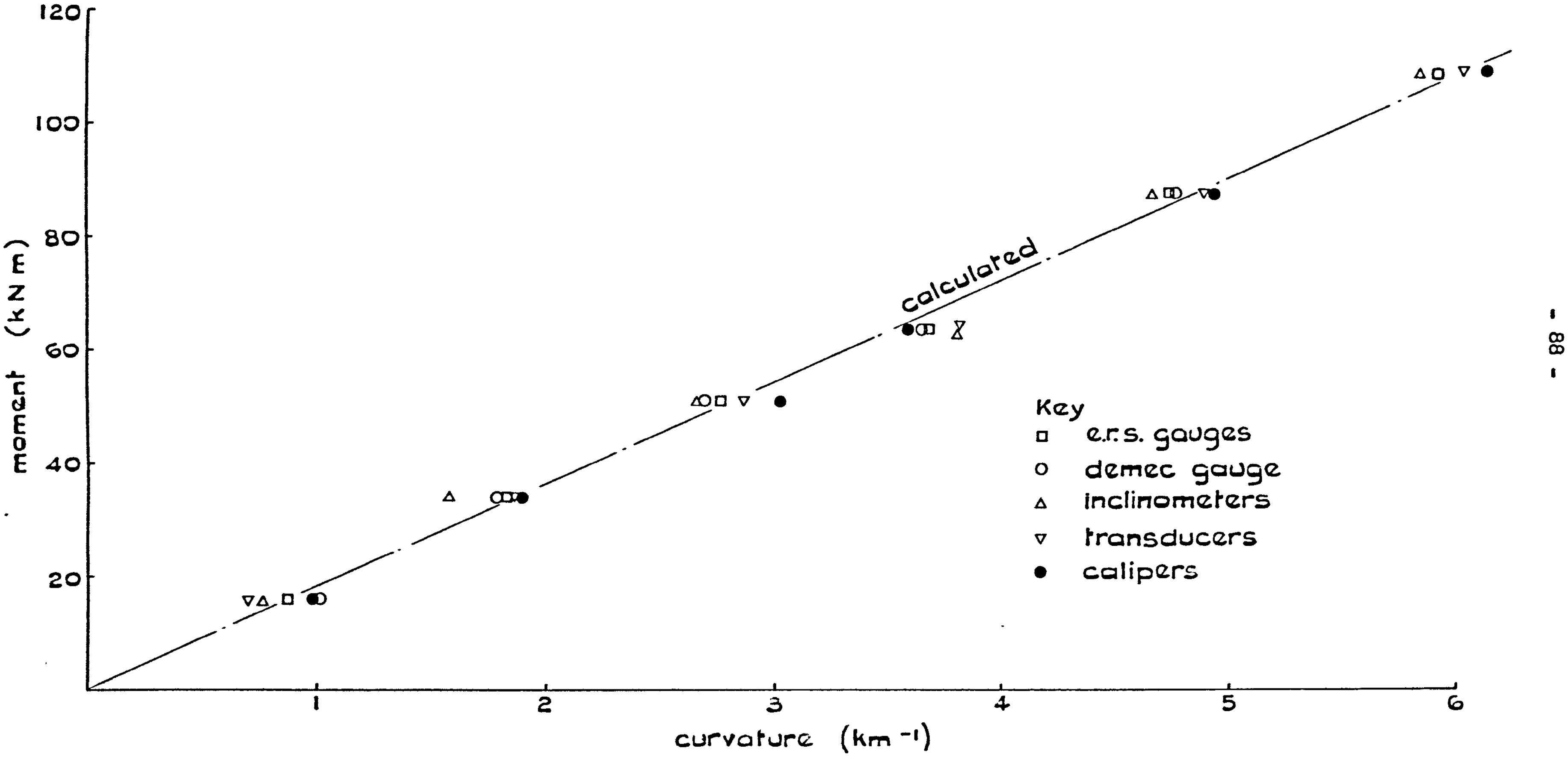

FIG.3.20 MOMENT-CURVATURE RELATIONSHIPS FOR BEAM UC6A

CHAPTER 4

ANALYSIS AND DISCUSSION OF TEST RESULTS

4.1 Introduction

Following a discussion of the accuracy of the results of the UC series of tests, it is shown that the drying shrinkage of the concrete slab has a significant effect on the behaviour of composite beams. A method of allowing for this effect quantitatively is described. The global behaviour of Beams UC1 to UC7 is then discussed with particular reference to the effects of shrinkage, and an equation for predicting the mean surface strain in uncased composite 'T' beams is derived.

Crack widths in composite beams are studied in Section 4.7 onwards. As noted (Section 3.1) only a statistical analysis of crack widths is practicable, and the method used is examined before the results of the analysis are presented and discussed.

The relationship between crack widths, surface strain and crack spacing is then considered, and it is established that spacing, as well as strain, determines crack widths. In Section 4.8 therefore, the parameters which determine crack spacing are discussed, and equations for predicting crack spacing in composite 'T' beams are derived. Design formulae for predicting crack widths are developed from these, and are compared with some of the existing formulae discussed in Chapter 1.

4.2 Accuracy of test results

4.2.1 Accuracy of experimental results

The calibration tests on the load cells showed that their response was linear to within 0.5% of the maximum load applied in the UC tests. Allowing for the inaccurate alignment of the bearings the difference between the derived moment in the test region and the true moment will not exceed 1.5% of its maximum value. Dead loads induce stresses in the

concrete slab which are equivalent to a maximum hogging moment of $0.011M_{ynt}$ at the jacks: dead load stresses have therefore been ignored.

The curvature of a beam cannot be measured directly, but several methods are available for deriving it. In this dissertation, curvature is derived from the gradient of the strain profile in the steel girder, as determined from the e.r.s.g.s. It is estimated that the maximum error in measuring the strain was approximately 2×10^{-5}, so the derived experimental curvatures may be in error by up to 2% of the maximum value. This is confirmed by the results of Test UC6A (Fig.3.20).

Test UC6A also confirmed an earlier suspicion that the strains output by the data-logger were much too large. The fault was traced to a program error, which resulted in the true strains being doubled before they were printed. The results presented here are, of course, based on the corrected values.

In some tests, strains in the steel girder were determined with demec gauges to provide an independent check on the e.r.s.g.s. The results from the two types of gauges were found to be similar (Figs.3.19 and 3.20). Allowing for the various techniques employed by different people when using demec gauges, strain can normally be determined to within $\pm 10^{-5}$ leading to an error of $\pm$ 1% in the curvature, but this was probably doubled due to the awkward position of the demec targets on the steel girder.

The use of transducers to measure deflection was found to be unsatisfactory, even though with an output of 1V per 50mm deflection and a digital volt-meter reading to the nearest micro-volt they are theoretically more sensitive to movement than dial gauges. In practice, they were only accurate to the nearest 0.1mm.

The curvature of Beams UC1 to UC7 may be obtained from the difference

between the deflections at the jacks and at mid-span. At maximum load, this was approximately 2.5mm, so the curvature may err by up to 1.5% when derived from dial gauge readings, and by 7% when dial gauge calipers or transducers are used. Fig.3.20 confirms this.

Trials showed that when an inclinometer was replaced on its bearing pads shortly after being removed, the previous reading could be repeated to within two divisions. Curvature is derived from the difference between two readings, which reached a maximum of about 250 divisions in Tests UC1 to UC7. This suggests an error in calculating the curvature from inclinometer readings of less than 2%. The results of UC6A show the error is closer to 4% of the maximum curvature, presumably due to insufficient care being taken in locating the gauge on its pads, and in keeping the pads free of dirt over the period of the test.

The mean surface strain along a grid line on the slab was determined from the average of 19 readings with an 8-in Demec gauge, so the error in $\bar{\varepsilon}$ will be virtually nil. In deriving the mean strain in the slab ($\bar{\varepsilon}_s$) from experimental readings the strain profile between grid lines has to be estimated, but this becomes awkward only when $\bar{\varepsilon}_s$ is large (see Fig.3.10). The percentage error is therefore quite low: it is estimated as less than 3% of the true value at each load stage.

Bending in plan will cause crack widths and strain at one side of the slab to exceed those at the other side. The only effect on the crack width-strain relationship is that for bending in plan, the slab will behave as a deep, narrow reinforced concrete beam, and not as a composite beam. Since the horizontal beam deflection is only 2.5% of the vertical deflection, this effect has been ignored.

The maximum slip measured in the test region of Beams UC1 to UC7 was in the order of 0.1mm, and dial gauge readings would be accurate to $\frac{1}{2}$ division, indicating an error of 5% of the maximum reading. The use of

transducers to measure slip in Tests UC5 and UC6 is seen now to have been a mistake, since their accuracy is of the same order as the quantity being measured; slip measurements for these two tests are therefore meaningless, and are not included here.

Crack widths were measured to the nearest 0.025mm, but errors also arise from the difficulty of measuring a crack at exactly the same position in successive load stages. It is estimated that crack width readings were accurate to within $\pm$ 0.05mm, so that for a crack 0.4mm wide the possible error is 13%. As will be shown in Section 4.7, however, the average width of all cracks crossing a grid line ($\bar{w}$) was quite high until several cracks had formed, so the error in predicting $\bar{w}$ would probably be about 7%.

4.2.2 Accuracy of theoretical calculations

In Sections 4.3 to 4.6, experimental values of curvature and surface strain are compared with theoretical predictions. The assumptions on which the latter are based are now considered.

The stiffness of each beam has been calculated on the basis of the nominal cross sectional area, which will not differ from the true area by more than 1%. Tests showed that the modulus of elasticity for the steel sections and reinforcement varied between 204kN/mm^2 and 211kN/mm^2, so an average value of 207kN/mm^2 was taken. The maximum error in the theoretical cracked stiffness of Beams UC1 to UC7 is therefore less than 3%.

Methods of calculating the modulus of elasticity of concrete for specific mixes give, at best, only an estimate of this property, so a nominal value of 27.6kN/mm^2 has been used to calculate the uncracked stiffness of Beams UC1 to UC7. This may be in error by as much as 25%, which will lead to an error in the calculated beam stiffness of about 10%. Since the study of uncracked composite beams was not a primary reason for

conducting the UC tests, this degree of accuracy is thought to be sufficient.

4.3 Moment-curvature and moment-strain relationships

As the extent of cracking in the slab of a composite 'T' beam increases, the beam stiffness is gradually reduced. However, provided the shear connection between the slab and the girder is sufficiently rigid to prevent slip, and the beam's response to load is elastic, the lowest possible stiffness corresponds to the condition of no tension-stiffening in the reinforced concrete. Values of minimum stiffness have been calculated for Beams UC1 to UC7, and are represented in Figs.3.2 to 3.8 and 3.11 to 3.16 by the lines labelled "no-tension".

Experimental values of curvature and surface strain often exceed those calculated on the basis of the theoretical minimum stiffness. Further, large values of residual curvature and strain are noted in those tests where measurements were taken as the load was reduced to zero, even though the theoretical elastic limit of the beam had not been exceeded. Three possible reasons for these phenomena are: slip between the concrete slab and the steel beam; residual stresses in the steel beams and the effects of using the same beam in several tests; and shrinkage of the concrete slab. These possibilities are now considered separately.

(a) Slip The slip measurements in Fig.3.17 have been used to calculate an equivalent slip strain over the length of the test region. It was found that slip of the magnitude observed in Tests UC1 to UC7 leads to an increase in the beam curvature of less than 4% of the value derived from a full-interaction analysis. Also, since the strain at the top surface of the concrete slab is reduced by slip, this phenomenon cannot account for the discrepancy between calculated and experimental curvatures and surface strains.

(b) Residual stresses These are always present in rolled universal beams and result in the moment-curvature response of the beam departing from the idealised elasto-plastic relationship, as illustrated in Fig.4.1. The true elastic limit of the beam is therefore lower than expected. Loading a beam beyond its elastic limit results in a non-linear response of the beam, but also gives rise to work-hardening and a consequent increase in the elastic limit.

The maximum stress in the steel beam in Test UC1, calculated on the basis of no tension-stiffening, was 233N/mm^2 in the tension flange. This stress was not exceeded in Tests UC2 to UC4 and UC7, which used the same beam, so the response of the steel beam in these tests would be purely elastic. (The moment-curvature and moment-strain curves are not linear of course, due to cracking in the concrete slab.) Therefore, if residual stresses were responsible for the difference between expected and measured curvatures and strains, the difference ought to be more marked in Test UC1 than in Tests UC2 to UC4 and UC7: this is seen not to be the case.

(c) Shrinkage Drying shrinkage of the concrete slab is thought to be the main cause of experimental strains and curvatures being larger than expected, and is now discussed in detail.

4.4 Drying shrinkage in the concrete slab

4.4.1 Theoretical consideration of shrinkage strain and curvature

Consider a composite beam in which the free shrinkage strain in the slab on the day of test is ε_{sh}. The shrinkage is restrained by the presence of the steel beam, which results in sagging curvature in the composite beam and a tensile stress at the top surface of the slab corresponding to a tensile strain of ε_{st}. These strains and curvatures develop before any external load is applied, and are shown by the lines ABC and OP in Figs.4.2 and 4.3 respectively. Initial readings of strain

and deflection in Tests UC1 to UC7 correspond to the points C and P.

If an external moment M_{cr}, not quite sufficient to cause cracking, is applied to the composite beam, the strains and curvatures increase as shown by lines CD and PQ. These changes will be detected by the instrumentation, and the lines AF and OS are plots of the experimental results. Since cracking has not yet occurred, there will be no release of shrinkage strain, and no alteration in the stiffness of the beam. The gradient of all four lines CD, AF, PQ and OS may therefore be calculated from the normal elastic theory of transformed sections.

The external moment is now increased until a value, M_f is reached such that all shrinkage stresses and strains are released. The amount of tension-stiffening in the concrete must then be zero. The lines DE and QR show the moment-strain and moment-curvature relationships, which are assumed linear for convenience. The experimental results are indicated by the lines FG and ST. The increments in strain and curvature during this load stage are due not only to the elastic response of the composite beam to the applied moment, but also to the release of shrinkage strains and curvatures.

A line through point O of Fig.4.3 and of gradient equal to the stiffness of the composite beam (assuming no tension-stiffening in the concrete) should pass through R and not T. This is because as the moment increases from M_{cr} to M_f, the initial sagging curvature due to shrinkage (ϕ_{sh}) is released. To predict the experimental curvature of a beam subjected to an externally applied moment M_f therefore, one must calculate the curvature due to the elastic response of the beam to this moment, then add the amount ϕ_{sh}. Hence, the experimental relationship ST relates to the line UT.

We now consider the moment-strain relationship. If all shrinkage stresses are released, the beam will return to its original, as-cast

length in the absence of any external moment. The concrete slab as a whole will return to this length also, although the mean strain in the concrete between cracks will then be $-\varepsilon_{sh}$. (The difference in length will be made up in the crack widths.) Release of shrinkage stresses therefore causes an increase in the mean surface strain of $(\varepsilon_{sh} - \varepsilon_{st})$: this amount must be added to the amount derived from the theoretical calculation of $\bar{\varepsilon}$ on the basis of no tension-stiffening. The experimental line FG therefore relates to the line HG.

4.4.2 Estimation of strains and curvatures due to shrinkage

This is the first of two stages to check the method of allowing for shrinkage described in Section 4.4.1. The second stage is to use the estimates in the prediction of total curvatures and strains for comparison with experimental results, which is dealt with in Sections 4.5 and 4.6 respectively.

The free shrinkage of the slabs of Beams UC2 to UC7 was estimated from the following equation:

$$\varepsilon_{sh} = (\text{predicted strain in slab from casting to day of test}) \times \frac{(\text{measured strain in prisms from day 7 to day of test})}{(\text{predicted strain in prisms from day 7 to day of test})}$$

The measured strain in the prisms is the value given in Table 3.1. The predicted shrinkage strain in both the slab and the shrinkage prisms was calculated using Appendix C of BS5400, Part 4[34], making due allowance for the reduction in ambient humidity when the damp hessian was removed from the slab.

The estimated value of free shrinkage strain in each slab is listed in Table 4.1. The strain distributions in the composite beams due to slab shrinkage are also given: they were calculated from ε_{sh} in the usual manner. In the absence of more reliable information, ε_{sh} for the slab of UC1 has been taken as equal to that of UC3, since the variation in cube

strength with time was virtually identical for both tests.

The above procedure to determine the free shrinkage strain in the slab may be criticised on the grounds that it relies on a theoretical prediction of the shrinkage effect. An attempt was made to eliminate this problem by using strain gauges and dial gauges to measure the effects of shrinkage directly (Section 2.6.1). This proved unsuccessful however, for the instruments used were not sufficiently accurate in relation to the small changes being measured to give consistent results.

4.5 Moment-curvature relationships

The poor correlation of experimental results and the theoretical "no-tension" lines in Figs.3.2 to 3.8 has been noted (Section 4.3). Two other theoretical relationships are shown in these figures, as follows. The line labelled "uncracked" assumes the concrete is effective in tension and that $E_s/E_c = 7.5$. The other line is labelled "no-tension (corrected)" and shows the curvature calculated on the basis of no tension-stiffening in the concrete, with the addition of ϕ_{sh} due to the release of shrinkage, taken from Table 4.1: it therefore corresponds to the line UT in Fig.4.3.

Initially the experimental results follow the "uncracked" theoretical line very closely; and at the maximum applied moment they are in reasonable agreement with the no-tension (corrected) line, which suggests that the calculation of shrinkage curvatures and the method of allowing for them is satisfactory, but is not conclusive. A proportion of the shrinkage curvature in a beam might still remain at maximum load, in which case agreement of the theoretical no-tension (corrected) line with the tests results would merely show that the allowance for shrinkage had been underestimated.

For Beams UC3 and UC5 to UC7, experimental values of curvature during the release of the maximum applied moment are shown in Figs.3.4 to

3.8. The gradient of the moment-curvature plot during unloading is equal to the beam stiffness, which is constant because no further cracks form. For Tests UC3, UC5 and UC6, the beam stiffness is seen to be very nearly equal to the theoretical "no-tension" value, showing that by the time a moment of $0.75M_{ynt}$ to $0.80M_{ynt}$ was applied, there was no tension-stiffening in the concrete slab. It follows that all shrinkage strains and curvatures were released, so the close agreement of experimental and theoretical results shows that the method described in Section 4.4 of allowing for shrinkage effects is satisfactory.

The stiffness of Beam UC7 at maximum load is greater than the value for no tension-stiffening (Fig.3.8), so it is unlikely that all the shrinkage curvature had been released. The correlation of the experimental results and the theoretical no-tension (corrected) line therefore indicates that the value of ϕ_{sh} has been underestimated for this beam.

The moment-curvature plots for UC5 to UC7 show the result of releasing and then re-applying the external moment before the maximum value is reached. The gradient of the curve during unloading and reloading is the beam stiffness as before, and the residual curvature at zero load is the amount of shrinkage curvature that has been released. The test results show that as the largest moment to which the beam has been subjected is increased, the beam stiffness decreases, and more shrinkage curvature is released. The expected behaviour of cracked composite 'T' beams is therefore confirmed.

4.6 Surface strains

4.6.1 Strain along individual grid lines

Fig.3.9 illustrates the large variation in surface strains averaged over individual gauge lengths; it is this variation which renders the individual crack width theory (Section 1.3.2) unsuitable for use in

design.

The line labelled "no tension at $0.79M_{ynt}$" in Fig.3.9 is the theoretical surface strain, calculated on the assumption of no tension-stiffening, and including an additional strain of $(\varepsilon_{sh} - \varepsilon_{st})$ to allow for the release of shrinkage effects. Of the five gauge lengths in which the theoretical strain is significantly exceeded, only one (the third from the left in Fig.3.9) spans more than one crack. The others each span a single crack whose width lies in the range 0.55mm to 0.63mm.

4.6.2 Average surface strain

The experimental $M - \bar{\varepsilon}_s$ relationships are shown in Figs.3.11 to 3.16, where they are compared with two theoretical relationships which are labelled "uncracked" and "no-tension". The first assumes that concrete is effective in tension, and that $E_s/E_c = 7.5$; the second assumes there is no tension-stiffening in the concrete.

The moment-strain relationships follow the same pattern as the moment-curvature relationships already discussed.

4.6.3 Prediction of mean surface strain

4.6.3.1 General

The work summarised in Chapter 1 shows that the mean surface strain of the concrete is an important parameter in determining crack widths, and design methods for predicting it are therefore required.

In Figs.3.11 to 3.16, strain is given with respect to the length of the slab at the start of the test, but this is only one of three alternatives. Strain may also be given with respect to:

(a) the length of the beam at the time of casting, corresponding to point A in Fig.4.2; or

(b) the length that the slab would adopt if entirely free of restraint (point B).

Alternative (b) is used throughout the remainder of this chapter, because it offers the following advantages:

(i) there will be a more definite relationship between $\bar{w}$ and $\bar{\varepsilon}$ defined as above than would exist if $\bar{\varepsilon}$ were given with respect to the length at some arbitrary time after casting the slab;

(ii) if strains were given with respect to the length at zero external load, in later stages of cracking the mean tensile strain at the surface of uncracked concrete (ε_{cm}) might well be compressive. For members loaded in tension this might be confusing.

Revised M - $\bar{\varepsilon}_s$ curves, where $\bar{\varepsilon}_s$ is given with respect to the unrestrained length of the slab, are shown in Figs.4.4 to 4.10. They are obtained by adding a strain ε_{st} to the experimental strains: the same strain must also be added to all theoretical values.

4.6.3.2 Before cracking

The derivation of the theoretical line "uncracked" has been given in Section 4.6.2, and is seen to give good predictions of $\bar{\varepsilon}_s$ until cracking occurs, as long as a value ε_{st} is added to the calculated strain to allow for the effects of shrinkage.

4.6.3.3 After cracking

The usual method of calculating strain after cracking is first to determine the strain on the assumption that the concrete is ineffective in tension (ε_{nt}), and then to subtract an amount ($\delta\varepsilon$) to allow for tension stiffening.

For composite beams, ε_{nt} must include an amount to allow for the effects of shrinkage: this amount is ε_{sh} when strains are given with respect to the unrestrained length of the slab. Calculated values of ε_{nt} are shown in Figs.4.4 to 4.10.

As noted in Section 1.4, current design methods[33,34] for calculating

$\delta\varepsilon$ are based on the equation:

$$\delta\varepsilon = k\, f_t\, f_{scr}/E_s\, \rho\, f_{nt} \qquad (4.1)$$

It has been assumed previously[39] that $f_t\, f_{scr}/E_s$ is roughly equal to 0.7×10^{-3}, but the effect of shrinkage will reduce the stress in the steel at first cracking. A smaller value of $f_t\, f_{scr}/E_s$ equal to 0.5×10^{-3} will therefore be taken. Substituting into Equation 4.1 gives the following expression for reduction in strain due to tension stiffening at any height in the slab of an unhaunched composite 'T' beam:

$$\delta\varepsilon = \frac{0.5 b_e\, h_f}{A_r\, f_{nt}} \left(\frac{a' - x}{h - x}\right) \times 10^{-3} \qquad (4.2)$$

where: A_r is the area of tensile reinforcement within the effective breadth of the slab.

The term $\delta\varepsilon$ has been calculated for Beams UC1 to UC7 at various values of applied moment, taking f_{nt} to be the amount due to external moment only. $\delta\varepsilon$ is then substracted from ε_{nt} to obtain the curved lines labelled "tension-stiffened" in Figs.4.4 to 4.10. Comparison of the experimental results with the "tension-stiffened" lines shows that the two are usually in agreement to within 10%. The equation proposed for predicting the mean strain in the concrete is therefore:

$$\bar{\varepsilon} = \varepsilon_{nt} + \varepsilon_{sh} - \frac{0.5 b_e\, h_f}{A_r\, f_{nt}} \left(\frac{a' - x}{h - x}\right) \times 10^{-3} \qquad (4.3)$$

The formula presently used[34] for predicting the mean surface strain in the slab of an unhaunched composite 'T' beam is Equation 1.38, which is repeated below:

$$\bar{\varepsilon} = \varepsilon_{nt} - \frac{1.2 b_e\, h_f}{A_r\, f_y} \left(\frac{a' - x}{h - x}\right) \times 10^{-3}$$

This equation has been used to calculate the strain in Tests UC1 to UC7,

and the results are plotted on Figs.4.4 to 4.10, where they are labelled "BS5400". The experimental values of strain are often underestimated at high loads, where a large proportion of shrinkage strains have been released, but overestimated at lower loads due to the tension stiffening term being a constant value.

Equation 4.3 therefore gives better agreement with the results of Tests UC1 to UC7 than existing equations, and its use in practice will require little extra design effort than previously, since f_{nt} and ε_{sh} will have to be calculated anyway.

4.7 Crack widths

Approximately 7000 measurements of crack width were taken during the UC series of tests, and these have been analysed by grouping together all readings along the grid line considered at each load stage. A typical histogram of the distribution of crack widths across a grid line is shown in Fig.4.11. The skewed distribution is common to the grid lines of all tests, so crack widths will be defined by two parameters: the average width across the grid line at the load considered ($\bar{w}$); and the width with a 20% probability of being exceeded (w_{20}).

Fig.4.12 illustrates plots of $\bar{w}$ and w_{20} against $\bar{\varepsilon}$ for two typical grid lines: w_{20} is not shown at low strains because it is a meaningless term when only two or three cracks have formed. The first cracks to form were very wide and although subsequent loading increased their width further, new and smaller cracks formed so that $\bar{w}$ and w_{20} did not increase in proportion to the strain until the latter exceeded about 1×10^{-3}. The same behaviour was observed in the biaxial tests on composite beams already described (Section 1.3.2) and is in direct contrast to the cracking behaviour in reinforced concrete elements, where crack widths and strain are directly proportional no matter how few cracks have formed.

Results from 9 of the 77 grid lines investigated were unusual in that crack width and strain were directly proportional throughout the loading history. This occurred when short cracks formed across a grid line either before or at the same time as the formation of larger cracks which penetrated the full width of the slab (Section 3.2). An example is illustrated in Fig.4.13a.

Results from three other grid lines displayed an opposite tendency, in that crack widths were never directly proportional to strain. This was most noticeable for Grid Lines 3 and 7 of Beam UC5 (Fig.4.13b) but even here, relationships of the form:

$$\bar{w} = k\,\bar{\varepsilon}; \quad w_{20} = k_1\,\bar{\varepsilon}$$

give a sufficiently accurate fit to the test data.

The presence of wide cracks at low strains is discussed in Section 4.11, but for the present we note that a surface strain of 1×10^{-3} in a composite 'T' beam corresponds to a stress in the reinforcement of less than $205N/mm^2$. This is only half the characteristic strength of high-yield reinforcing bars, so for the majority of composite beams it will be sufficiently accurate for design purposes to assume that crack width and strain are proportional.

For all grid lines of Tests UC1 to UC7 graphs of $\bar{w}$ against $\bar{\varepsilon}$ have been plotted, combining results from symmetrical grid lines of the same test. The gradients of the lines which pass through the origin and give the best fit to the test results for which $\bar{\varepsilon}$ exceeds 1000$\mu\varepsilon$ are listed in Table 4.2. They are referred to as the average crack slope and denoted by W_{ave}, since they correspond to the average crack slope in reinforced concrete elements, defined in Section 1.2.4.3. Similarly, crack slopes with a 20% probability of being exceeded (W_{20}) have been obtained from graphs of w_{20} against $\bar{\varepsilon}$, and are listed in Table 4.2. The lines W_{ave} and

W_{20} are shown in Figs.4.12 and 4.13.

W_{ave} and W_{20} are seen to be greater between reinforcing bars than directly over them, especially where the bar spacing is wide and the minimum cover small. Doubling the minimum cover whilst the bar spacing remains constant almost doubles W_{ave} and W_{20} over the reinforcement, and also results in larger crack widths elsewhere in the slab.

4.8 Crack spacing

4.8.1 Effect on crack widths

Consider part of the slab of a composite 'T' beam of original length L_o. At some subsequent load stage, the length of the slab element has increased by δL_o and n cracks of widths $w_1 .. w_i .. w_n$ have formed.

Hence:

$$L_o + \delta L_o = L_o + L_o\ \varepsilon_{cm} + \sum_{i=1}^{n} w_i \qquad (4.4)$$

Now define the crack spacing L as:

$$L = L_o/n$$

Substituting into Equation 4.4 gives:

$$\delta L_o/L_o = \varepsilon_{cm} + (1/L) \sum_{i=1}^{n} w_i/n$$

But $\delta L_o/L_o = \bar{\varepsilon}$, the mean surface strain as determined from the demec gauge readings; and

$\sum_{i=1}^{n} w_i/n = \bar{w}$, the mean crack width.

Hence:

$$\bar{w} = \bar{\varepsilon}\ (1 - \varepsilon_{cm}/\bar{\varepsilon})\ L \qquad (4.5)$$

Equation 4.5 predicts that $\bar{w}/\bar{\varepsilon}$ approaches the crack spacing as the ratio $\varepsilon_{cm}/\bar{\varepsilon}$ tends to zero. This will occur as the strain is increased,

for the mean crack spacing decreases and local failure around the bars will increase, both of which will have the effect of reducing the build-up of strain in the concrete between cracks. Hence, $\bar{w}/\bar{\varepsilon}$ ought to approach L as strain increases, and Figs.4.14 to 4.16 show this to be the case for Test UC5: the same is true for all other tests in the UC series. Crack widths therefore depend to a large extent on crack spacing.

4.8.2 Presentation and discussion of test results

The final crack patterns of the UC series of tests have already been considered (Section 3.2), but the relationship between crack spacing and surface strain is also important. Two typical plots of experimental results, with crack spacing defined as in Section 4.8.1 are shown in Figs.4.17 and 4.18. The same information is presented as graphs of crack spacing against inverse strain in Figs.4.19 and 4.20.

The crack spacing decreased rapidly until the surface strain was approximately 1×10^{-3}. Thereafter only a few extra cracks appeared, and a stable crack pattern may be said to have formed. The linear part of the crack width-strain relationship corresponds to the formation of the stable crack pattern.

Research on cracking in reinforced concrete construction has shown that an inverse relationship exists between crack spacing and strain (Sections 1.2.1 and 1.2.4.3). A least squares regression analysis has therefore been conducted on the results of Tests UC1 to UC7, grouping symmetrical grid lines of each test together. The equation of best fit for each grid line, or pair of grid lines, is listed in Table 4.3, and the appropriate equations are shown on Figs.4.19 and 4.20, where they are labelled "all results".

These lines give a poor fit to the test results: at low strains they indicate that the mean spacing decreases less rapidly with increasing strain than is actually the case, and at high strains they predict that

crack spacing continues to decrease indefinitely, whereas test results show that it approaches a minimum value in the region of 2000-3000με. Further, many of the lines of best fit indicate that the final crack spacing (at infinite strain) is less than 0, which is nonsense, of course.

Now, for many of the grid lines in Tests UC1 to UC7 the first value of crack spacing corresponds to only one or two cracks, and it would be reasonable to discard this result on the grounds that pure chance might have dictated either one crack more or one crack less, causing the spacing to either halve or double. A further linear regression analysis has therefore been conducted on the results of Tests UC1 to UC7, again assuming an inverse relationship between mean crack spacing and average strain, but ignoring all results where less than four cracks have crossed the grid line in question. The equations of best fit are listed in Table 4.3, and the appropriate ones plotted on Figs.4.19 and 4.20, where they are labelled "selected results".

The gradients of the lines of best fit are lower for the second analysis than for the first, with the desirable result that negative values of final crack spacing are predicted for fewer grid lines. However, the work on reinforced concrete summarised in Chapter 1 leads one to expect that the dominant factor in determining the final crack spacing along a grid line is the cover to the nearest reinforcing bar. Hence, for Beams UC2 to UC7, the final crack spacing along grid lines 1 and 9 should be of the same order as on grid lines 3 and 7, and both should be less than the final crack spacing along grid lines 2, 5 and 8. Table 4.3 shows that this is not the case. Therefore the assumed inverse relationship between crack spacing and strain does not appear to describe the cracking behaviour in composite beams as well as in reinforced concrete elements, and a different relationship must be sought.

Inspection of test results such as those in Figs.4.19 and 4.20

suggests that an exponential equation of the form:

$$L = a \exp(b/\bar{\varepsilon}) \qquad (4.6)$$

where: a and b are constants

would give a reasonable fit to the test data. When $\bar{\varepsilon}$ is zero, mean crack spacing would be infinite, but as $\bar{\varepsilon}$ tends to infinity, L tends to the final value, a.

Values of a and b for the grid lines of Tests UC1 to UC7 have been obtained from a least squares regression analysis, grouping data from symmetrical grid lines as before. The results are given in Table 4.4 and the appropriate curves drawn on Figs.4.19 and 4.20 where they are labelled "exponential". A good fit with test results is observed. Further, the final crack spacing (= a in Equation 4.6) is consistently low for grid lines over the reinforcement, and high for those between the reinforcement.

4.8.3 Prediction of final crack spacing

4.8.3.1 General

Many of the cracks in Beams UC1 to UC7, and especially those that were not concentrated around the reinforcement, penetrated the full depth of the slab. The same behaviour will occur in most composite 'T' beams subjected to hogging moment, since the neutral axis is usually below the slab soffit. Therefore, in a slab without reinforcement, or where the bond between the reinforcement and the concrete has broken down, the shear connection between the steel beam and the slab will determine the final crack spacing, as follows.

Consider the composite beam shown in Fig.4.21a. The concrete slab is unreinforced, and it is assumed that the strength of the bond between the surface of the steel beam and the soffit of the slab is negligible.

Fig.4.21b shows a plan of the beam when the applied moment is just

sufficient to cause a crack to form between (say) studs 'A' and 'B'. Once formed, the crack will prevent any tensile stresses developing in the slab between these studs, so their spacing will directly affect the final crack spacing.

Assuming a 45° spread of load from the studs, tensile stresses cannot develop in the area of slab shaded in Fig.4.21b. Subsequent loading may cause a crack to form at section x - x in Fig.4.21c but this crack will not extend further than shown. Cracks at sections y - y and z - z may however extend across the full width of the slab. The final crack spacing in an unreinforced slab therefore depends on the spacing of the shear connectors (S_t) and the distance between them and the grid line considered, measured transversely (H).

4.8.3.2 Final crack spacing midway between bars

For Tests UC2 to UC7, Grid Lines 2 and 8 were about 350mm from the steel beam, so the minimum crack spacing along these grid lines would be 350mm. At a surface strain of 2×10^{-3}, and assuming a mean residual strain in uncracked concrete of 0.5×10^{-3}, Equation 4.5 gives the minimum crack width as:

$$w_{min} = 2 \times 10^{-3} (1 - 2/0.5) \times 350 = 0.525\text{mm}$$

The minimum crack widths measured in Tests UC1 to UC7 were very much less than this; in fact not even the average crack width at 2000με ever reached 0.5mm. This shows that, even midway between reinforcing bars spaced as far apart as 315mm, the crack pattern is critically dependent on the presence of the reinforcement.

Equation 1.31, which is repeated below, may be used to predict crack spacings in terms of bar spacing and minimum cover:

$$2L_{cr} = 0.82 (S^2 + c^2)^{\frac{1}{2}} + 86$$

(all dimensions in mm)

The final crack spacing (L_f) is expected to fall within the range:

$$L_{cr} \leq L_f \leq 2L_{cr}$$

From Reference 7:

$$L_f = 1.33L_{cr}$$

hence: $$L_f = 0.55(S^2 + c^2)^{\frac{1}{2}} + 57 \qquad (4.7)$$

Equation 4.7 makes an average allowance for the effects of bond slip, which is sufficiently accurate for predicting crack spacing mid-way between reinforcing bars.

4.8.3.3 Final crack spacing over reinforcing bars

Both Broms and Beeby agree that if no slip occurs between the reinforcement and the concrete, the minimum final crack spacing will be c, and the maximum spacing 2c (Section 1.2.2). The average spacing would then be 1.33c. This conclusion was reached by studying cracking in reinforced concrete, but there is no reason to suppose different rules would apply to composite slabs: where there would be a difference is in the effect of bond failure before the final crack pattern has formed. This is because bond failure in reinforced concrete will cause crack spacing to tend to the h_o-controlled pattern, whereas in composite beams cracking would tend to a pattern controlled by the shear connection, as discussed in Section 4.8.3.1.

The term which defines the effect of bond failure on crack spacing in Equation 1.27 is $\exp(-K'_3\ c/h_o)$ so for composite beams this term ought to be replaced by one which is a function of $c/(2H + S_t)$. The equation for predicting the final crack spacing above reinforcing bars in the slabs of composite beams ought therefore to be:

$$L_f = 1.33c + (A/B)^{\frac{1}{2}}\ (cB/2\emptyset)\ f(c/[2H + S_t])$$

The final function is derived empirically by plotting λ against $c/(2H + S_t)$ where λ is $(L_f - 1.33c)/(A/B)^{\frac{1}{2}}(cB/2\emptyset)$.

This has been done in Fig.4.22, using values of L_f from Table 4.4. For reasons which are not apparent, the two results from Test UC1 lie well clear of all the other data and have therefore been ignored in deriving the line of best fit, which is:

$$\lambda = 0.51\exp(-12c/[2H + S_t])$$

Hence:

$$L_f = 1.33c + 0.51(A/B)^{\frac{1}{2}}(cB/2\emptyset)\exp(-12c/[2H + S_t]) \qquad (4.8)$$

Equation 4.8 is the one proposed for predicting the mean final crack spacing directly over a reinforcing bar. The last term in the equation determines the variation in mean crack spacing due to internal failure, and it reduces to zero as the term $c/(2H + S_t)$ approaches unity. This is the expected result, for when $c = 2H + S_t$ the patterns controlled by the cover and the shear connection will give much the same crack spacing, irrespective of the amount of bond failure.

4.8.3.4 Final crack spacing anywhere on the concrete slab

It has been shown (Section 1.2.4.3) that crack slopes are inversely proportional to a_{cr}, and a similar relationship might be expected to exist between L_f and a_{cr}. Experimental values of $1/L_f$ and $1/a_{cr}$ are compared in Fig.4.23, and although insufficient data is available to have any confidence in formulae derived from these graphs alone, a linear relationship is seen to give a reasonable fit to the test results.

The mean final crack spacing anywhere on the surface of the slab of a composite beam may therefore be found graphically by first calculating the final crack spacing over bars (L_b) and mid-way between them (L_m) and then plotting a graph of $1/L_f$ against $1/a_{cr}$. Equation 4.9 below gives the expression for calculating L_f directly, but it is a rather cumbersome

one: the graphical solution is sufficiently accurate and much simpler to use.

$$L_f = \frac{(a_m - c)\, a_{cr}\, L_b\, L_m}{a_m\, L_b(a_{cr} - c) + c\, L_m(a_m - a_{cr})} \qquad (4.9)$$

where: a_m is the distance from the surface of the reinforcement to the point on the concrete surface mid-way between bars.

4.8.3.5 Comparison with experimental results

Equations 4.7 to 4.9 have been used to predict the final crack spacing along all grid lines of Beams UC1 to UC7. The predicted values are compared with the experimental ones (from Table 4.4) in Fig.4.24 and are seen to be in reasonable agreement with them.

4.9 Prediction of crack widths

4.9.1 Introduction

In Sections 4.9.2 and 4.9.3 formulae are developed for predicting the crack widths on the surface of the slab of a composite 'T' beam, when the strain there exceeds 1×10^{-3}. Crack widths at lower strains are considered in Section 4.11.

4.9.2 Mean crack widths

As noted, once the surface strain exceeds about 1×10^{-3} the value of $\bar{w}/\bar{\varepsilon}$ is constant and very nearly equal to the crack spacing. However, the spacing still decreases slightly with increasing strain and Equation 4.5 shows that there must be a compensating reduction in the ratio $\varepsilon_{cm}/\bar{\varepsilon}$ to maintain the constant value of $\bar{w}/\bar{\varepsilon}$ (ie. W_{ave}).

It seems reasonable to assume that the equation for predicting W_{ave} will be of the same form as that for predicting the final crack spacing, and in Fig.4.25 experimental values of W_{ave} for Tests UC1 to UC7 are compared with L_f as calculated from Equations 4.7 to 4.9. The line:

$$W_{ave} = 1.25L_f$$

is seen to give a reasonable fit to the data.

The equations put forward for predicting the average crack width when the mean surface strain exceeds 1×10^{-3} are therefore:

$$W_b = 1.66c + 0.64(c\ B/2\phi)(A/B)^{\frac{1}{2}}\exp(-12c/[2H + S_t]) \qquad (4.10)$$

$$W_m = 0.70(S^2 + c^2)^{\frac{1}{2}} + 70 \qquad (4.11)$$

$$W = \frac{(a_m - c)\ a_{cr}\ W_b\ W_m}{a_m\ W_b\ (a_{cr} - c) + c\ W_m\ (a_m - a_{cr})} \qquad (4.12)$$

where: W_b is the crack slope directly over a reinforcing bar;

W_m is the crack slope on the surface of the concrete mid-way between reinforcing bars.

Using the term 'slope ratio' to denote the ratio of the experimental value of the crack slope to the predicted value, the mean of the slope ratios for the grid lines of Tests UC1 to UC7 is 1.00, and the standard deviation is 0.21.

To judge the usefulness of any crack width formulae it is first necessary to determine the degree of accuracy to be expected of them. Consider the worst possible formula for predicting crack widths in terms of crack slope:

$$W_{ave} = k$$

where: k is a constant.

In other words crack slope is assumed to be independent of all variables. The mean of all measured average crack slopes of Tests UC1 to UC7 is 126mm and the standard deviation is 54.0, so if we were to use for a crack width formula:

$$W_{ave} = 126\text{mm}$$

the mean slope ratio would be 1.00 and the coefficient of variation would be 54.0/126 or 0.43. Therefore, to be of any value a formula for predicting crack slopes must give a slope ratio coefficient of variation considerably less than 0.43.

Now, cracking is a random phenomenon and test results are subject to experimental error, so there will be a lower limit to the coefficient of variation associated with any crack width formula. Comparison of results from nominally identical grid lines (symmetrical grid lines of one test or the same grid line of two identical tests) shows that for Tests UC1 to UC7 this lower limit is of the order of 0.15.

Summarising, a formula which exactly predicted the effects of the known parameters (cover, bar spacing, etc.) would give a coefficient of variation for the slope ratios of approximately 0.15, and a formula which takes no account of any parameters, known or otherwise, gives a coefficient of variation of 0.43.

Equations 4.10 to 4.12 when applied to the grid lines of Beams UC1 to UC7 give a coefficient of variation of 0.21, which compares very favourably with the limits set out above.

4.9.3 Crack widths with a 20% probability of being exceeded

Current design requirements involve the calculation of the crack width with a 20% probability of being exceeded (w_{20}), which must be less than some specified limit. Any design formulae for determining crack widths in composite beams should therefore predict w_{20}.

It is now assumed that the equations for predicting W_{20} are of the same form as those for predicting the final crack spacing, although the relationship is not necessarily a linear one. Hence, one may write:

$$W_b = K_1 c + (A/B)^{\frac{1}{2}}(c\ B/2\phi)\ f(c/[2H + S_t]) \qquad (4.13)$$

and

$$W_m = K_2(S^2 + c^2)^{\frac{1}{2}} + K_3 \qquad (4.14)$$

where: K_1, K_2, K_3 are constants;

$f(c/[2H + S_t])$ is a function of $c/[2H + S_t]$

The constant K_1 determines the crack width directly over a bar in the absence of slip, and this should be the same for both reinforced concrete and composite construction. From Reference 25, $K_1 = 1.59$ for a 20% probability of the crack width being exceeded. The function of $c/(2H + S_t)$ is determined by plotting η against $c/(2H + S_t)$ where η is $(W_b - 1.59c)/(A/B)^{\frac{1}{2}}(c\ B/2\emptyset)$, and finding the line of best fit to the test data. This has been done in Fig.4.26 and gives the following equation for calculating crack widths with a 20% probability of being exceeded:

$$W_b = 1.59c + 0.95(A/B)^{\frac{1}{2}}(c\ B/2\emptyset)\exp(-2.5c/[2H + S_t]) \qquad (4.15)$$

To obtain the values of K_2 and K_3 in Equation 4.14 one should plot W_m against $(S^2 + c^2)^{\frac{1}{2}}$, but since the latter term is in the range 151mm to 157mm for all save one grid line of Beams UC1 to UC7 this method would be very unreliable. Instead, it is assumed that W_m is proportional to the mean final crack spacing and experimental values of W_m are plotted against L_f, calculated from Equation 4.7. The gradient of the line of best fit to the data is 1.70, which gives the following equation for predicting the crack width with a 20% probability of being exceeded:

$$W_m = 0.94(S^2 + c^2)^{\frac{1}{2}} + 97 \qquad (4.16)$$

As for final crack spacing, an inverse relationship between W_{20} and a_{cr} is assumed, so W_{20} anywhere on the surface of the slab of a composite 'T' beam may be found from W_b and W_m either graphically or by using Equation 4.12. The values of W_b and W_m must, of course, be those appropriate to the 20% level of probability.

Equations 4.12, 4.15, and 4.16 have been used to calculate W_{20} for each grid line of Beams UC1 to UC7, and the results are compared with the

experimental values in Fig.4.27. The mean value of all slope ratios is 1.05, and their standard deviation 0.23, which gives a coefficient of variation of 0.22. The range within which the coefficient of variation is expected to fall has been calculated by the method described in Section 4.9.2, using values of W_{20} rather than W_{ave}, and is found to be from 0.15 to 0.42. Equations 4.12, 4.15 and 4.16 therefore give good correlation with the test results.

4.10 Comparison of various crack width formulae

4.10.1 Introduction

The aim of this section is to determine whether or not existing formulae may be applied to cracking in composite 'T' beams. The work reported in Chapter 1 has shown that the bond-slip theory is inappropriate when high-yield reinforcement is used, so formulae based on this theory are not considered here. Neither are any purely empirical relationships based on research on plain reinforced concrete elements, since the cracking behaviour of these is dissimilar to that of composite 'T' beams.

The numerical comparisons are summarised in Table 4.5, the derivation of which is now described.

For each group of crack width formulae considered, the predicted crack slopes for the grid lines of Beams UC1 to UC7 have been calculated. Some formulae predict W_{ave} and others W_{20}: Table 4.5 indicates which. Slope ratios for each grid line and each method of prediction were then found, using experimental values of W_{ave} or W_{20} from Table 4.2, as appropriate. Table 4.5 gives the mean, standard deviation (S.D.) and coefficient of variation (C.V.) for various groups of slope ratios; the first two rows deal with the crack width formulae developed in Sections 4.9.2 and 4.9.3 respectively.

4.10.2 Equation based on stress-redistribution

This is Equation 1.17, which is repeated below:

$$\bar{w} = 2r_t\, c_e\, \varepsilon_s \qquad (4.17)$$

where: c_e is the effective cover, defined in Section 1.2.2.3.

Directly over a reinforcing bar, c_e equals the minimum cover, which gives:

$$\bar{w}/\bar{\varepsilon} = W_{ave} = 2c \qquad (4.18)$$

Equation 4.18 makes no allowance for the effect of bond failure in the region of a crack, and is expected therefore to underestimate crack slopes directly over bars. This is confirmed by the results of Tests UC1 to UC7 (see Table 4.5).

The average crack slope mid-way between adjacent reinforcing bars is given by:

$$W_{ave} = 2c_e \qquad (4.19)$$

Crack widths obtained from this equation are compared with those from the formula for predicting W_{ave} in composite beams (4.11) in Fig.4.28. Widths have been calculated for various values of bar spacing and minimum cover, assuming a mean surface strain of 1.6×10^{-3}. For small covers and small bar spacings, where the effects of local bond failure will be greatest, the formula based on stress redistribution is seen to underestimate the crack width calculated from the composite formulae by as much as 35%. For the values of cover and bar spacing in Beams UC1 to UC7 however, there is little to choose between the two methods, (see Table 4.5) save that the calculation of c_e for Equation 4.19 is rather complicated.

4.10.3 Equations based on the no-slip theory

The equations derived from the no-slip theory are the "tension formulae" (Equations 1.23, 1.25 and 1.27). The crack width equation used

in current codes of practice (1.28) has been derived from these, and is also studied here.

Equations 1.27 and 4.10 for predicting crack widths directly over a bar differ only in the term which defines the effect of bond failure: the former predicts that bond failure will result in the crack pattern being determined by the value of h_o, and the latter by the value of $(2H + S_t)$. In a composite slab where the steel beam spacing is 2.0m, say, h_o remains constant whereas $(2H + S_t)$ varies across the width so the two methods cannot give the same width for all points on the slab. This is illustrated in Fig.4.29 in which the predicted widths for two different composite slabs are compared. The two slabs have a similar cross section to those of Beams UC2, UC3, UC4 and UC7 respectively, and the range of $(2H + S_t)$ investigated in these specimens is indicated. There is good agreement between Equations 1.27 and 4.10 within this range - in fact Table 4.5 shows that the equation developed for cracking in reinforced concrete is the better of the two.

There is no single equation amongst the tension formulae which directly predicts crack widths on the surface of concrete mid-way between adjacent reinforcing bars, so comparisons between the tension formulae and Equation 4.11 may only be made for individual beams. Table 4.5 shows that the tension formulae give poorer predictions of W_m for the Tests UC1 to UC7 than does Equation 4.11.

The simplifications made to the tension formulae in order to obtain Equation 1.28 mean that its application is limited to predicting the crack width with a 20% probability of being exceeded mid-way between the reinforcing bars. Table 4.5 shows that these simplifications result in Equation 1.28 giving good predictions of W_{20} for the Tests UC1 to UC7. However, Fig.4.30 shows that there is little agreement between this equation and the one developed specifically for composite 'T' beams (4.16)

outside the range of S and h_o studied in Tests UC1 to UC7.

4.10.4 Equation based on individual crack width theory

This is Equation 1.35, which is used to predict the crack width with a 20% probability of being exceeded on the surface of the concrete midway between adjacent reinforcing bars. The equation is similar to the one developed in this thesis (4.16) although the two methods require the surface strain to be calculated in different ways. In Equation 1.35, strain is calculated on the assumption that tension-stiffening is zero, whereas in Equation 4.16 a reasonable estimate of the actual surface strain is required, and can only be obtained by considering the effects of tension-stiffening.

Where the effect of tension-stiffening is small, Equations 1.35 and 4.16 will give virtually the same answer, but Equation 1.35 will give larger values of w_{20} whenever tension-stiffening significantly reduces the mean surface strain.

4.11 Crack widths at low strain

4.11.1 Discussion of results

As noted, the first few cracks to form in Beams UC1 to UC7 were often much wider, in relation to the average surface strain, than cracks which formed at higher loads. For example, along Grid Line 7 of Beam UC5, the average crack width at a mean surface strain of 0.3×10^{-3} was 0.25mm, giving $\bar{w}/\bar{\varepsilon}$ = 833mm, whereas at higher strains the average value of $\bar{w}/\bar{\varepsilon}$ was approximately 90mm. Values of w_{20} did not fall as the strain increased (as did $\bar{w}$ in some cases), but neither did they increase in proportion to the strain until $\bar{\varepsilon}$ exceeded approximately 1×10^{-3}.

It is believed that the behaviour described above is due to the release of shrinkage strains as cracks form in the slab.

4.11.2 Crack widths due to release of shrinkage strain

Consider the short length of composite beam illustrated in Fig.4.31. The strains in the beam just before cracking occurs are shown in Fig.4.31a.

If the external moment (M) is increased slightly, a crack will form in the slab and a proportion of the shrinkage strains will be relieved. The following assumptions are now made in order to estimate the crack width:

(i) the first crack to form penetrates the full depth and breadth of the slab. This was always the case when wide cracks formed at low strain;

(ii) in the absence of the externally applied load, the steel beam would return to its original length between the studs A and B. This assumption is checked later;

(iii) there is no relative movement between the slab, the reinforcement and the steel beam at the studs, i.e. the shear connection is assumed to be rigid;

(iv) there is no bond between the slab soffit and the tension flange of the steel beam;

(v) the bond between the reinforcement and the slab is completely destroyed over a length $S_t/4$ on both sides of the crack, but is otherwise intact. This assumption cannot be checked, but crack widths are calculated for other assumed lengths of bond failure.

Fig.4.31b shows the composite beam and the idealised strain distribution (ignoring the strains due to external load for the time being).

Making the assumptions above, the crack width in Test UC5 due to the release of shrinkage alone is 0.11mm. The corresponding increase in the average surface strain between the two studs is 0.45×10^{-3}, so w/ε is equal to 244mm. This is of the same order as W_{ave} for grid lines between the reinforcing bars, but more than twice as large as W_{ave} for grid lines

over the bars. The difference is exaggerated by the method of averaging strains over the length of the grid lines, for a strain of 0.45×10^{-3} between two studs 250mm apart gives a value for $\bar{\varepsilon}$ of only 0.056×10^{-3}. Due to the release of shrinkage therefore, $\bar{w}/\bar{\varepsilon}$ for the first crack to form in the slab of UC5 is estimated as 1867mm, or six times larger than the maximum experimental value of W_{ave}.

A proportion of the measured widths and strains will be due to external moments for which $\bar{w}/\bar{\varepsilon}$ is comparatively small, so the experimental value of $\bar{w}/\bar{\varepsilon}$ is not expected to be as high as 1867mm. As the strain increases, cracking due to the external moment begins to dominate, and the experimental values of $\bar{w}/\bar{\varepsilon}$ drop. Also, once a large proportion of the shrinkage strain between two studs has been released by the formation of a single crack, further cracks between the same studs will be dominated by the external moment as soon as they form. This explains why the first cracks to appear in Beams UC1 to UC7 were large compared with the ones that formed later.

Assumption (ii) on p119 may be checked by comparing the restraining force (F) that the steel beam must exert on the cracked and uncracked slabs to retain its original length. For UC5, F for the cracked slab is less than 7% of that for the uncracked slab, so the assumption is reasonable.

Crack widths and strains due to the release of shrinkage effects in UC5 have been calculated, assuming different lengths of bond failure, and the results are shown in Table 4.6. The stud spacing has been taken as 250mm. We note that if the bond has failed over 20mm on each side of the crack, the restraining force in the cracked slab is 21% of the restraining force in the uncracked slab. Assumption (ii) would therefore be invalid and a sagging curvature would develop in the composite beam, reducing the crack width. Nonetheless, $\bar{w}/\bar{\varepsilon}$ due to the release of shrinkage would

still be very much greater than the largest experimental value of W_{ave}.

4.11.3 Prediction of crack widths at low strains

The calculations above show that the large crack widths at low strains observed in Tests UC1 to UC7 result from shrinkage of the slab. The method used is not suitable for design purposes however, because it requires an estimate of the length over which the bond between the concrete and the reinforcement is destroyed.

In Tests UC1 to UC7, w_{20} was often almost constant until at a strain of about 1×10^{-3}, it began to increase in proportion to strain. The value of w_{20} at $\bar{\varepsilon} = 1 \times 10^{-3}$ was never significantly exceeded while the strain was less than this. Pending further research into crack widths in composite beams at low strain, the following rule is therefore suggested: that in calculating the design crack width from Equations 4.12, 4.15 and 4.16, $\bar{\varepsilon}$ should never be taken as less than 1×10^{-3}.

Given this requirement, Equation 4.16 may be used to calculate an absolute maximum bar spacing in terms of the permitted crack width. For example, if the permitted crack width is 0.2mm, and the cover to the main reinforcement 40mm, the clear distance between bars must not exceed 205mm, no matter how small the tensile strain in the slab.

Test	Strain (10^{-6}) : extension positive					ϕ_{sh} (km^{-1})
	ε_{sh} (slab)	ε_{st}	ε_1	ε_2	ε_3	
UC1	-440	71	-272	168	43	1.10
UC2	-401	57	-260	141	37	1.04
UC3	-440	71	-272	168	43	1.10
UC4	-248	2	-170	78	25	0.68
UC5	-586	83	-358	228	72	1.62
UC6	-269	62	-149	120	23	0.58
UC7	-236	3	-162	72	25	0.65

Key:-

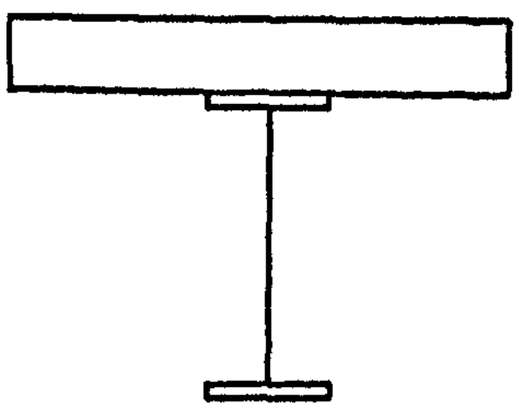

Section

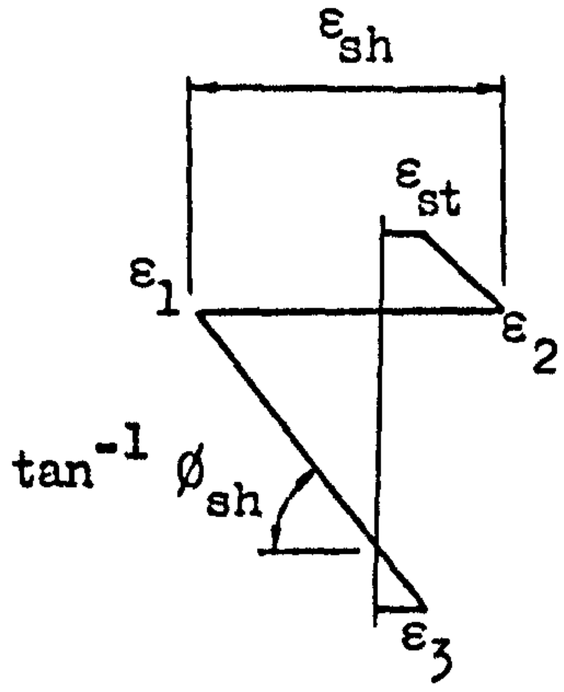

Strain diagram

TABLE 4.1 ESTIMATED STRAIN PROFILES IN UC1-UC7 DUE TO SHRINKAGE

Beam	Grid lines	W_{ave} (mm)	W_{20} (mm)
1	1,5	70	100
	2,4	120	143
	3	80	125
2A	1,9	60	81
	2,8	142	205
	3,7	70	125
	5	190	225
2B	1,9	51	63
	2,8	208	253
	3,7	63	112
	5	170	240
3A	1,9	69	109
	2,8	142	225
	3,7	61	95
	4,6	162	205
	5	140	155
3B	1,9	59	100
	2,8	174	230
	3,7	77	130
	4,6	118	195
	5	190	245
4	1,9	93	157
	2,8	200	270
	3,7	120	190
	4,6	165	250
	5	115	170
5	1,9	60	95
	2,8	140	250
	3,7	86	145
	4,6	165	243
	5	165	280
6	1,9	48	57
	2,8	168	250
	3,7	51	70
	3a,7a	57	90
	4,6	102	178
	5	131	220
7	1,9	142	260
	2,8	245	330
	3,7	150	225
	3a,7a	193	310
	4,6	205	340
	5	186	330

TABLE 4.2 EXPERIMENTAL VALUES OF W_{ave} AND W_{20} FOR BEAMS UC1-UC7

Test	Grid lines	$L = A + B/\bar{\varepsilon}$ (All results)		$L = A + B/\bar{\varepsilon}$ (Selected results)	
		A	B	A	B
1	1,5	31.8	.1266	31.8	.1266
	2,4	49.1	.1526	96.5	.1009
	3	21.7	.1841	21.7	.1841
2A	1,9	39.5	.0644	39.5	.0644
	2,8	52.5	.2093	122.3	.1164
	3,7	-93.6	.3286	-81.5	.3129
	5	40.7	.2660	165.6	.1001
2B	1,9	34.4	.0607	34.4	.0607
	2,8	-67.9	.3704	28.3	.2727
	3,7	-129.0	.3404	-22.1	.2162
	5	-117.6	.3989	-67.7	.3468
3A	1,9	-107.1	.2328	55.1	.0543
	2,8	56.0	.1680	56.0	.1680
	3,7	-22.3	.1367	-22.3	.1367
	4,6	134.2	.0981	134.2	.0981
	5	76.3	.0969	76.3	.0969
3B	1,9	-76.3	.1834	-3.1	.1104
	2,8	37.9	.2306	103.6	.1594
	3,7	-133.0	.2718	11.0	.1151
	4,6	-57.4	.2749	73.9	.1259
	5	0.0	.2703	131.9	.1187
4	1,9	20.2	.1159	74.7	.0620
	2,8	-40.1	.3911	43.8	.2927
	3,7	-15.9	.2314	49.0	.1432
	4,6	-156.0	.4146	82.7	.1556
	5	-57.2	.2377	-2.6	.1718
5	1,9	-12.3	.1241	-12.3	.1241
	2,8	-300.3	.6695	57.6	.2007
	3,7	-397.3	.7173	-18.6	.2184
	4,6	-289.2	.6781	68.0	.2098
	5	-43.4	.3616	61.5	.2236
6	1,9	-53.3	.1908	-33.2	.1329
	2,8	-71.3	.2809	99.8	.1236
	3,7	-259.6	.3635	-45.9	.1558
	3a,7a	-58.2	.1853	-58.2	.1853
	4,6	-8.1	.2050	16.1	.1756
	5	-176.5	.3750	51.1	.1578
7	1,9	8.5	.1961	22.1	.1802
	2,8	64.8	.3213	148.0	.1817
	3,7	-20.5	.2829	-33.3	.2974
	3a,7a	7.6	.3487	116.9	.1641
	4,6	-19.6	.3750	122.4	.1444
	5	-47.6	.3468	-23.1	.3164

TABLE 4.3 EXPERIMENTAL EQUATIONS OF BEST FIT: CRACK SPACING AND SURFACE STRAIN

(See Table 4.2 for location of grid lines)

Test	Grid lines	$L = ae^{b/\bar{\varepsilon}}$	
		a	$b(10^{-6})$
1	1,5	85	546
	2,4	118	494
	3	95	692
2A	1,9	65	423
	2,8	136	526
	3,7	74	862
	5	159	541
2B	1,9	53	538
	2,8	152	699
	3,7	59	1063
	5	105	883
3A	1,9	53	723
	2,8	114	583
	3,7	48	709
	4,6	160	325
	5	119	341
3B	1,9	53	609
	2,8	145	507
	3,7	55	739
	4,6	102	619
	5	145	540
4	1,9	88	410
	2,8	183	536
	3,7	99	604
	4,6	123	626
	5	70	767
5	1,9	49	650
	2,8	101	892
	3,7	58	1108
	4,6	113	872
	5	125	755
6	1,9	51	589
	2,8	139	441
	3,7	37	824
	3a,7a	42	864
	4,6	84	702
	5	111	547
7	1,9	93	645
	2,8	189	592
	3,7	108	703
	3a,7a	150	692
	4,6	137	760
	5	118	743

TABLE 4.4 EXPONENTIAL LINES OF BEST FIT TO TEST DATA: CRACK SPACING AND SURFACE STRAIN

(See Table 4.2 for location of grid lines)

Formulae used	Directly over reinforcement			Mid-way between reinforcement			Total		
	Mean	S.D.	C.V.	Mean	S.D.	C.V.	Mean	S.D.	C.V.
4.10,11,12 (W_{ave})	1.01	0.22	0.21	0.96	0.18	0.19	1.00	0.21	0.21
4.12,15,16 (W_{20})	1.07	0.26	0.25	1.00	0.19	0.19	1.05	0.23	0.22
Stress redistribution (W_{ave})	1.62	0.29	0.18	1.04	0.19	0.19	-	-	-
No-slip theory (W_{ave})	1.00	0.16	0.16	0.79	0.14	0.18	0.90	0.19	0.21
CP110 BS5400 (W_{20})	Not applicable			1.03	0.20	0.19	Not applicable		

TABLE 4.5 STATISTICS OF SLOPE RATIOS FOR VARIOUS CRACK WIDTH FORMULAE

Length on each side of crack over which bond destroyed (mm)	w (mm)	ε between studs ($\times 10^{-6}$)	Equivalent $\bar{w}/\bar{\varepsilon}$ (mm)	Restraint force (kN)
20	0.07	450	1280	231
62.5	0.11	450	1867	71
125	0.11	450	2000	0

TABLE 4.6 CRACK WIDTHS DUE TO RELEASE OF SHRINKAGE STRAINS

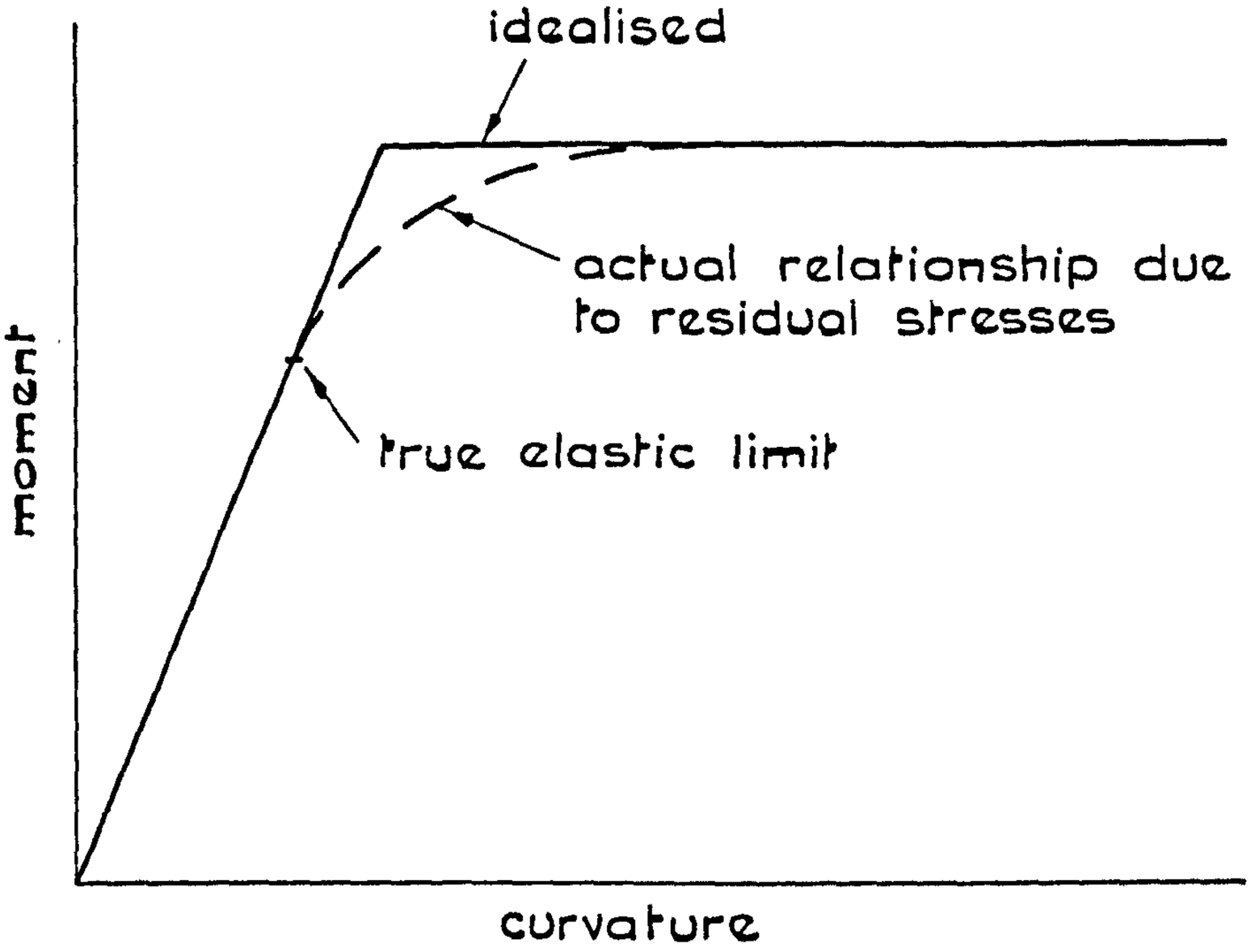

FIG. 4.1 MOMENT-CURVATURE RELATIONSHIPS FOR A ROLLED STEEL GIRDER

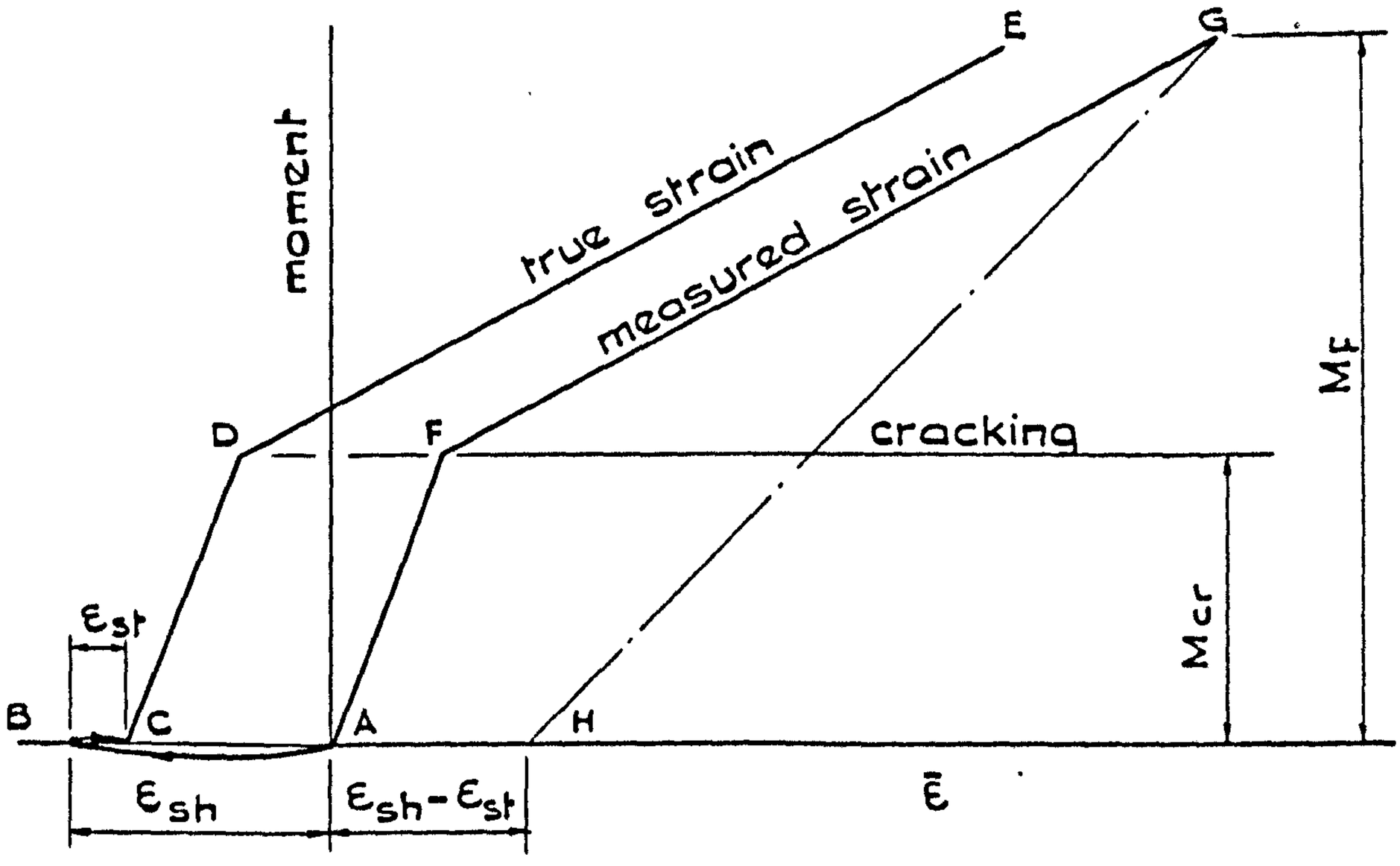

FIG. 4.2 RELATIONSHIP BETWEEN TRUE AND MEASURED STRAIN

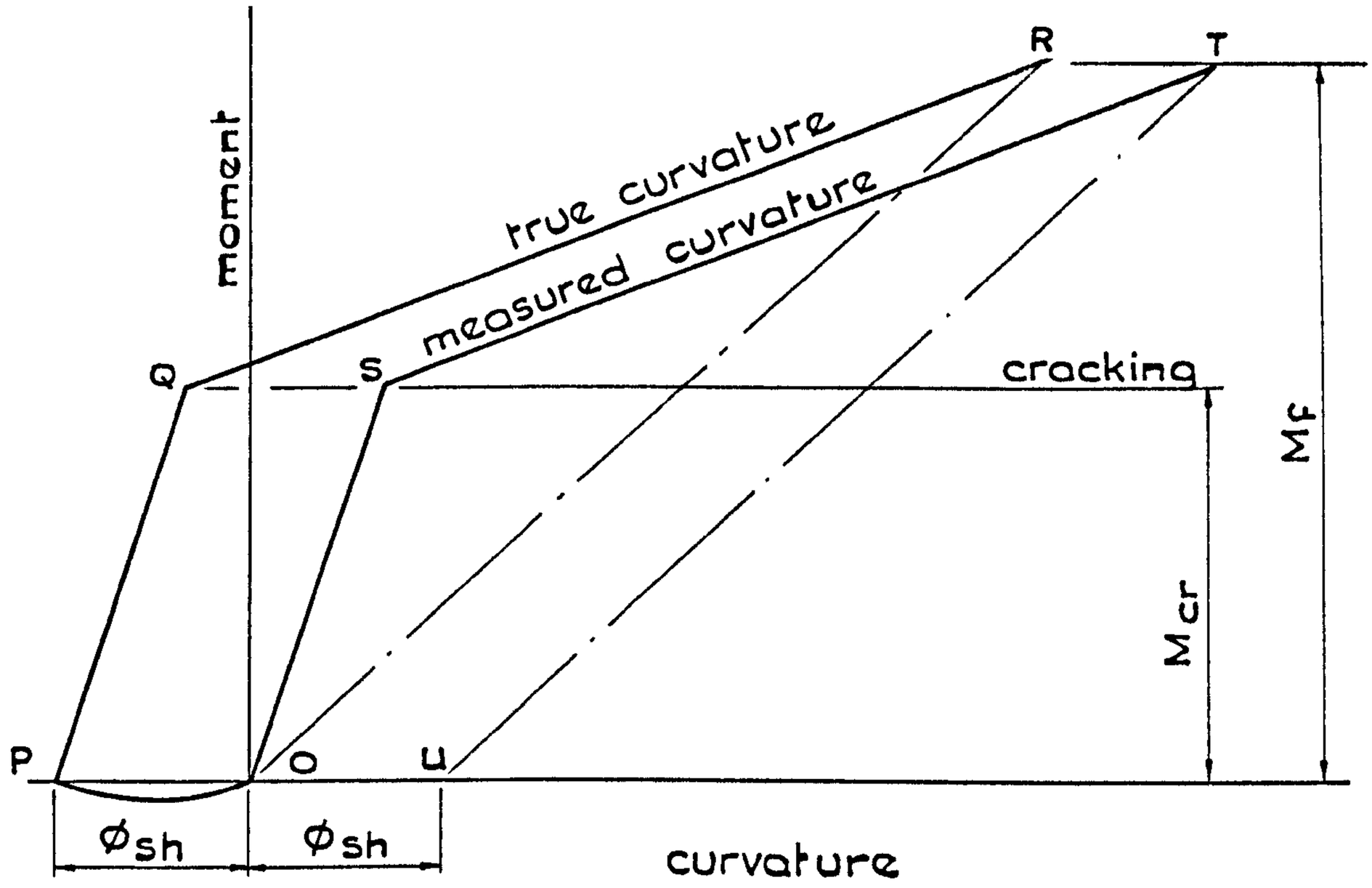

FIG. 4.3 RELATIONSHIP BETWEEN TRUE AND MEASURED CURVATURE

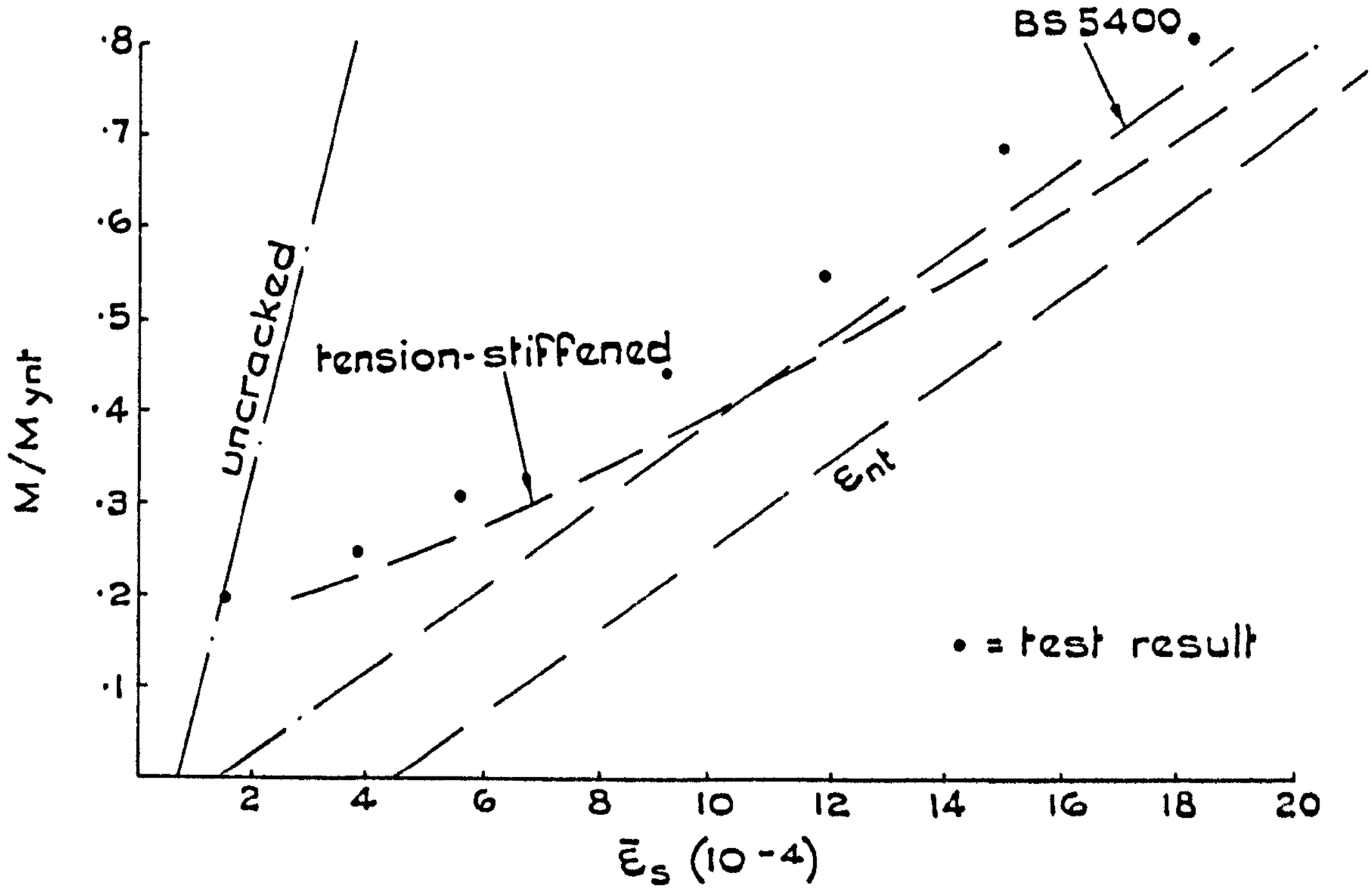

FIG. 4.4 MOMENT-STRAIN RELATIONSHIPS FOR UC1

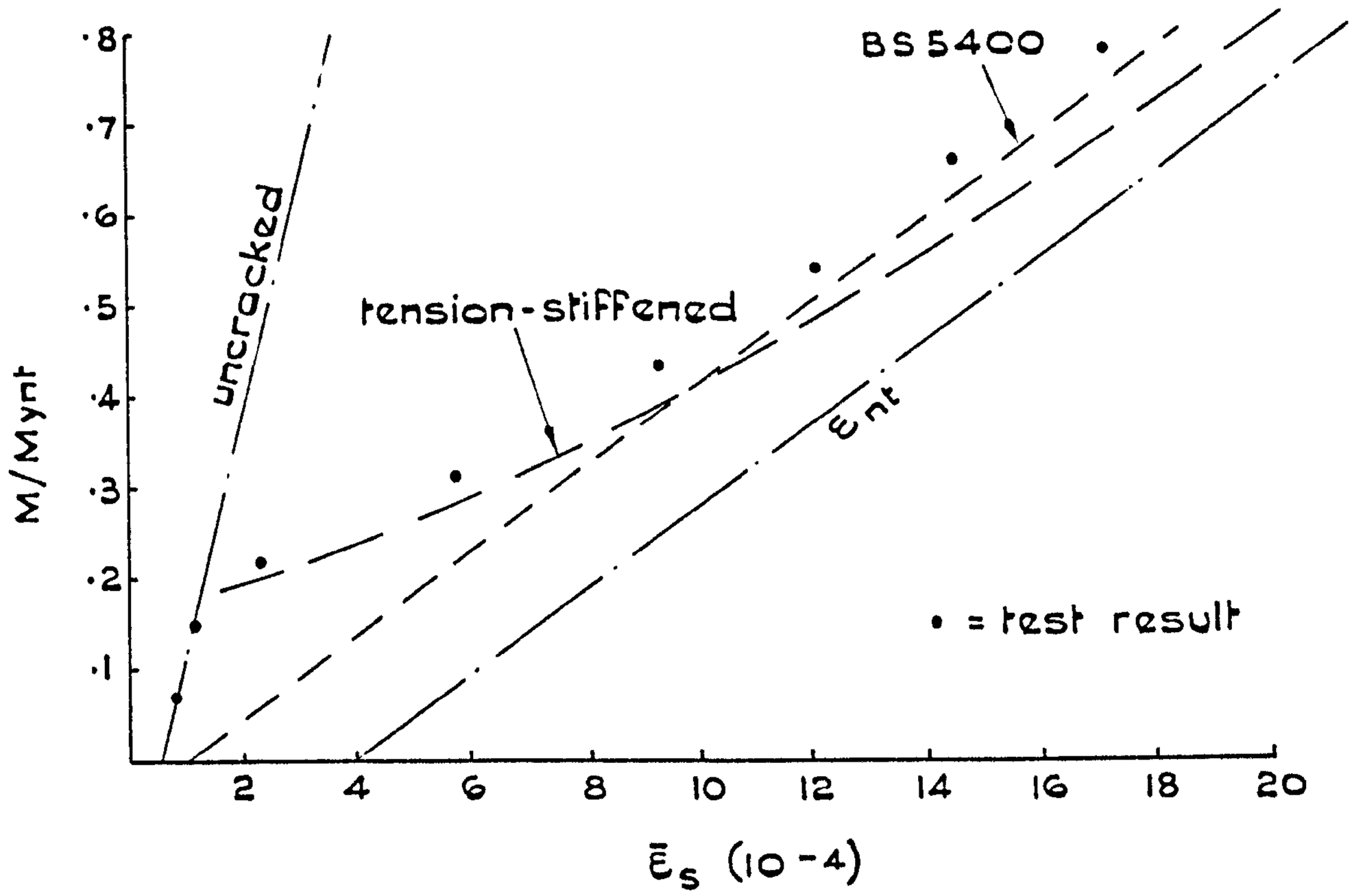

FIG. 4.5 MOMENT-STRAIN RELATIONSHIPS FOR UC2

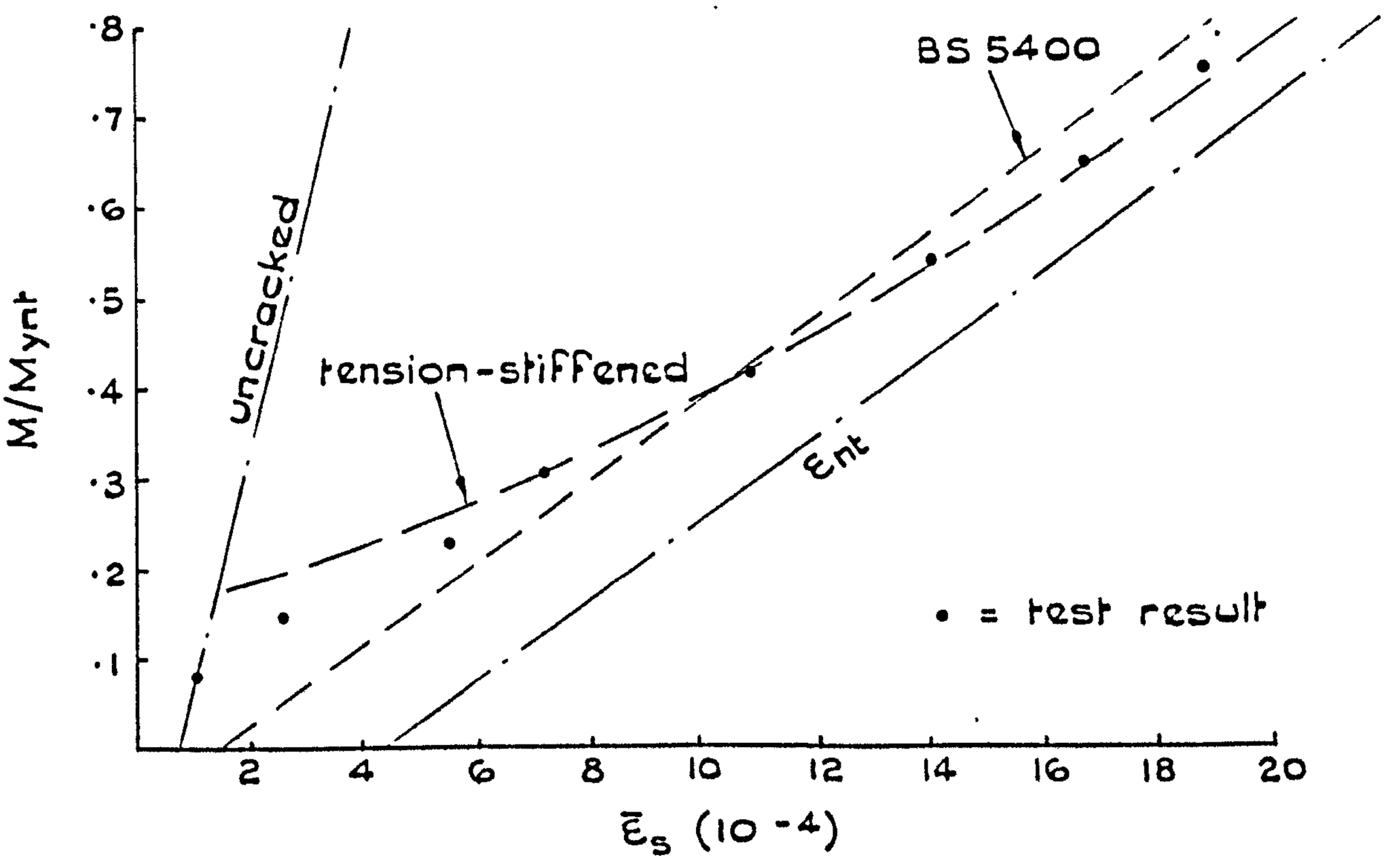

FIG. 4.6 MOMENT-STRAIN RELATONSHIPS FOR UC3

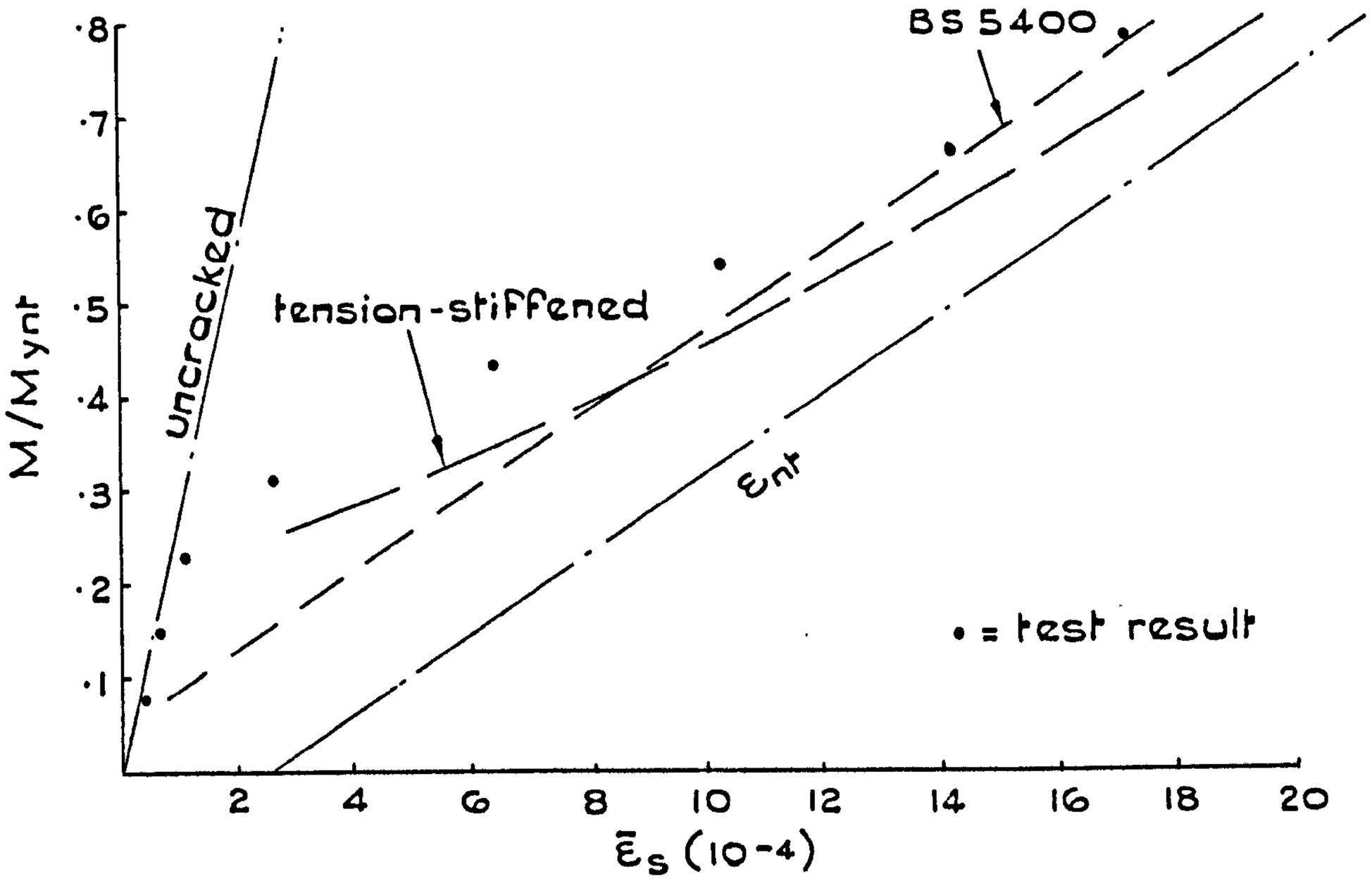

FIG. 4.7 MOMENT-STRAIN RELATIONSHIPS FOR UC4

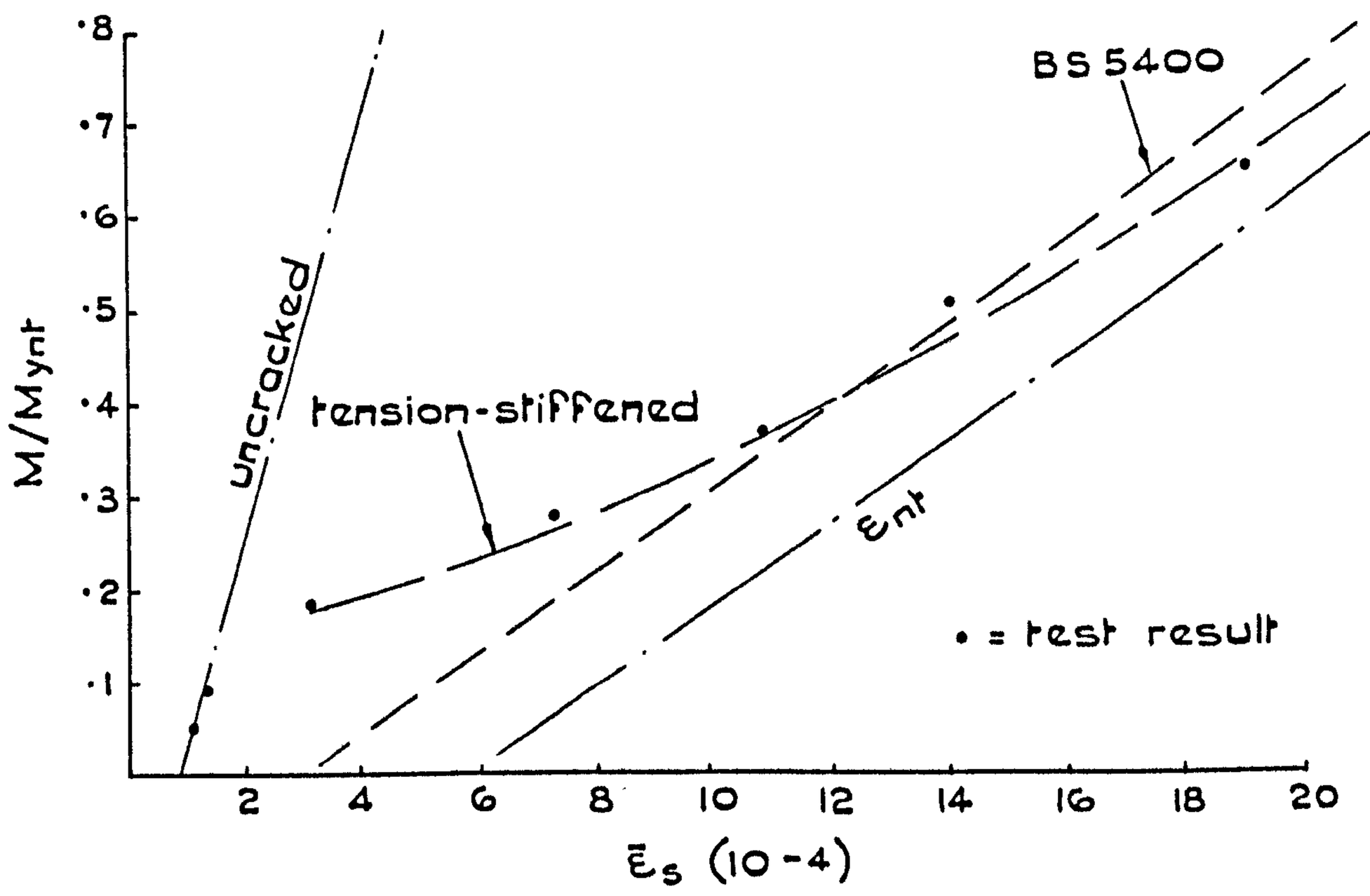

FIG. 4.8 MOMENT-STRAIN RELATIONSHIPS FOR UC5

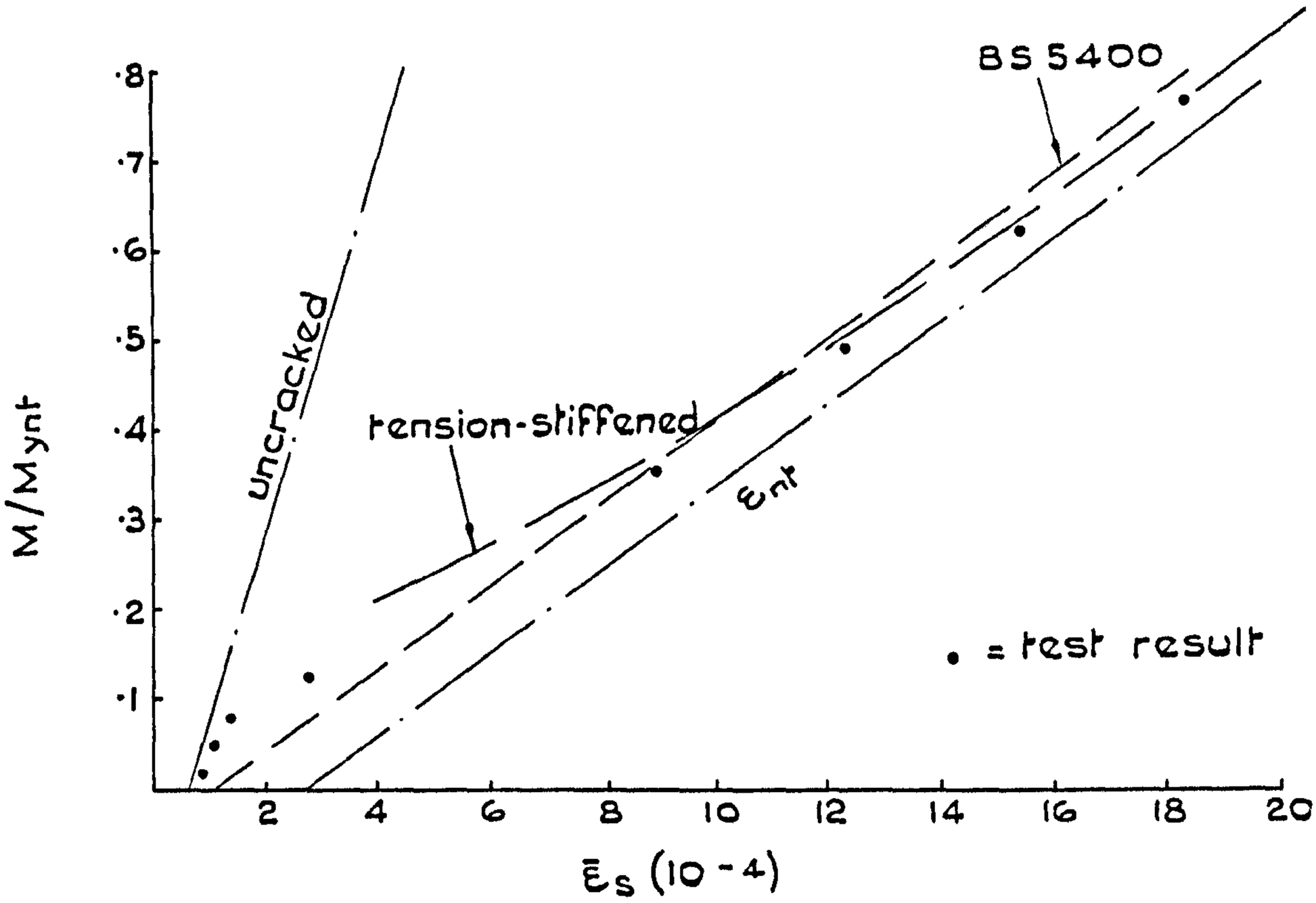

FIG. 4.9 MOMENT-STRAIN RELATIONSHIPS FOR UC6

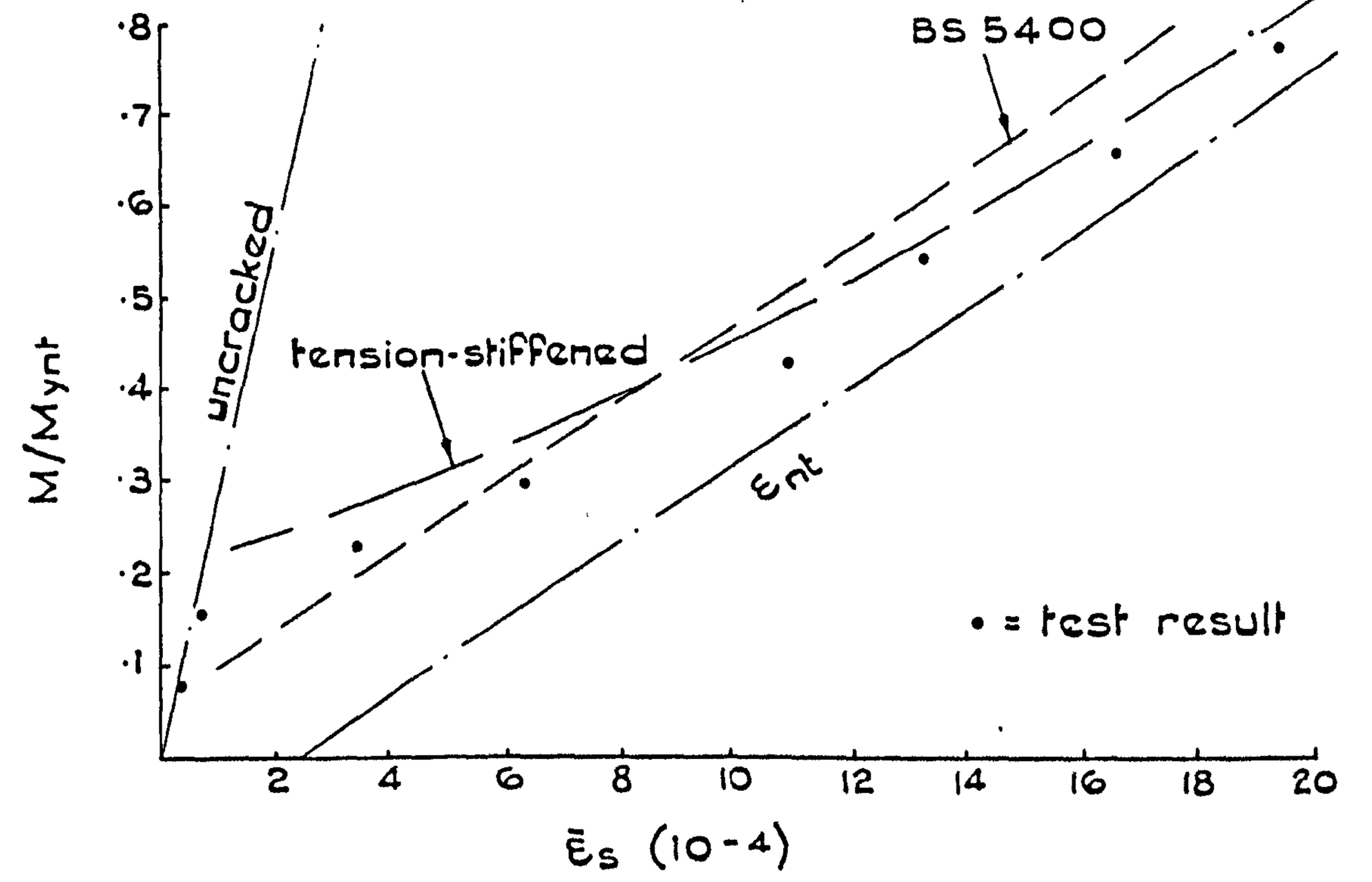

FIG. 4.10 MOMENT-STRAIN RELATIONSHIPS FOR UC7

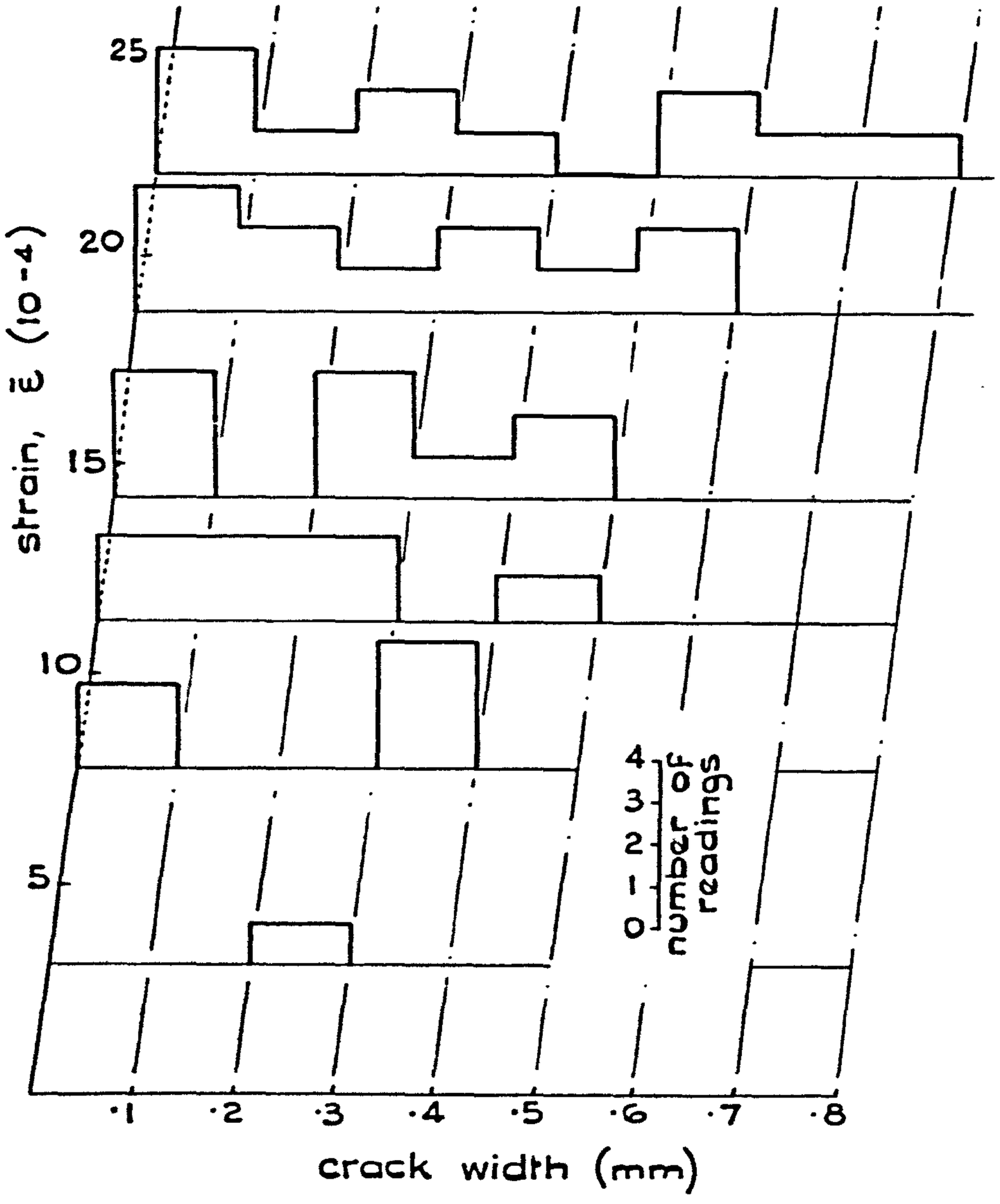

FIG.4.11 DISTRIBUTION OF CRACK WIDTHS
GRID LINE 8, BEAM UC5

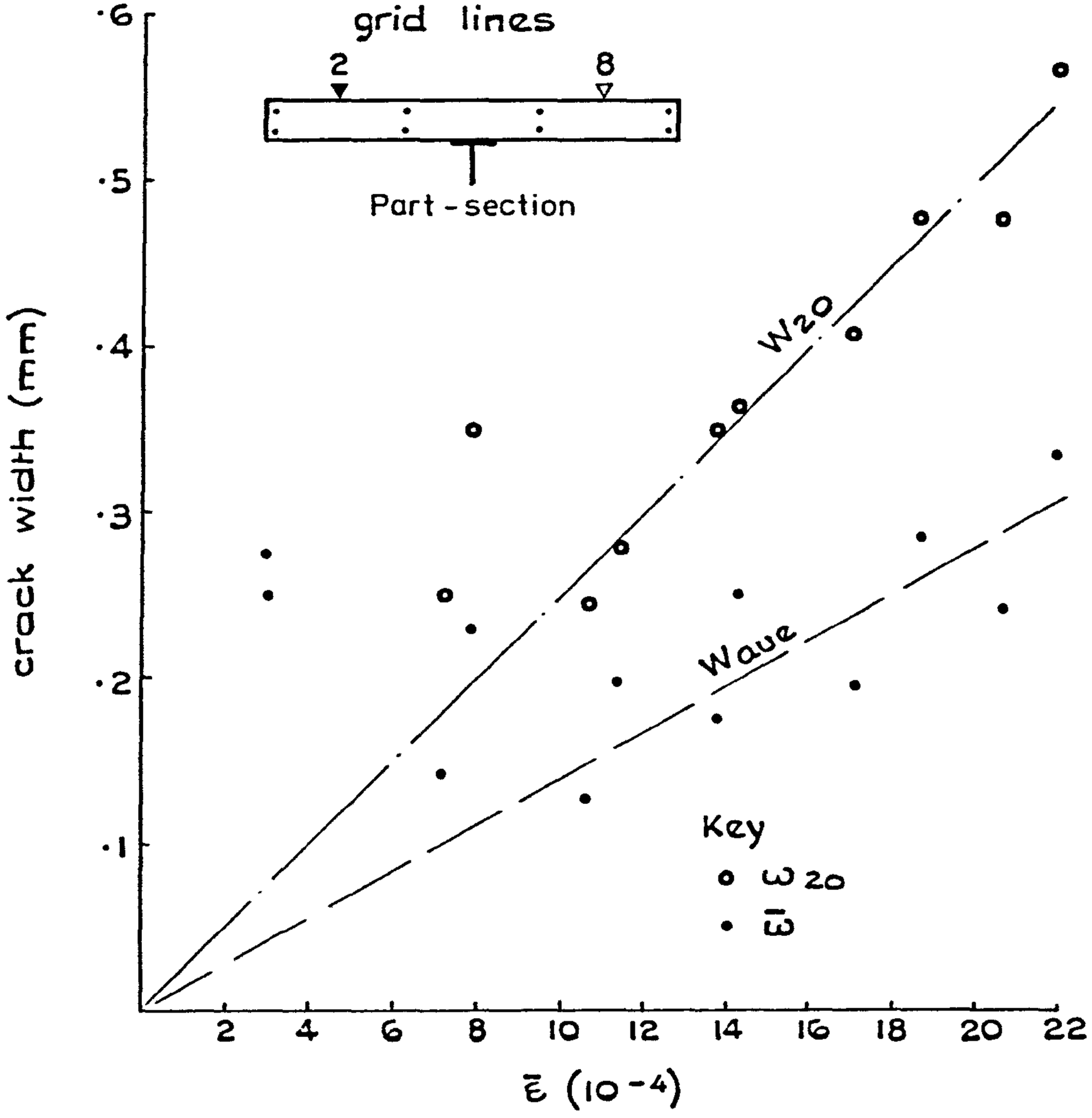

FIG.4.12 CRACK WIDTH-STRAIN RELATIONSHIPS
GRID LINES 2&8, BEAM UC5

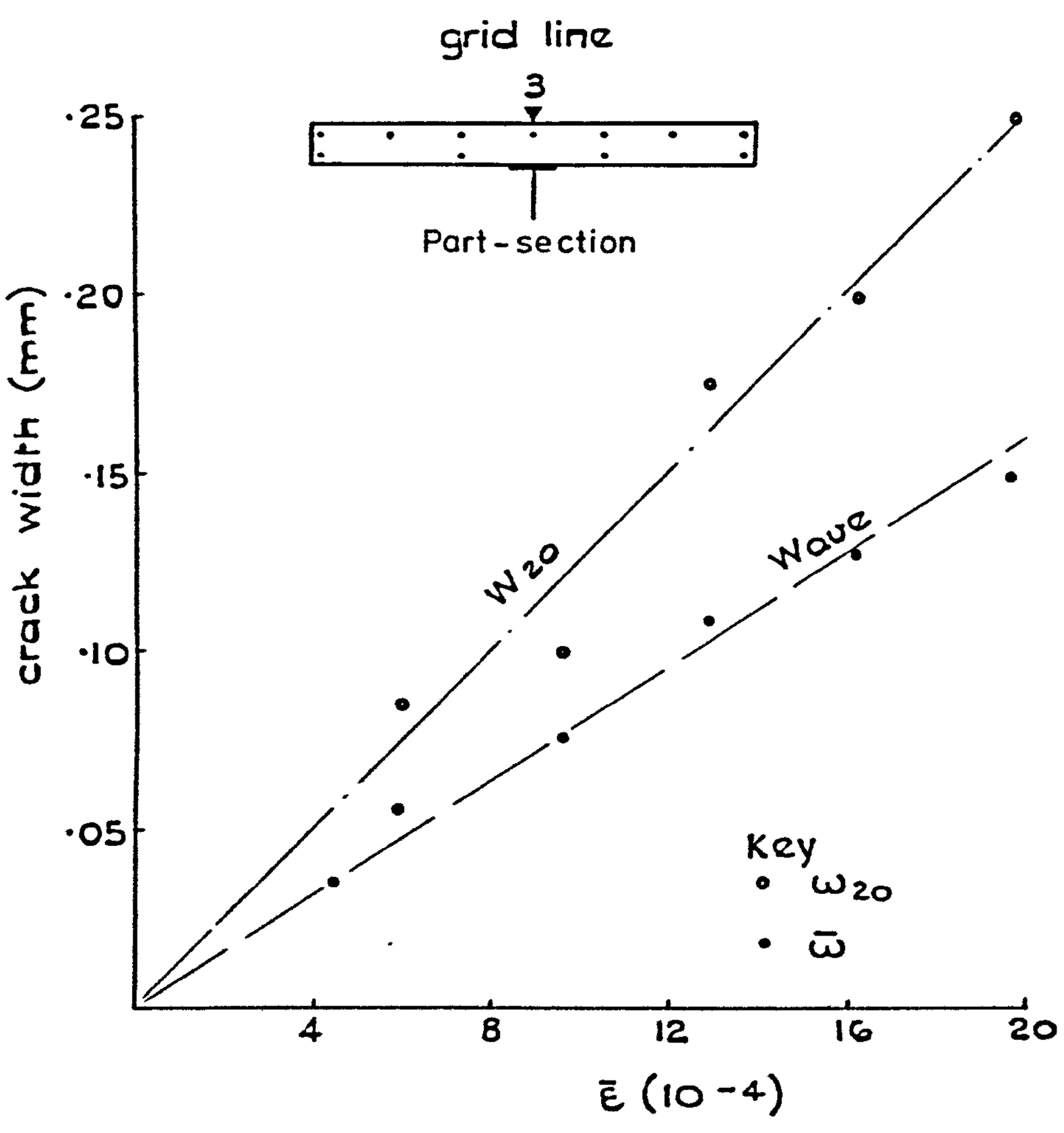

a) Grid line 3, Beam UC1

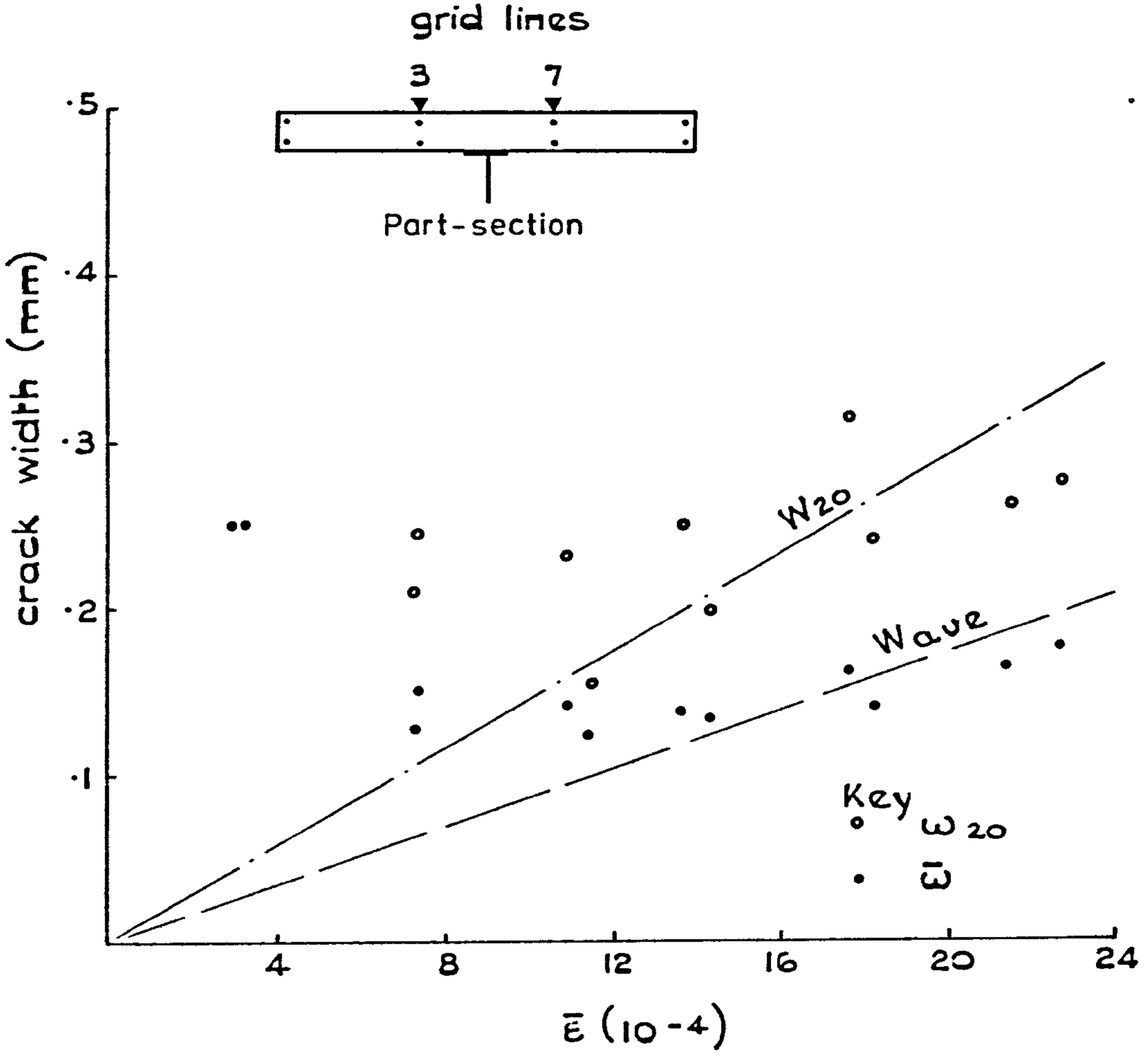

b) Grid lines 3&7, Beam UC5

FIG. 4.13 CRACK WIDTH-STRAIN RELATIONSHIPS

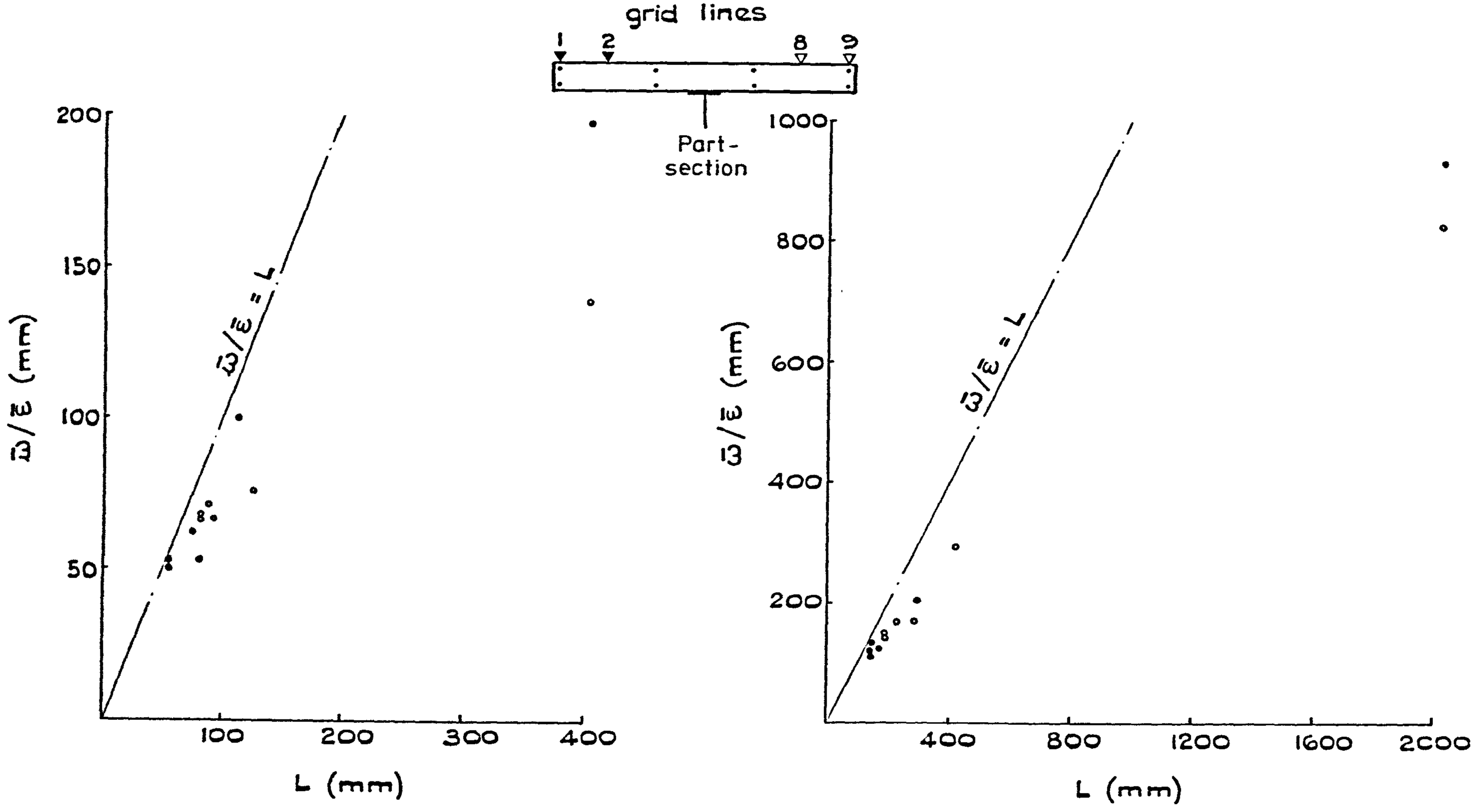

a) Grid lines 1&9

b) Grid lines 2&8

FIG. 4.14 RELATIONSHIP BETWEEN CRACK SLOPE AND CRACK SPACING, BEAM UC5

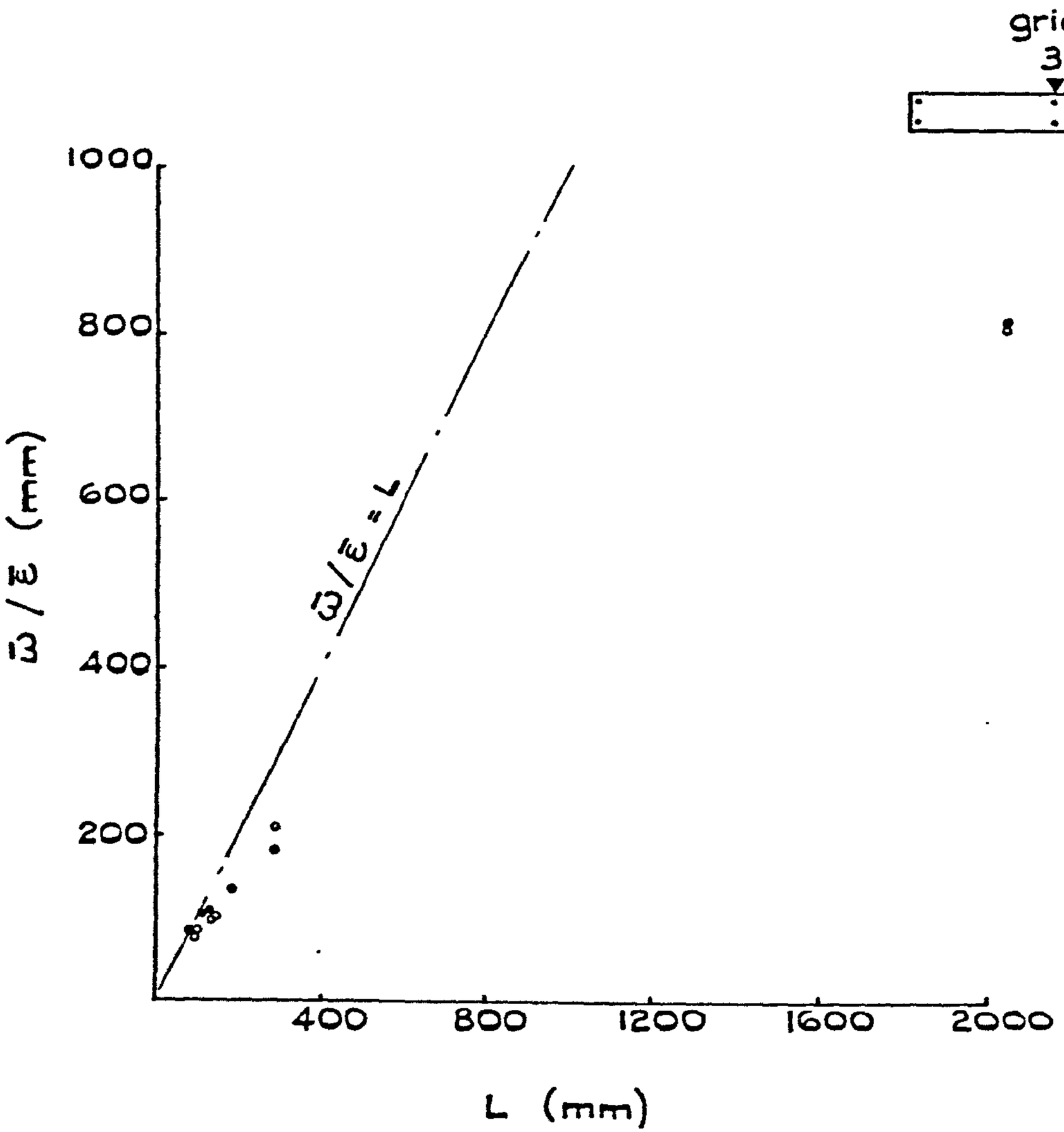

a) Grid lines 3&7

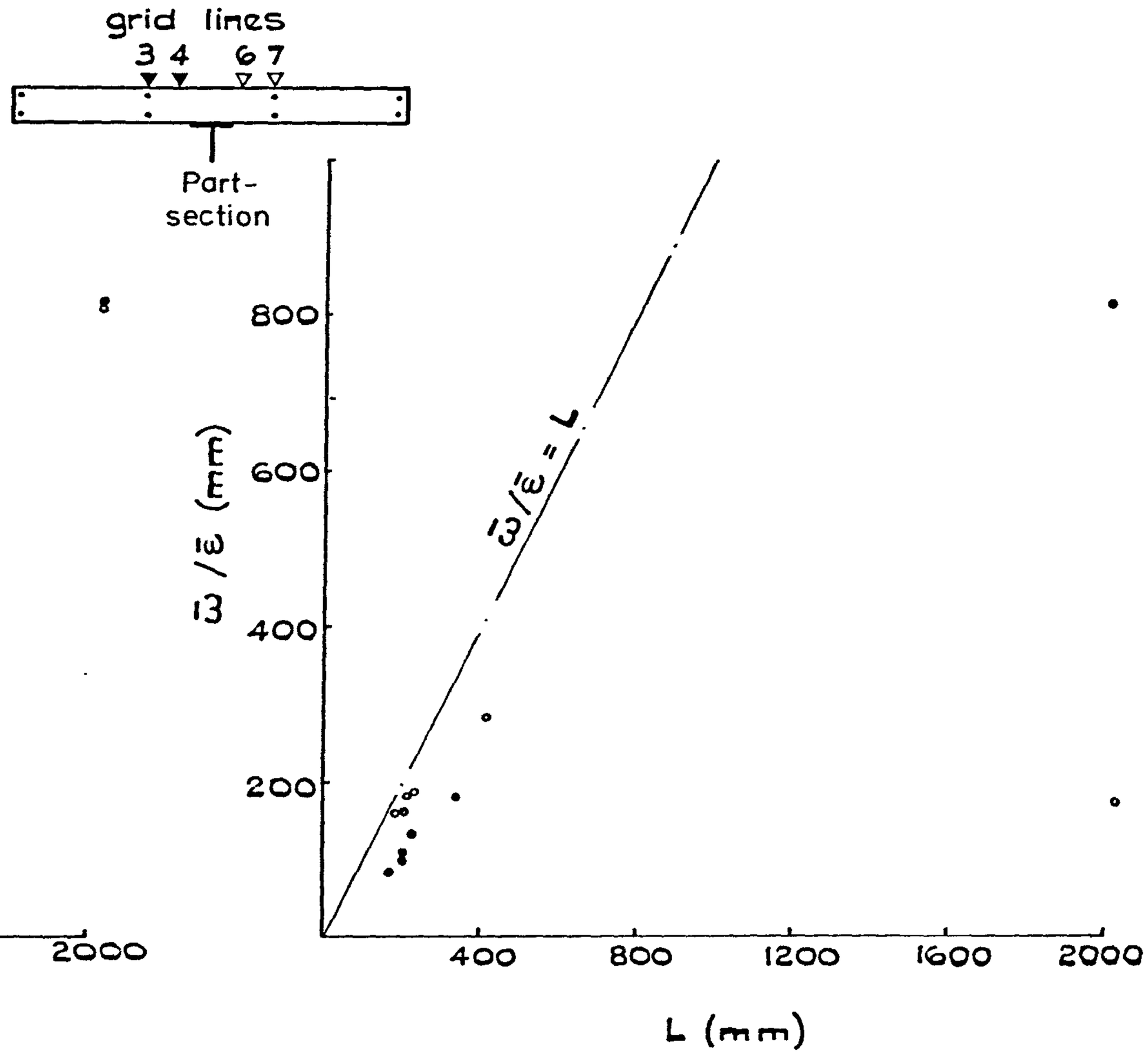

b) Grid lines 4 & 6

FIG. 4.15 RELATIONSHIP BETWEEN CRACK SLOPE AND CRACK SPACING, BEAM UC5

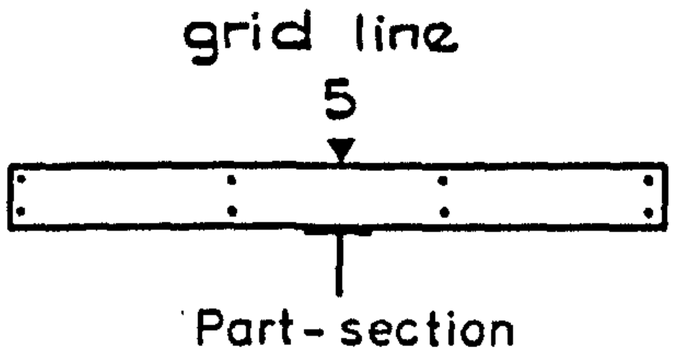

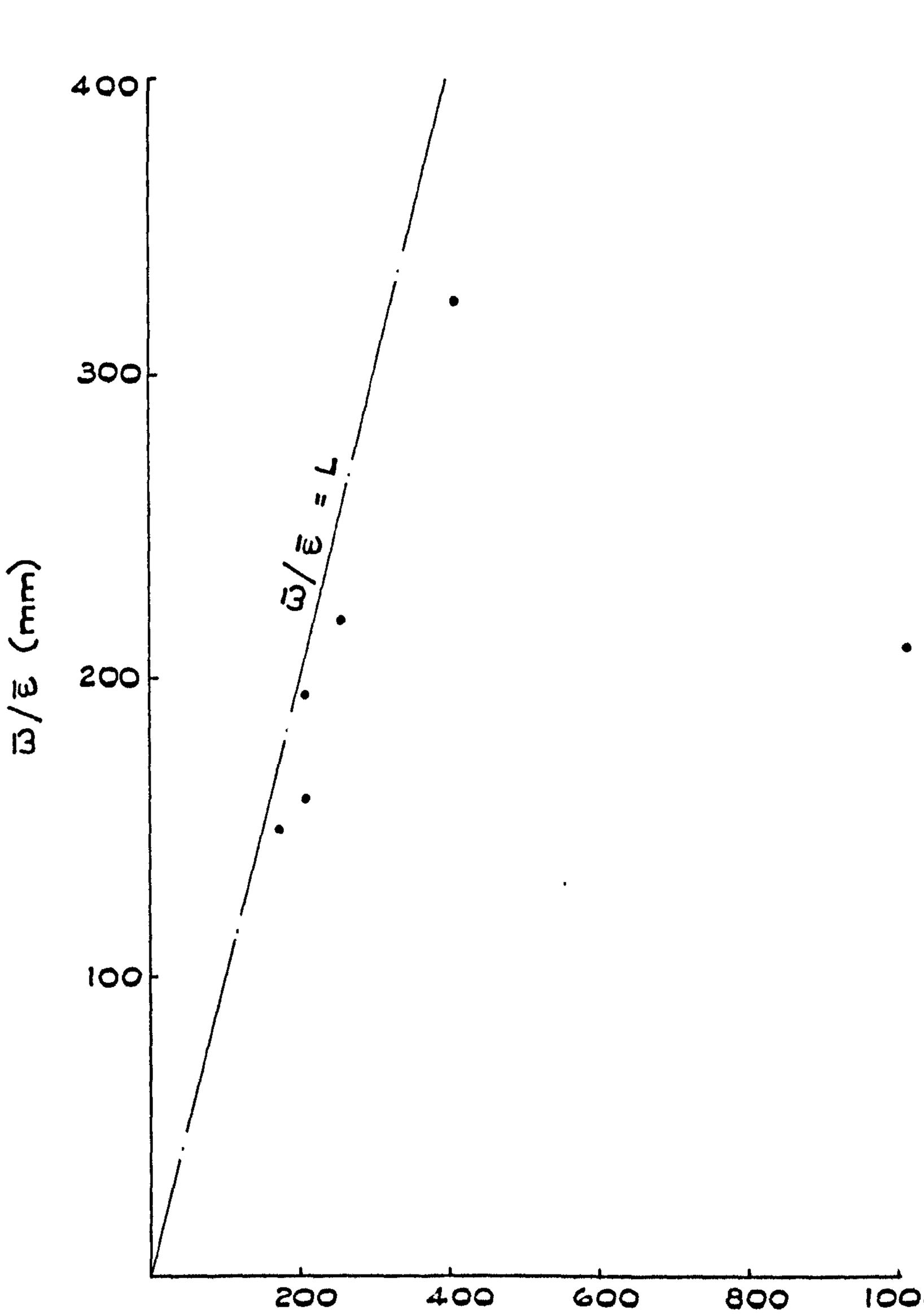

Grid line 5

FIG. 4.16 RELATIONSHIP BETWEEN CRACK SLOPE AND CRACK SPACING, BEAM UC5

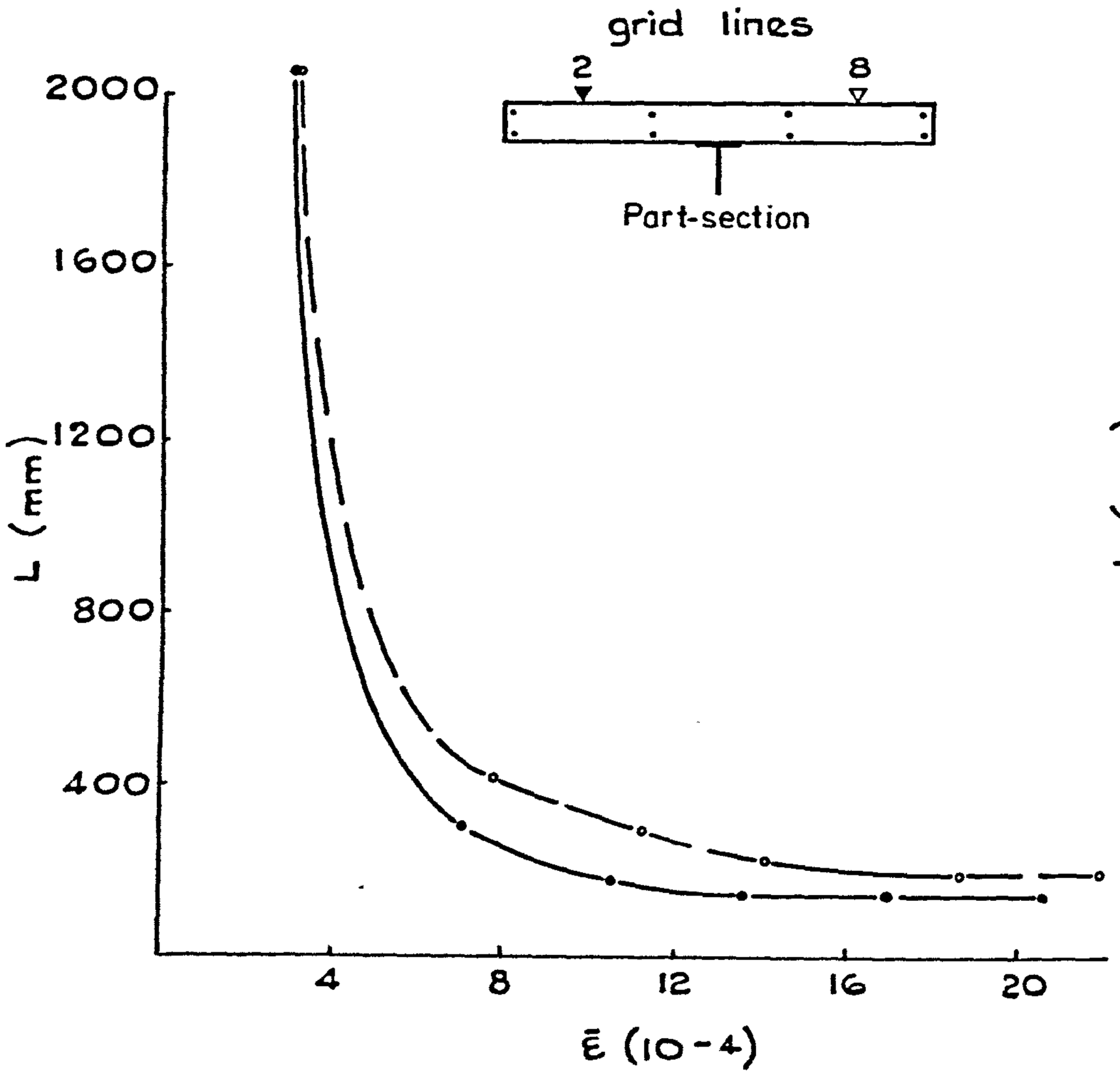

FIG. 4.17 CRACK SPACING-STRAIN RELATIONSHIP GRID LINES 2&8, BEAM UC5

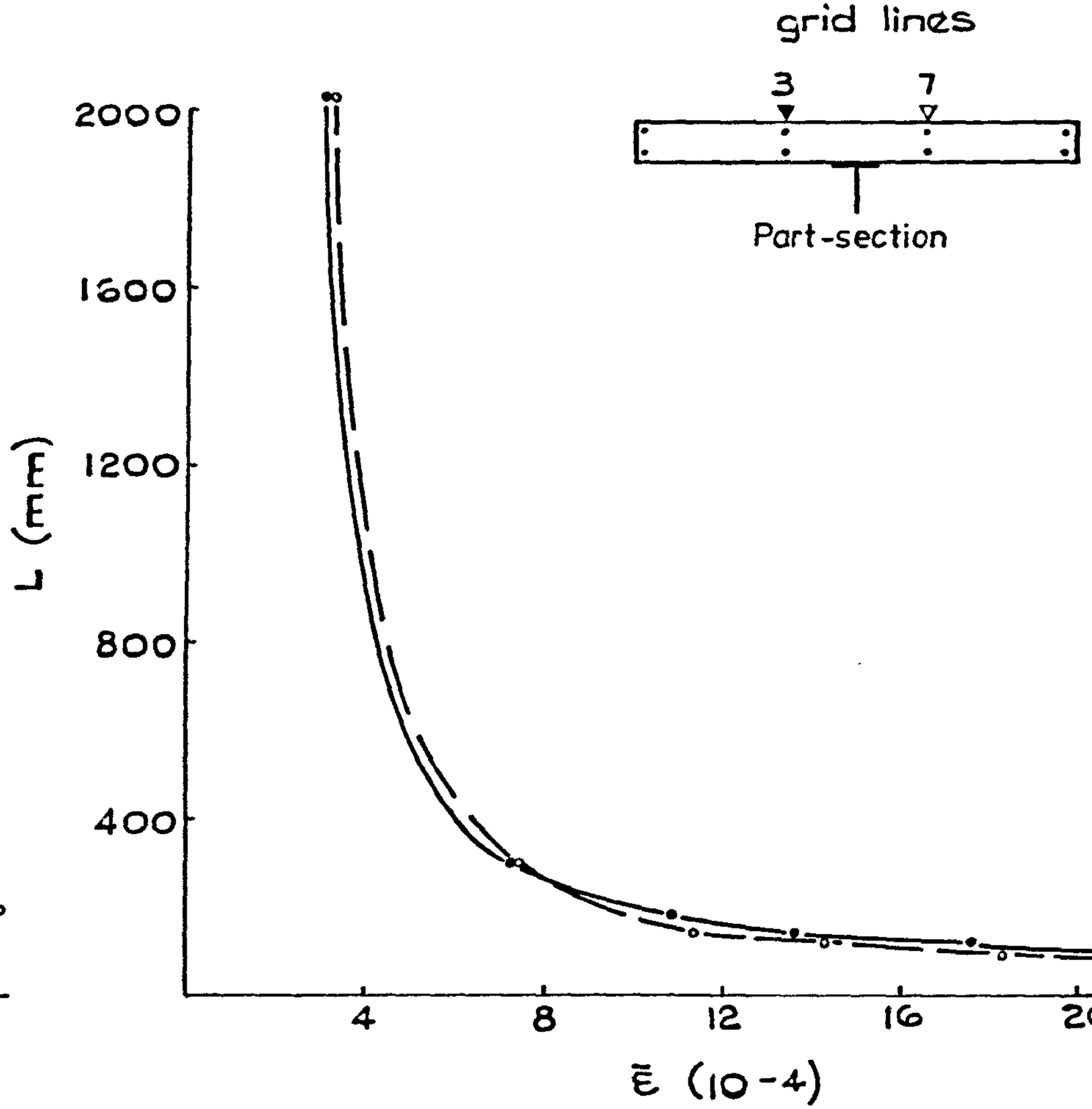

FIG. 4.18 CRACK SPACING-STRAIN RELATIONSHIP GRID LINES 3&7, BEAM UC5

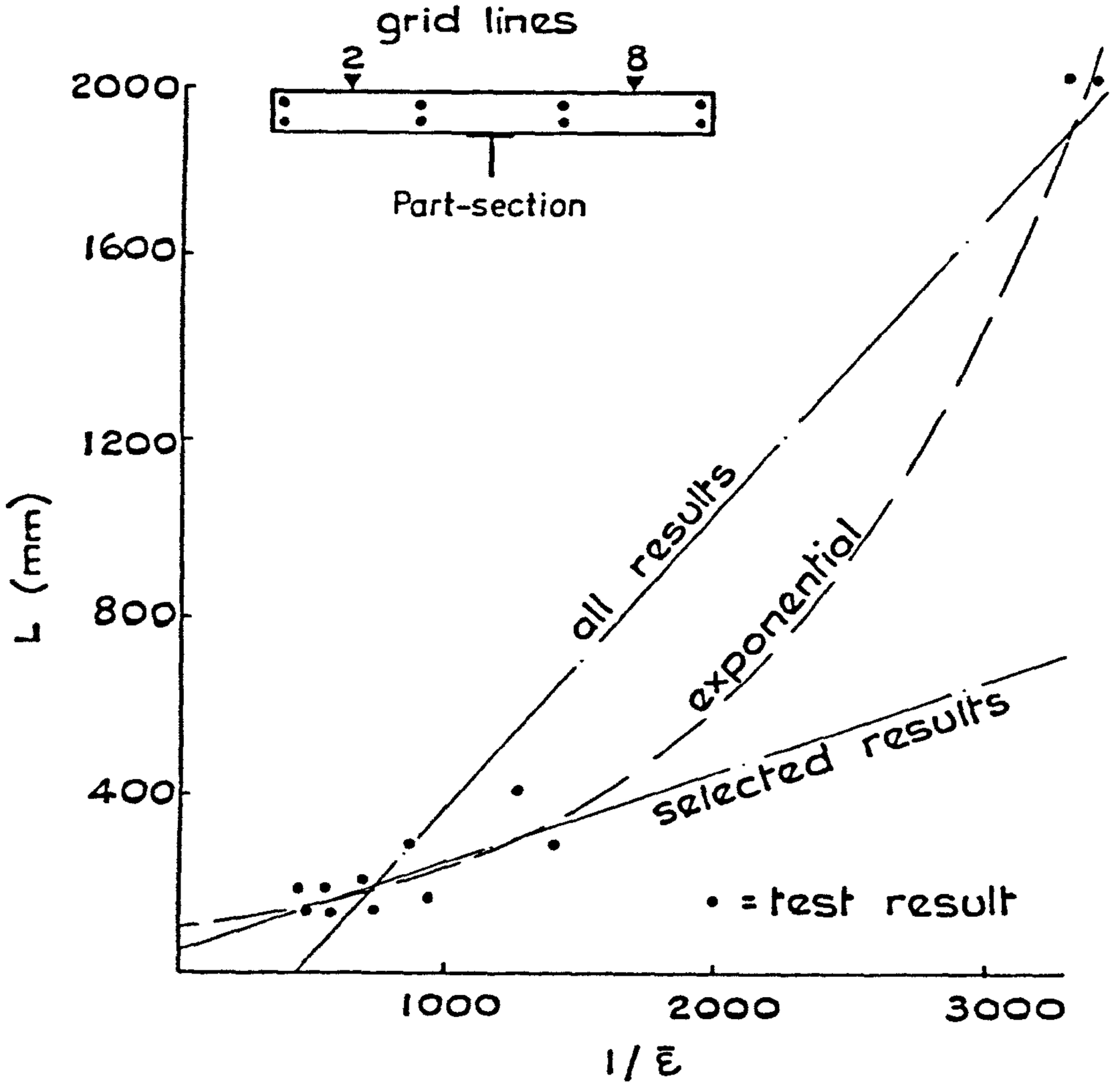

FIG. 4.19 CRACK SPACING-INVERSE STRAIN RELATIONSHIP: GRID LINES 2&8, BEAM UC5

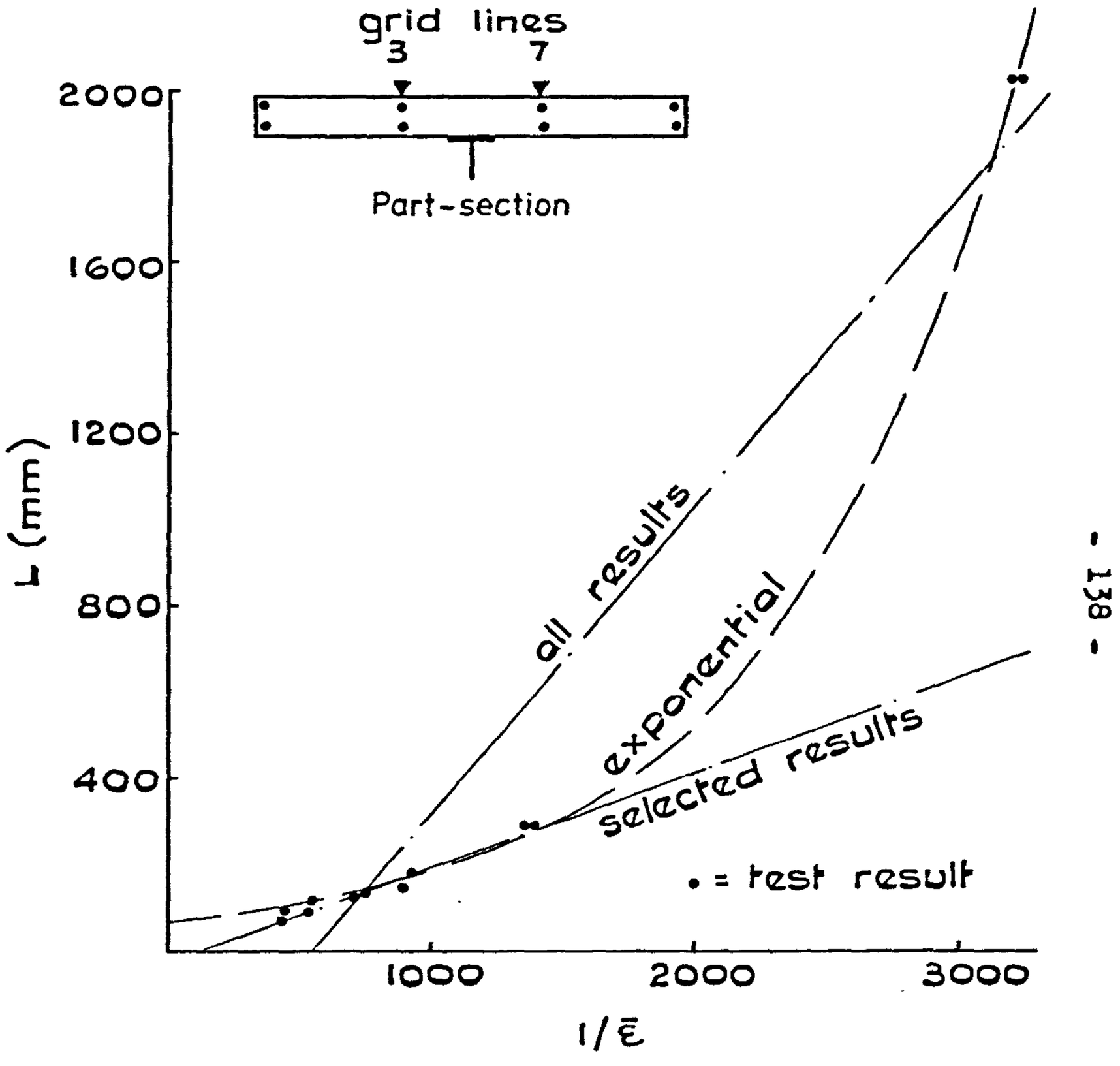

FIG. 4.20 CRACK SPACING-INVERSE STRAIN RELATIONSHIP: GRID LINES 3&7, BEAM UC5

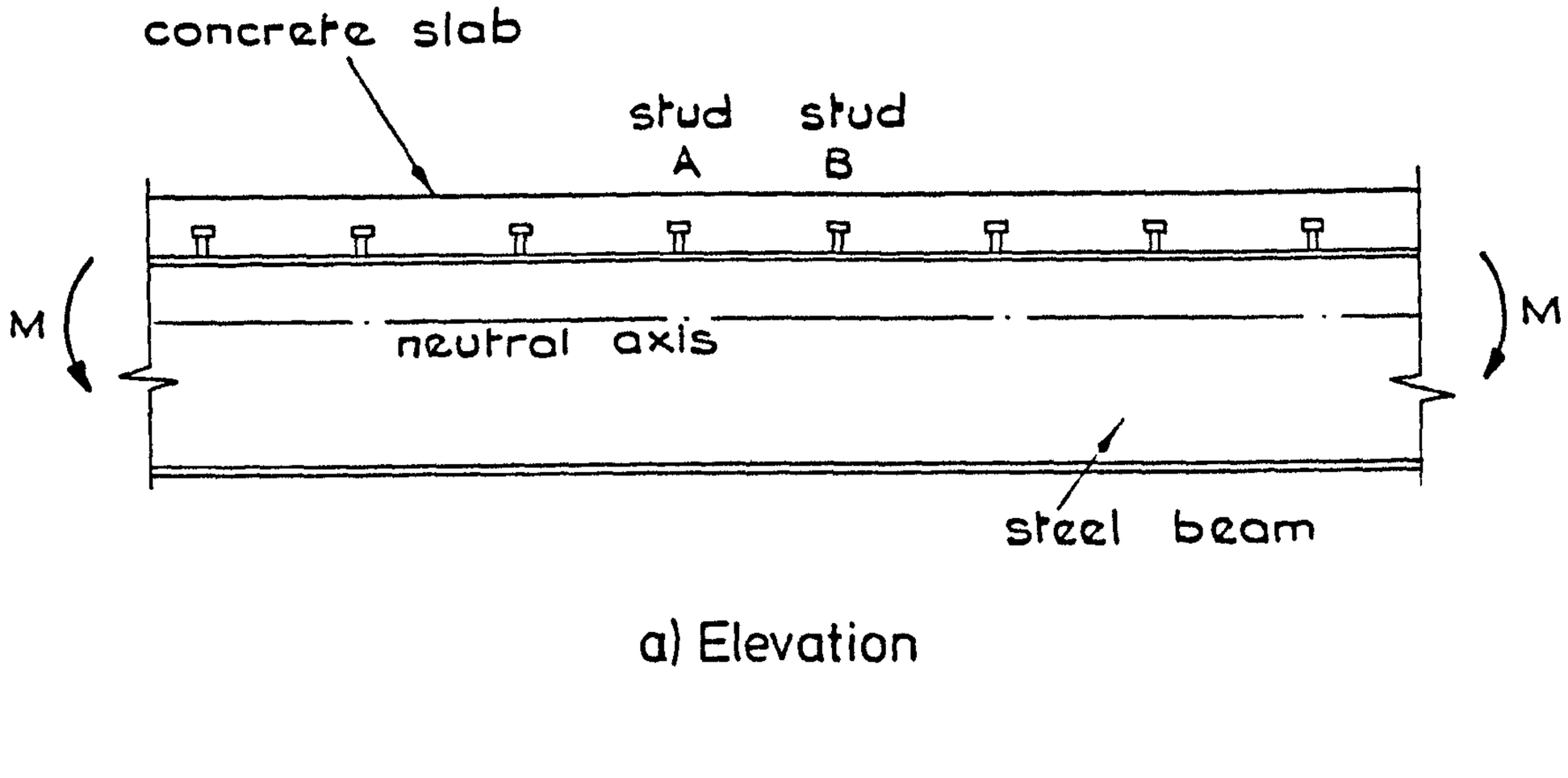

a) Elevation

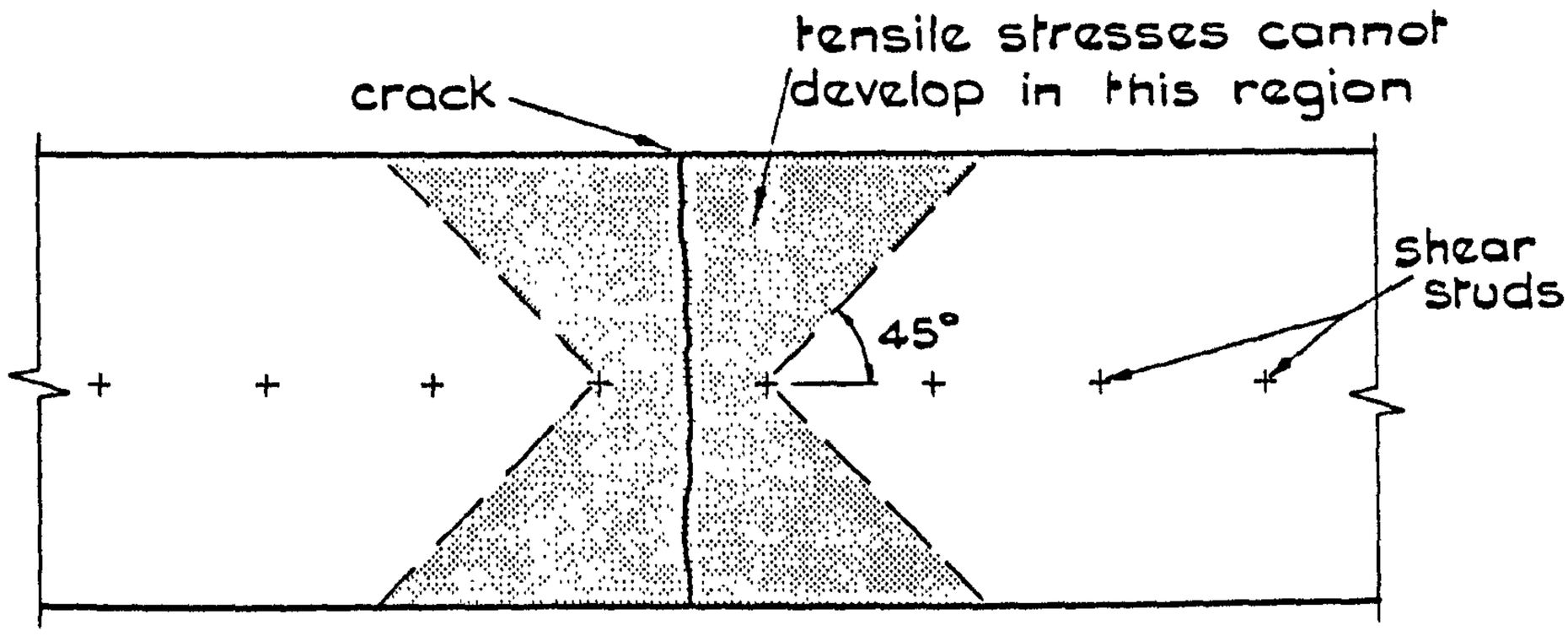

b) Plan showing initial crack

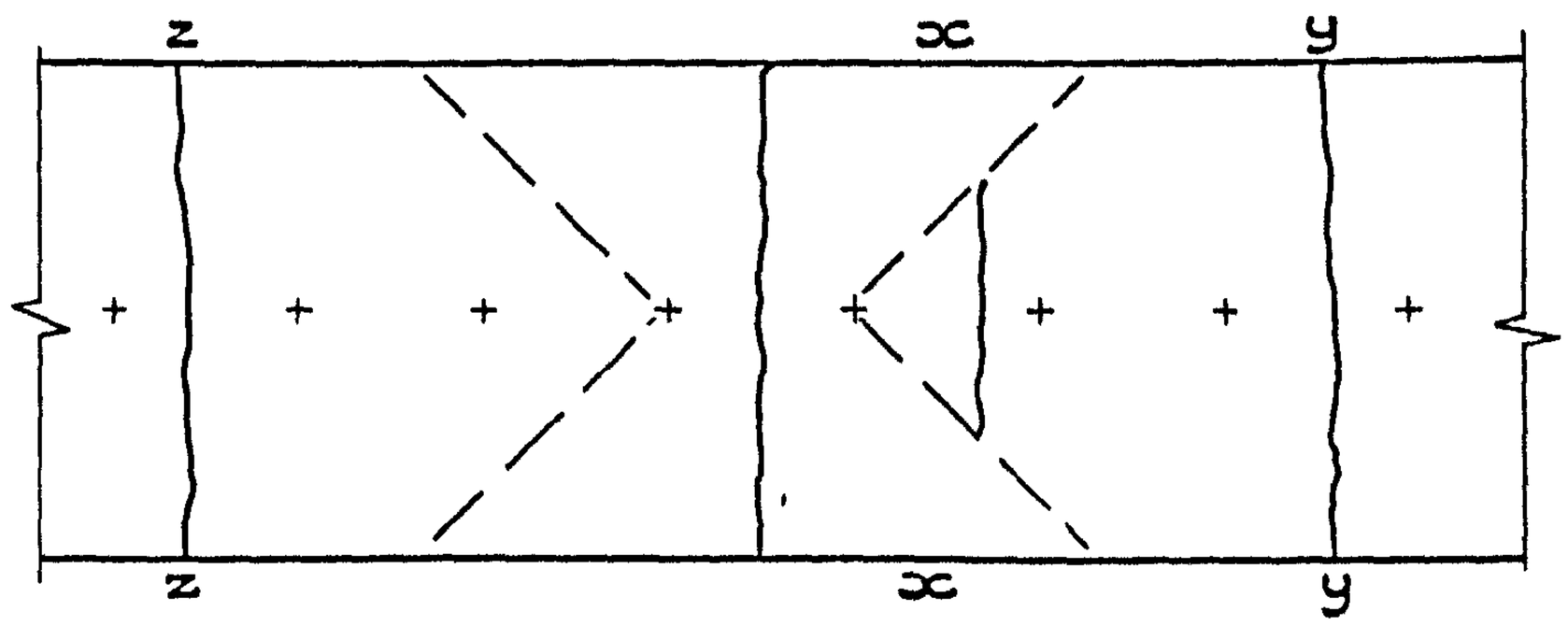

c) Plan showing subsequent crack pattern

FIG. 4.21 CRACKING IN UNREINFORCED SLAB OF COMPOSITE BEAM

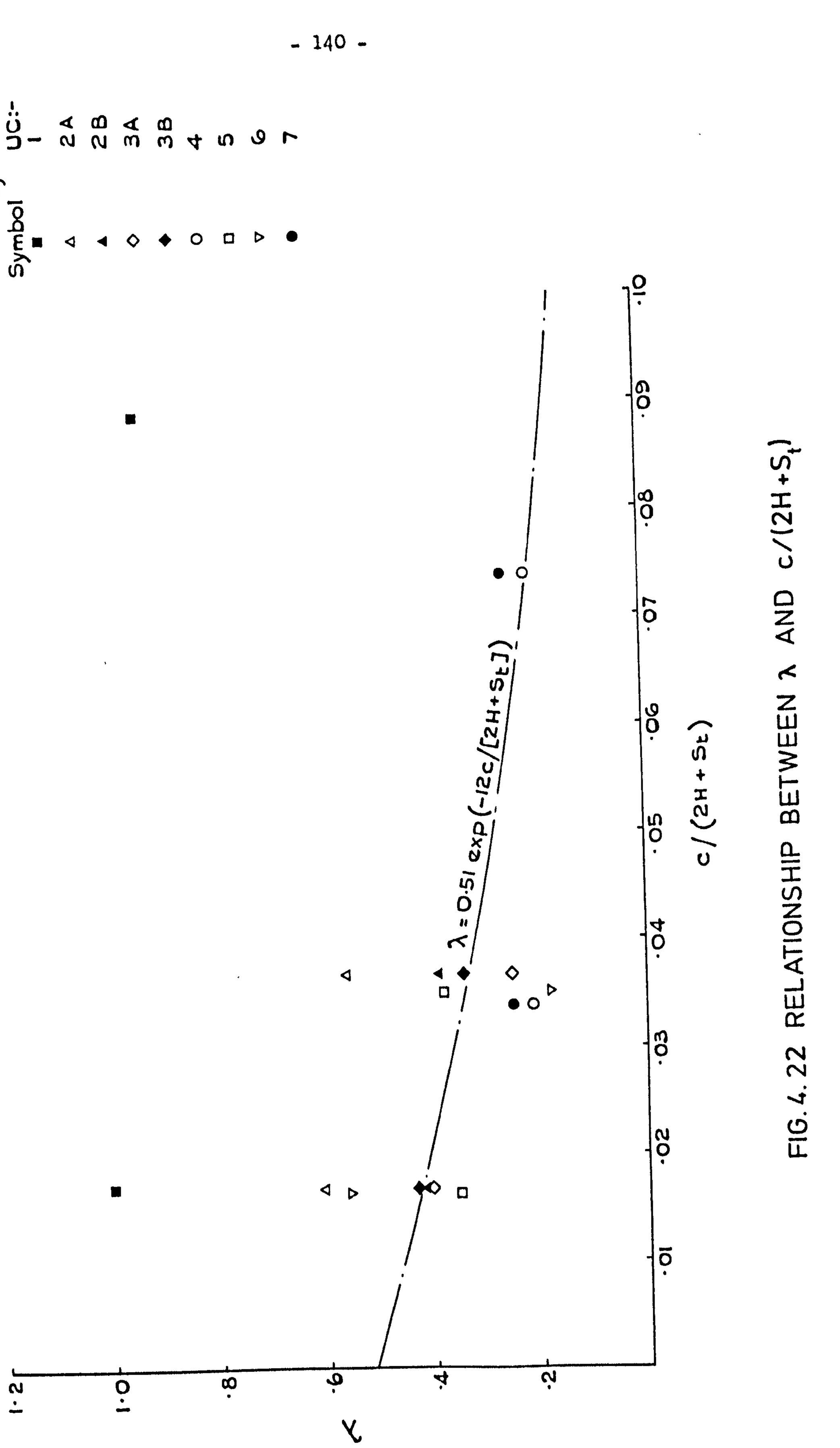

FIG. 4.22 RELATIONSHIP BETWEEN λ AND c/(2H+S_t)

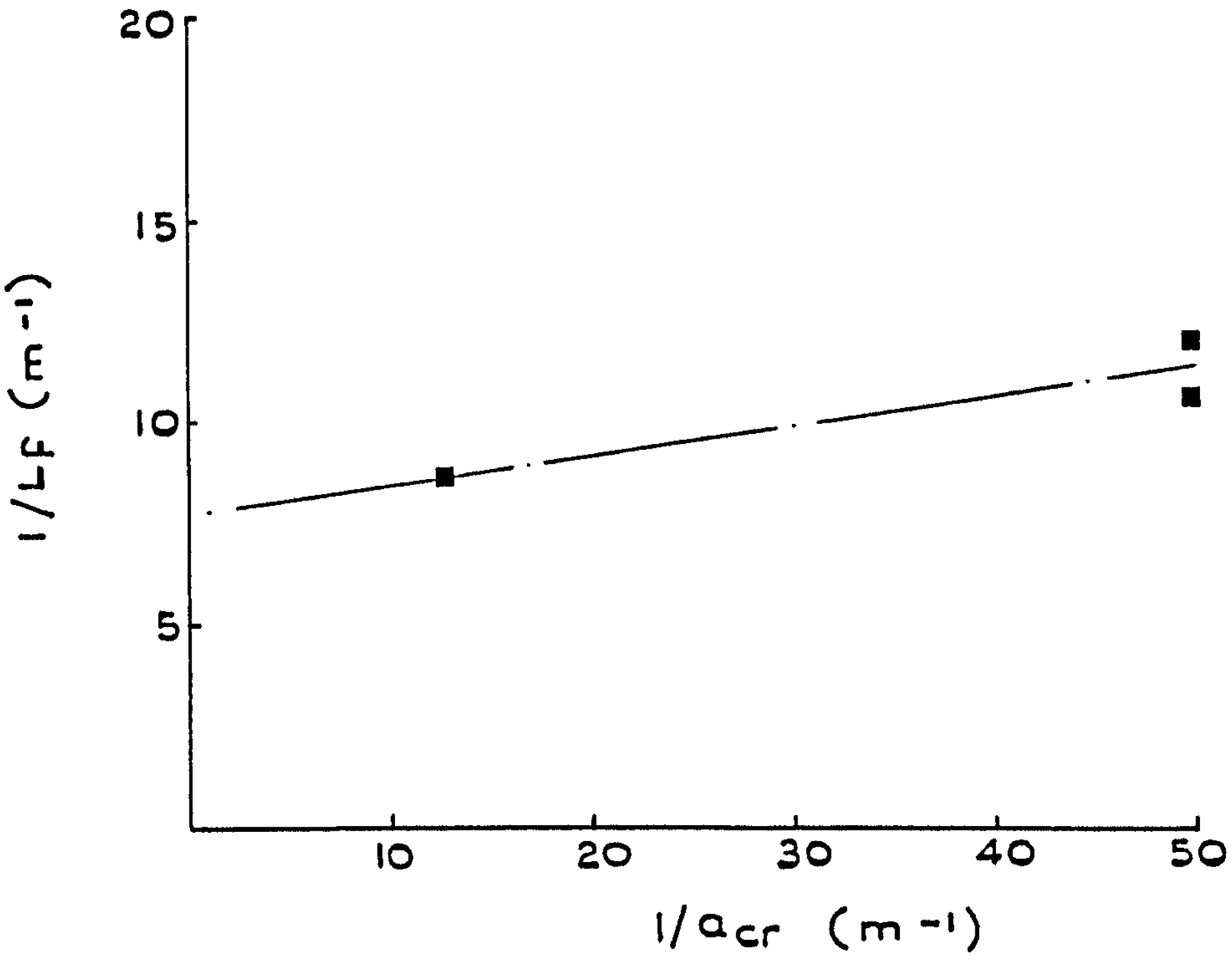

Beam UC1

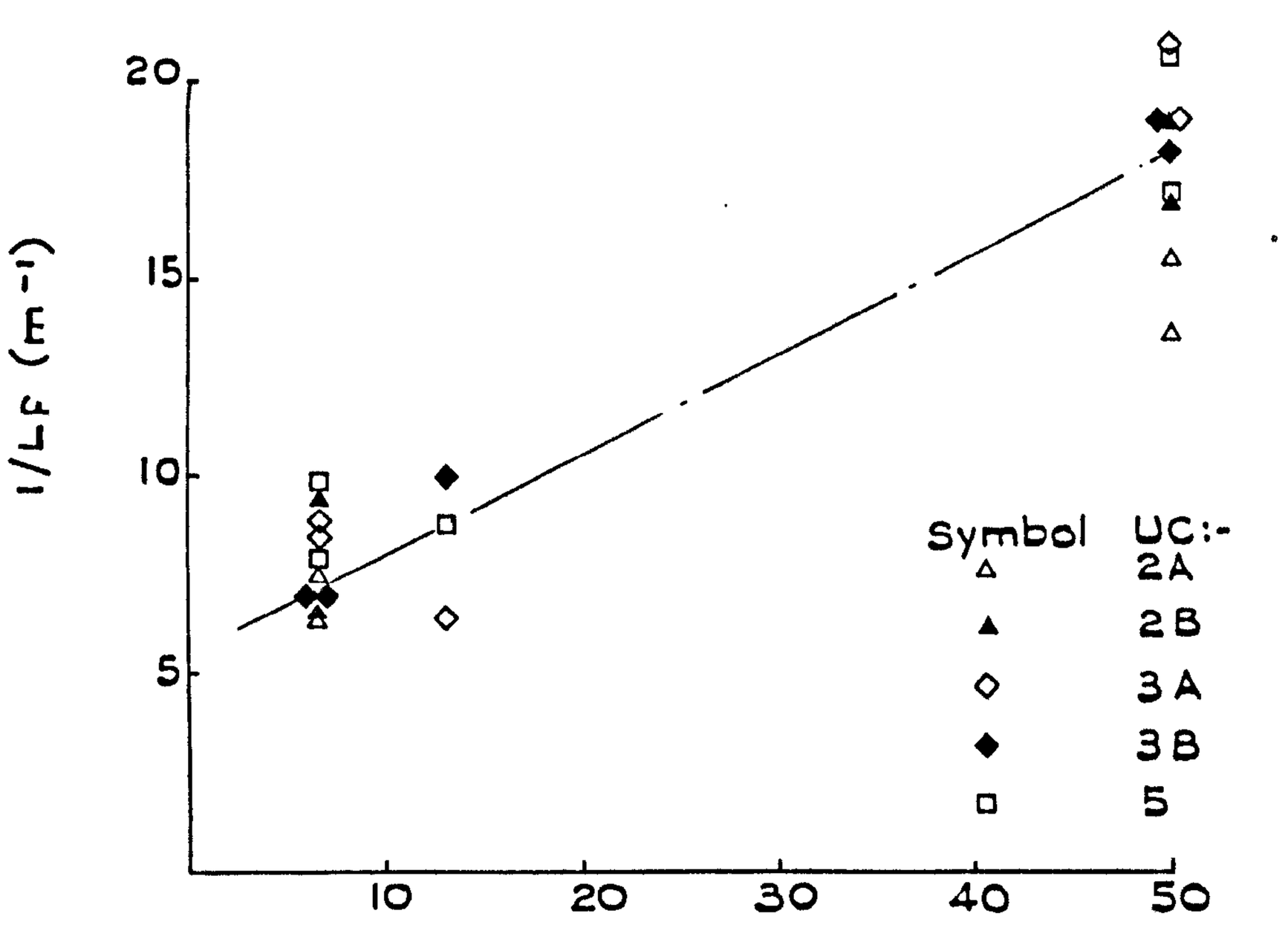

Beams UC2, 3 & 5

FIG. 4.23 RELATIONSHIP BETWEEN $1/L_f$ AND $1/a_{cr}$

(continued...)

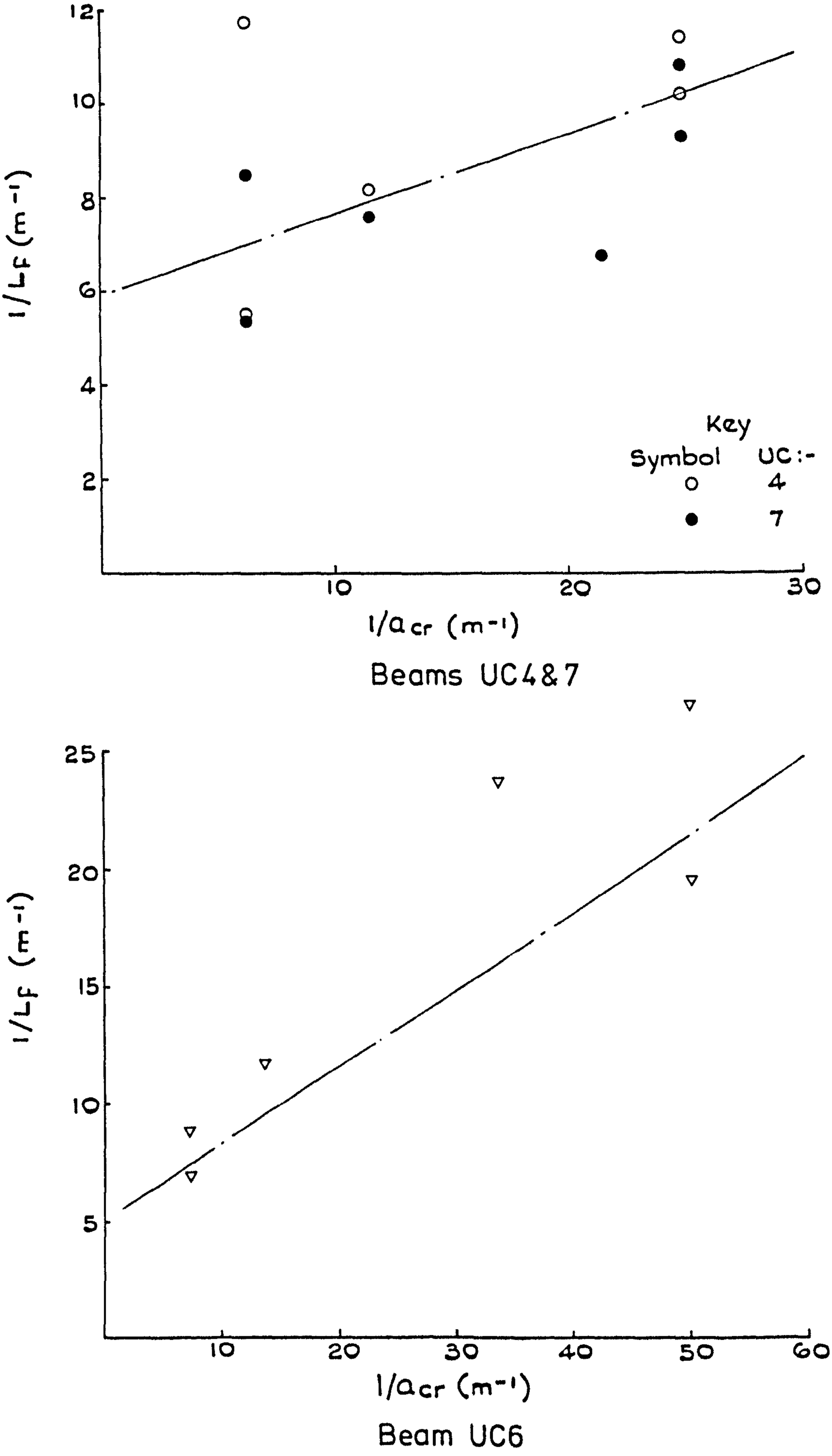

FIG.4.23 RELATIONSHIP BETWEEN $1/L_f$ AND $1/a_{cr}$ (concluded)

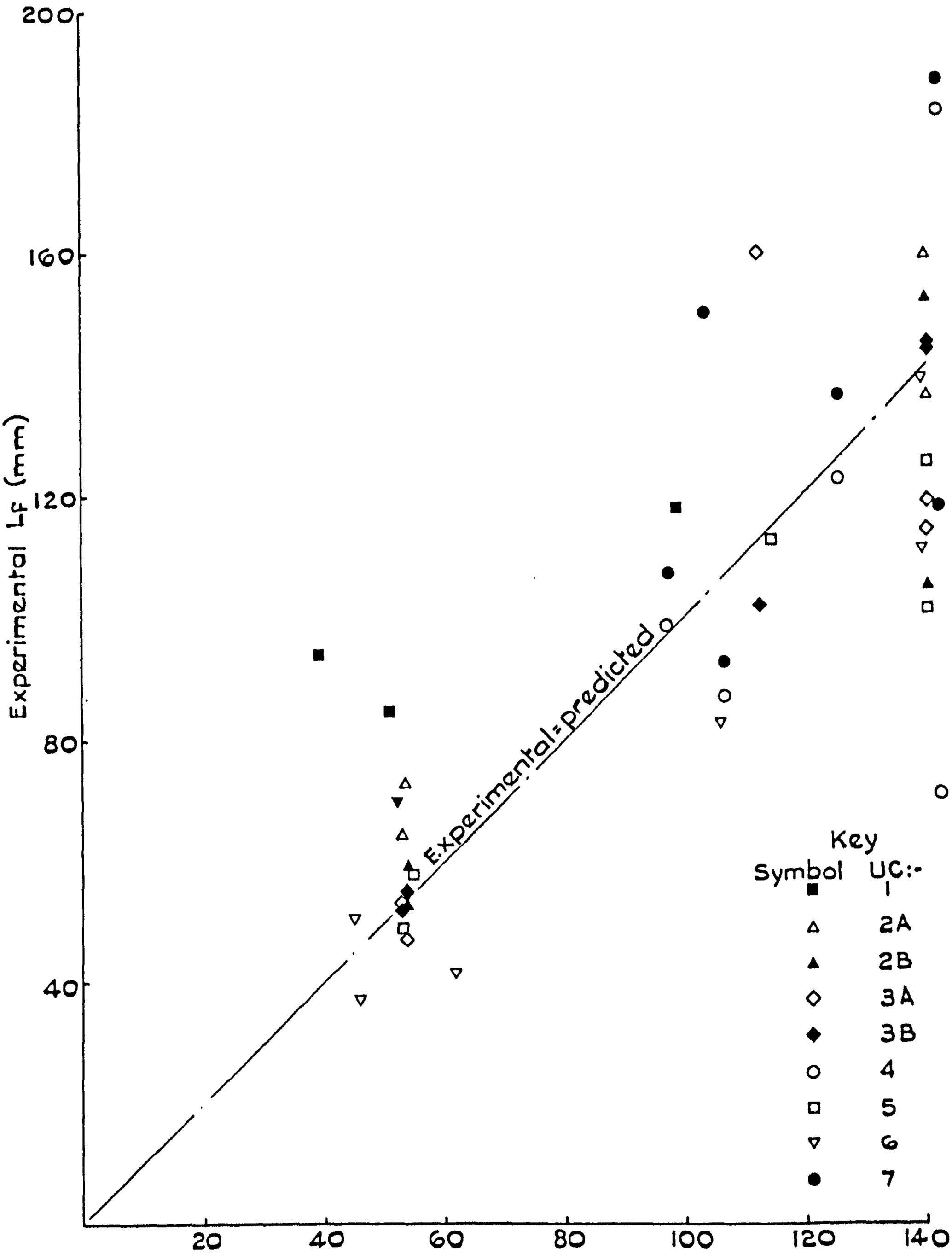

FIG. 4.24. COMPARISON OF EXPERIMENTAL AND PREDICTED FINAL CRACK SPACING

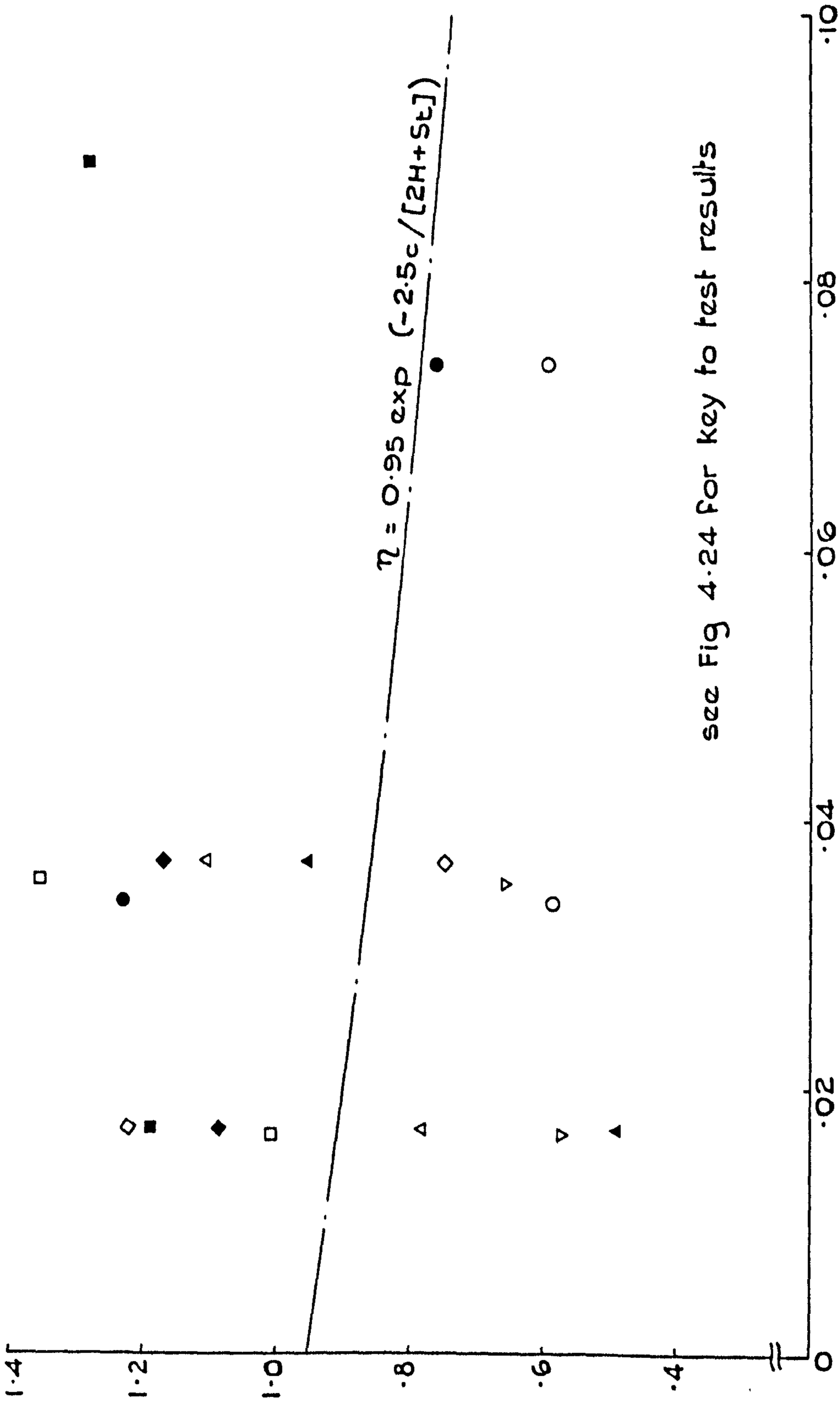

FIG. 4.26 RELATIONSHIP BETWEEN η AND $c/(2H+S_t)$

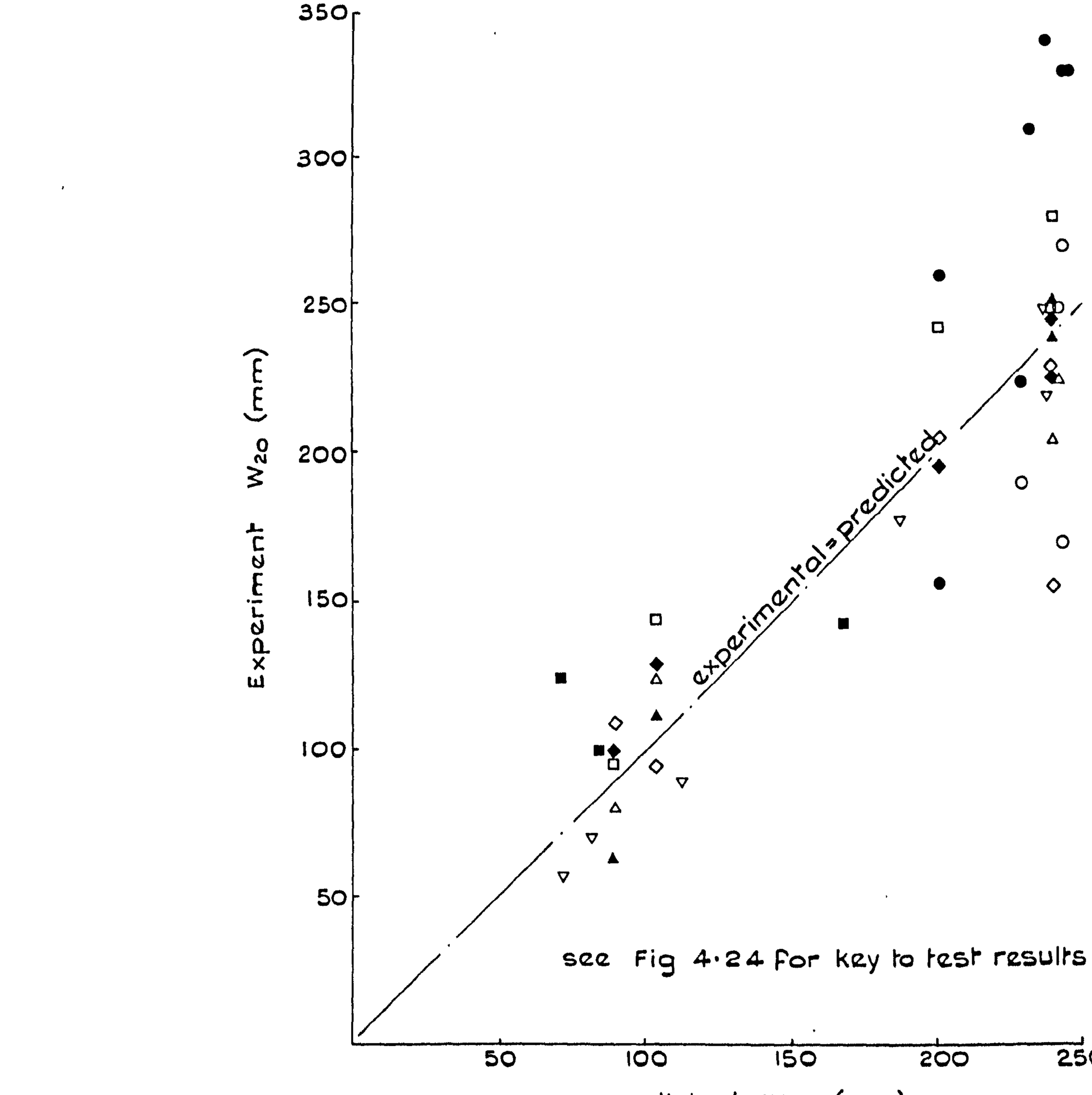

FIG. 4.27 COMPARISON OF EXPERIMENTAL AND PREDICTED VALUES OF W_{20}

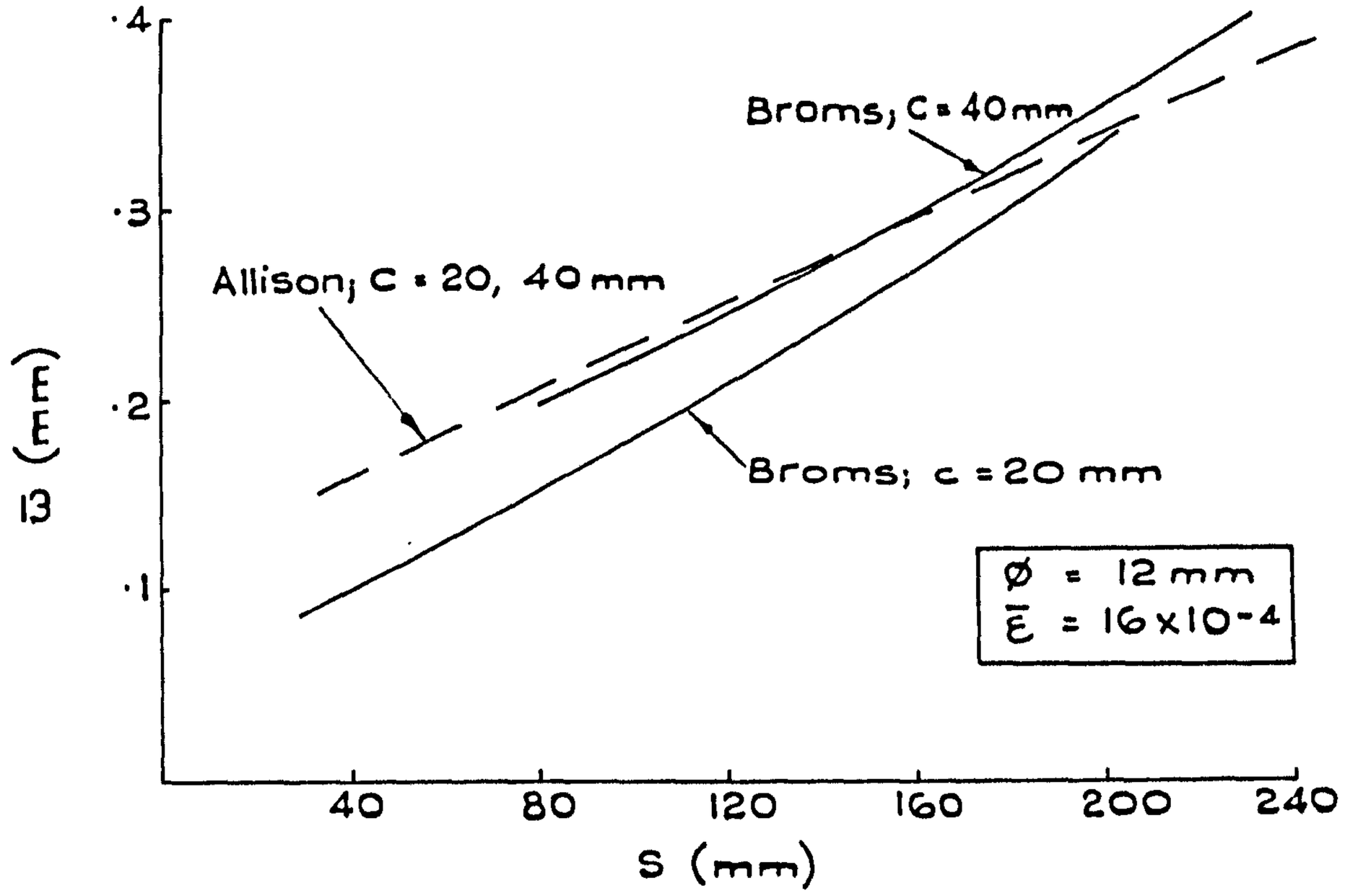

FIG. 4.28 PREDICTED CRACK WIDTHS MID-WAY BETWEEN BARS
Broms and Allison

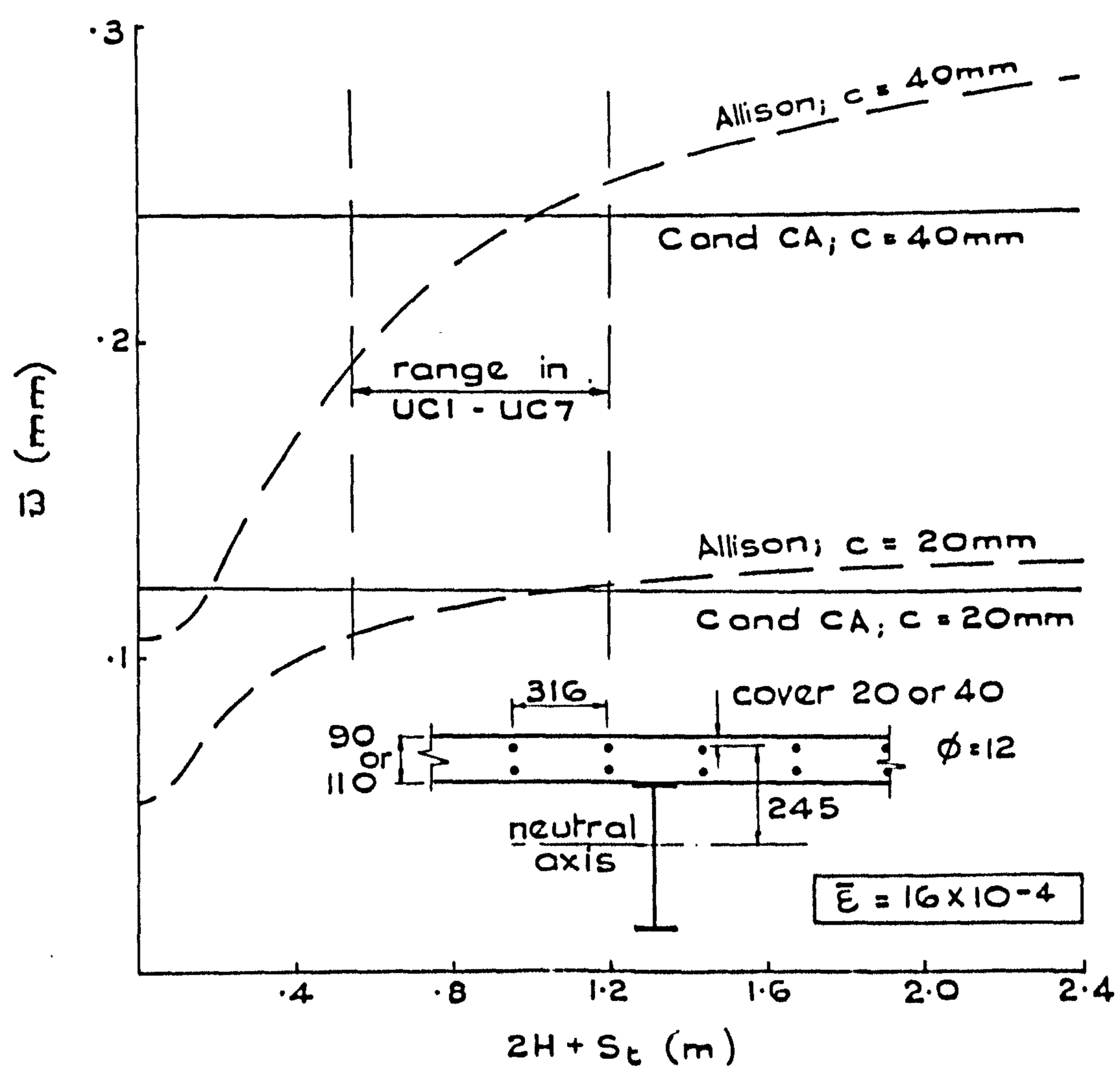

FIG. 4.29 PREDICTED CRACK WIDTHS OVER BARS
C & CA and Allison

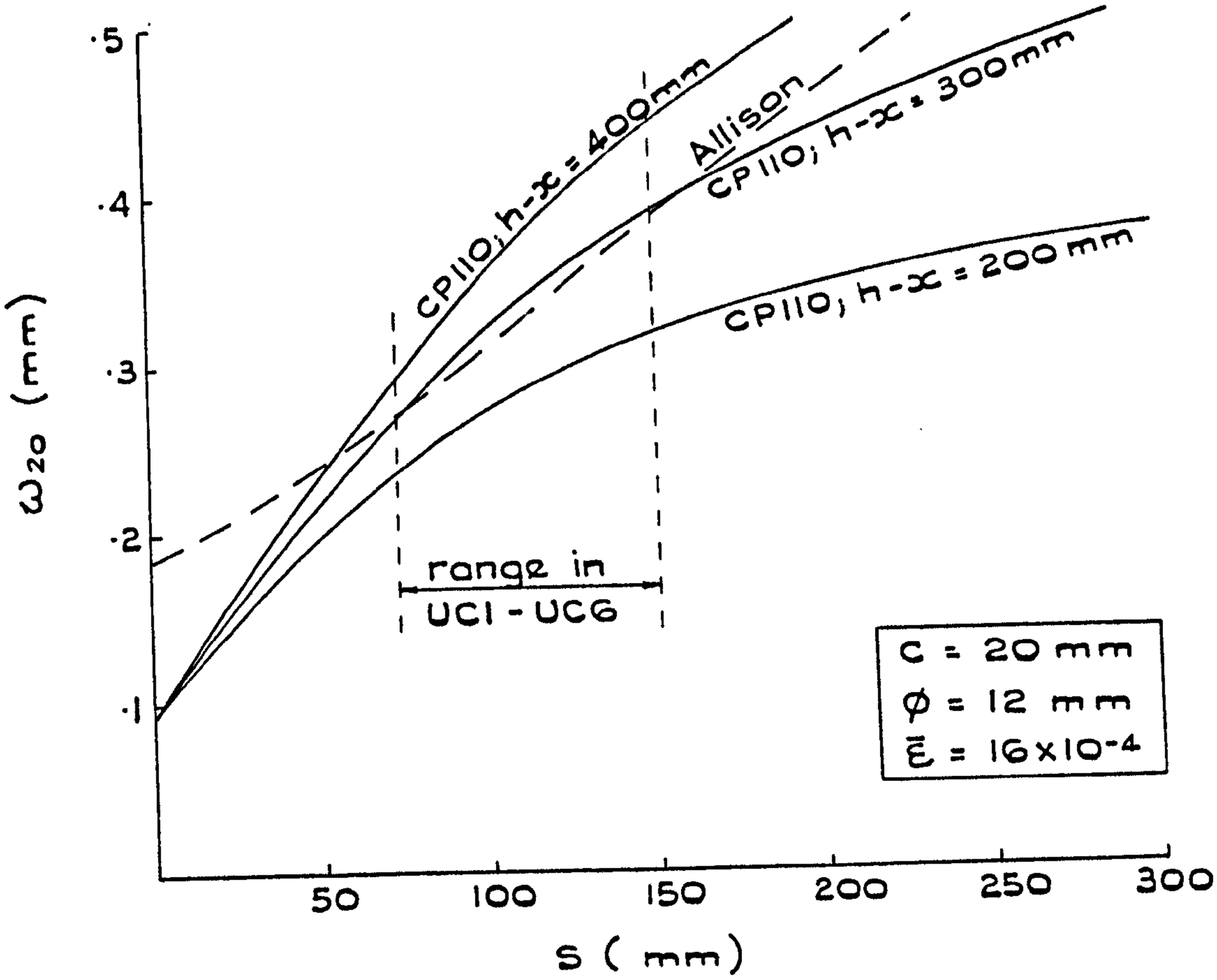

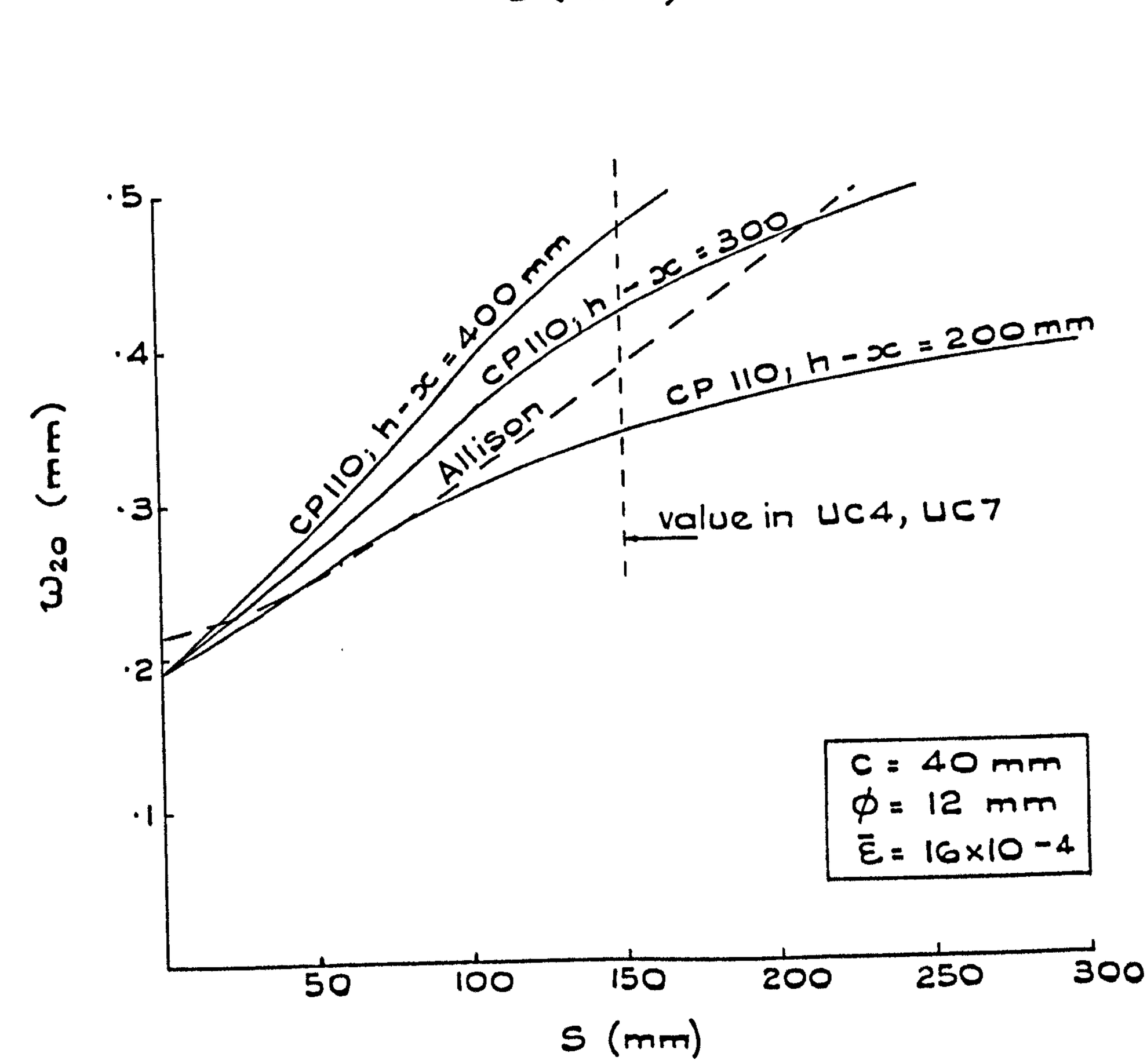

FIG. 4.30 PREDICTED CRACK WIDTHS MID-WAY BETWEEN BARS
CP 110 and Allison

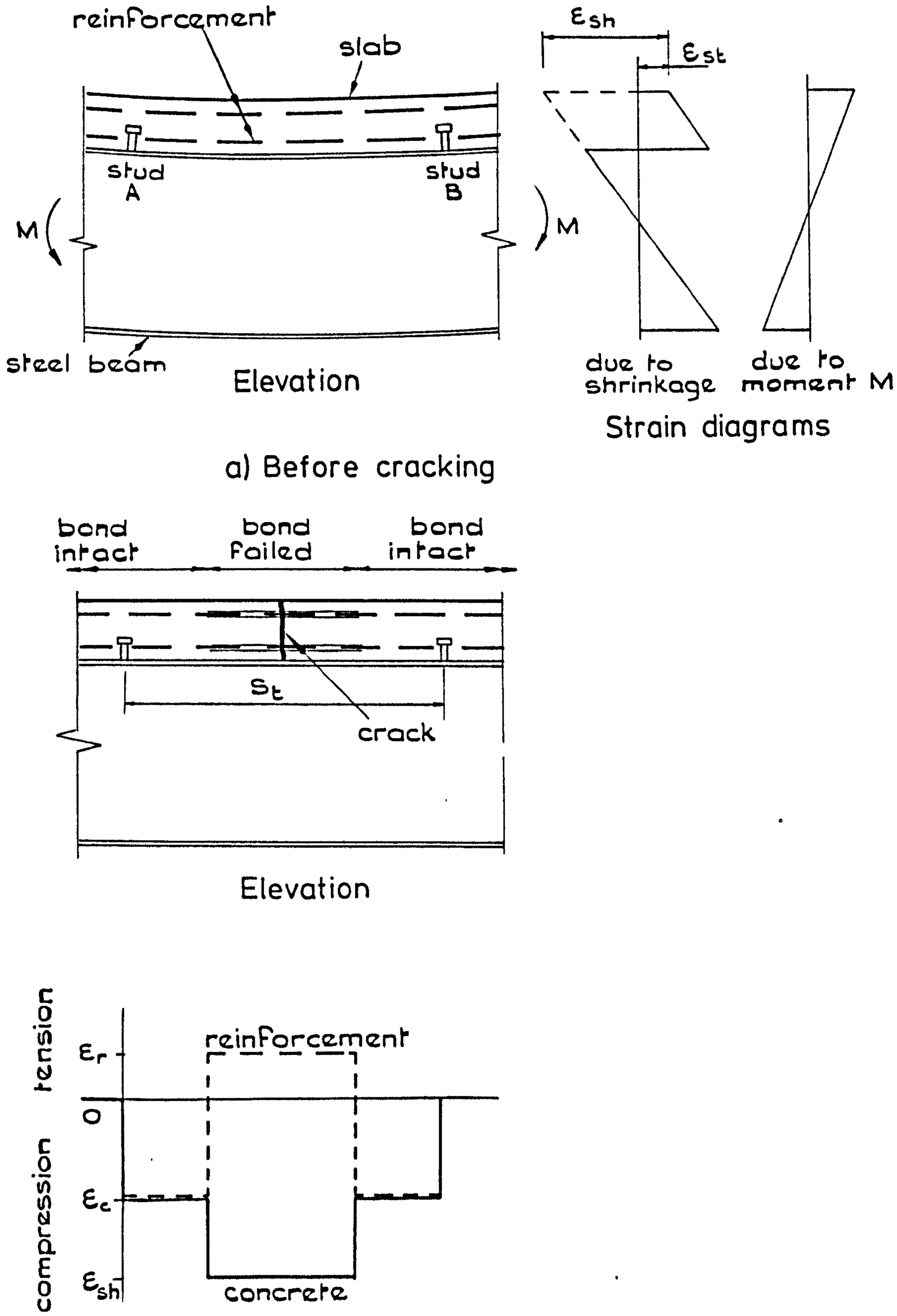

FIG. 4.31 CRACK WIDTHS DUE TO THE RELEASE OF SHRINKAGE STRAINS

CHAPTER 5

CONCLUSIONS OF THE WORK ON CRACKING

5.1 Summary of conclusions

The experimental work has shown that the first cracks to form in the slabs of composite 'T' beams penetrate the full width and depth of the slab, and those that form later are concentrated in the region of the reinforcing bars. This is similar to the behaviour of plain reinforced concrete, but the final crack spacing was approached much more rapidly with increasing strain in the composite beams.

The first cracks to form in Beams UC1 to UC7 were very wide in relation to the mean surface strain, and although this will not affect the design of most composite 'T' beams, it might cause problems where the crack width requirements are severe - in structures exposed to salt spray for example, where the maximum permitted width is 0.1mm. The release of tensile strain developed in the concrete slab due to drying shrinkage has been shown to be the cause of the large crack widths at low strain. Release of shrinkage strains can also have a significant effect on the moment-curvature response in a composite beam, as shown in Section 4.5.

By using both theoretical argument and experimental data, five equations have been derived which may be used to predict $\bar{w}$ and w_{20} anywhere on the surface of the slab of a composite 'T' beam. These equations (4.10.to 4.12, 4.15, 4.16) are in close agreement with the results of Tests UC1 to UC7. Some of the formulae which have been developed from research into plain reinforced concrete have been compared with the same results, and give good predictions of crack width either over the reinforcing bars or between them, but never at all points on the slab's surface.

5.2 Recommendations for design

As noted in Section 1.2.4.5, current design practice is to check

that w_{20} for points on the concrete surface mid-way between reinforcing bars does not exceed some specified limit. Equation 4.16 may therefore be used as a design formula, and to make it compatible with existing crack width equations, a_{cr} may be substituted for the term $(s^2 + c^2)^{\frac{1}{2}}$. This alteration results in an error which is always conservative, and which will usually be less than 5%. The resulting design formula is:

$$w = (0.9a_{cr} + 100)\ \bar{\varepsilon} \qquad (5.1)$$

Equation 4.16 is compared with the current design formula in Section 4.10.3.

The recommended design formula for calculating the mean strain at any level in the slab of a composite 'T' beam is Equation 4.3, but $\bar{\varepsilon}$ should not be taken as less than 1×10^{-3}. The minimum value is stipulated because without it crack widths at low strain may be seriously underestimated. The formula differs from the one currently in use (Equation 1.38) in two respects : a term is included to allow for shrinkage effects, and the reduction in strain due to tension-stiffening decreases in inverse proportion to the steel stress.

5.3 Scope of proposed design formulae

The proposed formulae rely in part on results from tests on uncased composite 'T' beams. The depth of the neutral axis below the top of the slab varied from 210mm to 285mm, and the diameter of reinforcement from 10mm to 16mm.

Strictly, the design formulae are applicable only to beams of similar cross section, but it is believed that the theoretical arguments in Chapter 4 extend their scope to any uncased composite 'T' beam likely to be used in practice, provided it is reinforced with high-yield deformed bars, and its neutral axis lies below the slab's soffit.

CHAPTER 6

REVIEW OF PREVIOUS WORK

6.1 Introduction

This chapter seeks to establish the parameters which affect the mode of failure and the ultimate load of continuous composite plate girders with slender webs in the region of an intermediate support.

The ultimate load behaviour of plain steel girders is considered first, and the pattern of loading on the concrete slab and shear connectors in a composite girder is determined. The work on slabs and composite beams which are loaded in a similar manner is then reviewed.

Finally, some current methods of designing plain and composite plate girders are described.

6.2 Plain steel girders

6.2.1 Behaviour in pure shear

Skaloud[47] has given a clear description of the three stages leading to collapse of steel plate girders with slender webs. In the first stage, the web plate is subjected to equal tensile and compressive forces at 45^{o} and 135^{o} to the flanges (Fig.6.1a). These stresses increase uniformly throughout the panel until a critical value is reached and the web buckles elastically. In the second stage, any further load in the web must be taken in tension alone, and the membrane stresses shown in Fig.6.1b develop.

Increasing the load causes yielding in a small zone in the web, which marks the onset of the third stage. The zone gradually expands to form a diagonal yield band (Fig.6.2), the final width of which is greater for stiff flanges than for flexible ones. The use of stiffer flanges also results in the angle between them and the buckles increasing to a

maximum of approximately 45^{o}.

Once the yield zone has reached the flanges, any additional load must be taken by the flanges alone and this, together with the membrane stresses already acting on them, leads rapidly to the formation of plastic hinges and the collapse mechanism of Fig.6.3a. Rockey and Skaloud[48-50] showed that the hinges B and E form very close to the edge of the yield band.

6.2.2 Design methods for girders subjected to pure shear

Research conducted before 1970 has been reviewed in a number of reports[51-53] and is considered only briefly here.

The ultimate load of the girder, V_{ult}, is given by:

$$V_{ult} = V_{cr} + V_m \qquad (6.1)$$

where: V_{cr} = the shear force when the web buckles;

V_m = the shear force developed by the plastic collapse mechanism.

All researchers agree that V_{cr} is given by:

$$V_{cr} = \tau_{cr}\, d\, t \qquad (6.2)$$

where: τ_{cr} = uniform shear stress to cause buckling;

d = clear depth of the web between flanges;

t = web thickness

but opinions differ concerning the support conditions of the edges of the web. Mackey[54] and Fujii et al[55] consider that the flanges provide rigid supports, and the transverse stiffeners simple supports, whereas Rockey et al[51] prefer the conservative assumption of simple supports throughout. For the latter case:

$$\tau_{cr} = K\, \pi^2\, E(t/d)^2/12(1 - \nu^2) \qquad (6.3)$$

where: $K = 5.35 + 4(d/b)^2$ for $b/d \geq 1$

$K = 5.35(d/b)^2 + 4$ for $b/d < 1$

b = clear width of web between vertical stiffeners;

ν = Poisson's ratio.

It is customary to ignore the effects of geometrical imperfections in the web, and of residual stresses due to welding. This practice is to some extent justified by the close agreement of predicted and calculated ultimate loads obtained by many workers who have made this assumption. Values of the buckling load are likely to be overestimated, however, and in view of this it would be better to assume that the web is simply supported all round when calculating τ_{cr}.

Several methods have been proposed[51,56-58] for calculating V_m, the main difference being in the assumed location of the flange hinges. Basler[56] made the very conservative assumption that the flanges of plate girders were too weak to support any membrane stresses, giving the mechanism of Fig.6.3b. Chern and Ostapenko[57] considered that the flanges could withstand small membrane stresses, and that they would form a picture frame mechanism before collapse occurred (Fig.6.3c).

In 1973, Calladine[58] conducted a thorough upper bound analysis on the plastic mechanism which Rockey and Skaloud had observed in their tests (Fig.6.3a). Girders with compact webs which yielded before they buckled were considered first. It was shown that the hinges at B and E actually formed at positions C and F, and that the whole web yields in a state of simple shear.

Calladine also analysed girders with slender webs by idealising the region ABDE in Fig.6.3a as a series of tendons in the direction of the principal tensile strain rate. The distance c_c, as defined in the figure, was left variable. Expressions for c_c and V_m were derived which showed that both increased as the flange size increased. In this respect,

Calladine's model reflects the true behaviour of steel girders, and is an improvement on earlier collapse models such as those in Fig.6.3b and 6.3c. However, it is not applicable to cases where the web develops shear stresses before it buckles, and it does not include the possible effect of the yield band extending beyond the region ABDE in Fig.6.3a.

Porter, Rockey and Evans[51] also used the collapse model of Fig.6.3a to predict the ultimate load of a plate girder. Analysis of the collapse mechanism gave:

$$V_m = 4M_p/c_c + c_c\ t\ \sigma_{ty} \sin^2\beta + \sigma_{ty}\ t\ d(\cot\beta - \cot\beta_d)\sin^2\beta \qquad (6.4)$$

where: M_p = the plastic moment of resistance of each flange acting individually;

σ_{ty} = the membrane yield stress;

β = the inclination of the tension field to the flanges;

β_d = the inclination of the web panel diagonal to the flanges.

In the above expression the membrane yield stress is the diagonal tensile stress which develops in the web after buckling, and which acts in addition to the buckling shear stress, τ_{cr}, to cause yielding of the web. The required value of σ_{ty} is calculated from the Von-Mises yield criterion.

The hinges B and E will form at the position of maximum moment in the flanges, and consideration of the equilibrium of flange element AB gave:

$$c_c = 2(M_p/\sigma_{ty}\ t)^{0.5}/\sin\beta \qquad (6.5)$$

The only unknown on the right hand side of Equation 6.4 is β, and this is calculated by trial and error: the value required is the one that maximises V_m.

Substituting Equations 6.5 and 6.4 into 6.1 gives the expression for

calculating the collapse load of a symmetrical girder subject to pure shear:

$$V_{ult} = \tau_{cr}\, d\, t + 2c_c\, t\, \sigma_{ty} \sin^2\beta + \sigma_{ty}\, t\, d(\cot\beta - \cot\beta_d)\sin^2\beta \quad (6.6)$$

This equation is not a true upper-bound solution (as was claimed) because the collapse mechanism analysed is for a web with a low yield stress equal to σ_{ty}. In fact the yield stress of the web is larger than this, and is only attained when the stress σ_{ty} acts in conjunction with the elastic critical stress, τ_{cr}. Equation 6.6 is a combination of terms from separate elastic and upper-bound (plastic) analyses.

Consideration of vertical equilibrium at the Section BE also gives Equation 6.6, and Porter et al[51] showed that the yield criteria is not violated in the wedges BCH and EFG. They did not, however, check for equilibrium at any other part of the girder, so Equation 6.6 is not necessarily a true lower-bound solution. Since it is not a true upper-bound solution either, it may not be the exact solution for the collapse mode of Fig.6.3a. Nonetheless, one would expect Equation 6.6 to give close estimates of V_{ult}, and this has been shown to be the case; for 16 plate girder tests the average value of the ratio V_{ult}:measured ultimate load was 1.00 and the standard deviation was 0.05.

6.2.3 Girders subjected to pure bending moment

Basler and Thurlimann[59] have described how buckling in the compression zone of the web causes direct stresses to be shed to the compression flange. Collapse of the girder occurs when the compression flange fails in one of three modes: vertical buckling (Fig.6.4), lateral-torsional buckling, or local buckling, when the flange rotates but does not translate.

Girders which fail due to vertical flange buckling were considered initially. Their ultimate moment is determined by the stability of the

compression flange, which is restrained vertically by the web, and Basler and Thurlimann derived the relationship shown in Fig.6.5 for a flange yield stress (σ_{yf}) of 228N/mm^2. M_{ult} is the collapse moment of the girder and M_y is the moment to cause yield in the extreme compression flange fibres. In the region PQ the flange buckles vertically before it reaches a stress (calculated on the basis of the effective section in Fig.6.4) equal to its yield stress. Decreasing the web slenderness in the region QRS improves the stability of the compression flange and leads to an increase in the collapse moment, until at S the full plastic moment of the girder is developed. When the web is very compact it can sustain such high strains that strain hardening occurs, and the collapse moment increases rapidly - ST.

It was found that the curve QRS could be replaced with sufficient accuracy by the straight line:

$$M_{ult}/M_y = 1 - 0.0005(A_w/A_f)\left[\frac{d}{t} - \left(\frac{d}{t}\right)_c\right]$$

where: A_w is the cross sectional area of the web;

A_f is the cross sectional area of the flange;

$(d/t)_c$ is the slenderness ratio when $M_{ult}/M_y = 1$, that is when the flange yield stress equals the flange buckling stress.

Plate theory gives values for $(d/t)_c$ for simply supported or rigidly supported panels, and an intermediate value of

$$(d/t)_c = 5.7(E/\sigma_{yf})^{0.5}$$

was taken. Hence:

$$M_{ult}/M_y = 1 - 0.0005(A_w/A_f)\left[d/t - 5.7(E/\sigma_{yf})^{0.5}\right] \qquad (6.7)$$

Local or lateral-torsional buckling is likely to be the limiting criteria for the bending strength of many girders, and Basler and

Thurlimann made an empirical modification to Equation 6.7 to allow for these modes of failure. The modified formula is:

$$M_{ult}/M_{cr} = 1 - 0.0005(A_w/A_f)(d/t - 5.7\left[E\ M_y/M_{cr}\ \sigma_{yf}\right]^{0.5}) \qquad (6.8)$$

where: M_{cr} = the lower critical moment obtained from separate local and lateral-torsional buckling analyses.

Basler and Thurlimann[59] recommended that the ratios M_{ult}/M_y and M_{ult}/M_{cr} should never be taken as greater than 1.0, but Cooper[60] showed that this was unnecessarily conservative. Eight full size girders with web slenderness ratios between 61 and 123 were loaded in pure bending, and all developed their full plastic moments of resistance (M_{pg}) before collapsing. A reasonable limitation to Equation 6.8 is therefore that M_{ult} should not exceed M_{pg}. It has been shown[62] that with this proviso, Equation 6.8 accurately predicts the ultimate bending strength of girders from several independent series of tests.

6.2.4 Girders subjected to combined shear and bending

6.2.4.1 Empirical methods

Basler[61] described the ultimate load behaviour of girders subjected to combined loads with the aid of the interaction curve shown in Fig.6.6a. V and M are the coexistent shear force and maximum panel bending moment, respectively.

It was assumed that the flanges of a girder are unable to resist any loads due to tension field action. The ultimate strength of a girder subjected to pure shear (point P on the interaction diagram) would therefore be underestimated for the size of flanges common in structural engineering. It was also assumed that web buckling results in all bending stresses being shed to the flanges, unless their moment capacity is exceeded. This moment capacity is equal to the plastic moment of resistance of the flanges alone (M_F), so the shear strength of a girder,

it was argued, is not reduced by moments less than M_F. In practice however, some direct stress will remain in the web even after buckling, and will reduce its shear capacity, so the line PQ ought to slope down towards Q.

The line QS represents a beam which yields throughout its section before bending failure occurs, and was assumed to be parabolic, with its apex at S. When failure of the girder results from buckling of the compression flange, in any of the modes described in Section 6.2.3, the line RT is appropriate. It is vertical because such modes of failure depend on the stress in the compression flange, which is assumed to be unaffected by vertical shear forces. M_{ult} may be calculated from Equation 6.8.

Fujii et al[55] have developed interaction curves (Fig.6.6b) which allow for the effect of tension field action on the flange stresses. The curve P'R'S' is appropriate for girders with compact webs which do not buckle; it assumes that all bending stresses are resisted by the flanges up to their yield stress, and that the flanges do not contribute to the shear strength of the girder. Hence the ultimate load under pure shear is equal to the shear yield strength of the web, V_y, and the line R'S' corresponds closely to the line QS in Fig.6.6a.

For girders with slender webs, buckling will occur and the interaction curve PQRS is appropriate. Points P and S are derived from analyses for pure shear and pure bending respectively. It was postulated that when the shear force equals the critical buckling load of the web, the web will not contribute to the strength in bending, but because there is no tension field action causing direct stresses in the flanges, these are able to develop their full plastic moment of resistance, M_F. Point R may therefore be located.

Point Q corresponds to the shear load developed by a girder with

flanges unable to resist any transverse stresses due to tension field action. This situation was said to arise when the direct flange stress due to tension field action, σ'_f, combines with the direct bending stress to cause yielding in the flange. Hence the moment at Q is $M_F(1 - \sigma'_f/\sigma_{yf})$. The coordinates of Q are therefore based on the conservative assumption that stresses in the flanges due to tension field action reduce the bending resistance, but do not add to the shear resistance.

Another conservative assumption is that the points P, Q, R and S may be connected by straight lines. Ultimate loads of 14 beams tested at Lehigh University were underestimated by as much as 20% using the interaction curve PQRS.

6.2.4.2 Analytical methods

Calladine[58] extended his upper-bound analysis (Section 6.2.2) to include the effects of bending by considering the collapse mode shown in Fig.6.7. Rotation of AB and DE causes the length AB to lengthen, and DE to shorten, because the location of the pivots in the plastic hinges is no longer at the centroid of the flanges. CD therefore rotates, and work is done by the applied moment. It was assumed that the distances c_c and c_t (where c_t is defined in the figure) were equal. This is by no means certain: in fact Evans et al[62] have shown that c_t exceeds c_c in a symmetrical girder. Expressions for c_c and z (as defined in Fig.6.7) were obtained in terms of M_p. Allowance was made for the reduction of M_p due to the direct stresses in the flange.

The interaction diagram derived from the equation of virtual work is shown in Fig.6.8, but it is not reliable when M/M_F approaches unity, because the possibility of compression flange buckling is not considered. The reservations concerning Calladine's analysis of a girder subjected to pure shear are also relevant.

Evans, Porter and Rockey[62] have described a method for calculating

the ultimate load of a girder when the shear ratio, defined as $(V/V_y)/(M/M_{pg})$, is large. It is assumed that the web stresses increase elastically until buckling of the web occurs. Further load is resisted by diagonal tensile stresses in the web, which are superimposed on the stresses at buckling and eventually lead to the formation of a diagonal yield band. The web buckling stresses are considered to remain constant up to the ultimate load of the girder; they are not increased or decreased as the amplitude of the buckles increases, but are merely added to by the diagonal stresses in the tension field. As noted in Section 6.2.2, this assumption was shown to lead to accurate prediction of V_{ult}[51].

The assumed collapse mechanism is that illustrated in Fig.6.9. It is an improvement on that used in Reference 58 in that c_c and c_t are not assumed to be equal. An equilibrium solution for the ultimate load of the girder is obtained by considering the forces and moments acting on Section BE, which are now explained.

V_{cr}, H_{cr} and M_w are the forces and moments associated with the buckling load of the web. The following equation was recommended for calculating the buckling stresses, but since it does not allow for the presence of a net axial force in the web, it is only applicable to symmetrical girders:

$$(\sigma_m/\sigma_{cr})^2 + (\tau_m/\tau_{cr})^2 = 1 \qquad (6.9)$$

where: $\sigma_{cr} = 23.9\ \pi^2 E\ (t/d)^2/12(1 - \nu^2)$ which is the critical bending stress of a panel subjected to pure moment;

σ_m and τ_m are the critical co-existent bending and shearing stresses. σ_m is the extreme compressive stress at the mid-panel section.

F_w is the resultant membrane force when the region ABDE has yielded, and acts at a perpendicular distance of q from the mid-height of the web. Its magnitude and position are obtained from the membrane stress

distribution, which varies through the depth of the web due to the buckling stresses, as follows:

$$\sigma_{ty} = -0.5X + 0.5(X^2 - 4[\sigma_m^2 + 3\tau_m^2 - \sigma_{yw}^2])^{0.5} \qquad (6.10)$$

where: $X = 3\tau_m \sin 2\beta + \sigma_m \sin^2\beta - 2\sigma_m \cos^2\beta$

The stresses in the above expression should strictly be those in the web at the ultimate limit state, when buckling in the compression zone of the web will have caused some redistribution of the direct stresses to the compression flange. However, it was found to be sufficiently accurate to take both σ_m and τ_m as the values corresponding to the critical buckling load, assuming plane sections remain plane.

Once F_w has been determined, the ultimate load on the girder is readily calculated from the expression of vertical equilibrium:

$$V_u = F_w \sin\beta + V_{cr} \qquad (6.11)$$

where: V_u = the ultimate shear strength of a girder subjected to combined shear and bending.

The forces acting on the length c_c of the compression flange are shown in the inset of Fig.6.9: similar (but not equal) forces act on the length c_t of the tension flange. The membrane stress varies little over the length c_c, and can reasonably be taken as that mid-way between E and D. The plastic moment of the compression flange M_{pc} is reduced by the axial force, which varies along the flange, but it was shown that the reduced value, M'_{pc} may be based with sufficient accuracy on the value mid-way between E and D (F'_c). Hence:

$$F'_c = A_{cf}\,\sigma_{cf} = F_c - c_c\, t(\sigma_{tyc} \sin\beta \cos\beta + \tau_m)/2 \qquad (6.12)$$

$$M'_{pc} = M_{pc}(1 - [\sigma_{cf}/\sigma_{yf}]^2) \qquad (6.13)$$

where: σ_{cf} = axial stress in compression flange mid-way between D and E;

A_{cf} = area of compression flange;

σ_{tyc} = membrane yield stress adjacent to the compression flange, mid-way between D and E;

F_c = axial force in the compression flange at the mid-panel hinge.

The location of E corresponds to the maximum moment in the flange, and is derived by taking moments about D:

$$c_c = 2(M'_{pc}/t\ \sigma_{tyc})^{0.5}/\sin\beta \qquad (6.14)$$

Similarly for the tension flange:

$$F'_t = A_{tf}\ \sigma_{tf} = F_t + c_t\ t(\sigma_{tyt}\ \sin\beta\ \cos\beta + \tau_m)/2 \qquad (6.15)$$

$$M'_{pt} = M_{pt}(1 - [\sigma_{tf}/\sigma_{yf}]^2) \qquad (6.16)$$

$$c_t = 2(M'_{pt}/t\ \sigma_{tyt})^{0.5}/\sin\beta \qquad (6.17)$$

where: F'_t = axial force in the tension flange mid-way between A and B;

A_{tf} = area of the tension flange;

σ_{tf} = axial stress in the tension flange mid-way between A and B;

F_t = axial force in tension flange at mid-panel hinge;

σ_{tyt} = membrane yield stress adjacent to the tension flange, mid-way between A and B;

M_{pt} = plastic moment of resistance of the tension flange;

M'_{pt} = reduced plastic moment of resistance of the tension flange.

Equations 6.13 and 6.16 are valid only for solid rectangular flanges, which marks a departure from earlier work by the same authors[51] in which M_p was calculated on the basis of an effective T-section. This comprised the flange and an effective depth of web, h_w, given by:

$$h_w = 30t(1 - 2\tau_{cr}/\tau_{yw})$$

No explanation is given for this change in approach. A large proportion of the web area adjacent to each flange hinge is already yielding in diagonal tension when the collapse mechanism forms, so the definition of an effective depth of web is a rather arbitrary one, but even so, to ignore the web completely seems over-cautious. This problem is discussed in the light of experimental results in Chapter 9.

Consideration of the element of girder in Fig.6.9b then gives:

$$F_c = V_u(0.5d\ \cot\beta + Z + 0.5[c_c - c_t])/d + (M'_{pt} + M'_{pc} + F_w\ q - M_w)/d$$
$$- 0.5V_{cr}\ \cot\beta - 0.5\tau_{cr}\ t(b - c_c - c_t) \qquad (6.18)$$

$$F_t = V_u(-0.5d\ \cot\beta + Z + 0.5[c_c - c_t])/d + (M'_{pt} + M'_{pc} + F_w\ q - M_w)/d$$
$$+ 0.5V_{cr}\ \cot\beta + 0.5\tau_{cr}\ t(b - c_c - c_t) \qquad (6.19)$$

where: Z is the lever arm of the external load about the mid-panel section.

A direct calculation of V_u would involve the solution of the simultaneous Equations 6.9 to 6.19, which would be difficult, so an iterative method was recommended. Since the value of β is unknown, the process must be repeated several times for different values of β to find the optimum one, β_o. It was argued that β_o would be the inclination that maximised V_m and, indeed, values of β_o so obtained were in very close agreement with the observed direction of the buckles in a number of plate girder tests[51]. None of the girders considered had a web-slenderness ratio of less than 255, however, and there is some doubt concerning the derivation of a satisfactory value of β for relatively compact webs. In such girders, the margin between the buckling and the ultimate loads is small, and may not be sufficient for the buckles to rotate from their initial direction (45^o to the flanges at the level of the neutral axis)

to their optimum direction, β_o. This matter is discussed further in Section 9.4.3.4.

Because Equations 6.10 to 6.19 have been derived without reference to the shape and size of the flanges, the above procedure may be used for asymmetrical girders as well as symmetrical ones, provided allowance is made for net axial forces in the web when calculating the buckling load. In contrast with other analyses for combined loading, it considers both the reduction in the shear capacity of the web due to direct stresses at low moments, and the effect of tension field action on the flange stresses.

6.2.4.3 Parametric study

Evans, Porter and Rockey[63] have conducted a parametric study on symmetrical steel plate girders which provides a useful insight into the behaviour of beams subjected to combined shear and bending. The results were used to develop a simplified design procedure[64], but the application of this to composite 'T' beams (which are asymmetrical by definition) is questionable.

A computer program based on Equations 6.9 to 6.19 was used to calculate the ultimate load of 31 plate girders subjected to shear and bending in various proportions. The interaction curve is given by the line PQR in Fig.6.10.

V_{ult} is derived, essentially, from Equation 6.6, but a term has been added to allow for the shear strength of the flanges. The argument for doing so is not clear, however, for the ability of the flanges to resist shear is implicitly assumed in both the upper and lower bound solutions: there is no other way in which the vertical component of that part of the yield band supported by the flanges can be resisted. Calculated values of V_{ult} therefore allow for the shear strength of the flanges twice over.

It was found that in the zone PQR, β may be taken as $2\beta_d/3$ with

reasonable accuracy unless the web slenderness ratio is below about 240. In this case, and especially if the panels are narrow so that β_d is large, β may be as low as $0.55\beta_d$.

Point R marks the transition between the shear mechanism failure and a bending type of failure. For most girders, M_R was found to be approximately equal to M_F, but for wide-flanged girders, M_R is as low as $0.85M_F$. Conversely, in girders with an aspect ratio (b/d) greater than 1.0 and d/t less than about 180, M_R increases to $1.25M_F$. All three situations might well arise in composite plate girders. The shear force V_R is obtained by resolving vertically at Section C-D in Fig.6.11:

$$V_R = \tau_{cr}\, d\, t + 0.5t \sin 2\beta\, \sigma_{ty}\, d_t$$

where: d_t is the depth of the yield band adjacent to the stiffener. It was recommended that d_t is calculated from the empirical formula:

$$d_t/d = (0.64 + 42.5M_p/M_F)(2 - [b/d]^{1/8})$$

This equation overestimates d_t, and therefore V_R, when the slenderness ratio is less than about 180. The resulting formula for V_R is:

$$V_R/V_y = \tau_{cr}/\tau_{yw} + D(0.554 + 36.8M_p/M_F) \qquad (6.20)$$

where: $D = \sigma_{ty} \sin(4\beta_d/3)(2 - [b/d]^{1/8})/\sigma_{yw}$;

τ_{yw} = the shear yield stress of the web.

The term in M_p has been queried[70] on the grounds that when a moment of M_F is applied to a symmetrical girder, the axial stresses in the flanges are such that they cannot resist any extra lateral forces. V_R should then be independent of M_p. This is true of very slender webs where the critical buckling stress is negligible, so that the tension flange force at B is equal to that at C, and both are equal to the yield force. A and B are therefore coincident. Even in less slender webs, where the shear stress at buckling has a finite value, the flange force at B will

be only slightly less than that at C, so that c_t will be almost zero. For symmetrical girders, the failure mode shown in Fig.6.11 is therefore inconsistent with the assumption of a moment of M_F at Section CD, so that Equation 6.20 is suspect.

An empirical method is used to plot the interaction diagram between P and R, and was found to be in close agreement with the results of the parametric study. M_Q is taken as b V_{ult} (the maximum moment in the end panel of a simply supported girder) but not greater than $0.5M_F$. The curve QR is assumed to be parabolic, with its apex at Q.

When the shear ratio is low, Evans et al use an interaction curve which is virtually identical to that proposed by Basler[61]. The curve RST corresponds to failure of a girder where web buckling is prevented and is assumed to be parabolic, with its apex at T. The vertical cut-off SU allows for the possibility of buckling in the compression flange; M_{ult} is calculated from Equation 6.8.

The theoretical collapse load of 58 vertically stiffened plate girders was calculated from the interaction chart of Fig.6.10, assuming that:

$$M_R = M_F \text{ and } \beta = 0.67\beta_d$$

The average value of the ratio of the calculated collapse load to the experimental collapse load was 0.995 and the standard deviation was 0.071, which indicates excellent correlation. Further, the values of c_c, c_t and β were found to agree well with experimental observation.

6.3 Composite beams

The author knows of no published account concerning the ultimate load behaviour of composite plate girders when the shear ratio is high. However, from the work reported in Section 6.2, the probable mode of failure if buckling of the compression flange is prevented is the one

sketched in Fig.6.12.

The shear sway mechanism observed in tests on plain steel girders is assumed to occur in composite beams also. If the shear connection between the slab and the girder is sufficiently strong, large hogging and sagging curvatures will occur in the slab at positions A and B. These will cause yielding in the reinforcement in tension, and may lead to local crushing in the slab, although the global tension in the slab due to bending might prevent the latter. The shear connectors at B will be subjected to large uplift forces as well as longitudinal shear, and this may cause local pull-out failure of the slab.

Willmington[65] conducted tests on composite beams with compact webs where the shear ratio exceeded unity. Although the steel beam does not develop the tension field action and the diagonal yield band associated with plate girders, the loads imposed on the shear connectors and the slab are similar to those described above. The observed collapse mode is shown in Fig.6.13. The web of the girder yields in shear over the length AC, and plastic hinges form in the flanges as shown. Large local curvatures were seen to form in the slab at A and C, and due to this and considerable slip, compressive forces developed in the bottom of the slab at the support. At the sagging hinge, however, measurements indicated that the whole depth of the slab remained in tension. Considerable uplift and slip were noted in this region, but the shear connectors did not fail, even though no account was taken of the uplift forces in their design.

The shear force carried by the reinforced concrete slab (αV) in these tests is of particular interest. Willmington[65] described how the normal elastic theory could be used to calculate the vertical shear stresses in the composite beam, assuming the concrete to be either fully effective (uncracked) or totally ineffective (cracked). The true stresses in the slab were expected to lie somewhere between these extremes, and

test results indicated that in the regions where the slab reinforcement remained elastic the uncracked value of α could be used.

Where the reinforcement has yielded, such as over the length AB in Fig.6.13, consideration of equilibrium leads to the conclusion that there is no shear force in the slab (unless the deformations are so severe that the reinforcement strain-hardens). The shear force αV must therefore be transferred to the steel girder at the boundary of the plastic zone, as shown. This was confirmed by Willmington's test results.

6.4 Shear in cracked reinforced concrete

It is now well established that cracked reinforced concrete can resist considerable shear force[66-68]. Taylor[68] conducted tests on simply supported beams subjected to a point load at midspan, and for a cube crushing strength of $45N/mm^2$ and a reinforcement ratio of approximately 1% found that less than 40% of the total shear was resisted in the compression zone. Between one-third and a half of the total load was taken by the interlocking of aggregate particles on opposite sides of a crack, and the remainder was taken by the dowel action of the reinforcement.

The maximum force transmitted by dowel action is determined by the formation of horizontal cracks at the level of the reinforcement, and thus depends on the net width of the concrete there, and its splitting strength.

The contribution of aggregate interlock to shear strength depends primarily on the crack width and the shear displacement. Fenwick and Paulay[67] tested plain concrete prisms in which the width of a pre-formed crack was held constant while an increasing shear force was applied parallel to it. They found that the shear force at failure was inversely proportional to the crack width. Taylor[68] argued that shear displacements (δ_s) and crack widths (w) increase simultaneously in reinforced concrete

beams, and conducted a series of tests in which the ratio δ_s:w for each specimen was maintained constant while the applied shear force was increased. The aggregate-interlock force was proportional to this ratio, which confirms the results of Fenwick and Paulay.

6.5 Design rules for composite girders

Part 5 of BS5400[34], and the 1977 draft of Part 3 of the same standard[69] make specific provision for the effects of tension field action in a manner which allows for the influence of the flange stiffness on the width of the yield band. A report by Horne, Ogle and Dowling[70] describes the derivation of the recommendations in the draft of Part 3.

For slender composite beams subjected to pure shear, the entire load is assumed to be resisted by the steel girder, whereas for beams subjected to pure moment, an elastic, full-interaction analysis, ignoring concrete in tension, is used to determine the stresses in the beam. In each case, the stresses should not exceed the limits laid down in Part 3 of the standard. No guidance on the method to be adopted for composite plate girders subjected to combined shear and bending is given, however, due to a lack of experimental data for such cases.

The design method given in Ref.69 is based on the interaction diagram of Fig.6.14. A partial safety factor for material strength is included in the expressions in the draft Part 3, but is taken as 1.00 in the following discussion, partly because its final value is not yet fixed, and partly to facilitate direct comparison of the design rules with test results.

M_{ult} is the ultimate bending moment capacity of the girder, which is derived from consideration of local buckling, lateral-torsional buckling, or inward collapse of the compression flange.

V_{ult} is the ultimate shear capacity of the panel and is determined

from graphs derived from Equations 6.5 and 6.6. As noted, these formulae do not include the extra term for shear in the flanges which Rockey added to his later solutions[63] and are more realistic for that reason. M_p is calculated for an effective flange section shown in Fig.6.15. b_f is the lesser of half the actual flange width and $10t_f(355/\sigma_{yf})^{0.5}$, where t_f is the flange thickness, and h_w is $12t(355/\sigma_{yw})^{0.5}$. β has been taken as $2\beta_d/3$ in the design charts, which are therefore subject to the reservations noted in Section 6.2.4.3 in this respect. More seriously, however, there is no provision for increasing M_p when a concrete slab acts compositely with the steel flange, and where the flanges are unequal the lower value of M_p is taken. These recommendations are likely to have a crippling effect on continuous composite beams in the region of an intermediate support, since the steel tension flange is often very small there: information on the effect of the concrete slab on the plastic moment of resistance of this flange would be very useful.

V_R and M_R are, respectively, the shear force and the maximum panel moment when the axial forces in the flanges are such that they cannot support the tension field. The collapse mechanism is the one shown in Fig.6.16. The forces acting on the flanges and the vertical stiffeners are shown - they are calculated on the assumption that the critical shear stress causes negligible variation of the flange forces along their length. V_R is derived from the design charts by substituting $M_{pc} = M_{pt} = 0$. M_R is calculated from:

$$M_R = F\ D' \qquad (6.21)$$

where: D' = the distance between the centroids of the two flanges;

F = the limiting flange force - to be taken as the lower value for the two flanges. This is the yield force in the case of the tension flange, but is determined by the critical buckling stress for the compression flange.

The contribution to M_R of the direct stresses in the web (M_w) is ignored. This is reasonable in the case of slender webs, but for relatively compact webs ($100 < d/t < 150$, say) M_w may be significant, so that M_R will be underestimated. Further inaccuracy arises because the force in the yield band is ignored: if the tension flange controls, F_w will add to the calculated value of M_R, but if the compression flange controls, M_R will be reduced because the lever arm of the compression flange force is no longer D'.

The shape of the interaction diagram between points P and R, and R and T is clearly an approximation introduced for the sake of simplicity. Evans et al[62,63] have shown that in the zone PR, the true interaction curve is a very shallow parabola and that V drops off rapidly with increasing moment only when M is almost equal to M_R. Further, the bending strength of a girder is not significantly decreased until the applied shear force exceeds $0.5V_R$. As long as the calculated values of V_R and M_R are reasonably accurate therefore, the interaction diagram PQRST is a good representation of the true curve.

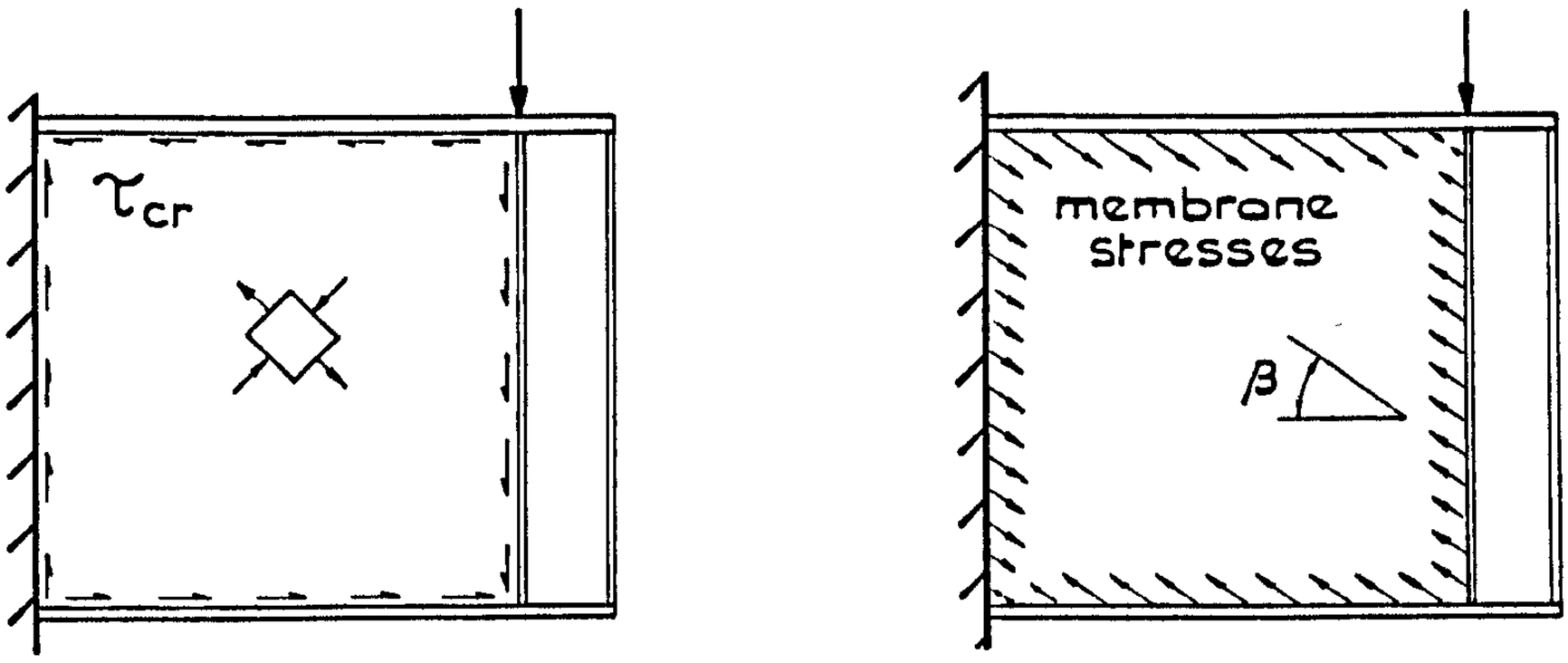

a) Stage 1 b) Stage 2

FIG. 6.1 STRESSES IN PLATE GIRDER SUBJECTED TO SHEAR

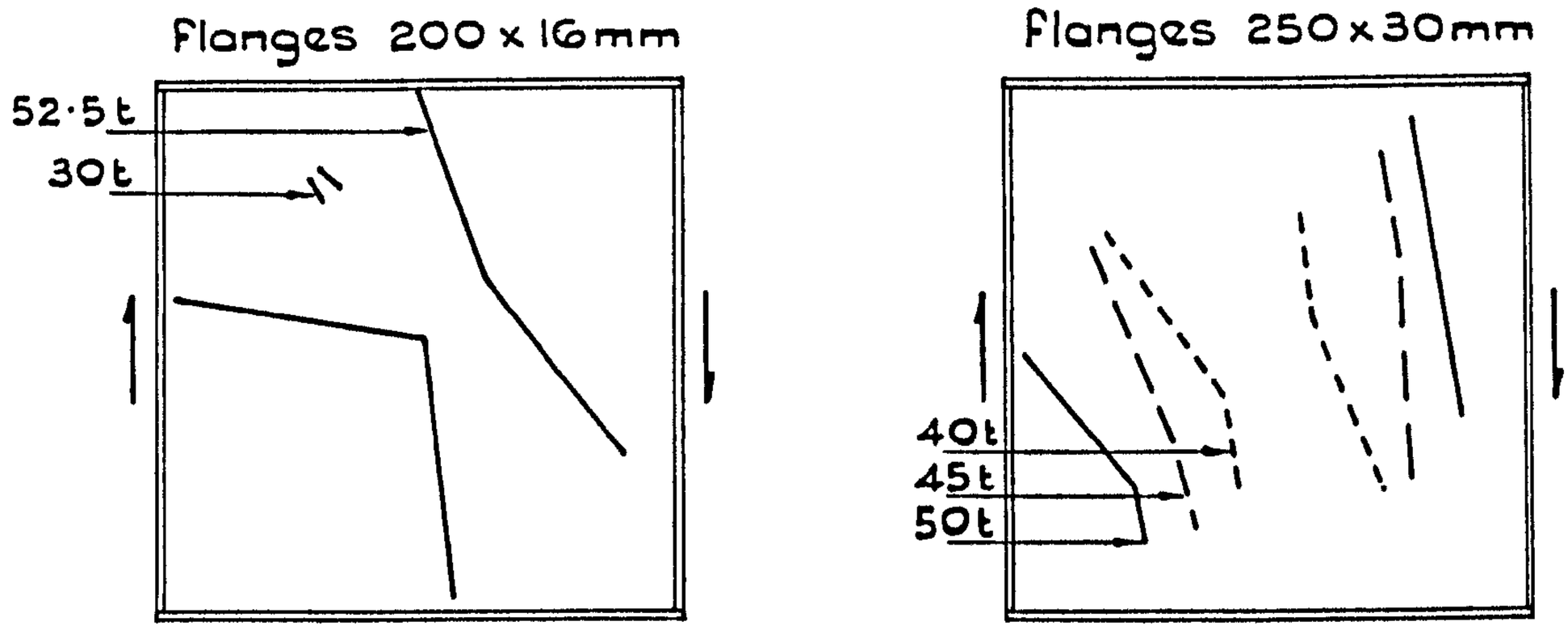

FIG. 6.2 EXTENT OF DIAGONAL YIELD BAND

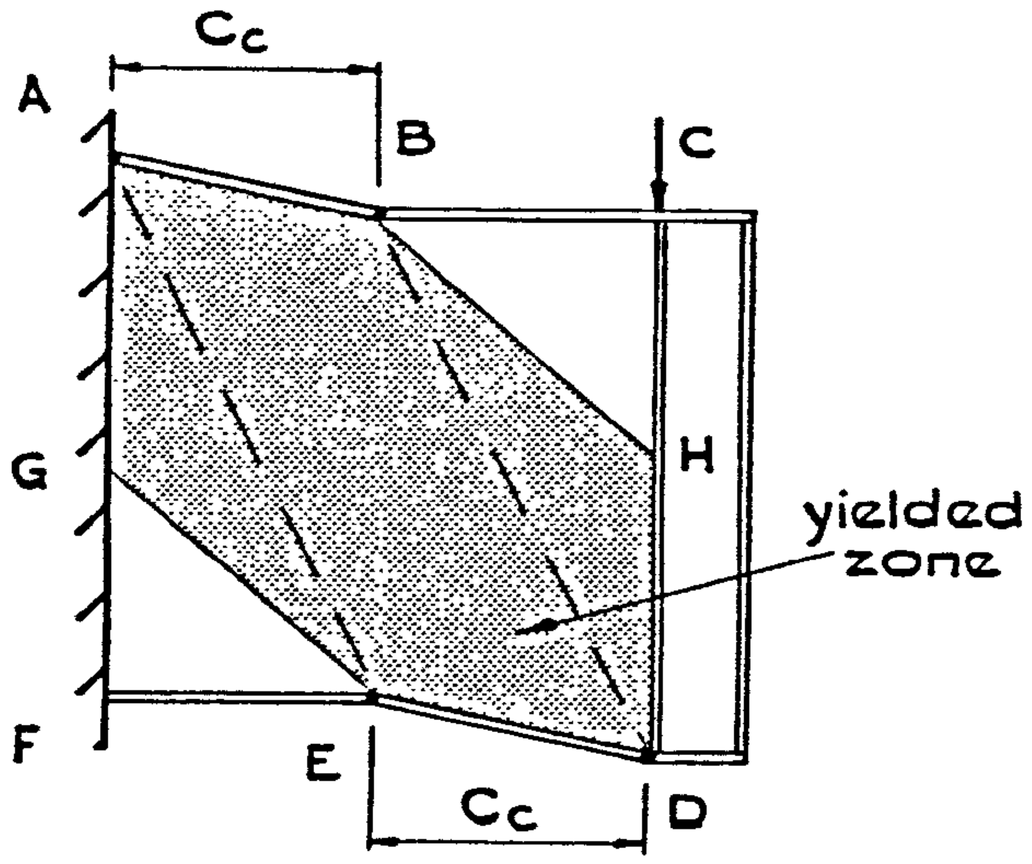

a) Rockey et al

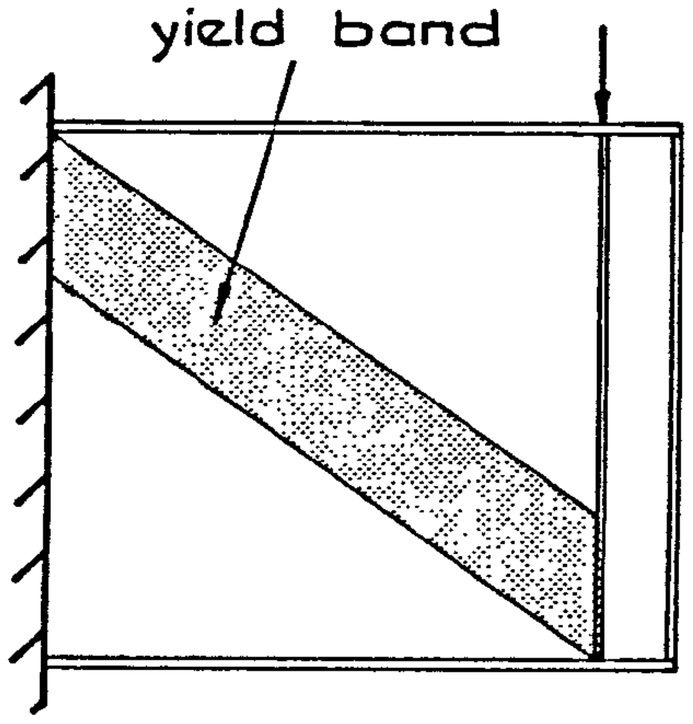

b) Basler

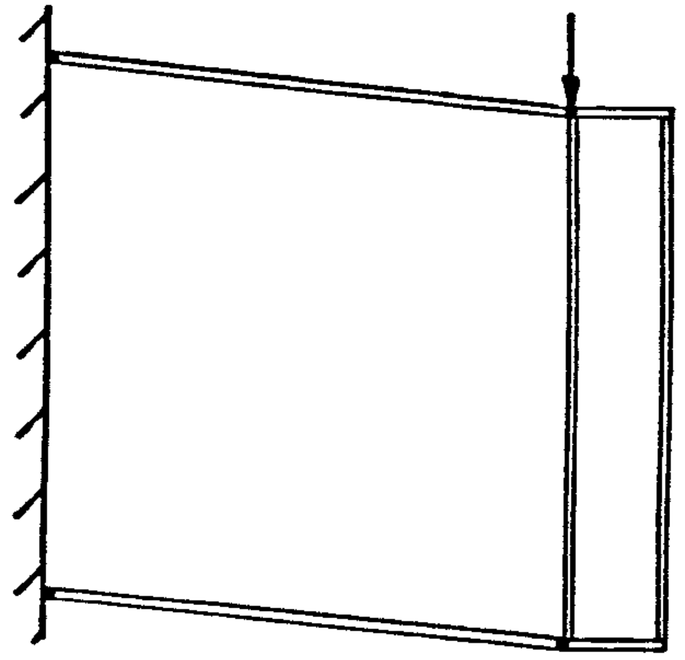

c) Ostapenko and Chern

FIG. 6.3 COLLAPSE MODES OF A GIRDER SUBJECTED TO SHEAR

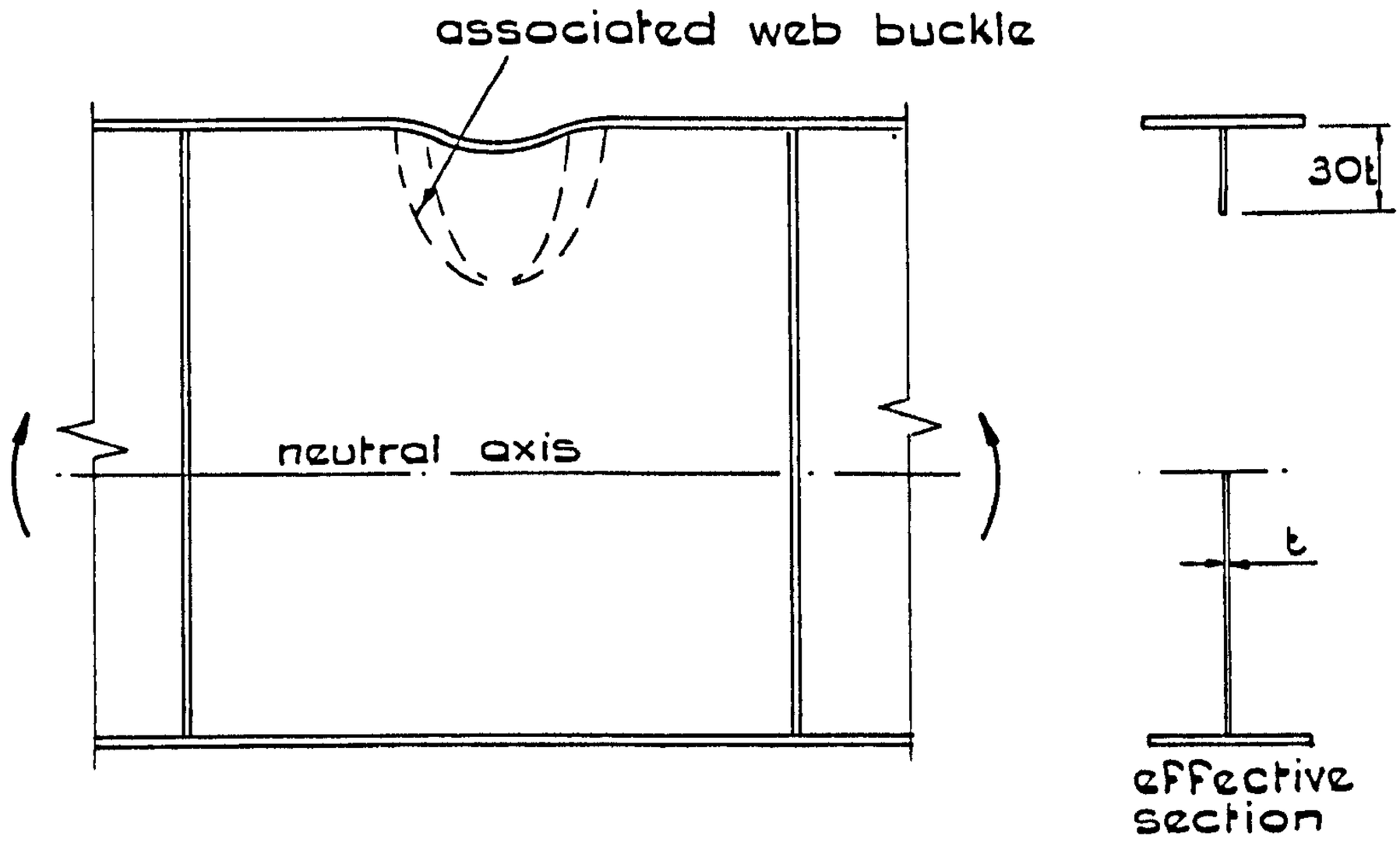

FIG. 6.4 VERTICAL FLANGE BUCKLING

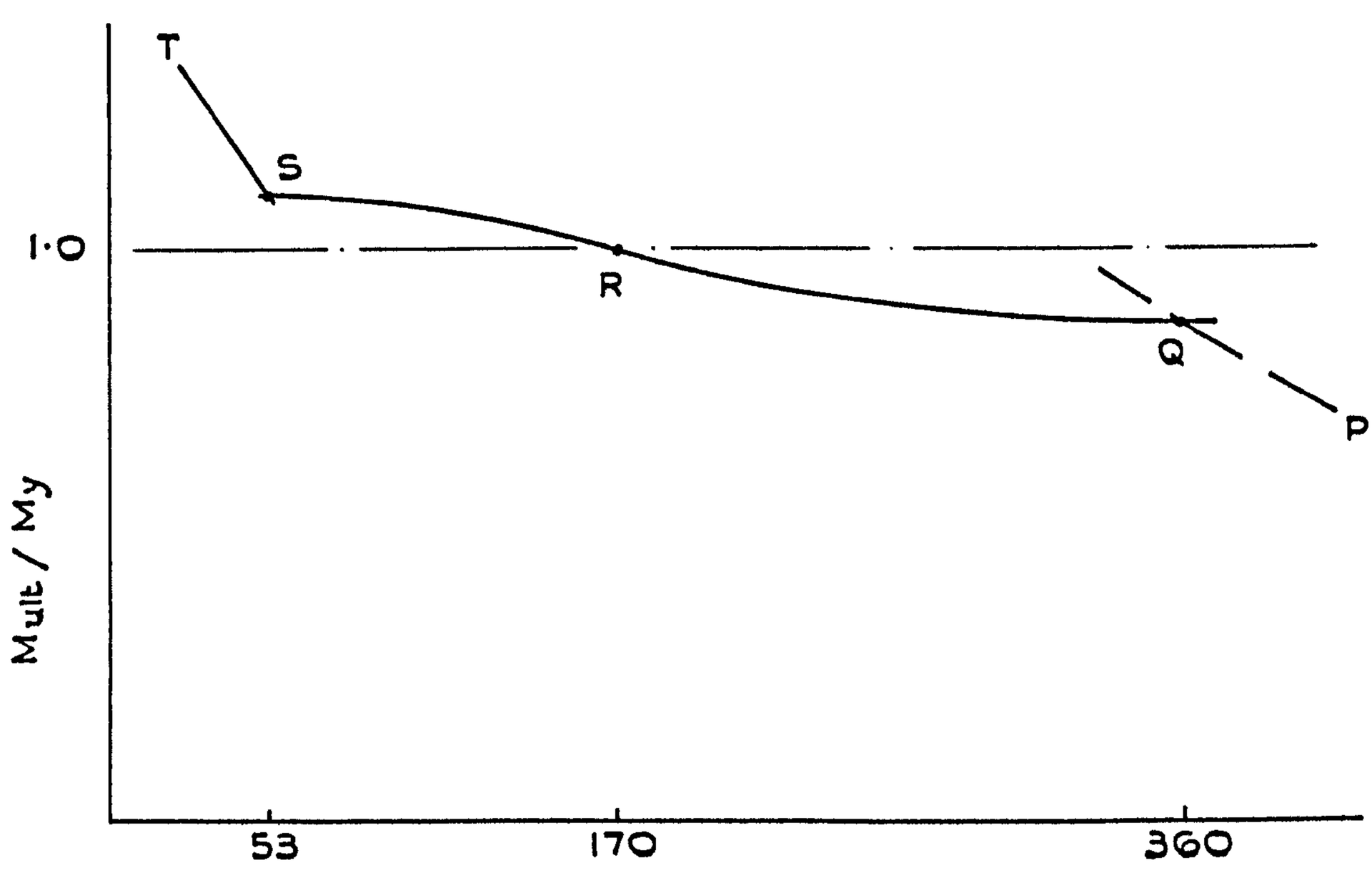

FIG. 6.5 EFFECT OF WEB SLENDERNESS ON ULTIMATE MOMENT

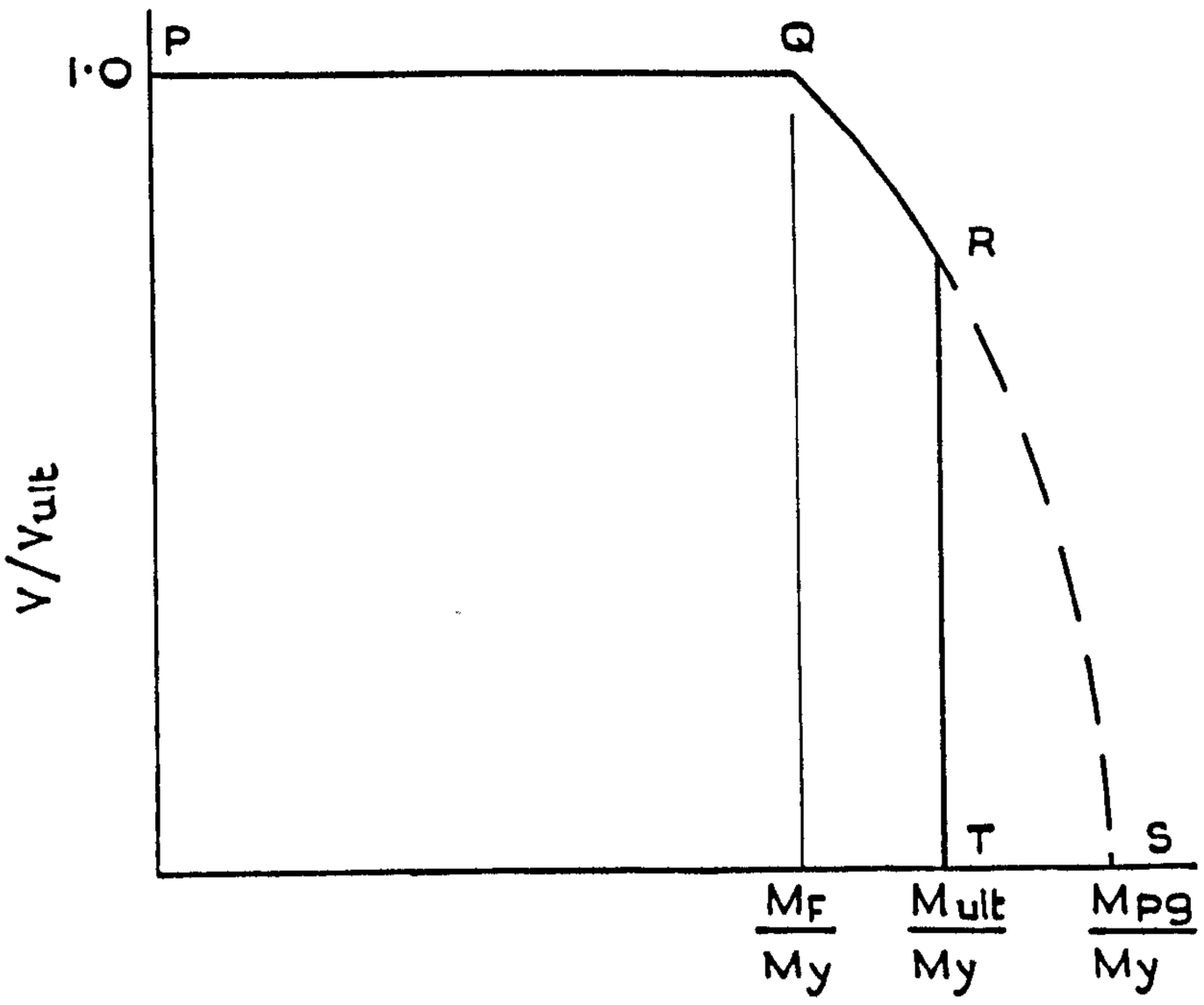

a) Basler

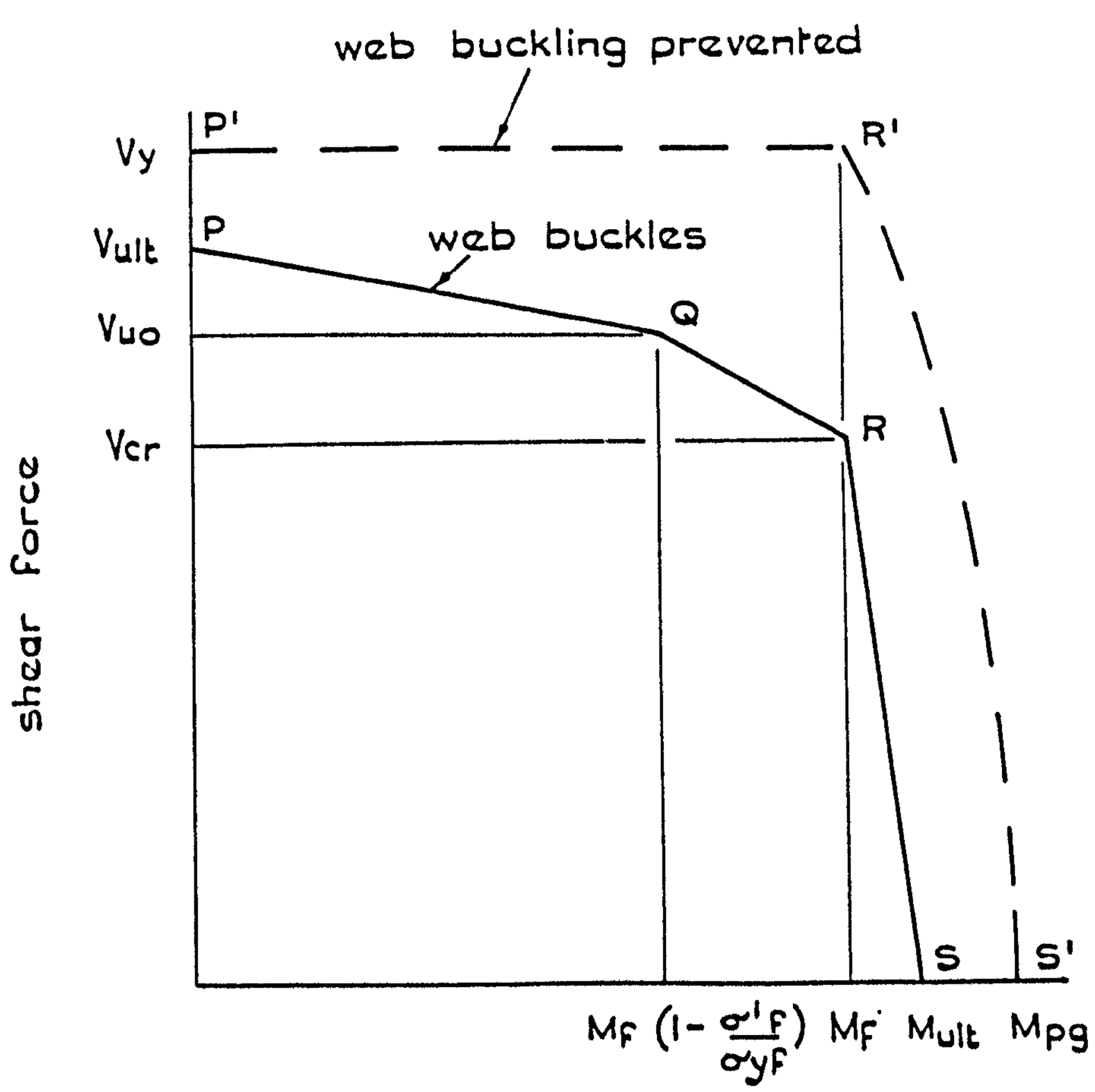

b) Fujji et al

FIG. 6.6 INTERACTION CHARTS FOR COMBINED LOADING

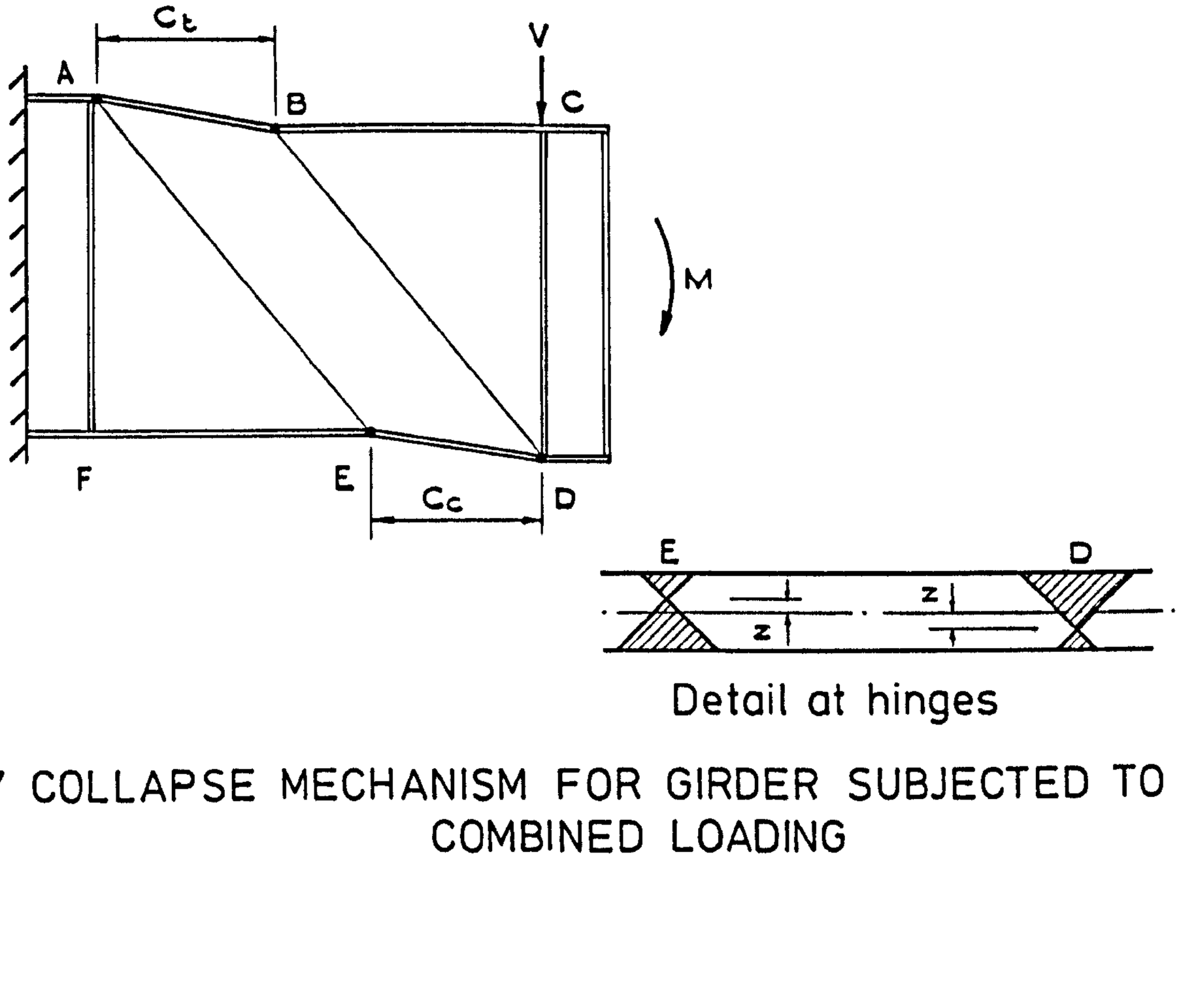

FIG.6.7 COLLAPSE MECHANISM FOR GIRDER SUBJECTED TO COMBINED LOADING

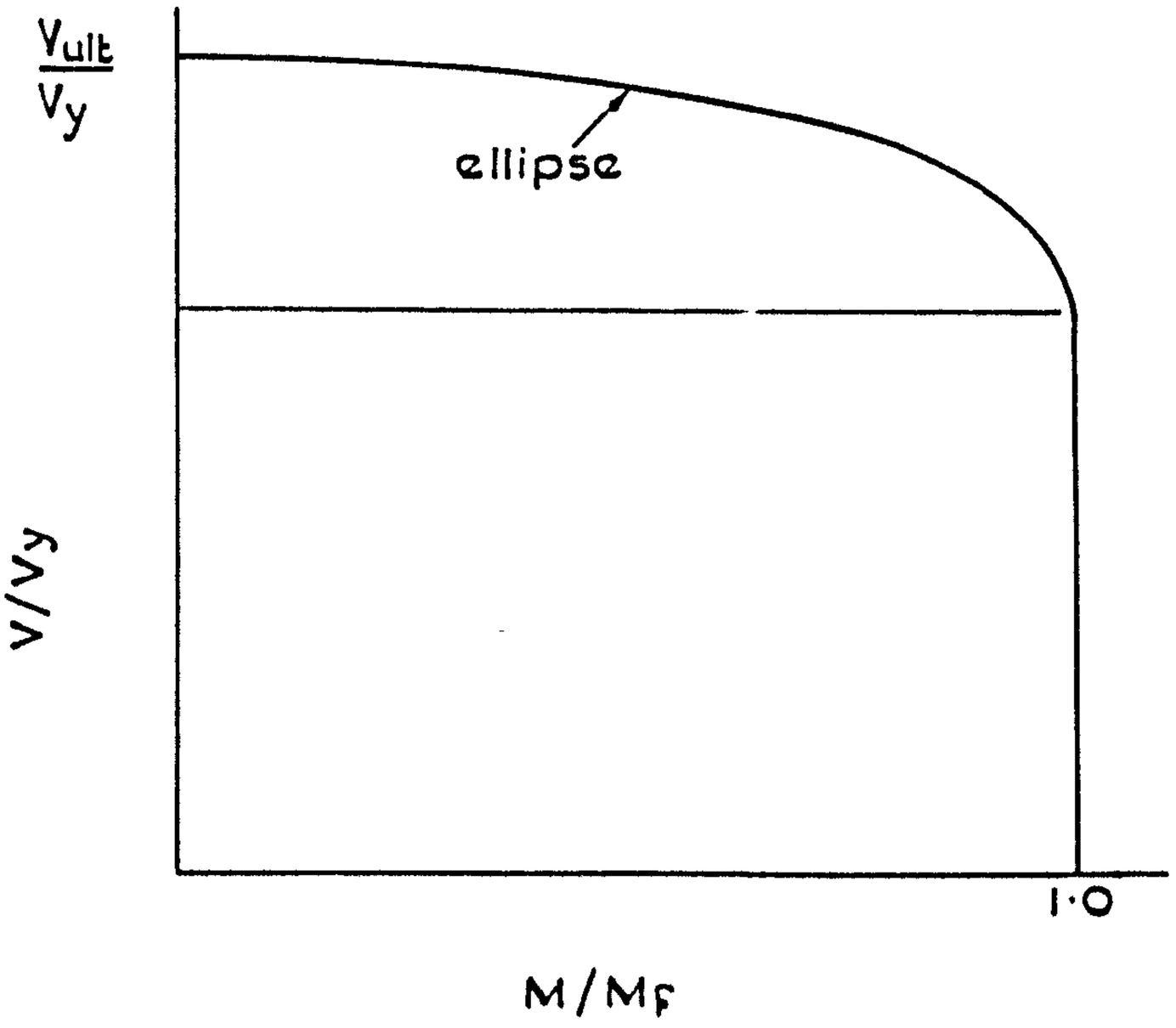

FIG.6.8 INTERACTION DIAGRAM FROM UPPER BOUND ANALYSIS

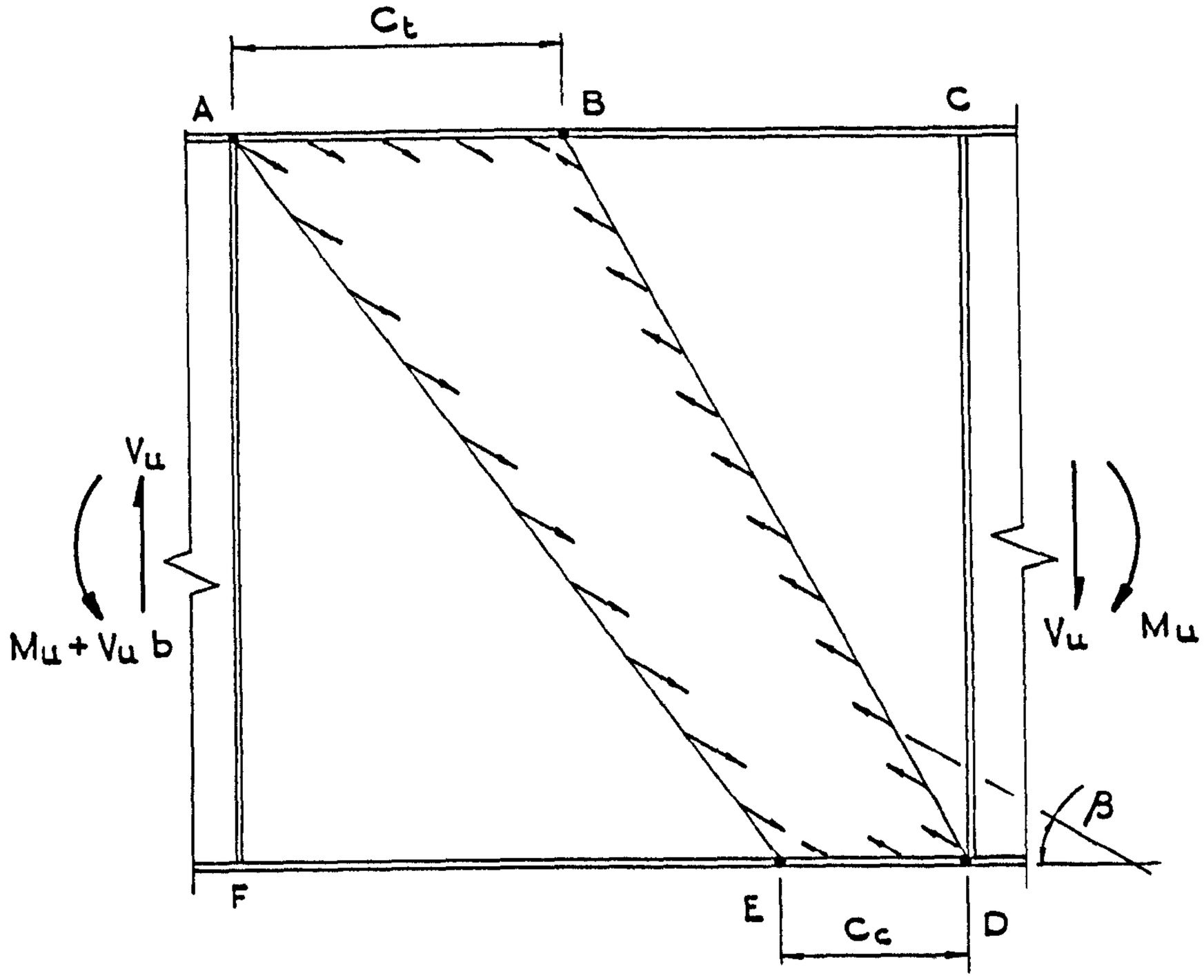

a) Failure mechanism

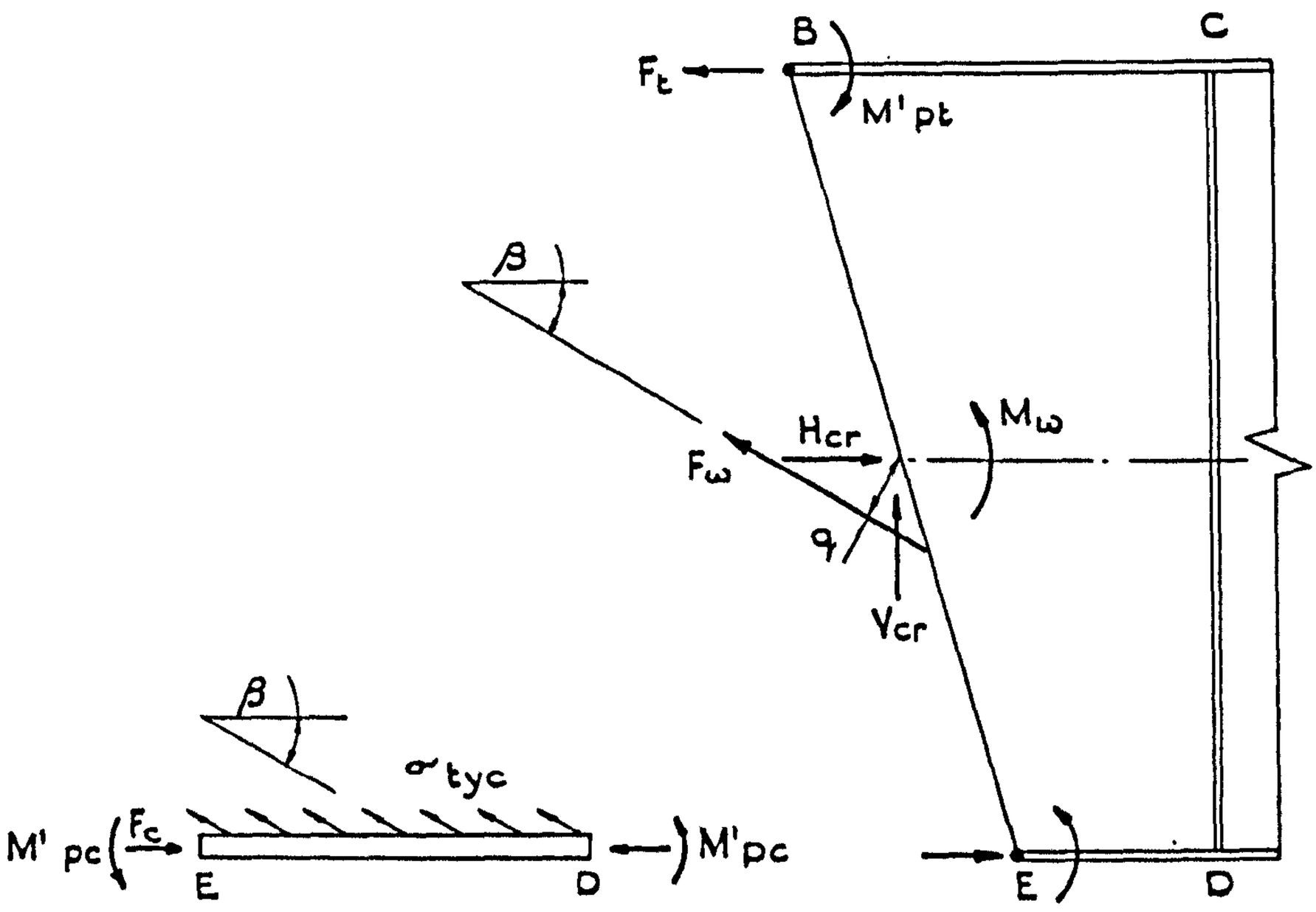

Forces on element DE

b) Forces on section BE

FIG. 6.9 FAILURE MECHANISM DUE TO EVANS ET AL

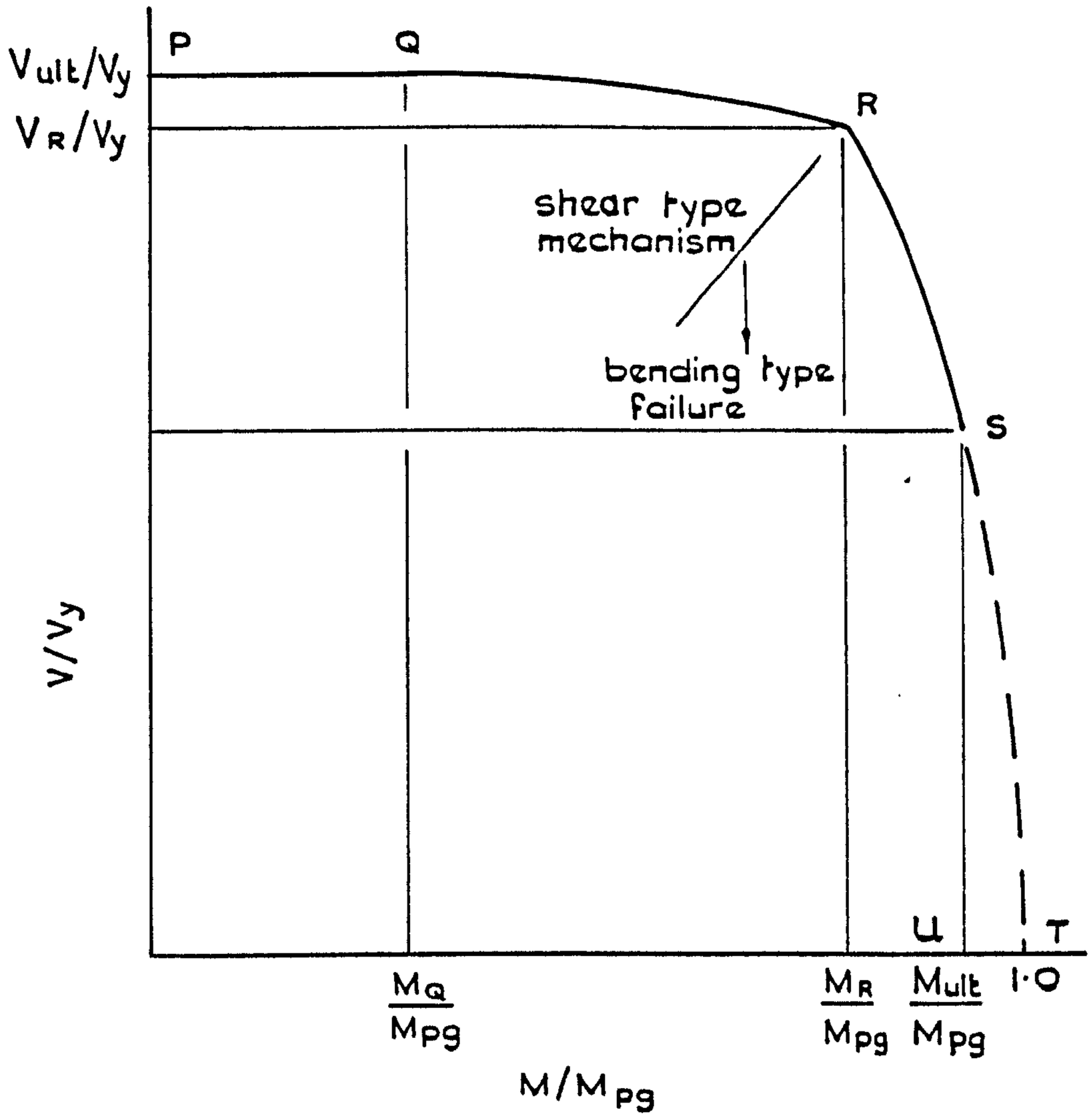

FIG. 6.10 INTERACTION CHART DUE TO EVANS ET AL

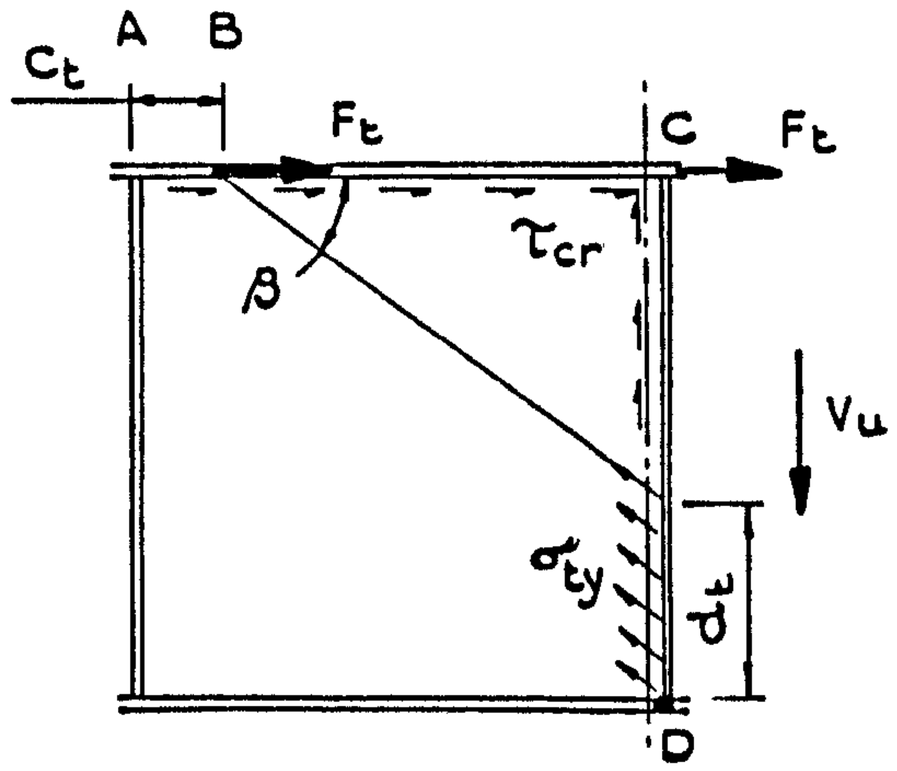

FIG. 6.11 WEB STRESSES AT YIELD IN COMPRESSION FLANGE

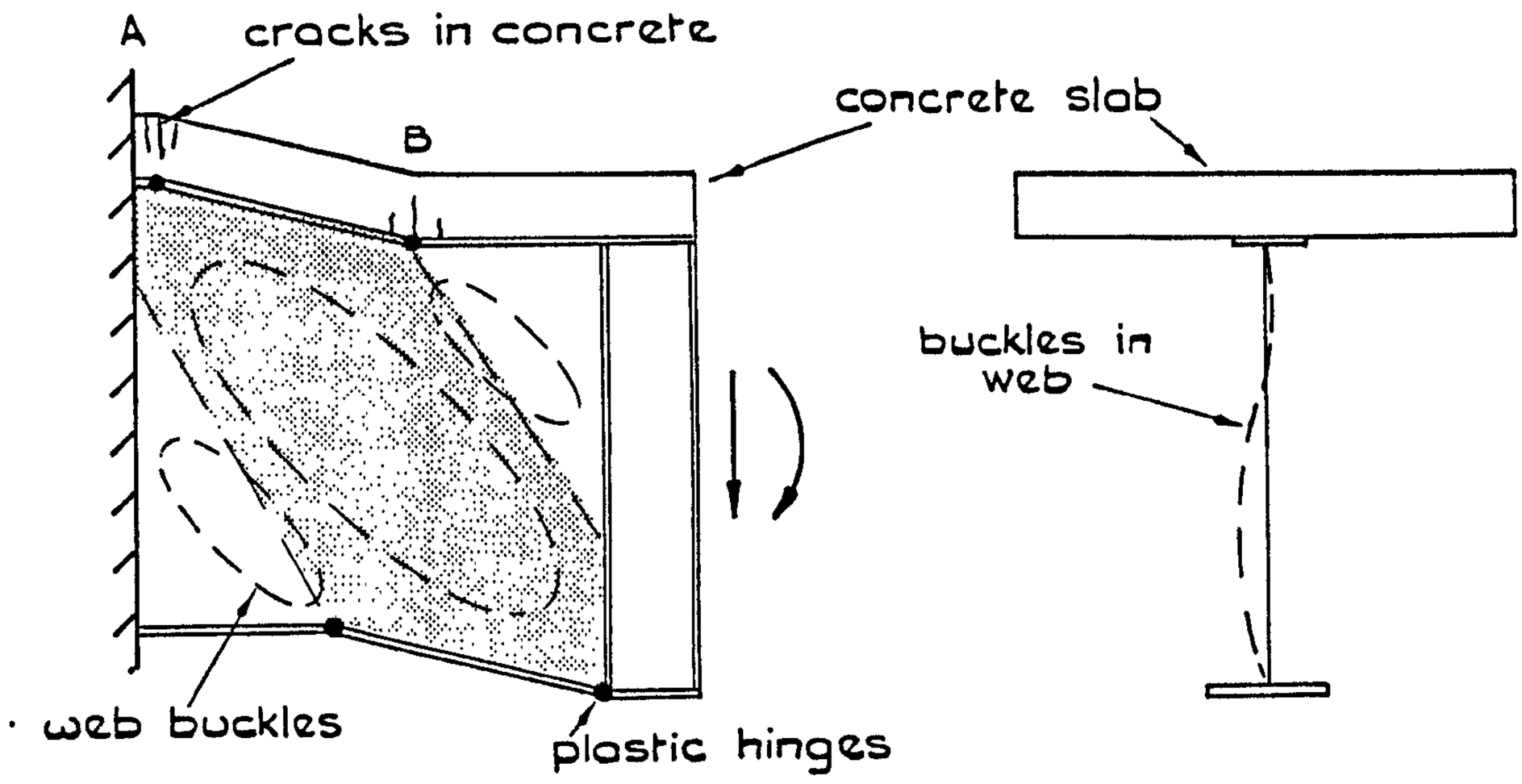

Elevation Section

FIG. 6.12 ANTICIPATED FAILURE MODE OF COMPOSITE PLATE GIRDER

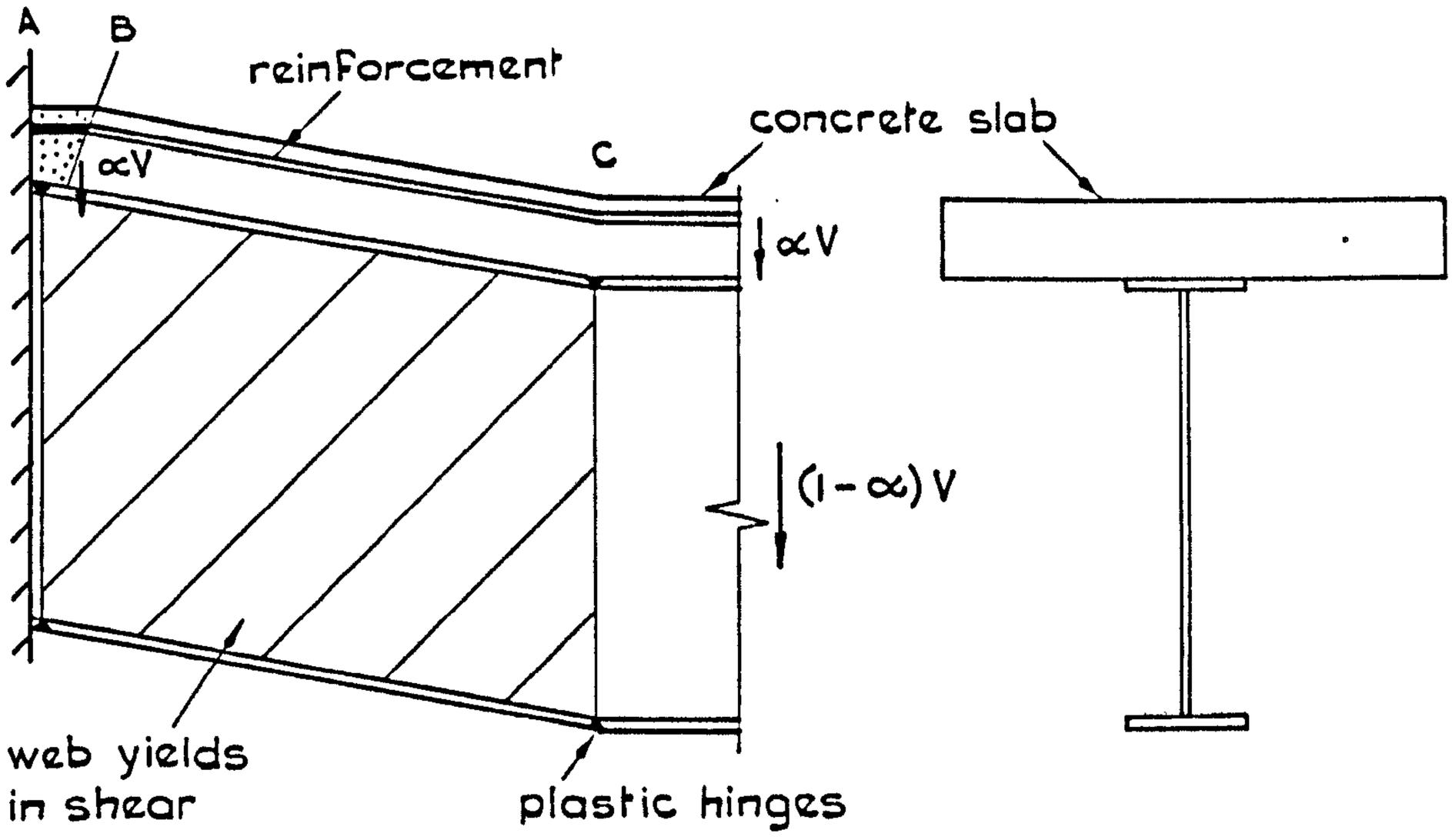

Elevation Section

FIG. 6.13 FAILURE MODE OF COMPACT COMPOSITE BEAM

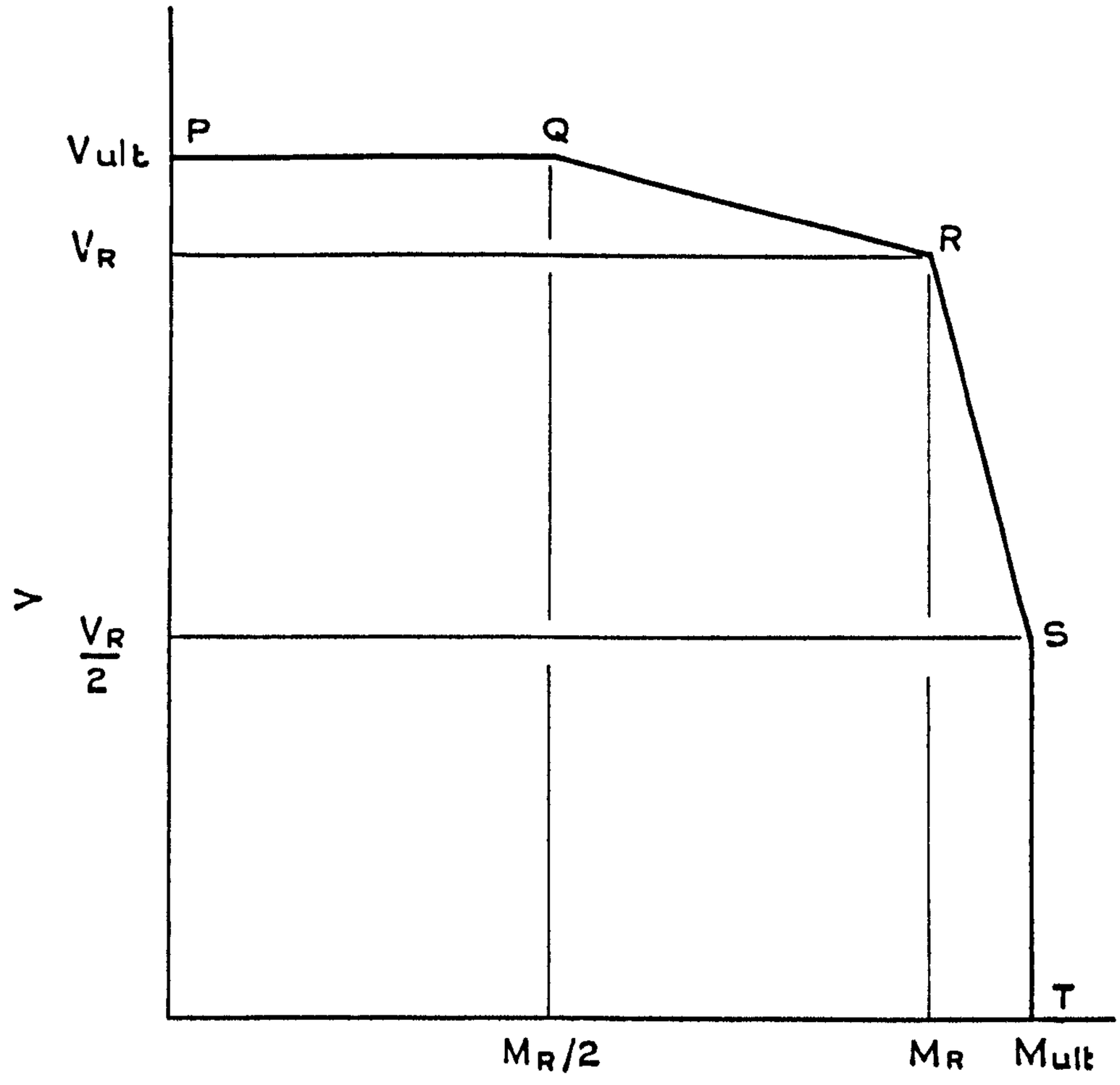

FIG. 6.14 INTERACTION DIAGRAM OF BS5400

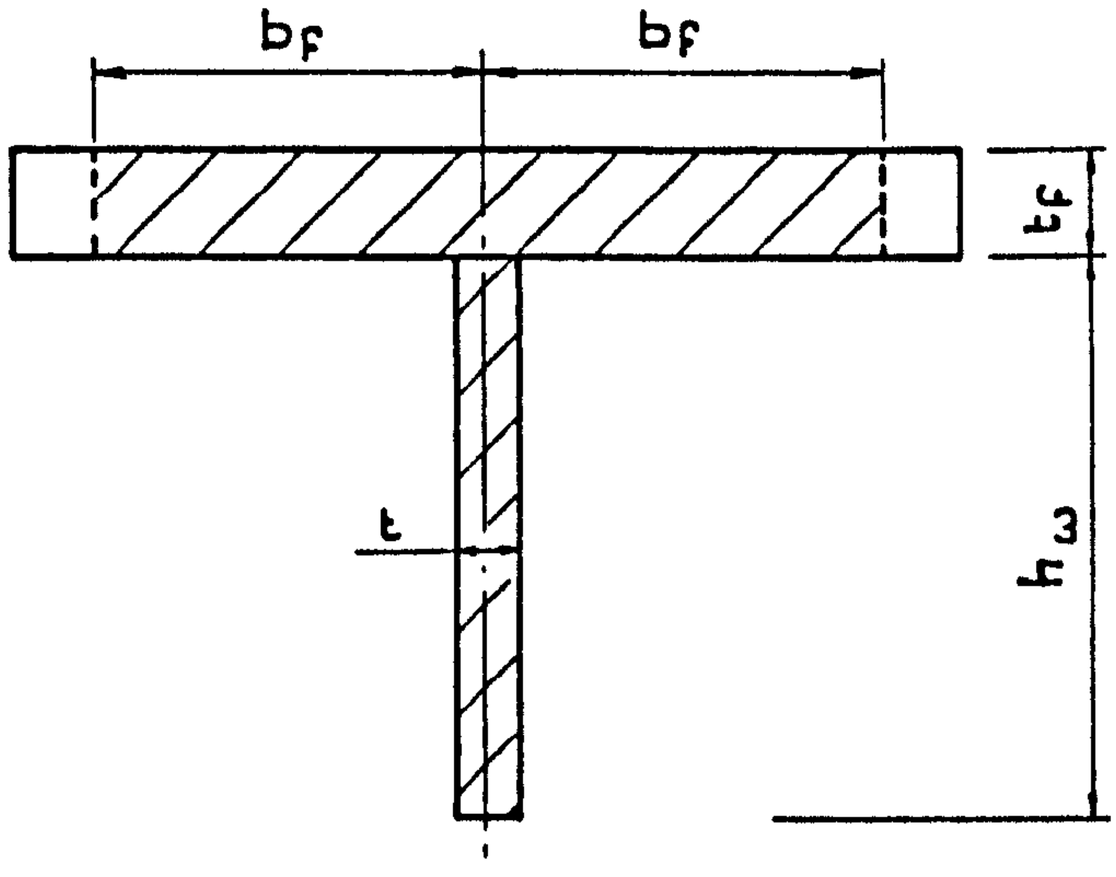

FIG. 6.15 EFFECTIVE FLANGE SECTION

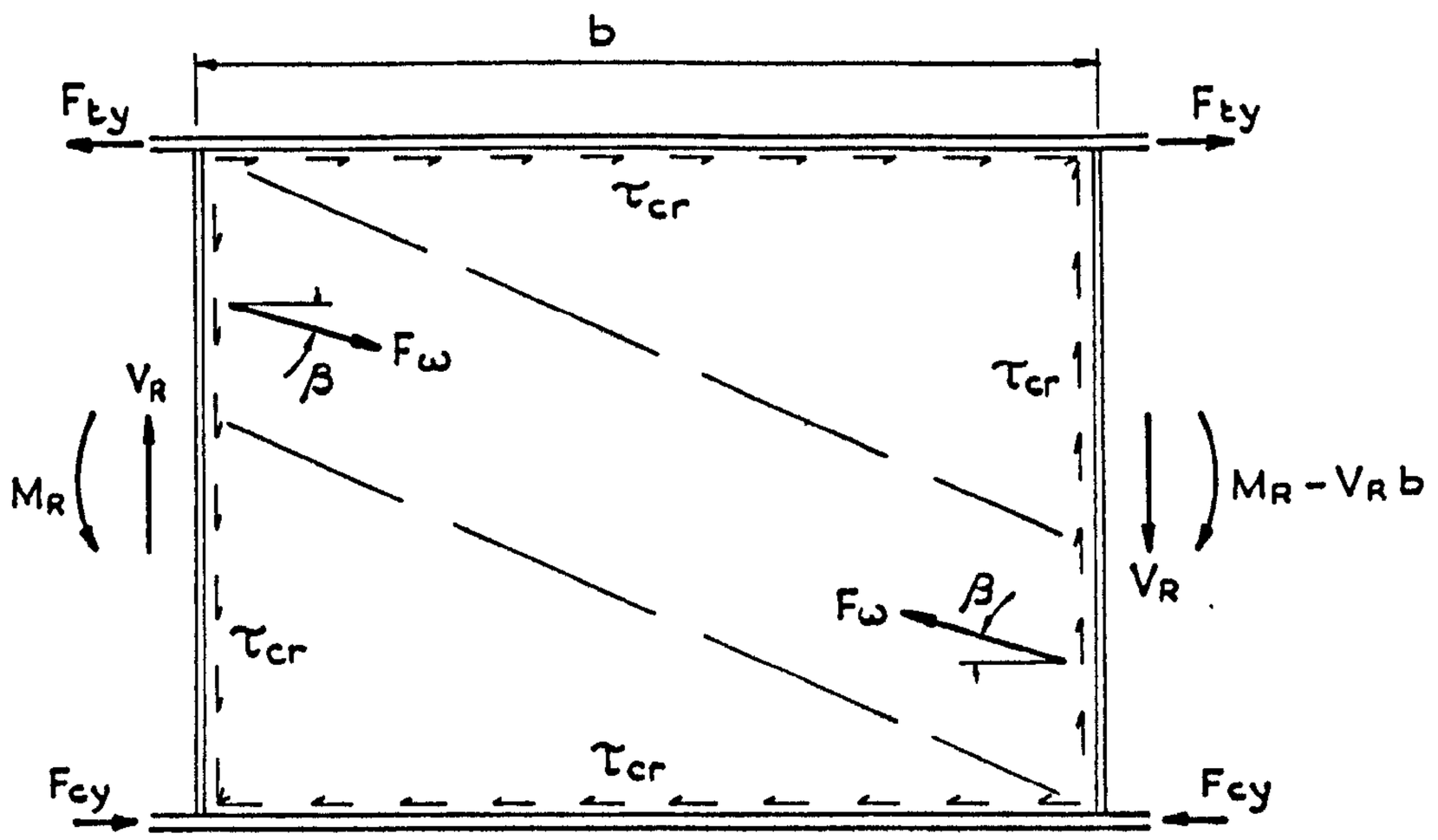

FIG. 6.16 COLLAPSE MECHANISM FOR LARGE AXIAL FLANGE STRESSES

CHAPTER 7

TESTS TO INVESTIGATE ULTIMATE STRENGTH

7.1 Introduction

Tests have been conducted on three uncased composite plate girders of 'T' cross-section. They represented that length of a continuous beam which is subjected to hogging moment and shear over an intermediate support. The purpose of the tests was to determine whether a slab acting compositely with the steel girder increased its ultimate strength in shear and bending. The behaviour of the shear connectors was of interest, because they would be subjected to a combination of uplift forces and longitudinal shear if tension field action occurred as in steel girders, and might fail as a result. This would probably lead to a loss of composite action.

The three test girders were numbered PG1 to PG3 and the two ends, which were tested separately, were denoted by 'A' and 'B' respectively. Only those parameters related to the concrete slab and its connection to the steel beam were varied.

7.2 Test specimens

7.2.1 Choice of specimens

Specimens PG1 and PG3 represented the main longitudinal girders of a bridge, and the two ends of PG2 simulated, respectively, a transverse diaphragm of a bridge and a main girder in a building.

The depth of the slab in composite bridges varies in practice between 200mm and 230mm, and it was thought that for the slab to have a significant effect on the beam behaviour, its depth should not be less than 10% of the total beam depth. The overall beam depth would therefore be approximately 2.0m, which precluded the possibility of testing a full-size beam in the laboratory. Conversely, a small-scale model was

undesirable because of the difficulty of manufacturing representative micro-concrete and, especially, of welding plate girders from very thin metal.

A scale of approximately 1:2 was therefore chosen for the models of longitudinal bridge beams, but the building girder and the transverse diaphragm were modelled almost full size. The overall dimensions of the specimens are listed in Table 7.1, which also gives the purpose of each test.

The method of conducting two separate tests on each beam is illustrated in Fig.7.1. The first test is conducted on end 'A', which is almost certain to fail before end 'B' because it is subjected to a much greater shear force (see Fig.7.1a). Once failure has occurred in one or more panels of end 'A', they may be stiffened with a diagonal brace before the beam is turned round to test end 'B' (Fig.7.1b). Changes in the dimensions of the slab or size and spacing of the shear connectors between one end of the beam and the other occur over panel 'C'.

7.2.2 Detailing of test specimens

7.2.2.1 Steel girder

The dimensions of all three plate girders for Beams PG1 to PG3 are shown in Fig.7.2. The slenderness ratio of the web is 130, which corresponds to a web thickness of approximately 13mm in a 2m deep composite beam.

The flange dimensions were chosen to avoid any possibility of local flange buckling, and all welds and stiffeners are over-scale to ensure that they do not fail prematurely.

7.2.2.2 Reinforced concrete slab

The dimensions and reinforcement of all the slabs are shown in Fig.7.3. Test PG3A was on a plain steel section, and the slab for PG3B

was cast while the steel beam alone was subjected to about 33% of the predicted ultimate load of the composite beam. The length of the slab was reduced for Specimens PG2 and PG3 to increase the clearance between the end of the slab and parts of the test rig.

7.2.2.3 Longitudinal shear

The magnitude of the longitudinal shear force at the interface of the steel beam and slab determines the design of the shear connection and the transverse slab reinforcement.

The shear connection in Girder PG2A was designed to the recommendations in the draft for public comment of Part 3 of the new BS449[44]. For the other specimens, the recommendations now in BS5400, Part 5[34] were used. Headed studs were used throughout, arranged as shown in Fig.7.4. The full width of the concrete slab was assumed to be effective and no allowance was made for uplift forces on the connectors which might have developed due to tension field action. Specimen PG2B is a model of a transverse beam framing into a main longitudinal beam (represented by the support stiffeners) and the gap of 500mm between adjacent groups of connectors is the one recommended by BS5400 in such circumstances.

The transverse reinforcement in Beam PG2A was designed to the recommendations in Ref.44. The longitudinal force in the slab at the critical section above the support was assumed to be that corresponding to a stress of 480N/mm^2 in the main reinforcement. For the other specimens, the transverse reinforcement was designed to the latest draft of BS5400, Part 5 available at the time[46]. It differs from the published standard in the calculation of shear flow at the interface of the girder and slab for the ultimate limit state. In the draft, the shear was derived from the difference in the longitudinal force in the slab between critical cross sections (as in Ref.44), whereas in BS5400 itself the cross section

is analysed elastically, assuming the slab to be uncracked and the loading appropriate to the ultimate limit state. For Specimens PG1 to PG3, the latter method gives a force in the slab above the support corresponding to four times the yield stress in the main reinforcement, so the draft rules are more appropriate here.

For the purpose of calculating longitudinal shear forces, the loads at serviceability and ultimate limit states were calculated as follows. It was assumed that the yield stress of the structural steel was 280N/mm^2, and its modulus of elasticity 207kN/mm^2.

(a) The load at the serviceability limit state generally was taken as the one that causes buckling in the web of the girder, calculated by the classical theory described in Chapter 6 and ignoring concrete in tension. By the time Specimen 3B was designed, it was clear that yield in the tension flange occurred before web-buckling, so for this test the serviceability load was taken as the one that resulted in a stress of 250N/mm^2 in the tension flange.

(b) The ultimate load was calculated from Rockey's method (Chapter 6). The area of longitudinal reinforcement in the slab was added to the area of the tension flange, but otherwise the effect of the slab was ignored. When designing PG2A, the "flexural strength" of the section was not calculated as recommended in Ref.44, but was taken as the maximum moment in the girder at the calculated ultimate load.

7.2.3 Construction of test specimens

The plate girders were fabricated by Clarke-Chapman Ltd., Horsely Piggot Division, using grade 43A steel throughout. The method and accuracy of fabrication followed as closely as possible the practice adopted for actual bridge girders up to 2.0m deep. Welds were made in

the sequence shown in Fig.7.5.

The concrete for the slabs was mixed in the laboratory using a $0.13m^3$ - capacity pan mixer. Two mixes were designed to give 7-day cube strengths of $25N/mm^2$ and $45N/mm^2$ respectively, using Rapid-hardening Portland cement and crushed aggregate of maximum size 20mm. Table 7.2 lists the mix used in each beam, and the number of batches required. Although only a standard strength concrete was needed in Test PG3B, the strong mix was used to reduce the delay between casting and testing.

The two halves of the slab for PG1 were cast on consecutive days.

Plywood shuttering was used for all tests.

The concrete was compacted with vibrating pokers and a vibrator mounted on a timber baulk which spanned the width of the slab. The slab was cured under damp hessian for seven days after casting.

Specimens were taken from each batch of concrete; the total number for each beam is shown in Table 7.3. They were stored under damp hessian for 24 hours before being demoulded. The shrinkage prisms were then placed alongside the test beam, but all other specimens were stored under water until they were tested.

7.3 The test rig

Two views of the test rig are shown in Figs.7.6 and 7.7. Standard laboratory "meccano" was used for most of the components.

The beam was loaded as a double-cantilever, using a 90-tonne hydraulic jack placed at one end of the beam and operated with a manual pump. The support for the girder was placed on a large concrete plinth to spread the load over a wide area of the strong floor, which was stiffened flexurally by connecting two 12-in channels to it with high-strength friction grip bolts.

Knife-edge bearings were used at all three loading points. They were essentially constructed to the design of May[45] who had developed crossed knife-edge bearings capable of withstanding a load of 2000kN for a column-testing rig[45]. Only one knife-edge is used in each bearing of the plate girder rig, to provide rotational freedom in the plane of bending.

Longitudinal freedom is provided in the two bearings at the ends of the beam by incorporating nineteen silver steel rollers 13mm diameter and 300mm long. Calculations based on the theory of elasticity showed that the measured yield stress of the silver steel rod would be exceeded two-fold at the design load of 1000kN. However, tests on a scale model subjected to an equivalent load revealed no sign of distress in either the rollers or the bearing plates, and the design was therefore thought to be satisfactory.

All the knife-edge bearings were carefully aligned to prevent torsional deformations being imposed on the beam.

Lateral and torsional stability of the beam was ensured by the system of braces shown in Fig.7.7, supplemented by guide plates bolted to the reaction frames at both ends of the beam and bearing against the edges of the tension and compression flanges.

The diagonal bracing to the reaction frames, and the two longitudinal channels which span between them (Fig.7.6) were added during Test PG1A. Previously, two attempts to load the beam to failure had had to be abandoned due to instability of the reaction frames and an unsatisfactory arrangement of the bearings there.

7.4 Instrumentation

A Phillips 100-tonne electrical strain gauge load cell was used to measure the load in the shorter cantilever (the 'test span'). A 50-tonne cell was used in the longer cantilever (the 'reaction span') except in

Test PG2 where an oil pressure gauge was inserted in the hydraulic system to determine the jacking force.

Rotations of the beam were measured at the points shown in Fig.7.8 using an inclinometer of sensitivity 333 x 10^{-6} radians/division. The rotation of the slab was not measured after Test PG1 because it was found to depend on local deformations only, which could be determined more accurately from deflection readings.

Deflections of the beam were measured at the positions shown in Fig.7.8 using dial gauges of sensitivity 0.01mm per divison. All gauges were mounted on the instrumentation rig which is illustrated in Fig.7.9, except as follows:

(a) In PG1A the dial gauges for measuring slab deflections were clamped to magnetic bases which were mounted on the underside of the steel tension flange. Uplift of the slab was therefore measured directly, but due to the limited space the gauges were difficult to read, and in subsequent tests they were mounted on the instrumentation rig.

(b) During the pre-loading and casting phases only of PG3B, measurements of deflection were limited to the vertical displacement of the extreme tips of the plate girder. The dial gauges were located underneath the compression flange and were mounted on a frame of 'Dexion' which was clamped rigidly to the supporting concrete plinth.

Strains on the surface of the steel girder and the reinforcing bars were measured with 10-mm temperature-compensated electrical resistance strain gauges. The output from them was recorded on the Solartron data-logger described in Chapter 2. The location of the gauges is shown in Fig.7.10. A diagonal grid of gauges was mounted on the web of PG1A to detect the effects of tension field action, but was replaced by a column

of strain-gauge rosettes in subsequent tests because buckling of the web did not occur until immediately before the beam collapsed.

At some cross-sections of PG1, strain gauges were placed on both sides of the longitudinal centre-line of the girder to check that deformations were symmetrical in the transverse direction.

A ripple scanner was used to measure the out-of-plane deformations of the web panel nearest the support in the test span. It is illustrated in Fig.7.11 and consisted of six transducers mounted on an aluminium channel which the operator could slide manually along two guide rails. The rails consisted of 20mm diameter steel rods and were mounted in self-aligning bearings clamped to the stiffeners of the girder. They were therefore located in the transverse direction, while avoiding distortion due to in-plane and out-of-plane deflections of the girder. Sensitivity of the transducers was either 50mm/volt or 25mm/volt, and the output was recorded by the Solartron data-logger.

Initial out-of-plane imperfections of the web were determined with a straight edge and feeler gauges.

The extension of the top surface of the concrete slab was measured along the grid lines shown in Fig.7.12 with a 200-mm demec gauge. Measurements were taken on consecutive gauge lengths. Crack widths were measured where they crossed the grid lines, using a microscope with 0.05mm graduations.

7.5 Test procedure

7.5.1 General

The procedure adopted for individual tests in the PG series is described in Sections 7.5.2 to 7.5.6, but some features are common to all tests and these are listed here. Where loads are given, they refer to the vertical shear force in the test span, and not the force in the jack.

In each test, the load was increased to 200kN and then dropped to zero three times to check the instrumentation. The load was applied in four equal increments and a complete set of readings was taken at each, apart from concrete surface strains and crack widths which were read during the first cycle only.

Once the instrumentation was checked, the load was increased in increments of 50kN until approximately 80% of the expected failure load was reached. Out-of-plane deflections of the web were measured at alternate load stages, but otherwise a complete set of readings was taken at each increment. In some tests, and for a variety of reasons as detailed below, the load was released before the beam failed. On continuing the test it was increased in increments of 100kN until the previous maximum load was attained.

As a beam approached the expected failure load, increments were decreased to a nominal 30kN. Only a few selected crack widths and concrete surface strains were measured, but otherwise a full set of readings was taken at each increment. When increasing the load, it was monitored very carefully and as soon as it showed any signs of falling off, a set of readings was taken as quickly as possible. Thereafter the test was deflection-controlled, applying a jack movement of approximately 5mm in each of six or seven load stages.

None of the tests were concluded in a single day, and the beams were left loaded overnight. The following morning the load had usually dropped off a little, but never by more than 5% of the overnight value.

7.5.2 PG1A

As noted, this test was abandoned twice due to instability in the rig; once at 600kN and again at 800kN. In each case, the load was released while modifications were made to the rig. Once the stiff

longitudinal bracing shown in Figs.7.6 and 7.7 had been added, the load was increased until the beam failed.

7.5.3 PG1B

The instrumentation was checked as usual, but in the third cycle the load was increased to 400kN before being released, in order to study the elastic behaviour of the beam. Thereafter, the load was increased steadily until the beam failed.

7.5.4 PG2A and PG3A

Once the instrumentation had been tested, the load was increased steadily until failure occurred in the test span. In each test the panel that buckled was the end panel, so the load was released while diagonal stiffeners of rectangular hollow section were welded in (Fig.7.13a). A further test was then conducted by reloading the beam in 100-kN increments until 80% of the expected failure load was applied, and thereafter in 30-kN increments until the panel adjacent to the support collapsed.

7.5.5 PG2B

In this test the concrete slab extended only half-way along the end panel, which would therefore represent neither a plain steel girder nor a composite one. It was therefore stiffened as shown in Fig.7.13b before the test, to prevent it buckling. Once the instrumentation had been checked, the load was increased steadily until the panel adjacent to the support failed.

7.5.6 PG3B

The end panel of this test was also stiffened as shown in Fig.7.13b. The test followed the normal procedure until the required prestress in the steel beam was reached. The corresponding load was 300kN, but 350kN was briefly applied to the beam to remove any slack from the rig. The shuttering was then constructed and the slab cast. The steel strains and

the vertical deflection at the tips of the beam were measured at regular intervals while the concrete was curing, and once it had reached the required strength, the test continued as usual.

7.6 Auxiliary tests

All transducers were calibrated immediately before each test using a micrometer of sensitivity 10^{-4}in per division. The calibration of the load cells was checked with a 3-MN Denison compression-tester when the PG tests were complete.

Tension tests were performed on three coupons cut from Girder PG3, using a 10-tonne Monsanto Extensometer machine and a Baty dial gauge of length 2in and sensitivity 1/20000 in per division. The dimensions and location of each coupon are shown in Fig.7.14.

Tests on the concrete specimens were carried out in accordance with BS1881[37] where appropriate, using a 3-MN Denison compression-tester. The shrinkage of the concrete prisms was determined as described in Section 2.6.1, except that 150-mm demec gauges were used.

Beam No.	End	Approx. scale	Total beam depth (mm)	Slab cross section (mm)	Concrete strength	Purpose
PG1	A	1 : 2	915	1000 x 90	Standard	General investigation and control
PG1	B	1 : 2	915	1000 x 90	Strong	To determine the effects of concrete strength
PG2	A	1 : 1	915	1000 x 90	Standard	Shear connection is approximately one-third as strong as that in PG1A: simulates a main girder in a building
PG2	B	1 : 1.2	1005	1000 x 180	Standard	Simulates a continuous transverse diaphragm
PG3	A	1 : 2	825	None		Test on plain steel girder for comparison
PG3	B	1 : 2	915	1000 x 90	Standard	Steel beam prestressed to approx. 33% collapse load before casting slab. Simulates unpropped construction

TABLE 7.1 LIST OF TESTS IN PG SERIES

Beam	Design strength of mix N/mm^2	Number batches
PG1A	25	3
PG1B	45	2
PG2	25	6
PG3B	45	4

TABLE 7.2 CONCRETE MIXES FOR BEAMS PG1 - PG3

Beam	No. of specimens		
	150mm cube	Cylinders 200mm x 100mm diam.	Shrinkage prisms 200 x 50 x 50mm
PG1A	6	3	2
PG1B	6	3	3
PG2	6	3	5
PG3B	2	3	5

TABLE 7.3 CONCRETE TEST SPECIMENS FOR BEAMS PG1 - PG3

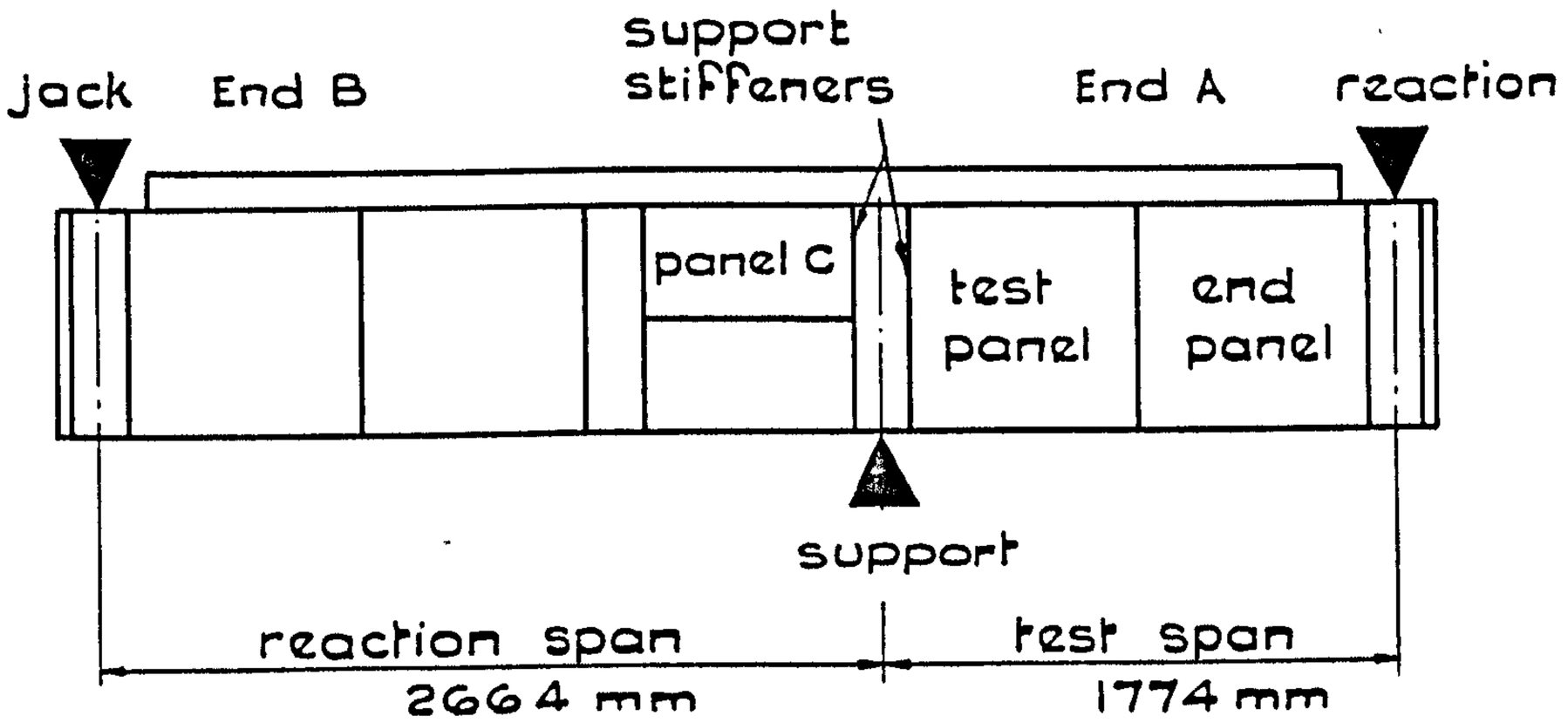

a) Test on end 'A' of beam

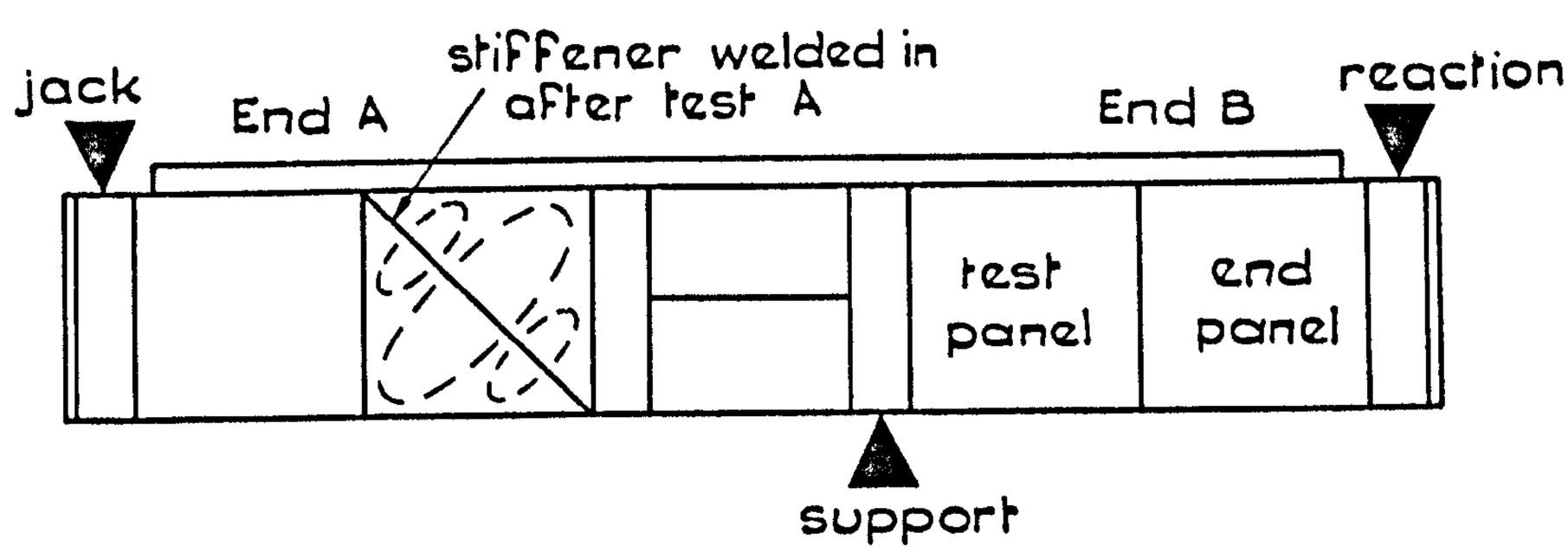

b) Test on end 'B' of beam

FIG. 7.1 METHOD OF CONDUCTING TWO TESTS ON ONE BEAM

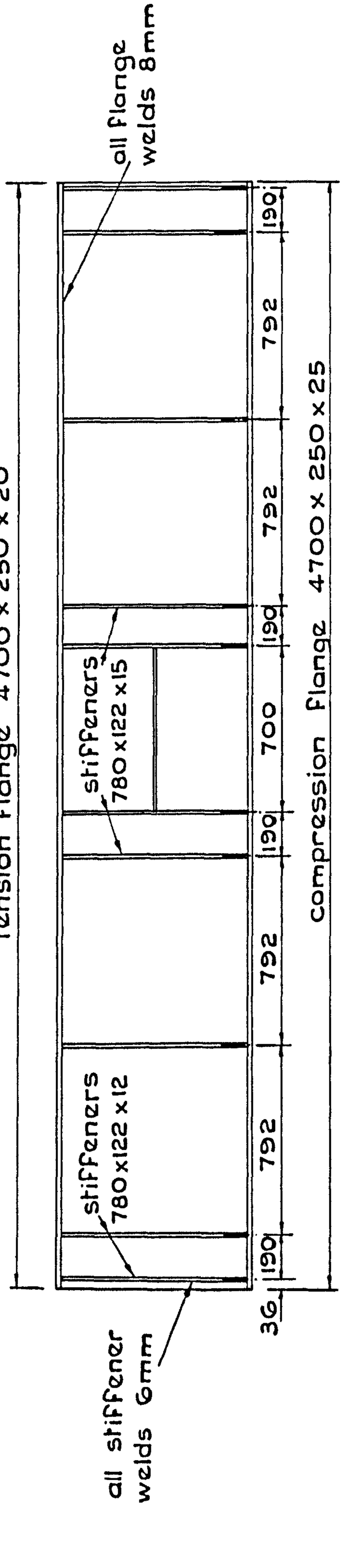

Notes
1) All steel to BS 4360 grade 43A
2) Dimensions in mm

FIG. 7.2 STEEL GIRDERS FOR BEAMS PG1-PG3

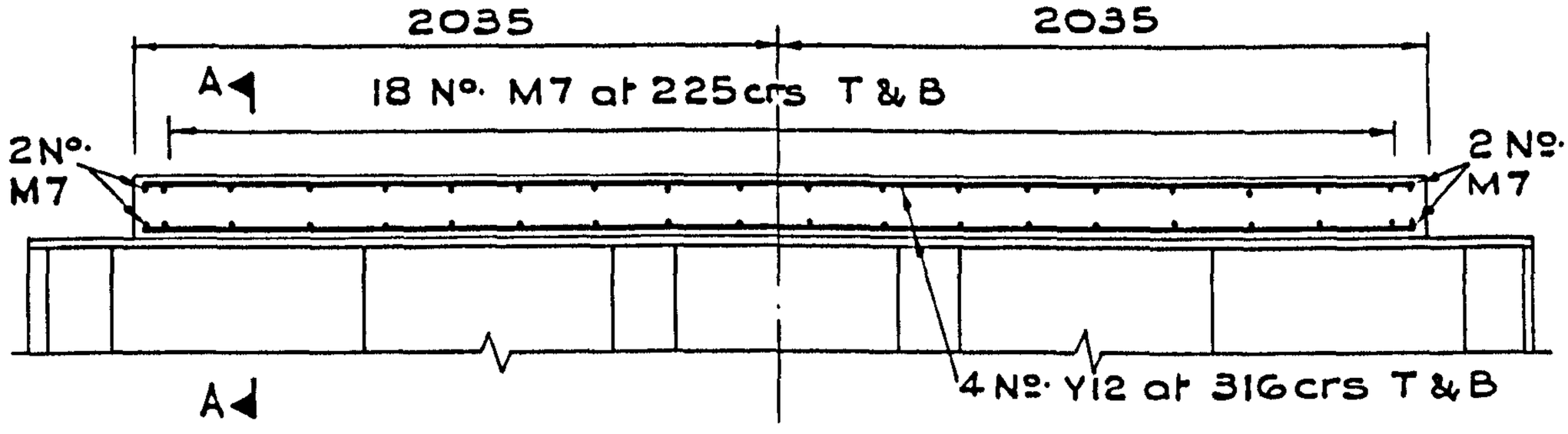

End A Beam PG1 End B

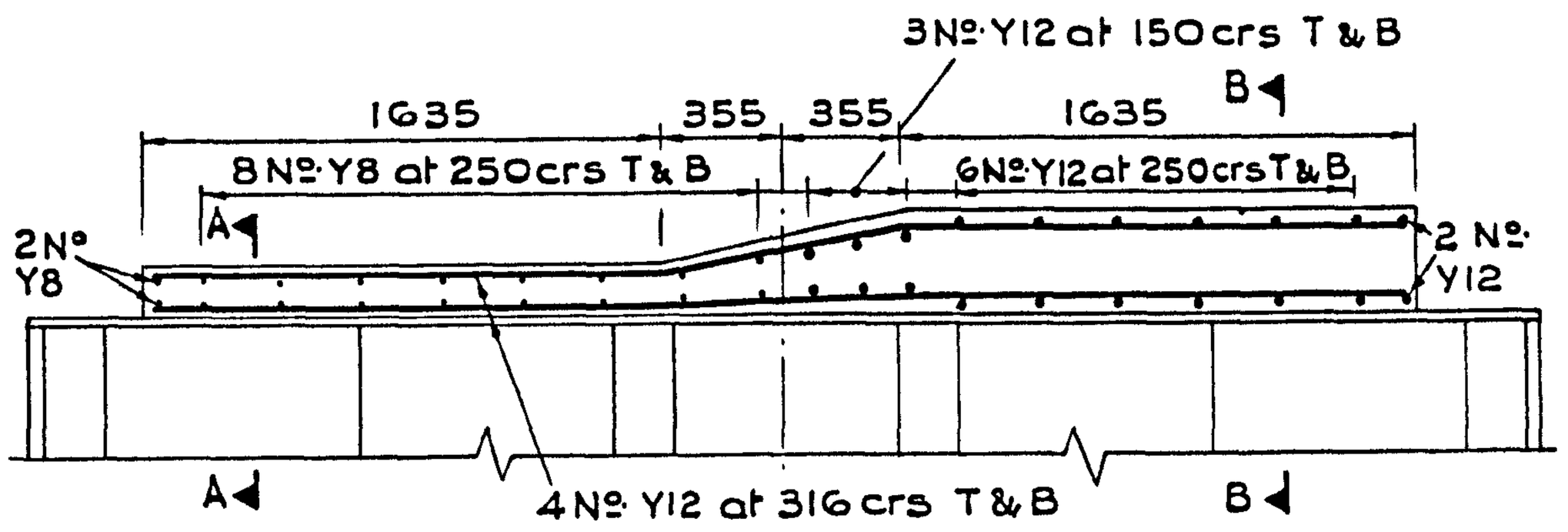

End A Beam PG2 End B

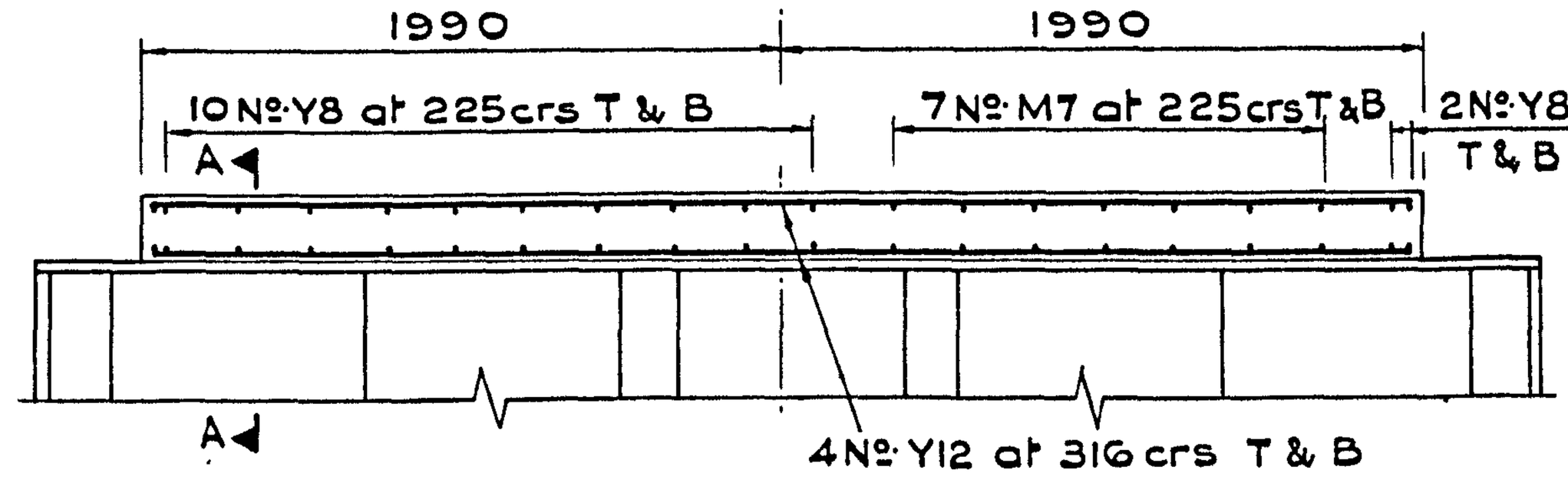

End A Beam PG3 End B

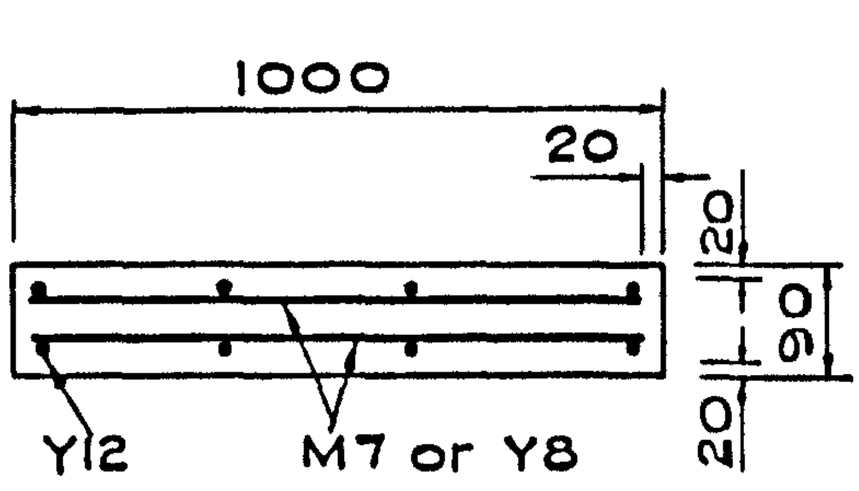

Section AA

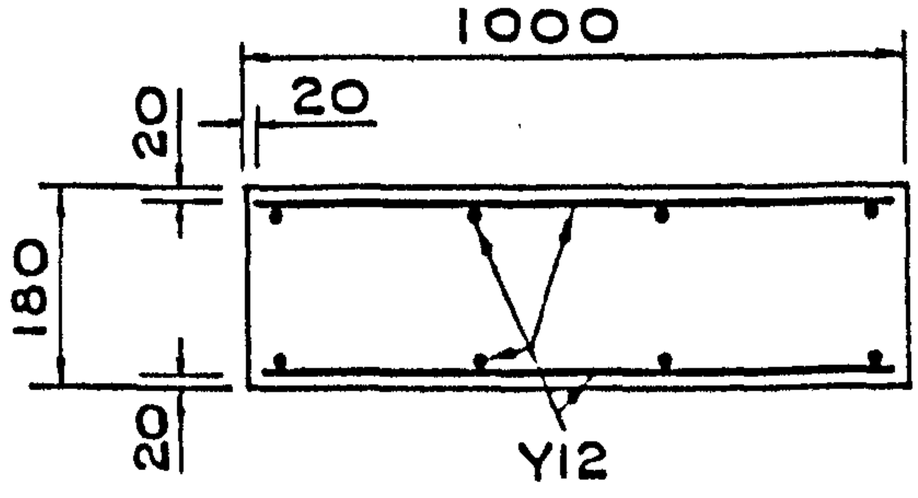

Section BB

FIG. 7.3 REINFORCED CONCRETE SLABS FOR BEAMS PG1-PG3

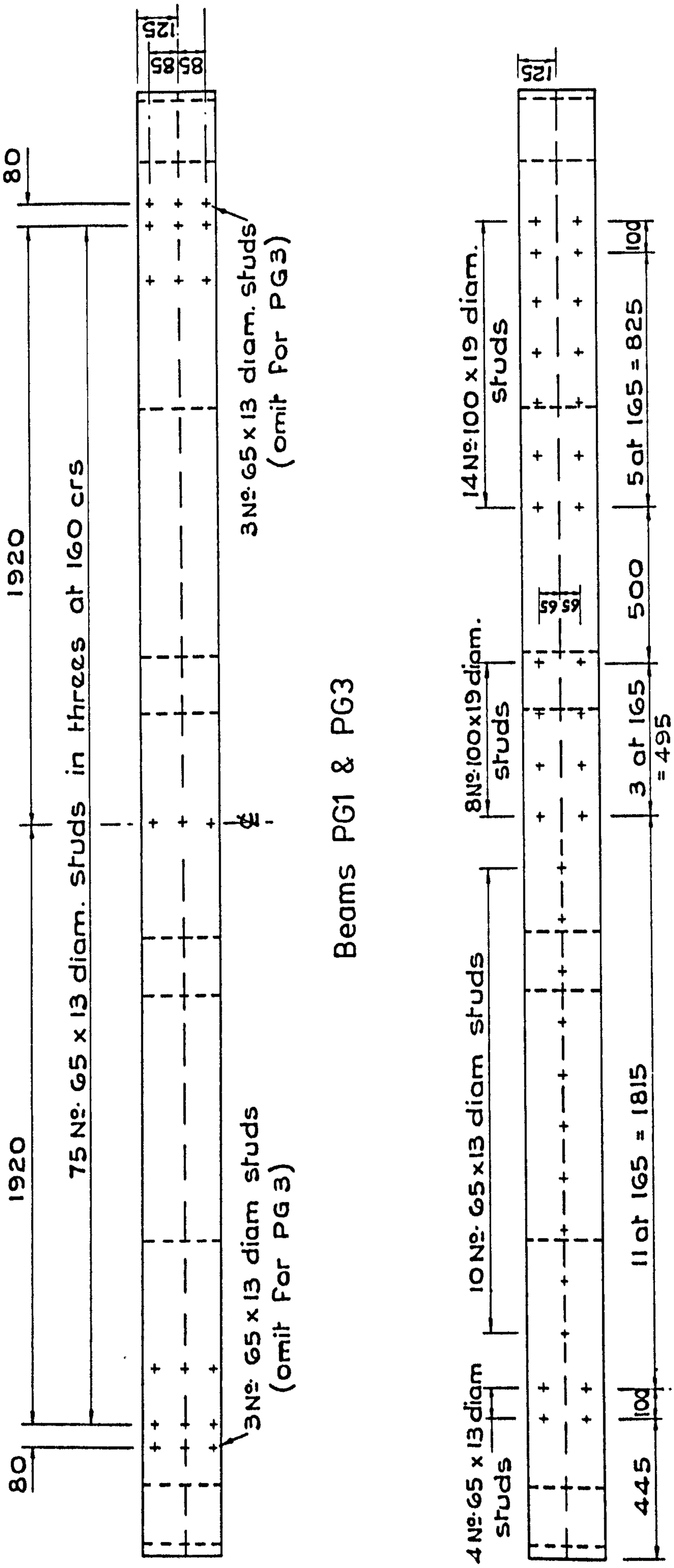

FIG. 7.4 LAYOUT OF SHEAR CONNECTORS FOR BEAMS PG1-PG3

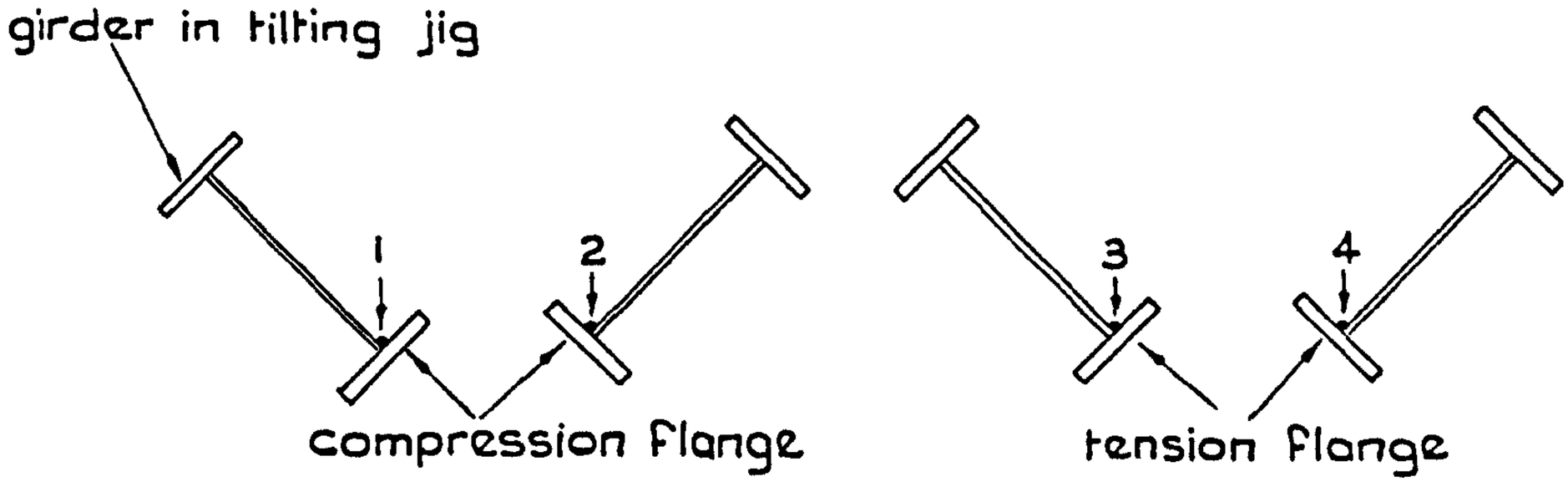

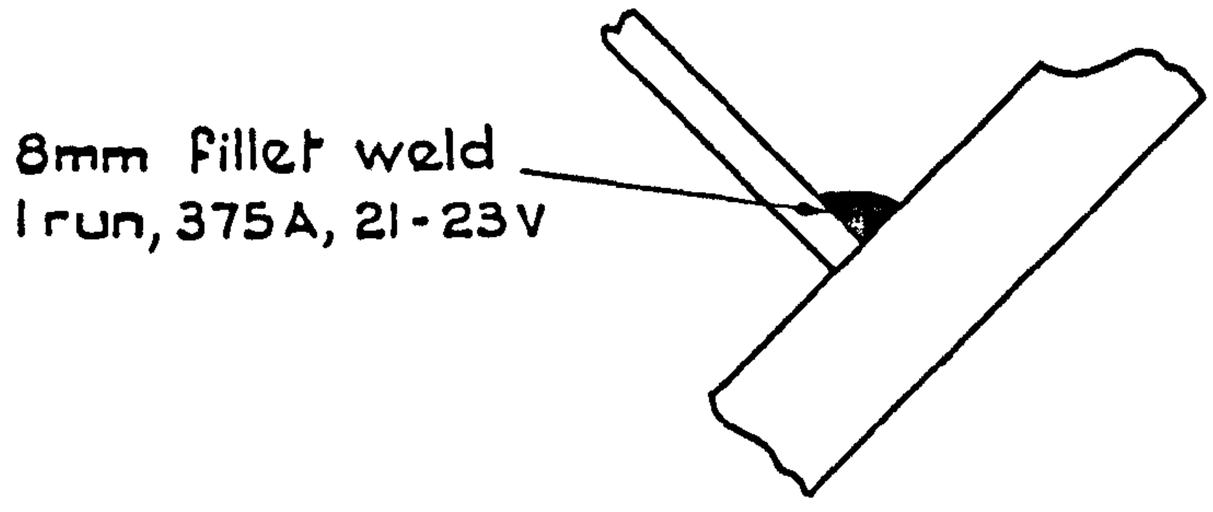

a) Flange-web welds

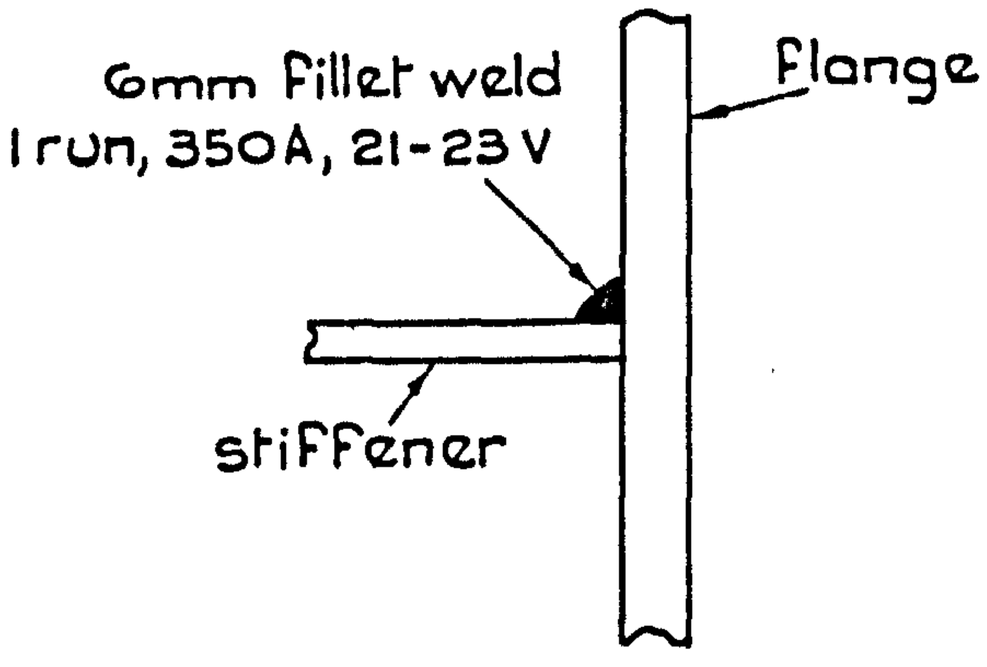

Sequence:
weld stiffener to
1) compression flange
2) tension flange
3) web

b) Stiffener welds

FIG. 7.5 WELDING OF STEEL PLATE GIRDERS

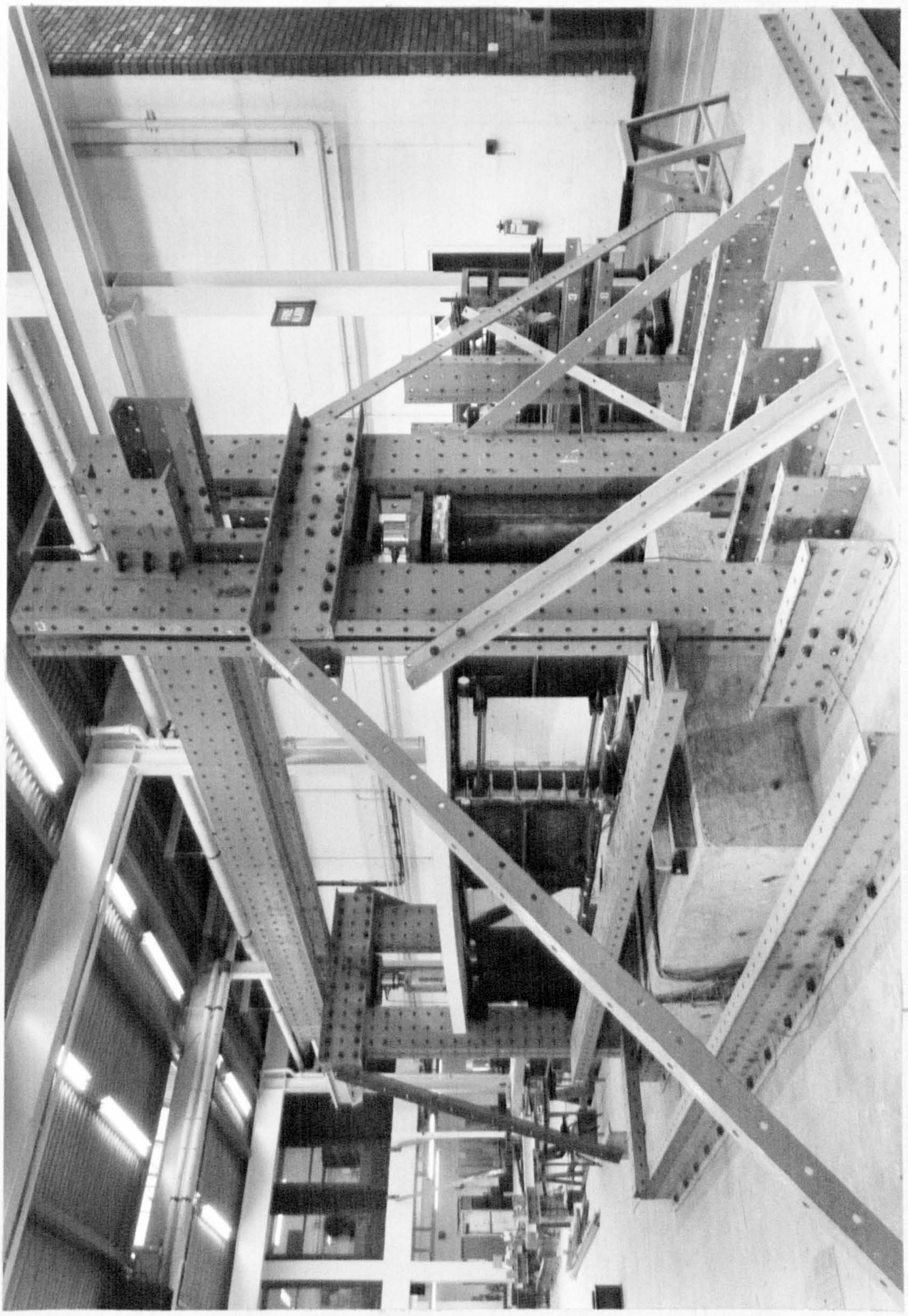

FIG. 7.6 VIEW OF TEST RIG FROM SOUTH WEST

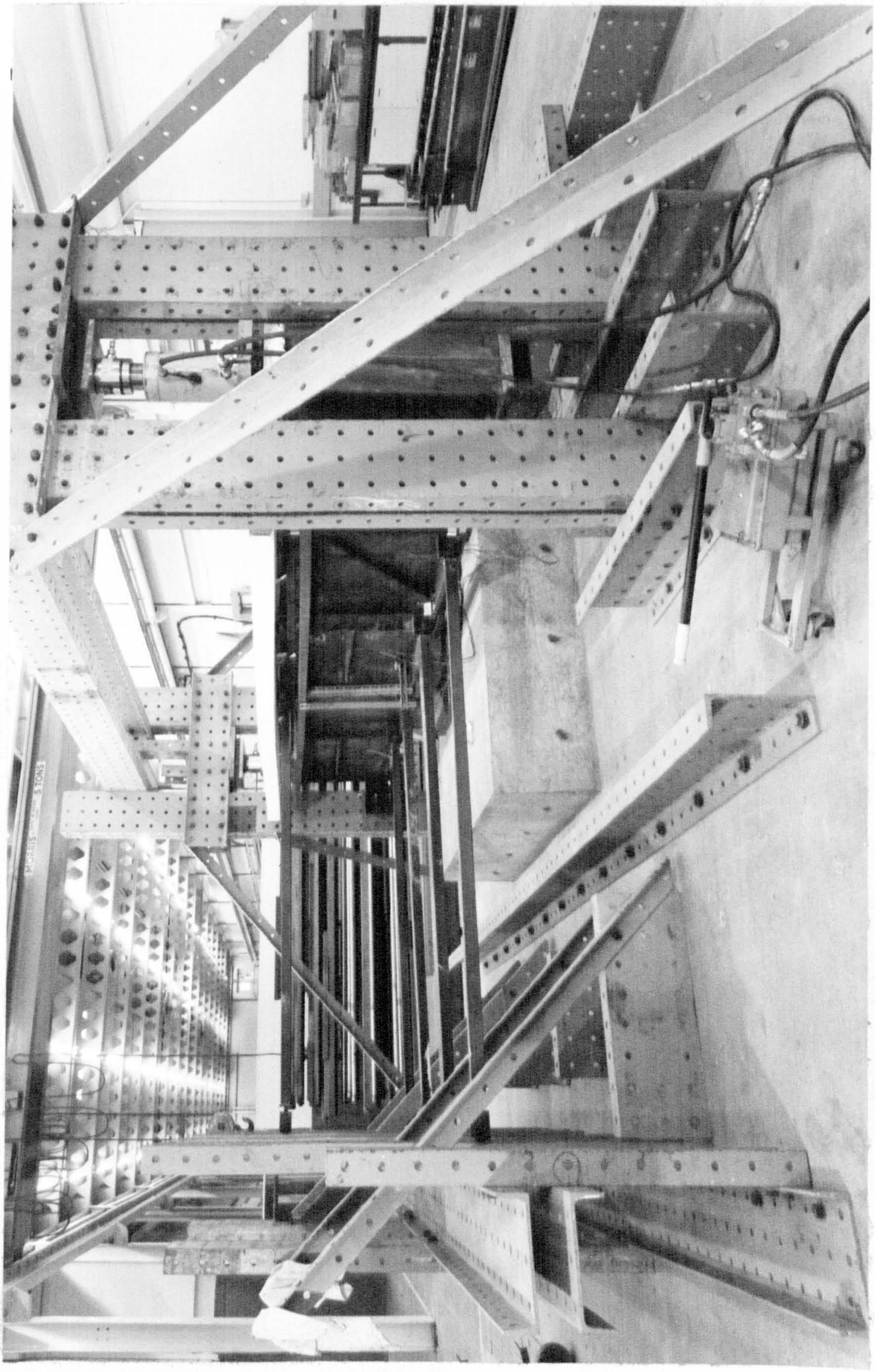

FIG. 7.7 VIEW OF TEST RIG FROM NORTH EAST

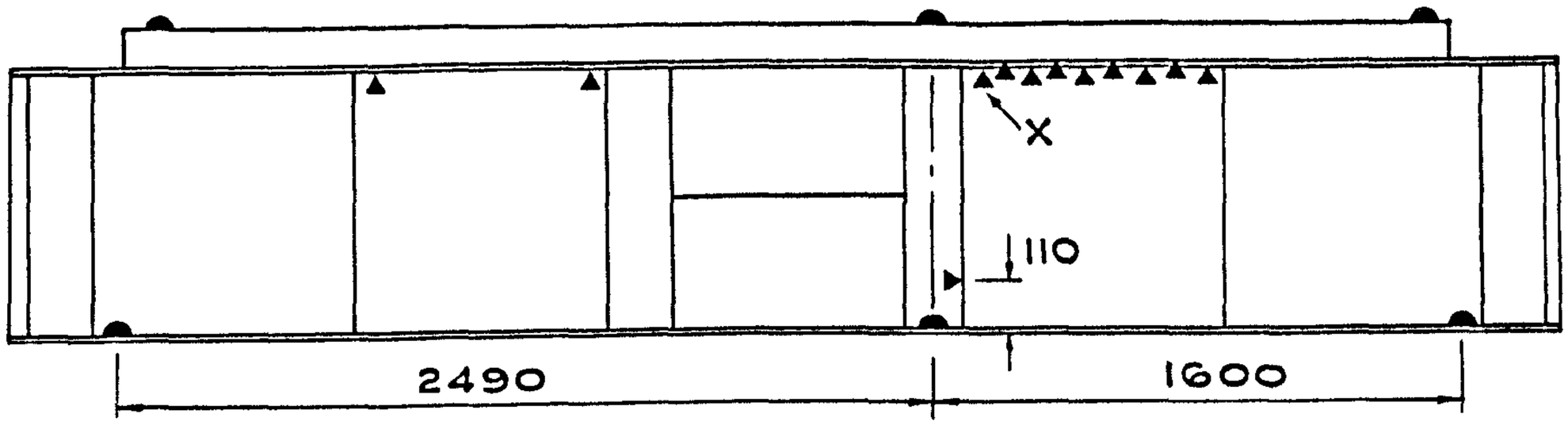

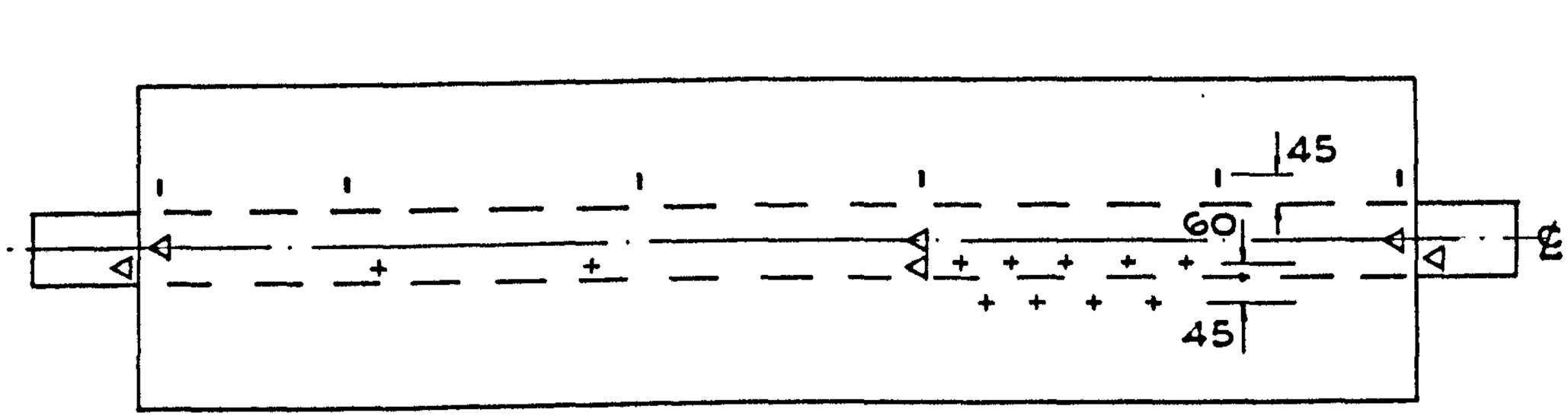

Elevation and plan: PG1

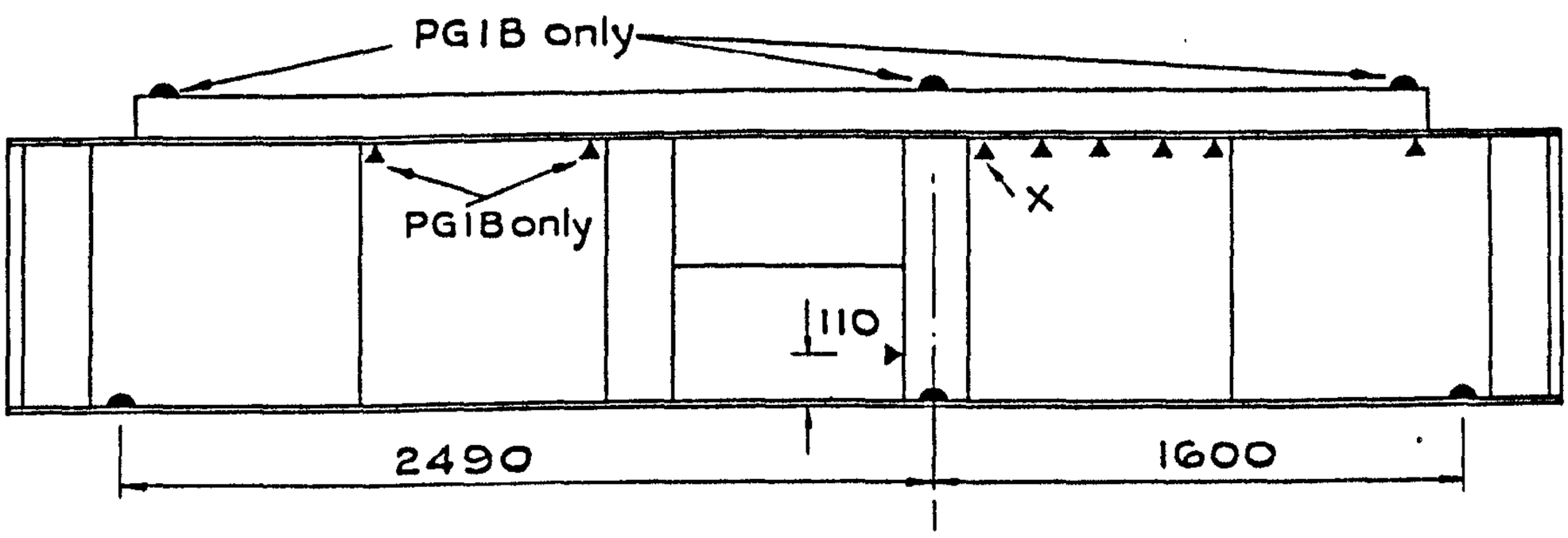

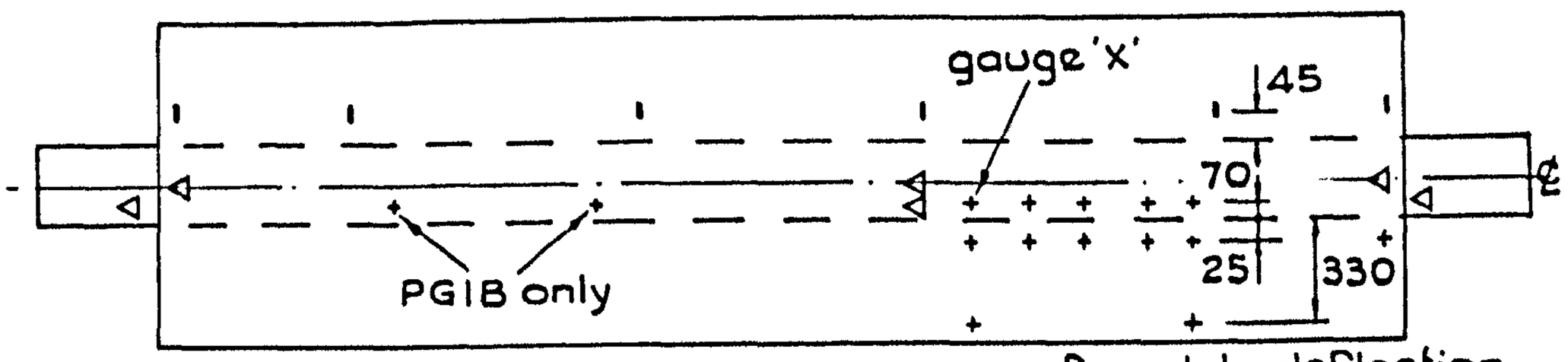

gauges for slab deflection not needed in PG3A

Elevation and plan: all other tests

Key

rotation gauge

deflection gauge

slip gauge

FIG. 7.8 DEFLECTION AND ROTATION READINGS: TESTS PG1-PG3

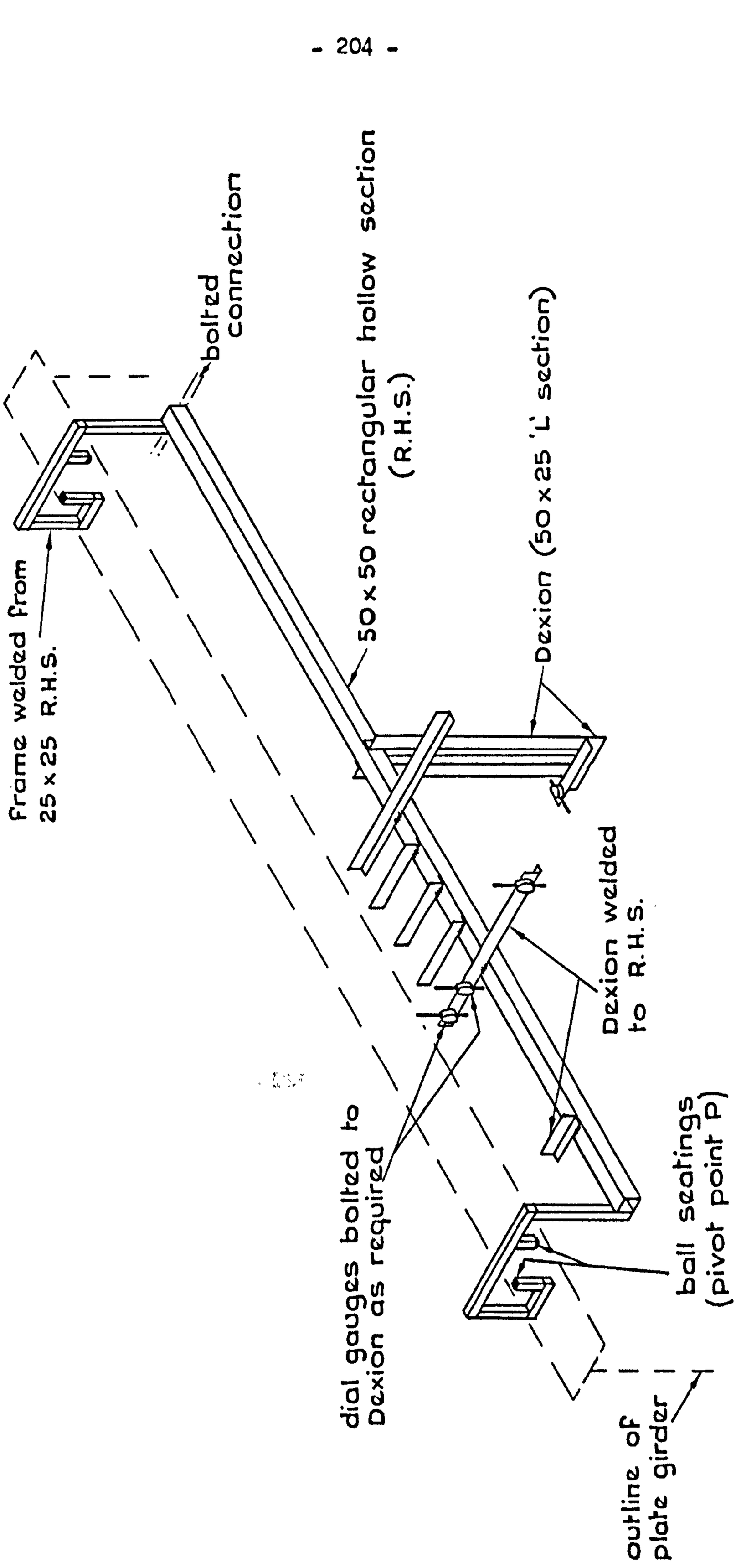

FIG. 7.9 INSTRUMENTATION RIG FOR TESTS PG1-PG3

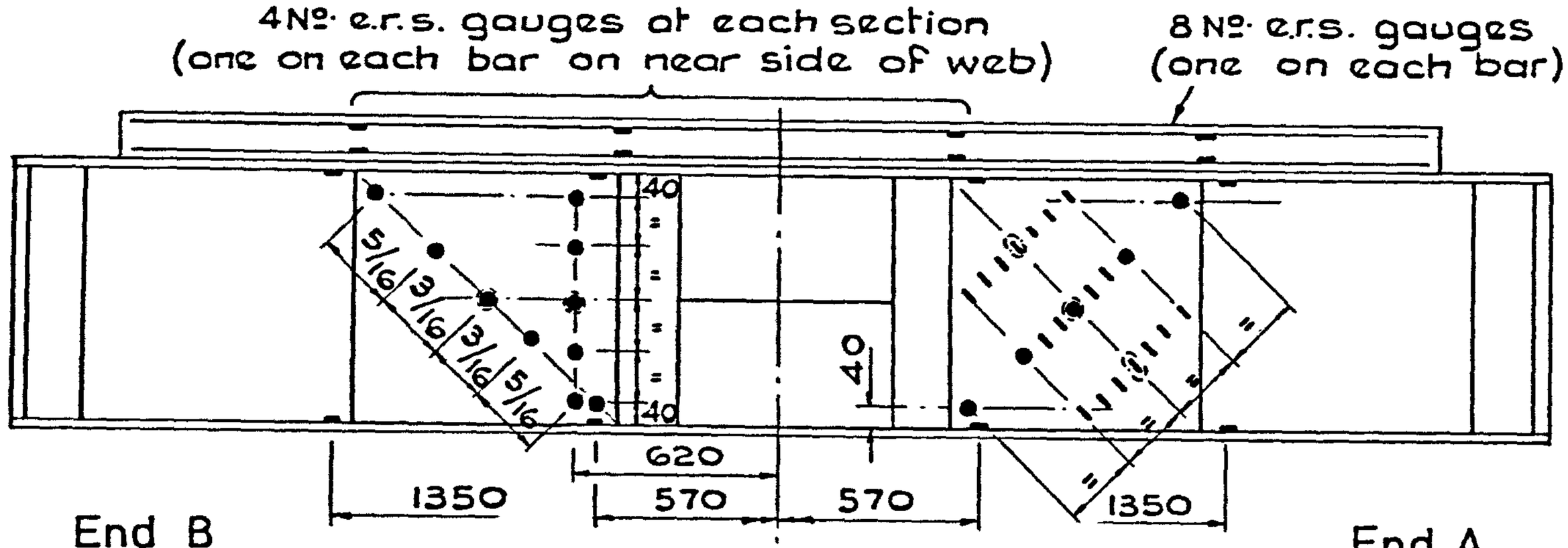

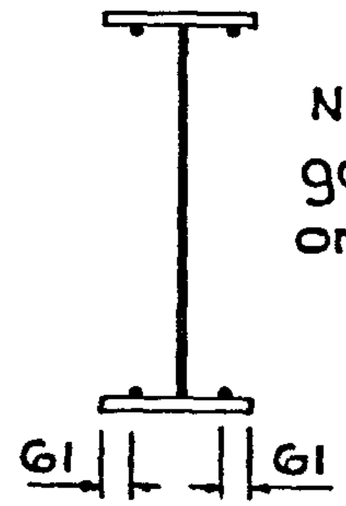

Note:- all flange gauges duplicated on far side of web

Section

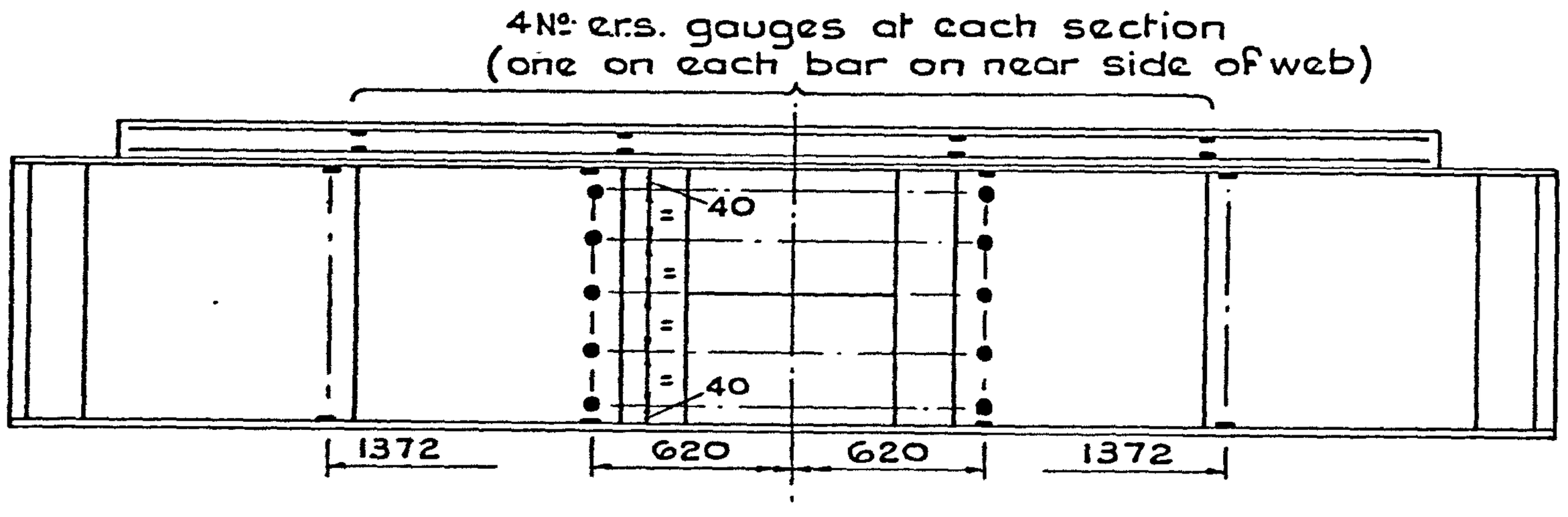

key

- single e.r.s. gauge
- e.r.s. gauge rosette (0 - 45° - 90°)
- web gauge duplicated on far side of web

FIG. 7.10 LOCATION OF ELECTRICAL RESISTANCE STRAIN GAUGES

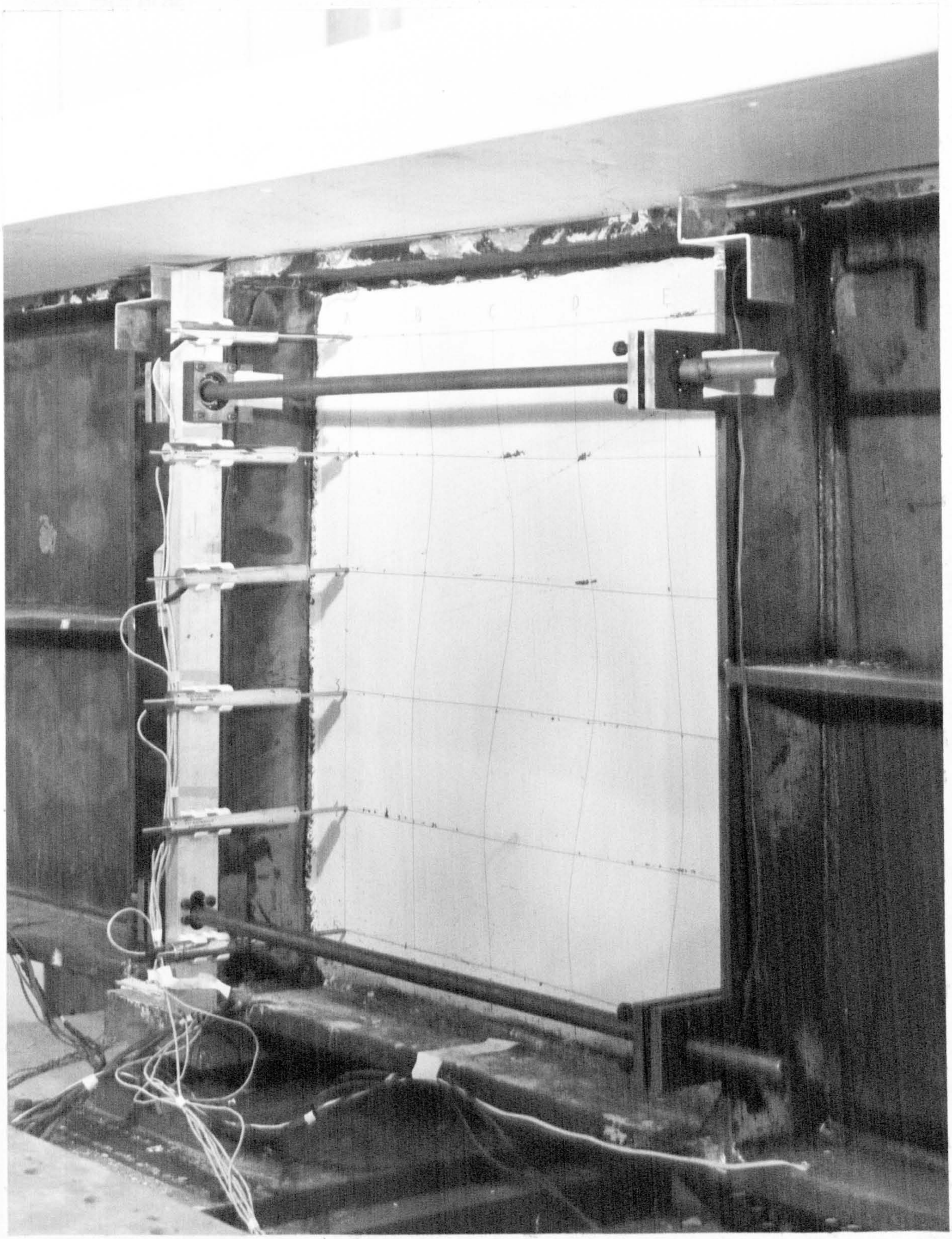

FIG. 7.11 RIG FOR MEASURING OUT-OF-PLANE WEB DEFORMATIONS

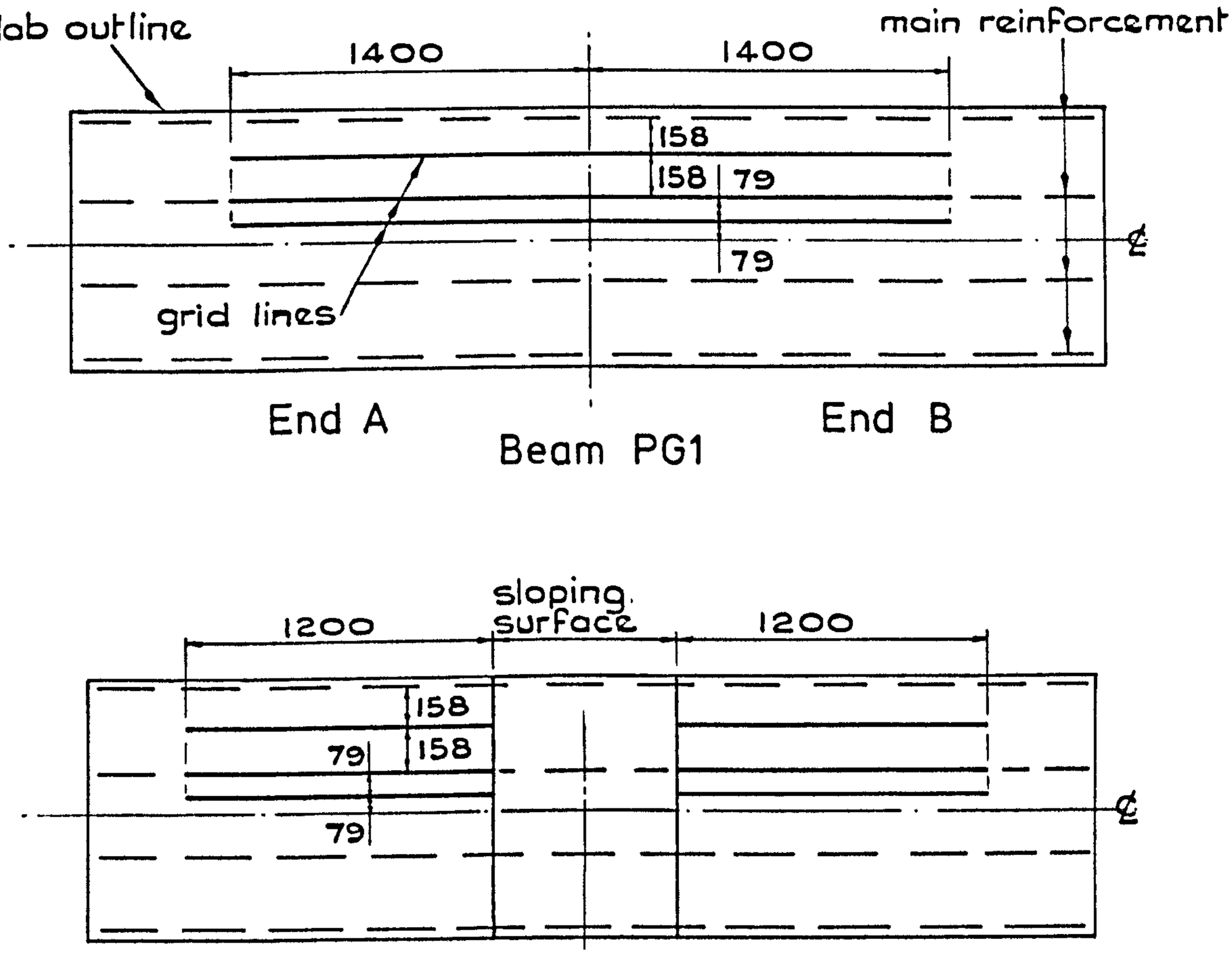

FIG. 7.12 GRID LINES ON TOP SURFACE OF SLAB

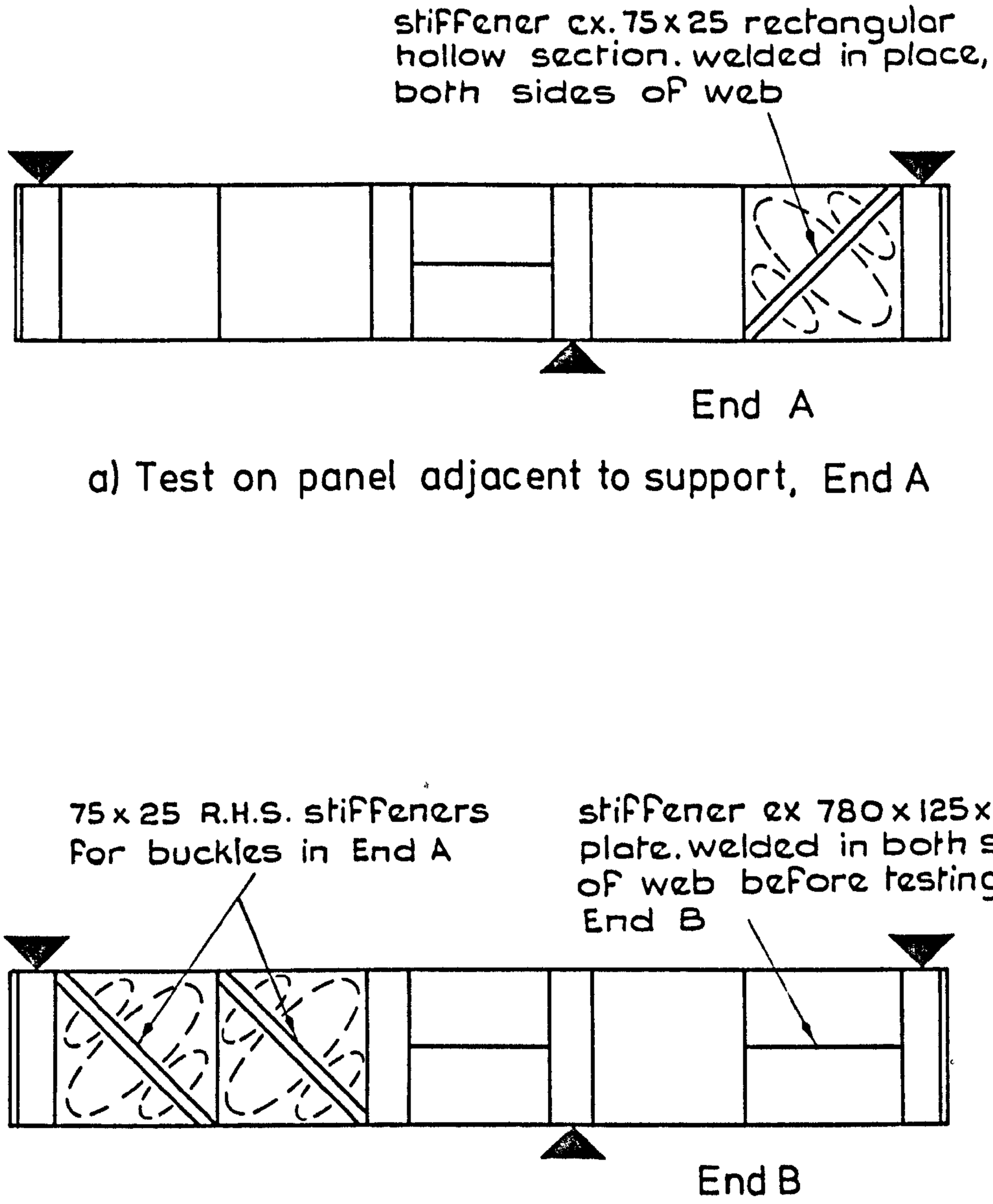

FIG. 7.13 EXTRA STIFFENING FOR BEAMS PG2 & PG3

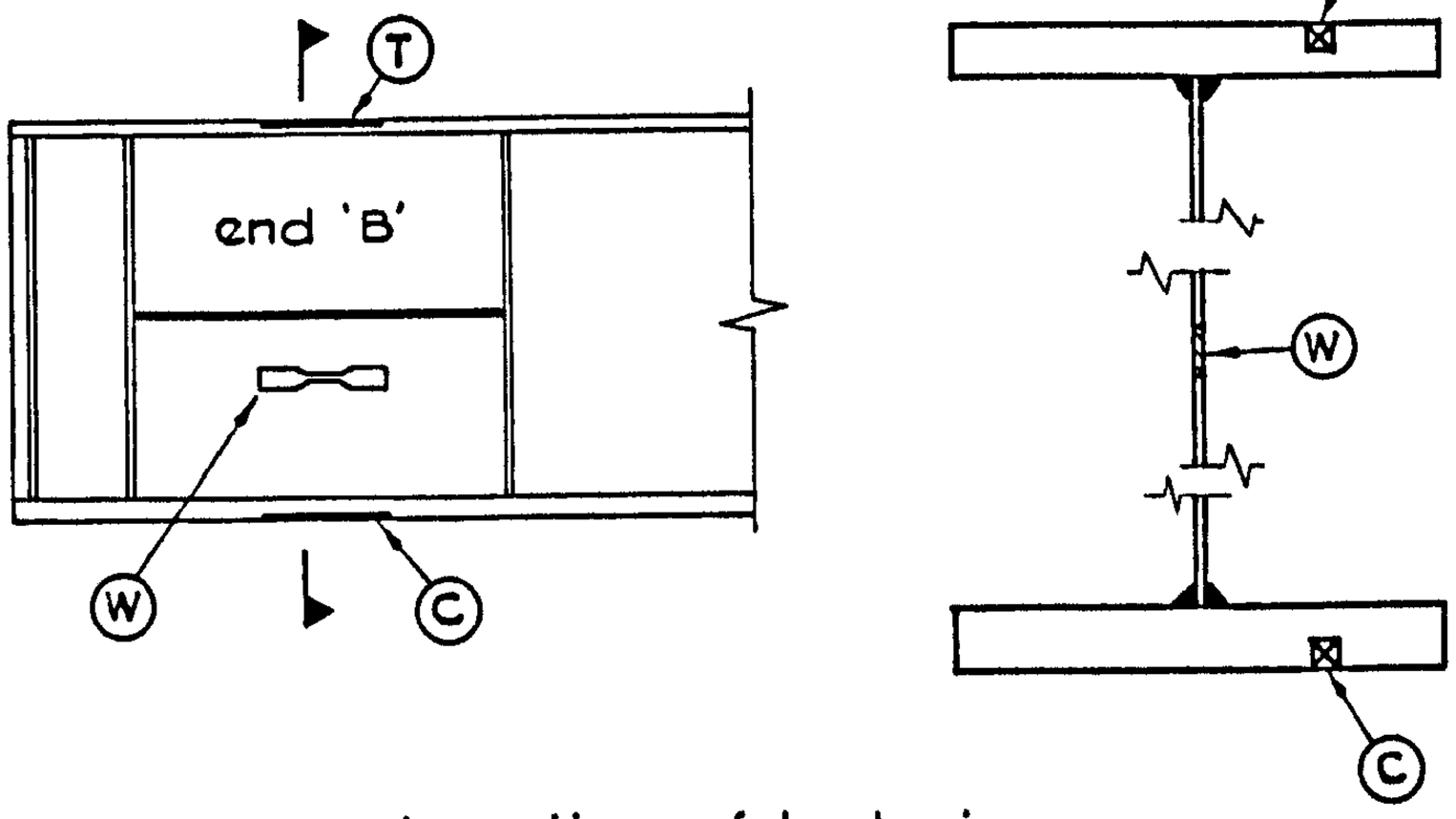

Location of test pieces

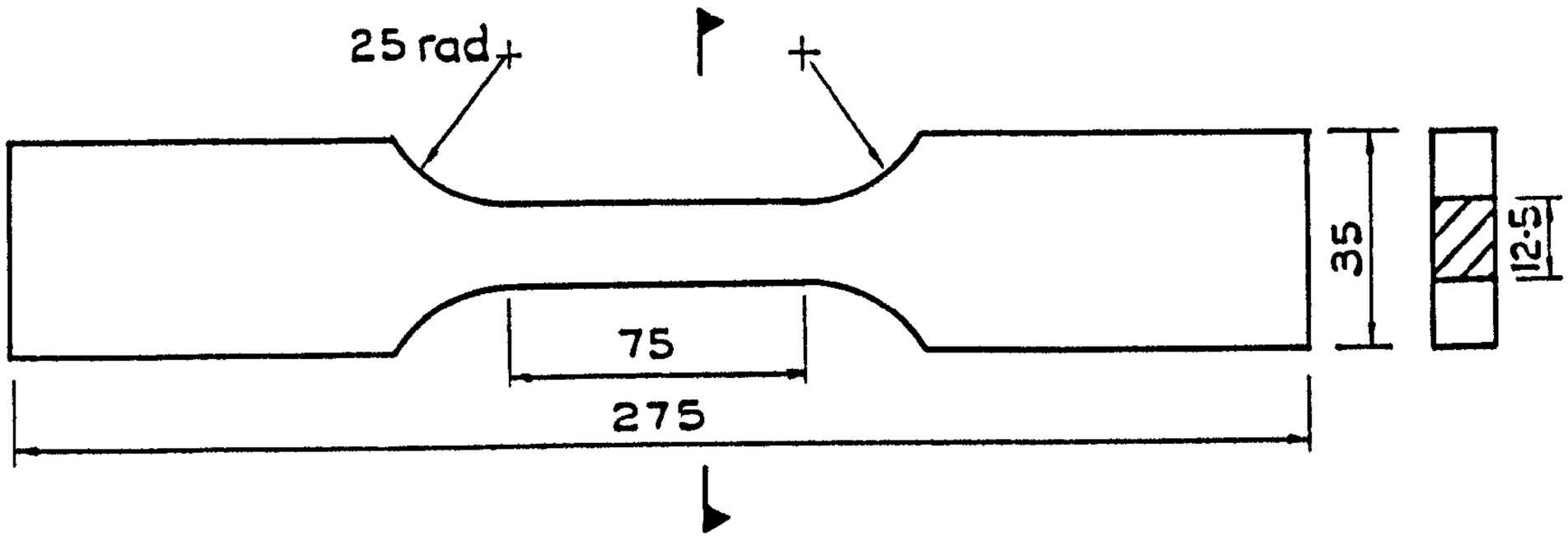

Coupon W

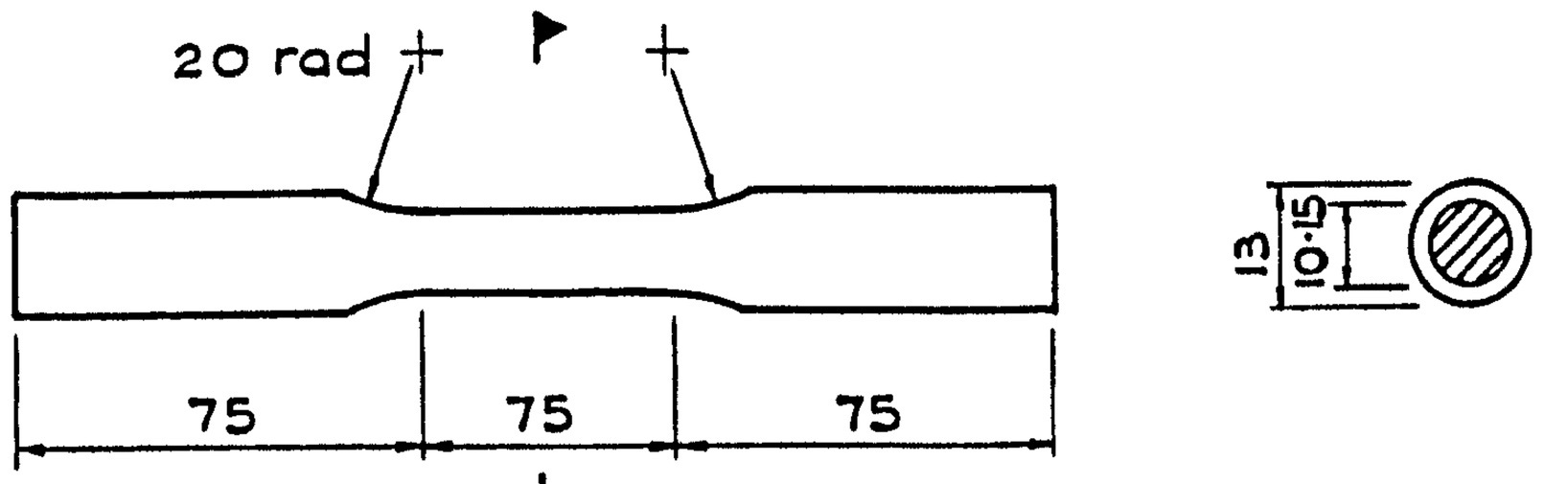

Coupons C & T

FIG. 7.14 COUPONS FOR PG1-PG3

CHAPTER 8

RESULTS OF TESTS ON PLATE GIRDERS

8.1 Introduction

The general behaviour of Beams PG1 to PG3 is described first in terms of their load-deflection (V-δ) curves, which are plotted in Figs.8.1 to 8.3. δ is the movement measured by the dial gauge marked 'X' in Fig.7.8, which was mounted on the instrumentation rig and therefore recorded the relative deflection of the support stiffeners and the tips of the beam. The load is the vertical shear force in the test span (V) and is expressed as a proportion of V_y.

The deformations in each beam after collapse are summarised in Fig. 8.4, and the final crack patterns are shown in Fig.8.5.

The detailed results from Tests PG1 to PG3 which are relevant to the discussion in Chapter 9 are given later in this chapter, as are the results of the auxiliary tests.

8.2 PG1A

The test on this beam was abandoned twice before the beam was loaded to failure, and the V-δ curve for all three phases is shown in Fig.8.1. The beam's response is non-linear, except when it is being reloaded to a previously applied maximum force.

At a load of $0.06V_y$ the first crack formed in the slab, at the boundary of the two concrete pours. At $0.11V_y$ a further crack spanning the full width of the slab formed adjacent to the support stiffeners and thereafter increasing the load caused cracks to develop over a greater length of the slab.

There were no signs of imminent collapse of the beam at a load of $0.9V_y$, which was then increased to $0.96V_y$. This caused the maximum

out-of-plane deflection in the test panel (δ_o) to increase suddenly from 1.7mm to 2.4mm. While applying the next load increment thin bands of whitewash and scale on the faces of the web were seen to flake off in a pattern resembling Lueders lines. A load of $1.02V_y$ was briefly sustained by the beam, but buckles formed in the test panel and δ_o increased to 13mm, which caused the load to fall off considerably. Simultaneously, a vertical shear deflection of 0.5mm developed across the flexural crack in the slab adjacent to the support stiffeners.

Imposing further deflection on the beam caused the load to decrease, and led to large rotations in the plastic hinges in the steel flanges. The concrete slab developed a sagging curvature over about one-third the length of the test panel (Fig.8.4). In the slab of PG1A, and in all other slabs where a region of local sagging curvature developed, additional cracks in this region formed first at the soffit of the slab, and did not penetrate its full depth. On the top surface of the slab, the width of existing cracks near to the sagging hinge decreased, and compressive strains were measured here when the hinge rotation was large.

When δ was increased to 23mm, serious local failure occurred in the soffit of the slab at the position marked 'L' in Fig.8.5. Failure was of the type shown in Fig.8.9, wherein the supporting knife edge is to the left of the picture, and the reaction frame to the right.

Fig.8.6 illustrates the permanent deformations in the slab of PG1 after both ends of the beam had been loaded to failure.

8.3 PG1B

The V-δ curve for this beam was approximately linear up to $0.69V_y$, which was the force applied to this end of the beam during the test on PG1A. Very few flexural cracks formed during this test (Fig.8.5). Lueders lines were visible on the web panel at $0.96V_y$, and between this

load and $0.99V_y$, δ_o increased from 0.25mm to 0.9mm. While applying the next increment of load, the shear force in the panel rose to $1.03V_y$, but this caused large buckles to form in the web (δ_o = 4.8mm) and the load then dropped off.

Imposing further deflection on the beam resulted in the load dropping off further, and in large rotations developing in the plastic hinges in the steel flanges. Sagging curvature developed in the concrete flange (Figs.8.4 and 8.6). When δ was increased to 26mm, local shear failure in the slab caused a horseshoe-shaped crack to develop on the top surface: this is illustrated in Fig.8.7, and marked 'H' in Fig.8.5.

8.4 PG2A

The first time this specimen was tested, the V-δ curve followed the plot labelled "end panel failing" in Fig.8.2. The first crack in the slab formed at a load of $0.06V_y$, across the full width of the slab at the root of the tapering section. Increasing the load caused the region of flexural cracking to spread out from this point.

A maximum load of $0.96V_y$ was applied to this specimen before gross out-of-plane deflections occurred in the end panel of the test span. At this stage δ_o for the test span was 1.3mm. When the beam deflection (δ) was increased to 13mm, δ_o in the test panel decreased to 0.7mm while that in the end panel increased to 22mm. Further deflection of the beam resulted in increased amplitude of the buckles in the end panel, and a small increase in those of the test panel. This test was terminated before local failure occurred in the slab.

After welding a stiffener into the end panel, Specimen PG2A was tested again and the V-δ curve is the one labelled "test panel failing" in Fig.8.2. At a load of $0.90V_y$, δ_o was approximately 1.33mm, but this increased suddenly to 5.9mm when a load of $0.97V_y$ was applied. The load

then dropped immediately, and further pumping of the jack caused it to drop further.

Plastic hinges in the steel flanges were first apparent when δ was 10.3mm, but the concrete slab remained in hogging curvature throughout the test, which resulted in larger separation between it and the girder than usual (Fig.8.8). Fig.8.9 illustrates the extent of the shear crack in the soffit of the slab at δ = 17.5mm.

8.5 PG2B

The load-deflection plot for this specimen (Fig.8.2) was linear up to a load of $0.68V_y$. The test was unusual in that very few cracks formed on the top surface of the slab.

Between $0.90V_y$ and $0.97V_y$, δ_o increased from 1.0 to 2.7mm. When a load of $0.99V_y$ was applied to the beam, severe buckling occurred in the web and the load dropped off rapidly. Imposing further deflections on the beam resulted in large rotations in the plastic hinges of the steel girder and sagging curvature in the slab over part of the test panel. When δ was equal to 24mm local failure had occurred at the soffit of the slab as shown in Fig.8.10. The crack is labelled 'L' in Fig.8.5.

8.6 PG3A

Failure of this specimen first occurred due to web buckling in the end panel. The V-δ plot is labelled "end panel failing" in Fig.8.3. Large values of δ_o were noted in the end panel at $0.82V_y$ (6mm) and at $0.88V_y$ (9mm), but the shear force in the beam was increased to $0.90V_y$ before δ_o increased rapidly and caused the load to drop off. This test was terminated when δ_o in the end panel had reached 26mm, at which stage the equivalent value in the test panel had attained a maximum of only 1.2mm.

A further test was conducted on this specimen after the end panel

had been stiffened, and the V-δ plot is labelled "test panel failing" in Fig.8.3. A load of $0.92V_y$ was sustained by the beam with no signs of distress, but a shear force of $0.93V_y$ could only be sustained by rapid pumping of the jack, even though δ_o in the test panel was only 1.0mm. A set of readings was taken at this stage, after which further deflection was imposed on the beam. This caused the load to increase to $0.941V_y$ and remain steady there. The same pattern of apparent failure, and subsequent pumping to a higher load occurred at $0.945V_y$, where δ_o was 2.0mm. When a load of $0.950V_y$ was applied however, δ_o increased to 4.1mm and the load dropped off more rapidly than ever. Subsequent deflection of the beam caused a reduction in the load and an increase in δ_o. Large rotations occurred in three plastic hinges in the steel flanges, but there was no evidence of the formation of a sagging hinge in the compression flange.

8.7 PG3B

The V-δ relationship for this specimen was linear up to a load of $0.34V_y$, when the concrete slab was cast. When the test continued after the slab was cured, a flexural crack appeared above the support stiffeners at a load of $0.45V_y$, and the region of cracking spread out from here as the load was increased. This part of the V-δ curve is not linear, even though this end of the beam had been subjected to a shear force of $0.63V_y$ during the test on PG3A.

At a load of $0.96V_y$, δ_o was only 1.2mm, but this increased suddenly to 3.7mm when a load of $0.97V_y$ was applied, and led to a rapid drop in the load.

When the beam deflection, δ was 16.5mm, a horseshoe-shaped crack of the type illustrated in Fig.8.7 developed; it is labelled 'H' in Fig.8.5. Sagging curvature was noted in the slab over part of the test panel. Increasing δ to 20mm led to the formation of the crack marked 'S' in Fig.8.5, which was similar to that in Fig.8.9. The vertical shear

deformation across this crack was less than 1mm, whereas at the same load, the deformation across the horseshoe crack on the top of the slab was 2-3mm.

8.8 Onset of plasticity

8.8.1 The steel girder

The output from the e.r.s.gauges mounted on the girder and reinforcement has been used to determine when yield occurred at the location of each gauge. The onset of plasticity in PG1A is described in detail first, and any differences in the behaviour of the other beams are then listed.

Plasticity was first detected at a load of approximately $0.5V_y$, when the web at location C in Fig.8.4 yielded due to the concentrated stresses there. A small area of the web yielded in diagonal tension when the applied shear force was equal to $0.84V_y$, but apart from this, no further plasticity was detected until the load stage immediately after the beam had failed. It was then found that a diagonal yield band had formed in the web, and that the tension flange had yielded at B.

In both of Girders PG2A and PG3A, the tension flange at location B in Fig.8.4 yielded before the beam failed, at approximately $0.84V_y$. The web at B yielded in diagonal tension at the same load, and plasticity extended throughout the depth of the web at B and C after failure of the beam due to collapse of the end panel. Following stiffening of this panel and the subsequent reloading of the beam, yield strains were not achieved in the tension flange until approximately $0.93V_y$ was applied. The whole depth of the web at B and C yielded in diagonal tension at a load of $0.97V_y$ in the case of PG3A, but not until the ultimate load had been applied in PG2A.

In PG1B, PG2B and PG3B, the tension flange at B yielded before collapse of the beam occurred, at loads of $0.98V_y$, $0.96V_y$ and $0.91V_y$

respectively.

8.8.2 Slab reinforcement

In all of the composite beams tested, yielding of the reinforcement was detected first in the top layer of bars at position B in Fig.8.4. In Beam PG1A, this happened when the ultimate load of the girder was reached, but for all the other beams it occurred just before then, at loads within the range $0.90V_y$ to $0.96V_y$. The lower layer of reinforcement at B did not yield until after the ultimate load of the beam had been reached but, as in the reinforcement above it, strains in the bars continued to increase with further jacking of the beam even when advanced plastic mechanisms had formed.

The top layer of bars at location A in Fig.8.4 never attained the yield strain; indeed the strain here fell slightly when large rotations developed in the adjacent sagging hinge. In the lower layer of bars at A, the large rotations resulted in an increase in the tensile strain, and eventual yielding in the case of Beams PG1A and PG2B.

8.9 Out-of-plane web deformations

Contours of web deformation for the test panels of each girder are shown in Fig.8.11: they are derived from measurements taken immediately after the maximum load in each girder was attained. The direction of the tension field has been estimated from the contours and is indicated by the diagonal straight line.

The development of web buckling is traced in Fig.8.12, wherein the out-of-plane deflection of a point near the centre of the panel is plotted against the applied shear force. Gross buckling did not occur until either just before or just after the ultimate load was reached, and was therefore elasto-plastic in nature, since it coincided with the formation of the diagonal yield band in the web.

8.10 Slip

Slip at the interface of the steel girder and the slab of Beams PG1 to PG3 is plotted against the vertical shear force in Figs.8.13 to 8.15.

8.11 Uplift and vertical deformations in the tension flange

The deflected shape of the tension flange in the region of the test panel has been determined at selected load stages, and the results are shown in Figs.8.16 to 8.18. Loads subscripted "F" are on the falling branch of the V-δ curve. The curves plotted are the relative displacement of the tension flange and the instrumentation rig shown in Fig.7.9. True deflections of the flange may be obtained by referring each curve to a straight line drawn through two points which are known not to have moved vertically. With sufficient accuracy, two such points may be taken as the pivot of the instrumentation rig (P in Fig.7.9) and the dial gauge nearest the support stiffeners, and the resulting reference lines are shown dotted in Figs.8.16 to 8.18.

The uplift of the concrete slab relative to the steel beam has been plotted below the curves of deflection, using the same horizontal scale but a much enlarged vertical one.

8.12 Auxiliary tests

The results of the tests on the steel coupons and the concrete specimens are given in Tables 8.1 and 8.2. The cube crushing strengths and moduli of elasticity for concrete are average results from tests on three specimens, except for PG3B, where only two cubes were cast. Tabulated values of shrinkage strain are the average of the strain in two sides of each prism (Table 7.3) between the seventh day after casting and the last day of the corresponding girder test.

The results of the tests to calibrate the load cells are given in Fig.8.19.

Girder coupons			Coupons from 12mm diam. reinforcement	
Location (Fig.7.14)	Yield stress (N/mm^2)	Modulus of elasticity (kN/mm^2)	Sample	0.2% proof stress (N/mm^2)
T	273	211	1	438
W	328	209	2	425
C	306	214	3	432

TABLE 8.1 RESULTS OF TESTS ON STEEL COUPONS

Specimen	Cube crushing strength (N/mm^2)	Modulus of elasticity (kN/mm^2)	Compressive strain in shrinkage prisms (10^{-6})
PG1A	36.3	28.1	271
PG1B	60.8	39.1	465
PG2 (Test on End 'A')	33.2	-	280
PG2 (Test on End 'B')	33.7	26.3	311
PG3B	43.7	28.3	257

TABLE 8.2 PROPERTIES OF CONCRETE ON LAST DAY OF GIRDER TEST

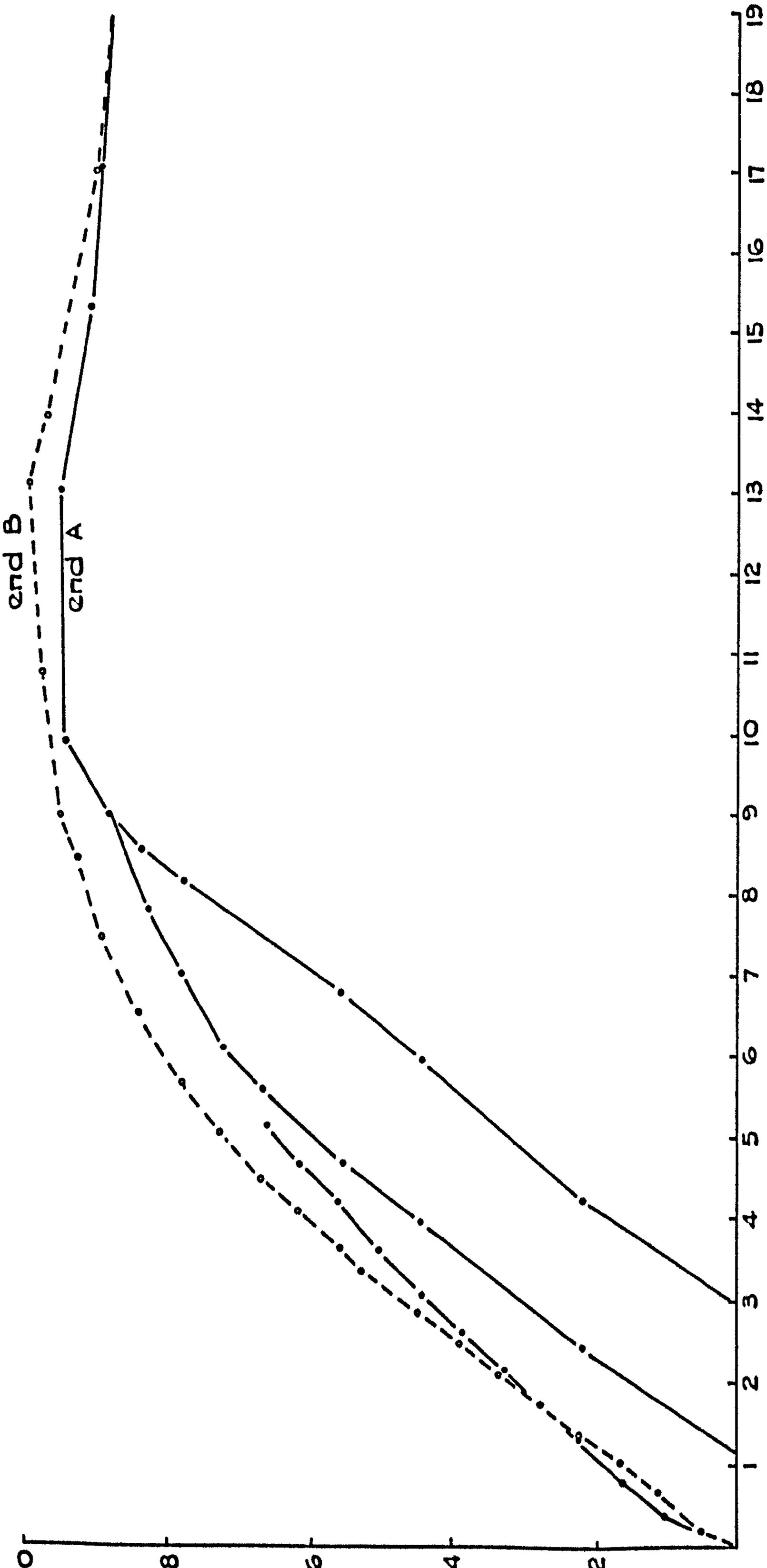

FIG.8.1 LOAD-DEFLECTION CURVES FOR BEAM PG1

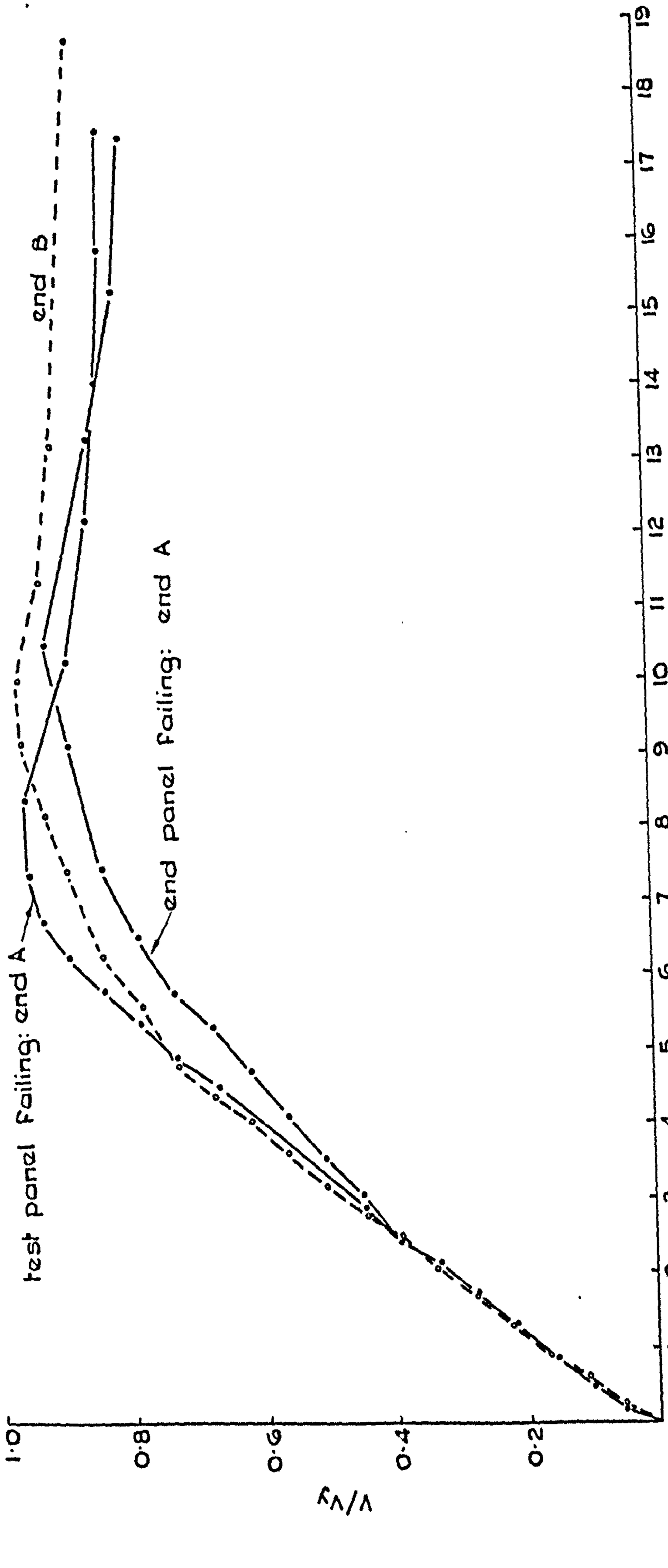

FIG.8.2 LOAD-DEFLECTION CURVES FOR BEAM PG 2

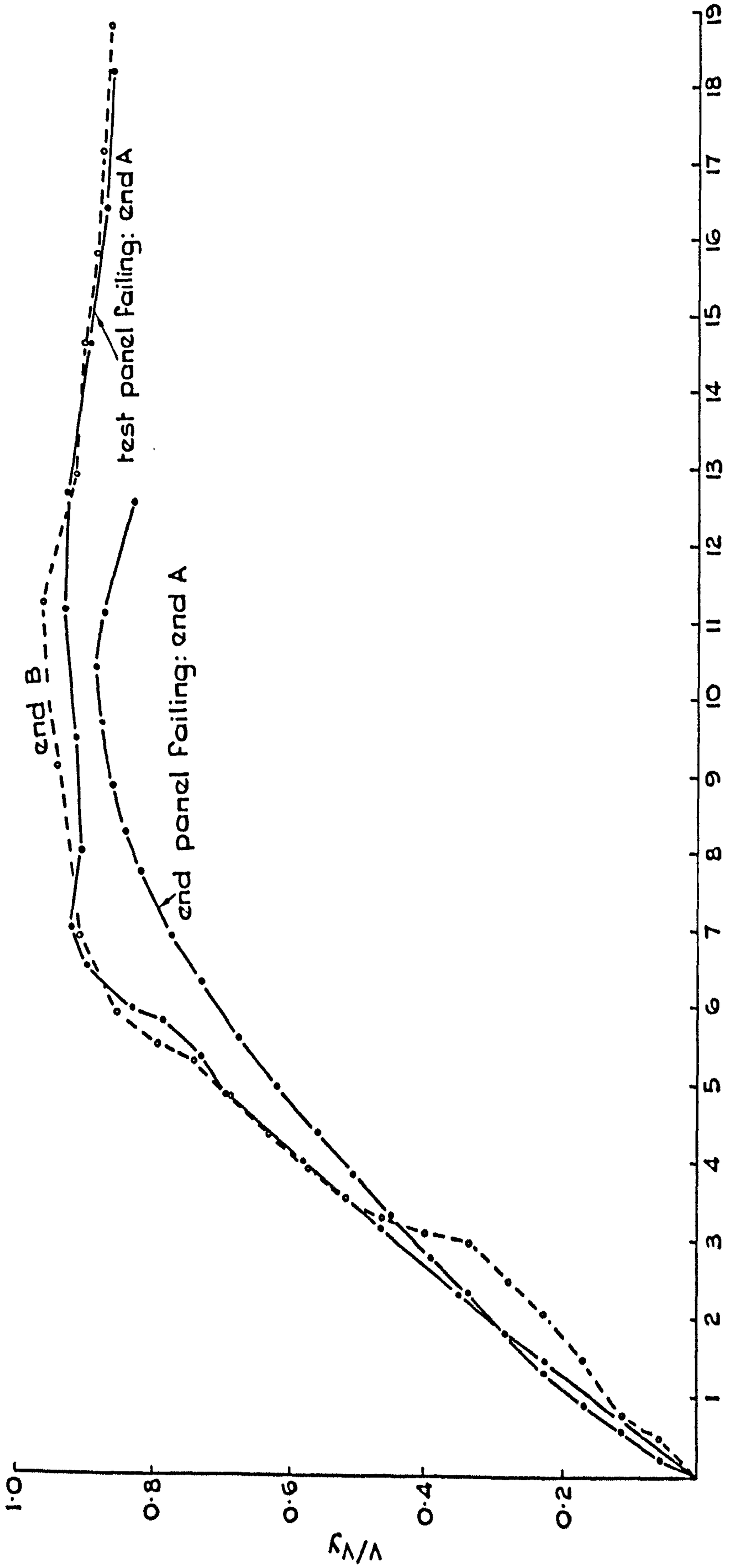

FIG.8.3 LOAD-DEFLECTION CURVES FOR BEAM PG3

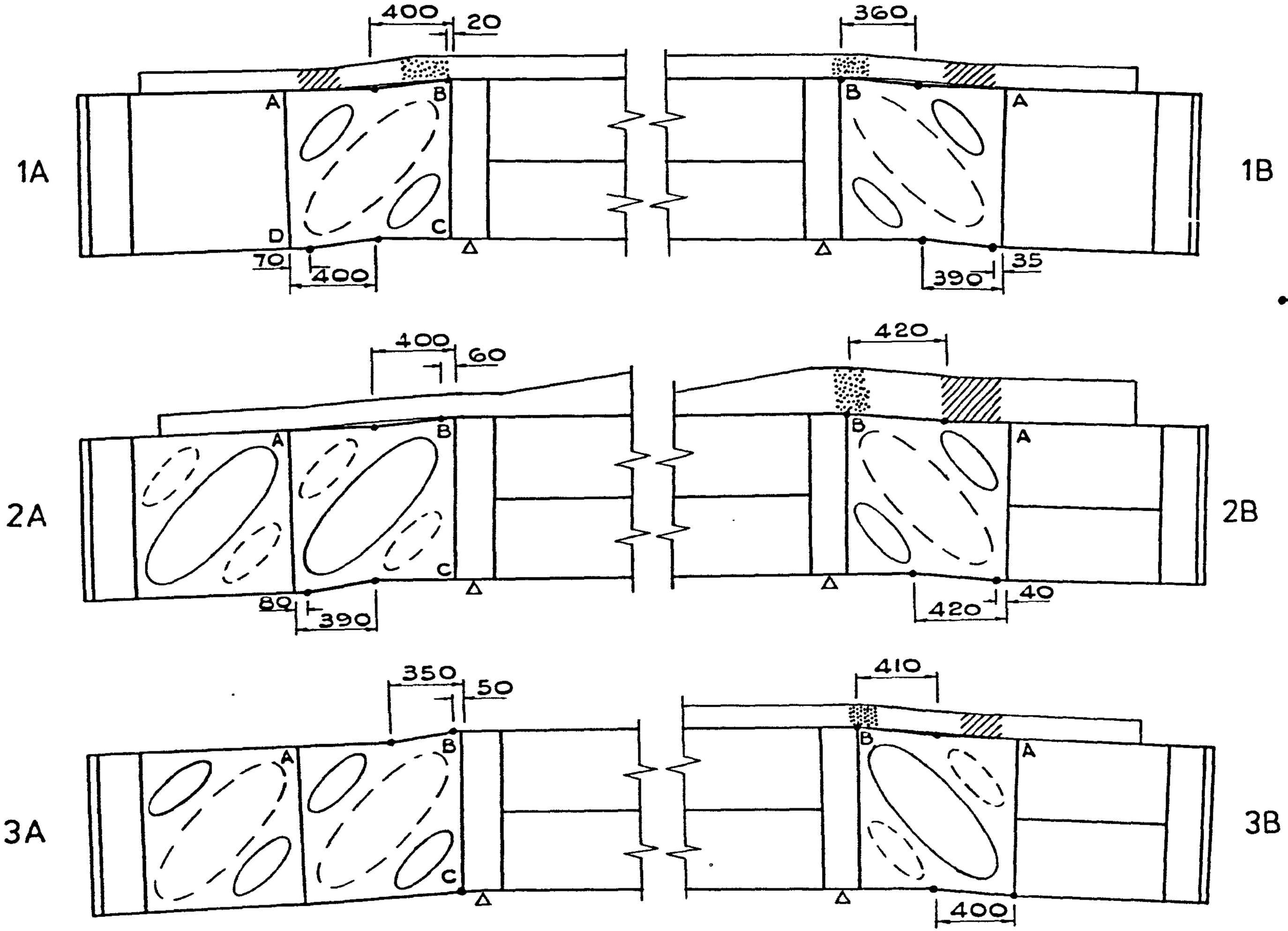

FIG.8.4 FINAL DEFORMATIONS IN BEAMS PG1-PG3

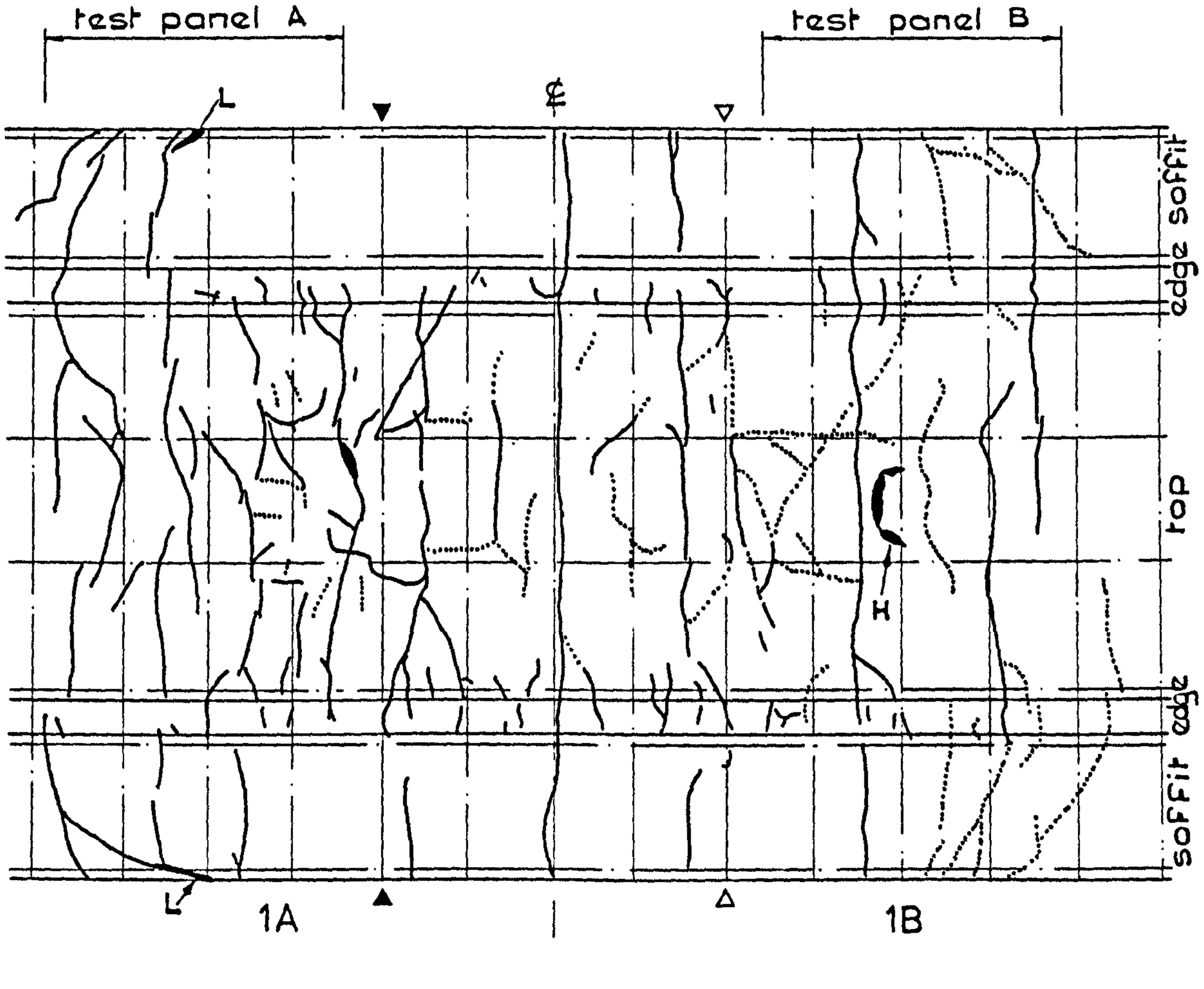

FIG.8.5 DEVELOPED SURFACE OF SLAB SHOWING FINAL CRACK PATTERN

(continued....)

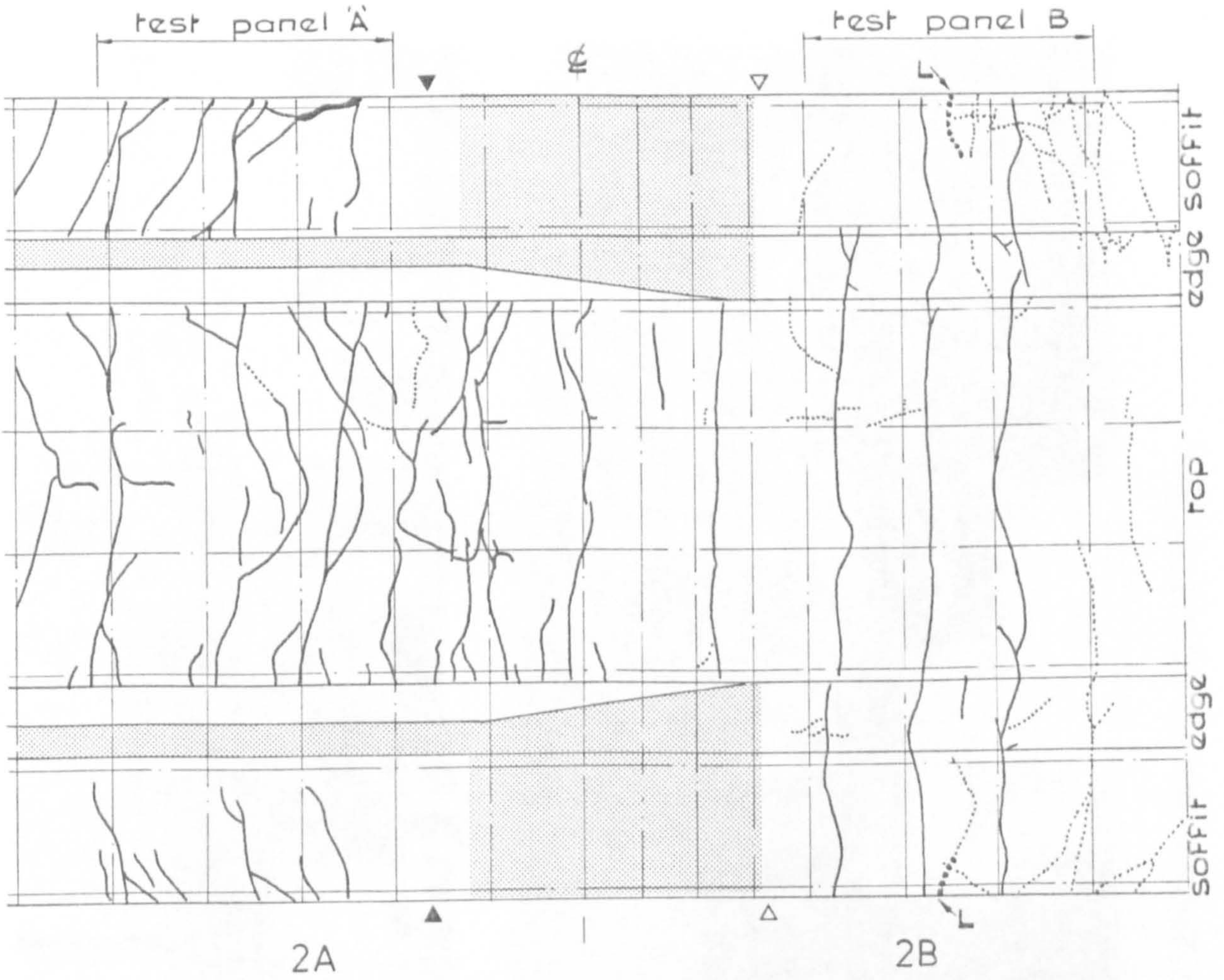

information not available

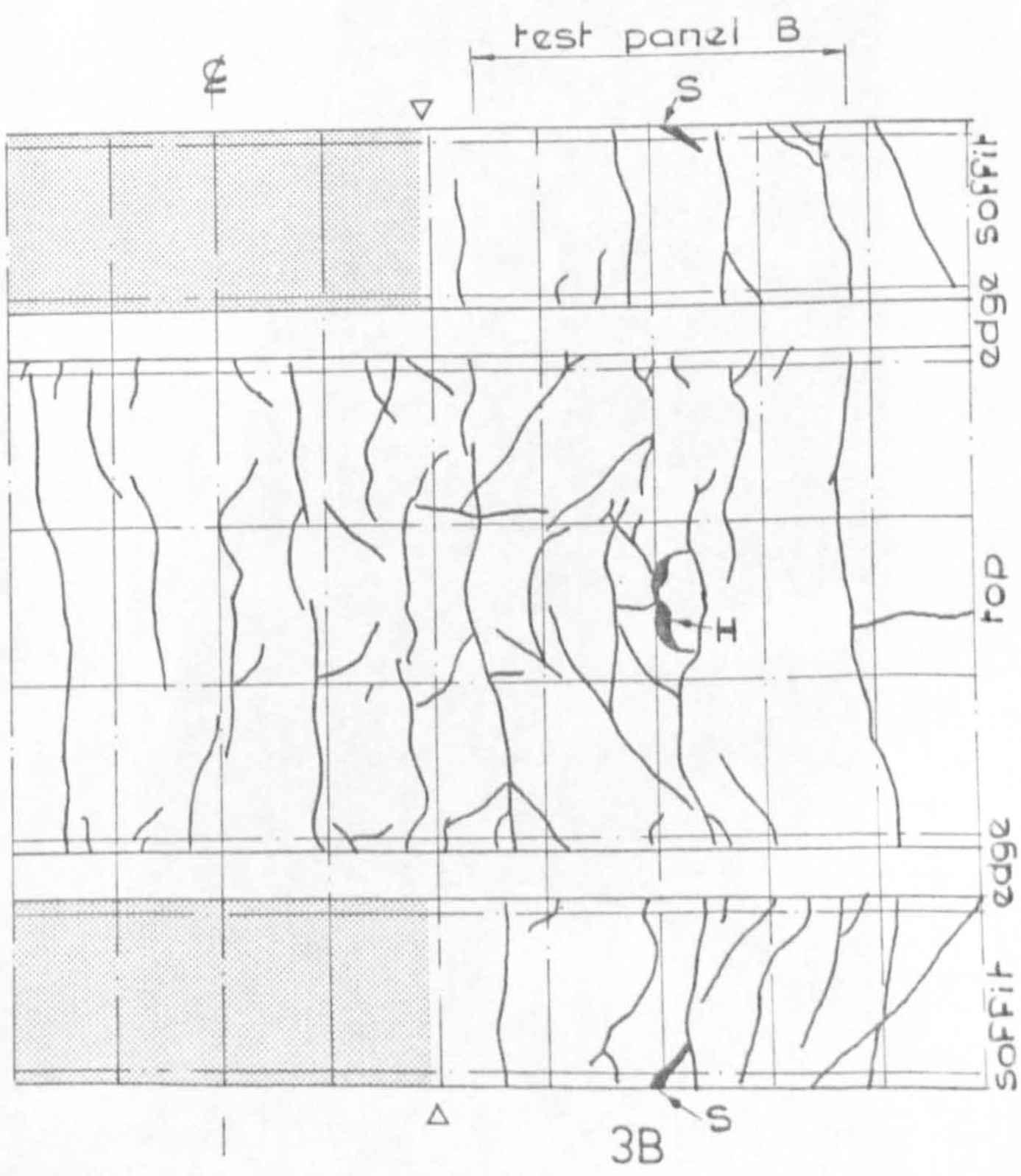

FIG. 8.5 (concluded)

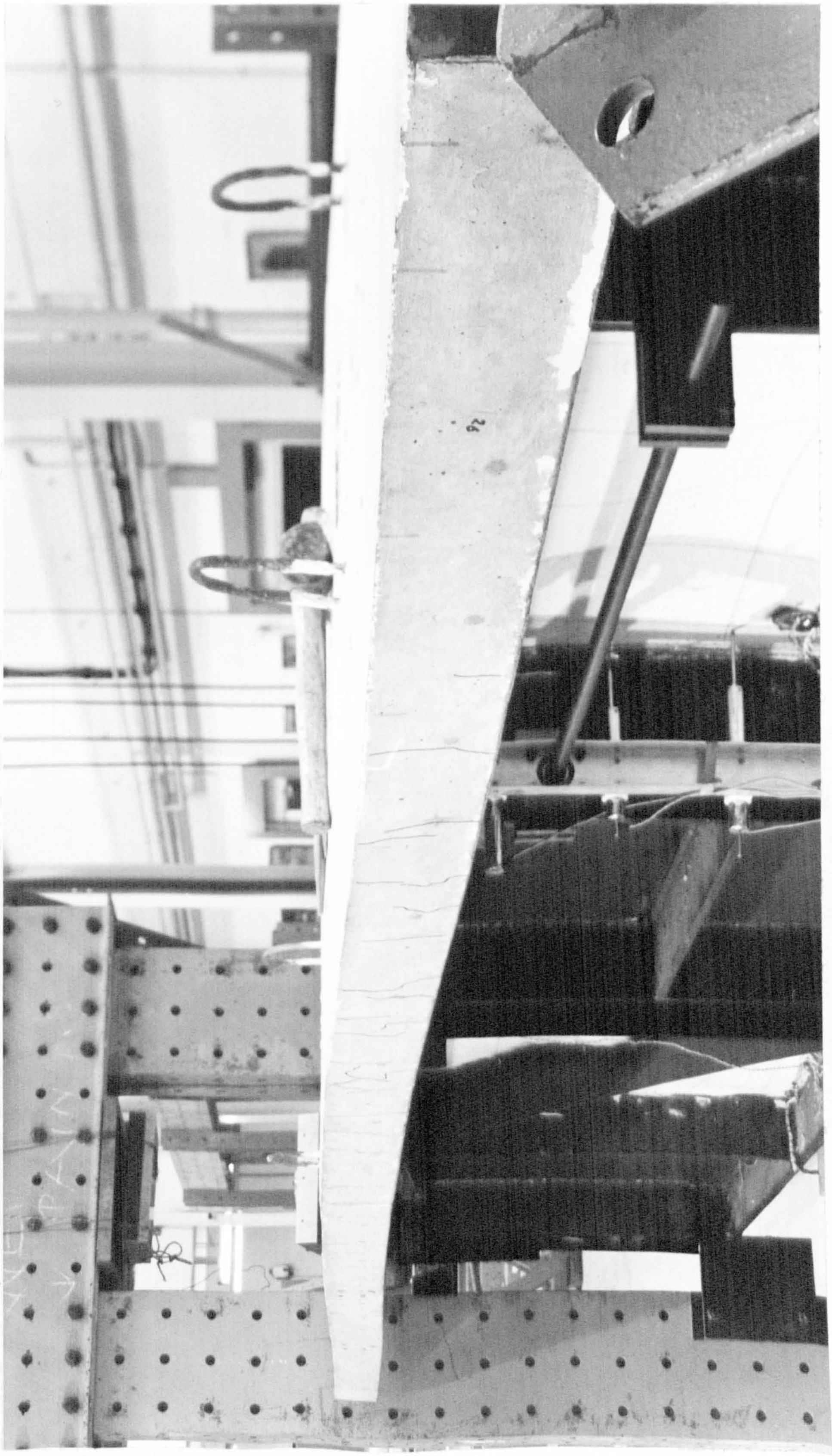

FIG. 8.6 RESIDUAL SLAB DEFORMATION IN BEAM PG1

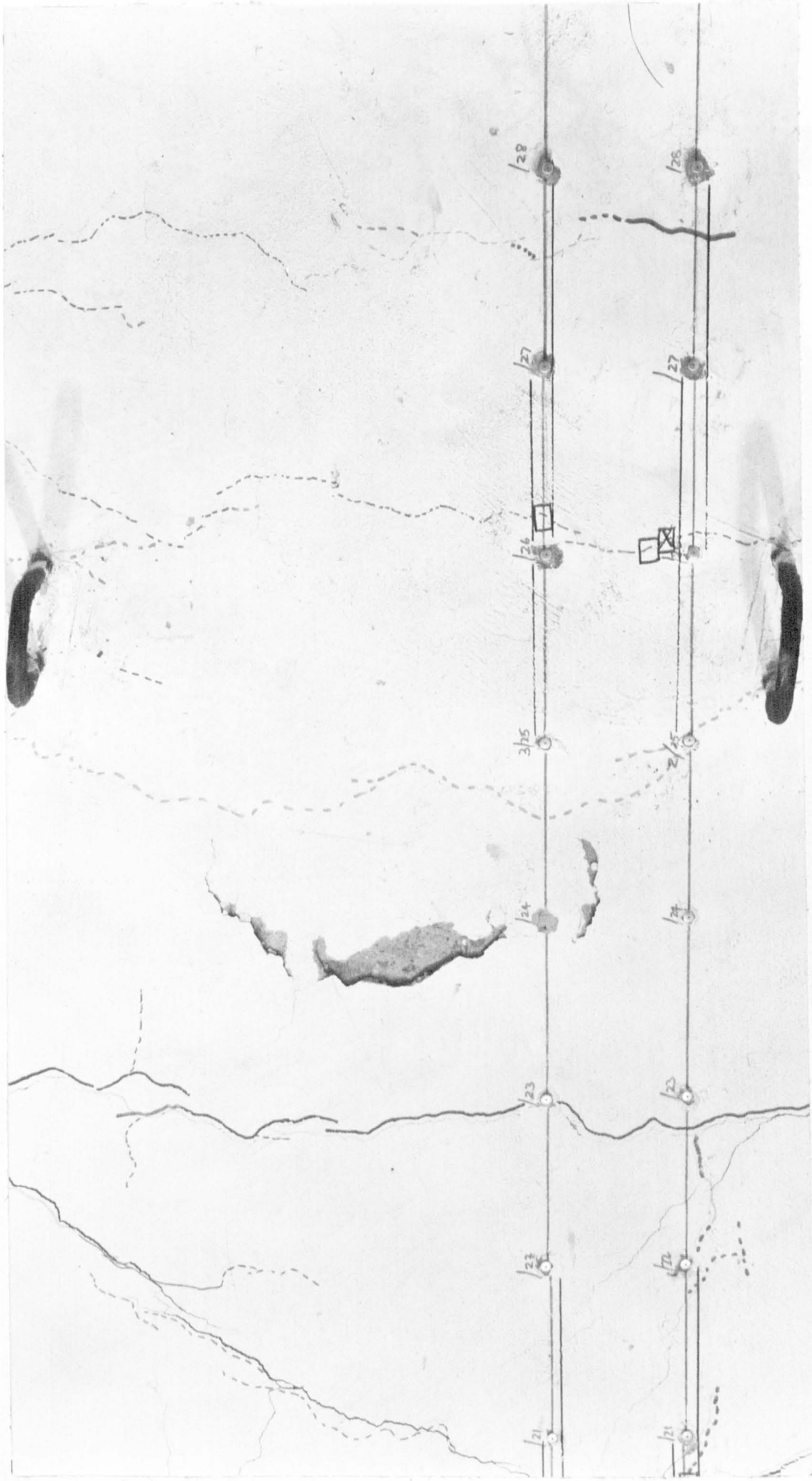

FIG. 8.7 CRACKING IN TOP SURFACE OF SLAB, BEAM PG1B

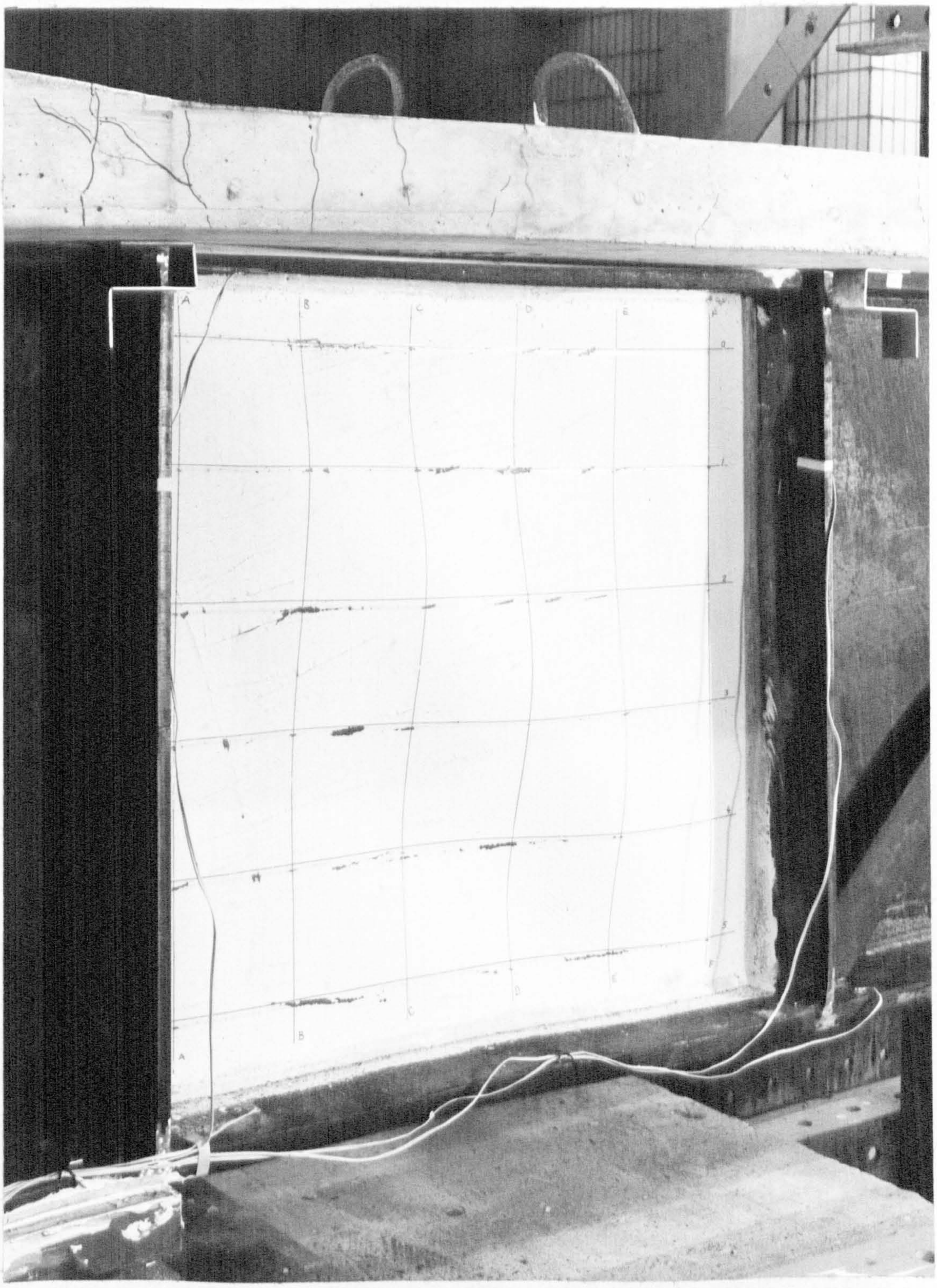

FIG. 8.8 SEPARATION OF SLAB AND GIRDER IN BEAM PG2A

FIG. 8.9 LOCAL FAILURE IN SOFFIT OF SLAB, BEAM PG2A

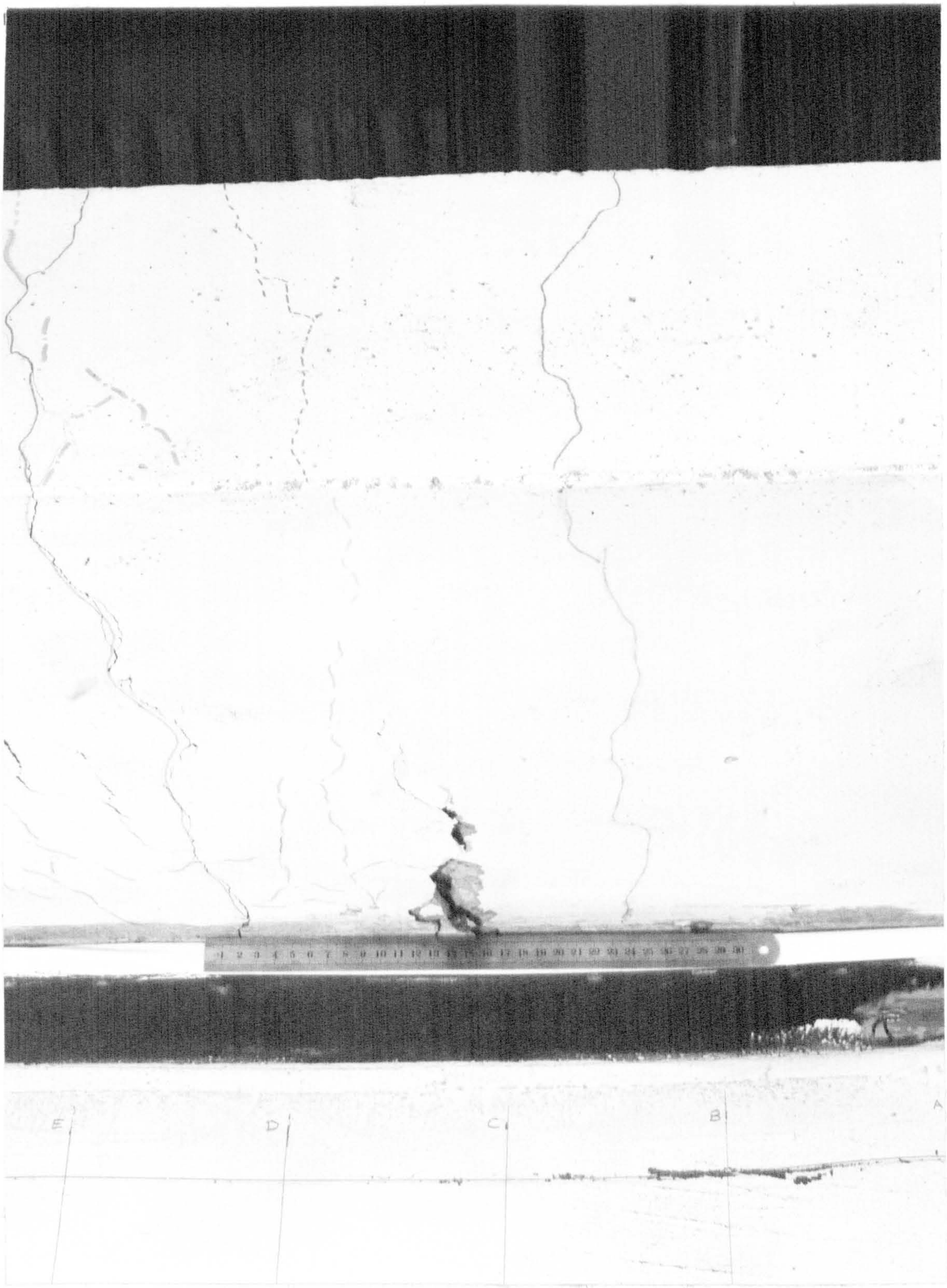

FIG. 8.10 LOCAL FAILURE IN SOFFIT OF SLAB, BEAM PG2B

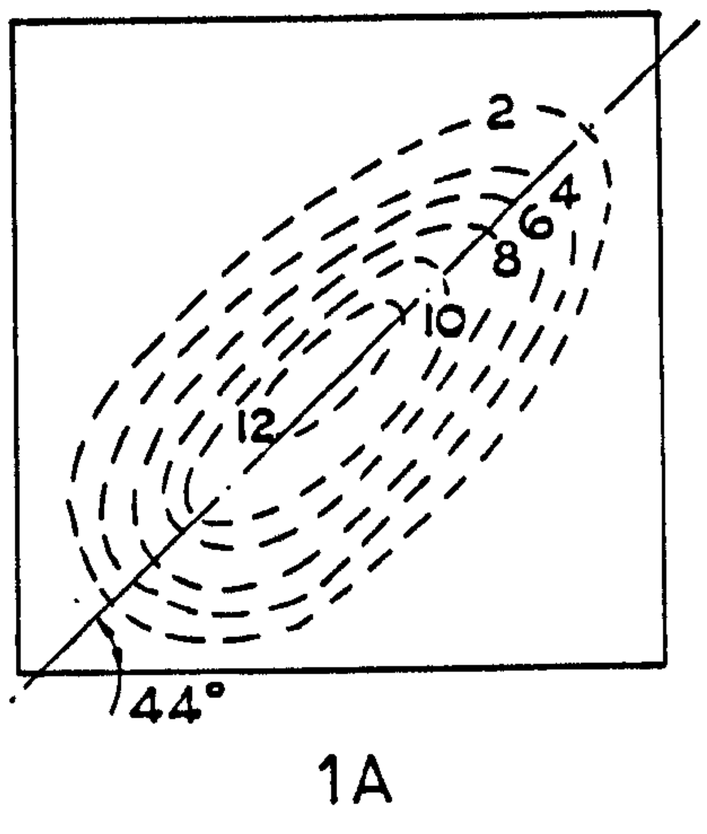

1A

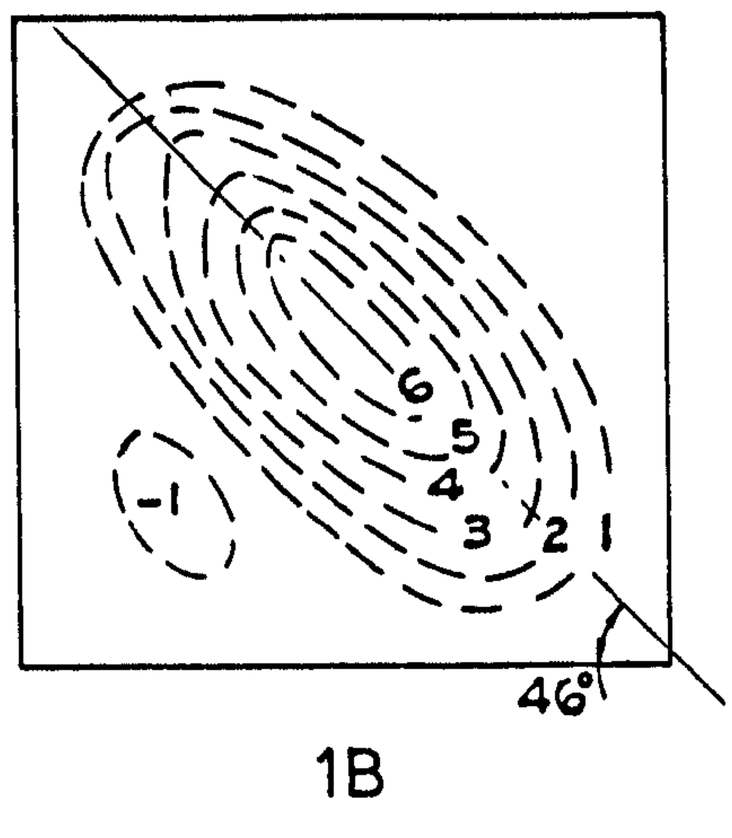

1B

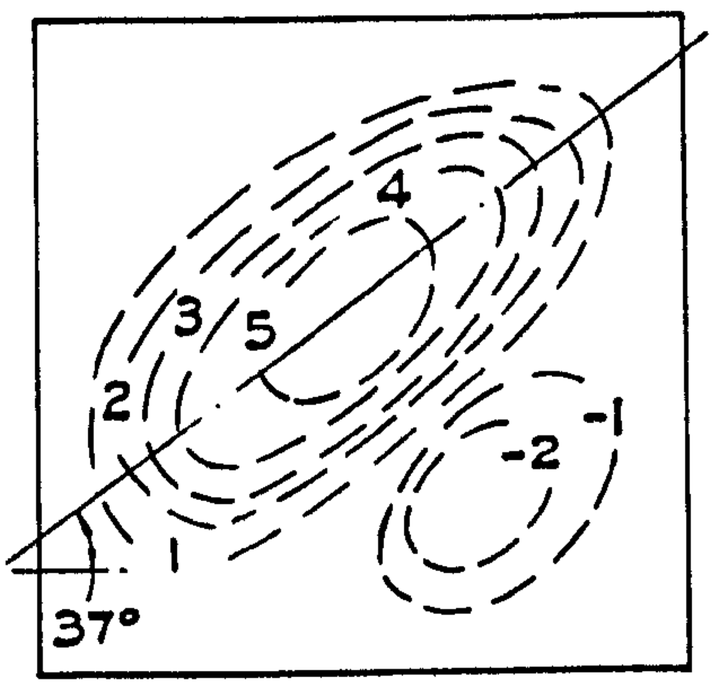

2A

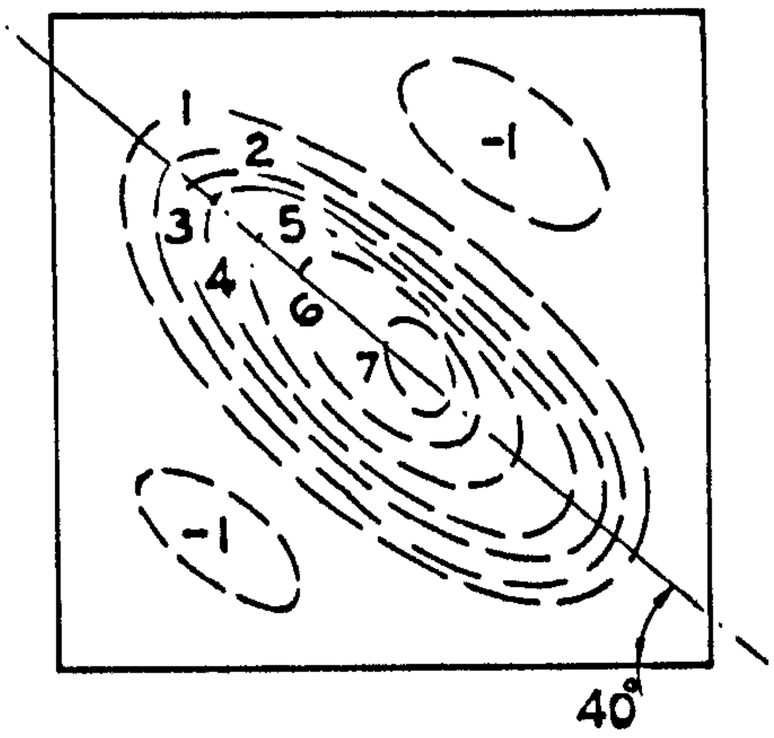

2B

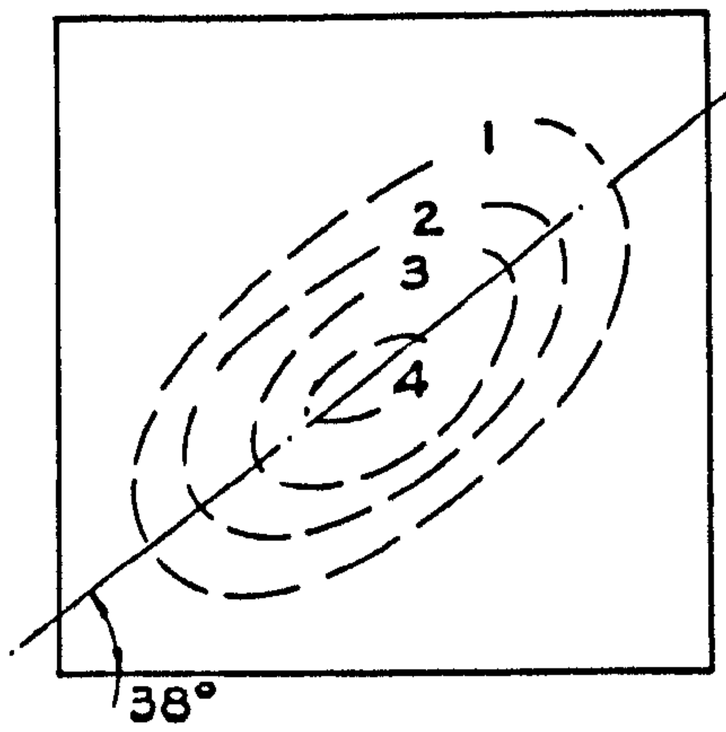

3A

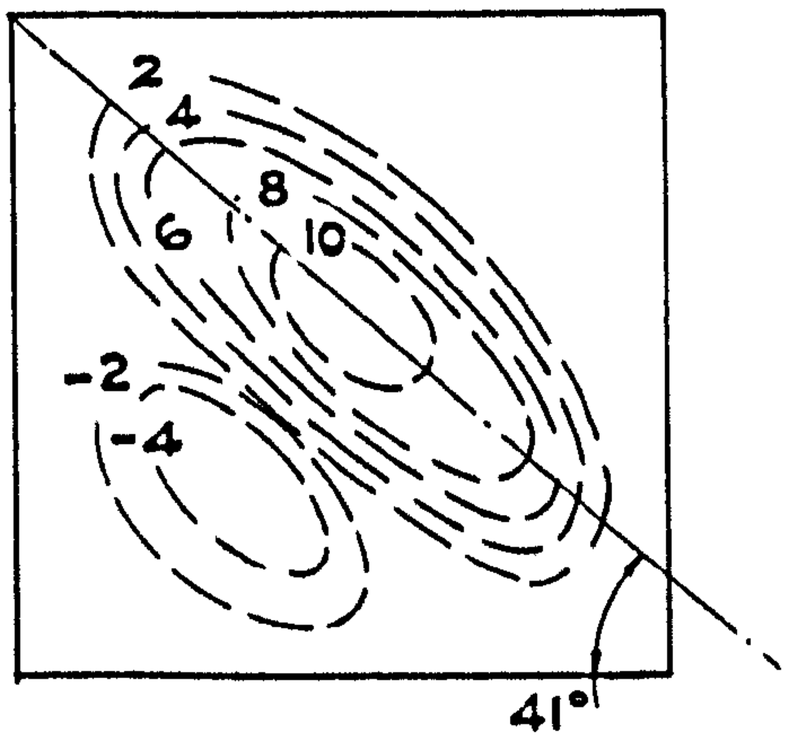

3B

Note: contour heights in mm

FIG. 8.11 CONTOURS OF WEB DEFORMATION IN TEST PANELS AT ULTIMATE LOAD

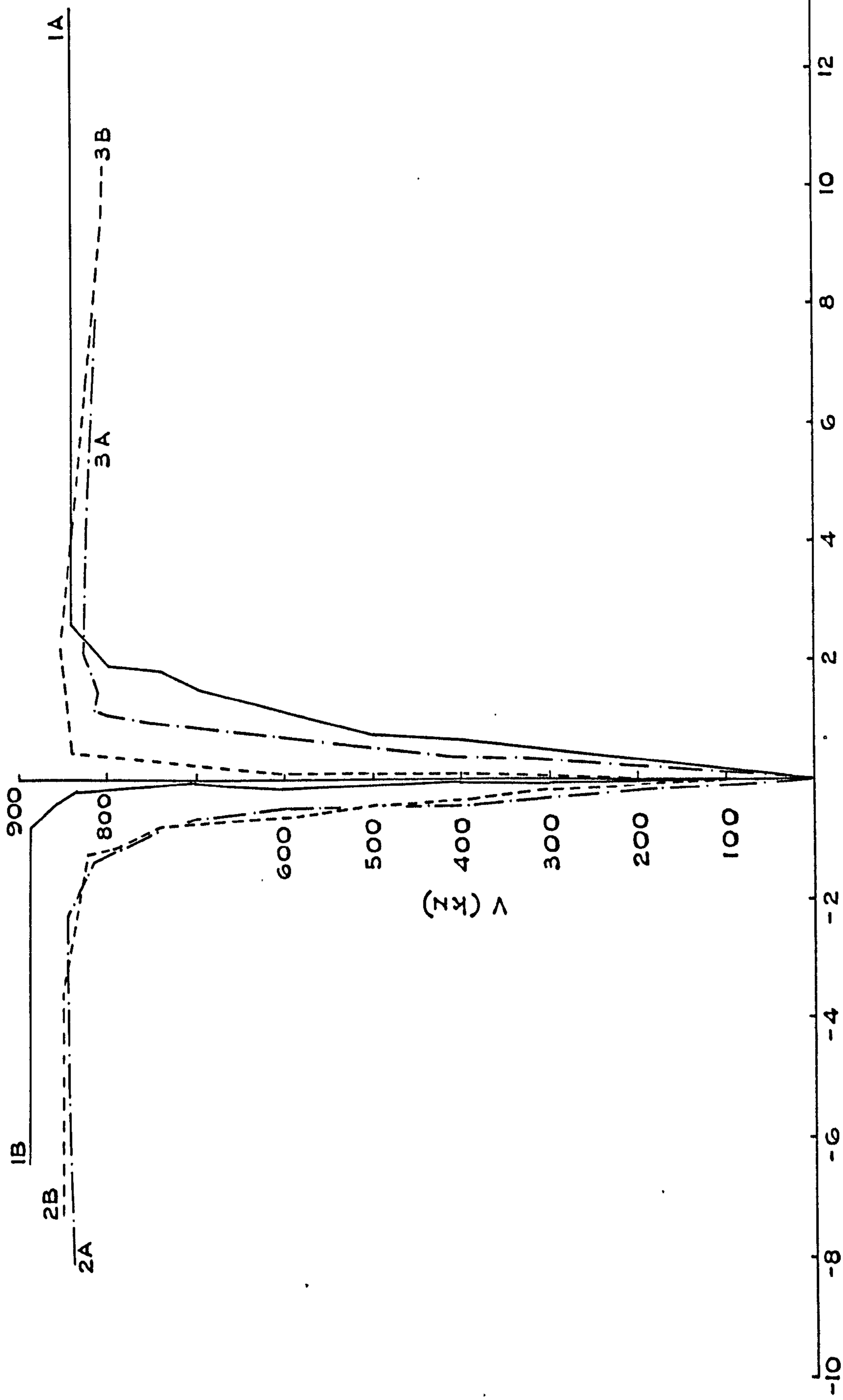

FIG. 8.12 V-δ_0 CURVES FOR BEAMS PG1-PG3

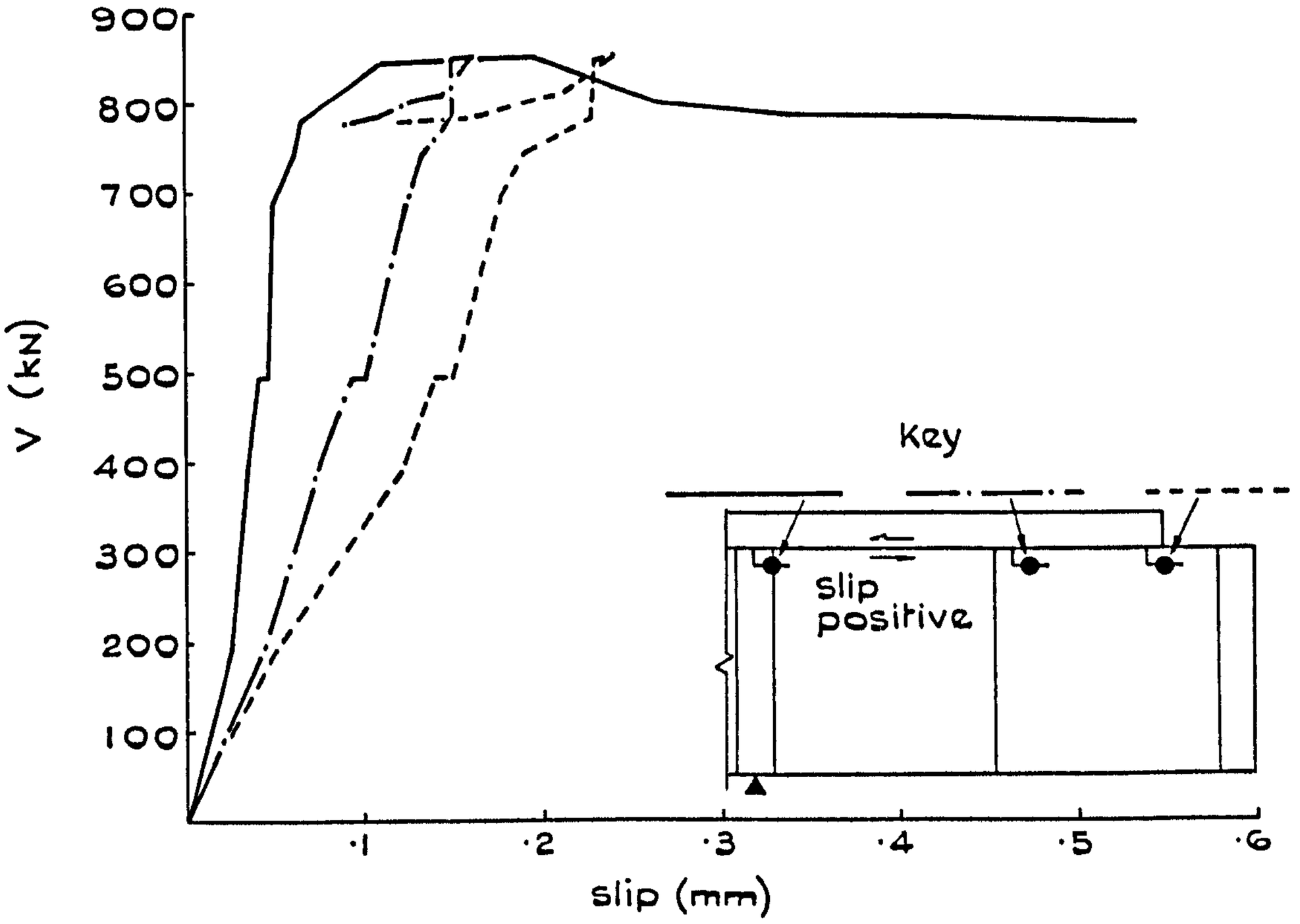

End A

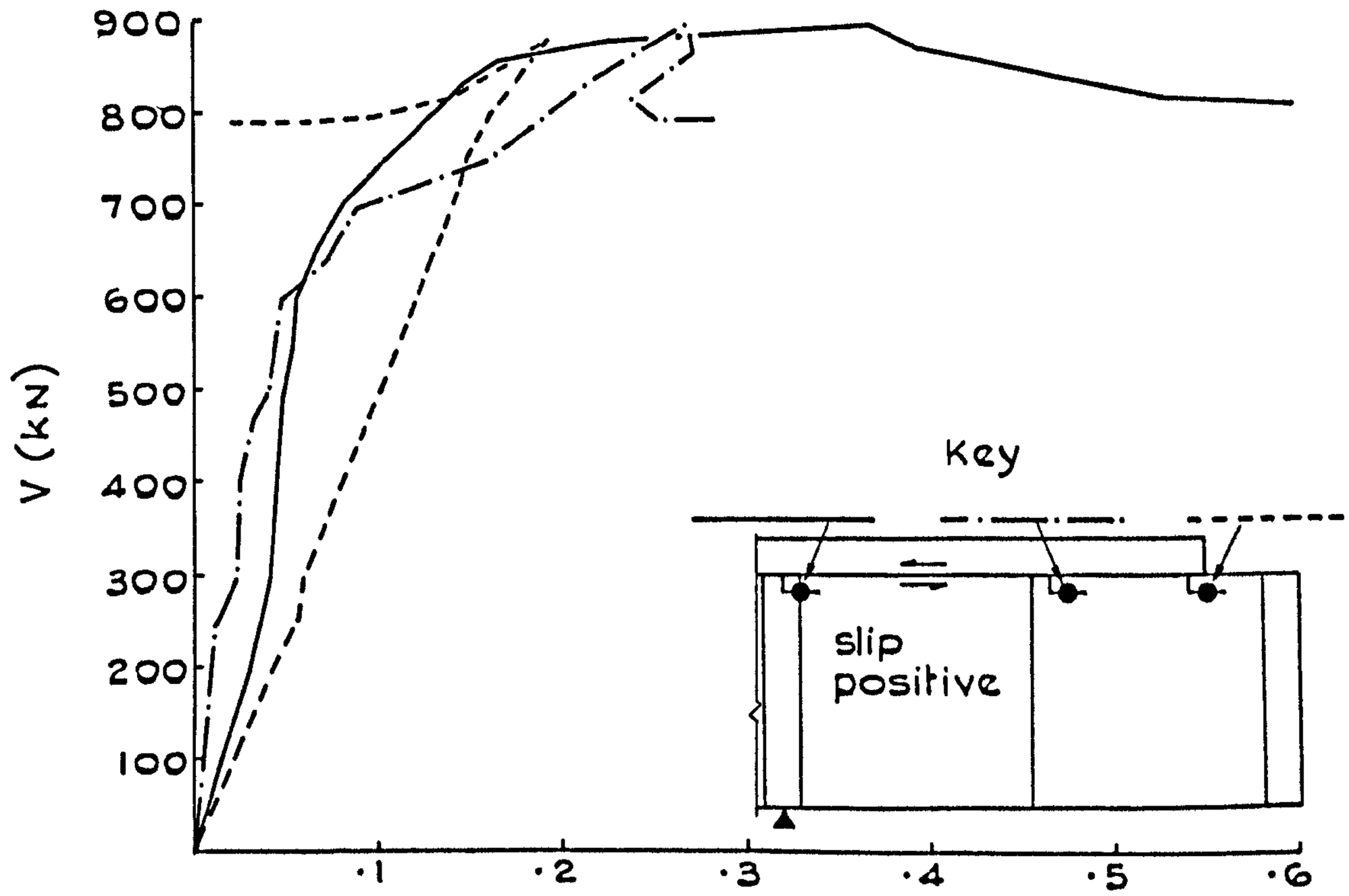

End B

FIG. 8.13 LOAD-SLIP CURVES FOR BEAM PG1

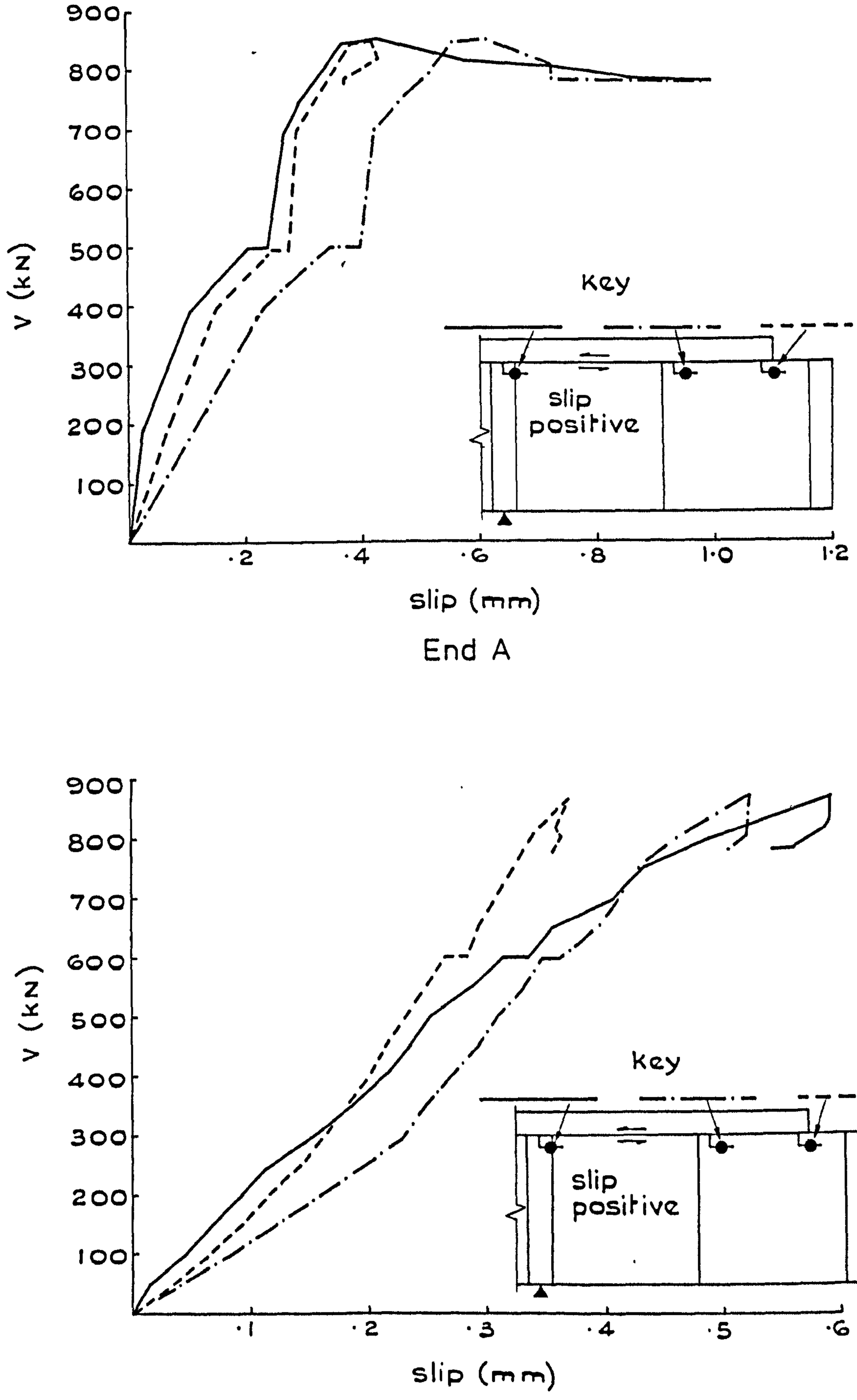

FIG.8.14 LOAD-SLIP CURVES FOR BEAM PG2

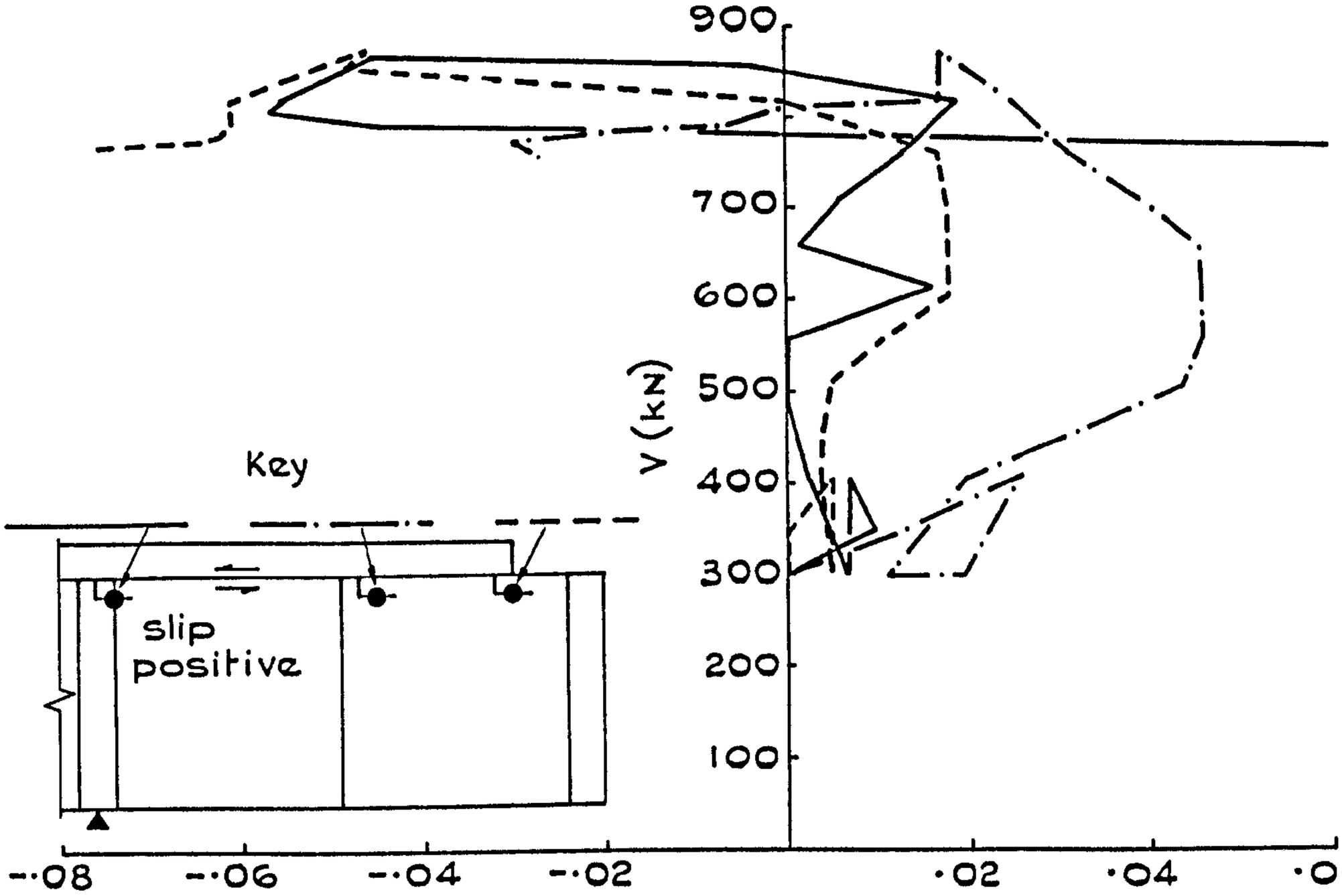

FIG. 8.15 LOAD-SLIP CURVES FOR BEAM PG3

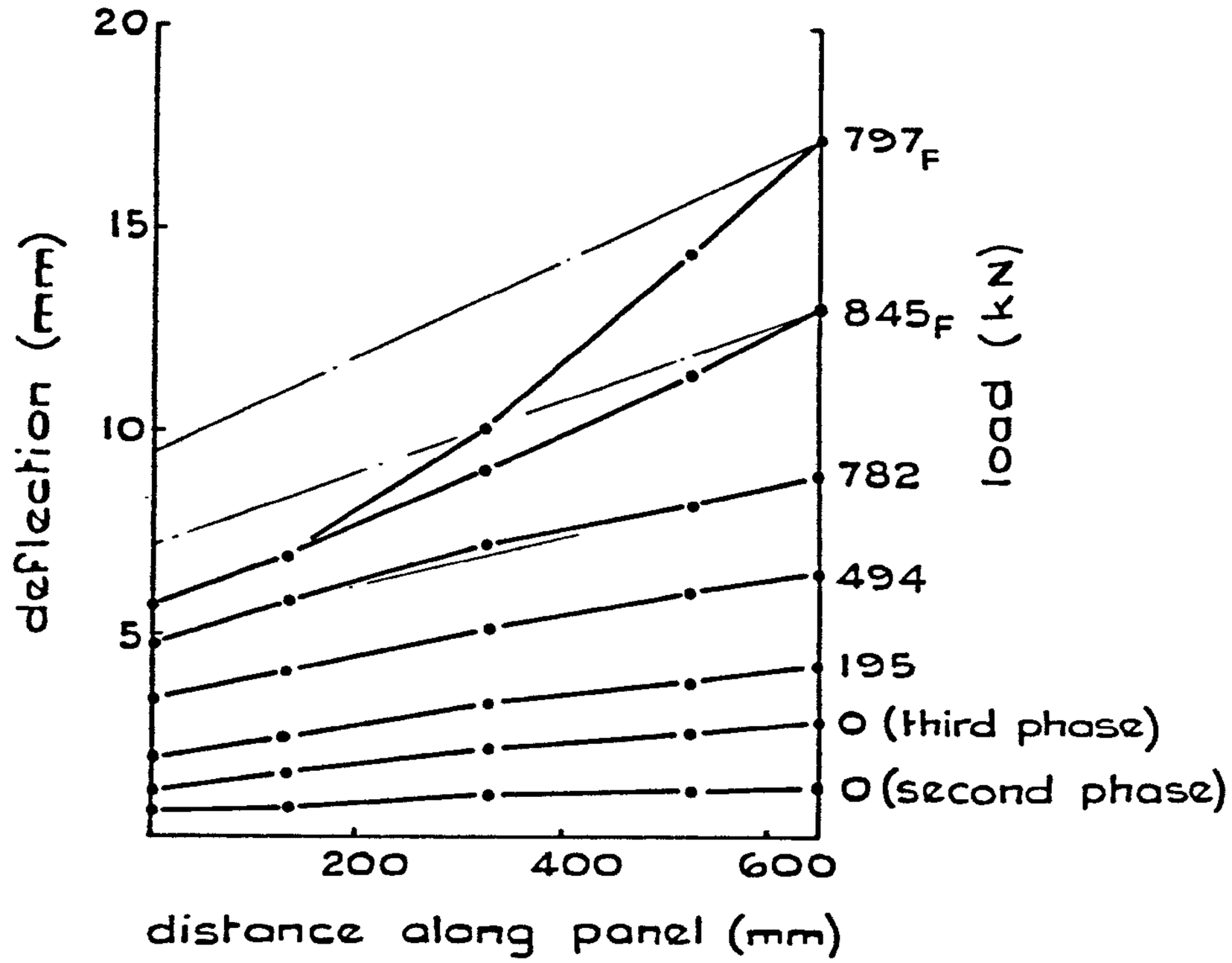

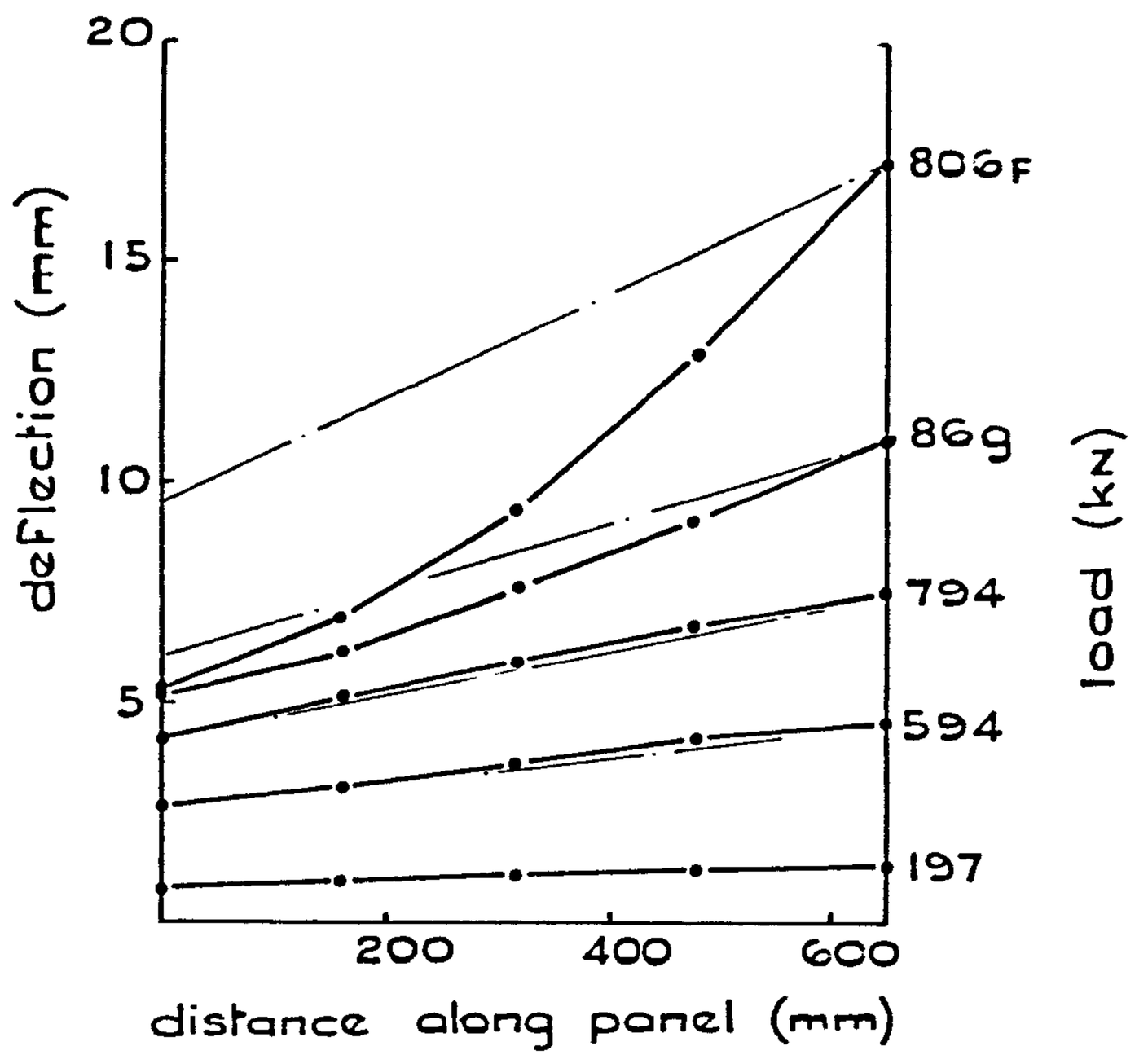

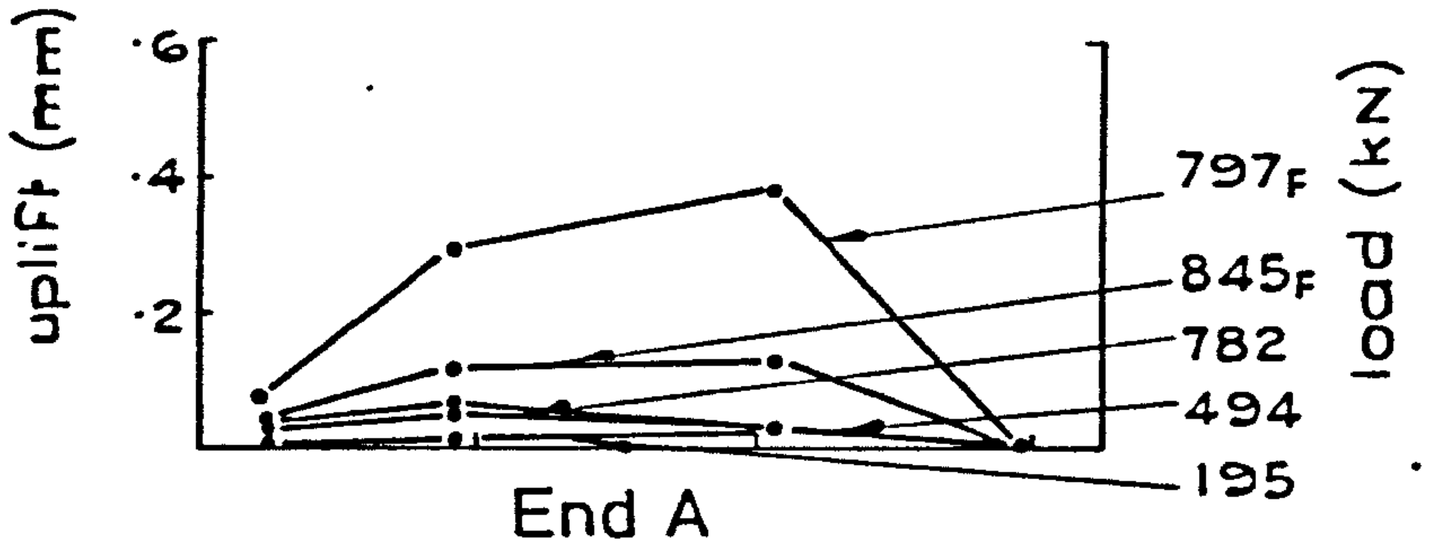

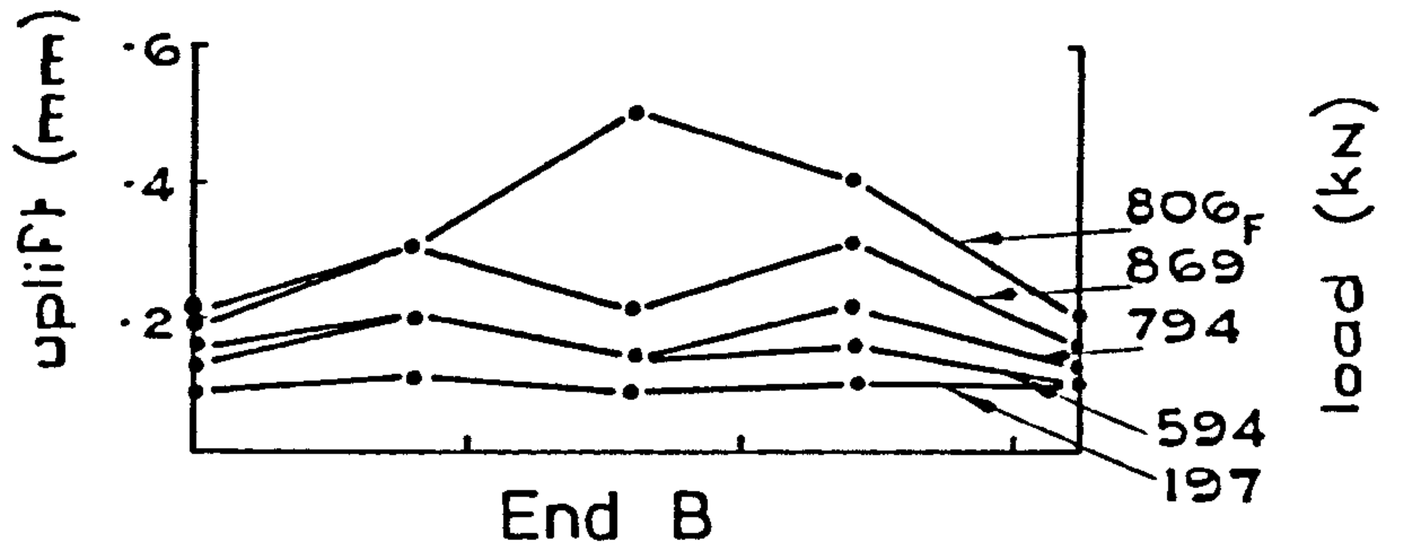

FIG. 8.16 DEFLECTION AND UPLIFT IN TEST PANELS OF BEAM PG1

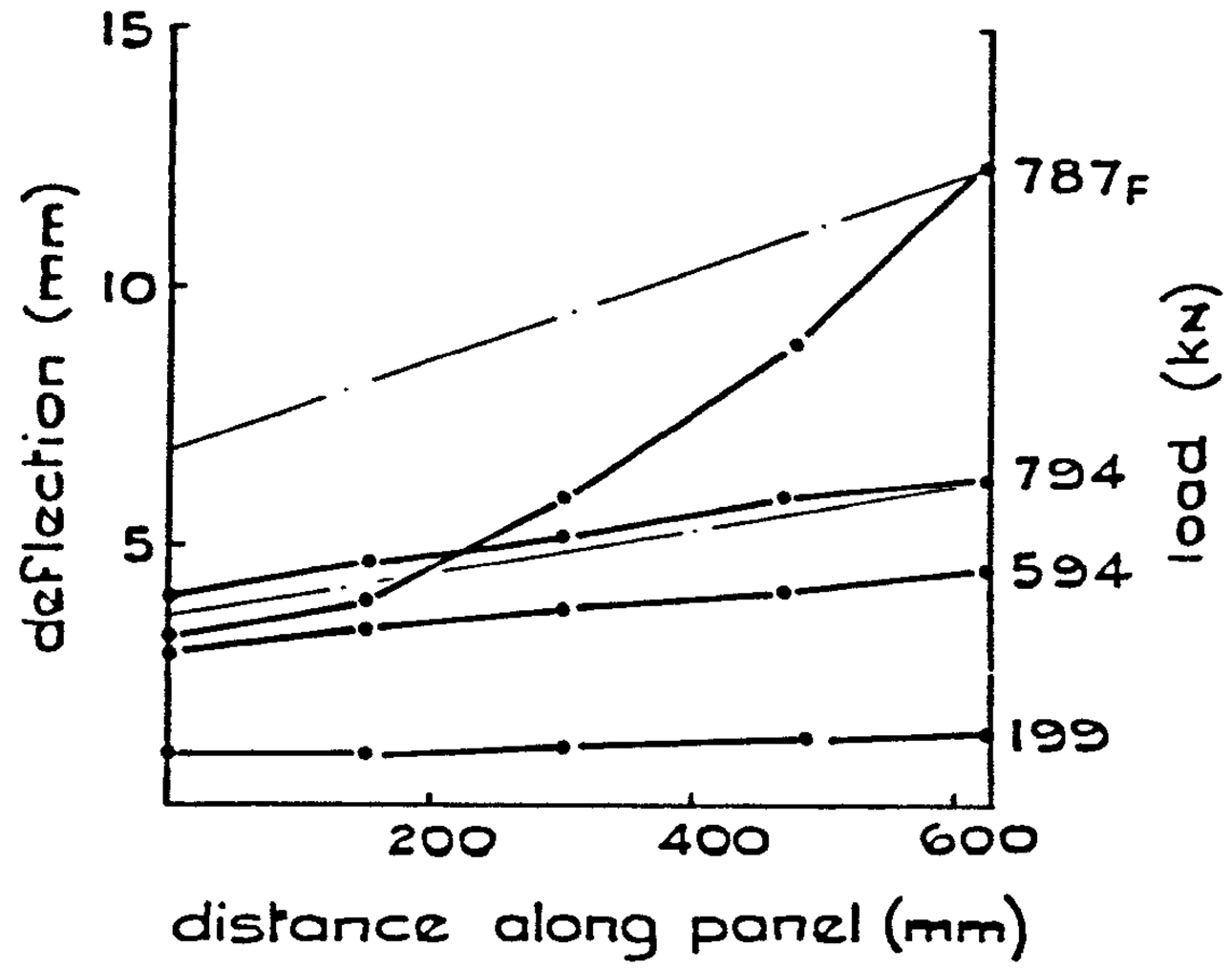

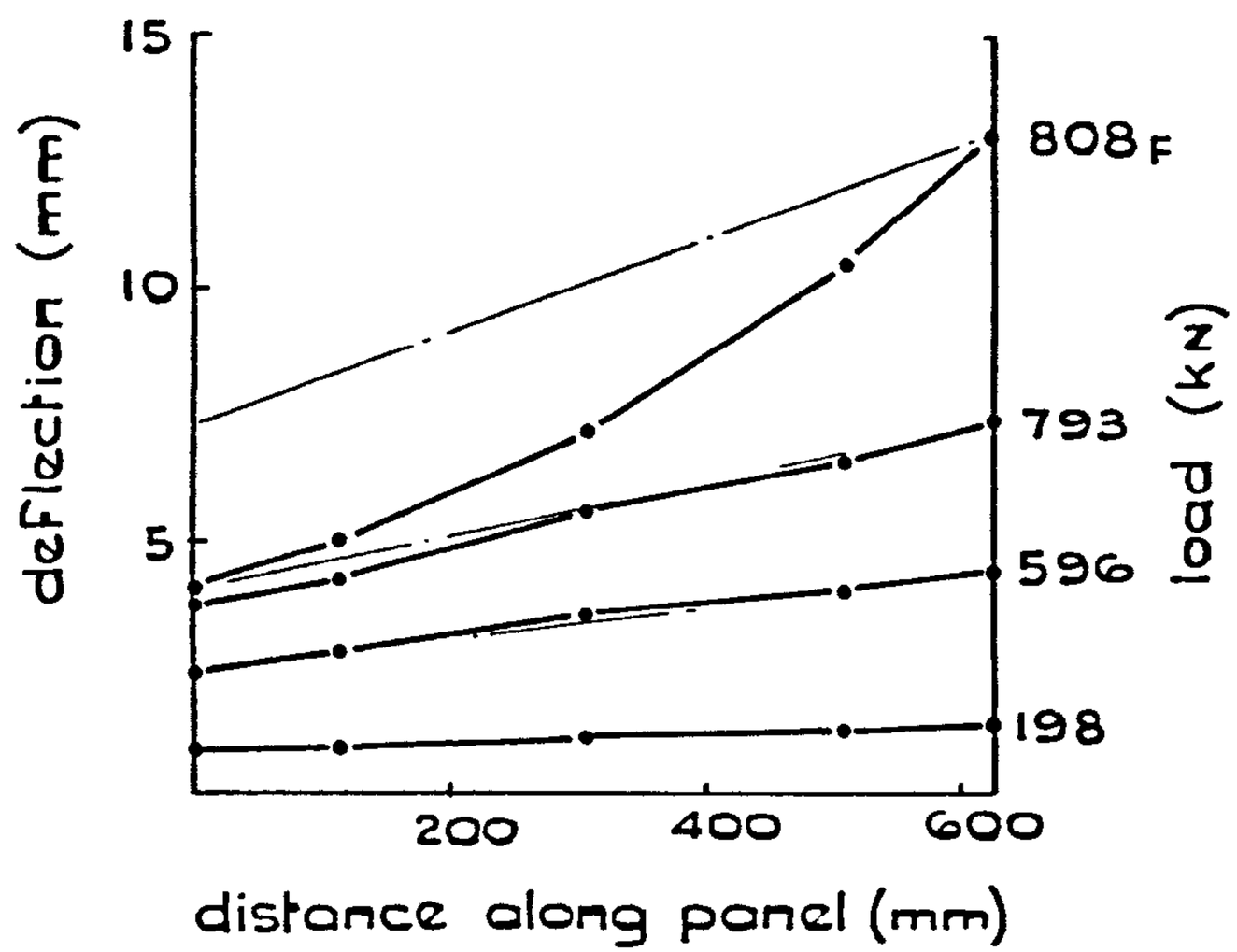

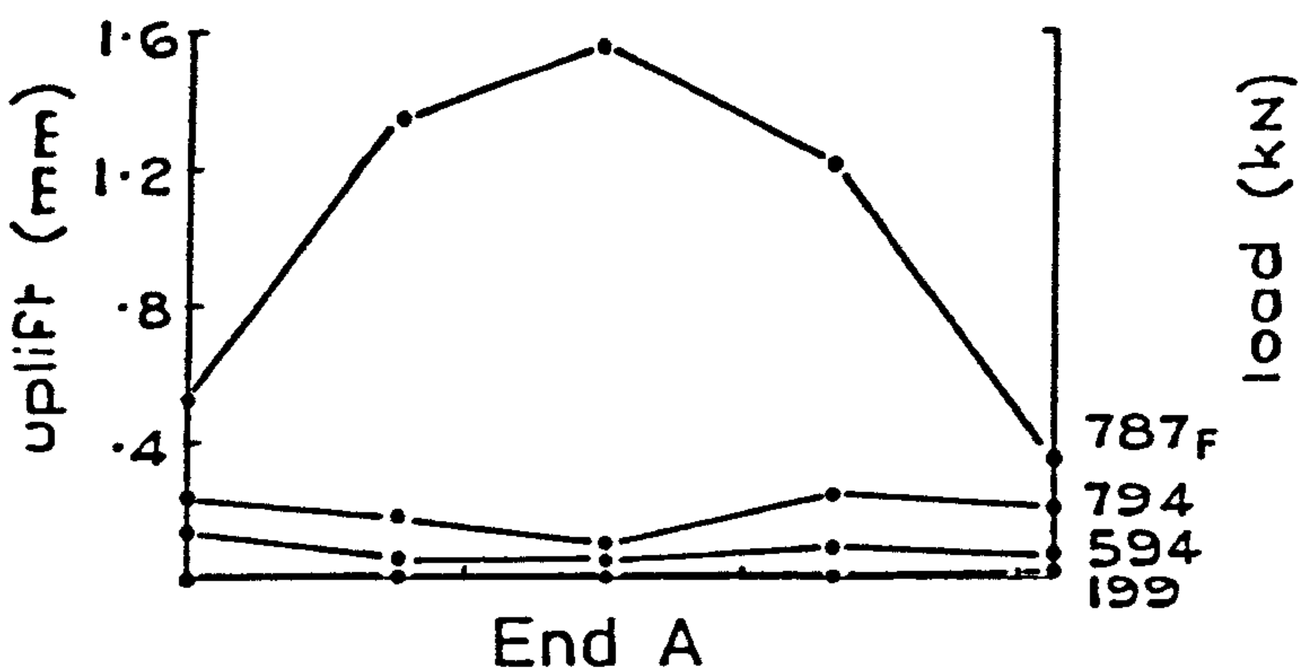

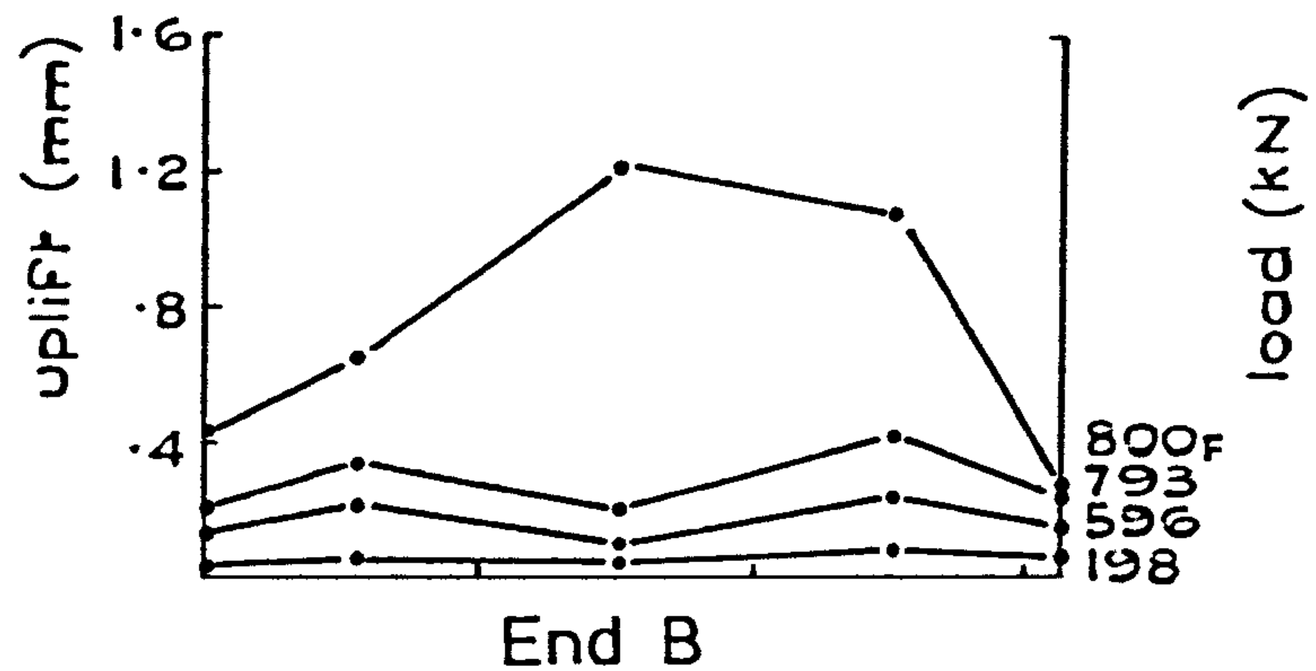

FIG. 8.17 DEFLECTION AND UPLIFT IN TEST PANELS OF BEAM PG2

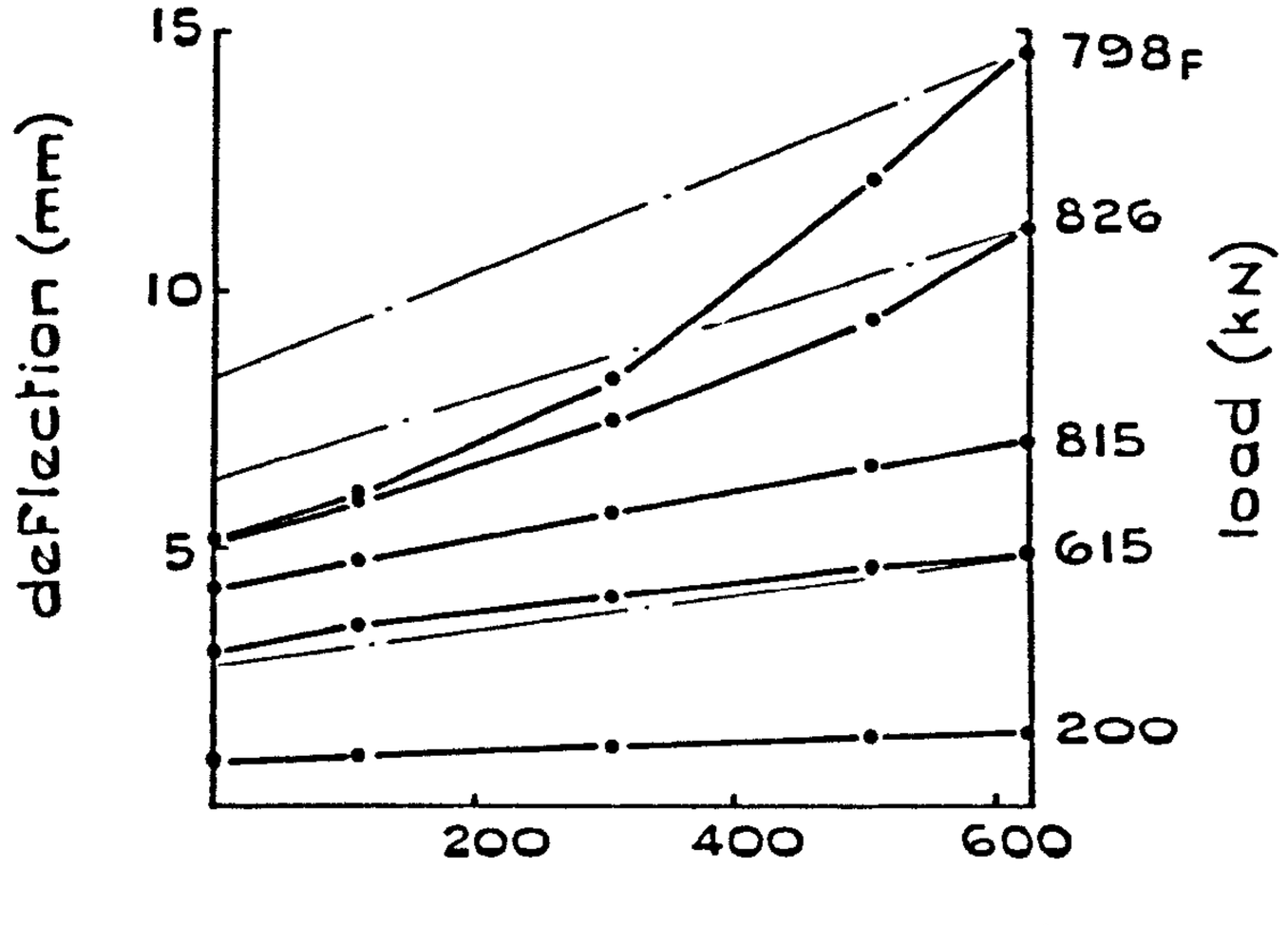

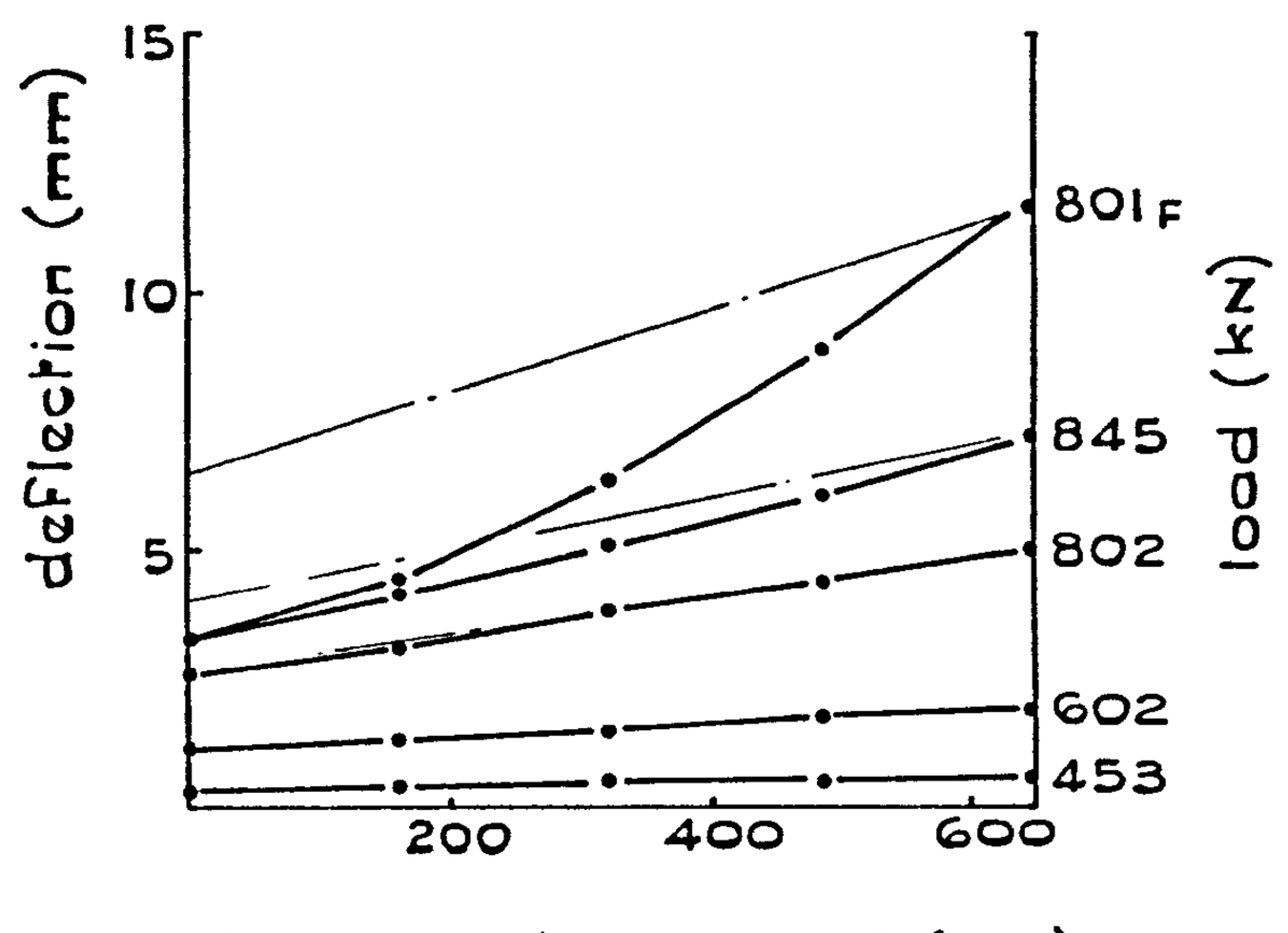

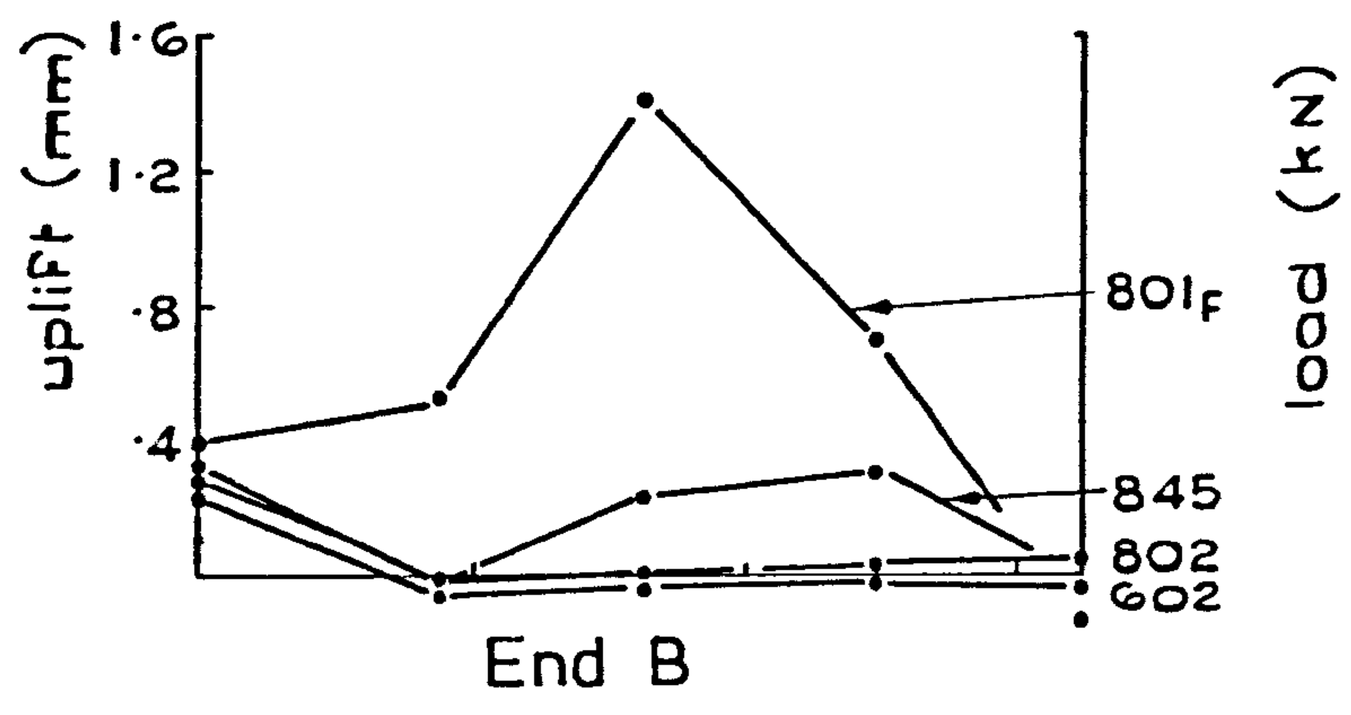

FIG. 8.18 DEFLECTION AND UPLIFT IN TEST PANELS OF BEAM PG3

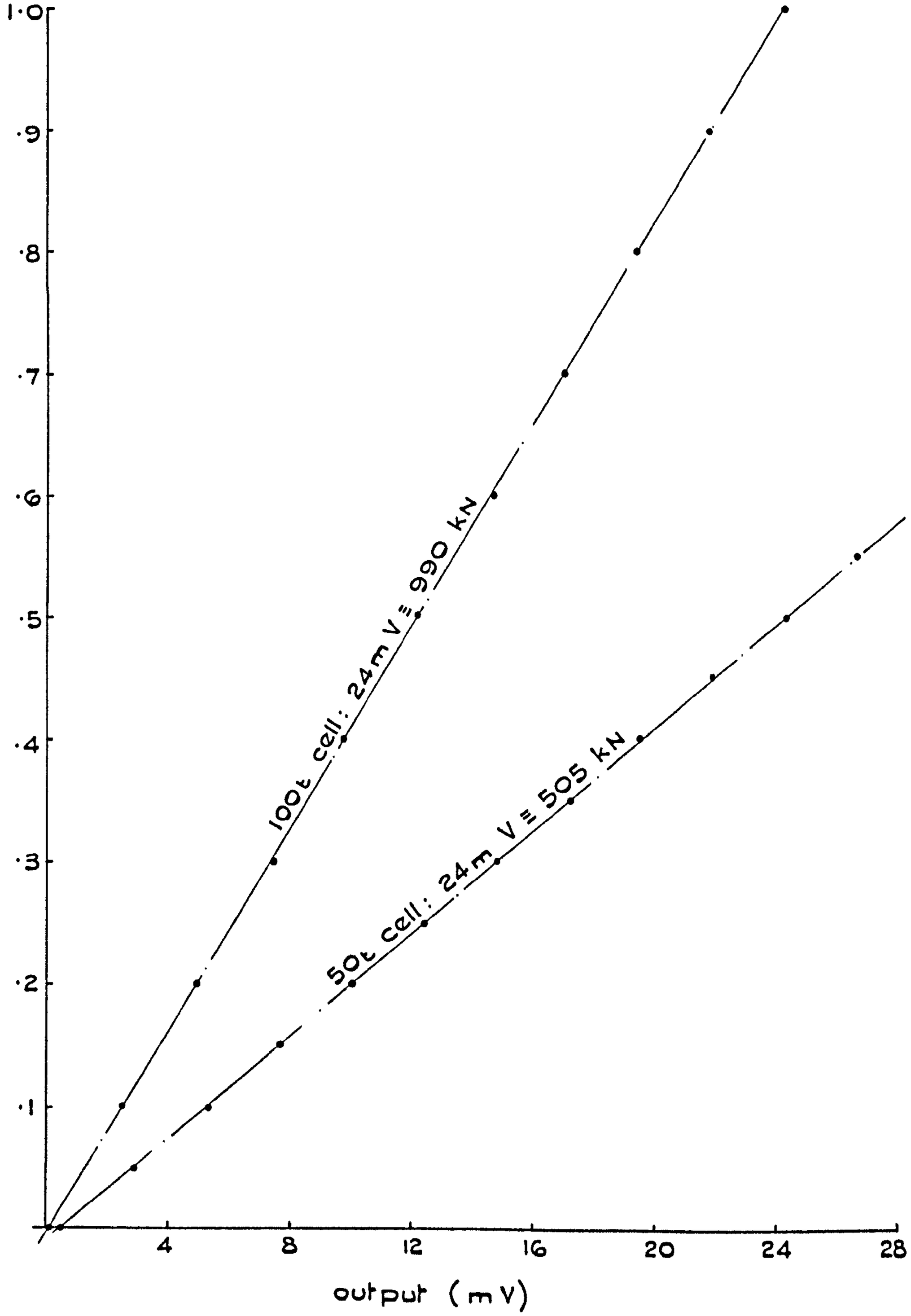

FIG. 8.19 CALIBRATION OF LOAD CELLS FOR PG TESTS

CHAPTER 9

ANALYSIS AND DISCUSSION OF TEST RESULTS

9.1 Introduction

In this chapter, the results of the PG series of tests are considered in order to determine a satisfactory collapse model for composite plate girders subjected to high shear ratios. It is shown that an established model for plain steel girders provides a satisfactory basis for further development, and the modifications required to allow for the presence of the concrete slab in composite beams are discussed.

A method of designing composite plate girders subjected to combined shear and hogging moment is then proposed. Finally, existing design rules for plain steel girders are discussed, and it is shown that they may be applied to composite girders with only slight modification.

9.2 Accuracy of results

9.2.1 Experimental results

The calibration test on the load cell showed it to be accurate to better than 0.5% of the maximum load. The use of knife-edge bearings permitted accurate positioning of the applied loads, and it is estimated that the shear force and bending moment derived from the load cell reading would be within 1% of the true values at the instant the measurement was taken.

The terms "ultimate load" and "maximum load", as used in this thesis, refer to the greatest load that the beam can sustain for an indefinite period of time. However, due to dynamic effects in the beam and the test rig the beam may develop instantaneously a load which exceeds the ultimate load, so test results can only give an estimate of the latter. It lies somewhere between the maximum recorded load and the load at the previous load stage, which was sustained while all readings were taken.

The error in estimating the ultimate load was minimised in Tests PG1 to PG3 by increasing the jacking force slowly as the beam approached failure, and monitoring the load cell readings constantly for any rapid reduction in load. Estimated values of the ultimate load of Beams PG1 to PG3 are thought to be accurate to within 2% - allowing for non-linearity of the load cell and errors in measuring the positions of the applied load.

Small variations in the strength of the three steel beams used for PG1 to PG3 are to be expected, but these were kept to a minimum by having all the girders fabricated at the same time by a firm with considerable experience in large-scale structural steelwork.

The ultimate load of the end panels of PG2A and PG3A was lower than that of the test panels. The higher shear force sustained by the test panels is too consistent to be ascribed to random deviation, and it is concluded that V_u for the end panels is unrealistically low. Draw-in of the end vertical stiffeners due to a lack of horizontal continuity and, in the case of PG2A, local effects due to the concrete slab terminating at mid-length of the panel, would account for this.

The onset of plasticity has been judged from e.r.s.g. readings which, of course, can only give information for specific locations. Reference is made to previous research on plain steel girders for more detailed information in this respect. Strain readings are accurate to within 2×10^{-5} (see Section 4.2.1) so the load at which yield occurs at the position of each gauge may be judged with insignificant error.

Strain gauge readings are also used to determine the average shear strain in the web before the onset of plasticity, and the accuracy of these will be affected by buckling in the web. Measurements of out-of-plane deflections show that the shear strain derived from readings of an individual gauge rosette may be in error by as much as 6 - 7%. For all beams except PG1A, however, web strains were measured by a vertical

column of gauges, so that convex out-of-plane bending at some gauge locations was balanced by concave bending at others. The error in the average web shear strain will therefore not exceed about 2%.

Deflections of the steel girder and the slab were measured with dial gauges mounted on a non-rigid frame (Fig.7.9), and errors would therefore accrue due to friction in the bearings of the frame. The deflected shapes of the girders are thought to be accurate to within 0.2mm which is satisfactory because they are not used in any quantitative analysis. The vertical separation of the girder and slab is determined from the difference in deflections recorded by adjacent dial gauges, the relative deflection of which would be very small. The plots of vertical separation should therefore be accurate to within .02mm.

9.2.2 Theoretical analyses

All theoretical analyses in this chapter are based on the measured yield stress of the component plates of the girders. An average value for E of 207kN/mm^2 has been used, and Poisson's ratio for steel was taken as 0.3. A yield stress of 430N/mm^2 was used for the longitudinal slab reinforcement, which is within 2% of the values determined by coupon tests. Properties of the concrete slab are not required.

The effects of residual stresses and initial imperfections of the web are not considered. This is thought to be reasonable because these phenomena were ignored in all the work reported in Section 6.2, without impairing the close agreement of theoretical predictions and experimental observations. Dead load accounts for less than 0.5% of the stresses at the ultimate load in Beams PG1 to PG3, so this also has been ignored.

9.3 Discussion of test results

9.3.1 Elastic response

The non-linear response of the girders which is evident in Figs.8.1

to 8.3 is to be expected because tension cracks form in the slab at low load, and lead to a gradual loss of stiffness as the cracked zone spreads outwards from the central support with increasing load. During parts of the loading history when no extra cracks form, either because the beam is being loaded for the second time or because there is no slab at all, the V-δ plot should be linear: Figs.8.1 to 8.3 show this to be the case.

A full-interaction elastic analysis has shown that shear strains account for approximately 40% of the total deflection of Beams PG1 to PG3 in their original condition. Adding heavy diagonal braces in one or more panels will significantly decrease the total shear deflection of the beam, and this explains why the apparent stiffness of Beams PG2A and PG3A is greater after the end panel has failed (and been stiffened) than before. It also explains why Beams PG1B and PG2B are as stiff as PG1A and PG2A, respectively, even though cracking in the slab was more extensive when the "B" end of each girder was tested.

Equation 6.9 has been used to calculate the theoretical shear force in the composite beam, V_{cr}, which causes elastic buckling in the webs of PG1 to PG3. It was found to lie in the range $0.47V_y$ to $0.54V_y$, the variation being due to the different depths of concrete slab on some of the girders which means that different loads must be applied to them in order to develop the same shear and bending stresses in the web.

In practice, initial imperfections in the web cause out-of-plane deflections to increase gradually with load, making it impossible to determine the elastic buckling load from experimental results. This was the case in Beams PG1 to PG3 (see Fig.8.12), but it is clear that web buckling is not significant until the load is almost double the calculated buckling load. The same behaviour was noted in other tests on plain steel girders with web-slenderness ratios of approximately 130[54,71].

9.3.2 Onset of plasticity

A full interaction analysis has been used to calculate the loads at which various elements of the composite beam are expected to yield, and the results are listed in Table 9.1. Concrete in tension has been ignored.

Discounting failure of the end panels for the present, yielding of the tension flange adjacent to the support stiffener occurred at a lower load than expected in all beams except PG3A. This was the plain steel girder, and the discrepancy is believed to be due to the existence of local hogging curvatures in the flange imposed by tension field action. In the composite beams, slip at the interface of the steel girder and the slab accounts for the higher strain measurements than calculated from full-interaction theory.

However, yield occurred in the top reinforcement of the composite beams at a load so much lower than expected that slip alone cannot be held responsible. The difference indicates the presence of local hogging curvature in the slab when the beam reaches its ultimate load, and is consistent with the presence of compressive strains in the soffit of the steel flange as described above. Compressive strains in the flange soffit will delay the onset of yield here, so the effect of slip in decreasing the load to produce plasticity in the flange is greater than is immediately apparent from the difference in the measured and calculated yield loads.

The spread of plasticity in the webs of PG1 to PG3 is, as far as could be determined from the strain gauge readings, the same as that reported in Chapter 6 for plain steel beams. Yield in diagonal tension was detected either just before or just after the ultimate load was reached, but this variation is to be expected because the margin in load between the web yielding and a plastic collapse mechanism forming is apparently small[47].

9.3.3 Behaviour at and beyond ultimate limit state

9.3.3.1 Uplift and deformation in the tension flange

The main cause of vertical separation of the concrete slab and the steel beam in Beams PG1 to PG3 is the development of the diagonal tension field in the web. It is resisted by bearing of the concrete against the underside of the head of the shear studs and, partly, by friction between the stud shank and the surrounding concrete.

The extent to which the slab and the steel girder act compositely with respect to vertical deformations of the flange is therefore closely related to the vertical strength of the shear connection. In Beam PG1 the shear connectors were designed to the stringent requirements of BS5400, and even though no specific allowance was made for uplift forces, the separation of the girder and slab remained small even when the ultimate load was applied (Fig.8.16). This resulted in the regions of severe sagging and hogging curvature in the slab, shown in Fig.8.4.

In PG2 the shear connection over both test panels was much weaker than in PG1, and the large separation of the slab and girder is not surprising. However, it does not follow immediately that the connectors should be designed to allow for uplift forces specifically: the value of doing so depends on the effect of large separations on the ultimate load of the composite beam, and is discussed later in this chapter.

In Beam PG3B, the vertical pull-in of the tension flange is of the same order as that in PG1A, yet the separation of the slab and girder is much larger. The arrangement of the shear connectors is identical in the two beams, so this indicates that the slab of PG3B offers greater resistance to the development of severe sagging and hogging curvature. This is as expected, because the prestress in the steel beam before casting the slab will reduce the extent of flexural cracking at a specified load, compared with a non-prestressed beam such as PG1A. The greater flexural

strength of the slab is, apparently, not counteracted by greater resistance to separation, and this agrees with the work done by Arnaouti[72], who showed that flexural cracking in the slab of a composite beam has no effect on its punching shear strength.

The plastic hinges which formed in the steel flanges of Beams PG1 to PG3 led to a shear-sway mode of collapse similar to the one proposed for plain steel girders (Fig.6.3a). There was surprisingly little variation in the position of these hinges, bearing in mind the differences in the flexural strength of the tension flange implied by the degree of vertical separation. For all three beams the sagging hinge in the tension flange fell within a distance of 0.44b to 0.52b from the support stiffener (Fig.8.4). Nor was the variation consistent: in PG1B the hinge formed closer to the support stiffener than in PG2A, where the tension flange was much weaker with respect to vertical forces.

The results of PG1 to PG3 therefore indicate that the resistance of the shear connectors to uplift has little effect on the position of the plastic hinges in the flanges, and that the small variation observed in these tests was probably due to random variations between the test specimens.

9.3.3.2 Web buckles

The inclination of the buckles to the flanges in PG1A and PG1B is noticeably larger than in the other composite beams due to the improved resistance of the shear connection to vertical separation. This increases the resistance of the tension flange to vertical loads, and attracts a greater proportion of the stresses in the tension field. In Beams PG2 and PG3B the considerable separation of the slab and girder causes a loss of composite action with respect to bending of the flange, and the inclination of the buckles is approximately equal to that in PG3A - the plain steel girder.

9.3.3.3 Slab behaviour

If local curvatures in the slab in the region of the plastic hinges become so severe that compression develops in the concrete, a considerable shear force will be required in the slab to maintain equilibrium, and this will add to the ultimate shear strength of the composite girder.

Strains in the top layer of reinforcement above the support stiffeners increased indefinitely as rotation occurred in the adjacent hogging hinge, as would be expected, but tensile strains in the lower layer of bars also increased and sometimes exceeded the yield strain, indicating that compression did not develop here. A normal plastic analysis of the assumed section of Fig.9.1 confirms this, for the neutral axis with respect to local bending is found to lie in the steel flange.

Crack width measurements on top of the slab at the sagging hinge show that for all beams except PG2A compression occurs there when large rotations develop. The reversal of slip both at the free end of the slab, and at point A in Fig.8.4 confirms this, but the beam deformation at this stage is so large that it would be unrealistic to allow for compression in the slab when calculating the ultimate load of the girder. Tensile strains in the lower layer of reinforcement at point A approached yield values at large deformations, indicating that these bars almost certainly yielded in tension at the mid-panel hinge where, apart from Beam PG2A, sagging curvatures were much greater.

9.3.3.4 Ultimate loads

The ultimate load of the test panels of Beams PG1 to PG3 has been derived as explained in Section 9.2 and the results are listed in Table 9.2. Fig.9.2 is an interaction diagram on which the coexistent shear force (V_u) and the maximum panel moment (M_u) at the ultimate limit state are plotted in terms of V_y and M_{pg} of Beam PG1. For composite 'T' beams,

M_{pg} is defined as the full plastic moment of the girder, including the reinforcement but ignoring concrete in tension. The various theoretical relationships plotted in Fig.9.2 will be described in due course.

There is very little variation in the ultimate load of Beams PG1 to PG3. Using a concrete with a cube crushing strength of 50N/mm^2 (PG1B) instead of 30N/mm^2 increases the ultimate load by 2%, and omitting the slab altogether (PG3A) reduces it by 2.5%. However, prestressing the steel beam, increasing the depth of the slab, or reducing the shear connection to the extent that considerable separation develops between the slab and the steel girder, had a negligible effect on the ultimate strength of the composite beam. These results will be discussed at length in the following sections, when realistic methods for calculating the strength of composite plate girders have been derived.

9.4 Ultimate strength of composite girders subjected primarily to shear

9.4.1 General

It is beyond the scope of this project to conduct a detailed investigation of the behaviour of plain steel plate girders, so one of the existing design methods described in Section 6.2 has been used as a basis for further development. That developed by Rockey et al[48-51,62-64] was chosen for several reasons: the assumed failure mode was the same as that in Beams PG1 to PG3; the behaviour of steel girders was thoroughly investigated and described in a series of reports; and calculations based on the design method correlate well with test results.

The elements that contribute to the shear strength of plain steel girders may be identified by combining Equations 6.1, 6.4 and 6.5 as follows:

$$V_{ult} = V_{cr} + 2c_c\ t\ \sigma_{ty} \sin^2\beta + \sigma_{ty}\ t\ d(\cot\beta - \cot\beta_d) \sin^2\beta \qquad (9.1)$$

The three terms in the expression for V_{ult} are, in order, the shear

buckling load and the loads due to the tension field supported by the flanges and the vertical stiffeners. A fourth term which is usually ignored in the case of steel girders, but which may be significant in composite construction, is the shear strength of the flanges.

9.4.2 Shear force in the slab

Four stages in the behaviour of the slab of a composite beam may be identified, as follows:

Stage 1 When the concrete slab is uncracked, a normal elastic analysis may be used to calculate α_u, the proportion of shear taken by it. This has been done for Beams PG1 to PG3, assuming full interaction, and the results are shown in Table 9.3. The proportion of shear is constant throughout the length of the composite beam.

Stage 2 When cracks have formed in the slab, an elastic analysis may still be used to determine α. Consider Fig.9.3a which illustrates the forces acting in a cracked composite beam subjected to combined shear and bending. Full interaction is assumed, but the slab and girder are shown separated for clarity.

Equilibrium dictates that:

$$\alpha_c = (\delta R_1 \, h_1 + \delta R_2 \, h_2)/V \, s \qquad (9.2)$$

where: α_c = value of α calculated on the basis of a cracked section;

R_1, R_2 = force in the top and bottom layers of reinforcement, respectively, at the section considered;

h_1, h_2 = height of top and bottom layers of reinforcement, respectively, above the slab soffit;

s = distance as defined in Fig.9.3a.

This formula has been used to calculate the proportion of the total shear carried by the cracked slabs of PG1 to PG3. Values of δR_1 and δR_2 were

derived from a full-interaction analysis, ignoring concrete in tension, and the results are shown in Table 9.3. The slab shear force will be transferred across the cracks by a combination of aggregate interlock and dowel action.

It is now assumed that Section B in Fig.9.3 is sufficiently far away from the nearest crack for the tensile stresses in the slab to have reached the value calculated from a full-interaction, uncracked analysis, so α here is the uncracked value. A total shear force of $(\alpha_u - \alpha_c)V$ must therefore be transferred to the steel beam over any length BC, and the proportion of the shear force carried by a slab varies between the limits α_u and α_c, dependent on the extent of cracking.

Stage 3 The onset of plasticity in the slab reinforcement marks the beginning of Stage 3. Yield will occur first in the zone subjected to the largest bending moment, so when this region reaches Stage 3 other parts of the slab will still be at Stage 2.

The slab reinforcement may yield in tension as a result of local bending due to tension field action, or global bending, or a combination of the two. As noted in Section 6.3, Johnson and Willmington have shown that if the reinforcement yields over the length PQ (Fig.9.3b) the slab takes no shear force in this region, and shear transfer occurs at P.

Stage 4 This is reached when severe deformations develop in the slab due to the formation of the shear-sway mechanism of Fig.6.12. Test results (Section 9.3.3.3) indicate that the forces acting on the slab are as shown in Fig.9.4a. F_y is the force to cause yield in tension in either the top or bottom layers of reinforcement, and F_{cs} is a compressive force in the slab.

Uplift forces develop at B and are balanced by vertical compressive forces between the girder and slab at A and C. Since these are unknown for Beams PG1 to PG3, the proportion of the shear force carried by the

slab cannot be calculated accurately. However, if it is assumed that the vertical forces P_c and P_t are equal in magnitude to αV, and act at the position shown, α may be estimated. Taking the resultant of F_{cs} and F_y to be the plastic moment of resistance of the reinforced concrete slab acting alone, gives:

$$\alpha_A V = \alpha_B V = 48kN; \quad \text{and}$$

$$\alpha_G V = 96kN$$

where: $\alpha_{A,B,G}$ = the proportion of the total shear force carried by the slab at locations A, B and G respectively.

From the discussion in Section 9.3.3.3, the composite beams tested in the PG series had reached Stages 2 and 3 at their ultimate limit state, and the problem of calculating the shear force in the slab resolves to one of determining which value of α is appropriate, and where shear transfer occurs due to yielding of the slab reinforcement.

Measurements of strain in the webs of the girders have been used to determine the shear force in the steel beam, and better correlation with these results is obtained if the uncracked value of α is assumed in theoretical calculations.

Small variations in the location of shear transfer will not be crucial, because the extra force applied to the girder here will seldom exceed 10% of the total, and will usually be as low as 4 - 5%. For composite beams which fail in the shear-sway mode, the top layer of reinforcement yields due to hogging curvatures imposed by tension field action, but this plastic zone will not extend further than the mid-panel section because local sagging develops there. The conservative assumption that shear transfer occurs at the position of the sagging hinge is therefore made, and the forces acting on the girder and slab are shown in Fig.9.4b.

The effect of this assumption is that in any upper-bound analysis based on the collapse mechanism of Fig.9.4, the entire shear force is taken by the steel girder. Such an analysis would be an approximation of a true upper-bound solution, since it depends on the top layer of reinforcement at B being at yield in tension, even though a sagging hinge is forming there: the two conditions are not compatible.

Later in this chapter, an estimate of the lower-bound solution is found by considering the equilibrium and yield criteria at Section BE in Fig.9.4b. The slab shear force is taken as acting to the right of this section (otherwise it would not be a critical one) so the region ABEF of the steel girder must resist the total applied shear force.

9.4.3 Shear strength of the steel girder

9.4.3.1 General

The shear force resisted by a plain steel girder may be obtained from Equations 6.9 to 6.19, but these will be modified slightly by the presence of the concrete slab, as follows.

9.4.3.2 Critical buckling load

As noted in Section 6.2.2, all researchers agree that

$$V_{cr} = \tau_{cr}\, d\, t \qquad (9.3)$$

but opinions differ concerning the support conditions at the edges of the web. Since the flanges of most girders are torsionally very stiff compared with the web, the addition of a concrete slab to the tension flange is unlikely to make much difference in this respect. The conservative assumption that the web is simply supported all round is now made, to balance the unsafe assumption that the buckling load is not affected by initial imperfections in the web.

The neutral axis in composite beams is usually above the mid-depth

of the web, which is therefore subjected to a combination of bending, shear and global compressive stresses. The critical shear stress is therefore obtained from Equation 9.4, rather than Equation 6.9:

$$\frac{\sigma_a}{\sigma_{acr}} + \left(\frac{\sigma_m}{\sigma_{cr}}\right)^2 + \left(\frac{\tau_m}{\tau_{cr}}\right)^2 = 1 \qquad (9.4)$$

where: σ_{acr} = $4(\pi^2 E/12[1 - \nu^2])(t/d)^2$, which is the critical axial stress of a panel subjected to pure compression;

σ_a = the net compressive stress at the mid-panel section which results in buckling in the presence of bending and shearing stresses.

Values of σ_m and σ_a are derived on the assumption of full-interaction between the slab and girder, ignoring concrete in tension. When calculating τ_m, allowance must be made for the shear force in the concrete slab, as follows:

$$\tau_m = V_{cr}(1 - \alpha_u)/t\ d \qquad (9.5)$$

9.4.3.3 Plastic moment of resistance of the flanges

As noted in Section 6.2.4.2, it is not clear whether M_p should be based on the flange alone, or on an effective 'T' section comprising the flange and part of the web, so both methods have been applied to the plain steel girder, PG3A.

If M_p is calculated for the flanges alone, Equations 6.9 to 6.19 may be used without modification. Taking β as equal to the measured inclination of the web buckles leads to calculated values of c_c, c_t and V_u which are considerably less than those observed in the test on Beam PG3A, indicating that M_{pc} and M_{pt} are underestimated.

As noted in Section 6.5, Reference 69 recommends that M_p is taken as the plastic moment of resistance of a 'T' section comprising the flange and a depth of web equal to $12t_w(355/\sigma_{yw})^{0.5}$. If M_{pc} and M_{pt} are so

defined for PG3A, satisfactory agreement between theoretical and experimental values of V_u, c_c and c_t is obtained. M'_{pc} and M'_{pt} for a 'T' beam are calculated not from Equations 6.13 and 6.16, but in the manner shown in Fig.9.5. Subject to the neutral axis of the section being in the flange, this gives the following equation:

$$M'_{pc} = M_{pc} - F'_c/4\sigma_{yf}\, b_f \qquad (9.6)$$

$$M'_{pt} = M_{pt} - F'_t/4\sigma_{yf}\, b_f \qquad (9.7)$$

In composite girders it will be conservative to ignore the increase in M_p afforded by the concrete flange, but not unduly so for several reasons. As noted, flexural cracks do not close up until the deformation of the beam is excessive, so the strength of the slab lies almost entirely in its reinforcement. Also, it is doubtful if the shear connection in a composite beam is sufficiently stiff to ensure full-interaction of the slab and the tension flange in the region AB of Fig.9.4b (the slip readings in PG1 to PG3 confirm this); but even if it were, the positive work done by the reinforcement at A would be balanced to some extent by the negative work at B. There is further experimental evidence that the assumption of full interaction of the flange and the reinforcement when calculating M_{pt} is optimistic. If this is done, M_{pt} is larger than M_{pc}, and because σ_{ty} is less in the region of the tension flange than it is near the compression flange, c_t should then be much greater than c_c. Fig.8.4 shows that this is not the case.

It follows from the assumption that the slab reinforcement yields over the length AB (Section 9.4.2) that the slab is unable to resist any transverse forces applied to the flange due to tension field action. This is consistent with the results of PG1 to PG3, in which large variations in the slab dimensions and the effectiveness with which vertical separation at the girder-slab interface was prevented, were seen to have minimal

effect on the position of the flange hinges. It is therefore recommended that the slab be ignored when calculating the full plastic moment of resistance of the tension flange.

Nonetheless, the presence of a concrete slab generally increased c_t in PG1 to PG3 (see Fig.8.4). This is because the tensile stress in the reinforcing bars at B will contribute to the flange force required to maintain equilibrium (F_t in Equation 6.15), so the reduction in M_{pt} due to the axial stress in the steel flange will be less if a concrete slab acts compositely with the steel girder. The results of PG1 to PG3 indicate that at the ultimate load the lower reinforcing bars yield in tension while the strain in the upper bars diminishes slowly. Bearing in mind the conservative approach in calculating M_{pt}, and the earlier assumption that both layers of reinforcement yield over the length AB, it is reasonable to take the tensile force in the slab as $A_r f_{yr}$.

The revised system of forces acting on BE of Fig.6.9 is shown in Fig.9.6. Consideration of the vertical, longitudinal and rotational equilibrium gives the following expressions for F_c and F_t:

$$F_c = V_u(d \cot\beta/2 + Z + [c_c - c_t]/2)/d + (M'_{pt} - M'_{pc} + F_w q - M_w)/d$$
$$- (V_{cr} \cot\beta/2 + \tau_{cr} t[b - c_c - c_t]/2) + F_r(0.5 - h_r/d) \qquad (9.8)$$

$$F_t = V_u(-d \cot\beta/2 + Z + [c_c - c_t]/2)/d + (M'_{pt} - M'_{pc} + F_w q - M_w)/d$$
$$+ (V_{cr} \cot\beta/2 + \tau_{cr} t[b - c_c - c_t]/2) - F_r(0.5 - h_r/d) \qquad (9.9)$$

where: F_r is the resultant of the forces in the reinforcing bars, assumed to be at yield in tension;

h_r is the lever arm of this force about the mid-depth of the web.

V_{cr}, τ_{cr} and M_w are the values calculated for the composite beam as described in Section 9.4.3.2.

In Beams PG1 to PG3, F_t is in the order of 1MN, and the yield force of the slab reinforcement for all the composite beams is approximately 400kN. The reduction of the full plastic moment of the tension flanges due to axial force is therefore almost equal for all the composite beams tested, and less than the reduction in the plain steel girder. In accordance with Equation 6.17, c_t should therefore be almost the same for all the composite beams, and greater than c_t for the steel beam. This correlates well with experimental results.

9.4.3.4 Inclination of the yield band

Evans et al[62] recommended that for any particular girder subjected to a given combination of loading, β be taken as the value that maximised the ultimate load (β_o). This method has been applied to Beams PG1 to PG3, using the following iterative approach:

(i) Estimate values of c_c and c_t.

(ii) Determine F_w and q from the membrane stress distribution, as given by Equation 6.10.

(iii) Calculate V_u from Equation 6.11. Since the slab is assumed to take no shear over the length AB, V_u is the total shear strength of the composite girder.

(iv) Calculate the average axial force in the compression and tension flanges from Equations 9.8, 6.12 and 9.9, 6.15 respectively.

(v) Obtain M'_{pc} and M'_{pt} from Equations 9.6 and 9.7, basing M_p on the effective 'T' section as described in Section 9.4.3.3.

(vi) Calculate new values for c_c and c_t, and repeat until convergence is obtained.

Various shear ratios were assumed, and for each several different values of β were used. The maximum value of V_u for each load combination was then plotted on the interaction chart of Fig.9.2.

Two curves are shown. One represents the plain steel beam (PG3A) in

which F_r is of course zero, and the other is applicable to all the composite beams. This is possible because the longitudinal reinforcement in each slab was identical, and its height above the steel flange varied only slightly between beams; it correlates well with the very small variation in the experimental ultimate loads of the composite beams. The variation in β_o as the shear ratio decreases is indicated by the figures adjacent to each interaction curve.

Although there is excellent agreement between the calculated and experimental ultimate loads for the test panels of PG1 to PG3, c_c and c_t are usually overestimated, and β_o is always less than the measured inclination of the web buckles. These differences are listed in Table 9.4, in which it is implicitly assumed that the experimental value of β_o is the inclination of the web buckles.

Further analyses have been conducted using the procedure above, but taking β_o as the measured inclination of the web buckles. Calculated values of V_u, c_c and c_t are different for each beam, and are compared with experimental values in Table 9.5. Each term is seen to be underestimated.

Two questions therefore arise: why are the inclinations of the web buckles in PG1 to PG3 so large, and are these necessarily the same as the inclination of the yield band?

We consider a plate girder subjected to pure shear, as shown in Fig.9.7. As noted in Chapter 6 buckling will first occur at an angle of 45° to the flanges, because the maximum tensile and compressive stresses in the web are at 45° and 135° respectively. A small increase in load will be taken by direct tension at an angle of 45°, but because the regions AB and DE are better anchored against lateral forces, there will be a small concentration of tensile force there relative to the regions BC and EF. The stresses acting on an inclined element of the web are therefore as shown in Fig.9.7b, and these result in the directions of

principal stress rotating by an amount $\delta\beta$. The buckles will re-orientate themselves to the new direction, and the process will repeat itself, with the inclination of both the tension field and the buckles gradually decreasing by equal amounts as the load increases. The process cannot continue indefinitely, of course, for a stage is reached when further reduction of the angle of the tension field would lead to a reduction of the vertical component of the force therein, and β has then reached its optimum value. If there is a sufficiently large difference between the buckling and ultimate loads (as in very slender webs) this optimum value will be attained. Porter et al[51] tested girders with web slenderness ratios between 250 and 400 and found that the inclination of the web buckles was very nearly equal to the calculated value of β_o, which varied between 20^o and 40^o.

The above argument indicates that for plate girders with relatively compact webs, the inclination of the web buckles may never attain the value β_o, and this is certainly the case with Beams PG1 to PG3, where d/t = 130. References 54 and 71 describe tests on plain steel girders with similar slenderness ratios, in which the web buckles formed at approximately 45^o to the flanges.

In PG1 to PG3, serious buckling did not occur until the ultimate load of the beam was exceeded, and it is possible that the angle $\delta\beta$ in Figure 9.7b was quite large at the maximum load. The inclination of the yield band in these tests is therefore not known accurately: but Fig.9.2 shows that good agreement with the experimental ultimate loads is obtained if it is assumed to equal β_o, while Table 9.5 shows that the ultimate load is underestimated if it is taken as equal to the inclination of the buckles. The first of these methods is seen to overestimate the values of c_c and c_t (Table 9.4) as would be expected, because assuming a low value of β results in a low value of the vertical forces on each flange. The second

method uses a high value of β and is therefore expected to underestimate c_c and c_t, which Table 9.5 shows to be the case.

9.5 Design method for composite plate girders

Steps (i) to (vi) in Section 9.4.3.4, repeated for several values of β to find the optimum one, constitute a design method for composite plate girders subjected to combined shear force and hogging moment. The limitations to its use are now discussed.

The method is not applicable to beams where the web yields before it buckles, because the yield band would then extend over the full width of the panel and all four flange hinges would form adjacent to the vertical stiffeners, as described in Section 6.2.2. This would invalidate the equilibrium equations on which the design method is based. Calladine[58] has shown that for plain steel girders with a slenderness ratio less than 100, the assumption of plastic buckling leads to better predictions of the ultimate load than does the assumption of elastic buckling and the consequent collapse mode of Fig.6.9.

For plate girders with very slender webs (d/t greater than 200, say) buckling will occur at an early stage of the loading history, and this will result in greater vertical forces on the flanges than were present in PG1 to PG3. The possibility of excessive separation of the steel tension flange and the slab then arises. Test results showed, however, that wide variations in separation caused a negligible change in the ultimate strength of the girder, which suggests that the design method is suitable for all slenderness ratios above 100 which are likely to be used in practice.

Equations 9.6 to 9.9 are based on the slab behaviour observed in Tests PG1 to PG3, where the applied moment was such as to cause wide flexural cracks at the ultimate load. When the shear ratio is high, such

cracks will be narrow or might not form at all, in which case the distribution of stresses in the slab will be different from that assumed. The loading arrangement for PG1 to PG3 was such as to represent a girder with a point of contraflexure distance 1.9h from the support, so if a typical span:depth ratio of 25 is taken, the point of contraflexure is 0.08 x span away from the support. It is therefore unlikely that the problem of high shear ratios will occur in practice.

As the shear ratio decreases, a stage is reached when the axial forces are so large they cause yielding of one or both of the flanges in either global compression or global tension. The flange is then unable to resist any lateral load, so that c_c or c_t will be zero, and the forces and moments acting on Section BE of the girder will be as shown in Fig.9.8. A further decrease in the shear ratio leads to a bending mode of failure, and the design method is no longer valid. The critical moment, M_R, is the sum of several terms, as follows:

(i) the moment of the yield force in the reinforcement about the mid-depth of the web;

(ii) the moment of the flange forces, F_c and F_t about the mid-depth of the web. One of these will be equal to the yield load of the effective section under pure axial load;

(iii) the moment exerted by the yield band, equal to F_w q;

(iv) the elastic critical moment in the web, M_w. It is the superposition of the diagonal stresses due to tension field action on the direct stresses due to M_w which lead to the formation of a diagonal yield band;

(v) the reduced plastic moment of resistance of the flange which has not yielded under the influence of the pure axial load.

The moment obtained by summing these terms must be corrected in the ratio of $Z:(Z + b + [c_c - c_t]/2)$ to find the required value of M_R at mid-length of the panel. Values of M_R for Beams PG1 to PG3 have been calculated,

and are plotted in Fig.9.2.

Of particular interest to designers is whether the moment capacity of a girder is reduced by shear, and whether the composite action between the slab and the girder is destroyed by tension field action. In PG1 to PG3 the strength of the shear connection in the region of the test panel varied from zero (PG2B) to that required by the stringent clauses of BS5400, Part 5 and yet the slip never exceeded 0.6mm at the maximum load. This compares with a slip of approximately 2.5mm at the ultimate load of the stud, and indicates that the slab is still acting compositely with the beam. Measurements of strain in the reinforcement at A in Fig.8.4 confirm this, for both layers of bars yield in tension - which would not be possible if composite action had broken down. The moment capacity of the girder is, nonetheless, decreased by the presence of shear forces, as shown by the interaction diagrams of Fig.9.2. Since lateral-torsional buckling was prevented in Specimens PG1 to PG3, Equation 6.7 may be used to calculate the ultimate moment capacity of these beams. This has been done, taking A_f to be the value appropriate to the compression flange and assuming full-interaction of the girder and slab, but ignoring concrete in tension. The results are plotted in Fig.9.2 where they are labelled 'M_{ult}': the reduction in bending capacity is seen to be approximately 14% for the composite beams.

A serious limitation of the proposed design method is its complexity, for steps (i) to (vi) in Section 9.4.3.4 have to be repeated three or four times for each β. However, it is a straightforward process to write a computer program which will calculate V_u for an assumed value of β, so that the maximum V_u may rapidly be found. Such a program is within the capabilities of the more powerful programmable "pocket" calculators introduced by various manufacturers during 1978-79: the interaction curves in Fig.9.2. were derived in a morning with the aid of a Texas

Instrument TI59.

9.6 Implications for design recommendations

The recommendations considered here are those in Reference 69, which are described in Section 6.5. Their application to PG3A (the plain steel girder) is straightforward, and the resulting interaction line is shown in Fig.9.9, where it is labelled PQRST. M_{ult} has been calculated from Equation 6.7, since lateral-torsional buckling was prevented. The ultimate loads of Beams PG1 to PG3 are plotted on Fig.9.9 for the purpose of comparison.

V_{ult} is expected to be underestimated by the draft recommendations since the calculations are based on the weaker flange, which in Beam PG3A is the tension flange: no allowance is made for the extra width of the yield band adjacent to the compression flange. The assumption made in the draft recommendations, that the inclination of the yield band is two-thirds that of the panel diagonal, is shown in Fig.9.2 to be a reasonable one.

Point R corresponds to the load at which the limiting force F is reached in the weaker flange. The forces and moments acting on the beam are the ones shown in Fig.9.8a, except that F_r is zero because there is no concrete slab. Reference 69 only allows for the buckling shear force in the web, the yield band supported by the vertical stiffeners and the moment F_t D' when calculating V_R and M_R: the width of the yield band supported by the compression flange, the moment M'_{pc} and the web moment are all ignored. The last term, especially, is significant in all Beams PG1 to PG3, since the webs are relatively compact (d/t = 130), and the result is that the simplified design recommendations in Reference 69 underestimate the ultimate load of PG3A by almost 20% of the true value. This degree of inaccuracy is not really acceptable, and suggests that more sophisticated rules are necessary for plate girders with asymmetrical flanges and relatively compact webs.

Before the interaction diagram of Reference 69 can be applied to composite plate girders, some means of allowing for the effect of the concrete slab must be determined. For the purpose of calculating M_{ult}, this is straightforward, and is covered in Part 5 of BS5400 - see Section 6.5. In the case of Beams PG1 to PG3, Equation 6.7 controls.

Realistic values of M_R and V_R may be derived as follows. Part 5 recommends that the entire shear force in a composite plate girder should be assumed to act on the steel girder, and it was shown in Section 9.4.2 that this is satisfactory for the shear ratios used in practice. It was also shown that when a shear-sway mode of failure occurs, both top and bottom layers of slab reinforcement yield at the section of the maximum panel moment, so that the limiting force in the tension flange now becomes the sum of the yield forces in the effective steel section and the reinforcement. If the conservative assumptions made by Reference 69 in defining M_R are deemed acceptable for the present, M_R may then be calculated from Equation 6.21, bearing in mind that the centroid of the tension flange will be raised by the slab reinforcement.

The draft recommendations assume that neither flange is able to support any tension field action for the purpose of calculating V_R, so the concrete slab will have no effect on this term. Even when allowance is made for the slab reinforcement, the yield force of the tension flange is likely to control in composite beams of practicable dimensions, so it is the width of the yield band adjacent to the compression flange that is ignored when calculating V_R. The errors in V_R will therefore be of similar magnitude for steel and composite beams.

A satisfactory value of V_{ult} is much more awkward to define, and the following discussion is based on the assumption that the slab behaviour is similar to that described in Section 9.4.2. As stated in Section 9.5, the actual behaviour of the slab at very high shear ratios may be quite

different, so V_{ult} as defined below has no physical meaning - it is merely a device for obtaining the ultimate load of composite plate girders subjected to realistic shear ratios.

It was shown in Section 9.4.3.3 that the effect of the slab reinforcement is simply to reduce the axial force in the tension flange: this increases the latter's ability to resist the vertical forces applied by tension field action and hence increases the shear strength of the girder. Any expression which attempts to define an effective M_{pt} for a composite beam must therefore include terms in the yield force of the slab reinforcement, the shape and size of the effective flange section, the yield stress of the flange and the web, and the shear ratio of the loading arrangement. The derivation of such an expression would require an extensive parametric study which is beyond the scope of this thesis. It is suggested that in the absence of any further information, the slab be ignored when calculating V_{ult} for design in accordance with Reference 69. (If this is thought to be too conservative for a specific girder, recourse may always be made to the more accurate, but more complex, design method discussed in Section 9.5.)

The interaction chart for the composite Beams PG1, PG2A and PG3B has been derived in accordance with the rules above and is shown in Fig.9.9, where it is labelled P'Q'R'S'T'. As expected, the same assumptions which cause the ultimate load of the plain steel girder to be underestimated lead to the predicted failure loads of the composite girders being 13% lower than the experimental values. The magnitude of the error is lower for the composite beams than for the plain steel one, because with the higher limiting force in the tension flange of the former the assumption that $M'_{pc} = 0$ when a moment of M_R is applied is nearly correct.

Beam (PG:)	Yield load/V_y		
	Tension flange soffit	Bottom reinforcement	Top reinforcement
1A	0.98	1.51	1.27
1B	0.98	1.51	1.27
2A	0.98	1.51	1.27
2B	1.01	1.38	1.12
3A	0.83	-	-
3B	0.92	1.85	1.61

TABLE 9.1 LOADS TO CAUSE YIELD AT VARIOUS LEVELS IN THE TENSION FLANGE

Beam (PG:)	Brief description	Ult load (kN)	Ult load $\div V_y$
1A	Datum	854	0.964
1B	Strong concrete	884	0.997
2A	Weak shear connection	852	0.961
2B	Deep slab	857	0.967
3A	No slab	829	0.935
3B	Prestressed girder	864	0.975

TABLE 9.2 ULTIMATE LOAD OF TEST PANELS

Beam (PG:)	α	
	Uncracked	Cracked
1A	0.043	0.0085
1B	0.043	0.0085
2A	0.043	0.0085
2B	0.109	0.0191
3B(1)	0.043(V-300)/V	0.0085(V-300)/V

Note: (1) for V expressed in kN

TABLE 9.3 PROPORTION OF TOTAL SHEAR CARRIED BY SLAB (α)

Beam (PG:)	V_u	β_o	c_c	c_t
1A	1.00	0.65	1.03	1.23
1B	0.97	0.63	1.05	1.36
2A	1.01	0.78	1.05	1.23
2B	1.00	0.72	0.98	1.17
3A	0.99	0.74	-	1.31
3B	1.01	0.70	1.03	1.20

TABLE 9.4 RATIOS OF THEORETICAL:EXPERIMENTAL VALUES FOR VARIOUS PARAMETERS, USING CALCULATED β_o

Beam (PG:)	V_u	β_o	c_c	c_t
1A	0.93	1.00	0.80	0.83
1B	0.89	1.00	0.82	0.92
2A	0.98	1.00	0.90	0.98
2B	0.96	1.00	0.79	0.86
3A	0.97	1.00	-	0.96
3B	0.94	1.00	0.83	0.88

TABLE 9.5 RATIOS OF THEORETICAL:EXPERIMENTAL VALUES FOR VARIOUS PARAMETERS, USING MEASURED INCLINATION OF WEB BUCKLES

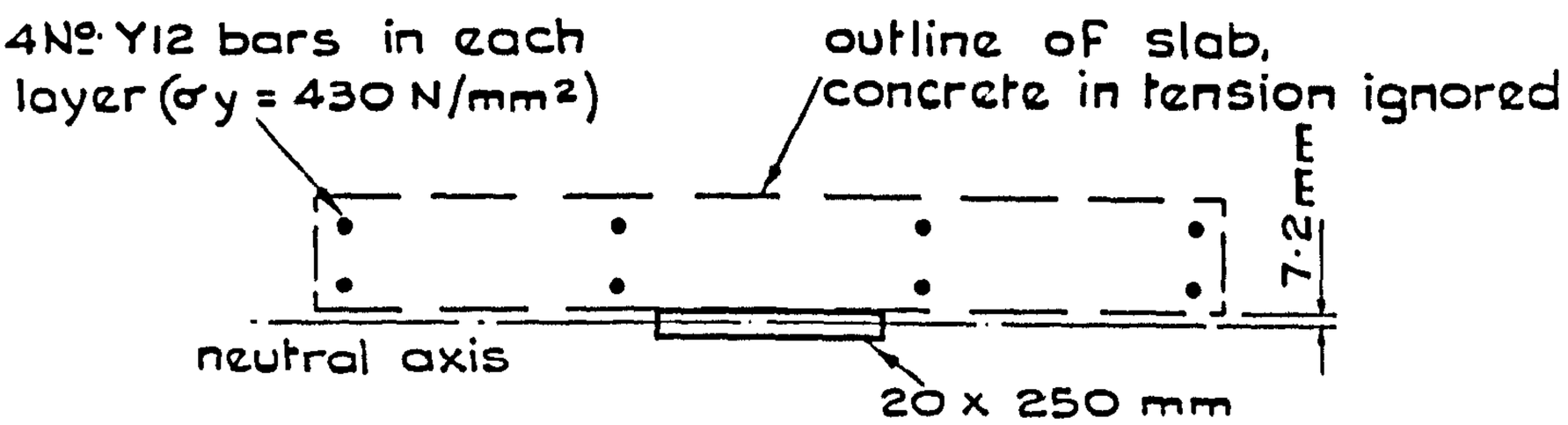

Mp = 27·67 kNm
Full interaction assumed

FIG. 9.1 PROPERTIES OF TENSION FLANGE AT HOGGING HINGE

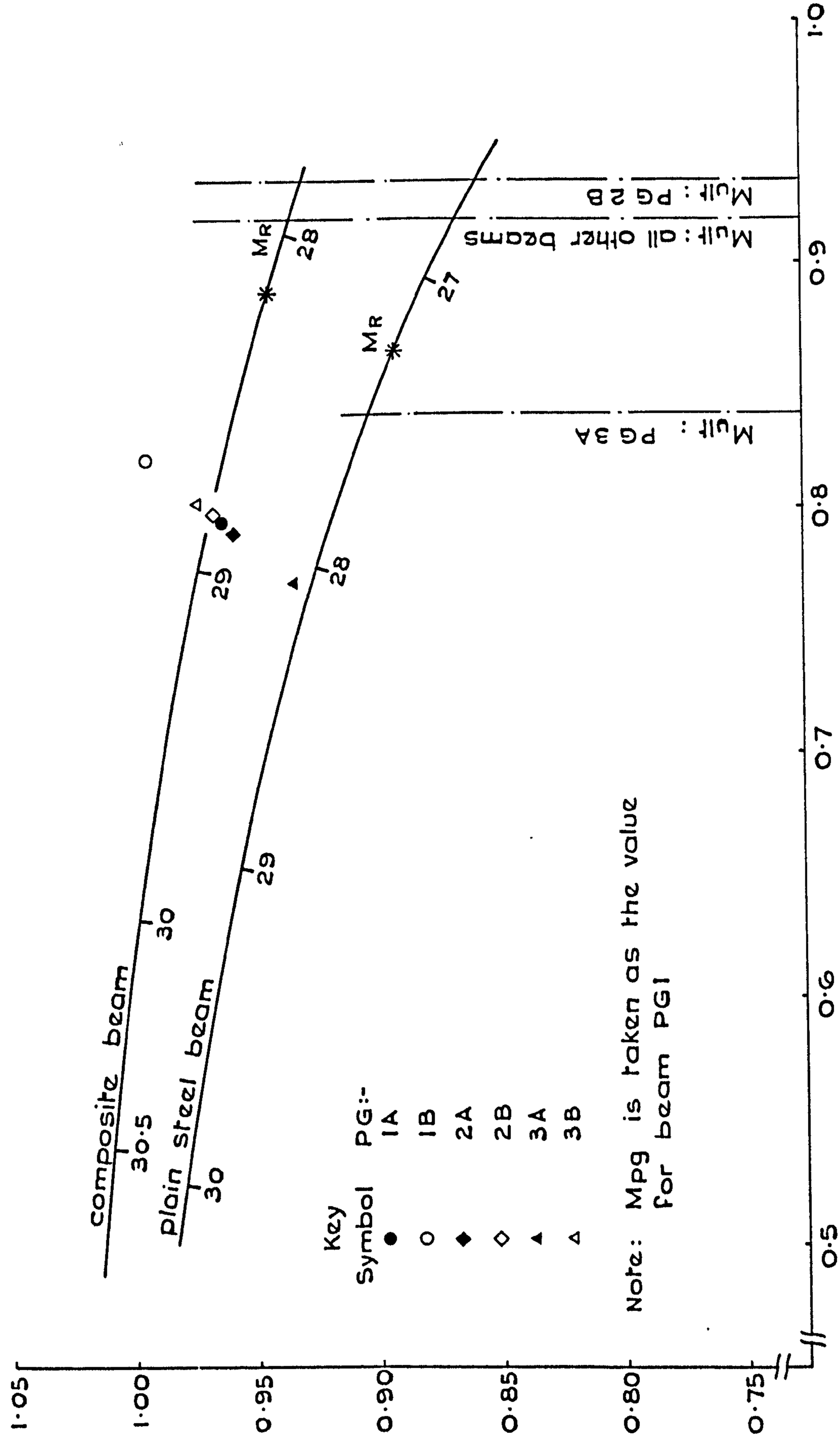

FIG. 9.2 INTERACTION DIAGRAM FOR BEAMS PG1-PG3

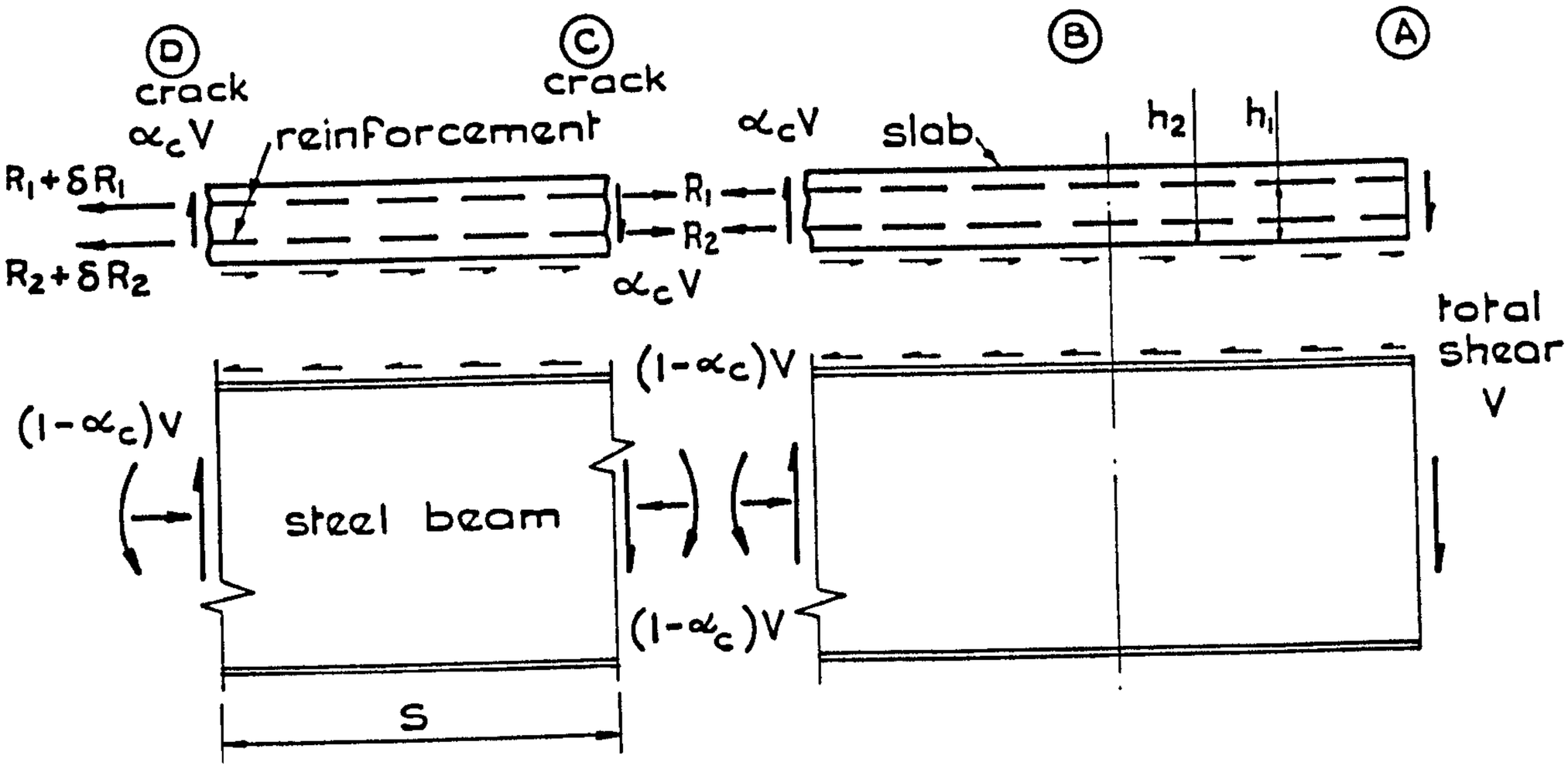

a) Cracked slab

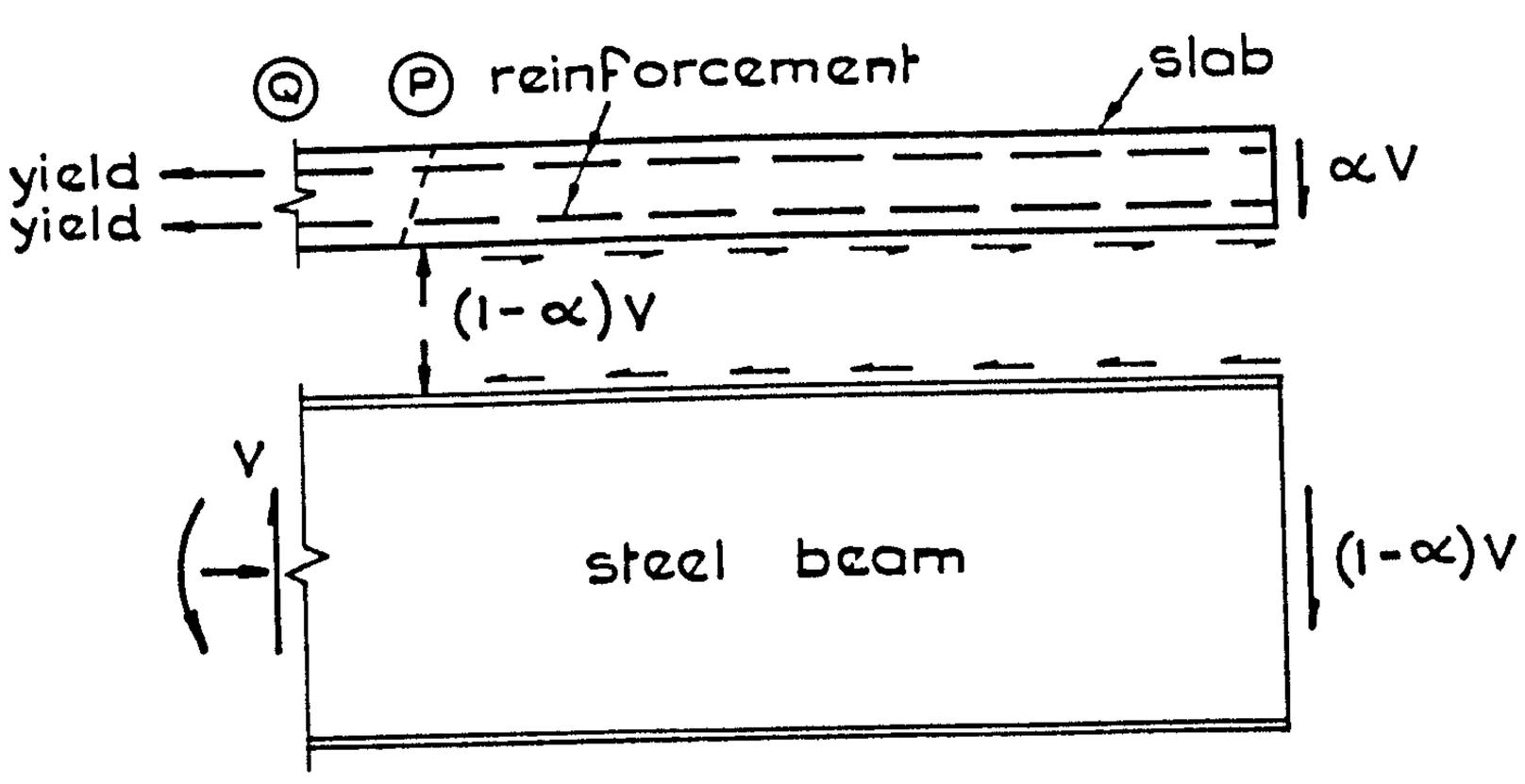

b) Yield in the reinforcement

FIG. 9.3 FORCES IN A COMPOSITE BEAM

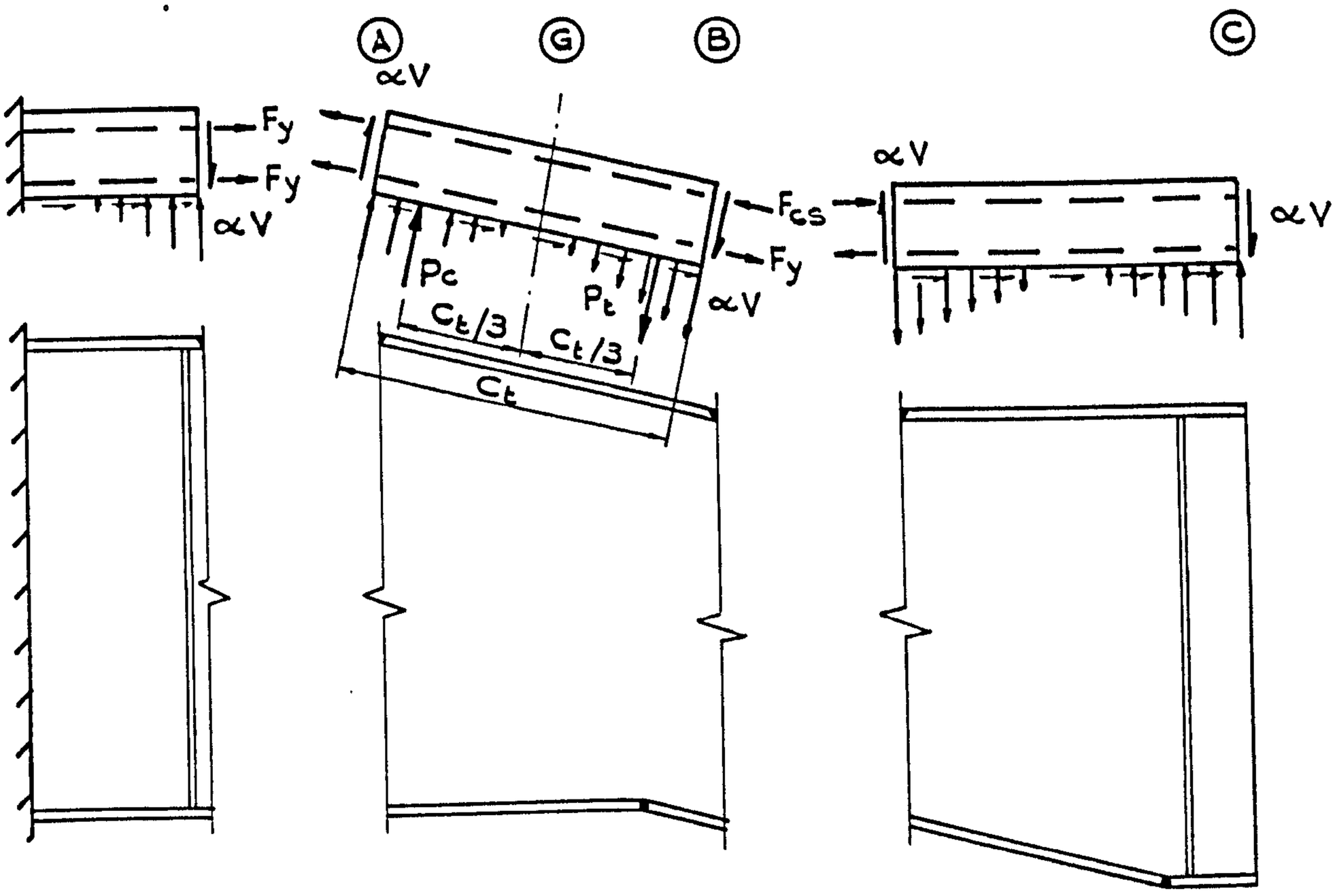

a) As deduced from experimental results

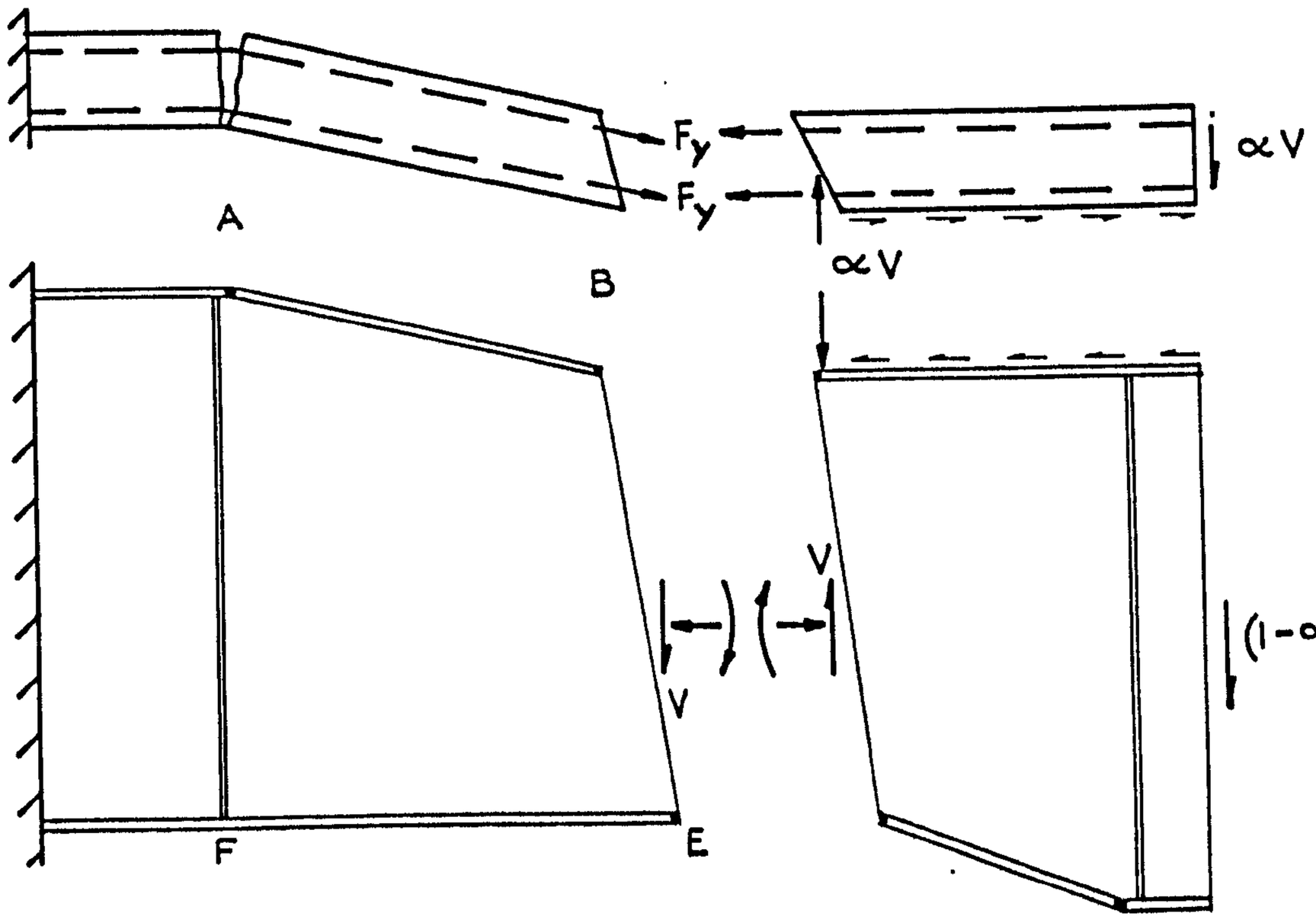

b) As idealised for analysis

FIG. 9.4 FORCES IN COMPOSITE PLATE GIRDER AT COLLAPSE

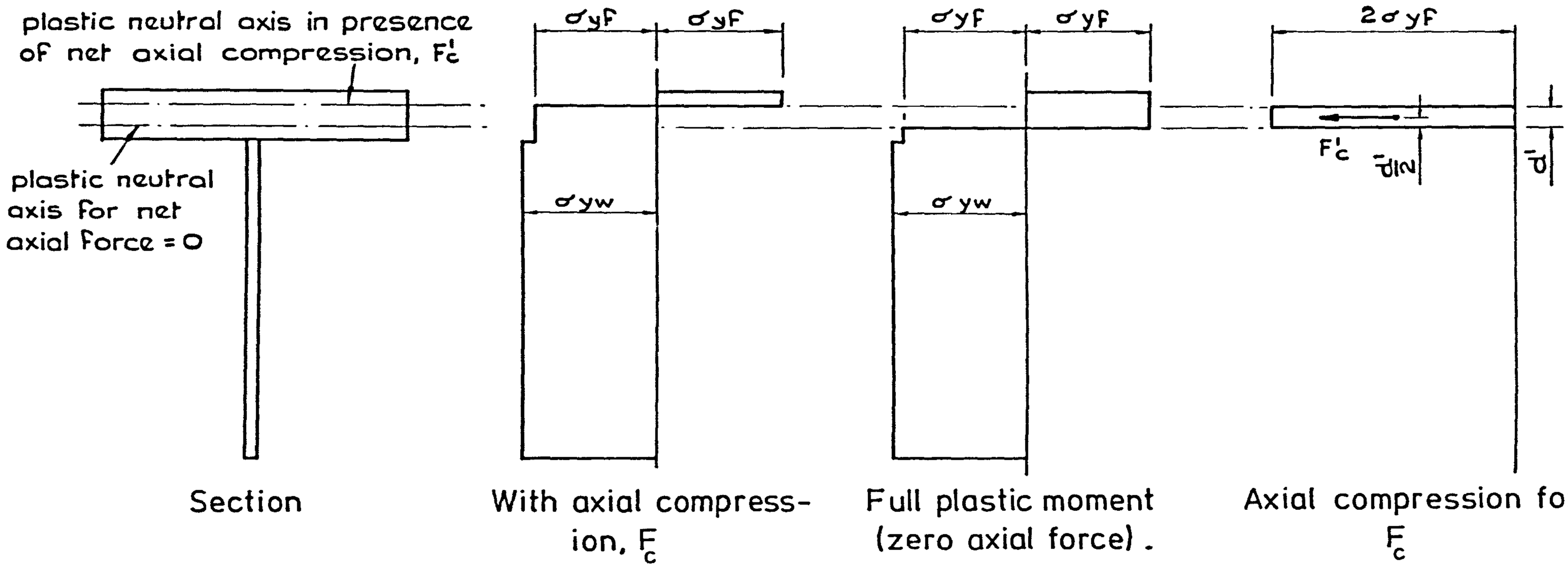

FIG.9.5 STRESSES IN 'T' SECTION AT LOCATION OF PLASTIC HINGE

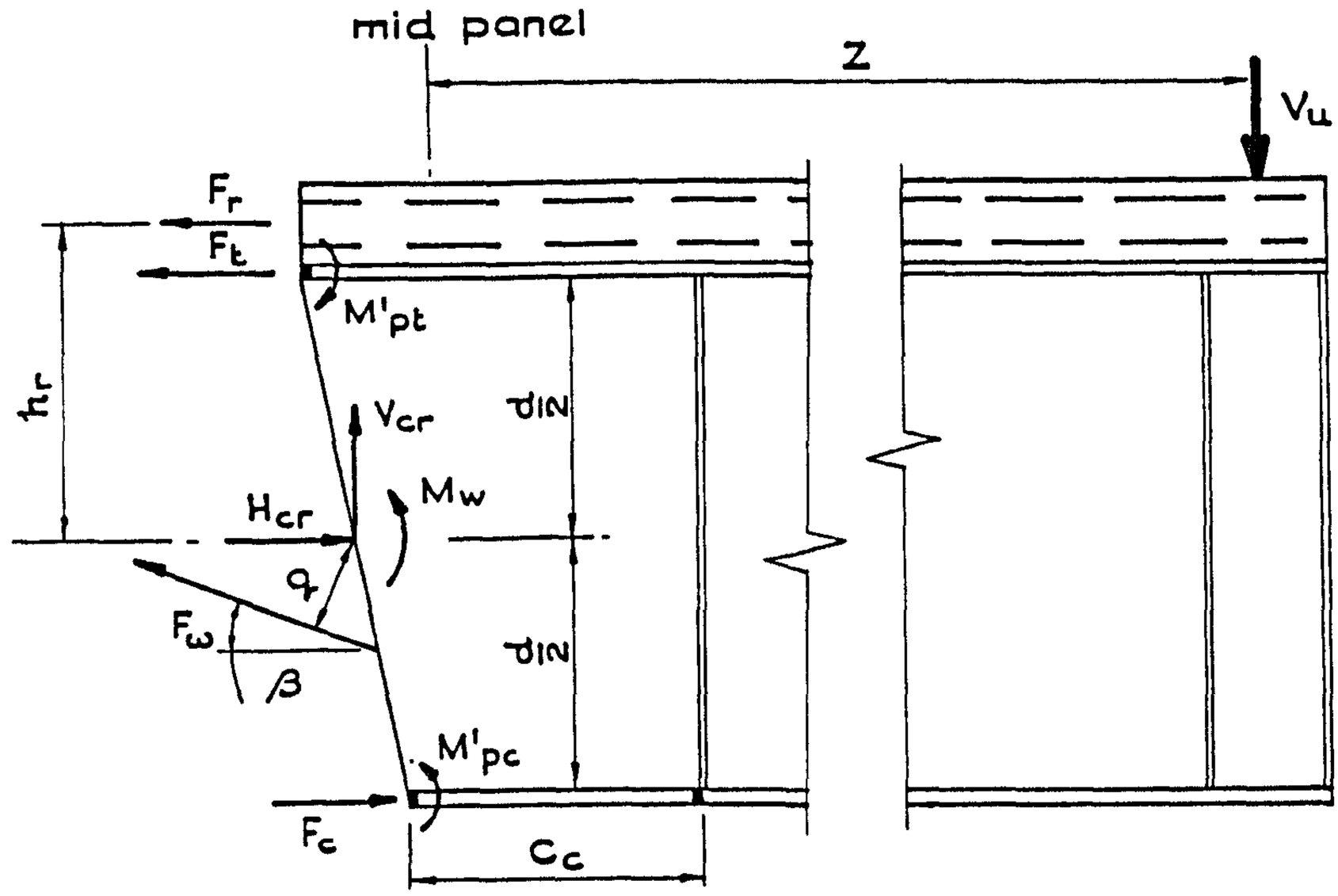

FIG. 9.6 EQUILIBRIUM FORCES IN COMPOSITE PLATE GIRDER AT COLLAPSE

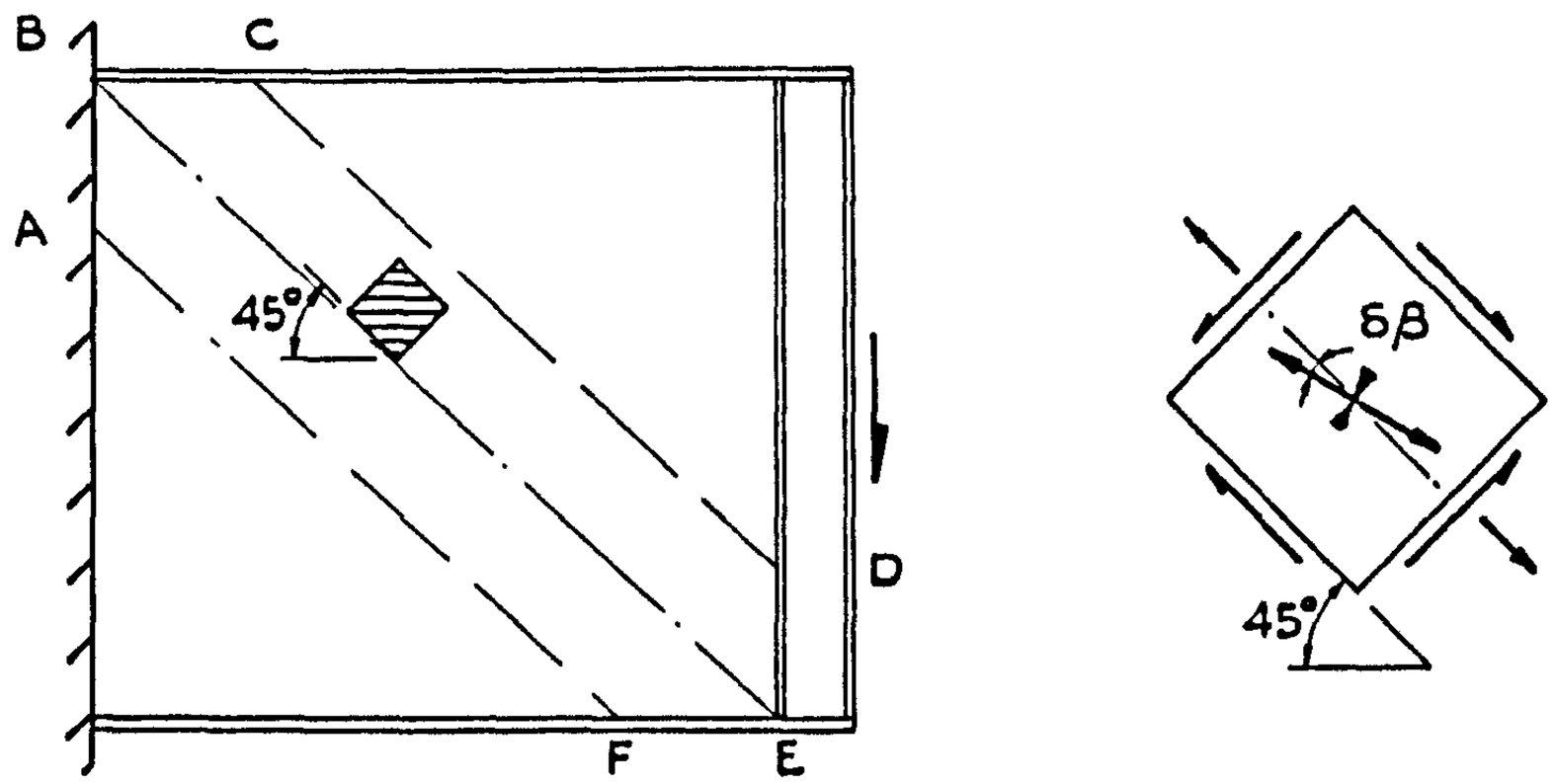

a) Elevation

b) Stresses in element of web

FIG. 9.7 STRESSES IN A BUCKLED WEB

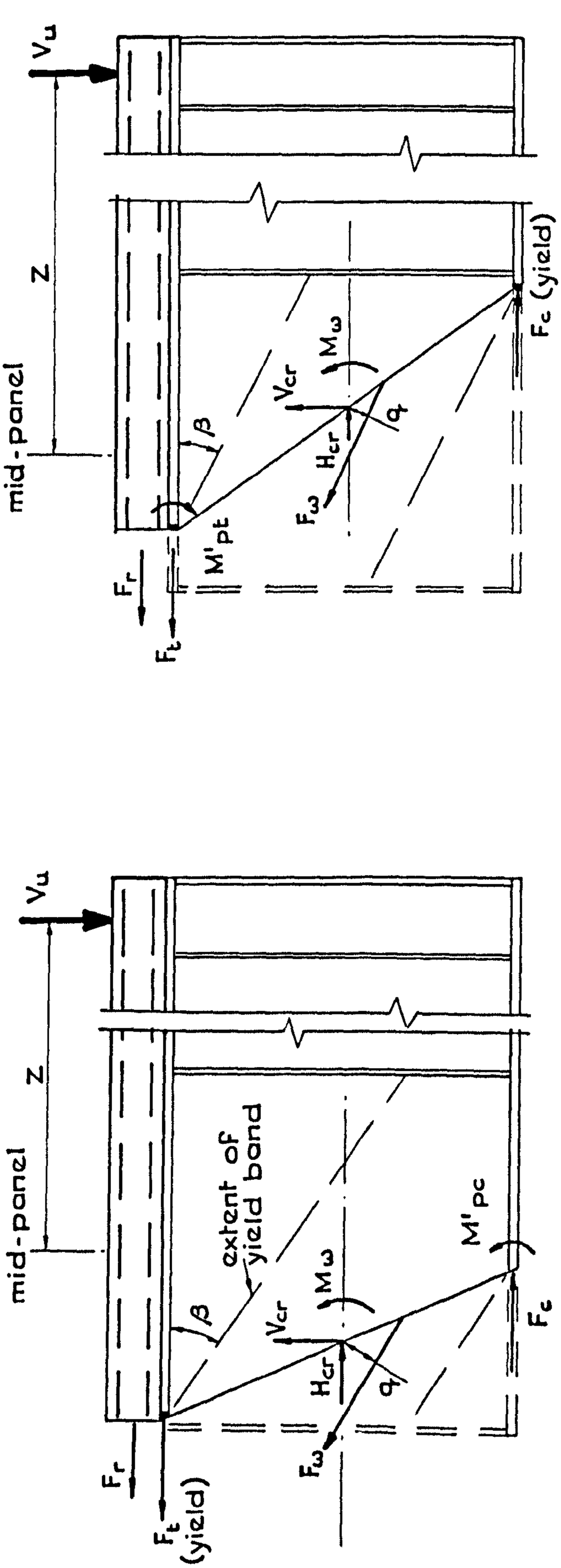

b) Axial yield in compression flange

a) Axial yield in tension flange

FIG. 9.8 COLLAPSE MODE FOR LARGE AXIAL FLANGE FORCES

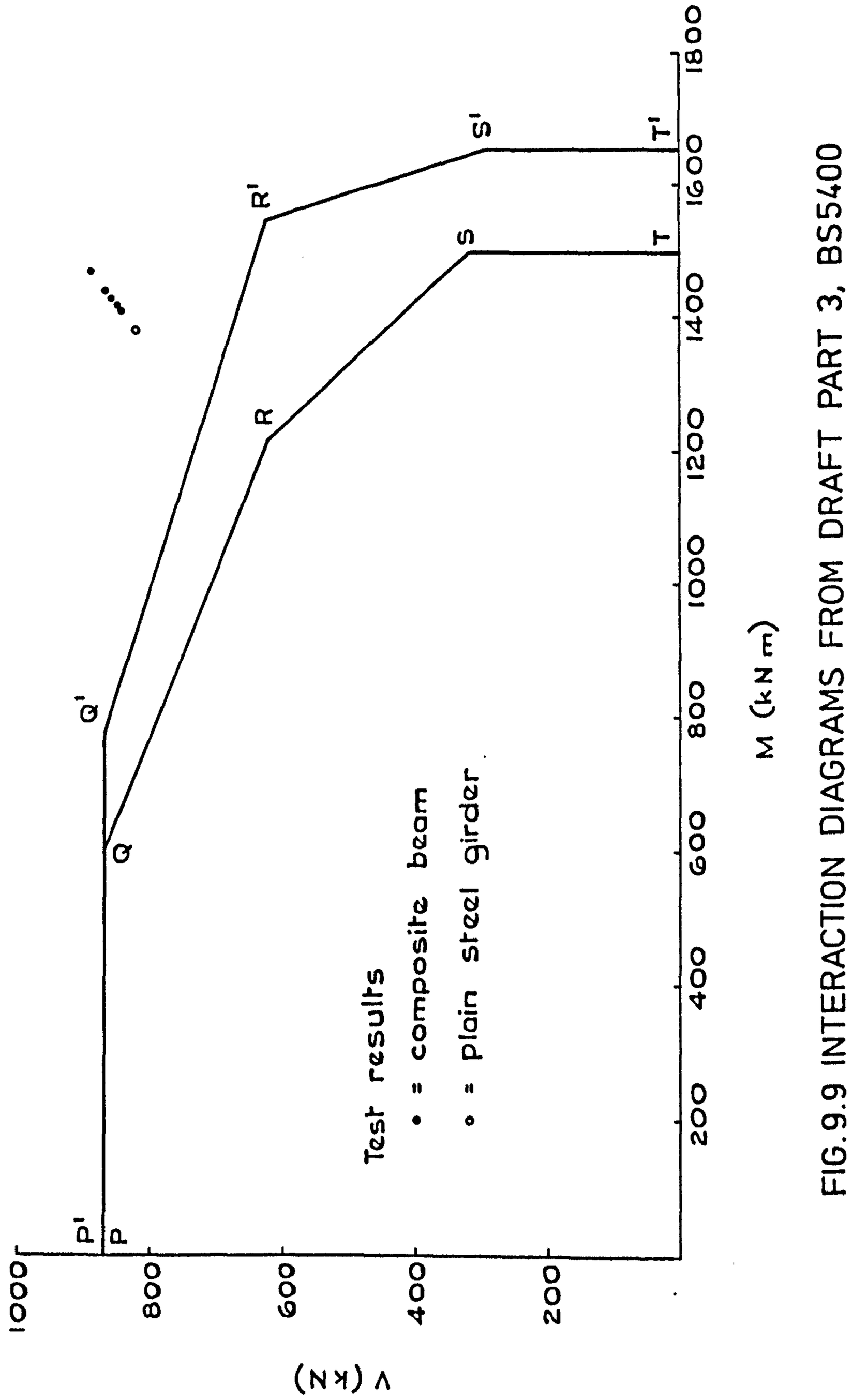

FIG. 9.9 INTERACTION DIAGRAMS FROM DRAFT PART 3, BS5400

CHAPTER 10

CONCLUSIONS OF THE WORK ON TENSION FIELD ACTION

10.1 Experimental observations

Tests have been conducted on five composite and one plain steel plate girders, subjected to a combination of shear and hogging bending. In all cases, failure occurred when the diagonal yield band in the buckled web combined with plastic hinges in the flanges to form a collapse mechanism. It was found that if the applied moment at the ultimate limit state is such that the slab is badly cracked due to flexural action, it does not contribute to the shear strength of the composite beam. It does, however, add to the bending strength, and because it resists some of the force that would otherwise be borne by the steel tension flange, the axial stress in the latter is reduced. This in turn enables the steel flange to withstand greater lateral forces applied by tension field action, and so increases the shear capacity of the steel girder.

The ratio of slab reinforcement was 1% in all the composite beams of the PG series, and data from tests on beams with heavier reinforcement would be useful.

Wide variation in the strength of the shear connection was found to have little effect on the shear capacity of composite beams that fail in a shear-sway mode. However, the strength of the shear connection, based on the full design shear strength of the studs, should be sufficient to develop the yield stress in both top and bottom layers of slab reinforcement in the region of an intermediate support of a continuous beam. The results of Tests PG1 to PG3 also showed that tension field action does not lead to failure of the shear connection and subsequent loss of interaction until deformations are such that, by any reasonable definition, the beam has already failed. It is argued (Section 9.5) that the same

will be true of beams with more slender webs than those of PG1 to PG3.

10.2 Design methods

The following comments on the design of plate girders are made on the understanding that the proportions of the compression flange, and the lateral bracing to it, are such that lateral-torsional buckling is not a problem in girders that fail in a shear-sway mode. It is also assumed that secondary modes of failure, such as fracture of the welds or yielding of the transverse slab reinforcement, are avoided by suitable detailing.

A method for designing composite plate girders of practicable dimensions subjected to high shear ratios has been developed. It is based on an iterative technique which is not particularly suitable for hand analysis, but which is readily programmed on a small desk-top computer. Several phenomena observed in Tests PG1 to PG3 are explained, and the ultimate loads are accurately predicted.

The simplified rules in the 1977 draft of Part 3, BS5400 are such that the ultimate load of asymmetrical plate girders with relatively compact webs is underestimated to an extent that could lead to significant loss of economy. If this error is deemed acceptable however, a sensible interpretation of the terms in the interaction diagram of the draft Part 3 permits the same rules to be applied to composite plate girders.

Unfortunately it has not been possible, in the time available, to develop a simple method of allowing for the increase in the shear capacity of the steel girder afforded by the concrete slab, and further study in this respect would be useful.

REFERENCES

1. CATTLEY, R.F. 'A review of research on the cracking behaviour of reinforced concrete beams and slabs.' Transport and Road Research Laboratory, Supplementary Report SR 47UC, 1974.

2. BIANCHINI, A.C., KESLER, C.E. and LOTT, J.L. 'Cracking of reinforced concrete under external load.' American Concrete Institute, Sp-20, 'Causes, mechanisms and control of cracking in concrete'. Paper 5, pp 73-86. Detroit, 1968.

3. BASE, G.D., READ, J.B., BEEBY, A.W. and TAYLOR, H.P.J. 'An investigation of the crack control characteristics of various types of bar in reinforced concrete beams.' Cement and Concrete Association, Research Report 18, Part 1. London, December 1966.

4. COMITÉ EUROPÉEN DU BÉTON. Proceedings of the Fifth Working Session, Vienna, April 1969. Bulletin d'Information, No.24, June 1970, pp 5.1-5.17.

5. HOGNESTAD, E. 'High strength bars as concrete reinforcement': Part 2 - 'Control of cracking'. Jnl. Portland Cement Association Research and Development Laboratories. Vol.4, January 1962, pp 46-62.

6. KAAR, P.H. and MATTOCK, A.H. 'High strength bars as concrete reinforcement': Part 4 - 'Control of cracking'. Jnl. Portland Cement Association Research and Development Laboratories. Vol.5, January 1963, pp 15-38.

7. BEEBY, A.W. 'The prediction of cracking in reinforced concrete members.' PhD Thesis, University of London, 1971.

8. KAAR, P.H. and HOGNESTAD, E. 'High strength bars as concrete reinforcement': Part 7 - 'Control of cracking in T beam flanges'. Jnl. Portland Cement Association Research and Development Laboratories. Vol.7, January 1965, pp 42-52.

9. KAAR, P.H. 'An approach to the control of cracking in reinforced concrete.' American Concrete Institute, Sp-20, 'Causes, mechanisms and control of cracking in concrete'. Paper 8, pp 141-158. Detroit, 1968.

10. DESAYI, P. 'A method for determining the spacing and width of cracks in partially prestressed concrete beams.' Proceedings of the Institution of Civil Engineers, Part 2. Vol.59, September 1975, pp 411-428.

11. BROMS, B.B. 'Stress distribution in reinforced concrete members with tension cracks.' Jnl.of American Concrete Institute. Vol.62, September 1965, pp 1095-1108.

12. BROMS, B.B. 'Crack width and crack spacing in reinforced concrete members.' Jnl. of American Concrete Institute. Vol.62, October 1965, pp 1237-1256.

13. BROMS, B.B. 'Technique for investigation of internal cracks in reinforced concrete members.' Jnl. of American Concrete Institute. Vol.62, January 1965, pp 35-44.

14. BROMS, B.B. and LUTZ, LeROY, A. 'Effect of arrangement of reinforcement on crack width and spacing in reinforced concrete members.' Jnl. of American Concrete Institute. Vol.62, November 1965, pp 1395-1410.

15. GOTO, Y. 'Cracks formed in concrete around deformed tension bars.' Jnl.of American Concrete Institute. Vol.68, April 1971, pp 244-251.

16. GERGELY, P. and LUTZ, LeROY, A. 'Maximum crack width in reinforced concrete flexural members.' American Concrete Institute, Sp-20, 'Causes, mechanisms and control of cracking in concrete'. Paper 6, pp 87-118. Detroit, 1968.

17. CLARK, A.P. 'Cracking in reinforced concrete flexural members.' Jnl. of American Concrete Institute. Vol.62, April 1965, pp 851-862.

18. RUSCH, H. and REHM, G. 'Versuche mit Betonformstahlen', Deutscher Ausschuss fur Stahlbeton. Bulletins No.140, Part 1, 1963; No.160, Part 2, 1963; and No.165, Part 3, 1964.

19. NAWY, E.G. 'Control of cracking in concrete structures': Chapter 4 - 'Control of flexural cracking in reinforced concrete'. Jnl. of American Concrete Institute. Vol.69, December 1972, pp 728-732.

20. ALBANDAR, F.A-A. and MILLS, G.M. 'The prediction of crack widths in reinforced concrete beams.' Magazine of Concrete Research. Vol.26, September 1974, pp 153-160.

21. BASE, G.D., READ, J.B., BEEBY, A.W. and TAYLOR, H.P.J. 'An investigation of the crack control characteristics of various types of bar in reinforced concrete beams.' Cement and Concrete Association, Research Report 18, Part 2. London, December 1966.

22. BEEBY, A. W. 'An investigation of cracking in slabs spanning one way.' Cement and Concrete Association, Technical Report TRA 433. London, April 1970.

23. CLARK, L.A. 'Crack similitude in 1:3.7 scale models of slabs spanning one way'. Cement and Concrete Association, Technical Report 42.455. London, March 1971.

24. BEEBY, A.W. 'An investigation of cracking on the side faces of beams.' Cement and Concrete Association, Technical Report 42.466. London, December 1971.

25. BEEBY, A.W. 'A study of cracking in reinforced concrete members subject to pure tension.' Cement and Concrete Association, Technical Report 42.465. London, 1970.

26. CLARK, L.A. 'Flexural crack similitude in slabs spanning one way.' Cement and Concrete Association, Technical Report 42.496. London, 1974.

27. FERRY-BORGES, J. 'Cracking and deformability of reinforced concrete beams.' IABSE. Vol.26, 1966, pp 75-95.

28. GARCIA, I., and DANIELS, J.H. 'Tests of composite beams under negative moment.' Lehigh University, Fritz Engineering Laboratory Report No.359.1. February 1971.

29. DANIELS, J.H. and GARCIA, I. 'Negative moment behaviour of composite beams.' Lehigh University, Fritz Engineering Laboratory Report No.359.4. April 1972.

30. ARNAOUTI, C. 'Research into composite bridge decks in biaxial tension.' Progress report No.7. Department of Engineering, University of Warwick. January 1977.

31. ARNAOUTI, C. 'Research into composite bridge decks in biaxial tension.' Progress report No.8. Department of Engineering, University of Warwick. June 1977.

32. JOHNSON, R.P. and ARNAOUTI, C. 'Cracking in composite bridge decks in uniaxial and biaxial tension.' Final report. Department of Engineering, University of Warwick. April 1978.

33. CP110, 'The structural use of concrete'. British Standards Institution, London, 1972.

34. BS5400, 'Steel, concrete and composite bridges': Part 4,'Code of practice for design of concrete bridges', 1978; Part 5, 'Code of practice for design of composite bridges', 1979. British Standards Institution, London.

35. OGUNRONBI, P.O. 'Cracking in negative moment regions of composite beams.' MSc Thesis, University of Warwick, 1975.

36. JOHNSON, R.P. 'Composite structures of steel and concrete.' Volume 1, 'Beams, columns, frames and applications in building'. Crosby Lockwood Staples, London, 1975.

37. BS1881, 'Methods of testing concrete': Part 4, 'Methods of testing concrete for strength': Part 5, 'Methods of testing hardened concrete for other than strength'. British Standards Institution, London,1970.

38. COMITÉ EUROPÉEN DU BÉTON. International recommendations for the design and construction of concrete structures. Vol.1 Principles and recommendations. Cement and Concrete Association, 1970.

39. BEEBY, A.W. 'The prediction of crack widths in hardened concrete.' The Structural Engineer. Vol.57A, January 1979, pp 9-17.

40. JOHNSON, R.P., VAN DALEN, K. and KEMP, A.R. 'The ultimate strength of continuous composite beams.' Proc. Conference on Structural Steelwork, London, 1966. British Constructional Steelwork Association, 1967, pp 27-35.

41. JOHNSON, R.P. and WILLMINGTON, R.T. 'Vertical shear in compact composite beams.' Proceedings of the Institution of Civil Engineers. Vol.53, September 1972, pp 189-205.

42. CLIMENHAGA, J.J. and JOHNSON, R.P. 'Local buckling in continuous composite beams.' The Structural Engineer, Vol.50, September 1972, pp 367-374.

43. HOPE-GILL, M.C. 'The ultimate strength of continuous composite beams.' PhD Thesis, University of Cambridge, 1974.

44. Draft standard for the use of structural steel in buildings. Part 3, Composite Construction. British Standards Institution, August 1976.

45. MAY, I.M. 'Crossed knife-edge joints for testing columns.' Proceedings of the Institution of Civil Engineers, Part 2. Vol.65, December 1978, pp 917-919.

46. Draft standard for steel, concrete and composite bridges. Part 5, The design of composite bridges. British Standards Institution, February 1976.

47. SKALOUD, M. 'Ultimate load and failure mechanism of thin webs in shear.' Proc. Colloquium on Design of Plate and Box Girders for Ultimate Strength. IABSE, London, 1971, pp 115-129.

48. ROCKEY, K.C. 'Factors influencing ultimate behaviour of plate girders.' Proc. Conference on Steel Bridges, London, 1968. British Constructional Steelwork Association, 1969.

49. ROCKEY, K.C. and SKALOUD, M. 'Influence of flange stiffness upon the load carrying capacity of webs in shear.' Final report, Proc. 8th Congress. IABSE, New York, 1968, pp 429-439.

50. ROCKEY, K.C. and SKALOUD, M. 'The ultimate load behaviour of plate girders loaded in shear.' The Structural Engineer. Vol.50, January 1972, pp 29-48.

51. PORTER, D.M., ROCKEY, K.C. and EVANS, H.R. 'The collapse behaviour of plate girders loaded in shear.' The Structural Engineer. Vol.53, August 1975, pp 313-325.

52. LALLY, A. (Chairman) 'Theory and design of longitudinally stiffened plate girders.' Jnl. Structural Division, American Society of Civil Engineers. Vol.104, April 1978, pp 697-716.

53. Introductory report, Second International Colloquium on Stability. European Convention for Constructional Steelwork. 1976, pp 145-208.

54. MACKEY, S. 'Investigation of plate girder behaviour under load.' Supplement, Proc. Institution of Civil Engineers. Paper 7307 (S). 1971.

55. FUJII, T., FUKUMOTO, Y., NISHINO, F. and OKUMARA, T. 'Research works on ultimate strength of plate girders and Japanese provisions on plate girder design.' Proc. Colloquium on Design of Plate and Box Girders for Ultimate Strength.' IABSE, London, 1971, pp 21-48.

56. BASLER, K. 'Strength of plate girders in shear.' Jnl. Structural Division, American Society of Civil Engineers, Part 1. Vol 87, October 1961, pp 151-180.

57. CHERN, C. and OSTAPENKO, A. 'Ultimate strength of plate girders under shear.' Lehigh University, Fritz Engineering Laboratory Report No.328.7. August 1969.

58. CALLADINE, C.R. 'A plastic theory for collapse of plate girders under combined shearing force and bending moment.' The Structural Engineer. Vol.51, April 1973, pp 147-154.

59. BASLER, K. and THURLIMANN, B. 'Strength of plate girders in bending.' Jnl. Structural Division, American Society of Civil Engineers. Vol.87, August 1961, pp 153-181.

60. COOPER, P.B. 'The ultimate bending moment for plate girders.' Proc. Colloquium on Design of Plate and Box Girders for Ultimate Strength. IABSE, London, 1971, pp 291-297.

61. BASLER, K. 'Strength of plate girders in combined bending and shear.' Jnl. Structural Division, American Society of Civil Engineers. Vol.87, October 1961, pp 181-197.

62. EVANS, H.R., PORTER, D.M. and ROCKEY, K.C. 'The collapse behaviour of plate girders subjected to shear and bending.' University of Wales, University College, Cardiff, 1975.

63. EVANS, H.R., PORTER, D.M. and ROCKEY, K.C. 'A parametric study of the ultimate load characteristics of plate girders.' University of Wales, University College, Cardiff, 1976.

64. ROCKEY, K.C., EVANS, H.R. and PORTER, D.M. 'A design method for predicting the collapse behaviour of plate girders.' University of Wales, University College, Cardiff, 1976.

65. WILLMINGTON, R.T. 'Vertical shear in composite beams.' PhD Thesis, University of Cambridge, 1969.

66. KREFELD, W.J. and THURSTON, C.W. 'Contribution of longitudinal steel to shear resistance of reinforced concrete beams.' Jnl. American Concrete Institute. Vol.63, March 1966, pp 325-344.

67. FENWICK, R.C. and PAULAY, T. 'Mechanisms of shear resistance of concrete beams.' Jnl. Structural Division, American Society of Civil Engineers. Vol.94, October 1968, pp 2325-2350.

68. TAYLOR, H.P.J. 'The fundamental behaviour of reinforced concrete beams in bending and shear.' Cement and Concrete Association. Paper for publication, PP/113, December 1972.

69. Draft standard for steel, concrete and composite bridges. Part 3, The design of steel bridges. British Standards Institution, 1977.

70. HORNE, M.R., OGLE, M.H. and DOWLING, P.J. Report on plated steel structures for the B/116/3 Steering Committee of the British Standards Institution, 1976.

71. COOPER, P.B., LEW, H.S. and YEN, B.T. 'Welded constructional alloy plate girders.' Jnl. Structural Division, American Society of Civil Engineers. Vol.90, February 1964, pp 1-36.

72. ARNAOUTI, C. Results of tests conducted at the University of Warwick, communicated personally to the author, 1978.